NUCLEAR ENERGY RESEARCH INITIATIVE

U.S. Department of Energy – Nuclear Energy Research Initiative
Award No. DE-FC07-05ID14656
Project No. 05-066

Development of an Engineered Product Storage Concept for the UREX+1 Combined Transuranic/Lanthanide Product Streams

Final Technical Report

March 1, 2009

Contact: Dr. Sean M. McDeavitt
Department of Nuclear Engineering
Look College of Engineering
Texas A&M University
3133 TAMU
College Station, TX 77843-3133
(979) 862–1745 (Phone) (979) 845–6443 (FAX)
mcdeavitt@tamu.edu

Collaborating Principal Investigators:

Prof. Thomas J. Downar, Univ. of Michigan, Ann Arbor, MI
Dr. Temitope A. Taiwo, Argonne National Laboratory, Argonne, IL
Dr. Mark A. Williamson, Argonne National Laboratory, Argonne, IL

Overview

The U.S. Department of Energy is developing next generation processing methods to recycle uranium and transuranic (TRU) isotopes from spent nuclear fuel. The objective of the 3-year project described in this report was to develop near-term options for storing TRU oxides isolated through the uranium extraction (UREX+) process. More specifically, a Zircaloy matrix cermet was developed as a storage form for transuranics with the understanding that the cermet also has the ability to serve as an inert matrix fuel form for TRU burning after intermediate storage. The goals of this research projects were: 1) to develop the processing steps required to transform the effluent TRU nitrate solutions and the spent Zircaloy cladding into a zirconium matrix cermet storage form; and 2) to evaluate the impact of phenomena that govern durability of the storage form, material processing, and TRU utilization in fast reactor fuel. This report represents a compilation of the results generated under this program. The information is presented as a brief technical narrative in the following sections with appended papers, presentations and academic theses to provide a detailed review of the project's accomplishments.

1.0 Introduction

This report describes results from a 2005 Nuclear Energy Research Initiative (NERI) project funded by the U.S. Department of Energy. ***Appendices A and B*** present an overview paper and accompanying presentation describing the project in more detail. The mission was to develop a storage form to secure extracted TRUs in a proliferation resistant state until a TRU-burning fast reactor infrastructure is in place. More specifically, the project was created to accomplish the following objectives.

1) Design and develop the individual processing steps required to transform reprocessing streams into a cermet storage form. This included nitrate solution conversion, Zircaloy cladding conversion, and form fabrication by hot extrusion

2) Evaluate the impact of phenomena that govern storage form durability, material processing, and eventual TRU utilization in fast reactor fuel. This included *calculations* to estimate the TRU burning performance in a reactor and the impact of helium and heat generation.

The proposed storage/fuel form is a zirconium matrix cermet is. Processing methods were designed to convert TRU bearing solutions from Uranium Extraction (UREX+) method and spent Zircaloy cladding into feed powders for the hot extrusion of cermet pins. The UREX+ reprocessing methods incorporate sequential aqueous solvent extraction schemes with optional ion exchange methods to separate uranium, selected fission products, and TRU elements from dissolved spent nuclear fuel. Figure 1 shows a high level flow diagram with three sequential steps named UREX, Cs/Sr Recovery, and TRU Recovery. The UREX process is a solvent extraction method that removes high purity uranium and technetium from the dissolved SNF using Tributyl Phosphate (TBP) in an organic solvent. The complexities of the UREX flowsheet are still under development and are not germane to this report, except to note the general flow of SNF materials through the UREX+ system and to highlight the Zircaloy and TRU source streams for this project.

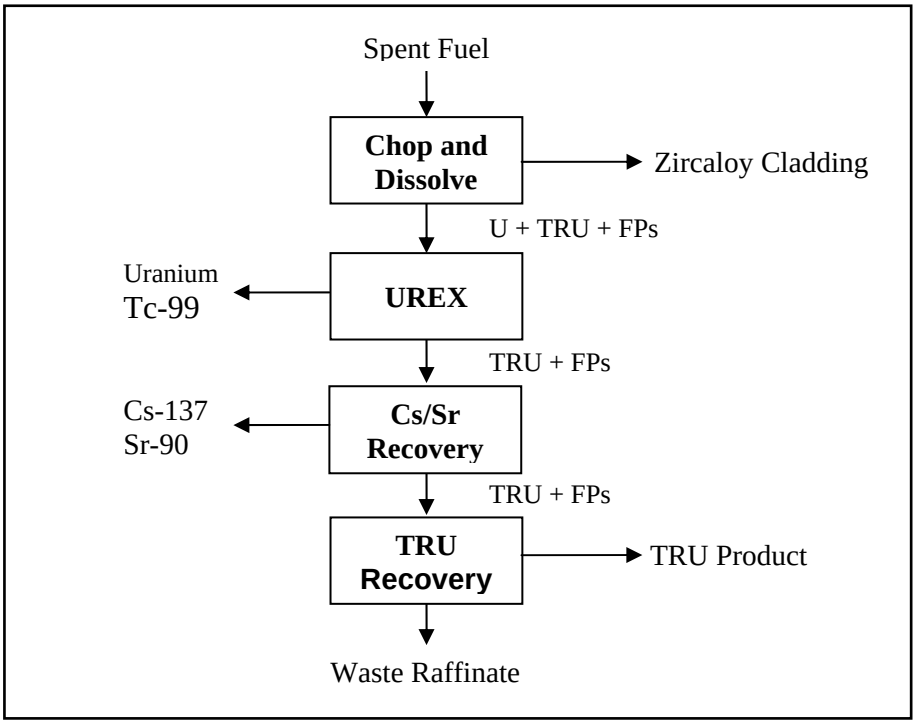

Figure 1. High-level process flow diagram for the AFCI aqueous separations plan.

As noted in Fig. 1, a significant amount of Zircaloy cladding is removed and prepared for waste disposal after the chop and dissolve step; a typical PWR fuel assembly contains ~115 kg of Zircaloy. At the other end of the process, a relatively small volume of TRU bearing solution is recovered from the fuel; the same hypothetical fuel assembly contains 5 to 10 kg of TRU. Therefore, there is an abundance of Zircaloy waste in the process and the Zircaloy recycle process does not need to be 100% efficient.

2.0 TRU Conversion Process Concept

The TRU conversion process was designed to follow the pattern of UO_2 microsphere production by the internal gelation (or sol-gel) method used for TRISO fuel kernel fabrication. For UO_2 production, a broth solution is prepared containing uranyl nitrate ($UO_2(NO_{3)2}$), HMTA ($(CH_2)_6N_4$), and urea ($(NH_2)_2CO$) to form low temperature (0ºC) precursors such as $UO_2(NO_3)_2$*$2(NH_2)_2CO$. This solution is inserted into warm (90ºC) silicone oil as spherical droplets to induce a sequence of self-consuming reactions that break up the complexes, consume the reaction products and gel into product microspheres of ammonium diuranate ($(NH_4)_2U_3O_7$) which are then fired to form and sinter into UO_2 microspheres.

The process studied here used cerium nitrate solutions to examine the gelation of cerium oxide as a surrogate for plutonium with the intent to continue this development using uranium and cerium nitrates to investigate the gelation of mixed oxides.. The primary questions are related to the relative stability of the complexes that form in the broth and how efficient the system is at forming mixed oxide precursors. The ultimate goal is to define the chemistry required to form (U,Ce)O2 ceramic microspheres, but the progress reported here only extends to the gelation of cerium oxide microspheres. Figure 2 shows a photo of cerium oxide microspheres produced in the sol-gel system built for this project.

Appendix C (Master's Thesis) and ***Appendix D*** (Thesis Defense Presentation) provide the detailed descriptions of the cerium oxide gelation project.

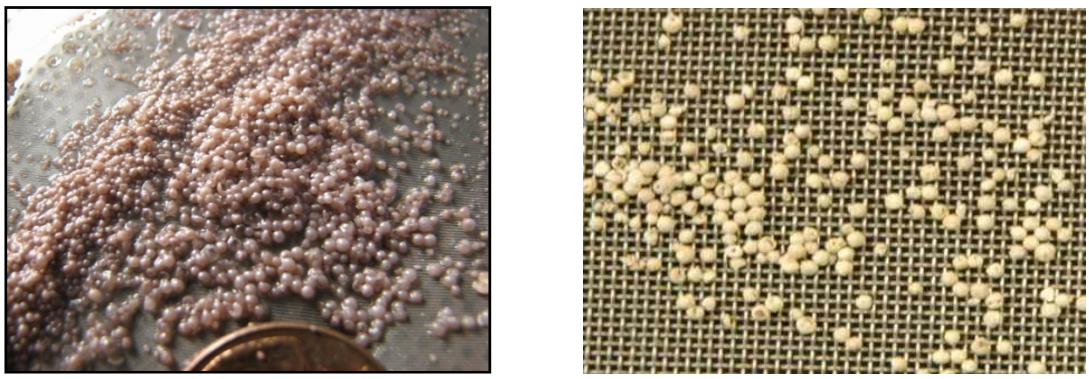

Figure 2. Example of cerium oxide microspheres fabricated via internal gelation.

3.0 Zircaloy Recovery Process

The Zircaloy recycle process is based on existing technology applied in a new way. The underlying principle is that Zr reacts with H_2 to form ZrH_2 according to the formation reaction

$$Zr + H_2 \rightarrow ZrH_2. \quad (1)$$

This is the same reaction that produces performance limiting ZrH_2 formations in reactor cladding. During reactor service, this embrittlement is considered negative. In the present application, this is the enabling phenomenon since the design is to completely embrittle the Zircaloy for milling. Once the alloy is pulverized into powder, the reaction in Eq. 1 may be reversed by raising the temperature to ~900ºC and reducing the ambient pressure to dehydride the ZrH_2 to metallic Zr.

Appendices E and F present a Master of Engineering project report and a Master of Science thesis describing the development of the hydriding process variables. ***Appendix G*** presents a data review prepared by Argonne National Laboratory summarizing the basic thermophysical properties of zirconium hydride and zirconium metal that are relevant to this project. These projects led to the establishment of a bench scale engineering system that is being established as a PhD project (not completed at the time of this report; continued funding from internal sources) that combines hydriding, milling, and dehydriding to produce fine zirconium

powder. When completed, the published results will acknowledge this NERI program as laying the foundation for this work.

4.0 Hot Extrusion Process

The hot extrusion process for Zr matrix cermets builds on experience gained during the development of a similar cermet system for the thorium fuel cycle. Figure 2 shows the microstructure of a representative Zr matrix cermet from an early experiment. The basic procedure for cermet production involves:

1. Combining fine Zr metal powder (-325 mesh) with the oxide microspheres (lab development with 100-400 μm ZrO_2-SiO_2 spheres) into copper billet holder,
2. Pre-heating the billet to ~900°C (above the α to β Zr transition temperature),
3. Pre-heating the extrusion die to ~600°C (T_{max} for die strength),
4. Inserting hot billet into hot die in 100-ton extrusion press and increasing pressure to extrude sample pin.

Appendices H, I, and J present the Master of Science thesis, a paper summary, and the accompanying presentation detailing the results of this research. A PhD thesis was begun under this project and is being completed under a different funding source, but ***Appendices K and L*** provide details on the work being performed there. This work is beyond the scope of the original proposal (value-added activity) but, as above, the published results from this continued research will acknowledge this NERI program as laying the foundation for this new work.

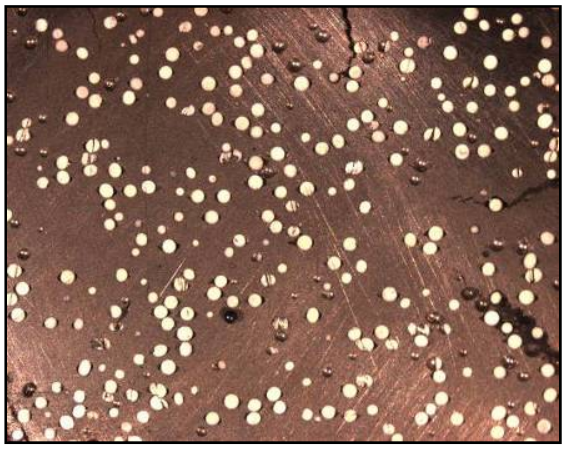

Figure 3. Sample of Zr-matrix cermet fabricated using ~400μm ZrO_2-SiO_2 micrispheres.

5.0 Computational Simulations of Nuclear Systems

Regarding the second major goal of this project (i.e., TRU utilization in a fast reactor), multiple neutronic and Zr/TRU cermet fuel parameters were calculated following the same protocols used in the development of a U-TRU metal fueled core. Input and computational databases were provided by Argonne National Laboratory for this work. These calculations were completed side-by-side with the development of a Monte Carlo depletion method for fast reactors using U?TRU metal fuels. ***Appendix M*** contains some startup data and initial criticality calculations related to the TRU cermet. ***Appendices N and O*** contain a paper summary and accompanying presentation materials describing the development of the Monte Carlo depletion method. ***Appendix P*** is the final Master of Science thesis describing the Monte Carlo depletion method including the reactor simulations for TRU burning and the comparison of the cermet fuel pin to U/TRU metal fuel.

6.0 Final Comments

As with any research program, there were objectives that were met and objectives that were missed. The objectives that were met include the following:

1. The cerium oxide gelation conditions have been well defined.
2. The Zircaloy hydride process has been well defined and the extension to a hydride-dehydride system is underway.
3. The hot extrusion system has been established and has been used to fabricate Zr-matrix cermet pins.
4. Nuclear simulations were completed indicating that this fuel form would succeed as a TRU burner.

The objectives that were not met include the following:

1. The oxide gelation development was not extended into mixed oxide gelation.
2. The all-in-one Zircaloy hydride-dehydride system is still under development, but is expected to be completed in 2009.
3. The impact of oxide fuel sphere interaction with the zirconium matrix was not investigated.

The reasons behind not meeting these objectives are common to many research programs: personnel changes and unexpected research opportunities. Personnel changes at Argonne National Laboratory caused the investigation of the internal gelation method to be carried out at Texas A&M University, diverting resources from the oxide-matrix interaction studies. In addition, the work required to develop, design and construct the hydride-dehydride system (still under development at this time) was underestimated in the original proposal. Even so, the Zircaloy recovery process research produced two Masters degrees and a PhD degree is still in progress.

Finally, this project has contributed to two "value-added" research activities that were not part of the original proposal:

1. Fuel performance data generation via ion bombardment of Zr cermet fuels (***Appendices K and L***), and
2. The Monte Carlo method development for TRU burning (***Appendices N, O, and P***).

Index of Appendices

Appendix A

Overview Paper of Process Development Scope (4 Pages)

S.M. McDeavitt, A. Parkison, A.R. Totemeier and J.J. Wegener "Fabrication of Cermet Nuclear Fuels Designed for the Transmutation of Transuranic Isotopes," Materials Science Forum, 561-565: 1733-1736 (2007).

Fabrication of Cermet Nuclear Fuels Designed for the Transmutation of Transuranic Isotopes

S. M. McDeavitt[a], A. Parkison, A.R. Totemeier and J.J. Wegener

Dept. of Nuclear Engineering, Texas A&M University,
3133 TAMU, College Station, TX 77843, USA

[a]mcdeavitt@tamu.edu

Keywords: Nuclear Fuel, Metal Matrix Composites, Material Fabrication Processes

Abstract. The Uranium Extraction (UREX) family of processes uses solvent extraction techniques designed to partition spent uranium and transuranic (TRU) isotopes from fission product waste. Once separated, the collective TRU elements (Np, Pu, Am, and Cm) can be recycled in advanced nuclear energy systems. A zirconium matrix cermet is proposed as a fuel form for this application. Processing methods have been designed to convert the TRU product and spent Zircaloy cladding into feed materials for the hot extrusion of the cermet fuel pins. The TRU conversion process is being developed using a surrogate mixture of uranium and cerium nitrate solutions to generate mixed oxide microspheres. The Zircaloy recovery process is a hydride-dehydride method that is being demonstrated at the bench scale. The powder products from these methods may be combined through hot extrusion into a cermet composite; demonstration experiments using zirconium powder and zirconia microspheres have been completed.

Introduction

The U.S. Department of Energy is developing next generation processing methods under the Advanced Fuel Cycle Initiative (AFCI) for the recycling of transuranic (TRU) oxides from spent nuclear fuel [1]. These methods are expected to be phased into existence over the next 20 to 40 years as the next generation nuclear energy systems are implemented. The TRU components of spent fuel have long half lives, significant fission energy content, and nuclear fission cross sections that make them fit for burnup (i.e., destruction) in a fast-spectrum nuclear reactor. The Uranium Extraction (UREX) family of processes uses solvent extraction techniques to partition spent uranium and transuranic (TRU) isotopes from fission product waste. Once separated, the collective TRU elements (Np, Pu, Am, and Cm) can be recycled in advanced nuclear energy systems.

This paper describes results from a 2005 Nuclear Energy Research Initiative (NERI) project funded by the U.S. Department of Energy that is developing processing methods to convert the TRU bearing solution into an acceptable mixed oxide form for short-term storage. The goal of the storage form is to secure the extracted TRUs in a proliferation resistant state until a TRU-burning fast reactor infrastructure is in place. Nominal projections for advanced reactor deployments are on the order of 20 to 30 years, so the required TRU storage form "lifetime" may be nominally stated to be 50 to 60 years.

A zirconium matrix cermet is proposed as a fuel form for this application. Processing methods have been designed to convert the TRU bearing solution and spent Zircaloy cladding into feed powders for the hot extrusion of cermet pins. The TRU conversion development is still incomplete so this paper will present the basis for that method and then highlight results from the Zircaloy recovery and hot extrusion experiments. This research is supported by the U.S. Department of energy through the Nuclear Energy Research Initiative.

Context with the UREX+ Process

The UREX+ reprocessing methods incorporate sequential aqueous solvent extraction schemes with optional ion exchange methods to separate uranium, selected fission products, and TRU elements from dissolved spent nuclear fuel. Figure 1 shows a high level flow diagram with three sequential steps named UREX, Cs/Sr Recovery, and TRU Recovery. The UREX process is a solvent extraction method that removes high purity uranium and technetium from the dissolved SNF using Tributyl Phosphate (TBP) in an organic solvent. The complexities of the UREX flowsheet are still under development and are not germane to this paper, except to note the general flow of SNF materials through the UREX+ system and to highlight the Zircaloy and TRU source streams for this project.

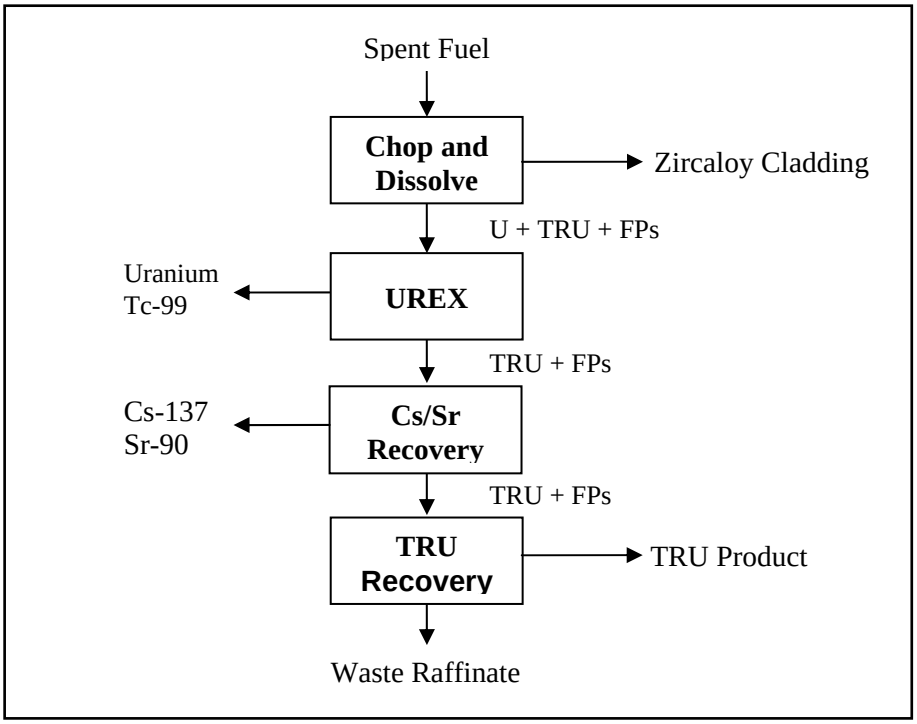

Figure 1. High-level process flow diagram for the AFCI aqueous separations plan.

As noted in Fig. 1, a significant amount of Zircaloy cladding is removed and cleaned for waste disposal after the chop and dissolve step; a typical PWR fuel assembly contains ~115 kg of Zircaloy. At the other end of the process, a relatively small volume of TRU bearing solution is recovered from the fuel; the same hypothetical fuel assembly contains 5 to 10 kg of TRU. Therefore, there is an abundance of Zircaloy waste in the process and the Zircaloy recycle process does not need to be 100% efficient.

TRU Conversion Process Concept

The TRU conversion process is designed to follow the pattern of UO_2 microsphere production by the internal gelation (or sol-gel) method used for TRISO fuel kernel fabrication [1]. For UO_2 production, a broth solution is prepared containing uranyl nitrate ($UO_2(NO_3)_2$), HMTA ($(CH_2)_6N_4$), and urea ($(NH_2)_2CO$) to form low temperature (0ºC) precursors such as $UO_2(NO_3)_2$*2$(NH2)_2CO$. This solution is inserted into warm (90ºC) silicone oil as spherical droplets to induce a sequence of self-consuming reactions that break up the complexes, consume the reaction products and gel into product microspheres of ammonium diuranate ($(NH_4)_2U_3O_7$) which are then fired to form and sinter into UO_2 microspheres.

The process being studied here is using mixed uranyl nitrate and cerium nitrate solutions to examine the co-gelation of mixed oxides an analog to this process. The primary questions are

related to the relative stability of the complexes that form in the broth and how efficient the system is at forming mixed oxide precursors. The ultimate goal is to define the chemistry required to form $(U,Ce)O_2$ ceramic microspheres.

Zircaloy Recovery Process

The Zircaloy recycle process is based on existing technology [2] applied in a new way. The underlying principle is that Zr reacts with H_2 to form ZrH_2 according to the formation reaction

$$Zr + H_2 \rightarrow ZrH_2. \quad (1)$$

The Gibbs Free Energy for this reaction (ΔG_f) ranges from -92.8 at 300ºC to -36.5 kJ/mole at 700ºC at 1 atm pressure. This is the same reaction that produces performance limiting ZrH_2 formations in reactor cladding. During reactor service, this embrittlement is considered negative. In the present application, this is the enabling phenomenon since the design is to completely embrittle the Zircaloy for milling. Once the alloy is pulverized into powder, the reaction in Eq. 1 may be reversed by raising the temperature to ~900ºC and reducing the ambient pressure to dehydride the ZrH_2 to metallic Zr.

Figure 2 shows the experimental setup used to evaluate process variables in the hydride process and Fig. 3 shows example products. Clean Zircaloy tubes are heated to various temperatures under flowing Ar-5%H_2. The typical result is a brittle collection of ZrH_2 shards (Fig. 2a) that are readily crushed into powder (Fig. 2b). The primary observations from the experimental results is that processing at temperatures far above the α-β-δ eutectoid (~540ºC on the Zr-H binary diagram) is not efficient for powder production because the body-centered cubic β-Zr(H) phase has a high solubility for hydrogen and is not brittle. The optimal hydriding temperature is just above or just below the α-β-δ eutectoid temperature. Processing in this range produces the shards in Fig. 2a and the material becomes brittle and millable well before 100% hydride formation.

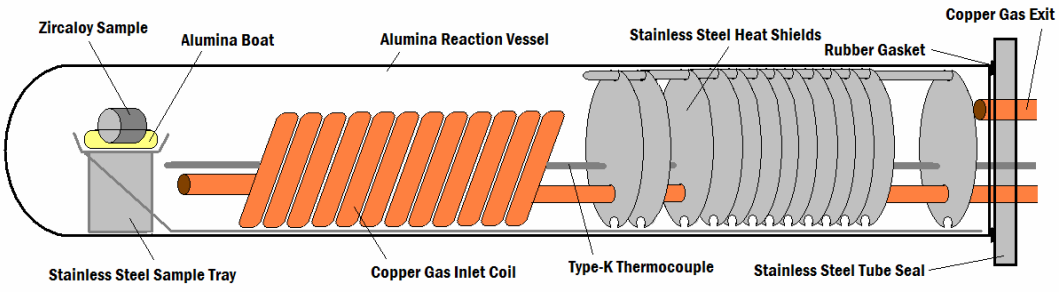

Figure 1. Schematic diagram of the process development experiment system designed to convert Zircaloy tube samples into zirconium hydride.

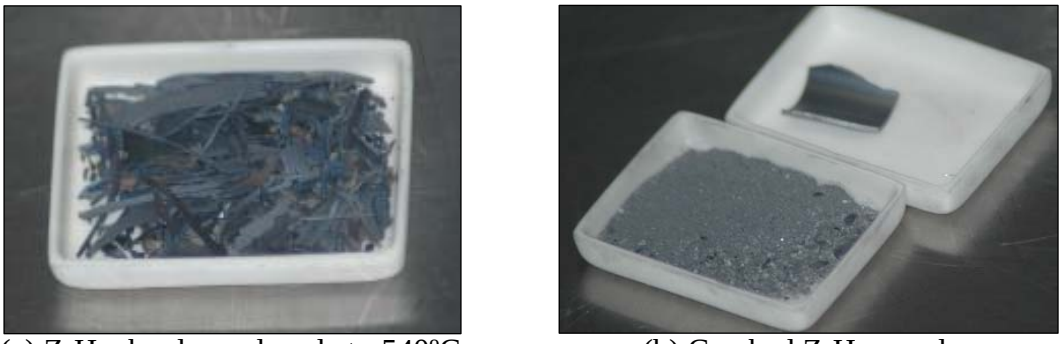

(a) ZrH_2 shards produced at ~540ºC (b) Crushed ZrH_2 powder

Figure 2. Photographs of hydrided Zircaloy tubes after processing (3 cm by 2 cm ceramic boat).

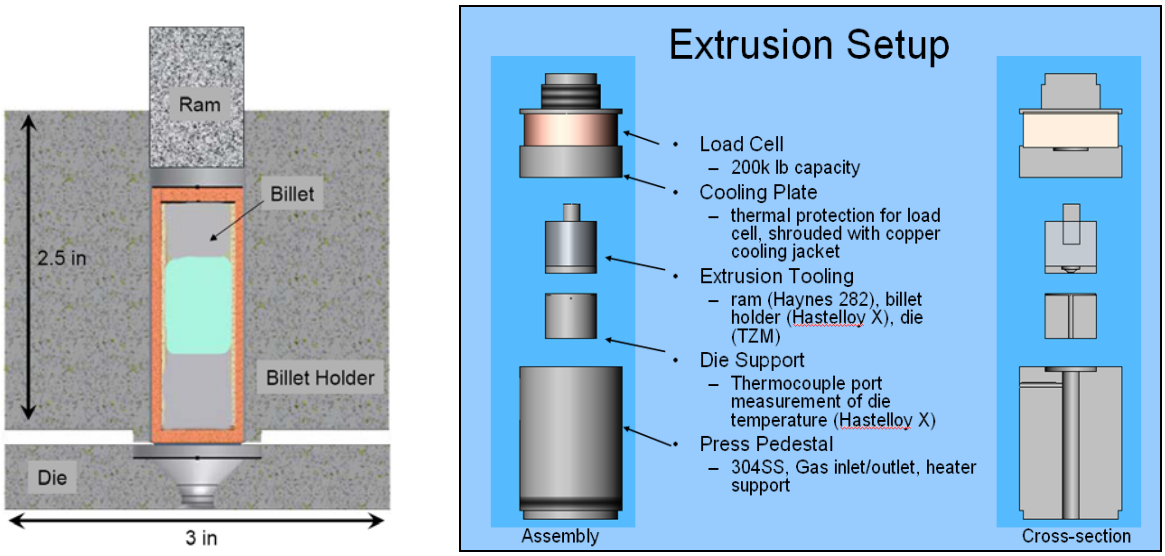

Figure 4. Schematics of the hot extrusion experiment setup to produce Zr-matrix cermet pins.

Hot Extrusion Process

The hot extrusion process for Zr matrix cermets builds on experience gained during the development of a similar cermet system for the thorium fuel cycle [3]. The experimental setup is presented schematically in Figure 4 showing a blowout of the extrusion die and an expanded view of the entire assembly. Initial experiments were performed using zirconium powder and yttria-stabilized zirconia microspheres to develop processing parameters. Powders were mixed in a controlled atmosphere glovebox and pressed into the extrusion die. Figure 5 shows the microstructure of a representative product.

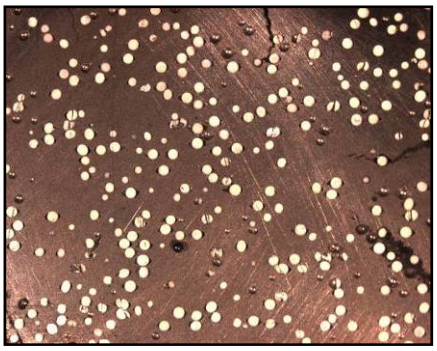

Figure 5. Sample of Zr-matrix cermet fabricated using ~400m zirconia micrispheres.

Experiments with copper containers were completed using a hydraulic press with low die temperatures of ~600ºC, but the particle damage rate was too high. The new extrusion system in Fig. 4 is designed for the bare extrusion of cermet pins at 900ºC. This modification will reduce the damage evident in the cermet microspheres (Fig. 5) by processing the cermet using the malleable β-Zr (cubic structure) instead of the rigid α-Zr (hexagonal structure).

Acknowledgements

The authors wish to acknowledge D.T. Kraemer, R.D. Kelley, P.M. Mews and E.C. Howell for their contributions to this research as well as P. Manning and S. Mathews of Haynes International for providing lab-scale samples of Haynes alloy 282 and Hastelloy X. This research is supported by the US Department of Energy under NERI Award No. DE-FC07-05ID14656.

References

[1] Rodney D. Hunt and Jack L. Collins, “Uranium kernel formation via internal gelation,” Radiochim. Acta Vol.92 (2004) pp.909–915.

[2] R.A. Hard and J.A. Megy, “Process for making titanium, zirconium and hafnium-based metal particles for powder metallurgy,” U.S. Patent 4,470,847 (1984).

[3] S.M. McDeavitt, Y. Xu, T.J. Downar and A.A. Solomon: “Zirconium Matrix Cermet for a Mixed Uranium-Thorium Oxide Fuel in a SBWR,” Nucl. Tech. Vol. 157(1) (2007), pp.37-52.

Appendix B

Overview Presentation of Process Development Scope (15 Pages)

S.M. McDeavitt, A. Parkison, A.R. Totemeier and J.J. Wegener "Fabrication of Cermet Nuclear Fuels Designed for the Transmutation of Transuranic Isotopes," Presented the 6th Pacific Rim International Conference on Advanced Materials and Processing (PRICM-6), Jeju Island, Korea, November 5-9 (2007).

Fabrication of Cermet Nuclear Fuels Designed for the Transmutation of Transuranic Isotopes

Presented at
The Sixth Pacific Rim International Conference on Advanced Materials and Processing

November 6, 2007 ICC Jeju, Jeju Island, Korea

Sean M. McDeavitt, A. Parkison, A.R. Totemeier and J.J. Wegener
Department of Nuclear Engineering, Texas A&M University

PRICM 6

Acknowledgements

- US Department of Energy funding under the Nuclear Energy Research Initiative
- Purdue University:
  Prof. T.J. Downar (now at UC Berkeley), Yunlin Xu, D.T. Kraemer, V. Seker.

  Prof. A.A. Solomon (emeritus) , V. Chandramouli, S Anthonysamy, S. Kuchibhotla

  SBWR core design team: Jere Jenkins, Daniel Mundy and Shaun Clarke
- Collaborators at Argonne National Laboratory:
  M.C. Hash, A.S Hebden, L. Leibowitz, J. Fink, N.L. Dietz Rago.
- Texas A&M University:
  A.R. Totemeier, A. Parkison, R. Kelley, and J. Wegener

The Nuclear Fuel Assembly

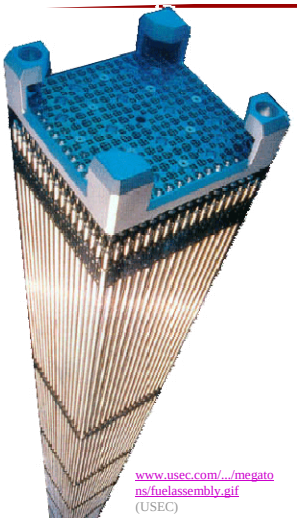

www.usec.com/.../megatons/fuelassembly.gif
(USEC)

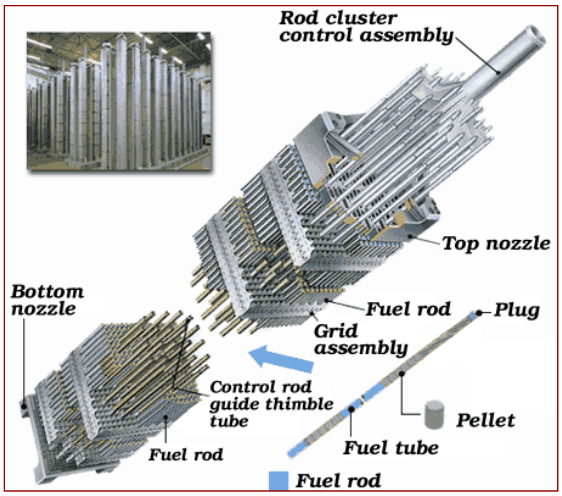

www.mnf.co.jp/images2/2img_pwr.gif
(Mitsubishi Nuclear Fuel)

Spent Nuclear Fuel

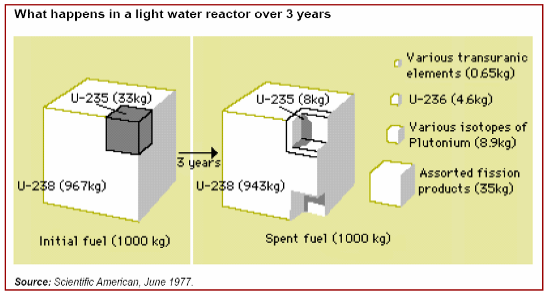

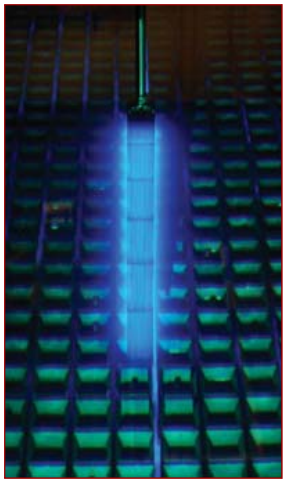

infocusmagazine.org/.../eng_nuclear_plants1.jpg

Fuel Recycle Strategies

Suite of UREX+ Processes

Process	Prod #1	Prod #2	Prod #3	Prod #4	Prod #5	Prod #6	Prod #7
UREX+1	U	Tc	Cs/Sr	TRU+Ln	FP		
UREX+1a	U	Tc	Cs/Sr	TRU	All FP		
UREX+2	U	Tc	Cs/Sr	Pu+Np	Am+Cm+Ln	FP	
UREX+3	U	Tc	Cs/Sr	Pu+Np	Am+Cm	All FP	
UREX+4	U	Tc	Cs/Sr	Pu+Np	Am	Cm	All FP

Notes: (1) in all cases, iodine is removed as an off-gas from the dissolution process.
(2) processes are designed for the generation of no liquid high-level wastes

U: uranium (removed in order to reduce the mass and volume of high-level waste)
Tc: technetium (long-lived fission product, prime contributor to long-term dose at Yucca Mountain)
Cs/Sr: cesium and strontium (primary short-term heat generators; repository impact)
TRU: transuranic elements (Pu: plutonium, Np: neptunium, Am: americium, Cm: curium)
Ln: lanthanide (rare earth) fission products
FP: fission products other than cesium, strontium, technetium, iodine, and the lanthanides

From "AFCI Separations Development," J. Laidler (Center fro Advanced Nuclear Fuel Cycles Meeting, 2006).

Zirconium Matrix Cermet Fuel

Brief Background on Cermet Nuclear Fuels

- Cermet fuels have a rich history in research and specialty applications (numerous experimental concepts from 1950 to present).
- Metallic matrix provides excellent strength and thermal performance.
- Ceramic dispersion useful for tailoring fuel composition and morphology through powder metallurgy methods.
- Disadvantage: lower "active" fissile volume due to non-fissile metal matrix. This often requires higher fuel enrichments.

Al-matrix fuel for research reactors

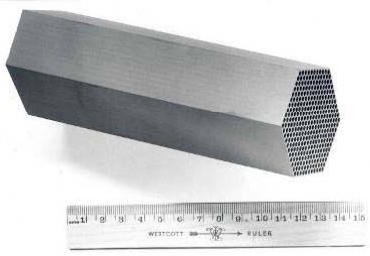

W-UO_2 Nuclear Rocket Concept

(photo from D. Walker, ANL)

Zr Matrix Cermet for $(Th,U)O_2$

Recent Publication:

Zirconium Matrix Cermet for a Mixed Uranium-Thorium Oxide Fuel in a SBWR, Sean M. McDeavitt, Yunlin Xu, Thomas J. Downar, and Alvin A. Solomon,

Published in the January 2007 Volume of Nuclear Technology.

NERI Project (1999 to 2003)

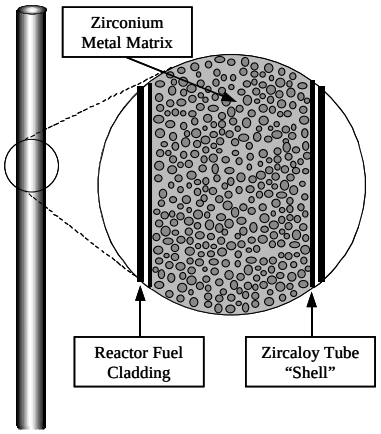

Purpose

- Explore the viability of using the thorium fuel cycle in an open fuel cycle with a cermet to enable direct disposal.
  - An open cycle was the targeted because it matched the internal U.S. goals in 1999.
  - The Zr matrix has many advantages beyond waste disposal.
- Three primary activities to demonstrate the concept.
  - Nuclear core simulations (Prof. Downar, Purdue University)
  - $(Th,O)_2$ fabrication (Prof. Solomon, Purdue University)
  - Zr-matrix cermet manufacturing (S.M. McDeavitt, ANL)

Cermet Fabrication Issues

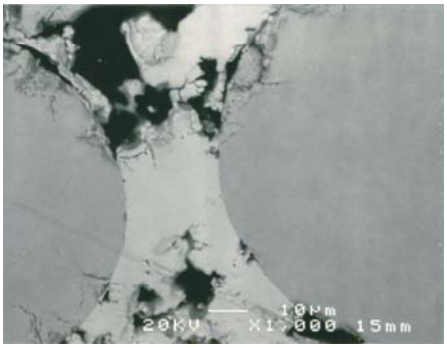

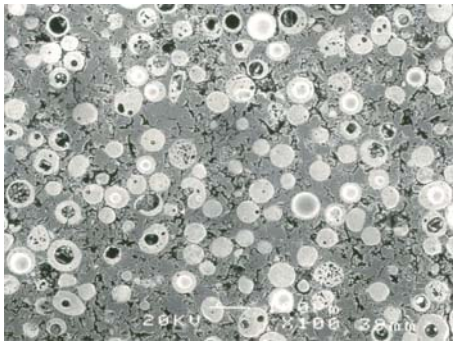

Comparison to Cold Drawing

Data from previous Zr-matrix cermet project (new pictures).

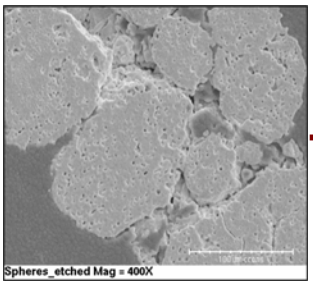

$(U,Th)O_2$ microspheres from A. Solomon (Purdue University)

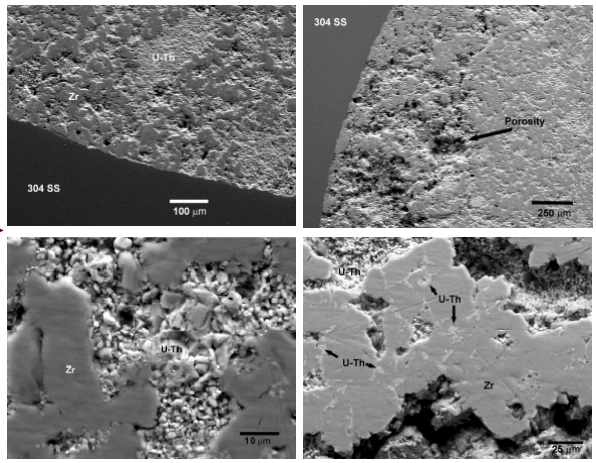

Micrographs of Zr-matrix cermet from N. Dietz Rago (Argonne National Laboratory)

Zr Matrix Cermet for Transuranic Storage/Transmutation

Design Basis Diagram for this Project

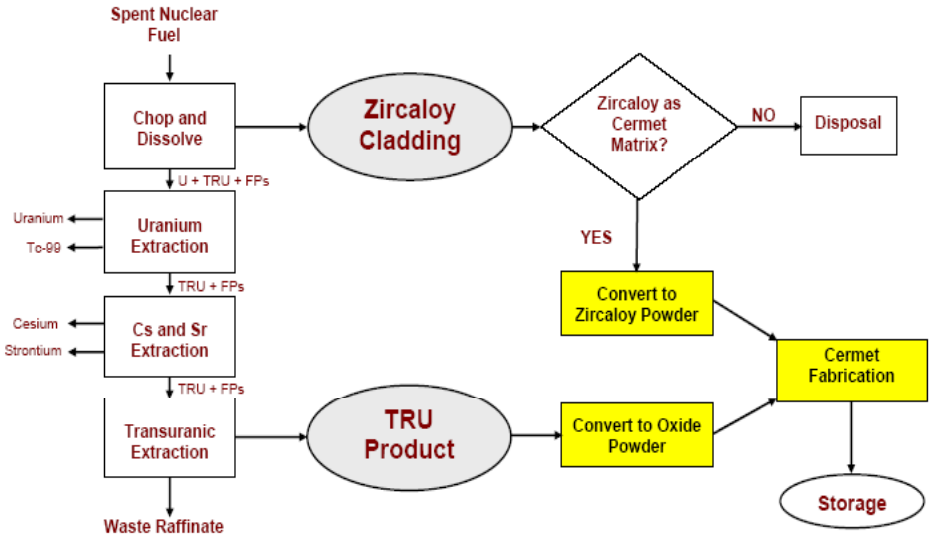

Design Basis Diagram for this Project

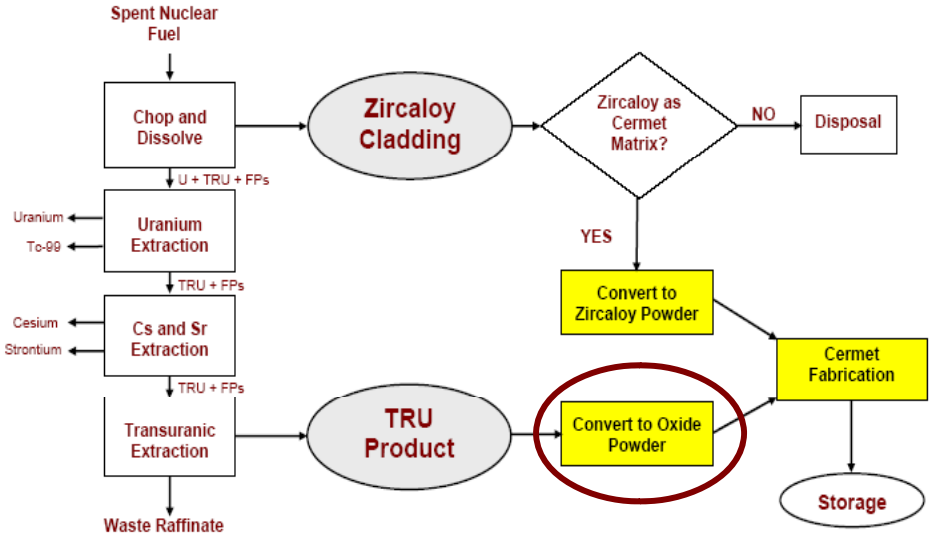

Oxide Conversion Chemistry

- Sol-Gel Process for pure UO_2 microspheres (J. Collins, ORNL)

"Broth" - Uranyl Nitrate $[UO_2(NO_3)_2]$ plus HMTA $[(CH_2)_6N_4]$ plus Urea $[(NH_2)_2CO]$

- Step 1: formation of low temperature (0°C) complex between the Uranyl Nitrate and Urea
  $UO_2(NO_3)_2{*}2(NH2)_2CO$
- Step 2: At higher temperature, the uranium naturally de-complexes via hydrolysis
  $UO_2 + 2H_2O \rightarrow UO_2(OH)_2 + 2H^+$
- Step 3: HMTA consumes the H^+ (protonation)
  $(CH_2)_6N_4 + H^+ \rightarrow [(CH_2)_6N_4H]^+$
- Step 4: The $HTMA^+$ breaks down after 70% to 90% conversion to $UO_2(OH)_2$ (excess H^+)
  $(CH_2)_6N_4H^+ + 3H^+ + 6H_2O \rightarrow 4NH_4 + 6CH_2O$
- Step 5: Decomplexed Urea reacts with formaldehyde to drive reaction to right (remove HTMA)
  $(NH_2)_2CO + CH_2O \rightarrow$ Copolymer that adds strength to gel structure
- Step 6: NH_4 from Step 4 complexes with $UO_2(OH)_2$ from Step 2 form Ammonium Diuranate
  $(NH_4)_2U_2O_7$ - solid
- Step 7: Thermal conversion to UO_2 followed by sintering

- Question: How will this work with mixed oxides?
  - Building apparatus to make $(U,Ce)O_2$ ceramic powders.

Sol-Gel Testing Apparatus

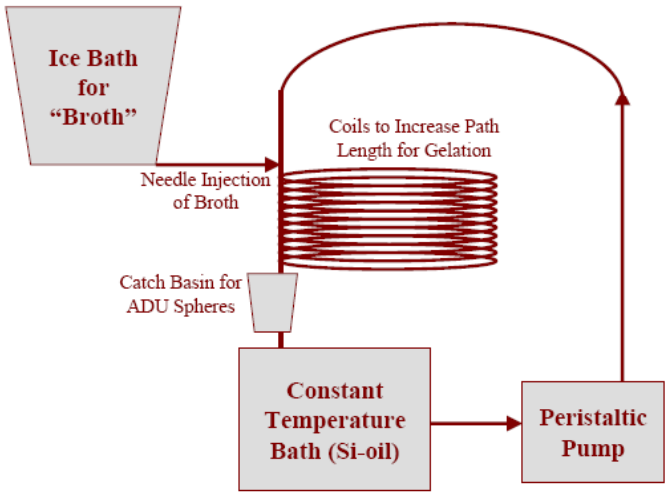

Design Basis Diagram for this Project

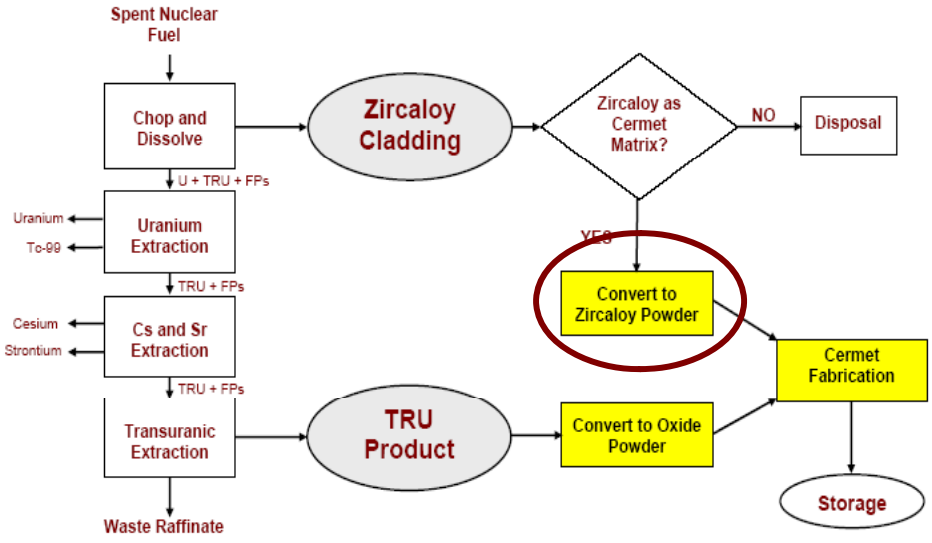

Condition of Real Zircaloy Cladding

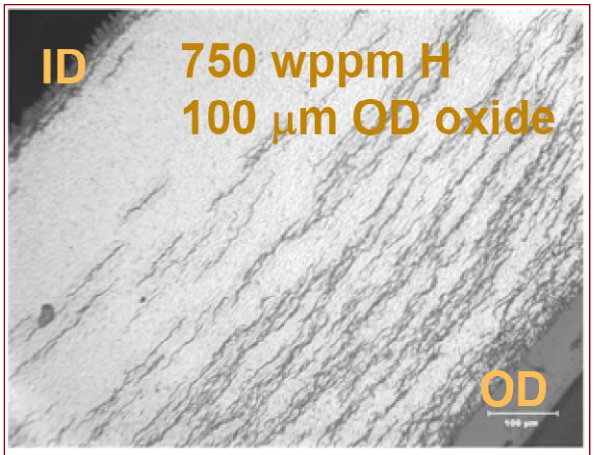

Zircaloy Recycle Process

$$Zr + H_2 \rightarrow ZrH_2$$

ΔG = -92.8 to -36.5 kJ/mole (300℃ to 700℃)

- Vapor phase synthesis of zirconium hydride (hydriding)
- Conversion of the hydride to powder (milling)
- Conversion of the hydride back to metallic powder (dehydriding)

- Industrial production experience
  - US patent 4,470,847: Method for Ti, Zr, and Hf.
  - Milling after hydriding to make fine powder.
  - Decomposition to metal enabled by fine particle size.

Process Vessel Design

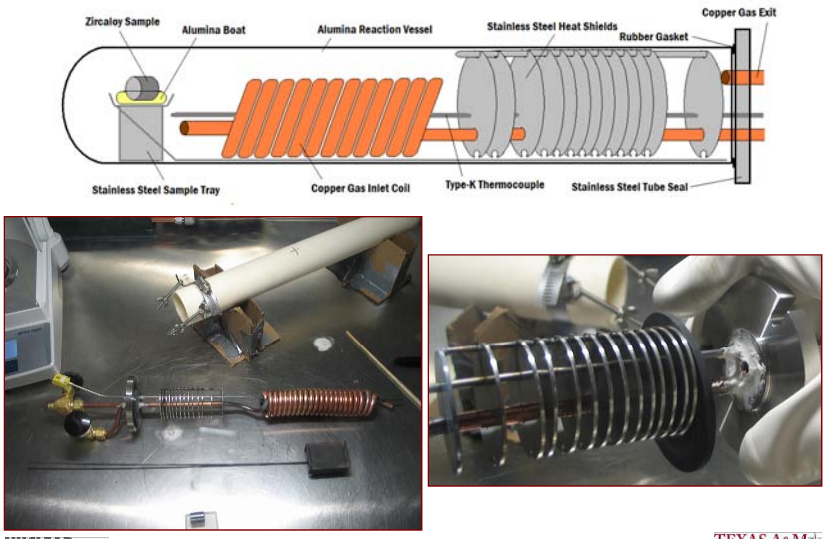

Process Development Experiments

- Phase 1: Process Variable Screening
  - Temperature: 350ºC to 750ºC
  - Pressure: 4.5 to 28 in H_2O
  - Process Time: 6, 12, and 24 h
  - Flow Rate: 3 to 8 SCFH
- Phase 2: Definition of Nominal Operation
  - New student researcher
  - Reproduction of previous results to learn experimental system
  - Relocation of experiment to Texas
  - Modify and upgrade system seals to improve performance
- Phase 3: Process Rate Evaluation
  - Measurement of basic rate constants for hydride reaction
  - Provide design basis data for “all-in-one” engineering device

Results from Process Development Tests

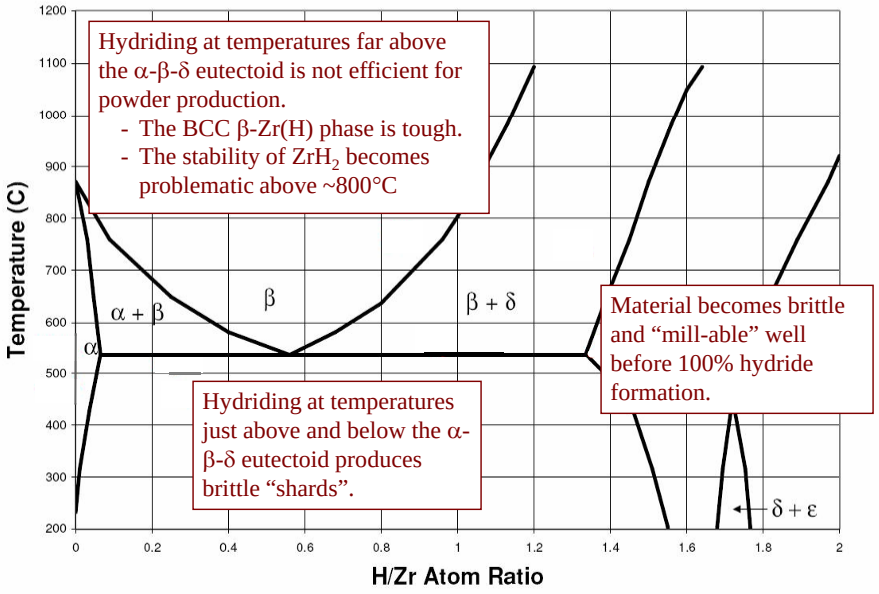

Hydrided Zircaloy Tubes

(before milling)

Post-test handling in an inert atmosphere glovebox

Hydrided Zircaloy Easily Pulverized

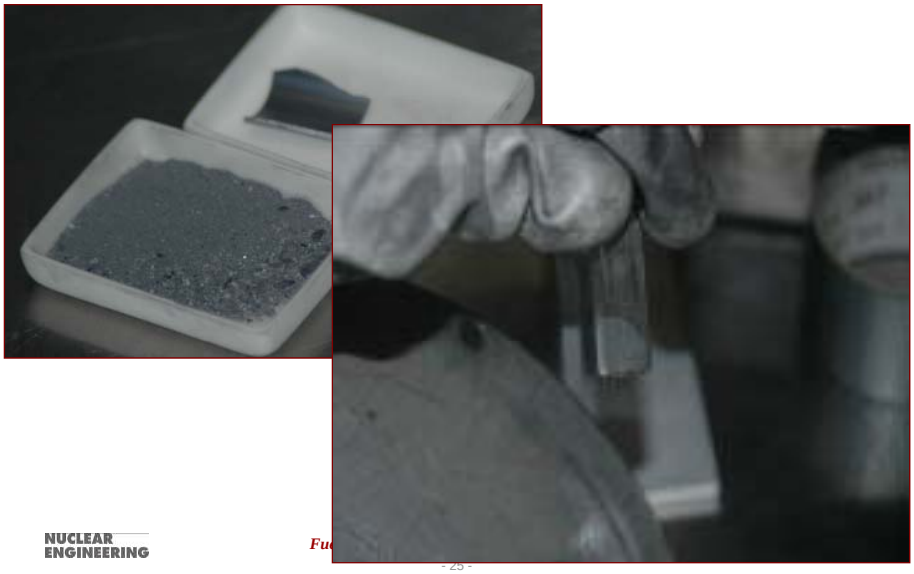

Rate Study Results

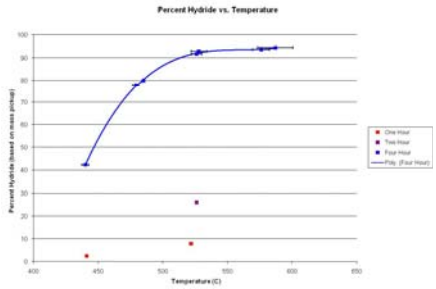

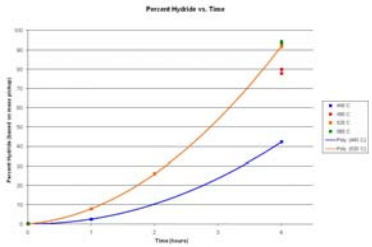

All-in-One Process "Concept"

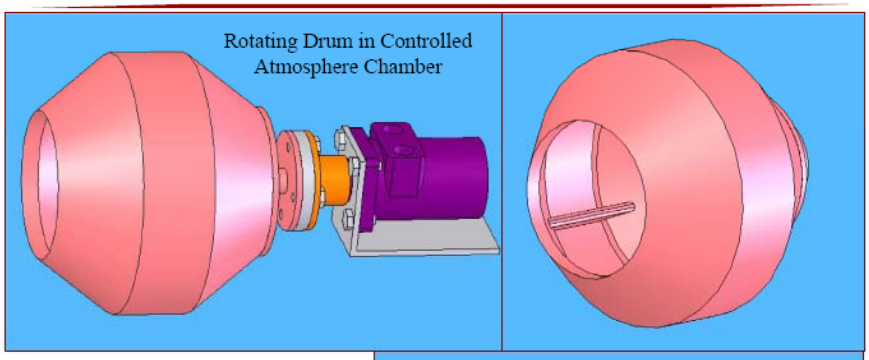

1. Hydride metal at ~550°C
2. Mill material $_{\text{in situ}}$
3. Dehydride to metal powder at ~900°C (TBD)

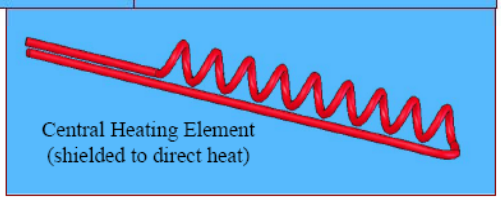

Design Basis Diagram for this Project

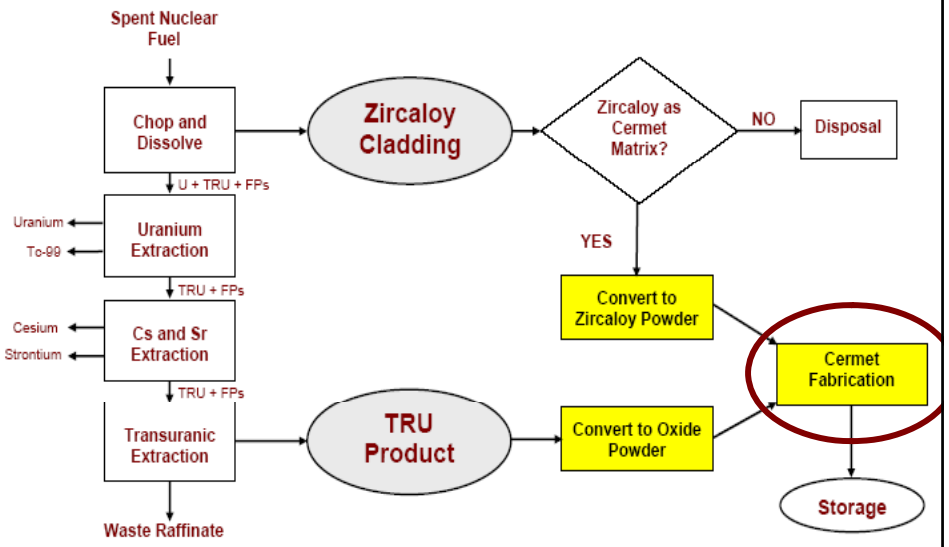

Initial Extrusion Die

- NuDie V (AISI H-13)
  - Low carbon tool steel with Cr, Mo, V additions
  - High temperature strength, moderate wear resistance
- Heat treatment
  - Austenitize
    - 1025ºC 45 min, equilibrate at 630ºC and 830ºC
  - Quench
    - 25 ºC/min (in air); forced convection
  - Temper
    - 2x at 540ºC for 2 h (air cool)

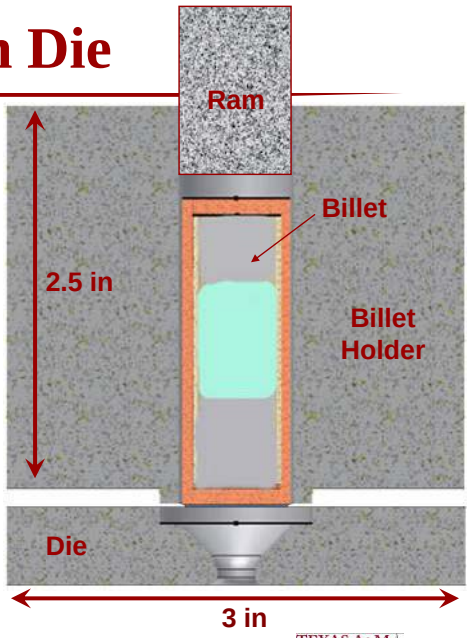

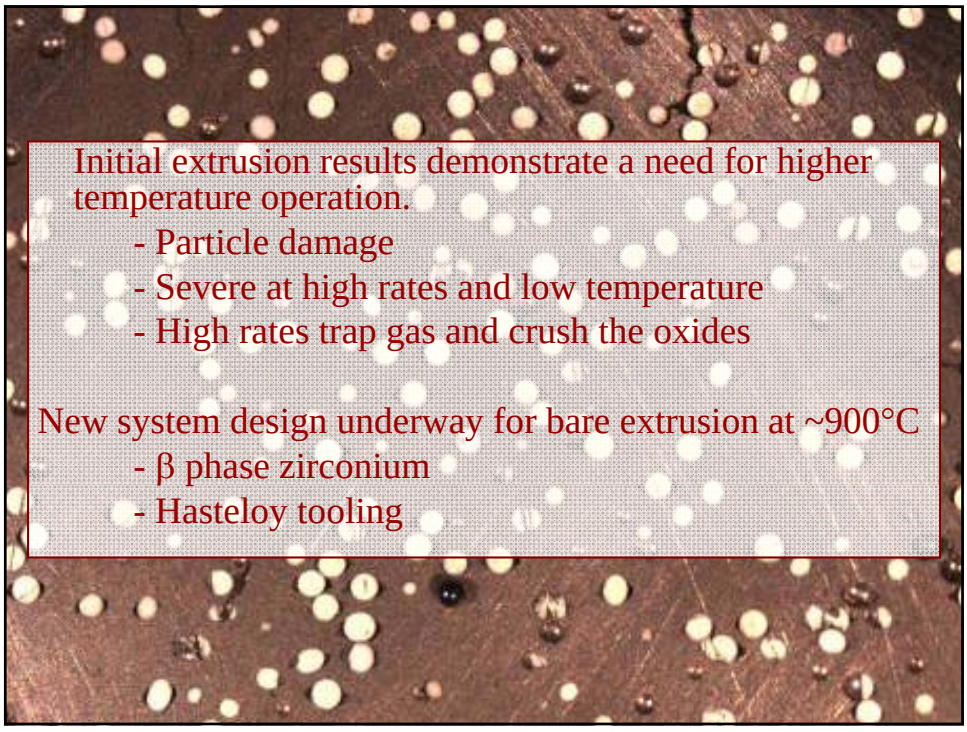

Initial extrusion results demonstrate a need for higher temperature operation.

- Particle damage
- Severe at high rates and low temperature
- High rates trap gas and crush the oxides

New system design underway for bare extrusion at ~900°C

- β phase zirconium
- Hasteloy tooling

Appendix C

Master of Science Thesis: Sol-Gel Fabrication Method (140 Pages)

PRODUCTION OF CERIUM OXIDE MICROSPHERES BY AN INTERNAL GELATION SOL-GEL PROCESS

A Thesis

By

JEFFREY JOHN WEGENER

Submitted to the Office of Graduate Studies of Texas A&M University
in partial fulfillment of the requirements for the degree of

MASTER OF SCIENCE

December 2008

PRODUCTION OF CERIUM OXIDE MICROSPHERES BY AN INTERNAL GELATION SOL-GEL PROCESS

A Thesis

by

JEFFREY JOHN WEGENER

Submitted to the Office of Graduate Studies of
Texas A&M University
in partial fulfillment of the requirements for the degree of

MASTER OF SCIENCE

December 2008

Major Subject: Nuclear Engineering

PRODUCTION OF CERIUM OXIDE MICROSPHERES BY AN INTERNAL GELATION SOL-GEL PROCESS

A Thesis

by

JEFFREY JOHN WEGENER

Submitted to the Office of Graduate Studies of
Texas A&M University
in partial fulfillment of the requirements for the degree of

MASTER OF SCIENCE

Approved by:

Chair of Committee,	Sean McDeavitt
Committee Members,	John Poston
	Miladin Radovic
Head of Department,	Raymond Juzaitis

December 2008

Major Subject: Nuclear Engineering

ABSTRACT

Production of Cerium Oxide Microspheres by an Internal Gelation Sol-Gel Process.

(August 2008)

Jeffrey John Wegener, B.S., Purdue University

Chair of Advisory Committee: Dr. Sean M. McDeavitt

The experiments performed for this research were completed to produce solid cerium oxide microspheres by an internal gelation sol-gel process. The motivation for this work was to develop a process that would enable the fabrication of a storage or transmutation form for the plutonium and transuranics (TRU) from the Uranium Extraction Plus (UREX+) used fuel reprocessing process. This process is being investigated by the Department of Energy (DOE) and the Advanced Fuel Cycles Initiative (AFCI) through the Nuclear Energy Research Initiative.

The internal gelation production of cerium oxide involves the combination of hexamethylenetetramine (HMTA), urea, and cerium nitrate solutions at ~100^{o}C. Microspheres were produced by injection of a broth solution into a flowing stream of hot silicone oil. The captured microspheres were aged, washed, and then underwent Thermogravimetric Analysis (TGA), Differential Scanning Calorimetry (DSC), and X-Ray Diffraction (XRD) analysis. The process variables examined in this study include the concentrations of HMTA, urea and cerium nitrate, the process temperature, the post-gelation aging time, and the product washing conditions.

Over a series of 70 experiments, it was determined that a broth solution containing a mixture of 1.45 M cerium nitrate and 1.65 M HMTA and urea (1:1 ratio) solutions produced the best cerium oxide microspheres. The spheres were aged for 30 to 60 minutes and then washed in hexane to remove the silicone oil and a subsequent series of ammonium hydroxide washes to remove unreacted product and to fully gel the microspheres.

Through DSC analysis it was determined that excess wash or unreacted product may be removed by an exothermic reaction at approximately 200^{o}C. The XRD analysis of unheated spheres showed the presence of cerium oxide with additional cerium-bearing organics. Following heating, the microspheres were completely converted to cerium oxide.

DEDICATION

This thesis is dedicated to my parents John and Susan Wegener, my brother Michael Wegener, and my sister Sarah Wegener.

ACKNOWLEDGEMENTS

I would like to thank my committee chair Dr. Sean McDeavitt for his support and the opportunity to study at Texas A&M University. I would also like to thank my committee members Dr. John Poston and Dr Miladin Radovic for their assistance. Thanks go to Zane Adams, Michael Naramore, and Jeffrey Hausaman for assisting in the analysis work, and to Luis Ortega, Adam Parkison, and Aaron Totemeier for their encouragement and advice along the way. Finally, I would like to thank my family for everything along the way, big and small, that has made this possible.

NOMENCLATURE

AFCI	Advanced Fuel Cycle Initiative
DSC	Differential Scanning Calorimetry
DOE	Department of Energy
HMTA	Hexamethylenetetramine
MOX	Mixed Oxide
NERI	Nuclear Energy Research Initiative
ORNL	Oak Ridge National Laboratory
PUREX	Plutonium and Uranium Extraction
RTV	Room Temperature Vulcanizing
TGA	Thermogravimetric Analysis
TRISO	Tristructural-Isotropic
TRU	Transuranic
TRUEX	Transuranic Extraction
UREX	Uranium Extraction
XRD	X-Ray Diffraction

TABLE OF CONTENTS

LIST OF FIGURES

LIST OF TABLES

1. INTRODUCTION

Presently in the United States, used nuclear fuel is accumulating at power plants at a rate of ~2,000 metric tons per year. As of 2007, over 55,000 metric tons were awaiting long term disposal in used fuel storage pools and dry casks [1]. The amount of recoverable energy stored in this volume of used fuel is extraordinary when compared to other long term energy options. To produce 8000 kWh from coal would require 3 metric tons of high quality black coal. This much coal would produce 8 metric tons of carbon dioxide and up to 100 kg of sulfur dioxide. The same amount of energy can be produced from between 30 and 70 kg of natural uranium, or about 30 grams of enriched fuel [2]. Assuming an enrichment of 1% on used nuclear fuel, the same energy load could be obtained from 21 to 49 kg.

The United States Department of Energy is exploring two different pathways to address the issue of this accumulating nuclear waste. The first option is long term storage at a repository. Yucca Mountain, located approximately 90 miles from Las Vegas, has been designated as the site for the long term repository. Under this plan, as outlined in the recently filed license application, 63,000 metric tons of used fuel from commercial reactor sites would be deposited in tunnels within the mountain [3]. Given current generation rates, in less than a decade more commercial used fuel would have been produced than the capacity of Yucca Mountain can accommodate. Using only repositories to store the waste, by the end of the current century several more deep

---

This thesis follows the style of Journal of Nuclear Materials.

geologic storage facilities would be required.

The second option being investigated would attempt to avoid long term storage by reprocessing and recycling used nuclear fuel. Under this pathway, the 8 to 11 kg of U-235 present in one metric ton of used fuel will be put back into service along with the useful energy content retrievable from plutonium and other transuranics. Two processing options are being put forward to accomplish the recycling process and produce usable fuel [1]. The first option, Plutonium and Uranium Recovery by Extraction (PUREX), separates high purity uranium and plutonium from the waste stream. PUREX is used worldwide for fuel reprocessing and the production of weapons grade fissile materials. The second recycling option, which is currently being promulgated by the US Department of Energy, is a modified PUREX process designed to eliminate pure plutonium extraction. This process is named UREX (Uranium Extraction) and it has the potential to save space inside a repository site such as Yucca Mountain by removing the uranium which makes up the vast majority of the mass of used fuel as well as some of the more active fission products. By utilizing UREX, the plutonium remains in the raffinate, or waste, stream with the other transuranics (TRU) and fission products, mitigating the proliferation issue. It will take a social policy decision to determine whether these Pu and TRU isotopes will be stored as waste or burned as fuel, but the research described here will support either mission.

The US Department of Energy is developing UREX and associated processes under the Advanced Fuel Cycle Initiative. One of the mechanisms used to advance this

technology with university research is the Nuclear Energy Research Initiative (NERI). The research presented in this thesis represents a portion of the larger NERI project designed to investigate the ultimate disposition form for the plutonium and TRU isotopes from the raffinate stream A complete family of separation processes, referred to as UREX+, have been designed to perform multiple operations to selectively isolate specific isotopes for individual treatment. The effluent stream containing the PU/TRU nitrate effluent comes from the TRUEX (TRU Extraction) process at the tail end of the UREX 1a scenario.

The focus of this project is on the development of a conversion process to transform mixed uranium and Pu/TRU nitrate solutions into solid mixed oxide microspheres. The results demonstrate the preliminary process methodology using cerium nitrate as a surrogate for plutonium nitrate. The overall NERI context for this cerium nitrate conversion process is a larger project designed to develop a comprehensive conversion scheme involving three processes: 1) the conversion of the U/Pu/TRU nitrates to oxide powder, 2) the recovery of a portion of the spent Zircaloy cladding as a metal powder via a hydride/dehydride process, and 3) the fabrication of cermet pins by combining both powders via hot extrusion. The final cermet is a candidate storage form that may also serve as a TRU-burning inert matrix fuel. The Zircaloy recovery and hot extrusion processes have been developed as separate projects [4, 5, 6, 7]. In addition to these process development activities, computational simulations evaluating the Pu and TRU-burning potential of this extruded fuel form in

advanced reactors are being performed at Purdue University and the University of California, Berkeley [7].

As the first process development stage for nitrate conversion, an internal gelation sol-gel system was created based on the conversion of cerium nitrate. In this method, a "broth" containing the nitrate solution, urea, and hexamethylenetetramine (HMTA) was injected into a hot flowing stream of silicone oil. Through the temperature driven sol-gel process, solid microspheres were produced, washed, and sintered for evaluation. This conversion process is similar to that used in the fabrication of UO_2 tristructural-isotropic (TRISO) fuel kernels for pebble bed and prismatic nuclear reactor systems [8]. Since the UO_2 process is well developed, this research focused on the gelation of cerium oxide as a first step toward the gelation of mixed uranium-cerium oxide microspheres.

The design of the sol-gel apparatus and the baseline processing data generated by this research will serve as a foundation for further work into mixed oxide microsphere gelation. A sequence of seventy internal gelation experiments were completed. The initial testes were used to identify appropriate processing variables and multiple system modifications were required as the process was developed. Through a set of parametric studies, it was discovered that the highest quality cerium oxide spheres were produced from a broth of 1.45 M cerium nitrate and 1.65 M HMTA and urea. Spheres produced from this broth composition were fully washed in hexane and underwent a series of ammonium hydroxide washes. These washed and dried spheres underwent varying levels of heat treatment and were then analyzed through x-ray diffraction (XRD), differential scanning calorimetry (DSC), and thermogravimetric analysis (TGA). The

final sintered microspheres were clearly identified as cerium oxide, whereas the freshly gelled and washed spheres were comprised of cerium oxide along with a remnant of organic impurity compounds. The following Sections describe the theoretical basis (Sections 2), experimental design (Section 3), experimental results (Section 4), and discussion (Section 5) from the research that created this conclusion.

2. PREVIOUS WORK

2.1. Sol-Gel Processing of Metal Oxide Ceramics

The name “sol-gel” refers to a family of liquid-to-solid conversion processes that produce solid materials from an initial chemical solution. The name itself is a reference to the starting solution, or “sol”, and the solid material produced from the “gelling” of inorganic polymers that form networks to produce a solid. In the case described here, the solid being produced is cerium oxide and the method is based on a sol-gel process developed for uranium dioxide fabrications.

There are two sol-gel process types that are used extensively in materials processing applications: external gelation and internal gelation. In both cases, the sol-gel reaction is driven by the presence of ammonia (NH_3). For external gelation, an external solution of ammonia is used to drive the gel-forming reaction [9]. However, external gelation is not practical for the production of microspheres because it would require many gallons of ammonia to be used as a heat transfer medium and a host for the reactant droplets that gel during the process. Therefore, internal gelation is commonly used to produce powders. For internal gelation, the required ammonia is produced internally by the decomposition of HMTA [9]. Internal gelation was used for this project and the basis for the experimental method is described in the next section.

2.2 Chemistry of UO_2 Internal Gelation

As stated above, the internal gelation sol-gel process involves the reaction of a nitrate salt with ammonia to produce a spherical gel and the ammonia is produced

internally by the decomposition of HMTA [9]. The discussion in this section outlines the sol-gel process designed for UO_2 TRISO kernels, as developed by Oak Ridge National Laboratory [9]

The starting uranyl nitrate is prepared as an aqueous solution (in contrast, cerium nitrate is used to generate cerium oxide spheres). The active chemical reagents for UO_2 internal gelation are the uranyl nitrate salt combined with urea ($(NH_2)_2CO$) and HMTA ($(CH_2)_6N_4$) inside of an inert heat transfer medium, such as silicone oil. The combination of the nitrate, urea, and HMTA is commonly referred to as the "broth" [9]. Before this broth can be used to produce microspheres, it first must be chilled to approximately 0°C. By doing this, urea combines with the nitrate salt to stabilize the solution and prevent early gelation [10]. This stabilizing reaction is given as equation 1.

$$UO_2\left(NO_3\right)_2 + 2(NH_2)_2CO \rightleftharpoons UO_2(NO_3)_2 \cdot 2(NH_2)_2CO \qquad [1]$$

After the broth is stabilized, the temperature is increased by introduction of the broth into the silicone oil at 90 to 110°C, the urea decomplexes and the above reaction is driven to the left. When the broth introduction is accomplished using a small needle, the liquid forms spherical droplets in the silicone oil. The reaction sequence that follows takes place within the spherical solution. First, the nitrate salt loses its nitrate group and undergoes hydrolysis [10], as shown in Equation 2.

$$UO_2^{2+} + 2H_2O \rightleftharpoons UO_2(OH)_2 + 2H^+ \qquad [2]$$

At this point, all species are still soluble and the hydrogen ions produced by the hydrolysis reaction then undergo a protonation reaction with the HMTA [10], as shown in Equation 3.

$$(CH_2)_6N_4 + H^+ \rightleftharpoons (CH_2)_6N_4 \cdot H^+ \quad [3]$$

Protonation of the HMTA continues until at least 95% of the HMTA molecules have picked up an extra hydrogen ion. At this point the decomposition reaction will occur reducing the protonated HMTA to ammonium and formaldehyde [11], as shown in Equation 4.

$$(CH_2)_6N_4 \cdot H^+ + 3H^+ + 6H_2O \rightleftharpoons 4NH_4^+ + 6CH_2O \quad [4]$$

All species are still soluble at this point.

The urea ($(NH_2)_2CO$) that had originally complexed with the nitrate salt at 0°C according to equation 1 and then decomplexed back into solution at ~100°C now has a second role to play in the reaction sequence. Urea and formaldehyde readily react together to produce monomethylol urea [10]. As this goes on, the reaction in Equation 4 is driven completely to the right as the formaldehyde product is consumed as fast as it is produced and the reactants strive for equilibrium.

Once the ammonium is produced, the final product is precipitated as a solid. This occurs as a rigid gel structure of hydrated uranium oxide with ammonia (a solid at 100°C) is formed by the cross linking of weakly bonded particles [12]. Since the reaction sequence transpires within the spherical solution droplet suspended in the silicone oil, the final product is a solid sphere. The sphere forms rapidly, but the

reaction needs time to go to completion, so the spheres are "aged" in the hot oil to ensure completeness.

2.3 Microsphere Production for TRISO Fuel Kernels

In the past several years, several research teams have investigated the production of microspheres by internal gelation sol-gel. The research team at Oak Ridge National Laboratory produced microspheres of 1200, 300, and 30 μm and they investigated the details for most of the steps in the gelation process described above. For all but the fine spheres, trichloroethylene was used as the gelation medium with temperatures ranging from 54 to 64^{o}C. The height of the gelation column in these experiments was 180 cm, allowing for a slower heat transfer rate. The broth for these sets of experiments consisted of a 1.3 M uranium solution and an HMTA / uranium and urea / uranium mole ratio of 1.25. After removal of the organic medium, the produced spheres were washed in a solution of 50% isopropyl alcohol and 50% 1.5 M NH_4OH. The next wash was a 0.5 M solution of NH_4OH. The final wash was 75% isopropyl alcohol and 25% water. Each of these washes was for 45 to 70 minutes. Drying of the spheres was accomplished by flow of air over the spheres. The first step in the sintering process involved placing the spheres into a flowing stream of argon – 4% hydrogen increasing in temperature to 450^{o}C for one hour. Finally they are loaded into molybdenum trays and rapidly heated to 1600 ^{o}C for four hours, then allowed to cool. The spheres produced had upwards of 99% theoretical density, were 88.2 weight percent uranium and had an oxygen to uranium ratio of 1.98 to 2.0 [13].

Other work at Oak Ridge was completed to produce 500 μm for use as TRISO fuel kernels [14]. This setup used a vibrating needle to deliver the broth into a veil of falling oil. The height of the gelation column used was 550 mm with a flowing oil temperature of 60^{o}C. Stock solutions of 2.7 M acid deficient uranyl nitrate were produced. Acid deficient refers to the ratio of NO_3^- to U. The lower this number, the more acid deficient the solution is. The final broth solution had an HMTA and urea ratio to uranium of 1.3. After production of spheres, they were allowed to age in the silicone oil for up to 30 minutes then washed in four solutions of trichloroethylene for a minimum of 15 minutes per wash to remove the silicone oil. The next series of washes was 30 minutes of 0.5 M NH_4OH until the electrical conductivity was below 800 μmhos; the spheres are then allowed to air dry. Sintering of the spheres was carried out in either a pure nitrogen or 5% hydrogen – argon environment. The heating profile was 80^{o}C for two hours, 150^{o}C for three hours, 600^{o}C for five hours, and finally 1550^{o}C for five hours [14].

Subsequent research at Oak Ridge was completed to produce both 350 and 500 μm spheres [8]. The broth for this series of experiments has been optimized to work for a wider range of sphere sizes. Uranium concentration within the broth is between 1.29 and 1.30 M, HMTA and urea are both 1.68 M, and NO_3^- is 2.00 to 2.08 depending on the acid deficiency of the uranyl nitrate. The sintering of the spheres is the same as above except a 4% hydrogen – argon flow was used at approximately 3 L per minute. During sintering, the spheres shrink from their original size. Dried spheres of 1000 μm in size were observed to shrink to between 500 and 532 μm after sintering [8].

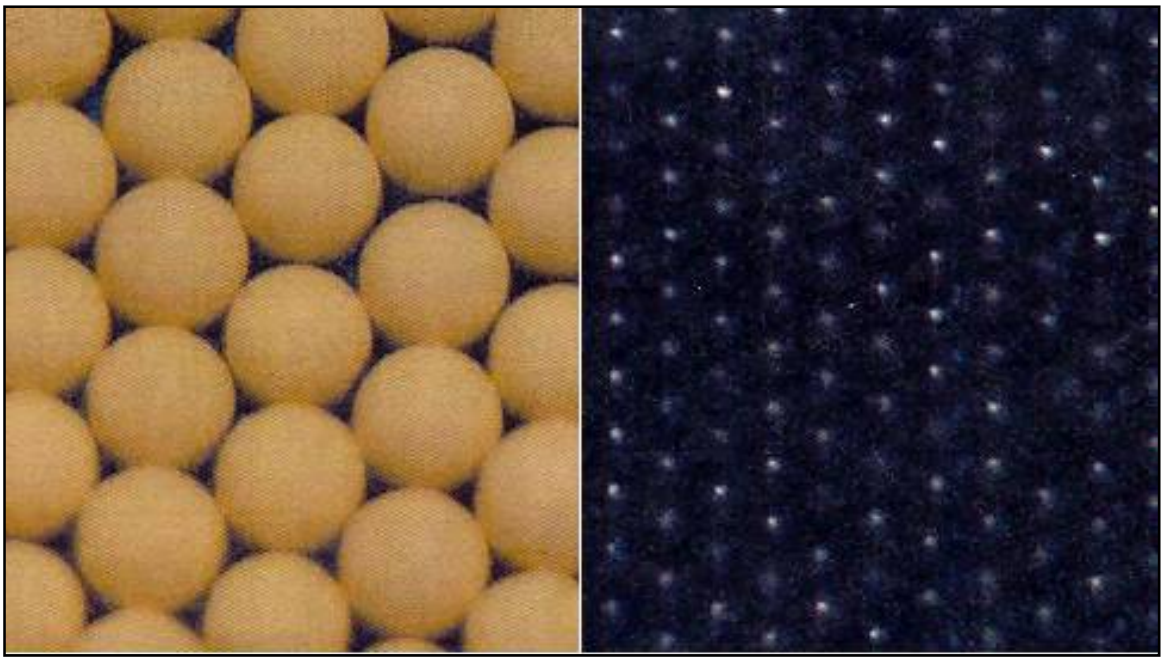

Figure 1. Dried UO_2 spheres (~1000 μm diameter, left) and sintered UO_2 spheres (500 to 532 μm diameter, right) [8].

Two main injection methods have been used in the creation of oxide microspheres. The first involves the spheres flowing through a vibratory nozzle into a veil of silicone oil. The second method involves directly inserting a needle into the flowing oil. One of the systems at Oak Ridge employed this latter setup [15] and a schematic is shown in Figure 2. Oil was heated in a reservoir where the collection basket was also located. From the reservoir, a pump drew the oil through the system where it went into the sphere-forming column from both the top and bottom. The broth was injected into the oil upstream of the column using a forced air injection method. After forming in the column, the spheres were carried through a section of tubing back into the reservoir [15].

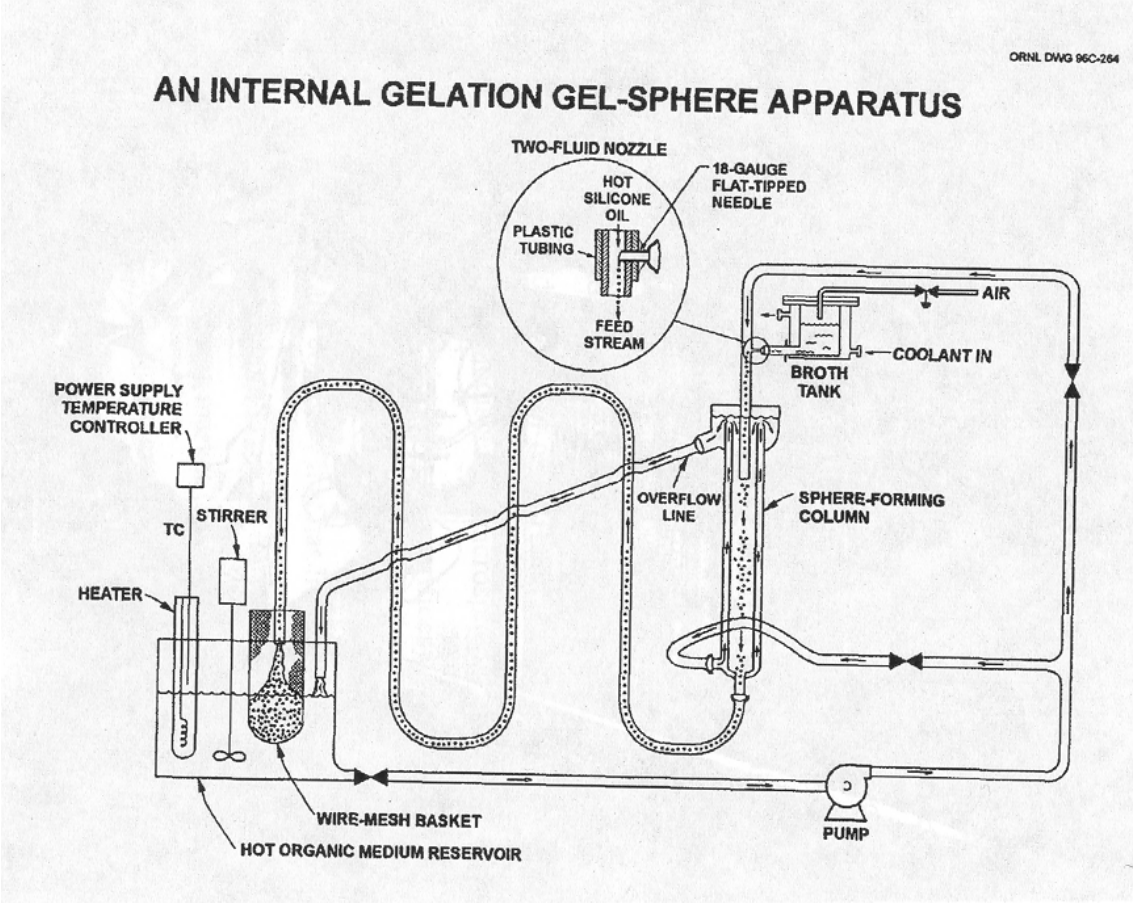

Figure 2. Diagram of Oak Ridge internal gelation sol-gel system [15].

While the work described previously focuses on UO_2 microsphere production, many oxide materials may be formed by sol-gel. For the presented research, cerium is used as a surrogate for plutonium. Cerium is able to be used due to the physical similarities between cerium oxide and plutonium oxide in a batch handling and compaction manner. The similarities also extend to the sintering process, where the two oxides exhibit nearly identical shrinkage behavior [16].

3. EXPERIMENTAL DESIGN AND PROCEDURE

The experimental sol-gel apparatus created for this project was based on the system used at Oak Ridge National Laboratory (Fig 2) [15] with custom modifications made as the experimental experience was gained. Figure 3 shows a schematic diagram of the final configuration of this device (used for experiments 17 through 70) and Figure 4 is a photograph of the installed apparatus.

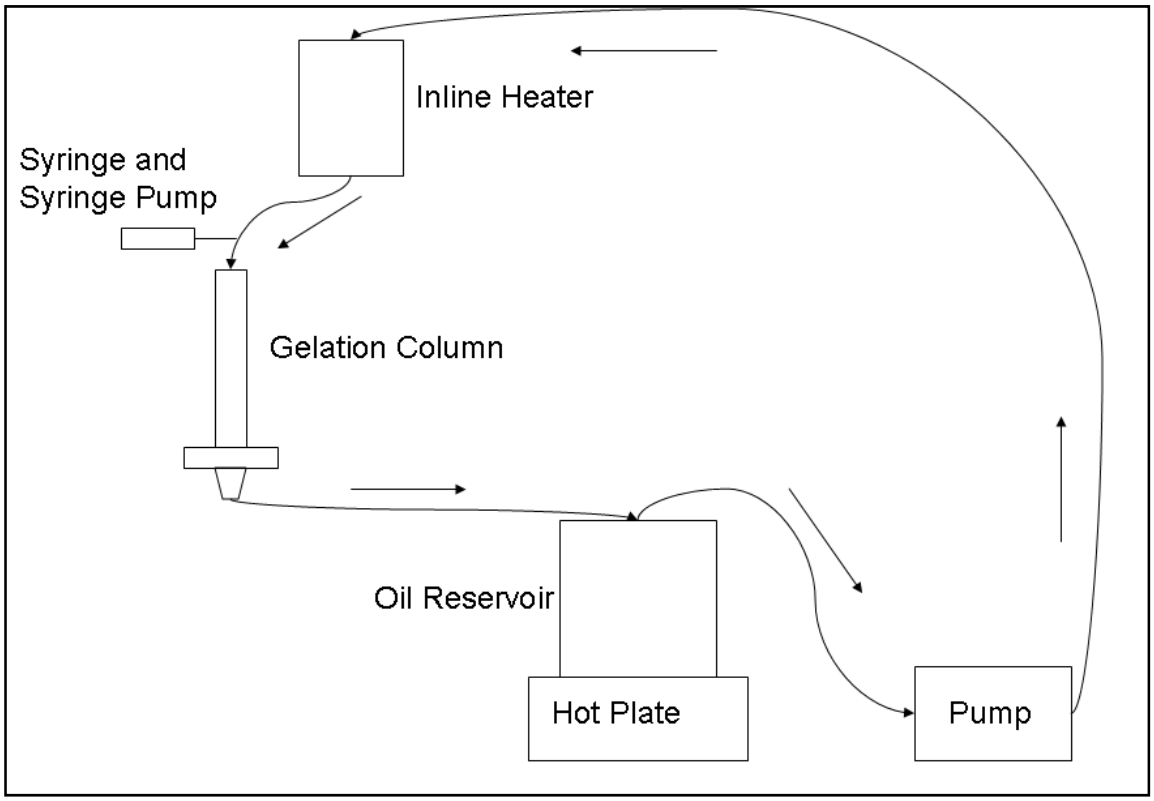

Figure 3. Schematic diagram of the final experiment configuration.

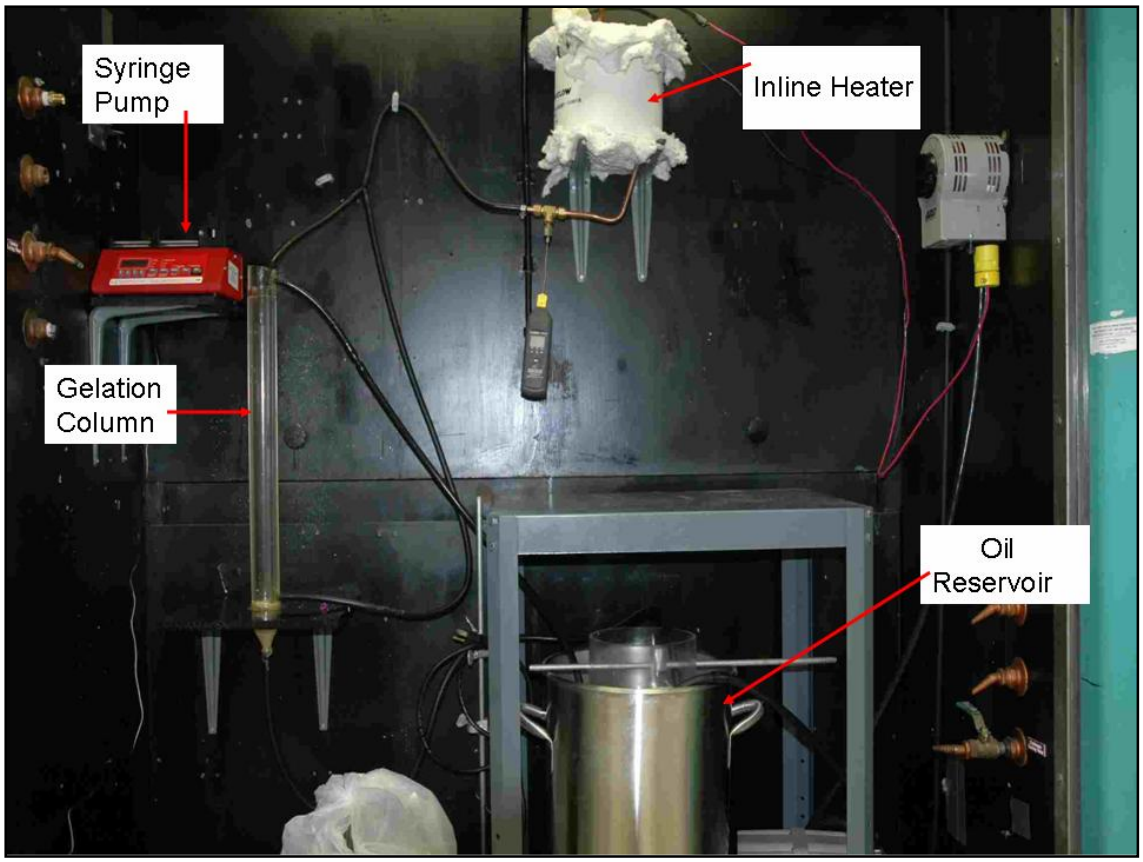

Figure 4. Photograph of the final experiment configuration.

In this system, an oil reservoir is heated by a hot plate, drawn through the system by a peristaltic pump, and the temperature of the flowing oil is then controlled to the desired operating temperature (nominally an experimental variable set near ~100^{o}C) while passing through a copper coil inside of an inline ceramic fiber heater. The precursor mixture of reactants, or the broth, is injected into the system using a syringe pump that is located directly upstream of the gelation chamber. The chemical consumption of the broth begins immediately upon insertion into the warm oil. The oil is an inert host to the gelation process and serves to provide heat and to carry the gelled

spheres to the catch basket at the end of the flowpath. Once the oil passes through the gelation chamber and into the catch basket it flows back into the reservoir.

3.1 Experimental Design

3.1.1 Oil Heating and Delivery

The silicone oil used in the system is stored in the oil reservoir. This reservoir is a 6 gallon stainless steel batch can. This reservoir is a seamless stainless steel pan that prevents oil from escaping the system, even when heated. Providing heat to the reservoir is a Thermolyne Type 2200 Hot Plate. The oil in the reservoir and microspheres present during aging are maintained at 90 to 100^{o}C by the hot plate heater.

The hot oil is pumped through the system by an Anko Mityflex peristaltic pump. The pump operates by placing the rubber tubing within the pump housing where three rollers force the oil through the tubing driving it through the rest of the system. The tubing is inserted into the reservoir on one end and sent to the gelation chamber on the other. By driving the oil through the system in this way, no part of the pump is contaminated by anything present within the oil. This is especially necessary for the future work where uranium gelation may be performed. Precautions must be taken to ensure that the section of tubing present in the pump housing does not become worn.

The hot plate is able to heat the oil to the correct temperature near 100^{o}C, but it is not able to give fine control over the oil that is flowing through the system. After pumping, it was observed that the oil was cooling in the line and needed a second heater to control the oil temperature prior to its entrance to the gelation chamber. Therefore, a Watlow 1100 W ceramic heater with an internal copper coil was installed between the

pump and the gelation chamber. Within the heater, a section of copper tubing has been coiled to provide a longer flow path inside of the furnace and to enable better heat transfer and higher temperatures than are achievable with rubber tubing.

3.1.2 Broth Delivery and Gelation

The initial method used to deliver the cerium-loaded broth into the gelation chamber was a pressurized broth pot and a forced air system. The broth pot was constructed using a section of acrylic tubing with a ball valve at the bottom to allow flow to the injection needle. At the top of the cylinder was a Swagelok tube fitting allowing connection to the air system. This was based on the setup observed at Oak Ridge National Laboratory for TRISO fuel kernel gelation.

Several variations of the forced air system were considered before the concept was abandoned altogether. The first involved a direct line from the building air supply into the broth chamber; although this was soon discovered to be far too much pressure. The next step involved several different pressure regulators, with the most time spent using a Control Air Inc. Type 700 Pressure Regulator in conjunction with a 15 psi pressure gauge. The whole broth pot system and forced air system was scrapped when it was discovered that the injection rate required for success was much lower than could be provided by any of the regulators (in other words, the insertion was too fast and difficult to control).

The final injection system installed on this system, and the method used for most of the experiments, involves a 5mL syringe and a New Era NE-300 syringe pump. In this method the syringe is loaded with the broth then placed into the syringe pump. The

needle from the syringe is placed in the flowing oil, the desired injection rate is set, and then the dispense button is pressed. Flow rates were on the order of 0.2 – 0.3 mL/min; much below what any of the air pressure regulators could provide.

The volume of the system where the gelation occurs is referred to as the gelation column and a schematic of this setup is shown in Figure 5. It was constructed using two differing diameters of acrylic tubing, an ABS plastic sheet, and a funnel. The outer, larger tube is slightly higher to allow an overflow spout for the oil. This tube is then secured to the plastic sheet at the bottom. The inner tube is connected to nothing at the top and is sealed onto the funnel at the bottom using epoxy. The top of the funnel is secured to the bottom of the plastic sheet. A photo of the final setup is shown in Figure 6.

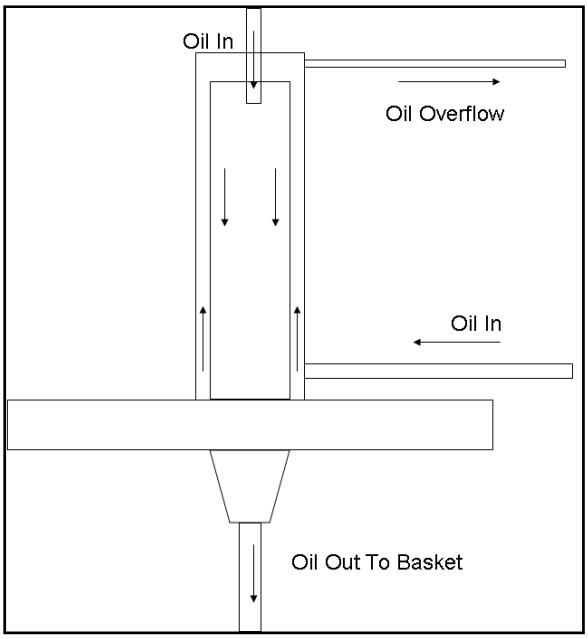

Figure 5. Schematic diagram of the gelation column

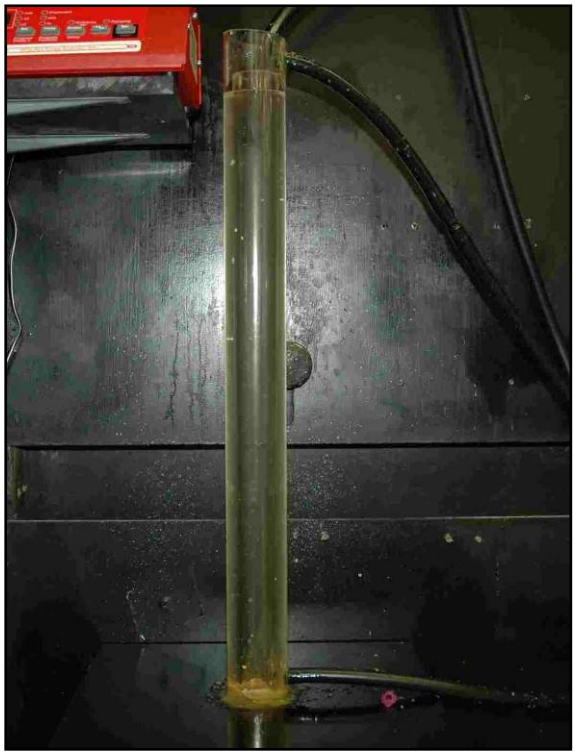

Figure 6. Photograph of the installed gelation column.

Once the oil leaves the gelation column it flows back into the oil reservoir where all gelation products are collected in the catch basket. Three types of mesh basket were used in the experiments, as described in Section 4. The first type of catch basket was constructed using sheets of woven stainless steel wire mesh (250 by 250 wires per inch). Using a 12" x 24" sheet of mesh, a cylinder was made approximately 5.75" in diameter. To one end of the cylinder a circle of the same mesh was attached using Room Temperature Vulcanized (RTV) Silicone Sealant. The second basket model used 80 x 80 mesh woven stainless steel wire. The final basket model was constructed using 40 x 40 mesh stainless steel wire. The courser mesh is better for post gelation washing since the washing fluids must drain through the mesh, allowing all washing steps to be performed with the sol-gel spheres in the constructed baskets rather than removing them spheres from the basket. In all cases, the mesh collection baskets were placed inside of the oil reservoir using an open acrylic cylinder to suspend it above the reservoir oil level. The acrylic cylinder has drain holes on the sides and a sheet of the wire mesh across the bottom to allow for drainage and filtration. This entire system (basket and acrylic cylinder) is then suspended in the reservoir such that the basket is above the oil and the cylinder does not touch the floor of the reservoir.

3.2 Experimental Procedure

The procedure described here represents the final procedure developed during the experiments described in Section 4. In a way, this procedure is a result of the research, but it is included in this section to provide understanding of how the experiments were

performed. Variations from this procedure are described throughout Section 4, especially for the earlier experiments. In the final experiment, solid microspheres were produced using this method.

The first step in running an internal gelation experiment is to prepare stock solutions of the primary broth constituents. The two reactants are kept apart to prevent gelation from occurring during storage. The first solution contains 3.0 M cerium nitrate, and the second solution is a mixture of both HMTA and urea (3.2 M for each). To create a stock solution containing HMTA and urea, the solid form of each compound is dissolved in deionized water and brought to the desired volume and molarity. The two solutions are both stored at room temperature as they are stable at that point. The experimental solutions used in the tests described in Section 4 were all diluted from these stock solutions to the experiment-specific desired concentrations.

For an experiment run, the first step is to turn on the hot plate under the oil reservoir. Doing this first allows a majority of the oil to heat when the system does not need to be attended. Typically the hot plate is set to 125^{o}C. While the oil is heating, the broth to be used in the run can be prepared. Calculated amounts from the stock 3.2 M HMTA/Urea and 3.0 M cerium nitrate solutions are measured corresponding to the desired concentrations of each in the run to be performed. To accurately measure out the solutions, 2 mL pipettes and a pipette pump are used. Each of the solutions were measured into test tubes and placed into a freezer for an hour to adequately chill them. At the beginning of each experiment the two solutions are combined together, stirred

thoroughly, and then placed back into the freezer until it is time for the run to begin. This allows the urea to complex with the nitrate according to the reaction in Equation 1.

When the oil has heated sufficiently, the peristaltic pump and the ceramic fiber heater are turned on. The heater is powered through a variac and is generally needed to be at approximately 50% power to heat the oil passing through the system to approximately 100^{o}C. Constant attention needs to be paid to the system when the pump is in operation so that the oil does not overflow the gelation column. For this reason it is typically turned to the lowest level possible setting to bring the oil up to the overflow weir located near the top of the column. Once the oil heats and its viscosity decreases, it flows faster through the column and the speed of the pump can be adjusted. For an experiment run, the pump is set to 30%.

The last step before performing an experiment run is to prepare the broth solution and syringe. The syringe is readied by removing it from the freezer and attaching the desired needle (the needle gauge size is an experimental variable). Having the syringe chilled helps in the prevention of premature gelation of the broth in the syringe and needle. The broth from the freezer is loaded into the syringe, air is removed from the syringe by plunging until broth is released, and then the system is placed into the syringe pump and secured. The final pre-experiment step is to insert the needle into the oil stream by either piercing the tubing or placing it into a pre-existing hole. Once everything is secure and ready the syringe pump is started and the broth is injected into the oil stream.

After the desired amount of broth has been injected into the system the syringe pump is stopped and the syringe and needle are removed from the pump. The spheres that have been formed must remain in the catch basket for an additional amount of time for the gelation process to be completed. This step is called aging. During this time the heaters and peristaltic pump remain on to keep hot oil flowing through the system and over the gelling spheres.

When the aging process is complete, the catch basket is removed and placed into the wash basin. The spheres are first washed with hexane to remove the silicone oil. The next series of three washes are designed to remove any reaction products still on the microspheres and to provide ammonium hydroxide to allow further gelation for improved sphere properties [13].

The three washes in the main process are each for 60 to 75 minutes and 200 mL of wash solution for each. First in the process is a solution of 50% isopropyl alcohol and 50% 1.5M Ammonium Hydroxide. The second primary wash involves a solution containing only 0.5M Ammonium Hydroxide. The final wash step is 75% isopropyl alcohol in water [13]. Once this has been completed the spheres are removed from the catch basket and placed aside to dry. After drying is completed, the spheres ready for sintering and further characterization. As evidenced by the results in Section 4, this washing procedure is a critical component of the production of the final microspheres.

4. RESULTS

A series of 70 experiments was performed using the apparatus and procedures described in Section 3. The experimental apparatus underwent several changes in design to address issues that arose as the research progressed. Throughout the series of experiments, equipment was replaced, added, and removed in the quest to produce solid, reproducible microspheres. Major system additions involve the removal of the forced air system and broth chamber, addition of the gelation column and syringe pump, and replacement of the oil reservoir system (each of these items are described in Section 3). Additionally, since the majority of literature on this subject deals with uranium oxide (U_3O_8 and UO_2) microsphere production, additional experiments were required to evaluate the impact of changes in chemical composition of the broth.

Figure 7 shows a chronological flowchart of the experiments performed for this project. The experiments are divided into three stages of development: 1) system development experiments (Section 4.1), 2) process development experiments (Section 4.2), and 3) microsphere production and characterization (Section 4.3).

Experiment 1 (Section 4.1.1) was an initial trial run using several equipment items that are no longer part of the system. In experiments 2 through 12 (Section 4.1.2) the broth chamber and flow regulator were replaced and the gelation column was added. Section 4.2.1 reports a series of small scale process development tests completed in test tubes to evaluate the optimum broth composition for sphere production. In experiments 13 to 16 (Section 4.1.3) the forced air system was removed and a manual injection via

syringe was used. In experiments 17 and 18 (Section 4.1.4) a syringe pump replaced manual injection. Experiments 19 to 36 (Section 4.2.2) explored variation in the broth composition and experiments 37 to 48 (Section 4.2.3) continued this process while also changing the catch basket designs. Experiment 49 through 53 (Section 4.2.4) continue with the evaluation of the broth concentrations, but a three-stage wash system developed at Oak Ridge National Laboratory was also implemented [7]. Experiments 54 to 59 (Section 4.2.5) used the same fixed broth composition with varying aging times, and Experiments 60 through 66 (Section 4.2.6) used diluted solution in an effort to obtain quality washed spheres. The final experiments performed, 67 through 70 (Section 4.3.1), focus on the final broth composition while exploring variations in the temperature of the silicone oil and the times for aging and washing. The X-Ray Diffraction (XRD), Thermogravimetric Analysis (TGA), and Differential Scanning Calorimetry (DSC) analyses (Section 4.3.2) were performed to characterize the product and evaluate the post-washing sintering of the microspheres

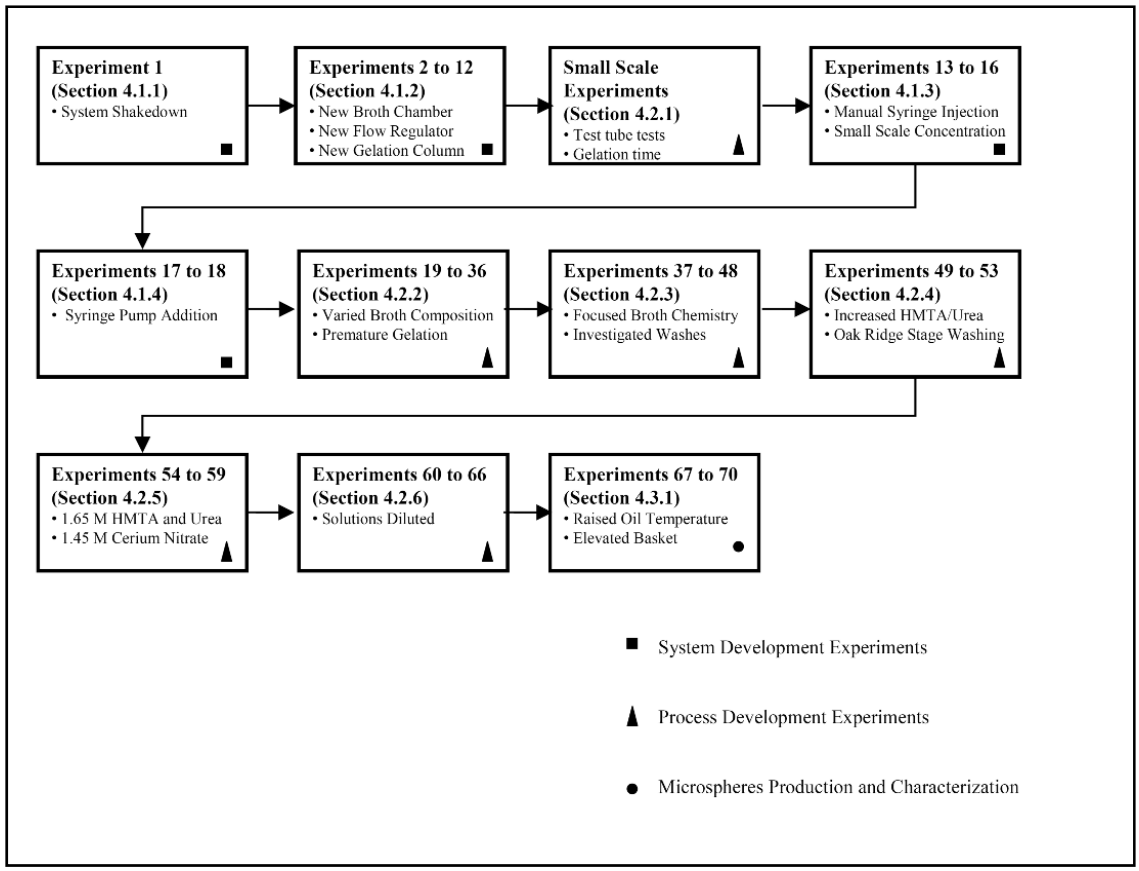

Figure 7. Chronological flowsheet of system and process experiments.

4.1 System Development Experiments

Experiments 1 to 18 were all performed to gain understanding of microsphere production and to establish the proper system components to enable that production. Throughout these tests, the sol-gel system evolved and the equipment changes mentioned in Section 3 were implemented as systematic flaws were discovered or to simplify operations.

4.1.1 System Shakedown (Exp. 1)

The first experiment used an experimental apparatus that only slightly resembles the system used in later runs. The oil reservoir was a steel pan suspended in a NesLab constant temperature bath. A glass separatory funnel was used as the broth chamber with forced air provided by a gas tank regulator. The microsphere catch basket was a sheet of stainless steel mesh (250 x 250 wires per inch) folded into a funnel shape that was placed over the steel pan reservoir.

For this experiment the constant temperature bath was set to 110^{o}C and the oil flowing through the system was maintained at 90^{o}C. The broth composition was 1.3 M cerium nitrate, 1.68 M HMTA, and 1.68 M urea and the total broth volume was 75 mL. The solutions of HMTA/urea and cerium nitrate were kept separate and chilled in an ice bath while the oil in the system was rising in temperature; before being poured into the broth chamber, the solutions were combined and stirred.

When the 18 gauge needle (0.838 mm inner diameter) was inserted into the tubing and the stopcock opened, no broth was initially injected into the system so the pressure on the regulator was increased until injection occurred. After a short time, a gelled substance began to form in the mesh funnel that eventually began to limit drainage flow. To counter this, the speed of the pump was manually adjusted until all of the broth had been injected and drainage flow was stabilized in the funnel. After 10 minutes of aging it was noted a gel surface had also formed on the bottom of the oil reservoir. After an hour of aging, the material in the funnel never fully gelled and a solid yellow crust formed on the bottom of the reservoir.

4.1.2 System Modification Tests (Exp. 2 to 12)

Several system changes were made after experiment 1. The first change made was the replacement of the oil reservoir and redesign of the catch basket. The second change involved replacing the broth chamber and air pressure regulator. Finally, the gelation column was added to allow a volume of slow, non-turbulent flow for the broth droplets to flow through while undergoing the gelation process.

Experiment 2 used the same broth composition, volume, and flowing oil temperature as experiment 1. Initially, a pressure of 4 psi was used to inject the broth but this was increased to 4.5 psi as broth was not flowing out of the broth chamber. Once this pressure was reached the broth was forced out too quickly and produced a result that initially looked similar to experiment 1. Examining the product after it was allowed to age and dry showed that it maintained its globular form rather than being a powder. Experiment 3 netted a product similar to experiment 2 using an injection pressure of 3.75 psi before the needle became clogged; a representative photo of the product is presented in Figure 8.

Figure 8. Photograph of product obtained from experiment 3.

For experiment 4 a system was developed to keep the broth chilled up to the point of injection in an attempt to overcome the clogged needle that had occurred in experiment 3. The same chemistry was used with an initial pressure of 3.75 psi that was increased to 4 psi until the nozzle on the broth chamber became clogged preventing any air from forcing broth into the system. Before clogging occurred, small white flecks were observed flowing from the output hose into the catch basket. After drying, these flecks were observed to be several gel spheres of varying size. Experiment 5 produced

nearly identical results of white specks in the output stream before the flow was clogged. It appeared, on inspection of the broth delivery system, that the broth was frozen around the metallic parts in the system. This prompted the replacement of the metal ball valve and nozzle with plastic.

For experiment 6, the injection ice bath was removed to prevent broth freezing. Before the needle was inserted into the oil line, the ball valve was opened to initiate flow before insertion to allow the broth to be flowing out of the needle as it is inserted into the tubing. A pressure of 4 psi was used initially, although this was determined to be too high as a mixture of gel globs and spheres were produced. Experiment 7 used the same conditions as 6, but with an injection pressure of 3.75 psi that enabled slow-flowing broth injection. After injecting 15 mL of solution, the product in the basket evolved into more of a thin film rather than spheres.

Experiments 8 and 9 explored minor variations in the broth composition by increasing the concentration of HMTA and urea. The product in experiment 8 initially appeared to be large spheres and after pulling the catch basket from the oil the spheres on top looked to have aged more and to be in a more stable form than those on the bottom. After washing, many of the spheres seemed to break down but many gelled spheres were still observable. During experiment 9 the oil backed up into the injection system at first so the pressure was increased to nearly 6 psi. This released in too much broth being released at once and created a sludge-like surface on the bottom of the catch basket.

Experiments 10 to 12 were the first tests performed using the gelation column described in Section 3.1.2, although the forced air system and broth chamber were still used. It was evident during experiments 10 and 11 that the air flow system was forcing the broth out of the injection system too fast and agitating the oil. Problems also persisted with the broth freezing or gelling early in the line leading up to the point of injection. Experiment 12 was the final run carried out using the forced air system and broth chamber. A pressure of less than 0.5 psi was used but the broth was still being injected too fast for spheres to be formed with a consistent, reproducible geometry. At this point, the system development was put on hold while a series of small scale process development tests were performed to determine the broth composition that would produce fastest gelling spheres (the results from these tests are described in Section 4.2.1).

4.1.3 Syringe Insertion: Manual Injection (Exp. 13 to 16)

Following completion of the small scale tests (Section 4.2.1), the forced air system was removed and a syringe was used to manually inject the broth into the tubing rather than the forced air system. Experiments 13 to 16 were all performed with a 2.13 M solution of HMTA and urea and a 1 M solution of cerium nitrate, as this was the fastest gelling concentration found through the small scale tests. The oil flowing through the system was 100^{o}C, as measured before flowing into the gelation column. However, the needle size was varied to explore differences in sphere formation. Experiments 13, 14, 15, and 16 used 18, 30, 24, and 24 gauge needles respectively (corresponding to 0.838, 0.140, and 0.292 mm inner diameters). In experiment 16 the needle was placed in

the freezer in an effort to prevent clogging by not allowing the broth material to increase in temperature until it is injected into the stream of oil. Experiments 13, 15, and 16 all produced spheres that were able to be aged and washed with hexane and a 0.1 M solution of ammonium hydroxide. All were placed into an 80^{o}C oven overnight to expedite the drying process. Upon examination the next day, those from 15 and 16 appear to have crumbled during the drying process, while 13 remained in good shape (Figure 9). No spheres were produced from experiment 14 as the needle became clogged and only a coating of unformed gel material was obtained.

The spheres produced during experiments 13 through 16 were of varying sizes due to the uneven manual injection rates. When injected too fast, either large spheres or unformed gel was produced.

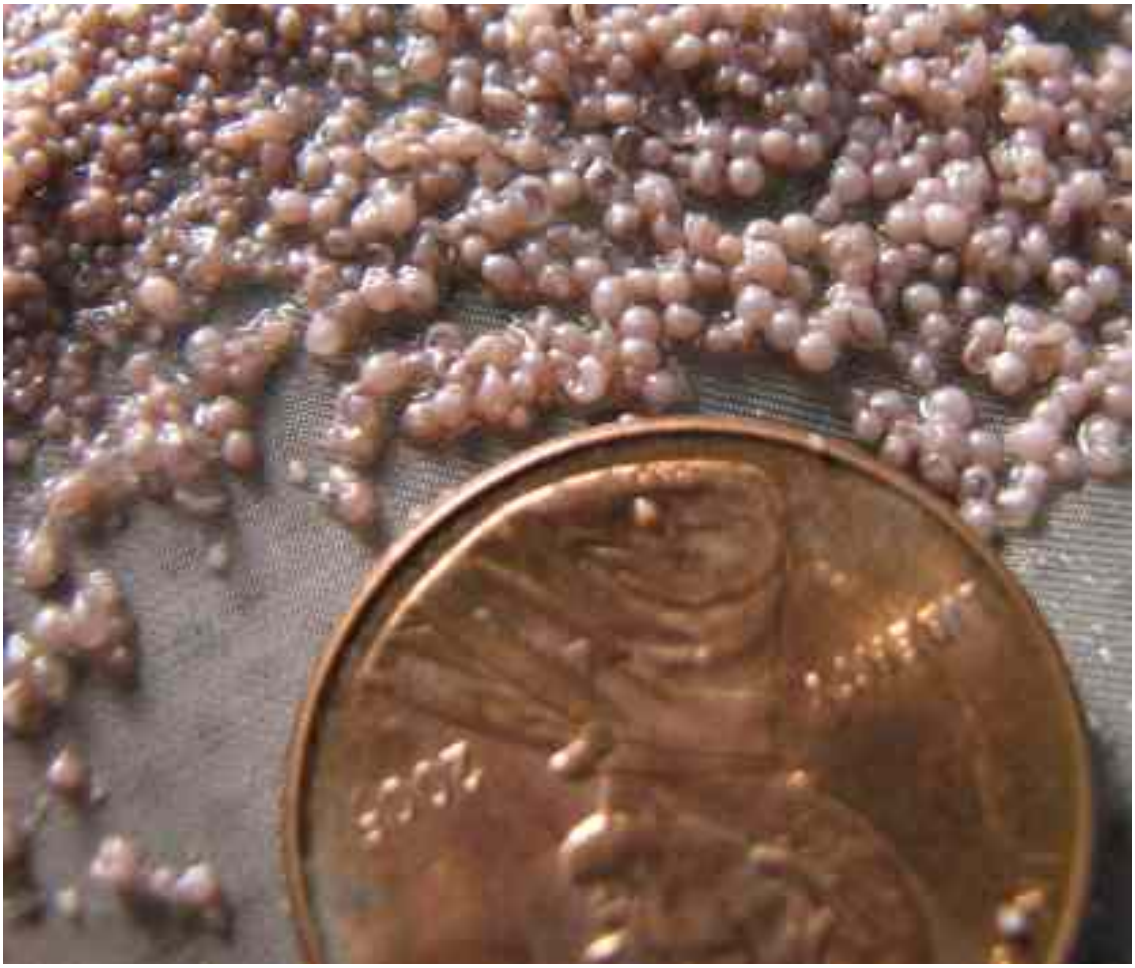

Figure 9. Photograph of product obtained from experiment 13.

4.1.4 Syringe Insertion: Automated Injection (Exp. 17 and 18)

The automatic syringe pump was added for experiment 17 and 18. The syringe pump was added to inject the broth into the oil at a constant rate and avoid the problems of inconsistent sphere size that occurred in Section 4.1.3. By using the pump, a steady slow injection rate could be obtained. This also allowed the attention of the operator to be focused elsewhere.

The same broth composition and washing procedures from experiments 13 to 16 were used (2.13 M HMTA and urea and 1 M cerium nitrate), as various chilled needles and injection rates were used on the syringe pump. During the course of the run the pump would be stopped and a new needle added for testing. A 26 gauge needle (0.241 mm) and an injection rate of 0.2 mL/min was finally decided upon and used for a majority of the run. Also tested were needles of 22 and 24 gauge (0.394 and 0.292 mm) and injection rates between 0.15 and 0.33 mL/min. The spheres produced were washed in hexane then in 0.1 M ammonium hydroxide. Experiment 18 used the same broth, temperature, and washing parameters as 17, although with a varied injection rate and only a 26 gauge needle.

Both experiments produced a large number of spheres that were free flowing when removed from the oil rather than fixed in place. When examined the next day after being placed in a 40^{o}C oven, the spheres from both appeared to have either popped or crumbled.

At this point, the system evolution was complete and the remaining experiments were focused on the process chemistry. The system remained relatively unchanged for the rest of the experiments.

4.2 Process Development Experiments

This section describes the series of small scale tests completed between experiments 12 and 13 as well as the process development experiments numbered 19 through 66. The focus of this section is on the development of optimum processing conditions to produce solid cerium oxide microspheres. The process variables that were

studied include the broth concentration, oil temperature, aging time, and washing conditions.

4.2.1 Small Scale Internal Gelation Experiments

Between system development experiments 12 and 13, a series of 38 small-scale process development experiments were performed in test tubes using small quantities of HMTA, urea, and cerium nitrate to quantify the gelation time as a function of broth composition. All test solutions were taken from the stock solutions prepared with concentration of 3.2 M HMTA and urea and 3.0 M cerium nitrate. The test tube solutions were prepared containing 1 mL of 3.0 M cerium nitrate and between 1 and 2.1 mL of 3.2 M HMTA and urea. This corresponds to a volume ratio of HMTA and urea to cerium nitrate of 1 to 1 and 2.1 to 1.

Once the solutions were mixed, the test tubes were immediately placed in a beaker filled with silicone oil heated to 100^{o}C and the solution was stirred until gelation occurred. The time to gelation for these experiments was defined to be when the solution fully underwent its color change to white. All data from the series of tests is listed in Appendix B. A trend was seen showing that the tests completed with higher volumes of HMTA and urea tended to have a shorter gel time per milliliter of solution present (Figure 10). The ratios shown in the plot correspond to volume of HMTA and urea within the test (both the same), and dividing it by the volume of cerium nitrate.

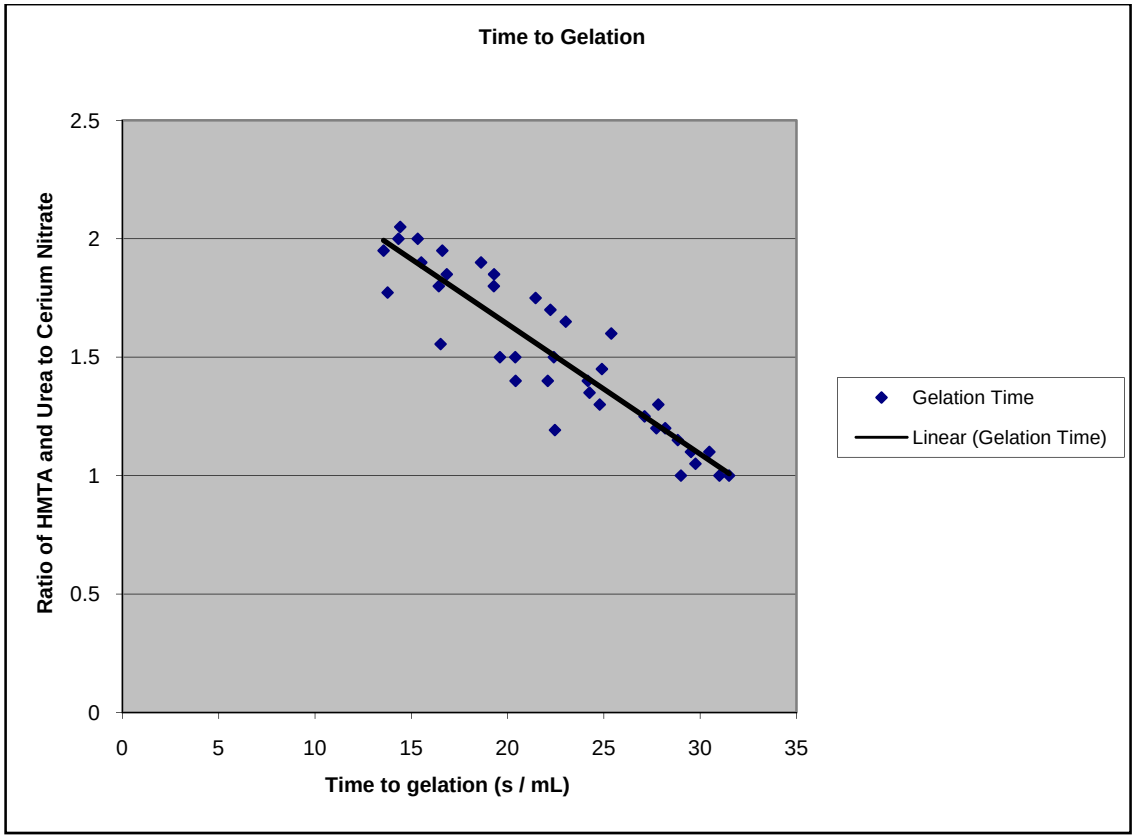

Figure 10. Plot of broth concentration versus time to gelation.

From the data in Appendix B and Figure 10, an HMTA+urea to cerium nitrate volume ratio of 2 to 1 was selected because of the rapid gelation time. This ratio corresponds to a broth concentration with 2.13 M HMTA, 2.13 M urea and 1 M cerium nitrate. This concentration was used to prepare a small solution that was loaded into a syringe and manually injected into the gelation column; the result was that if injected slowly enough, spheres were formed. Approximately 5.5 mL of solution was injected and, after being allowed to age, many noticeable spheres were formed with a small amount of unformed gel material connecting them. This was the first manual syringe

test and it was followed by the system development tests described in Section 4.1.3. From these small scale tests and the introduction of the syringe insertion method, it was possible for the system development stage (Section 4.1) to near its end and begin the process development.

4.2.2 Chemical Feed Variations (Exp. 19 to 36)

Experiments 19 to 36 were carried out to evaluate the impact of varying the broth concentrations to determine the composition of broth that would produce solid spheres when fully washed and dried. In addition, the temperature of the broth was altered, various needle sizes were used, and aging times were varied. It was observed that needle contamination was an important issue; needles not entirely cleaned clogged prematurely. The test conditions for this series of experiments are laid out in Table 1. From these tests, it became evident that increased levels of HMTA and urea produce spheres that are already cracked when removed from the oil. (The practice of placing the broth into the freezer before the experimental run rather than just using an ice bath was also started in the experiments described in this section.)

Table 1. Conditions for experiments 19 through 36.

Exp.	HMTA/Urea Conc.	Cerium Nitrate Conc.	Oil Temperature (^{o}C)	Needle Size (ga)	Aging Time (min)
19	1.92 M	1.2 M	100	26	20
20	1.78 M	1.33 M	100	26 (f)	15
21	1.68 M	1.43 M	100	24	15
22	1.78 M	1.33 M	100	24 (f)	30
23	1.78 M	1.33 M	100	18	30
24	1.68 M	1.3 M	100	24 (f)	45
25	1.6 M	1.5 M	100	26 (f)	---
26	1.92 M	1.2 M	110	24 (f)	30
27	1.78 M	1.33 M	110	24 (f)	---
28	1.6 M	1.5 M	100	22 (f)	30
29	1.64 M	1.46 M	100	22 (f)	120
30	1.68 M	1.3 M	100	22 (f)	30
31	1.62 M	1.48 M	100	22 (f)	30
32	1.68 M	1.3 M	100	22 (f)	---
33	1.64 M	1.46 M	100	22 (f)	---
34	1.52 M	1.58 M	100	18 (f)	30
35	2.06 M	1.07 M	100	18 (f)	30
36	1.42 M	1.67 M	100	18 (f)	30

(f) connotes that the needle was placed into a freezer prior to the experimental run.

With the exception of experiment 35, performed with a 2.06 M solution of HMTA and urea, all were carried out with 1.92 M solutions or less and all were performed at 100^{o}C except for experiment 27 performed at 110^{o}C. Experiments 19, 20, and 21 involved decreasing concentrations of HMTA and urea and increasing levels of cerium nitrate. The results of all three were then allowed to age for 15 to 20 minutes, washed in hexane, and then in a solution of 0.1 M ammonium hydroxide. The product from experiment 19, after removal from a low temperature oven, appeared cracked with some of the remaining spheres not hollow. While washing the spheres from experiments 20 and 21, the ammonium hydroxide wash appears to break down the spheres and leave a sludge surface on them. After one day, the spheres from experiment 20 were solid while those from experiment 21 were hollow and cracked.

Experiments 22 and 23 were both completed with a cerium nitrate concentration of 1.33 M and a 1.78 M solution of HMTA and urea. Both produced solid spheres after injecting over 3 mL of solution and washing in hexane. When washed in 0.1 M ammonium hydroxide, the product of experiment 22 became cloudy and formed a crud layer. Washing of experiment 23 was terminated after the hexane wash. When examined after drying, the spheres did not appear cracked or hollow (Figure 11). Experiment 24 decreased the HMTA and urea ratio slightly and produced spheres that were free flowing when washed in hexane. The product was then rinsed in water rather than an ammonium hydroxide wash, although the same results were obtained.

Figure 11. Picture of product obtained from experiment 23

Experiments 26 through 31 began another series of decreasing HMTA and urea concentrations while also raising the amount of cerium nitrate. The oil temperature was raised to 110^{o}C in experiment 26 and the product was washed with hexane and water. After drying, the spheres were observed to be hollow, as had been observed in previous experiments. Experiment 28 lowered the temperature back to 100^{o}C and stopped the wash process after hexane. The product obtained had an excess of white unformed gel

that appeared to be formed around many of the spheres. After drying, many of the formed spheres did not appear to be hollow when observed under an optical stereo microscope. Experiment 29 used a further decrease in the HMTA and urea concentrations and a longer aging time of two hours before removal from the oil. The product appeared to be made of spheres of two different colors. The first group was white with a slight pink tint that appeared solid. The second product was a lavender color that cracked and crumbled during the hexane wash, as seen in Figure 12.

Figure 12. Photograph of dried product from experiment 29.

For experiment 30 the HMTA and urea concentration was increased and the resulting product contained more of the white spheres with the crumbly lavender spheres in the minority. Experiment 31 lowered the HMTA and urea ratio to below the level for experiment 29 and obtained a product that consisted of spheres connected by unformed gel. When washed in ammonium hydroxide, the unformed material was partially removed leaving only the spheres connected by unformed gel, shown in Figure 13.

Figure 13. Photograph of product obtained from experiment 31.

Experiment 33 began the practice of placing the unmixed broth into a freezer approximately an hour before being injected into the system. The concentration was the same as experiment 31 and roughly the same product was obtained. Experiment 34 was carried out with a cerium nitrate concentration of 1.58 M and a 1.52 M concentration of HMTA and urea. After 30 minutes of aging, the product contained many spheres connected by unformed gel that remained after the hexane wash. Experiment 35 was performed with a concentration of 2.06 M HMTA and urea and 1.07 M cerium nitrate; this combination was produced by operator error. The product contained unformed gel, white spheres, lavender spheres, and dark spheres already cracked. Experiment 36 was performed with a cerium nitrate concentration of 1.67 M and HMTA and urea of 1.42 M. This experiment was also the first to use baskets made of 80 x 80 wires per inch stainless steel mesh and of a smaller overall size. Results obtained for this run were some spheres with an excess of unformed gel connecting them. After washing in hexane it was discovered that even the new baskets would not allow the ammonium hydroxide to drain during the washing process.

Experiments 25, 27, and 32 were all terminated early as the syringe began gelling before a significant portion of broth could be injected into the system.

4.2.3 Narrowed Broth Concentration (Exp. 37 to 48)

Experiments 37 to 48 were all carried out with cerium nitrate concentrations between 1.44 and 1.46 M with HMTA and urea molarity spanning 1.65 to 1.67 M. From previous results in Section 4.3.1, it was found that the spheres that stood up the best after

being dried came from this range and therefore these conditions were warranted. All tests were performed at 100^{o}C, an 18 gauge needle, and 30 minutes of aging time, as seen in Table 2. Wash conditions for this portion of the experiments were varied. The initial experiments were washed in hexane and 0.1 M ammonium hydroxide. A portion received only a hexane wash after it was discovered the dried product was not cracked and crumbling using this method. The final series underwent hexane a hexane wash and then an ammonium hydroxide varied from 0.5 to 3 M.

Table 2. Conditions for Experiments 37 through 48

Exp.	HMTA/Urea Conc.	Cerium Nitrate Conc.	Oil Temp. (^{o}C)	Needle Size (ga)	Aging Time (min)
37	1.66 M	1.44 M	100	18 (f)	30
38	1.65 M	1.46 M	100	18 (f)	30
39	1.65 M	1.45 M	100	18 (f)	30
40	1.65 M	1.46 M	100	18 (f)	30
41	1.67 M	1.44 M	100	18 (f)	30
42	1.65 M	1.45 M	100	18 (f)	30
43	1.65 M	1.45 M	100	18	30
44	1.65 M	1.45 M	100	18	30
45	1.65 M	1.46 M	100	18 (f)	30
46	1.65 M	1.45 M	100	18	30
47	1.65 M	1.45 M	100	18	30
48	1.65 M	1.45 M	100	18	30

Experiments 37 and 38 were carried out with slight variations of concentrations of solution and identical operating conditions after finding the optimum injection rate for an 18 gauge needle, 0.1 to 0.2 mL/min. Initial examination of experiment 37 showed a wide variety of spheres due to the varying injection rates. After washing in hexane and then a solution of 0.1 M ammonium hydroxide, the product appeared to remain solid.

The spheres were then rinsed with water and placed in a 60^{o}C oven overnight to dry. The final dried product was partially cracked, with a portion of the spheres sticking to each other during the drying process. Experiment 38 started at the lower end of the injection rate span identified in experiment 37 then moved to the middle of that span. When first removed from the oil after aging 30 minutes the spheres are all white in color with a minimum amount of unformed product. After the hexane wash a solution of 0.1M ammonium hydroxide was used that appeared to dissolve a majority of the spheres.

Since it appeared that the ammonium hydroxide wash was breaking down the spheres, the product from experiments 39 through 41 was only washed in hexane. The product obtained from experiment 39 was placed into a warm oven overnight to dry, and when examined the next day had not broken down in any way, shown in Figure 14.

Figure 14. Photograph of product from experiment 39.

Experiment 40 involved a slightly lower HMTA and urea concentration and a needle change was required almost immediately as the first became clogged. The final washed and dried product did not turn out as well as experiment 39. Connecting the spheres was unformed gel that remained after the hexane wash. Experiment 41, using the highest of the HMTA and urea concentrations, obtained a product that was similar to 39. The products from all three of these runs retained a wet, slightly oily look to them,

even after being allowed to dry in the oven. This was caused by too short of a hexane wash or the lack of an ammonium hydroxide wash. Experiment 42 used the same broth concentrations as 38, although the needle clogged quickly and was replaced. After 0.857 mL of broth was injected, the entire syringe began to gel and injection was stopped at this point. During the hexane wash it was discovered there was a hole in the bottom of the basket that allowed all the spheres to escape into the beaker. After the wash was finished, a second wash was then performed using a 3 M solution of ammonium hydroxide. The spheres did not break down during this wash, and after the wash completed the spheres were placed onto a mesh screen to dry.

Beginning with experiment 43, the needles were no longer placed in the freezer after the previous few experiments utilizing this method experienced clogs early in the runs. Experiments 43 and 44 both used a cerium nitrate solution of 1.45 M and a 1.65 M solution of HMTA and urea. After aging 30 minutes, the spheres were found to be of a high quality, appearing like those of 39 (Figure 14). The product from 43 was only washed in hexane, while half of those from 44 were washed in two 40 minutes washes of 3 M ammonium hydroxide. The next day those washed in hexane only remained intact, while the portion washed in ammonium hydroxide appear chalky and were crumbling. Experiment 45 used a broth solution that had been prepared the previous day and kept in the freezer overnight. When injected into the oil solution, the spheres began to gel well down in the column, rather than halfway up as had been observed in previous experimental runs. After 2.5 mL of injection, two needles had become clogged and were replaced by interrupting the experiment. The product was allowed to age for ~30

minutes. After washing in hexane and dried, the product was very sticky with few well defined areas of spheres. The needle clogging and needing replacement contaminated the system and caused the poor quality of the product.

Experiments 46 through 48 comprised an investigation to determine the proper molarity of ammonium hydroxide in the post hexane wash. All three experiments used the same broth concentration as experiment 39, which had the best product spheres from the previous runs (1.65 M HMTA and urea and 1.45 M cerium nitrate). Experiment 46 experienced no clogging and the spheres aged for 30 minutes. Once the hexane wash was completed, half of the product was washed in two consecutive steps of 3 M ammonium hydroxide then rinsed in water. After drying, this product was cracked and crumbling. The products from experiments 47 and 48 were also washed with hexane and then split into two groups for individual washes of varying ammonium hydroxide molarity followed by a rinse in water. The two washes for experiment 47 were 2 M and 1 M for 40 minutes, and experiment 48 used solutions of 0.75 M and 0.5 M for slightly under 40 minutes. One day later, both of the washed products from 47 appeared dry and cracked, and those from 48 appear a mess of material, shown in Figures 15 and 16.

Figure 15. Product from experiment 47 washed in 2 M ammonium hydroxide.

Figure 16. Product from experiment 48 washed in 0.5 M ammonium hydroxide.

4.2.4 Multi-Stage Washing (Exp. 49 to 53)

The next sequence of experiments was performed to further refine the wash procedure. Even though spheres washed in hexane and not ammonium hydroxide were the only ones to remain solid after washing, the lack of a complete wash resulted in unreacted product on the outside and within the spheres. If this is not removed, sintering of the spheres cannot occur. All experiments from this point used catch baskets with the bottom portion produced from 40 x 40 wires per inch stainless steel mesh. This bottom allows complete washing of the spheres within the baskets without the need to remove the product from the basket. This change allowed the ammonium hydroxide wash solution to completely drain during the wash.

After the failed attempts above of washing the microspheres in ammonium hydroxide using a 1.45 M solution of cerium nitrate and a 1.65 M solution of HMTA and urea (Section 4.2.3), changes were made in the concentrations of experiments 49 through 53 in an attempt to find a solution that would withstand washing. These changes are outlined in Table 3, which shows how the concentrations of HMTA and urea were increased within the broth solution. In this series, the spheres were washed with hexane and then washed using several wash stages with varying concentration of ammonium hydroxide.

Table 3. Conditions for experiments 49 through 53

Exp.	HMTA/Urea Conc.	Cerium Nitrate Conc.	Oil Temp (^{o}C)	Needle Size (ga)	Aging Time (min)
49	1.68 M	1.43 M	100	18	30
50	1.75 M	1.36 M	100	18	30
51	1.81 M	1.3 M	100	18	30
52	1.68 M	1.3 M	100	18	30
53	1.68 M	1.43 M	100	18	30

Experiment 49 used a cerium nitrate solution of 1.43 M and a 1.68 M solution of HMTA and urea. After the hexane wash, two consecutive washes of 3 M ammonium hydroxide were performed for 40 minutes each followed by a water rinse. After drying, the spheres crumbled, though some remained intact with an off white color and solid, shown in Figure 17.

Figure 17. Photograph of dried product from experiment 49.

Starting with experiment 50, the 3-stage wash system used at Oak Ridge National Laboratory for UO_2 was implemented [13]. The wash, a three step process for 60 to 75 minutes each, consists of a first wash in a solution of 50% isopropyl alcohol and 50% 1.5 M ammonium hydroxide. The next step is a 0.5 M solution of ammonium hydroxide. The final stage involves a solution of 75% isopropyl alcohol and 25% water [13].

Experiments 50 through 53 were all carried out with slightly raised amounts of HMTA and urea and a lower concentration of cerium nitrate. After aging 30 minutes and undergoing a hexane wash, in the product form experiment 50 did not appear to stick together as they had in previous washes. When dried, the spheres appear cracked and crumbling. The spheres produced in experiment 51 were darker in color than those of 50, and they began breaking down during the first step of the wash. The spheres produced in 52 and 53, after aging for 30 minutes, appeared solid with no visible cracking after the wash process. They were then placed into a warm oven overnight to dry. As with the previous experiments, the dried product was cracked and crumbled into powder, Figure 18 shows the product from experiment 53.

Figure 18. Photograph of dried product from experiment 53.

4.2.5 Constant Broth Concentration (Exp. 54 to 59)

Experiments 54 through 59 were all run with the same broth concentrations used in experiment 39 (Section 4.2.3), 1.45 M for cerium nitrate and 1.65 M for HMTA and urea, which had produced the best dried spheres to this point. These experiments evaluated variations of temperature of the oil, amount of time for aging, and the initial wash steps.

Table 4. Conditions for Experiments 54 through 59

Exp.	HMTA/Urea Conc.	Cerium Nitrate Conc.	Oil Temp (^{o}C)	Needle Size (ga)	Aging Time (min)
54	1.65	1.45	100	18	30
55	1.65	1.45	100	18	60
56	1.65	1.45	100	18	90
57	1.65	1.45	100	18	60
58	1.65	1.45	100	18	0
59	1.65	1.45	90	18	60

Experiments 54 and 55 were completed with an aging of 30 and 60 minutes respectively then washed in hexane. After the full wash process, 54 was placed into a 40^{o}C oven overnight to dry, while 55 was placed in front of a fan for forced convection at room temperature. Examining each of them the next day revealed that the product from experiment 54 was dry and cracked and the product from experiment 55 also appeared dry and crumbling at first. However, under a microscope many of the spheres from experiment 55 were found to be solid with no hollow sections. Experiment 56 was aged for 90 minutes and washed in hexane. After removing from the oil, the spheres did not look to be the same quality as previous experiments. During the second stage of the wash process, 50% solution of 1.5 M ammonium hydroxide and 50% isopropyl alcohol, the basket failed and the spheres were released into the beaker. After the wash step was finished, the spheres were placed onto a screen and placed in front of a fan to dry.

Examining the next day showed the spheres to very brittle with cracking also occurring, shown in Figure 19.

Figure 19. Photograph of dried product from experiment 56.

Experiment 57 was aged for 60 minutes then the hexane wash was skipped in an effort to produce better washed spheres. After the rest of the washing process, the spheres were placed in front of a fan for 15 minutes to dry. The final dried product was cracked and crumbling. The change made for experiment 58 was to allow no aging to

occur after 3.65 mL of solution was injected. The product was immediately washed in hexane for 10 minutes and then underwent the rest of the wash process before being placed in front of a fan to air dry. The next day, it was observed that the product had some dark spheres and some lighter colored ones that appeared to remain solid. Experiment 59 was run at a temperature of 90^{o}C and allowed to age for 60 minutes before being washed in a hexane solution. When removed from the oil there was an abundance of unformed gel present in the basket. Gelation had not occurred until near the bottom of the gelation column, whereas normally it occurred near the halfway point. When gelation does not occur in the column, the droplets do not have an opportunity to gel into a spherical shape before being deposited into the catch basket. During the first stage of the wash process the basket failed, as had happened in experiment 56. After finishing the 60 minute wash, the product was rinsed in water before being allowed to dry in front of a fan. It was noticed when undergoing the first wash stage that most of the unformed gel dissolved when lowered into the wash. The product appeared cracked and crumbling when examined the next day.

4.2.6 Feed Broth Dilution (Exp. 60 to 66)

Experiments 60 through 66 involved the addition of water to the broth solution of HMTA, urea, and cerium nitrate in an attempt to obtain spheres that would better withstand the washing process. This series of experiments was performed with dilution to examine the possibility that the overall broth solution was too strong and dissolving itself during the drying process. For experiments 60, 61, 62, and 66, the same initial

concentrations (1.45 M cerium nitrate and 1.65 M HMTA and urea) were used as in Section 4.2.5, but with varying amounts of water added to dilute the solution.

Table 5. Conditions for Experiments 60 through 66

Exp.	HMTA/Urea Conc.	Cerium Nitrate Conc.	Oil Temp (^{o}C)	Needle Size (ga)	Aging Time (min)
60	1.48	1.29	100	18	30
61	1.42	1.25	100	18	60
62	1.56	1.37	100	18	30
63	1.35	1.05	100	18	30
64	1.65	1.29	100	18	30
65	1.64	1.46	100	18	60
66	1.62	1.42	100	18	30

Experiment 60 used a 1.29 M solution of cerium nitrate and a 1.48 M solution of HMTA and urea and the product was aged for 30 minutes and washed in hexane for 10 minutes. After finishing the 3-stage wash process described above, the spheres were placed in front of a fan to air dry. The dried product appeared mostly dark and cracked, although a portion of the product was better than in previous experiments. Experiment 61 used a broth consisting of a 1.25 M solution of cerium nitrate and a 1.42 solution of HMTA and urea. After injection, the product was aged for 60 minutes and had a large amount of unformed gel when removed from the oil. The product was washed in hexane

and then underwent the full wash where most of the unformed gel was removed during the first step. The finished product was semi-spherical and caked together. Experiment 62 used a 1.37 M solution of cerium nitrate and a 1.56 M solution of HMTA and urea. This product was allowed to age for 30 minutes and then underwent a 25 minute hexane wash before continuing with the rest of the wash process. The final product was a yellowish powder with a few solid spheres scattered throughout, as seen in Figure 20.

Figure 20. Photograph of dried product from experiment 62.

Experiments 63 and 64 were completed with the same initial broth concentrations (1.36 M cerium nitrate and 1.75 M HMTA and urea) before water was added to dilute the solutions. Experiment 63 was run with a solution of 1.05 M cerium nitrate and 1.35 M HMTA and urea. This was originally not meant to be as diluted, however an error occurred during addition of the water. Gelation occurred near the bottom of the column, if at all, for this broth solution. After aging for 30 minutes it was noted that a few spheres were present in the catch basket as well as a large volume of unformed gel. In the hexane wash a portion of the unformed gel broke down, and after the first step of the wash process, it was canceled since all that remained was sludge. The final dried material was just a layer of gel with a few spheres present within. Experiment 64 used a much less diluted solution of 1.29 M cerium nitrate and 1.65 M HMTA and urea. After aging for 30 minutes the product was then washed in hexane. During the first step of the wash process the bottom fell off the basket once again. All steps of the wash process were completed, although for 75 minutes rather than the typical 60. After being dried, the product appeared even more crumbled than usual.

Experiment 65 decreased the amount of HMTA and urea within the solution to below the level used in Section 4.2.5, as this had not been attempted since beginning the full wash system. After aging for 60 minutes it was noticed that in addition to the spheres, there was unformed gel present in the basket. The spheres that were present were oblong and not spherical in shape. The product was washed in hexane and the 3-stage ammonium hydroxide process, where most of the unformed gel dissolved during the first stage. Not many spheres remained after the stage washing, and after being dried

they appeared cracked, but not as crumbling as those from 64. Experiment 66 was the final one performed with a diluted broth solution. When the product was pulled from the oil there was quite a bit of unformed gel present mixed in with the spheres. During the wash process the unformed gel dissolved leaving only the spheres. The dried spheres appeared crumbling and cracked.

4.3 Microsphere Production and Characterization

Over the span of the previous 66 experiments it was observed that the highest quality microspheres were produced from a broth of 1.45 M cerium nitrate and 1.65 M HMTA and urea. Also observed was that if the temperature of the oil is too low, the spheres will not form until near the bottom of the column, generally resulting in the production of unformed gel. The final set of experiments used the ideal broth composition and the final two experiments raised the temperature of the oil above the 100^{o}C that had been common.

Following the completion of the experimental series, a number of analysis techniques were performed on the microspheres. To sinter the spheres and identify the presence of any reaction occurring during the process, Differential Scanning Calorimetry (DSC) and Thermogravimetric Analysis (TGA) were performed to evaluate the mass changes and identify any possible reaction during the heating process. Also, x-ray diffraction (XRD) was used to characterize the crystal structure and identify the phases present in the product microspheres.

4.3.1 Increased Oil Temperature (Exp. 67 to 70)

It was observed previously that the highest quality spheres came from a broth composed of 1.45 M cerium nitrate and 1.65 M HMTA and urea. The final experiments completed, 67 through 70, all used this broth composition. Varied for the experimental series was the temperature of the oil and the aging and wash times.

Table 6. Conditions for Experiments 67 through 70

Exp.	HMTA/Urea Conc.	Cerium Nitrate Conc.	Oil Temp (^{o}C)	Needle Size (ga)	Aging Time (min)
67	1.65	1.45	100	18	30
68	1.65	1.45	100	18	70
69	1.65	1.45	110	18	60
70	1.65	1.45	115	18	60

Experiment 67 did not have any unformed gel when removed from the oil. During the 3-stage washing process it appeared that a large portion of the microspheres were breaking down. The final dried product was cracked and crumbled into powder. Within the dried product, there were a few solid spheres that appeared soft. Experiment 68 suspended the basket above the oil reservoir to ensure equal aging for all spheres. When all the broth was injected, the basket was then lowered into the oil and aged for 70 minutes. After washing and drying, the product was cracked and crumbled into powder.

Experiments 69 and 70 were both performed with higher silicone oil temperatures; 110^{o}C and 115^{o}C respectively. Experiment 26 had been performed with an oil temperature of 110^{o}C, but did not use the broth composition that has been determined to be ideal (1.65 M HMTA and urea and 1.45 M cerium nitrate). Each was allowed to age for 60 minutes, washed in hexane, then underwent washing for 75 minutes in each step of the 3-stage wash process. The final dried product from each was very white and powder like. When examined under a microscope the spheres are solid, but were brittle and crumbled with a small amount of force. Earlier experiments that had produced solid, washed spheres were darker in color, as like those from experiment 56. Product from experiment 69 is seen in Figure 21.

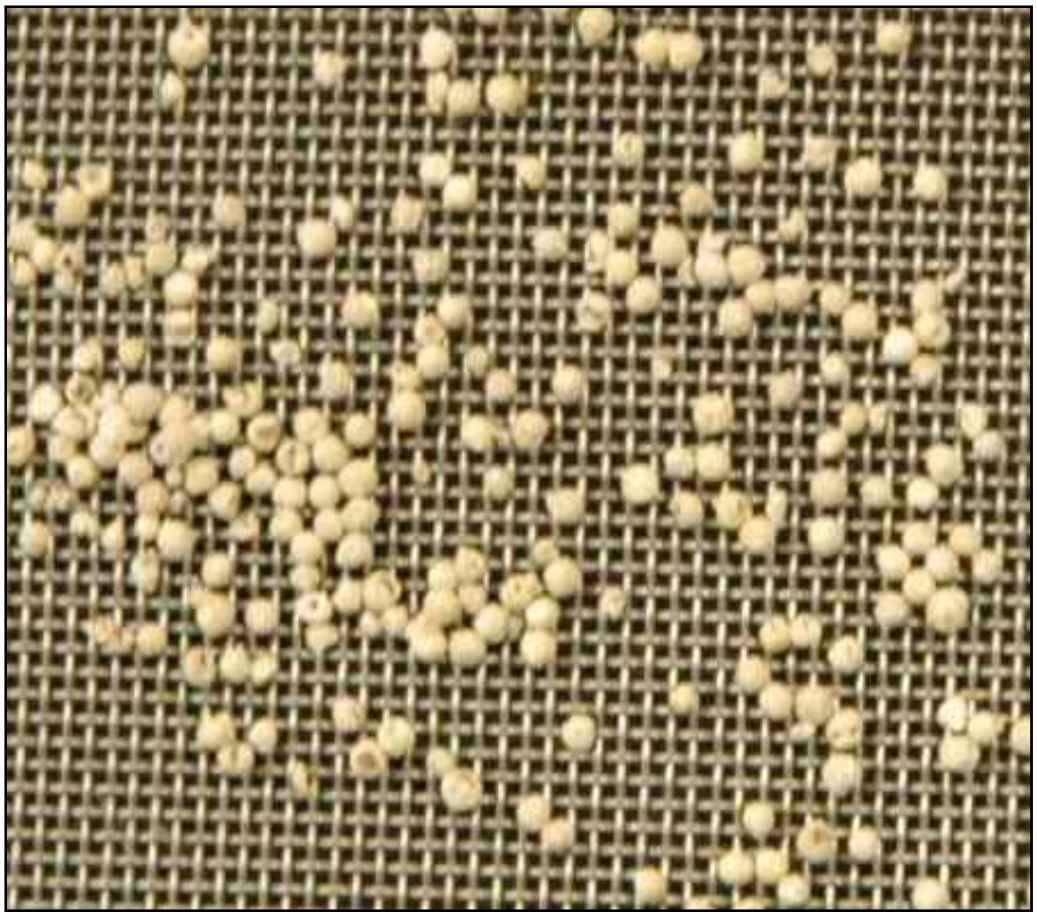

Figure 21. Photograph of product from experiment 69.

4.3.2 Differential Scanning Calorimetry and Thermogravimetric Analysis

One of the analytical needs for the process development experiments was the characterization of the particles after washing and drying to determine the nature of the solid product from the tests. To this end, Differential Scanning Calorimetry (DSC) and Thermogravimetric Analysis (TGA) measurements were made for a select set of product microspheres using a Netzsch STA 409 PC. Table 7 lists the spheres that were analyzed and the principal results. The goal of the measurements was to determine the

thermochemical response to temperature. The DSC measurement involves heating the sample to a set temperature, and then measuring the heat and energy required to heat a reference to the same temperature. As a reaction occurs in the sample, more or less energy is required to keep the reference at the same temperature. The TGA measurement involves using a fine balance to measure the mass change of the sample as it is heated.

Table 7. List of samples analyzed by DSC and TGA methods

Experiment Number	Type of Analysis	Principal Observations
56	TGA to 1400°C	40% mass loss during exothermic reaction 60% overall mass loss
56	DSC to 1400°C	Exothermic reaction observed at ~205°C
69	TGA to 500°C	Initial mass gain ~40% overall mass loss
69	DSC to 500°C	Exothermic reaction begins ~200°C, but not as sharp as experiment 69
69	TGA to 175°C	Small mass gain observed Gradual loss of less than 6% mass
69	TGA to 300°C	Sharp 6% mass loss at 200°C
69	TGA held 300°C	Slight mass loss as temperature held
70	TGA to 1450°C	Quick mass loss of ~15% at 200°C

For the spheres to be pressed into a cermet storage or fuel form, they must first be able to withstand high temperature and sintered to high density. To examine this requirement, a small portion from experiment 56 underwent a mock sintering profile within the Netzsch STA 409 PC instrument. The spheres were heated under an argon atmosphere and the temperature was increased to slightly over 1400^{o}C at a rate of 10 degrees per minute, held there for 30 minutes, then allowed to cool. This heating profile is shown in Figure 22. The product from experiment 56 was chosen since it was one of the first to be have solid spheres produced from the ideal concentration and to complete at least a portion of the 3-stage wash process.

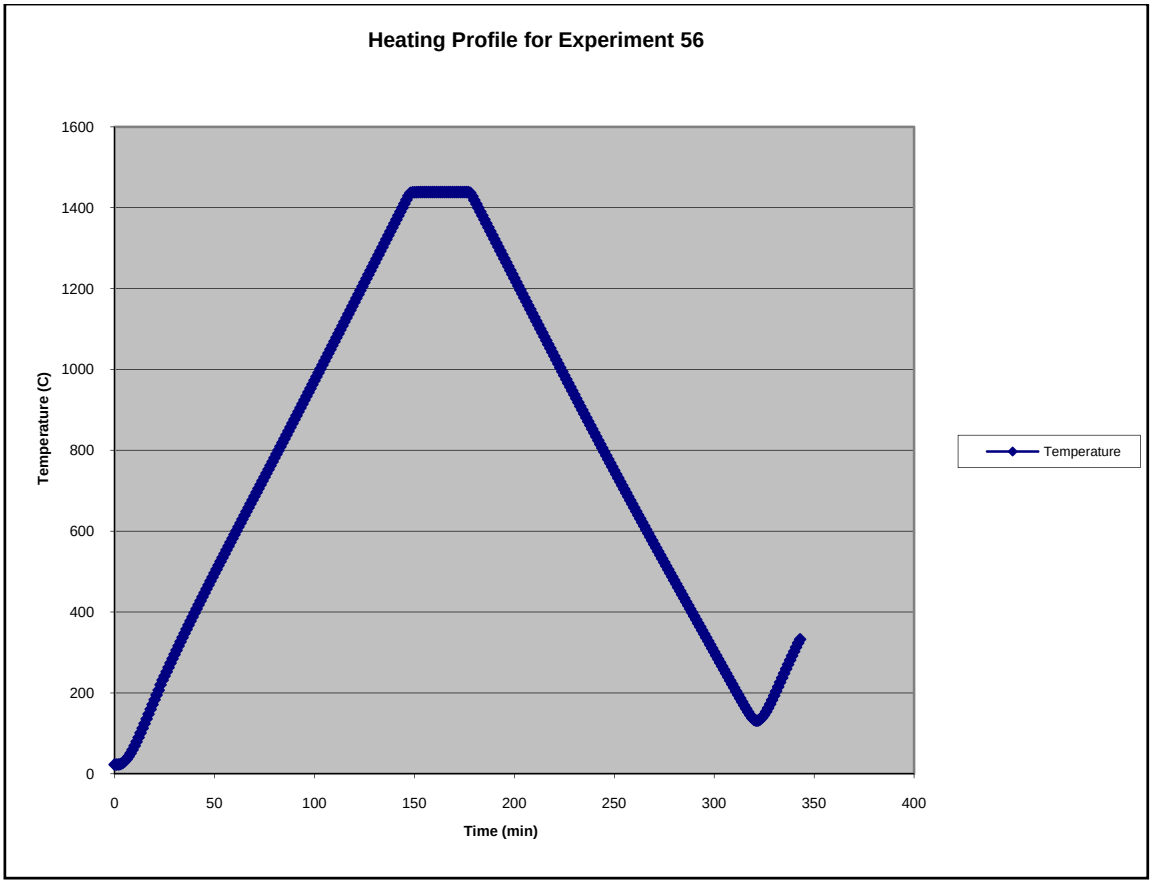

Figure 22. Plot of the heating profile used for experiment 56 sample.

At roughly 205^{o}C, the DSC data indicated that a strong exothermic reaction occurred and the TGA data revealed that the product mass decreased by nearly 40% at that point (Figure 23). Following this, the mass slowly decreased with temperature. After cooling, the product was removed from the system and the spheres had become a fine gray powder. As mentioned previously, experiment 56 was chosen because the spheres were solid and the result seemed to indicate that the washing step was incomplete.

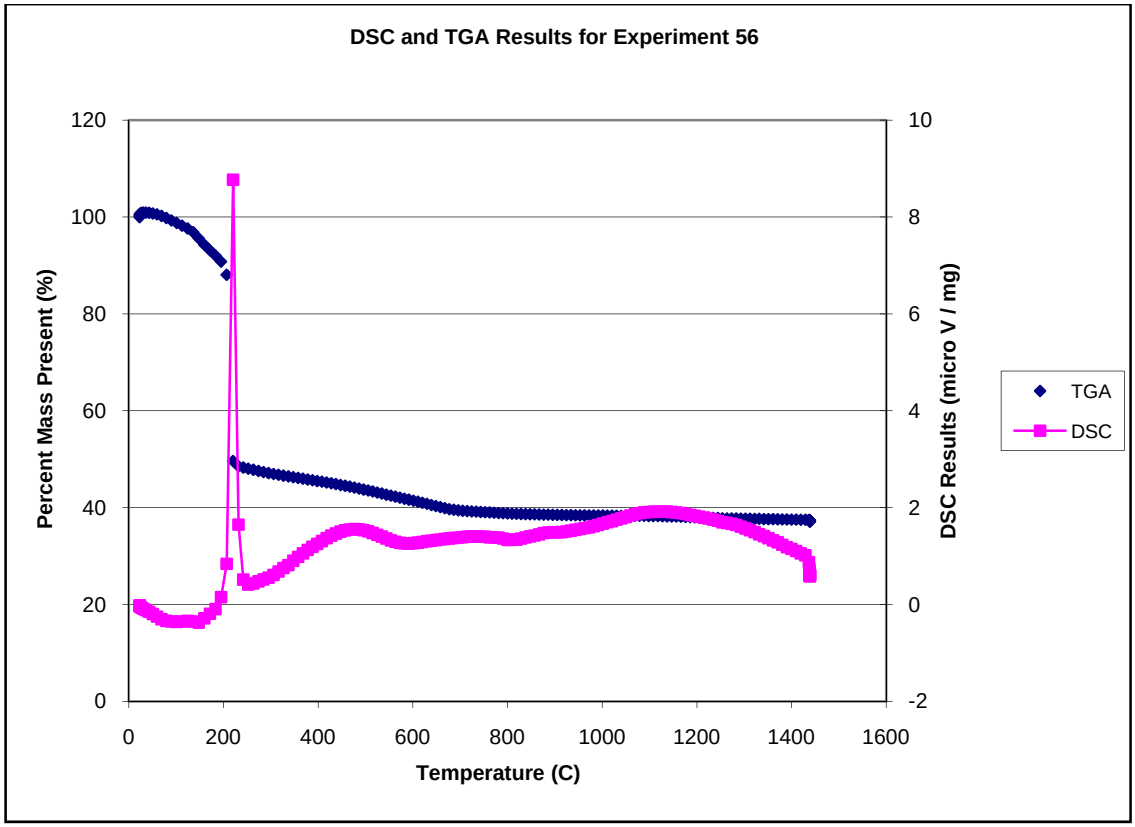

Figure 23. DSC and TGA results for experiment 56.

The second product that was analyzed came from experiment 69. These microspheres were from the final two batches that were well formed, well aged, and well washed. In this test, the DSC/TGA chamber was only heated to 500°C in an argon environment. This temperature was selected because the exothermic reaction occurred at 205°C and the intent of the test was to evaluate the impact of the final optimized processing method on the spheres (see Section 4.3.1 for more detail on the procedures used to generate the spheres. As observed in the previous test, an exothermic reaction was indicated between 200 and 250°C by the DSC trace (Figure 24). In this case the

mass loss was dramatically reduced, indicating that there were fewer leftover reagents in the product spheres.

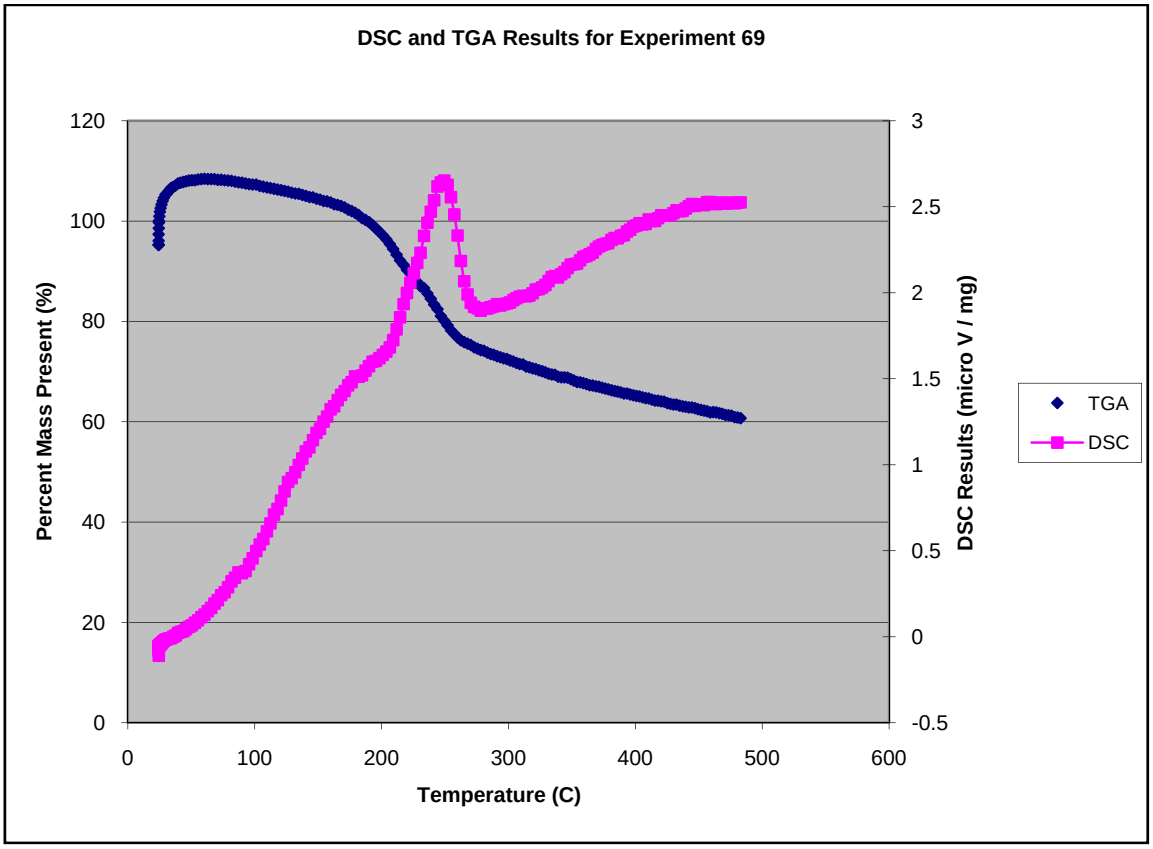

Figure 24. DSC and TGA results for experiment 69.

When removed from the system, the spheres had not swollen and crumbled as they had when product from experiment 56 was tested in the STA. Instead, they had turned from an off white color to a faded yellow, as seen in Figure 25.

Figure 25. Image of spheres from experiment 69 heated to 500^{o}C.

Next, additional product from experiment 69 was used to investigate the nature of the exothermic reaction. The remaining microspheres were split into two batches and separate samples were analyzed using a large TGA sample cup. The first sample was heated to 175^{o}C and held for two hours (Figure 26). The second sample was heated to 300^{o}C (Figure 27). The first of the samples, held below the exothermic reaction temperature of ~200^{o}C, experienced only a small mass loss, ~5%, during the span of its heating (Figure 26). The second sample underwent an exothermic reaction at

approximately 200°C and lost over 12% of its mass in the process (Figure 27). This sample was meant to be heated to 300°C for two hours; however, when this temperature was reached an over temperature safety was thrown and the run was cancelled.

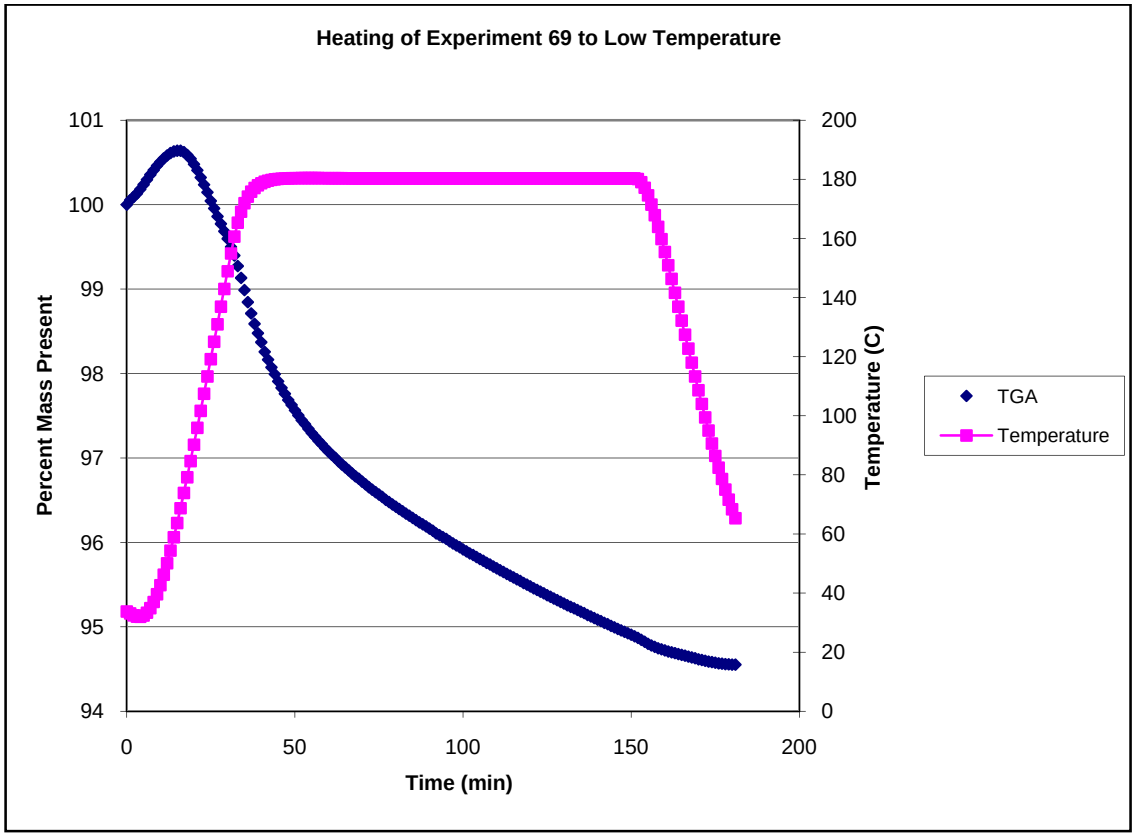

Figure 26. TGA results from heating experiment 69 to below 200°C.

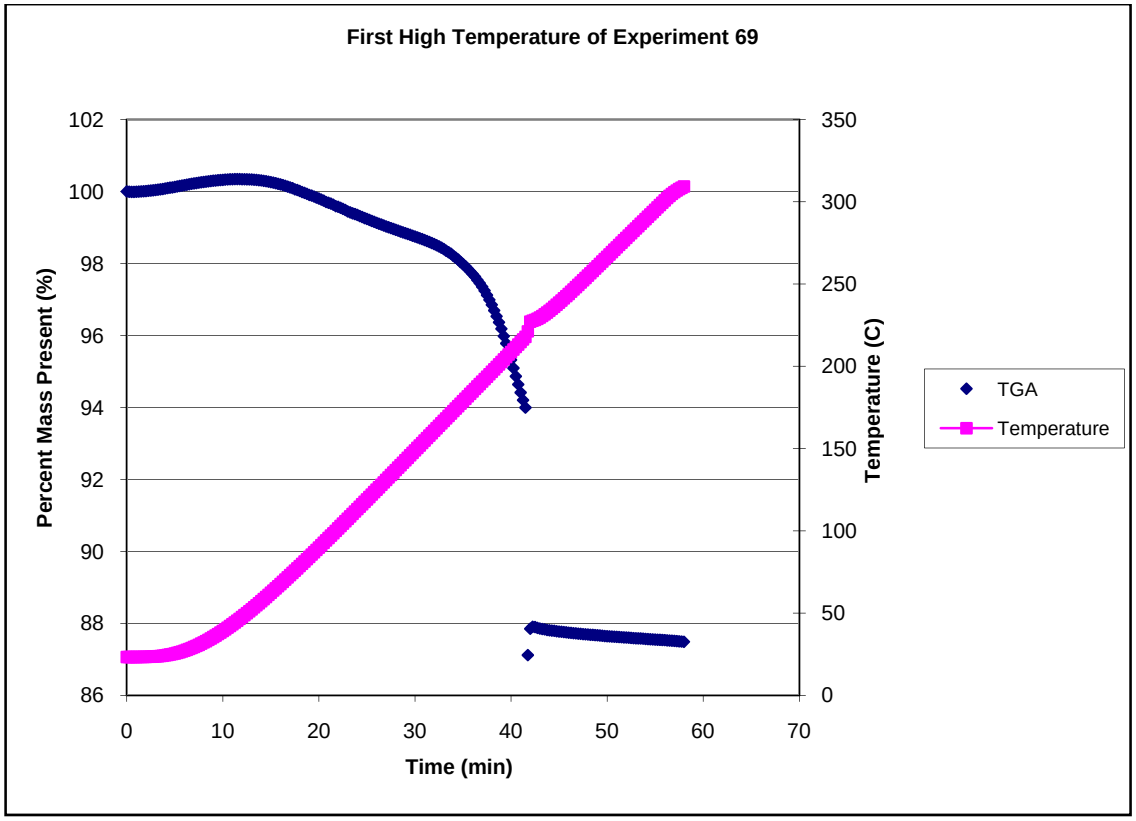

Figure 27. TGA results from heating experiment 69 to 300°C.

When the sample cooled to 210°C the run was reactivated and completed at 300°C for the full two hours (Figure 28). The sample initially gained mass, most likely from being reheated, and the sample proceeded to gradually lose mass as the temperature was held constant, although a much smaller percentage than was observed in the previous runs. When the sample was removed from the system it had turned the same faded yellow color as the small portion that had been heated to 500°C. It is evident from these results that the product from experiment 56 has a significant quantity of volatile reagent left in the spheres whereas the product from experiment 69 had a much lower

amount of this material (but it was still there). The X-ray diffraction data in the following section confirms this observation.

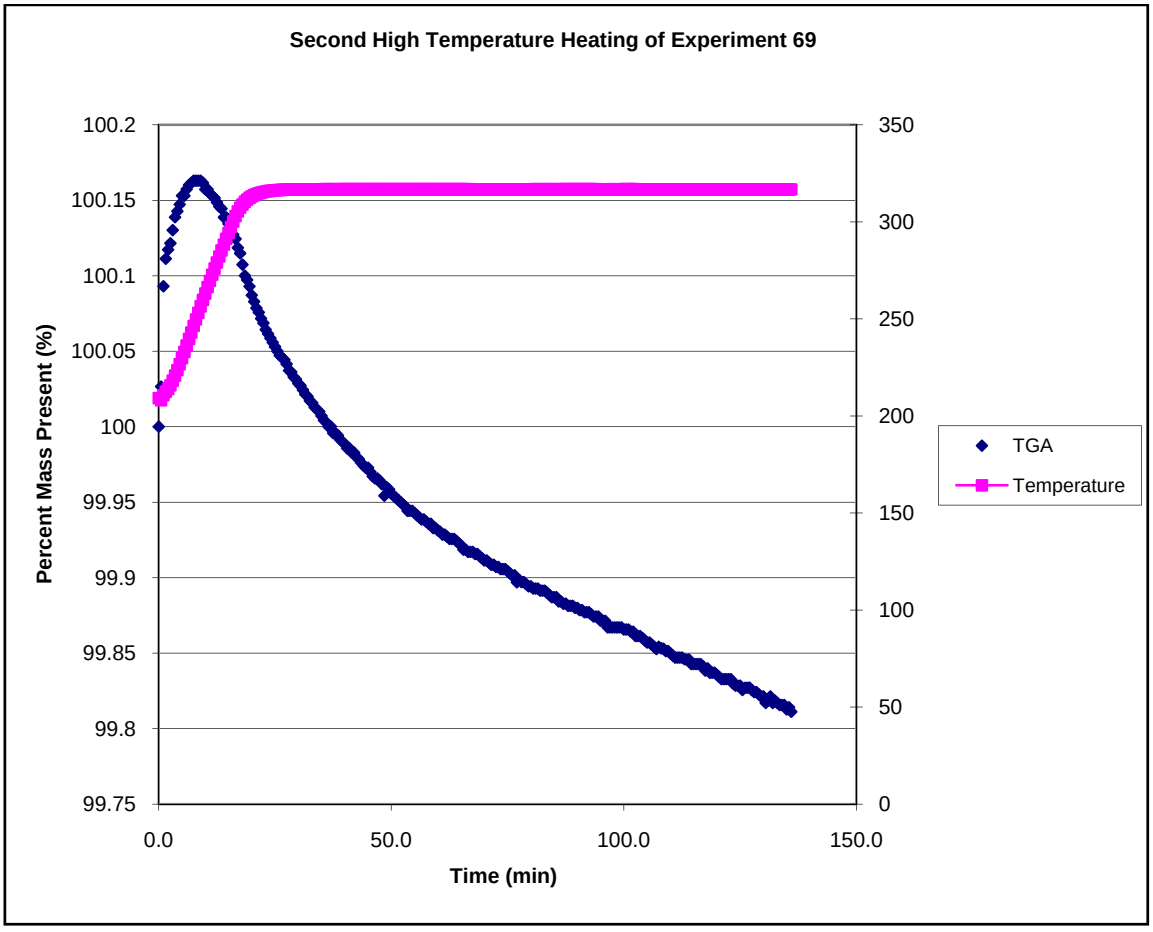

Figure 28. TGA results from holding experiment 69 at 300°C for 2 hours.

None of the spheres from experiment 69 exhibited the same ballooning problem as had affected those from 56, so an attempt was made to take fully washed spheres up to sintering temperatures. However, the entire product from experiment 69 was consumed in the various DSC and TGA trials, so spheres produced from experiment 70

were used instead. The only difference between the two experiments was that experiment 70 was gelled 5°C higher than experiment 69.

The STA instrument was used to sinter a portion of the produce from experiment 70. To do this, the large TGA sample cup was used. The product was heated to 1450°C and held for four hours. Figure 29 shows that the exothermic reaction and mass loss was again evident in this sample at ~200°C. The mass loss was significant, yet not as extreme as seen in experiment 56.

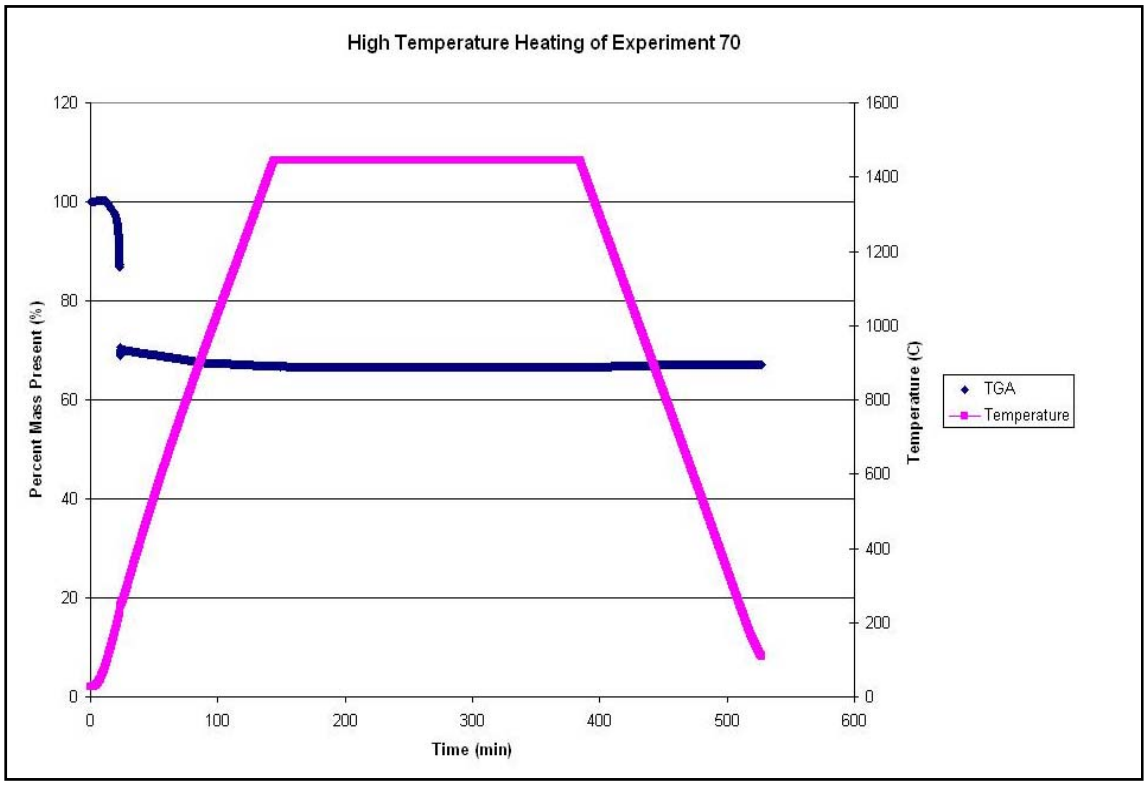

Figure 29. TGA results from sintering of experiment 70.

When the product was examined following the run, no ballooning was seen and the spheres had not turned a faded yellow color. A comparison of the product from experiment 70 is shown in Figure 30. By examining the figure, the non-heated microspheres are roughly 1000 μm in diameter. The sintered microspheres look to be ~500 μm. Both sets of microspheres are brittle and crumble easily. The spheres are solid though, setting the groundwork for future investigation.

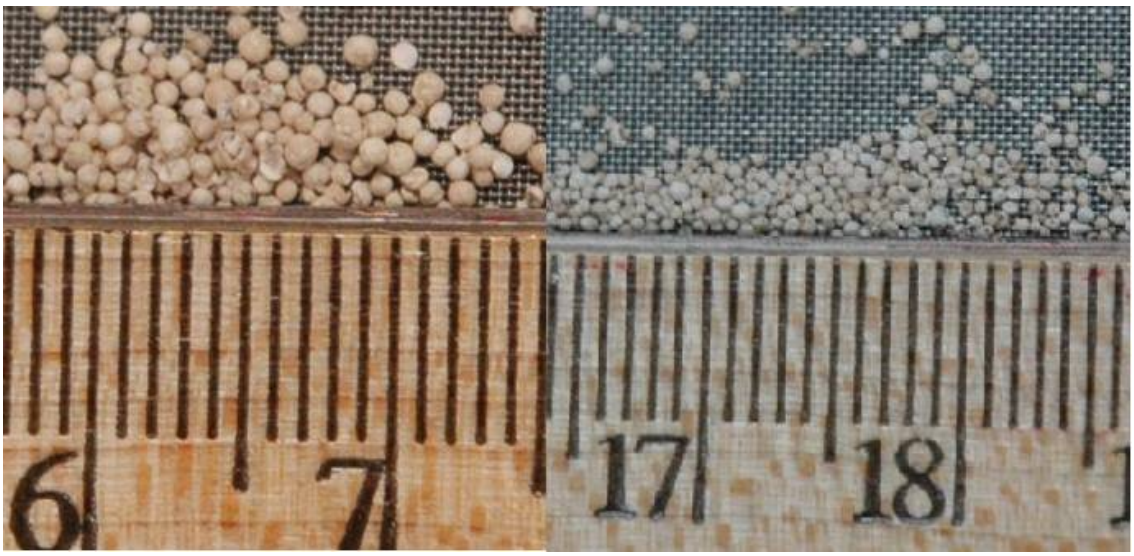

Figure 30. Photo of experiment 70 product; non-heated on left and sintered on right.

4.3.2 X-Ray Diffraction Analyses

To further characterize the sol-gel products from the experiments, X-Ray Diffraction (XRD) analysis was completed on several different products. The very first XRD spectra collected was for the poorly formed product from experiment 1. The gel that became caught in the funnel was washed in hexane and in a solution of 3 M

ammonium hydroxide. The XRD spectrum analysis (Figure 31) shows the product from experiment 1 was primarily cerium oxide or CeO_2. This indicates that even though the solid form was inadequate, the chemical form was exactly what was planned from the very first experiment.

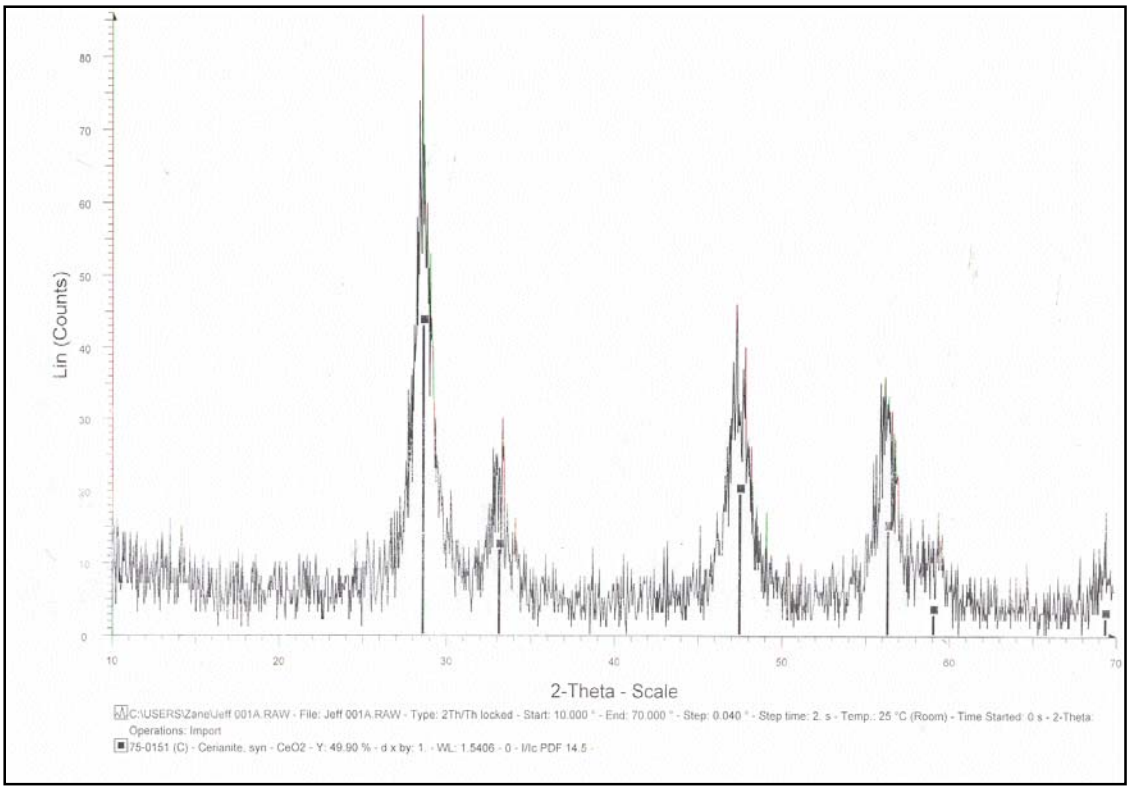

Figure 31. XRD analysis of experiment 1.

The second analysis was performed on the spheres produced during experiment 39. This experiment was the first to obtain solid quality spheres after drying; although only a hexane wash was used. In this case, the XRD analysis was unable to identify the product that was produced, as seen in Figure 32. This spectrum looks like an amorphous

collection of material, so this indicates that either the operator of the XRD system made a significant error during the test setup or the reaction was not complete. The first option is more likely since the reagents and conditions produced a product containing CeO_2 in every other case analyzed.

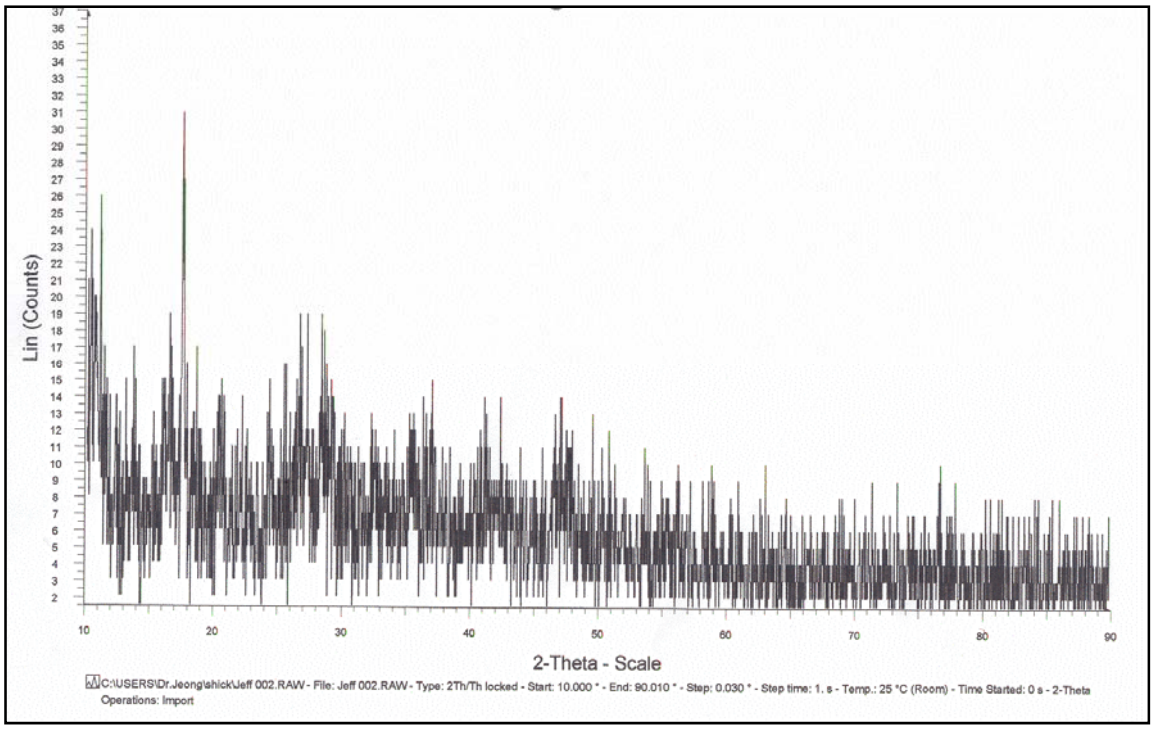

Figure 32. XRD analysis of experiment 39.

Two sets of analysis were performed on the spheres from experiment 56. This product was from the first batch of dried spheres that had been washed in hexane and then underwent a portion of the 3-stage washing process. These spheres, while brittle, were solid and did not dissolve or appear "popped" after drying. The analysis was able to determine that the microspheres were primarily cerium oxide along with an unknown

impurity material (Figure 33). The unknown impurity phase is evident from the minor peak at the 2θ value located between 11° and 12°.

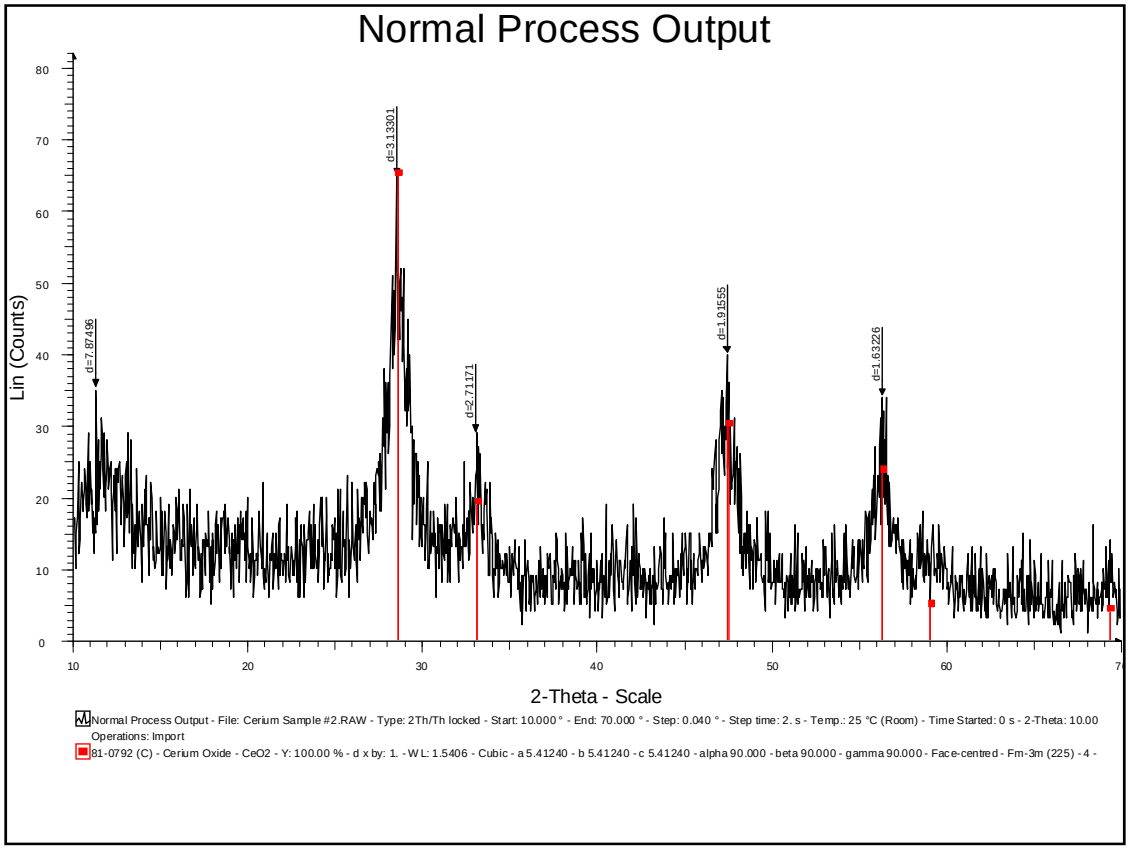

Figure 33. XRD analysis of non-heated product from experiment 56.

A second analysis was performed on material from experiment 56 using a sample that was meant to be heated to 1400°C in the STA to produce a reacted product for XRD analysis; however, at the exothermic range of 200°C the heating program was cancelled due to the evolution of vapor from the system exhaust and an automatic shutdown due to the transient. The product had swollen to several times its original size and turned black.

This was evidently due to the large volume of leftover chemicals within the spheres, as observed in experiment 56 in the previous section. The powder product was analyzed using XRD analysis; the product is shown in Figure 34 to be cerium oxide without the trace impurity phase noted above.

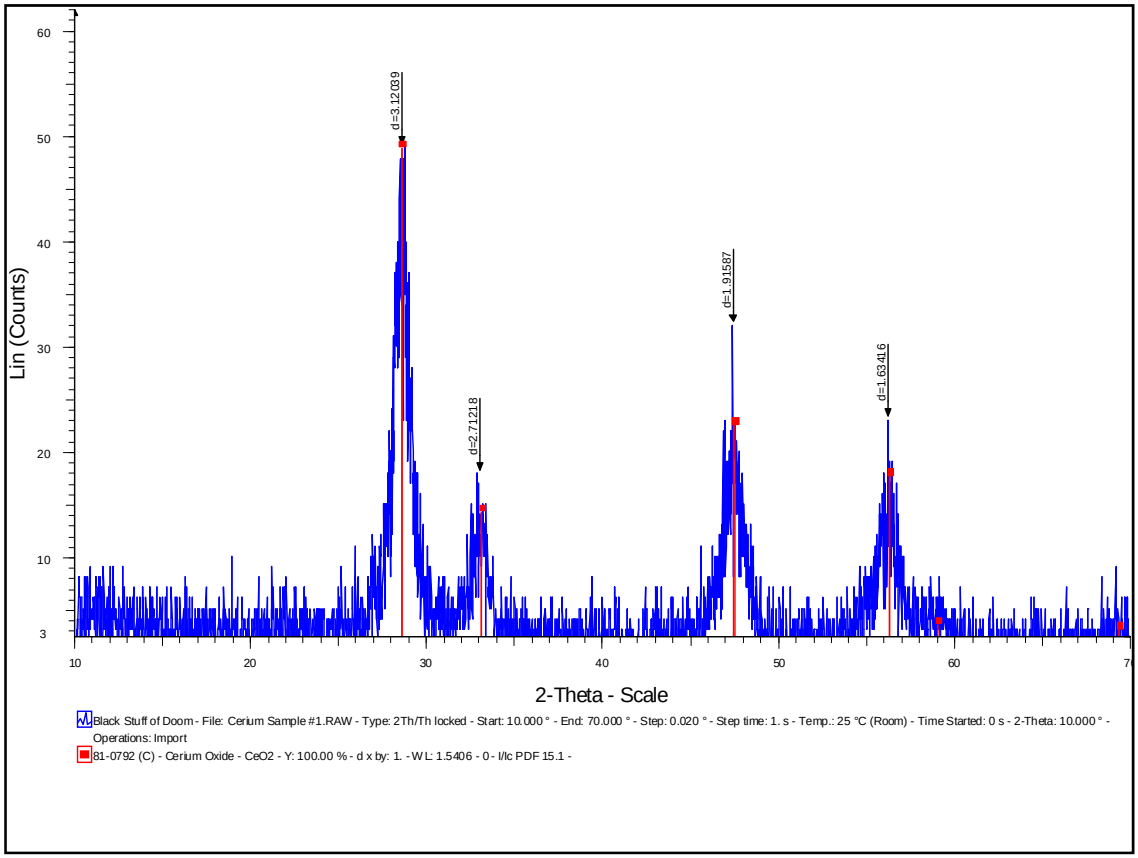

Figure 34. XRD analysis of heated product from experiment 56.

At the end of the process development tests, a number of XRD analyses were completed on spheres produced in experiment 69. The first analysis was carried out on "as-washed" spheres that had not been exposed to any heat treatment. The product was

identified as cerium oxide with an impurity material present as had happened with the unheated sample from experiment 56 (Figure 35). The analysis software selected guanidinium pentacarbonatocerate tetrahydrate as the most likely compound to match the impurity peak, but this was not confirmed by other methods. At the very least it seems that the impurity represents a cerium bearing organic compound that may be exothermically volatile at ~200°C.

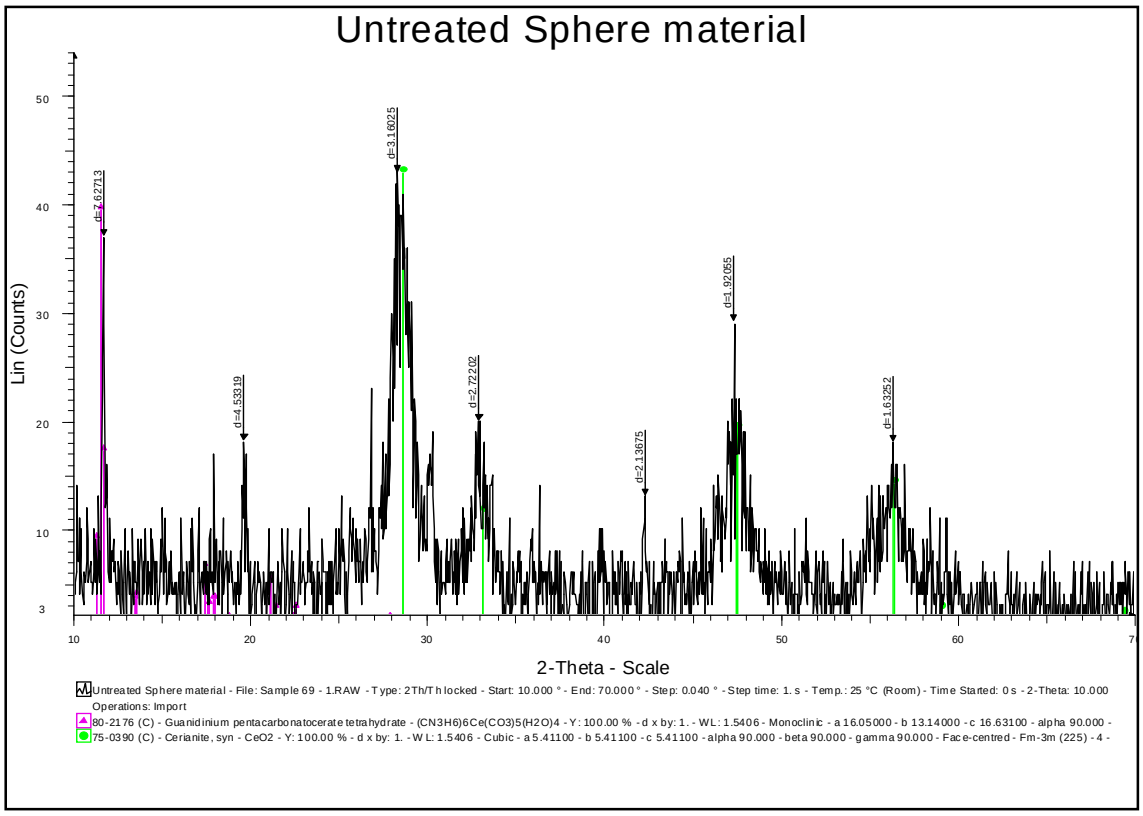

Figure 35. XRD analysis of non-heated product from experiment 69.

The second XRD analysis from experiment 69 was performed on spheres that had been heated to 175°C and then held at that temperature for two hours. The product

was identified as cerium oxide and there was no presence of the impurity that is present in unheated spheres, even though this sample was not taken up to the exothermic reaction temperature (Figure 36).

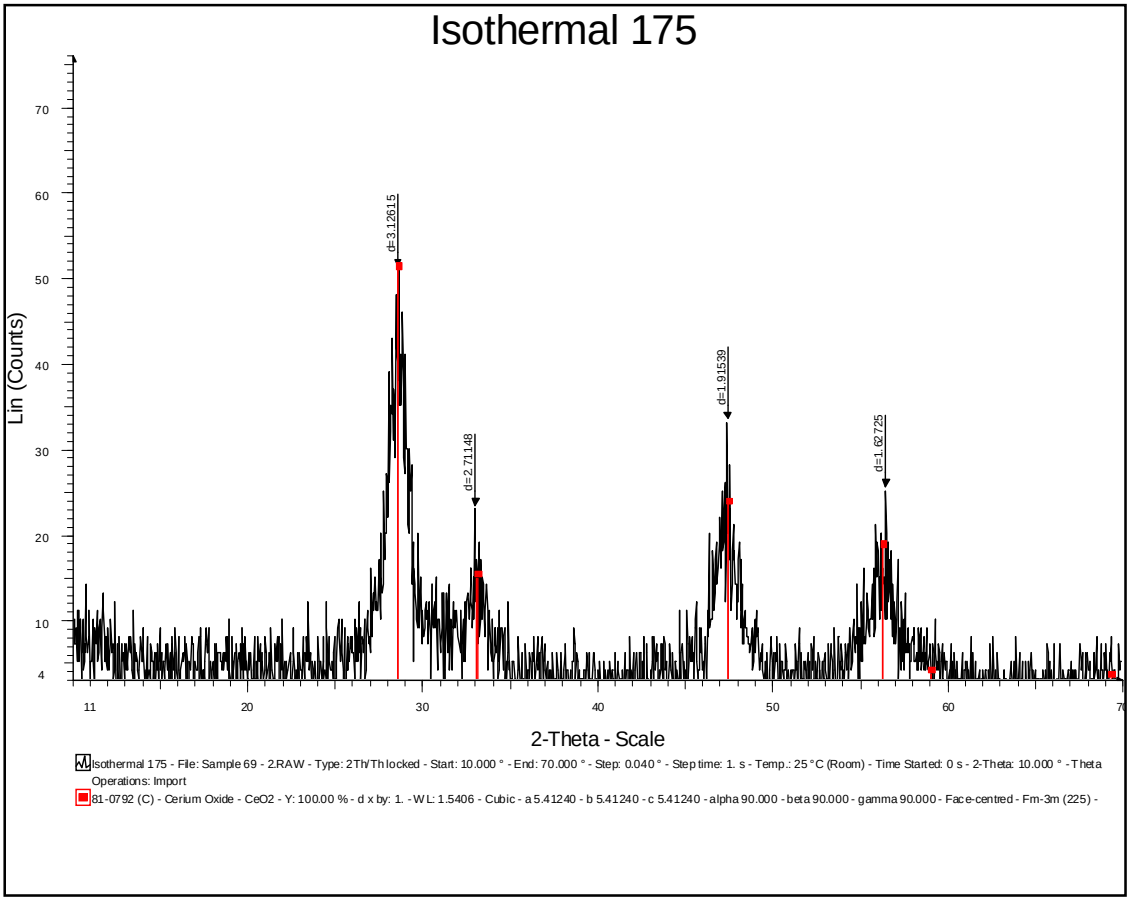

Figure 36. XRD analysis of experiment 69 product heated to 175^{o}C.

The final XRD analysis on experiment 69 was performed on spheres that had been heated at 300^{o}C for two hours. The product was clearly identified as only cerium

oxide (Figure 37), which is the expected result after the impurity is removed during the heating process.

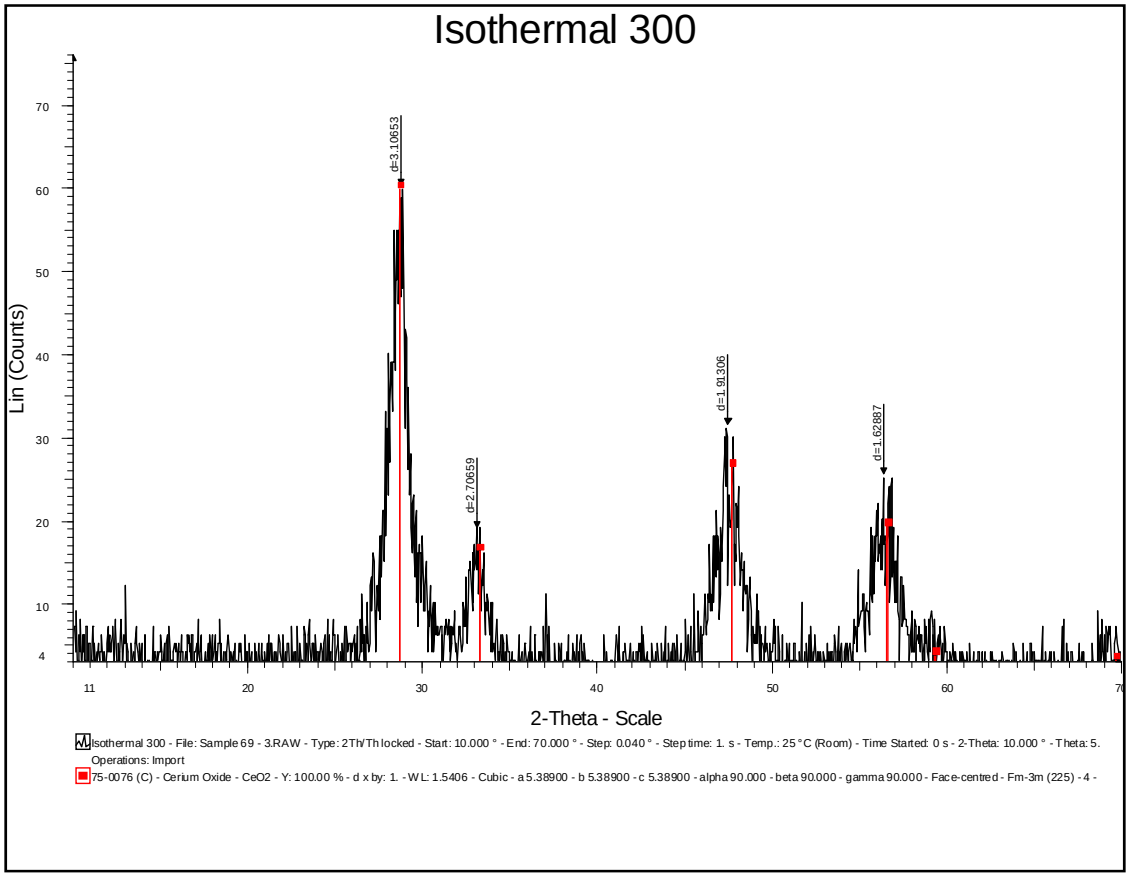

Figure 37. XRD analysis of experiment 69 product heated to 300^{o}.

Finally, two samples from experiment 70 were analyzed by XRD analysis. The first sample comprised as-washed spheres and the product was identified as cerium oxide containing two possible cerium-bearing organic compounds (Figure 38). The second sample was the sintered portion that had been heated to 1450^{o}C for four hours.

This analysis, seen in Figure 39, showed that the sintered microspheres only contained cerium oxide.

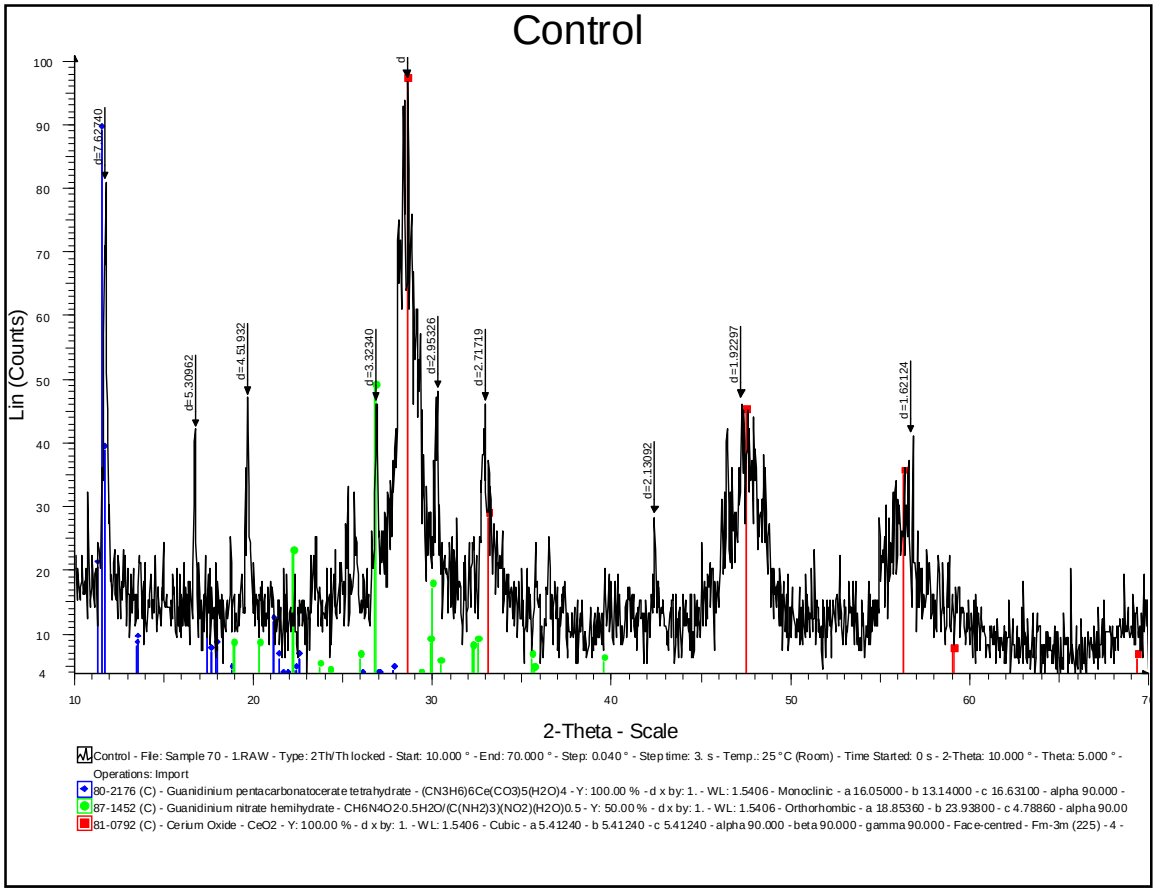

Figure 38. XRD analysis of non-heated product from experiment 70.

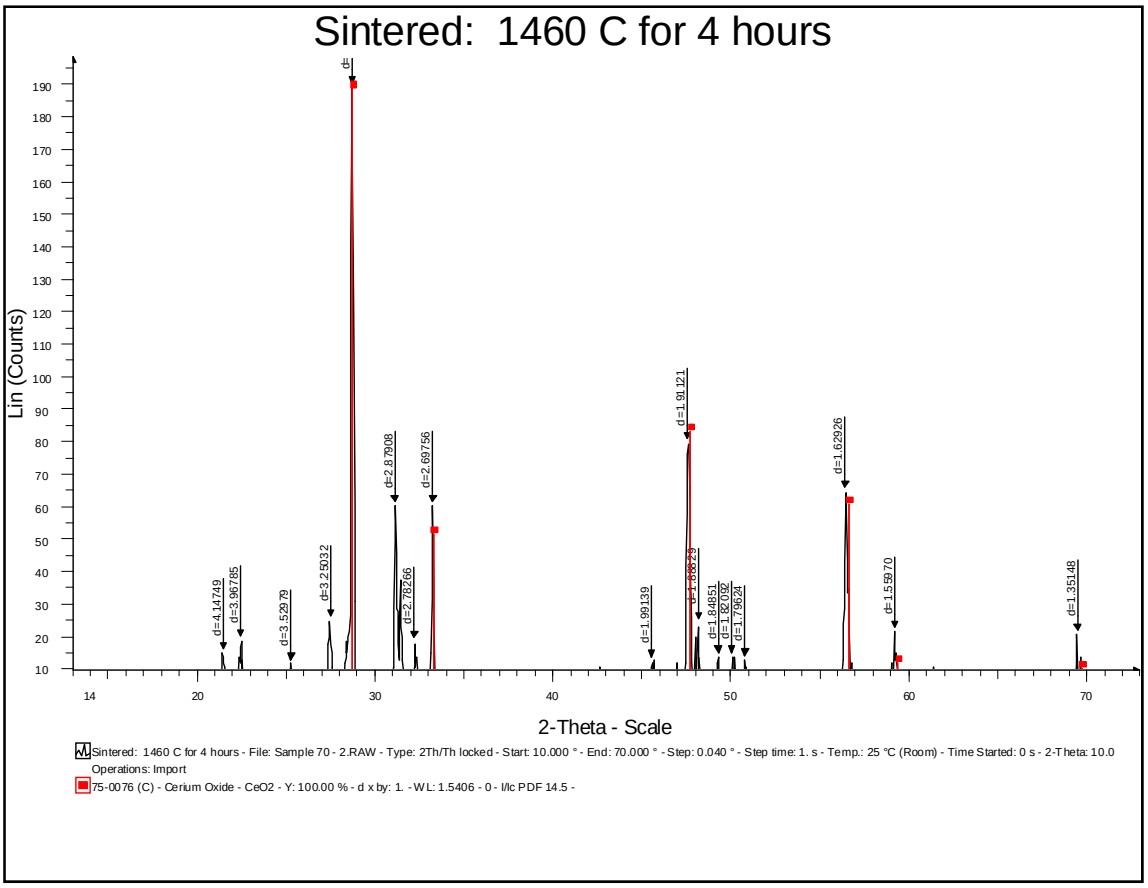

Figure 39. XRD analysis of sintered product from experiment 70.

5. DISCUSSIONS OF EXPERIMENTAL RESULTS

The experiments described in Section 4 were performed to develop and demonstrate a process designed to produce sintered cerium oxide microspheres by an internal gelation sol-gel process. The initial experiments were performed to gain an understanding into the sol-gel process itself and to establish the optimum equipment configuration within the experimental system. Changes were made to the apparatus as the experiments progressed and the later experiments were used to refine the concentration of the broth constituents and the washing procedure to produce the best usable spheres. A total of 70 experiments were completed, using varied concentrations, aging times, wash conditions, and other factors.

5.1 Experimental Observations

The early experimental runs, 1 through 12, all created a mass of unformed gel with few, if any microspheres present. The leading cause of the unformed material was the forced air system that was injecting the broth too rapidly from the broth storage chamber. Most of the forced air broth injections took place with pressures between 4 and 6 psi. While an actual flow measurement was never taken, it was much faster than the 0.15 mL/min used for the majority of the experiments after the syringe pump was installed. Another significant cause of unformed gelation in the early experiments was the absence of the gelation column that was introduced after experiment 9. The column provides a volume of low, non-turbulent flow for the broth spheres to form and to gel. The addition of the column also allowed the visual observation of the sphere gelation

reaction which enabled the operator to adjust the broth injection and silicone oil flow rates as needed.

The first observation after the first 12 experiments was that the composition of the broth may have been the cause behind the failure to create quality spheres. However, it eventually became evident the process procedures and equipment were the true cause of the problem. The 38 small scale tests (Section 4.2.1) revealed that the broth did indeed gel properly and that as the concentration of HMTA and urea is increased compared to the concentration of cerium nitrate, the internal gelation reaction is faster (Figure 10). The fact that the internal gelation reaction was occurring properly was further supported by the XRD data from experiment 1 that revealed that the unformed gel was still cerium oxide and not some other compound.

The small scale tests also showed that the outer shell of the gelled material became harder as the HMTA and urea to cerium nitrate ratio was increased. However, these tests did not evaluate the quality of the gel that was being produced. The increased ratio may have produced a faster gelling material, but later experiments have shown that an increased HMTA and urea level leads to cracked and hollow spheres before washing occurs. Due to the trend shown in those small scale tests, an increased HMTA and urea concentration was used for the next several experiments.

Another point of interest is that during the final small scale tests it was discovered that viable spheres could be produced if a syringe was manually used to inject the broth into the flowing oil rather than using the forced air system and a pressurized broth chamber. Therefore, these initial processing experiments proved to be

very informative. First, the gelation reaction was confirmed and the rate was quantified. Second, the true problem with the broth insertion rate was discovered and the transition was made to syringe injection.

The spheres produced using the manual injection syringe method (experiments 13 to 16) were of non-consistent size and many of the experiments had quantities of unformed gel due to inconsistencies in the manual injection speed. Also in this span, several different sized needles were used with mixed results. It was found that the 30 gauge needle easily clogged and the product was a layer of unformed gel. These experiments also used the same washing method, which consisted of a quick rinse in hexane and then a wash in 0.1 M ammonium hydroxide. When the product was placed into ammonium hydroxide, it appeared that many of the spheres dissolved. Due to the increased amount of HMTA and urea present within those experiments, it is possible that the ammonium hydroxide was causing the breakdown by interacting with unreacted reagents within the spheres.

Prior to experiment 17, the syringe pump was installed. The injection rate was varied slightly during experiment 18 while using a 28 gauge needle showing that the sphere size relied more on the size of the needle used rather than the injection rate over a small range of rates. Due to the inability of spheres to remain intact during washing, the concentration of HMTA and urea was decreased beginning in experiment 19, but the same washing procedure continued to be used. Also, starting at experiment 20 the needles were put in the freezer before the experiment run in an effort to prevent early

gelation. Until other process changes were made, freezing the needle before the experiment enabled more broth to be injected before clogging occurred.

As the amount of HMTA and urea within the broth was decreased, the quality of spheres upon removal from the oil increased. No longer were they cracked with a dark lavender color, instead they were an off white solid that was free flowing on top of the screen. In experiment 22 when the spheres were washed in the 0.1 M ammonium hydroxide solution, rather than breaking down as they had with a higher HMTA and urea concentration, the liquid instead only became cloudy, leaving many of the spheres intact. This indicated that the wash was removing reagents but the gelation process had matured farther than in previous experiments.

Some of the product from experiment 23 that was washed only in hexane was placed into an oven at 160^{o}C, after an undocumented amount of time the spheres had swollen, turned a shade of yellow, and had begun to smolder. The reason for this was likely an abundance of unreacted reagents on or within the spheres. The lack of complete gelation in the early experiments may account for the hollowness of the early product spheres and their breakdown upon washing in ammonium hydroxide.

Experiment 28 was the first test to approach the final 1.45 M cerium nitrate and 1.65 M HMTA and urea concentrations used for a large portion of the experiments. It was also the first test to produce spheres that did not appear hollow after drying; although they only received a hexane wash. Around this time it was noted that if any product began depositing in the syringe during injection, the entire run needed to be stopped, as any spheres produced beyond this point would be of the dark lavender

variety and not be of a good quality. Although the gelation reaction is temperature driven, once it begins it is autocatalytic and consumes the reagents wherever they are regardless of the temperature. Experiments 29 and 30 both provided a significant portion of quality spheres and it was noted that the proper broth concentration was likely to be between 1.64 to 1.68 M HMTA and urea and 1.43 to 1.46 M cerium nitrate. These concentrations bound the combination mentioned previously that consistently produced the best quality spheres. When the concentrations are dropped below these ranges, more unformed gel is produced with fewer spheres. This is likely due to the lack of ammonium being created from the decomposition of HMTA. This leads to some gelation, yet not enough to create a quality microsphere. When the experiments with a low HMTA concentration were washed in ammonium hydroxide, nearly all the unformed gel product dissolved away; leaving very little remaining. This is in contrast to the higher ratios where material does not dissolve, but the spheres are already cracked when removed from the oil reservoir.

After experiment 32 the significance of needle contamination became evident, and it was decided that syringes could not be reused after an experiment regardless of the amount of cleaning they undergo. Experiment 39 was the first of several runs where the spheres were only washed in hexane, skipping the ammonium hydroxide wash. The product from these experiments was solid and did not crack or crumble. Even after being set out to air dry and placed in a warm oven overnight they still maintained an oily, slightly wet feel. This could be a result of too short of a hexane wash or the

presence of unreacted reagents that were not removed with an ammonium hydroxide wash.

Experiment 42 was the final test to use a syringe that had been placed into a freezer before the run, and also the final test to experience early gelation in the syringe; which had been prevalent while using the frozen syringes. Earlier experiments, including those using the pressurized broth chamber, had experienced early gelation, but it was considered to be frozen broth. With this experiment, it became evident that this phenomenon was actually a premature manifestation of the gelation process, just at a slower speed than when introduced into the hot silicone oil. Experiment 42 was also the first to attempt to wash the spheres outside the stainless steel catch baskets and directly in beakers. A 3 M solution of ammonium hydroxide was used for an undocumented amount of time before the spheres were placed onto a section of mesh screen to dry. The resulting product had a chalky appearance, a condition that continued throughout the rest of the experiment runs.

After several attempts at washing with varying solutions of ammonium hydroxide, the standard wash procedure developed at Oak Ridge National Laboratory for UO_2 gelation spheres was implemented after a further literature review. The first stage of the wash consists of 50% isopropyl alcohol and 50% 1.5 M ammonium hydroxide. Stage two involves a solution of 0.5 M ammonium hydroxide, and the final stage is 75% isopropyl alcohol [13]. The ability to do multiple stage washing was enabled by the introduction of baskets with a bottom made from 40 x 40 stainless steel mesh. The body of the baskets remained 80 x 80 mesh until experiment 63, when the entire basket

became 40 x 40 mesh. Initially each step was performed for 50 minutes; however, that was increased to 60 minutes for most of the following experiments.

The first observation from the new multi-stage wash procedure was that the washed spheres did not stick together or to the mesh after washing. The inclusion of isopropyl alcohol in the wash process is the likely reason for this. During the first washing stage any unformed gel present dissolves and leaves only the product spheres behind. Even if no unformed gel is present, some material is removed from the spheres, evidenced visually by the wash solution becoming cloudy during the process. This is likely to be unreacted reagents on the outer surface of the spheres. During the second wash not as much material is removed from the spheres, but they begin a noticeable color change. By the end of the second wash, most of the spheres will have gone from a white color to a darker white with a yellow hue. Also, some of the spheres agglomerate together and some are more likely to become attached to the bottom of the basket or the side wall. No color change was observed during the third wash. However, spheres that stick to each other in the second wash tend to come apart during the third wash. In experiment 62 a magnetic stirrer was implemented during the wash process. It was used intermittently throughout the remaining experiments as various techniques were used in an attempt to elevate the basket above the spinning bar.

From experiment 50 through 59, all materials were allowed to age for a varying amount of time, washed in hexane, then washed using the Oak Ridge 3-stage washing process. When finished, nearly all of the spheres looked to be solid and were not cracked or crumbling. After being allowed to dry, all of the spheres exhibited the dry,

chalky appearance noted above. It was thought that the concentration of active material may have been too high within the broth, so beginning with experiment 60, water was added to the broth solution in an effort to dilute it.

The ratio of HMTA and urea to cerium nitrate was kept consistent throughout most of the next several experiments; just the amount of the diluting water added was varied. Experiment 63 showed that the addition of too much water led to a product that consisted almost entirely of unformed gel. That solution was accidentally diluted to 1.35 M HMTA and urea and 1.05 M cerium nitrate. The resulting product of unformed gel dissolved during the wash process. Experiments 64 and 66, also with diluted broths, obtained no better spheres than those that had not been diluted. From these experiments it was determined that the strength of the solutions was not responsible for the cracked spheres produced during drying.

The final two experiments run, 69 and 70, raised the temperature of the oil flowing through the system and kept the basket elevated above the oil reservoir until the aging process was completed. The temperature was raised due to the variations seen in the gelation speed with different oil temperatures. At lower temperatures, the gelation process did not occur until near the bottom of the column. These tests were performed to determine if higher quality spheres could be produced if the oil temperature was raised. The spheres produced from these runs were solid, although brittle. At this point, the process development was concluded and the final characterization tests were completed. The product from these two experiments provided the majority of the materials analyzed in Section 4.3

5.2 Product Characterization

Products from experiments 1, 39, 56, 69 and 70 were analyzed using TGA, DSC and XRD analysis methods. The product from experiment 1 was confirmed by X-ray diffraction to be cerium oxide (Fig. 31); the ceramic material that was the object of these experiments. Since the form of the cerium oxide product was not spherical, but rather an amorphous blob, the remaining work was focused on generating the desired spherical product (It should be noted as well that approximately 3 months elapsed before the product of experiment 1 underwent XRD analysis). Throughout all of the tests, it is apparent that the internal gelation product was primarily cerium oxide. "Extra" peaks were observed in the unwashed, partially washed, and thermally-processed samples indicating that some leftover reagents or rogue compounds are always present in the washed spheres.

The spheres formed in experiment 39 were the next to undergo analysis. Through XRD, the form of the product was not able to be identified (Fig. 32). After aging, the spheres were washed in hexane and did not undergo an ammonium hydroxide wash. Unreacted product from the gelation process, leftover hexane, or unremoved silicone oil could all be responsible for the inability to identify the product. The spectrum indicated that the product was an apparently amorphous collection of material. As noted, this indicates that either the operator of the XRD system made a significant error during the test setup or the reaction was not complete. The first option is more likely since the reagents and conditions produced a product containing a significant quantity of CeO_2 in every other sample that was analyzed.

Spheres produced in experiment 56 underwent TGA, DSC, and XRD. The portion not undergoing heat treatment was identified through XRD as being partially cerium oxide with other material present (Fig. 33). The spheres from experiment 56 underwent a hexane wash and the first step of the 3-stage wash until the basket failed. The DSC/TGA results indicated that a volatile species was being liberated at ~200^{o}C (Fig. 23). It is suspected that this represents the evaporation of leftover reagents that were not removed by washing.

The product from experiment 69 was split into several small samples before undergoing the various analysis techniques. Recall that experiments 69 and 70 were the final production tests that produced the best available microspheres. A small portion was heated to 500^{o}C for TGA and DSC evaluation. The exothermic reaction observed in experiment 56 was again observed, but the magnitude of the reaction was significantly reduced (compare Figs. 23 and 24). The spheres from experiment 69 were washed with the complete washing process, as opposed to experiment 56 that only went through the first stage. By going through the full wash process, more unreacted product was removed from the spheres. The same results were seen for a larger sample of spheres taken above the 200^{o}C reaction point. The product turned a pale yellow color and remained intact. The XRD results from the three samples from experiment 69 (Figs. 35 to 37) show that even being heated below 200^{o}C is enough to remove the impurity phase, leaving the cerium oxide as the only observable phase. And although Figure 35 shows a strong peak matching guanidinium pentacarbonatocerate tetrahydrate, the data was not conclusive enough to identify that species as the impurity phase.

Product from experiment 70, produced using the same conditions as experiment 69, was taken up to over 1400^{o}C to simulate sintering. The portion undergoing just TGA underwent the typical mass drop around 200^{o}C with minimal mass loss above that point (Fig. 29). The final product was a slightly smaller sphere caused by densification through sintering (Fig. 30). The product would not be usable for pressing due to the cracking observed, but it was able to survive the temperatures needed for the sintering process without the destructive reactions from remnant reagents. If the microspheres sintered in experiment 70 were to be used in the production of cermet fuels, they would not be able to withstand the pressures involved in the pressing process. Even after sintering, the microspheres were brittle and crumbled under very little pressure.

6. SUMMARY AND RECOMMENDATIONS

Seventy process development experiments were performed to establish a system to produce cerium oxide microspheres through internal gelation. To accomplish this task, various process variables were altered, including broth composition, oil temperature, injection rate, and wash steps and times. Through the techniques investigated in this research, it is possible to produce cerium oxide microspheres that are solid, but brittle, and are able to withstand washing and sintering.

The following are the observations and results obtained from the experiments performed:

1. Increased concentrations of HMTA and urea lead to faster gelation, but the quality of the spheres is decreased. Results of the small scale tests show a 2:1 ratio of HMTA and urea to cerium nitrate produces the fastest gelling material for the conditions studied. However, experiments performed with this composition produced spheres that were cracked when removed from the oil
2. Spheres of the highest quality came from a broth composed of 1.45 M cerium nitrate and 1.65 M HMTA and urea. When not washed in ammonium hydroxide, the product spheres were solid and did not crack or crumble while drying. Cracking occurs when undergoing the full wash process, but the produced spheres were the best produced in this study.
3. Introduction of the gelation column and syringe pump was a key to the production of microspheres. The gelation column created a volume of low

disturbance and low flow for the initial structure of the spheres to be formed. It also allowed real time correction to the injection speed as the spheres could be observed flowing through the column. The syringe pump allowed the broth to be injected slowly enough for microspheres to be produced.

4. Contamination became a serious issue when working with the optimum broth solution. Due to this, new syringes were used for every experiment run and the needles were thoroughly washed to remove product from previous runs. Introduction of any foreign material may lead to the needle clogging and early gelation in the syringe.

The following are recommendations for any future research into this area:

1. Only a small investigation of sphere production at greater than 100^{o}C was completed. Further analysis may show a higher temperature will allow production of spheres that are not cracked during the drying process
2. The gelation column used was originally to be longer, but it was cracked during the installation process and had to be shortened. A column of greater length would allow the spheres a longer time in the low flow region to provide superior gelation.
3. The final experiments were completed using baskets of 40 x 40 mesh and washed by placing these baskets into a beaker. Attempts were made to use a magnetic stirrer to flow the wash over the baskets, but the experimental setup was unstable.

By designing a better washing stand, more waste may be removed from the spheres by a flowing wash.

4. Further analysis is needed of the produced spheres before and after sintering to determine particle size and density. Densification should occur during the sintering process, it is desired to know the extent.
5. The next stage of this research should include the extension to mixed oxides, especially uranium-cerium oxides.

REFERENCES

[1] G.J. Suppes and T.S. Storvick, Sustainable Nuclear Power, Academic Press, New York, 2007.

[2] I. Hore-Lacy, Nuclear Energy in the 21st Century, Academic Press, New York, 2007.

[3] Yucca Mountain Repository License Application, DOE/RW-0573 (2008).

[4] A.J. Parkison, (2008). Hydride Production Zircaloy-4 As A Function of Time and Temperature. M.S. Thesis, Texas A&M University, College Station, TX.

[5] A.R. Totemeier, (2006). Evaluation of a Zirconium-Matrix Cermet for the Storage and Transmutation of Transuranic Isotopes. M.S. Thesis, Purdue University, West Lafayette, IN.

[6] S.M. McDeavitt, A. Parkison, A.R. Totemeier and J.J. Wegener, Fabrication of Cermet Nuclear Fuels Designed for the Transmutation of Transuranic Isotopes, Materials Science Forum, 561-565: 1733-1736 (2007).

[7] S.M. McDeavitt, Development of an Engineered Product Storage Concept for the UREX+1 Combined Transuranic/Lanthanide Product Streams, Quarterly Progress Report, July 1, 2005.

[8] J.L. Collins, R.D. Hunt, G.D. Del Cul and D.F. Williams, Production of Depleted UO_2 Kernels for the Advanced Gas-Cooled Reactor Program For Use in TRISO Coating Development, ORNL/TM-2004/123 (2004).

[9] P. Naefe and E. Zimmer, Preparation of Uranium Kernels by an External Gelation Process, Nuclear Technology. 42 (1979), p. 163-71.

[10] J.L. Collins, M.H. Lloyd, and R.L. Fellows, The Basic Chemistry Involved in the Internal-Gelation Method of Precipitating Uranium as Determined by pH Measurements, Radiochimica Acta. 42 (1987), p. 121-34.

[11] J.L. Collins, Experimental Methodology for Determining Optimum Process Parameters for Production of Hydrous Metal Oxides by Internal Gelation, ORNL/TM-2005/102 (2005).

[12] V.N. Vaidya, S.K. MukerJee, J.K. Joshi, R.V. Kamat, and D.D. Sood, A Study of Chemical Parameter of the Internal Gelation Based Sol-Gel Process for Uranium Dioxide, Journal of Nuclear Materials. 148 (1987), p. 324-31.

[13] P.A. Haas, J.M. Begovich, A.D. Ryon and J.S. Vavruska, Chemical Flowsheet Conditions for Preparing Urania Spheres by Internal Gelation, Ind. Eng. Chem. Prod. Res. Dev. 19 (1980), p. 459-67.

[14] R.D. Hunt and J.L. Collins, Uranium kernel formation via internal gelation, Radiochim. Acta. 92 (2004), p. 909-15.

[15] J.L. Collins and J.S. Watson, Economic Evaluation for the Production of Sorbents and Catalysts Derived from Hydrous Titanium Oxide Microspheres Prepared by the HMTA Internal Gelation Process, ORNL/TM-1999/212 (2000).

[16] J.C. Marra, A.D. Cozzi, R.A. Pierce, and J.M. Pareizs, Cerium as a Surrogate in the Plutonium Immobilized Form, DE-AC09-96SR18500.

APPENDIX A

EXPERIMENTAL CONDITIONS AND RESULTS

Experiment 1

HMTA / Urea:	1.68 M	Cerium Nitrate:	1.3 M	Flowing Oil:	90 C
Needle:	18 ga	Air Pressure:	Undocumented	Aging Time:	10 min

Wash: Undocumented

Product Result: Solid yellow crust at bottom of oil reservoir; material in catch funnel never fully gels

Notes: Experiment used Neslab constant temperature bath and funnel for catch basket

Experiment 2

HMTA / Urea:	1.68 M	Cerium Nitrate:	1.3 M	Flowing Oil:	90 C
Needle:	18 ga	Air Pressure:	4 psi	Aging Time:	Undocumented

Wash: Undocumented

Product Result: Unformed gel product filling catch basket

Notes: Pressure increased to 4.5 psi during run; used large oil reservoir

Experiment 3

HMTA / Urea:	1.68 M	Cerium Nitrate:	1.3 M	Flowing Oil:	90 C
Needle:	18 ga	Air Pressure:	4 psi	Aging Time:	Undocumented

Wash: Hexane and Ammonium Hydroxide

Product Result: Unformed gel product filling catch basket

Notes: Pressure started at 4 psi, reduced during run to obtain lower flow rate

Experiment 4

HMTA / Urea:	1.68 M	Cerium Nitrate:	1.3 M	Flowing Oil:	90 C
Needle:	18 ga	Air Pressure:	3.75 psi	Aging Time:	Undocumented
Wash:	Hexane and Ammonium Hydroxide				
Product Result:	Some small sphere "flecks" in unformed gel				
Notes:	Pressure increased up to 4 psi before needle blockage				

Experiment 5

HMTA / Urea:	1.68 M	Cerium Nitrate:	1.3 M	Flowing Oil:	90 C
Needle:	18 ga	Air Pressure:	4 psi	Aging Time:	Undocumented
Wash:	Hexane and Ammonium Hydroxide				
Product Result:	Small amounts of white "specks" in output stream before injection flow stops				
Notes:	Early gelation around points of metal in injection system stops run				

Experiment 6

HMTA / Urea:	1.68 M	Cerium Nitrate:	1.3 M	Flowing Oil:	90 C
Needle:	18 ga	Air Pressure:	4 psi	Aging Time:	Undocumented
Wash:	Hexane and Ammonium Hydroxide				
Product Result:	Mixture of unformed gel with some small spheres				
Notes:	Running start used; broth flowing out of tip of needle when inserted into flowing oil				

Experiment	7				
HMTA / Urea:	1.68 M	Cerium Nitrate:	1.3 M	Flowing Oil:	90 C
Needle:	18 ga	Air Pressure:	3.75 psi	Aging Time:	Undocumented
Wash:	Hexane and Ammonium Hydroxide				
Product Result:	Appears more as film than unformed gel or spheres				
Notes:	Running start used again				

Experiment	8				
HMTA / Urea:	1.92 M	Cerium Nitrate:	1.2 M	Flowing Oil:	90 C
Needle:	18 ga	Air Pressure:	5 psi	Aging Time:	Undocumented
Wash:	Hexane and Ammonium Hydroxide				
Product Result:	Some very large spheres and unformed gel				
Notes:	First experiment with altered chemistry				

Experiment	9				
HMTA / Urea:	2.13 M	Cerium Nitrate:	1 M	Flowing Oil:	90 C
Needle:	18 ga	Air Pressure:	4 psi	Aging Time:	Undocumented
Wash:	---				
Product Result:	Oil backed up into system; experiment stopped				
Notes:	Slime like surface created when pressure increased to counter oil back flow				

Experiment 10

HMTA / Urea:	1.92 M	Cerium Nitrate:	1.2 M	Flowing Oil:	90 C
Needle:	18 ga	Air Pressure:	4 psi	Aging Time:	Undocumented

Wash: Hexane and Ammonium Hydroxide

Product Result: Mass of unformed gel

Notes: First experiment with gelation column; still using forced air injection

Experiment 11

HMTA / Urea:	1.92 M	Cerium Nitrate:	1.2 M	Flowing Oil:	90 C
Needle:	18 ga	Air Pressure:	4 psi	Aging Time:	Undocumented

Wash: Hexane and 3 M Ammonium Hydroxide

Product Result: Some spheres seen falling through column, although not all gelling; washed product has some spheres and unformed gel

Notes: Early gelation occurs around ball valve area of broth chamber

Experiment 12

HMTA / Urea:	1.6 M	Cerium Nitrate:	1.5 M	Flowing Oil:	90 C
Needle:	18 ga	Air Pressure:	< 0.5 psi	Aging Time:	Undocumented

Wash: Hexane and 3 M Ammonium Hydroxide

Product Result: Unformed gel with some spheres within

Notes: With flow only from the air valve turned off still injecting at too high of a rate

Experiment 13

HMTA / Urea:	2.13 M	Cerium Nitrate:	1 M	Flowing Oil:	100 C
Needle:	18 ga	Manual Syringe Injection		Aging Time:	Undocumented

Wash: Hexane and 0.1 M Ammonium Hydroxide

Product Result: Many spheres, although unformed gel by manual injection

Notes: Following small scale tests, learned can create spheres by using syringe manually

Experiment 14

HMTA / Urea:	2.13 M	Cerium Nitrate:	1 M	Flowing Oil:	100 C
Needle:	30 ga	Manual Syringe Injection		Aging Time:	Undocumented

Wash: ---

Product Result: Needle clogged within seconds; only unformed gel produced

Notes: 30 gauge needle is much to small to inject spheres without clogging

Experiment 15

HMTA / Urea:	2.13 M	Cerium Nitrate:	1 M	Flowing Oil:	100 C
Needle:	24 ga	Manual Syringe Injection		Aging Time:	Undocumented

Wash: Hexane, 0.1 M Ammonium Hydroxide, and Water

Product Result: Spheres produced during run; placed in 80 C oven overnight, seem to have "melted"

Notes: Rough measurements on sphere sizes show to be between 560 and 690 μm

Experiment 16

HMTA / Urea:	2.13 M	Cerium Nitrate:	1 M	Flowing Oil:	100 C
Needle:	24 ga (f)	Manual Syringe Injection		Aging Time:	Undocumented

Wash: Hexane, 0.1 M Ammonium Hydroxide, and Water

Product Result: Spheres produced during run; placed in 80 C oven overnight, seem to have "melted"

Notes: First run with frozen needle; appeared to be able to inject much more

Experiment 17

HMTA / Urea:	2.13 M	Cerium Nitrate:	1 M	Flowing Oil:	100 C
Needle:	26 ga	Injection Rate:	0.2 mL/min	Aging Time:	Undocumented

Wash: Hexane, 0.1 M Ammonium Hydroxide, and Water

Product Result: Many small spheres produced during run; product seems "popped" or "melted"

Notes: First experiment with syringe pump; injection rate variable removed

Experiment 18

HMTA / Urea:	2.13 M	Cerium Nitrate:	1 M	Flowing Oil:	100 C
Needle:	26 ga	Injection Rate:	Varied	Aging Time:	Undocumented

Wash: Hexane, 0.1 M Ammonium Hydroxide, and Water

Product Result: Solid spheres after aging; placed in 40 C oven to dry; appear "popped" or "melted"

Notes: Variation of injection rate over a small range does not seem to alter sphere size

Experiment 19

HMTA / Urea:	1.92 M	Cerium Nitrate:	1.2 M	Flowing Oil:	100 C
Needle:	26 ga	Injection Rate:	0.2 mL/min	Aging Time:	20 min

Wash: Hexane, 0.1 M Ammonium Hydroxide, and Water

Product Result: Spheres appear good after washing, some appear "melted" after drying in oven overnight

Notes: Under scope some of the spheres appear not hollow

Experiment 20

HMTA / Urea:	1.78 M	Cerium Nitrate:	1.33 M	Flowing Oil:	100 C
Needle:	26 ga (f)	Injection Rate:	0.2 mL/min	Aging Time:	15 min

Wash: Hexane and 0.1 M Ammonium Hydroxide

Product Result: Free flowing after hexane wash; Ammonium Hydroxide made them stick in place; broken down next day

Notes: Continuing decreasing HMTA and urea concentration; some spheres lost to hole in basket

Experiment 21

HMTA / Urea:	1.68 M	Cerium Nitrate:	1.43 M	Flowing Oil:	100 C
Needle:	24 ga	Injection Rate:	0.1 mL/min	Aging Time:	15 min

Wash: Hexane and 0.1 M Ammonium Hydroxide

Product Result: Solid product after aging and hexane wash; following Ammonium Hydroxide and aging appear "melted"

Notes: Further decreasing of HMTA and urea concentration

Experiment 22

HMTA / Urea:	1.78 M	Cerium Nitrate:	1.33 M	Flowing Oil:	100 C
Needle:	24 ga (f)	Injection Rate:	0.1 mL/min	Aging Time:	30 min

Wash: Hexane and 0.1 M Ammonium Hydroxide

Product Result: Solid spheres out of aging, once washed in Ammonium Hydroxide becomes cloudy with "crud" forming

Notes: Needle clogged after 1.3 mL injected, 22 ga used for remainder

Experiment 23

HMTA / Urea:	1.78 M	Cerium Nitrate:	1.33 M	Flowing Oil:	100 C
Needle:	18 ga	Injection Rate:	0.7 mL/min	Aging Time:	30 min

Wash: Hexane

Product Result: Non-melted spheres after drying; some appear hollow

Notes: Seeing effects of not washing with Ammonium Hydroxide

Experiment 24

HMTA / Urea:	1.68 M	Cerium Nitrate:	1.3 M	Flowing Oil:	100 C
Needle:	24 ga (f)	Injection Rate:	0.2 mL/min	Aging Time:	45 min

Wash: Hexane and Water

Product Result: Free flowing spheres during hexane wash; breaking down when in contact with water

Notes: Needle clogged after 1.6 mL injected, 26 ga used for remainder

Experiment	25				
HMTA / Urea:	1.6 M	Cerium Nitrate:	1.5 M	Flowing Oil:	100 C
Needle:	26 ga (f)	Injection Rate:	0.2 mL/min	Aging Time:	---
Wash:	---				
Product Result:	Needle clogged almost immediately; experiment scrapped				
Notes:	After needle clogged, entire syringe began to gel				

Experiment	26				
HMTA / Urea:	1.92 M	Cerium Nitrate:	1.2 M	Flowing Oil:	110 C
Needle:	24 ga (f)	Injection Rate:	0.2 mL/min	Aging Time:	30 min
Wash:	Hexane and Water				
Product Result:	Many small spheres and some unformed gel; appear hollow when dried				
Notes:	Increased amount of HMTA and urea				

Experiment	27				
HMTA / Urea:	1.78 M	Cerium Nitrate:	1.33 M	Flowing Oil:	110 C
Needle:	24 ga (f)	Injection Rate:	---	Aging Time:	---
Wash:	---				
Product Result:	Sediment formed as soon as loaded into syringe; experiment scrapped				
Notes:	Realized had been using same syringe for all experiments				

Experiment 28

HMTA / Urea:	1.6 M	Cerium Nitrate:	1.5 M	Flowing Oil:	100 C
Needle:	22 ga (f)	Injection Rate:	0.2 mL/min	Aging Time:	30 min

Wash: Hexane

Product Result: Excess of unformed gel; upon drying appears many are not hollow

Notes: New syringes used and made sure that broth is chilled thoroughly

Experiment 29

HMTA / Urea:	1.64 M	Cerium Nitrate:	1.46 M	Flowing Oil:	100 C
Needle:	22 ga (f)	Injection Rate:	0.2 mL/min	Aging Time:	120 min

Wash: Undocumented

Product Result: Two different color products; white / light pink that is solid and purple / lavender that is cracked

Notes: Several attempts required to get experiment set up, end up pouring broth into syringe through the top rather than drawing in through the needle

Experiment 30

HMTA / Urea:	1.68 M	Cerium Nitrate:	1.3 M	Flowing Oil:	100 C
Needle:	22 ga (f)	Injection Rate:	0.2 mL/min	Aging Time:	30 min

Wash: Hexane

Product Result: Majority of spheres are lighter colored; next day white product is not hollow while darker is dried and cracked

Notes: Paid extra attention to make sure no early gelation occurring in syringe

Experiment	31				
HMTA / Urea:	1.62 M	Cerium Nitrate:	1.48 M	Flowing Oil:	100 C
Needle:	22 ga (f)	Injection Rate:	0.2 mL/min	Aging Time:	30 min
Wash:	Hexane and 0.1 M Ammonium Hydroxide				
Product Result:	Spheres with unformed gel connecting; during washing unformed gel dissolves leaving spheres only				
Notes	Extra effort put into removing contamination from system components				

Experiment	32				
HMTA / Urea:	1.68 M	Cerium Nitrate:	1.3 M	Flowing Oil:	100 C
Needle:	22 ga (f)	Injection Rate:	0.2 mL/min	Aging Time:	---
Wash:	---				
Product Result:	Needles clogged early in run; scrapped				
Notes:	Last experiment attempted with reused and washed syringes, new ones for each experiment from here on out				

Experiment	33				
HMTA / Urea:	1.64 M	Cerium Nitrate:	1.46 M	Flowing Oil:	100 C
Needle:	22 ga (f)	Injection Rate:	0.2 mL/min	Aging Time:	Undocumented
Wash:	Hexane				
Product Result:	Many white spheres connected by unformed gel;				
Notes:	First two attempts gelled as soon as loaded into syringe; realized broth was not freezing as had thought earlier since second attempt was not chilled				

Experiment 34

HMTA / Urea:	1.52 M	Cerium Nitrate:	1.58 M	Flowing Oil:	100 C
Needle:	18 ga (f)	Injection Rate:	0.3 mL/min	Aging Time:	30 min

Wash: Undocumented

Product Result: Many spheres with unformed gel

Notes: Broth was chilled in a freezer for over an hour rather than using ice bath

Experiment 35

HMTA / Urea:	2.06	Cerium Nitrate:	1.07	Flowing Oil:	100 C
Needle:	18 ga (f)	Injection Rate:	0.3 mL/min	Aging Time:	30 min

Wash: Undocumented

Product Result: After aging, some unformed gel, some white spheres, and some dark that are already cracked

Notes: This concentration was an accident, meant to be much lower; already knew this was too high

Experiment 36

HMTA / Urea:	1.42 M	Cerium Nitrate:	1.67 M	Flowing Oil:	100 C
Needle:	18 ga (f)	Injection Rate:	0.3 mL/min	Aging Time:	30 min

Wash: Hexane and 0.1 M Ammonium Hydroxide

Product Result: Some spheres and lots of unformed gel after aging; nearly all product dissolved or "melted" after washing

Notes: New smaller baskets made from 80 x 80 mesh

Experiment 37

HMTA / Urea:	1.66 M	Cerium Nitrate:	1.44 M	Flowing Oil:	100 C
Needle:	18 ga (f)	Injection Rate:	0.3 mL/min	Aging Time:	30 min

Wash: Hexane and 0.1 M Ammonium Hydroxide

Product Result: Large light colored and small darker spheres after aging; washed product placed in oven to dry

Notes: Small variations of injection rate show it needs to be between 0.1 and 0.2 mL/min

Experiment 38

HMTA / Urea:	1.65 M	Cerium Nitrate:	1.46 M	Flowing Oil:	100 C
Needle:	18 ga (f)	Injection Rate:	0.15mL/min	Aging Time:	30 min

Wash: Hexane and 0.1 M Ammonium Hydroxide

Product Result: Many spheres with very little unformed gel; majority of product melted when washed in Ammonium Hydroxide

Notes: This injection rate allowed a slow stream of uniform sized spheres to be produced

Experiment 39

HMTA / Urea:	1.65 M	Cerium Nitrate:	1.45 M	Flowing Oil:	100 C
Needle:	18 ga (f)	Injection Rate:	0.15 mL/min	Aging Time:	30 min

Wash: Hexane

Product Result: Many spheres with little if any unformed gel; after drying appear solid with no cracking

Notes: Spheres were placed in warm oven to dry

Experiment	40				
HMTA / Urea:	1.65 M	Cerium Nitrate:	1.46 M	Flowing Oil:	100 C
Needle:	18 ga (f)	Injection Rate:	0.15 mL/min	Aging Time:	30 min
Wash:	Hexane				
Product Result:	Not as well formed as #39; possibly caused by switching of needles in run				
Notes:	First needle clogged almost immediately				

Experiment	41				
HMTA / Urea:	1.67 M	Cerium Nitrate:	1.44 M	Flowing Oil:	100 C
Needle:	18 ga (f)	Injection Rate:	0.15 mL/min	Aging Time:	30 min
Wash:	Hexane				
Product Result:	Appear about the same as #39				
Notes:	Slightly higher HMTA and urea than #39, but similar results				

Experiment	42				
HMTA / Urea:	1.65 M	Cerium Nitrate:	1.45 M	Flowing Oil:	100 C
Needle:	18 ga (f)	Injection Rate:	0.15 mL/min	Aging Time:	30 min
Wash:	Hexane and 3 M Ammonium Hydroxide				
Product Result:	Spheres do not dissolve in Ammonium Hydroxide wash performed in a beaker; dried product appears chalky				
Notes:	First needle clogged right away then entire syringe began to gel				

Experiment	43				
HMTA / Urea:	1.65 M	Cerium Nitrate:	1.45 M	Flowing Oil:	100 C
Needle:	18 ga	Injection Rate:	0.15 mL/min	Aging Time:	30 min
Wash:	Hexane				
Product Result:	Appeared well formed after aging and still did after drying				
Notes:	Needle no longer placed in freezer after several clogged needles in previous runs				

Experiment	44				
HMTA / Urea:	1.65 M	Cerium Nitrate:	1.45 M	Flowing Oil:	100 C
Needle:	18 ga	Injection Rate:	0.15 mL/min	Aging Time:	30 min
Wash:	Hexane for all, and portion in two >40 minute washes of 3 M Ammonium Hydroxide				
Product Result:	Those undergoing second washing appear chalky and are crumbling				
Notes:	No longer experiencing early gelling since not freezing needles				

Experiment	45				
HMTA / Urea:	1.65 M	Cerium Nitrate:	1.46 M	Flowing Oil:	100 C
Needle:	18 ga (f)	Injection Rate:	0.15 mL/min	Aging Time:	30 min
Wash:	Hexane				
Product Result:	No defined areas of spheres; very sticky				
Notes:	Broth kept in freezer overnight; gelation is occurring near bottom of column				

Experiment 46

HMTA / Urea:	1.65 M	Cerium Nitrate:	1.45 M	Flowing Oil:	100 C
Needle:	18 ga	Injection Rate:	0.15 mL/min	Aging Time:	30 min

Wash: Hexane then half in two washes of 3 M Ammonium Hydroxide and Water

Product Result: Portion from second wash is dried, cracked, and crumbling

Notes: Have realized that this broth composition gives good quality spheres

Experiment 47

HMTA / Urea:	1.65 M	Cerium Nitrate:	1.45 M	Flowing Oil:	100 C
Needle:	18 ga	Injection Rate:	0.15 mL/min	Aging Time:	30 min

Wash: Hexane then half in 2 M Ammonium Hydroxide and rest in 1 M for 40 minutes then rinsed with Water

Product Result: All appear dry and cracked after dried

Notes: Trying to find the right concentration of Ammonium Hydroxide to wash in

Experiment 48

HMTA / Urea:	1.65 M	Cerium Nitrate:	1.45 M	Flowing Oil:	100 C
Needle:	18 ga	Injection Rate:	0.15 mL/min	Aging Time:	30 min

Wash: Hexane for all then half in 0.75 M Ammonium Hydroxide and rest in 0.5 M for under 40 minutes

Product Result: After drying product appears as a "goo"

Notes: Continued effort to find optimum wash solution

Experiment	49				
HMTA / Urea:	1.68 M	Cerium Nitrate:	1.43 M	Flowing Oil:	100 C
Needle:	18 ga	Injection Rate:	0.15 mL/min	Aging Time:	30 min
Wash:	Hexane, two 40 minute washes of 3 M Ammonium Hydroxide, then Water wash				
Product Result:	Most appear crumbling; some appear off white and still solid				
Notes:	Baskets now using 40 x 40 mesh on the bottom, allows washing in basket				

Experiment	50				
HMTA / Urea:	1.75 M	Cerium Nitrate:	1.36 M	Flowing Oil:	100 C
Needle:	18 ga	Injection Rate:	0.15 mL/min	Aging Time:	30 min
Wash:	Hexane then Oak Ridge Wash System				
Product Result:	Dried product appears cracked and crumbling				
Notes:	Discovery of Oak Ridge Wash in literature				

Experiment	51				
HMTA / Urea:	1.81 M	Cerium Nitrate:	1.3 M	Flowing Oil:	100 C
Needle:	18 ga	Injection Rate:	0.15 mL/min	Aging Time:	30 min
Wash:	Hexane then Oak Ridge Wash System				
Product Result:	More darker spheres produced as HMTA and Urea increased; product appears to be dissolving during wash; final dried product is cracked and crumbling				
Notes:	Increased amount of HMTA and urea				

Experiment	52				
HMTA / Urea:	1.68 M	Cerium Nitrate:	1.3 M	Flowing Oil:	100 C
Needle:	18 ga	Injection Rate:	0.15 mL/min	Aging Time:	30 min
Wash:	Hexane and Oak Ridge Wash for 60 minutes each step				
Product Result:	After washing placed in 50 C oven overnight; dried product is cracked and hollow				
Notes:	Attempt at broth composition that is used for uranium				

Experiment	53				
HMTA / Urea:	1.68 M	Cerium Nitrate:	1.43 M	Flowing Oil:	100 C
Needle:	18 ga	Injection Rate:	0.15 mL/min	Aging Time:	30 min
Wash:	Hexane then Oak Ridge Wash for 60 minutes each stage				
Product Result:	Placed in 40 C oven overnight; dried product is cracked and hollow				
Notes:	Increase amount of cerium nitrate to reduce amount of cracked and dried spheres				

Experiment	54				
HMTA / Urea:	1.65 M	Cerium Nitrate:	1.45 M	Flowing Oil:	100 C
Needle:	18 ga	Injection Rate:	0.15 mL/min	Aging Time:	30 min
Wash:	Hexane then Oak Ridge Wash for 60 minutes each stage				
Product Result:	Placed in 40 C over overnight; dried product is cracked and hollow				
Notes:	First attempt with broth composition that produced best spheres when only washed in hexane				

Experiment 55

HMTA / Urea:	1.65 M	Cerium Nitrate:	1.45 M	Flowing Oil:	100 C
Needle:	18 ga	Injection Rate:	0.15 mL/min	Aging Time:	60 min

Wash: Hexane then Oak Ridge Wash for 60 minutes each stage

Product Result: Washed product placed in front of fan to dry; some dried product appears brittle, under scope appears solid though

Notes: To dry faster, begin placing the washed spheres in front of a fan to dry

Experiment 56

HMTA / Urea:	1.65 M	Cerium Nitrate:	1.45 M	Flowing Oil:	100 C
Needle:	18 ga	Injection Rate:	0.15 mL/min	Aging Time:	90 min

Wash: Hexane then first stage of Oak Ridge Wash and a Water rinse; basket failed in middle

Product Result: Placed product in front of fan to dry; dried product is hollow and cracked

Notes: Increasing aging time while keeping other factors constant

Experiment 57

HMTA / Urea:	1.65 M	Cerium Nitrate:	1.45 M	Flowing Oil:	100 C
Needle:	18 ga	Injection Rate:	0.15 mL/min	Aging Time:	60 min

Wash: Oak Ridge Wash for 60 minutes each stage

Product Result: Placed in front of fan for 15 minutes to dry; dried product is cracked

Notes: No hexane wash in effort to produce quality washed spheres

Experiment 58

HMTA / Urea:	1.65 M	Cerium Nitrate:	1.45 M	Flowing Oil:	100 C
Needle:	18 ga	Injection Rate:	0.15 mL/min	Aging Time:	0 min

Wash: Hexane for 10 minutes then Oak Ridge Wash for 60 minutes each stage

Product Result: Placed in front of fan to dry, looked good when left; dried product has some very dark cracked spheres and some lighter ones

Notes: No aging done in effort to produce quality washed spheres

Experiment 59

HMTA / Urea:	1.65 M	Cerium Nitrate:	1.45 M	Flowing Oil:	90 C
Needle:	18 ga	Injection Rate:	0.15 mL/min	Aging Time:	60 min

Wash: Hexane then first stage of Oak Ridge Wash for 60 minutes and Water rinse

Product Result: Upon removal from oil had some unformed gel which dissolved during wash; dried product looks chalky but solid

Notes: Dropped temperature by 10 C; gelation occurred near bottom of column

Experiment 60

HMTA / Urea:	1.48 M	Cerium Nitrate:	1.29 M	Flowing Oil:	100 C
Needle:	18 ga	Injection Rate:	0.15 mL/min	Aging Time:	30 min

Wash: Hexane for 10 minutes ten Oak Ridge Wash for 60 minutes each stage

Product Result: Placed in front of fan to dry, look good upon leaving; dried product is dark and "crusty"; some appear good though

Notes: Diluting solutions by adding water; thought broth may have been too strong

Experiment	61				
HMTA / Urea:	1.42 M	Cerium Nitrate:	1.25 M	Flowing Oil:	100 C
Needle:	18 ga	Injection Rate:	0.15 mL/min	Aging Time:	60 min
Wash:	Hexane then Oak Ridge Wash for 60 minutes each stage				
Product Result:	Spheres and unformed gel formed, with unformed gel dissolving during washing				
Notes:	Further dilution of the broth by addition of water				

Experiment	62				
HMTA / Urea:	1.56 M	Cerium Nitrate:	1.37 M	Flowing Oil:	100 C
Needle:	18 ga	Injection Rate:	0.15 mL/min	Aging Time:	30 min
Wash:	Hexane then Oak Ridge Wash for 60 minutes each stage				
Product Result:	Dried product is a yellowish power with a few solid spheres				
Notes:	Used magnetic stirrer for washing; finding way to suspend basket over the spinning stirrer is an ordeal				

Experiment	63				
HMTA / Urea:	1.35 M	Cerium Nitrate:	1.05 M	Flowing Oil:	100 C
Needle:	18 ga	Injection Rate:	0.15 mL/min	Aging Time:	30 min
Wash:	Hexane then first stage of Oak Ridge Wash for 60 minutes				
Product Result:	Out of oil is few spheres and majority unformed gel; unformed gel dissolved in washing leaving just a sludge product				
Notes:	Too much water added in dilution process; gelation near bottom of column				

Experiment 64

HMTA / Urea:	1.65 M	Cerium Nitrate:	1.29 M	Flowing Oil:	100 C
Needle:	18 ga	Injection Rate:	0.15 mL/min	Aging Time:	30 min

Wash: Hexane wash for 10 minutes then Oak Ridge Wash for 75 minutes each stage

Product Result: Dried product is very crumbly

Notes: Basket fell on top of stirrer and bottom was torn off; length of wash increased because of this issue

Experiment 65

HMTA / Urea:	1.64 M	Cerium Nitrate:	1.46 M	Flowing Oil:	100 C
Needle:	18 ga	Injection Rate:	0.15 mL/min	Aging Time:	60 min

Wash: Hexane then Oak Ridge Wash for 60 minutes each stage

Product Result: Out of oil has some spheres and some unformed gel; most spheres look oblong and nonspherical; dried product is cracked and crumbling

Notes: Took amount of HMTA and urea below level typically used

Experiment 66

HMTA / Urea:	1.62 M	Cerium Nitrate:	1.42 M	Flowing Oil:	100 C
Needle:	18 ga	Injection Rate:	0.15 mL/min	Aging Time:	30 min

Wash: Hexane then Oak Ridge Wash for 60 minutes each stage

Product Result: Quite a bit of unformed gel when removed from oil; unformed product dissolves in wash; dried product is cracked and crumbling

Notes: Last attempt at diluting solution

Experiment	67				
HMTA / Urea:	1.65 M	Cerium Nitrate:	1.45 M	Flowing Oil:	100 C
Needle:	18 ga	Injection Rate:	0.15 mL/min	Aging Time:	30 min
Wash:	Hexane wash for 10 minutes then Oak Ridge Wash for 60 minutes each stage				
Product Result:	No unformed gel when removed from oil; lot of product dissolves in washing process; dried product is cracking; some solid spheres, but they are soft				
Notes:	Another attempt at this concentration with 30 minutes of aging				

Experiment	68				
HMTA / Urea:	1.65 M	Cerium Nitrate:	1.45 M	Flowing Oil:	100 C
Needle:	18 ga	Injection Rate:	0.15 mL/min	Aging Time:	70 min
Wash:	Hexane, Water rinse, then Oak Ridge Wash for 75 minutes each stage, Water rinse				
Product Result:	Placed in front of fan to dry; dried product is cracked and crumbling				
Notes:	Same as #67 with increased aging and longer wash times				

Experiment	69				
HMTA / Urea:	1.65 M	Cerium Nitrate:	1.45 M	Flowing Oil:	110 C
Needle:	18 ga	Injection Rate:	0.15 mL/min	Aging Time:	60 min
Wash:	Hexane wash for 15 minutes then Oak Ridge Wash for 75 minutes each stage				
Product Result:	Dried product is white and very powder like				
Notes:	Begin to increase oil temperature to speed the gelation process				

Experiment	70				
HMTA / Urea:	1.65 M	Cerium Nitrate:	1.45 M	Flowing Oil:	115 C
Needle:	18 ga	Injection Rate:	0.15 mL/min	Aging Time:	60 min
Wash:	Hexane wash for 15 minutes then Oak Ridge Wash for 75 minutes each stage				
Product Result:	Dried product looks a lot like #69, very white and powder like				
Notes:	Further increase of the oil temperature				

APPENDIX B

DATA FROM SERIES OF SMALL SCALE INTERNAL GELATION TESTS

Volume 3.2 M HMTA/Urea (mL)	Vol. 3.0 M Cerium Nitrate (mL)	(Vol. HMTA and Urea) / (Vol. Cerium Nitrate)	Time to gelation per mL solution (s/mL)	Arbitrary Hardness
1	1	1	29	3
1	1	1	31	3
1	1	1	31.5	3.5
1.05	1	1.05	29.8	1.5
1.1	1	1.1	30.5	5
1.1	1	1.1	29.5	5
1.15	1	1.15	28.8	5
1.2	1	1.2	27.7	5
1.2	1	1.2	28.2	5
1.25	1	1.25	27.1	5
1.3	1	1.3	24.8	6
1.3	1	1.3	27.8	5
1.35	1	1.35	24.3	5.5
1.4	1	1.4	20.4	6

Volume 3.2 M HMTA/Urea (mL)	Vol. 3.0 M Cerium Nitrate (mL)	(Vol. HMTA and Urea) / (Vol. Cerium Nitrate)	Time to gelation per mL solution (s/mL)	Arbitrary Hardness
1.4	1	1.4	24.2	5.5
1.4	1	1.4	22.1	6
1.45	1	1.45	24.9	5.5
1.5	1	1.5	20.4	6.5
1.5	1	1.5	19.6	6
1.5	1	1.5	22.4	5
1.55	1.3	1.2	22.5	4.5
1.6	1	1.6	25.4	4.5
1.65	1	1.65	23.0	4.5
1.7	1	1.7	22.2	4.5
1.75	1	1.75	21.5	5
1.8	1	1.8	16.4	6
1.8	1	1.8	19.3	5
1.85	1	1.85	19.3	5.5
1.85	1	1.85	16.8	6
1.9	1	1.9	15.5	6
1.9	1	1.9	18.6	5.5

Volume 3.2 M HMTA/Urea (mL)	Vol. 3.0 M Cerium Nitrate (mL)	(Vol. HMTA and Urea) / (Vol. Cerium Nitrate)	Time to gelation per mL solution (s/mL)	Arbitrary Hardness
1.94	1	1.95	16.6	6
1.95	1	1.95	13.6	7
1.95	1.1	1.77	13.77	2
2	1	2	15.3	6
2	1	2	14.3	6
2.05	1	2.05	14.4	6
2.1	1.35	1.56	16.5	---

VITA

Name: Jeffrey John Wegener

Address: Department of Nuclear Engineering, Texas A&M University, 3133
TAMU College Station, TX 77843-3133

Email Address: wegenerj@tamu.edu

Education: B.S., Nuclear Engineering, Purdue University, 2004
M.S., Nuclear Engineering, Texas A&M University, 2008

Appendix D

Master of Science Presentation: Sol-Gel Fabrication Method (35 Pages)

PRODUCTION OF CERIUM OXIDE MICROSPHERES BY AN INTERNAL GELATION SOL-GEL PROCESS

Thesis Defense Presentation

By

JEFFREY JOHN WEGENER

June 12, 2008

TEXAS A&M ENGINEERING

Production of Cerium Oxide Microspheres by Internal Gelation Sol-Gel

Jeffrey Wegener

Texas A&M School of Nuclear Engineering

June 12th, 2008

TEXAS A&M ENGINEERING

Outline

- Project Scope
- Sol-Gel Background and Chemistry
- Experimental Setup and Procedure
- Experiment Results
- Analysis of Spheres
- Summary

Project Scope

Overall NERI Project Goals

- Investigate the ultimate disposition form for the plutonium and TRU isotopes from the raffinate stream of UREX and TRUEX process.
  - Conversion of U/Pu/TRU nitrates to oxide powder
  - Recovery of Zircaloy cladding by hydride/dehydride
  - Fabrication of cermet pin by hot extrusion pressing of combined mateials

Location of Sol-Gel Within Overall Project

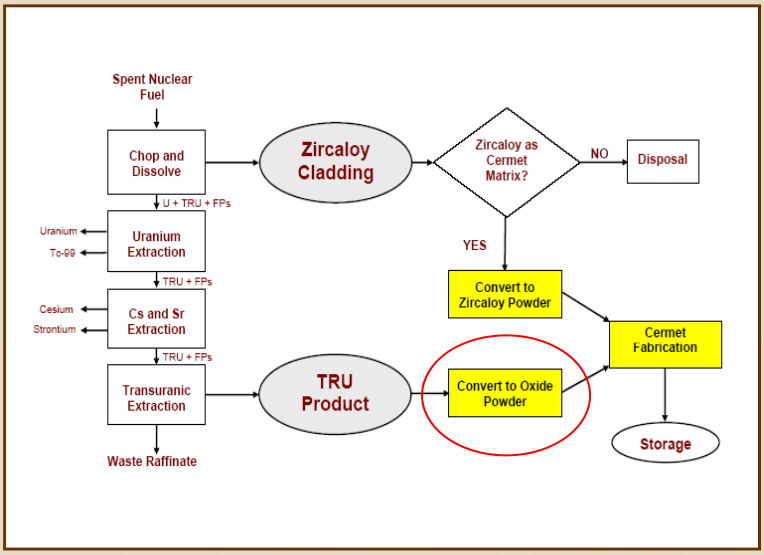

TEXAS A&M ENGINEERING

Sol-Gel Background and Chemistry

Sol-Gel Process and Definition

- Liquid to solid conversion of a material from a chemical solution to a stable solid form.
  - Metal oxide for this research
- “Sol” refers to the starting solution.
- “Gel” comes from inorganic polymers networking to form a solid.

TEXAS A&M ENGINEERING

Sol-Gel Process

- External Gelation
  - Relies on external source of ammonia to drive reaction.
    - Gallons of ammonia would be required to produce microspheres by this method
- Internal Gelation
  - Ammonia produced internally by the decomposition of hexamethylenetetramine (HMTA).

Internal Gelation Sol-Gel Chemistry

- Nitrate Salt: Cerium Nitrate, Uranium Nitrate…
- Hexamethylenetetramine (HMTA): $(CH_2)_6N_4$
- Urea: $(NH_2)_2CO$
- Hot Organic Medium: Silicone oil

Combination of Urea and Nitrate Salt

$$UO_2\left(NO_3\right)_2 + 2(NH_2)_2CO \rightleftharpoons UO_2(NO_3)_2 \cdot 2(NH_2)_2CO$$

- Prevents early gelation and creates a stable broth.
- Temperature activated reaction at approximately 0°C.
- As temperature increases product decomplexes and reaction proceeds to left.

Nitrate Salt Hydrolysis

$$UO_2^{2+} + 2H_2O \rightleftharpoons UO_2(OH)_2 + 2H^+$$

- After urea decomplexes, nitrate salt loses it's nitrate group
- Oxide then undergoes hydrolysis

HMTA Protonation

$$(CH_2)_6N_4 + H^+ \rightleftharpoons (CH_2)_6N_4 \cdot H^+$$

- Hydrogen atoms from hydrolysis undergo protonation with HMTA
- Reaction continues until at least 95% of HMTA atoms have undergone reaction

Decomposition of HMTA

$$(CH_2)_6N_4 \cdot H^+ + 3H^+ + 6H_2O \rightleftharpoons 4NH_4^+ + 6CH_2O$$

- Once 95% of HMTA atoms have undergone protonation, decomposition reaction begins.
- Urea drives decomposition by reacting with formaldehyde to produce monomethylol urea.

TEXAS A&M ENGINEERING

Production of Final Gel Product

- Weakly bonded particles create rigid gel by cross linking if conditions are right.
  - Temperature
  - pH
  - Constituent concentrations
- Precipitated product is hydrated uranium oxide with ammonia.

Cerium as Surrogate for Plutonium

- Focus of NERI project is producing a storage form for Pu and TRU
  - Not feasible to proceed with Pu
- Cerium (Ce) is used as a surrogate
  - Behave the same under batch handling
  - Similar sintering behavior

Oak Ridge Research into Uranium Oxide Microspheres for TRISO Fuel Kernels

- 30 to 1200 µm spheres produced with 1.3 M uranium solution and HMTA/U and Urea/U ratios of 1.25
- 500 µm spheres produced with vibratory nozzle and HMTA/U and Urea/U ratios of 1.3
- 350 and 500 µm spheres produced with 1.29 – 1.30 M uranyl nitrate and 1.68 M HMTA/Urea broth

Oak Ridge TRISO Kernel Sintering Process

- Completed in either pure Nitrogen or 5% Hydrogen in Argon.
  - 80°C for 2 hours
  - 150°C for 3 hours
  - 600°C for 5 hours
  - 1550°C for 5 hours

Air Dried and Sintered Microspheres

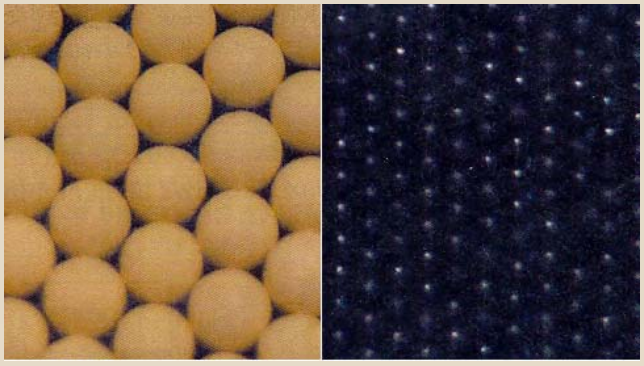

- 1000 µm air dried spheres on left
- 500 – 532 µm sintered spheres on right

Oak Ridge Sol-Gel System

- Oil flows from heating reservoir through gelation column back into reservoir.
- Gelation column is where broth undergoes gelling process.
  - Provides area of slow, non-turbulent flow for gelation to occur
- Two methods used to inject broth into silicone oil.
  - Vibratory nozzle sends broth into a flowing veil of oil
    - Nozzle is expensive and difficult to control
  - Needle is directly inserted into tubing upstream of gelation column

TEXAS A&M ENGINEERING

Diagram of Oak Ridge Direct Broth Injection Apparatus

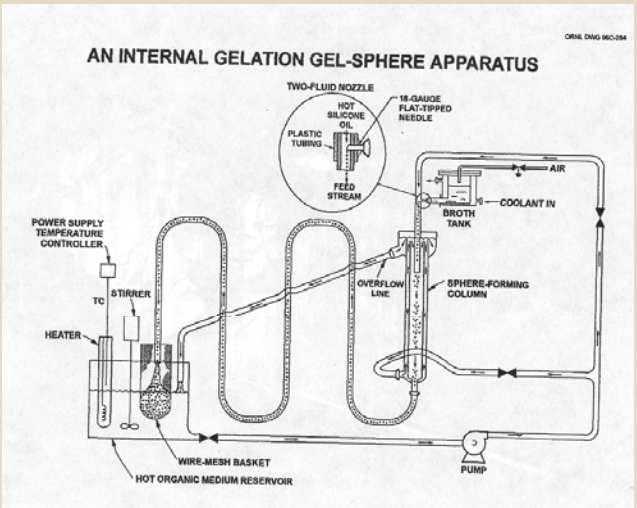

Experimental Setup and Procedure

Evolution of Experimental Apparatus

- Initial system utilized NesLab constant temperature bath, funnel suspended above, and high pressure gas regulator.
- Constant temperature bath replaced with stainless steel batch can. Funnel replaced with stainless steel mesh baskets in oil.
- Gelation column introduced along with low pressure air regulator.

Experimental System Using Pressurized Broth Chamber and Air Injection

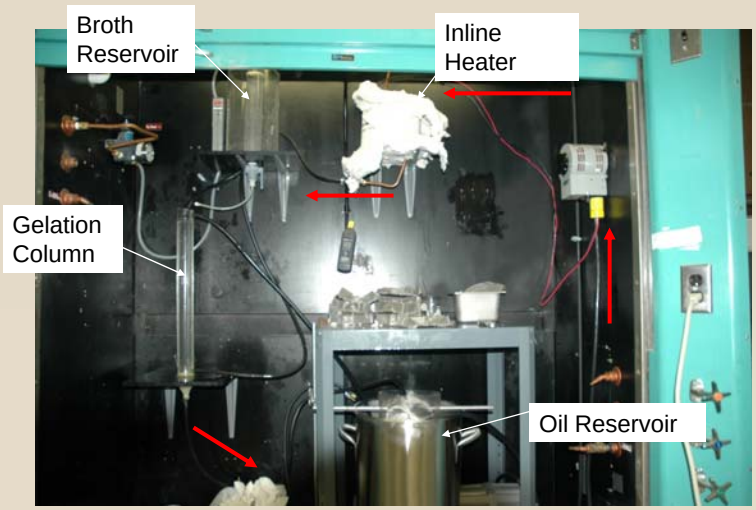

Final Changes to Experimental System

- Syringe and syringe pump replaced broth chamber and forced air system
- Large baskets of 250 x 250 wires per inch mesh are replaced first with smaller 80 x 80 mesh baskets, then finally 40 x 40 mesh.

Finalized Experimental Apparatus

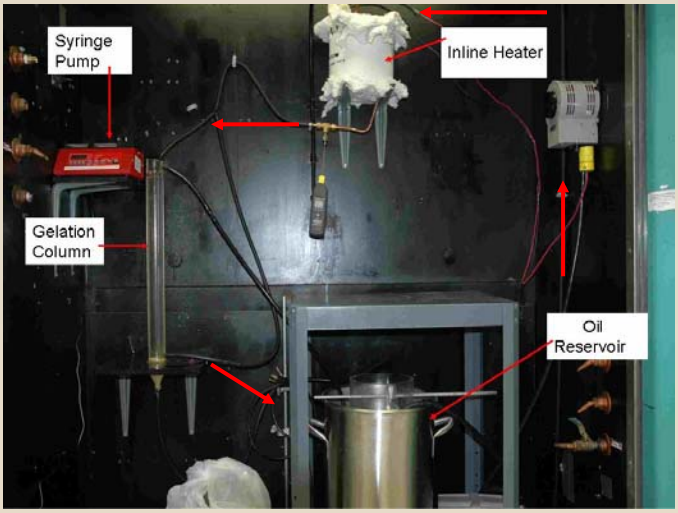

TEXAS A&M ENGINEERING

System Preparation

- Several hours before run, hot plate is turned to approximately 125°C.
- Solutions readied and placed into freezer with syringe.
- Peristaltic pump and ceramic fiber heater turned on to bring flowing oil to desired temperature of 90-110°C.

Experimental Procedure

- Catch basket placed into holder in oil reservoir.
- Broth is poured into syringe, placed in syringe pump, and the needle is placed in the oil stream.
- Syringe pump is started at desired injection rate and broth flows into gelation column.
- After injection finished, spheres allowed to age in oil for set period of time.

Washing of Spheres

- Spheres are first washed in hexane to remove silicone oil.
- Washed in 3 stage process for 60 – 75 minutes per stage. (ORNL Method)
  - 50% isopropyl alcohol; 50% 1.5 M Ammonium Hydroxide
  - 0.5 M Ammonium Hydroxide
  - 75% isopropyl alcohol in water

Experiment Results

Master Solutions

- 3.2 M of both HMTA and Urea produced from dry forms.
- 3.0 M solution of Cerium Nitrate produced from dry form.
- Kept separate and chilled until nearing time of injection.

First Experiments (1-9)

- Experiments 1-9 performed with air injection system and without gelation column.
  - 1.3 M cerium nitrate and 1.68 M HMTA/Urea for all
- Product is amorphous blobs with slight hints of spheres visible.
- Problems finding ideal injection pressure and keeping broth from early gelation in broth chamber and feed line.

- Experiment 3 product.

TEXAS A&M ENGINEERING

Addition of Gelation Column

- Experiments 10-12 run with addition of gelation column.
- Air pressure system injecting broth too fast and agitating oil.
  - 4 psi to below 0.5 psi
- No spherical product.

Small Scale Tests

- Series of ~2 mL tests done in test tubes to determine fastest gelling broth composition.
- Results show higher concentrations of HMTA and urea leads to faster gelling.

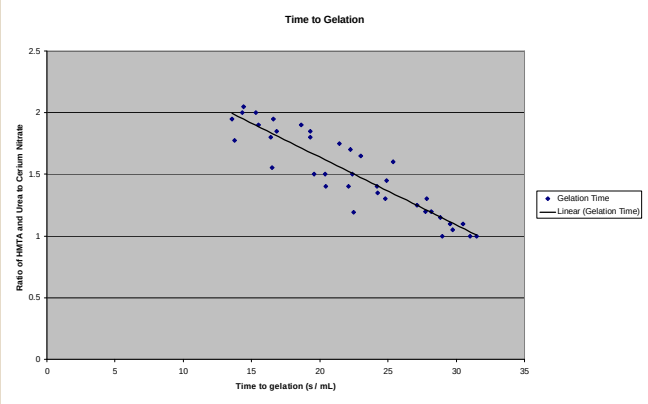

TEXAS A&M ENGINEERING

Manual Syringe Injection

- Experiments 13-16 use 2.13 M HMTA/Urea and 1 M cerium nitrate
- First batches of all spheres
- No constant sphere size and sizeable amounts of unformed gel produced by inconsistent injection rates.

- Experiment 13 product.

Addition of Syringe Pump (Exp 17 and 18)

- 2.13 M HMTA/Urea and 1 M Cerium Nitrate
- Allows for constant injection rate.
- Hands free device, allows attention elsewhere during injection.
- Real time injection volumes.

Broth Concentration Changes (Exp 19-36)

- HMTA/Urea varied between 2.06 M and 1.52 M.
  - Lowered below 1.64 M and an excess of unformed gel is produced.
  - Raised above 1.78 M and product is cracked out of oil (brittle and hollow).
- Most experienced breakdown during wash in ammonium hydroxide.
- Contamination because issue.

Product formed from Experiments 23 and 31

- 1.78 M HMTA/Urea and 1.33 M Cerium Nitrate.
- Washed in Hexane.

- 1.62 M HMTA/Urea and 1.48 M Cerium Nitrate.
- Washed in Hexane and 0.1 M Ammonium Hydroxide.

TEXAS A&M ENGINEERING

Premature Gelation Problems

- Needles became clogged in Experiments 22, 24, 25, and 32.
- Entire syringe became gelled and run scrapped in Experiments 25, 27, and 32.
- Several new syringes bought prior to Experiment 28 with each run getting fresh syringe beginning with Experiment 33.

Investigation of Stable Point (Exp 37-48) and Wash Methods

- HMTA/Urea levels of 1.65 to 1.67 M.
- Cerium nitrate between 1.44 and 1.46 M.
- Spheres washed only in hexane do not breakdown during drying.
- Investigation into proper molarity of ammonium hydroxide wash.

Exp. #	Am. Hyd. Wash (M)
47A	2
47B	1
48A	.75
48B	.5

TEXAS A&M★ENGINEERING

Product formed in Experiments 39, 47A, and 48B



- All performed with broth of 1.65 M HMTA/Urea and 1.45 M Cerium Nitrate.
- 18 ga. needle and 30 minute aging time for all.

Increased HMTA/Urea Concentration (Exp 49-53)

- Attempt to find broth that would remain solid after full washing and drying.
- Implementation of Oak Ridge Stage Washing
  - 50% isopropyl alcohol; 50% 1.5 M ammonium hydroxide
  - 0.5 M ammonium hydroxide
  - 75% isopropyl alcohol in water
- Spheres do not stick together during washing.
- Product appears good after washing, but cracked after drying.

TEXAS A&M ENGINEERING

Washed Spheres from Experiments 49 and 53

- 1.68 M HMTA/Urea : 1.43 M Cerium Nitrate.
- Two Washes of 3 M Ammonium Hydroxide.

- 1.68 M HMTA/Urea : 1.43 M Cerium Nitrate.
- Oak Ridge Wash System for 60 minutes each stage.

TEXAS A&M ENGINEERING

Stage Washing With Stable Broth (Exp 54-59)

- All performed at 1.65 M HMTA/Urea and 1.45 M Cerium Oxide.
- Variations in aging time and oil temperature.
  - 90°C oil gelled near bottom of column producing unformed gel
- Washed and dried spheres were brittle and showing cracks.

- Spheres from Exp. 56 after undergoing first stage of Oak Ridge Wash.

TEXAS A&M ENGINEERING

Addition of Water to Dilute Solutions (Exp 60-66)

- Diluted to examine possibility that broth was too strong and dissolving itself during drying.
- Large amounts of unformed gel present when removed from oil.
- Washed and dried product was still powder like and brittle.

Exp #	HMTA/ Urea (M)	Ce. Nitrate (M)
60	1.48	1.29
61	1.42	1.25
62	1.56	1.37
63	1.35	1.05
64	1.65	1.29
66	1.62	1.42

Powder Product from Experiment 62

- 1.56 M HMTA/Urea : 1.37 M Cerium Nitrate.
- Aged for 30 minutes.

Results of Experiments 67-70

- Elevated basket out of oil during injection; lowered in to age.
- Exp. 69 and 70 performed at elevated oil temperatures and washed for 75 minutes each step.
  - Product is white and brittle, but solid
  - Extended analysis performed

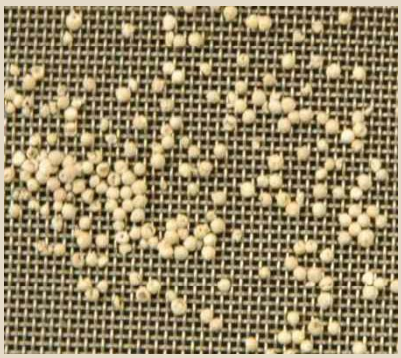

- Unheated sample from Experiment 69

Analysis of Spheres

Analysis Techniques

- Thermogravimetric Analysis (TGA)
  - High precision analysis of weight change in relation to temperature
- Differential Scanning Calorimetry (DSC)
  - Measure of difference in amount of heat required to maintain sample and a reference at same temperature
- X-Ray Diffraction (XRD)
  - Used to identify sample product by comparison of diffraction data

Experiment 1 Analysis (poor formation)

- Product identified as Cerium Oxide through XRD.
- Extended period of time between gelation and analysis.

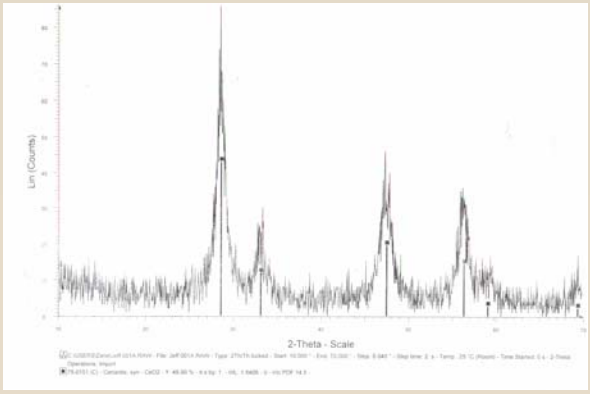

Experiment 39 Analysis

- Spheres washed only in hexane; oily texture even after dried.
- Unidentified product through XRD analysis.
- 1.65 M HMTA/Urea and 1.45 M Cerium Nitrate

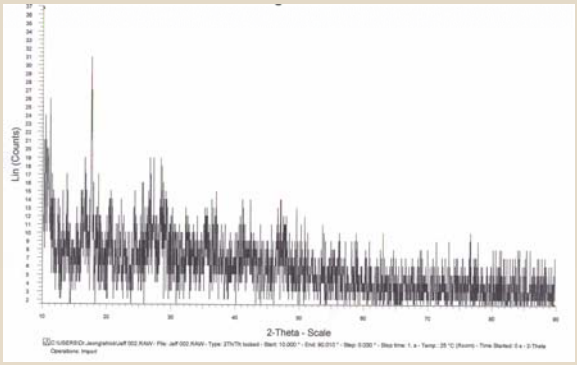

TGA and DSC for Experiment 56

- Product washed in hexane, aged for 90 minutes, then underwent first step of stage washing before basket failure.
- Strong exothermic reaction occurs at roughly 205°C resulting in a rapid 40% mass loss. 60% total loss when heated to 1400°C.
- Large sample run cancelled due to smoke and equipment failure.

TEXAS A&M ENGINEERING

DSC and TGA Results for Experiment 56

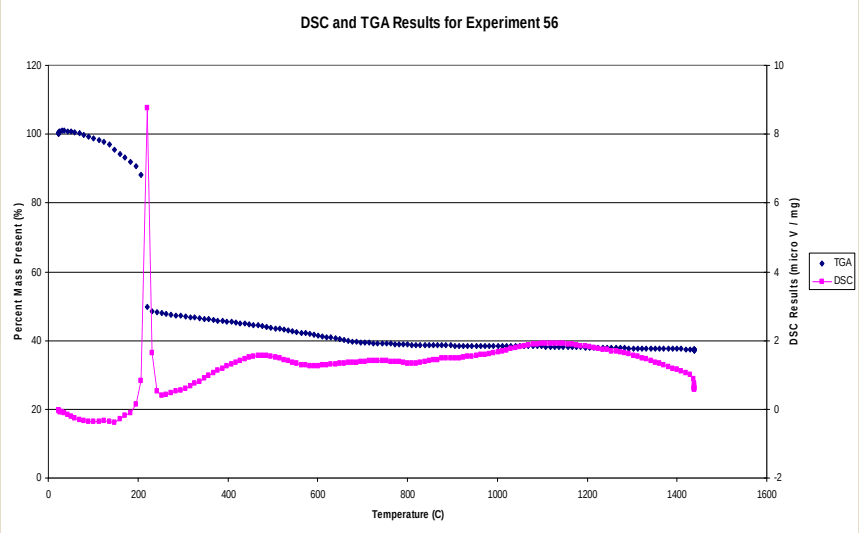

TEXAS A&M ENGINEERING

XRD Results for Experiment 56 (Non-heated)

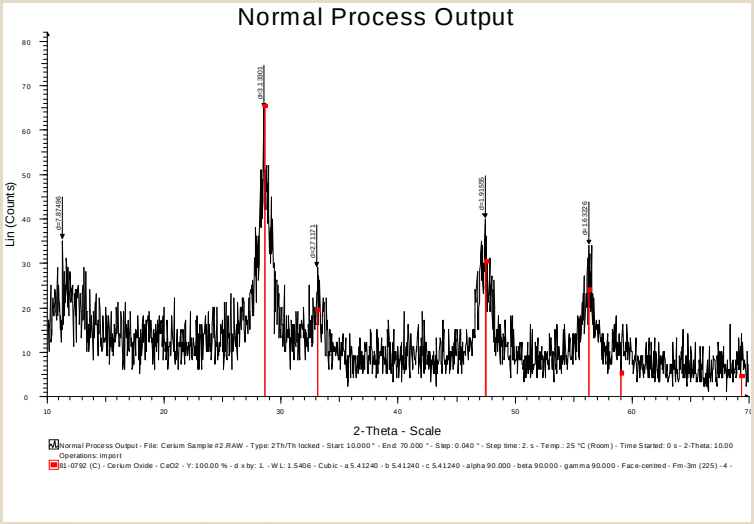

TEXAS A&M ENGINEERING

XRD Results for Experiment 56 (Heated)

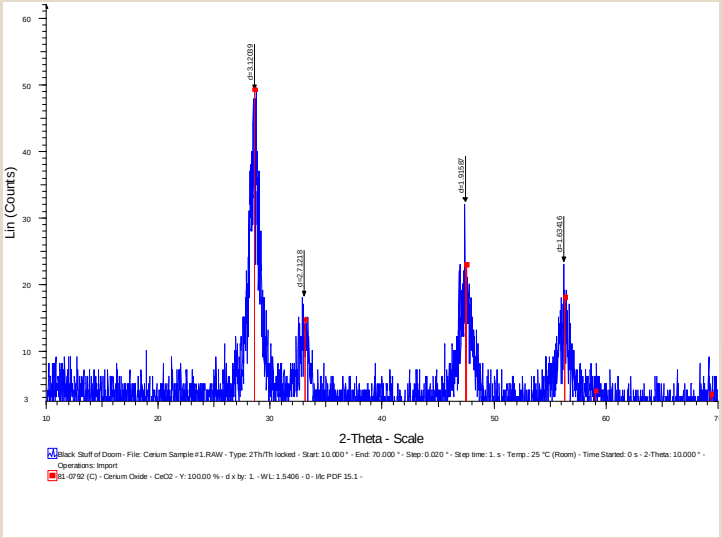

TEXAS A&M ENGINEERING

Experiment 69 Analysis

- Small sample underwent DSC and TGA to 500°C.
  - Exothermic reaction and mass drop at 200°C
- Unheated sample analyzed through XRD.
  - Identified as Cerium Oxide and an “organic” cerium-bearing impurity
- Large sample heated to 175°C and held for 2 hours, then underwent XRD.
  - Identified as Cerium Oxide
- Large sample heated to 300°C and held for 2 hours, then underwent XRD.
  - Identified as Cerium Oxide

TEXAS A&M ENGINEERING

DSC and TGA for Experiment 69

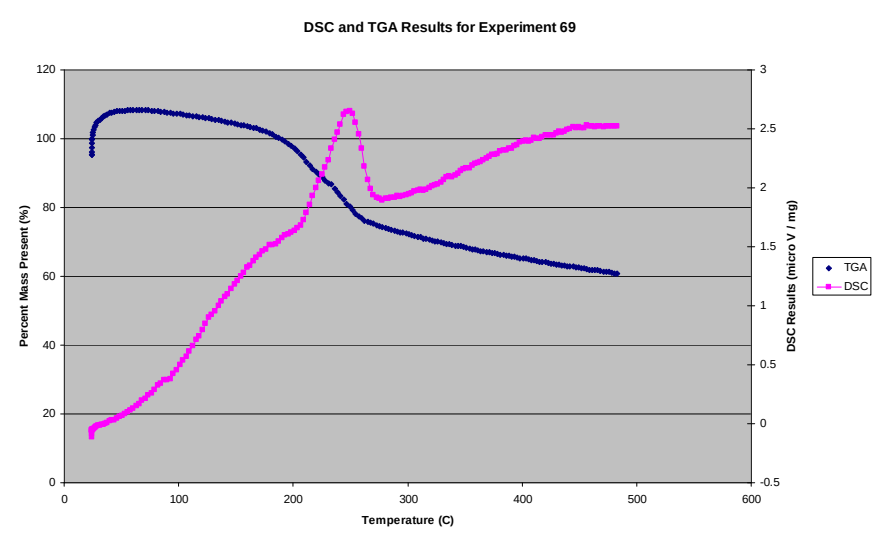

TEXAS A&M ENGINEERING

Experiment 69 XRD Results (No Heating)

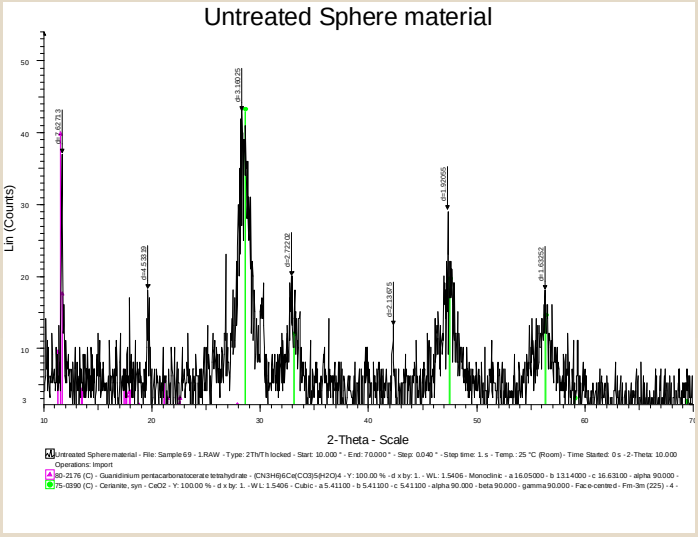

TEXAS A&M ENGINEERING

Experiment 69 XRD Results (Heated to 175ºC)

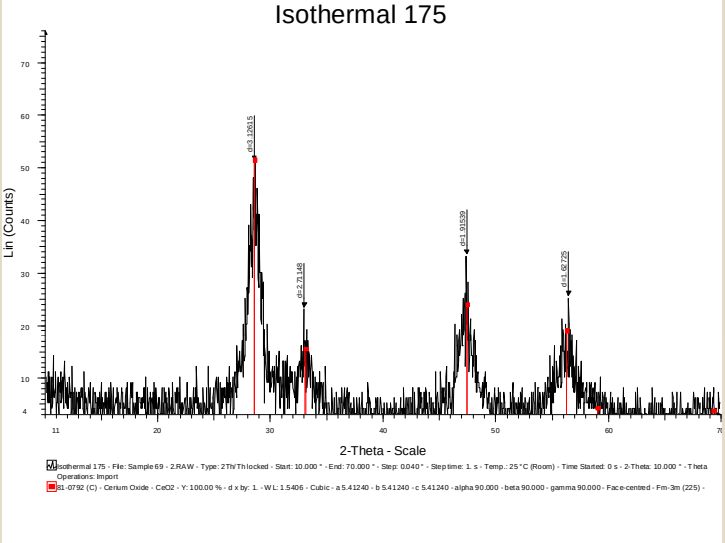

TEXAS A&M ENGINEERING

Experiment 69 XRD Results (Heated to 300°C)

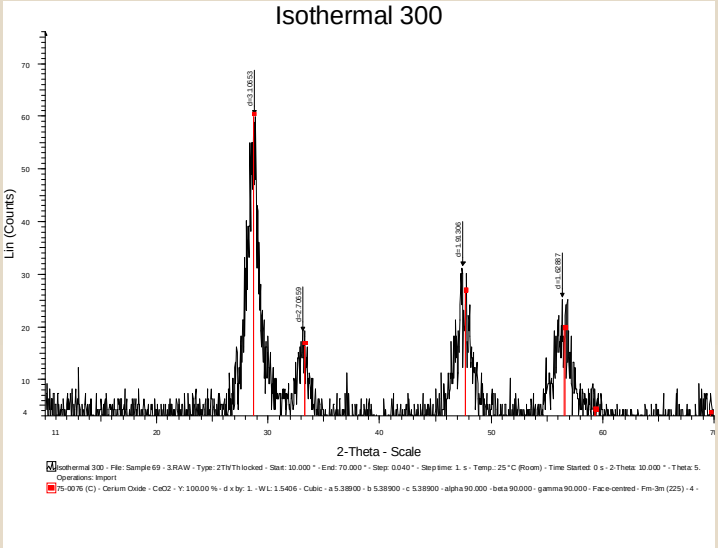

TEXAS A&M ENGINEERING

Experiment 70 Analysis

- Small portion underwent DSC and TGA.
- Half of remaining heated to 1460°C for 4 hours for sintering followed by XRD.
  - Product identified as cerium oxide
- Non-heated portion underwent XRD.
  - Identified as cerium oxide and two possible “organic” cerium-bearing impurities

Experiment 70 Product

- Non-heated portion on left, sintered product on right.

TEXAS A&M★ENGINEERING

Experiment 70 TGA

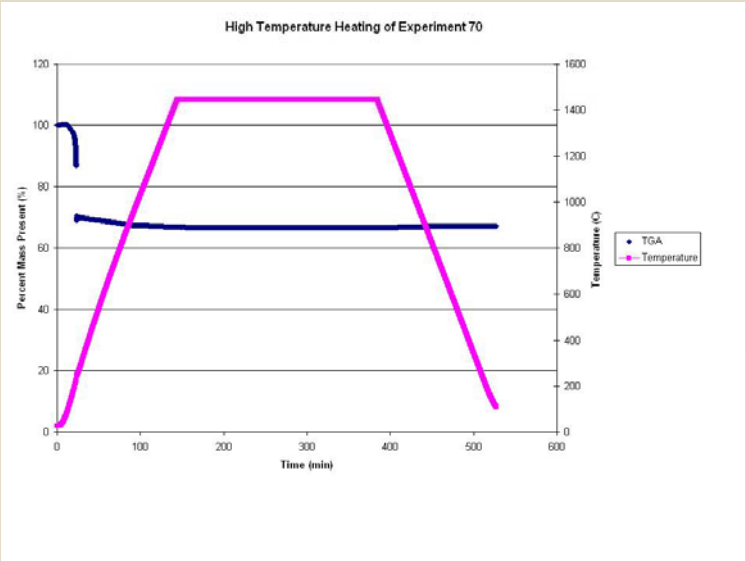

TEXAS A&M ENGINEERING

XRD for Non-Heated Experiment 70 Sample

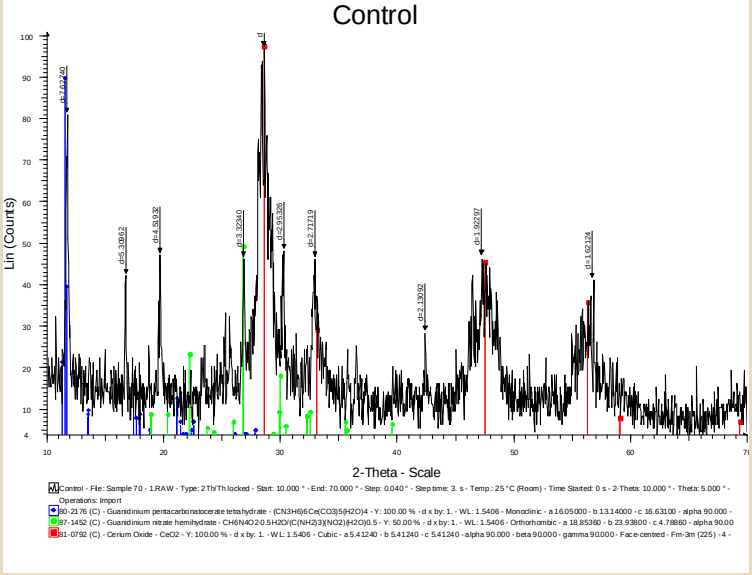

TEXAS A&M ENGINEERING

XRD for Heated Experiment 70 Sample

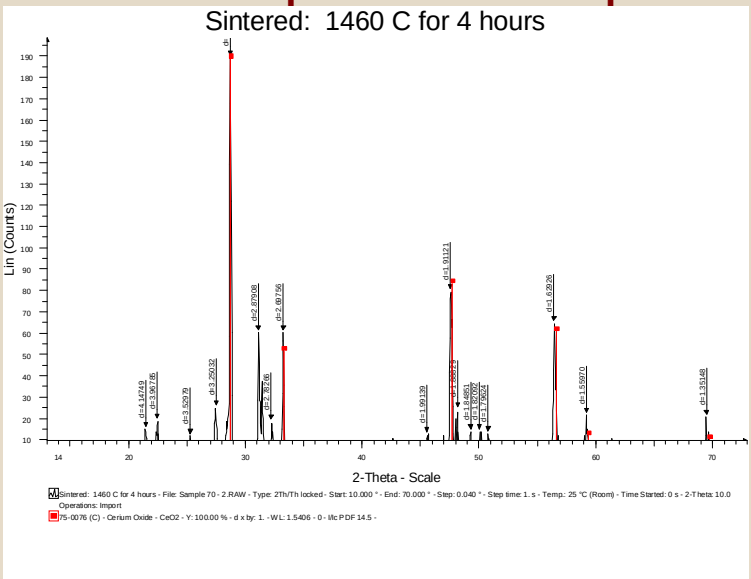

Summary

TEXAS A&M ENGINEERING

Summary

- Increased concentrations of HMTA and urea produce faster gelling spheres with decreased quality.
- Solution of 1.65 M HMTA/Urea and 1.45 M Cerium Nitrate produces highest quality spheres after aging that best withstand washing.
- Addition of gelation column and syringe pump were the key to producing microspheres.
- Cerium oxide microspheres were obtained by fully washing and heating the spheres from several experimental runs.

Recommendations

- Further analysis of gelation occurring above 100°C.
- Larger gelation column would allow a longer time of gelation.
  - Original was longer, but cracked during construction.
- Density and size measurements on spheres will be required.

Acknowledgements

- Dr. McDeavitt for guidance and the opportunity to finish at Texas A&M
- Jeff Hausaman, Michael Naramore and Zane Adams for help in completing analysis work
- Luis Ortega, Adam Parkison, and Aaron Totemeier for encouragement and advice along the way
- All members of FCML for assistance in completing the project

References

- A.J. Parkison, (2008). Hydride Production in Zircaloy-4 As A Function of Time and Temperature. M.S. Thesis, Texas A&M University, College Station, TX.
- A.R. Totemeier, (2006). Title. M.S. Thesis, Purdue University, West Lafayette, IN.
- S.M. McDeavitt, A. Parkison, A.R. Totemeier and J.J. Wegener, Fabrication of Cermet Nuclear Fuels Designed for the Transmutation of Transuranic Isotopes, Materials Science Forum, 561-565: 1733-1736 (2007).
- S.M. McDeavitt, Development of an Engineered Product Storage Concept for the UREX+1 Combined Transuranic/Lanthanide Product Streams, Quarterly Progress Report, July 1, 2005.
- J.L. Collins, R.D. Hunt, G.D. Del Cul and D.F. Williams, Production of Depleted UO2 Kernels for the Advanced Gas-Cooled Reactor Program For Use in TRISO Coating Development, ORNL/TM-2004/123 (2004).
- P. Naefe and E. Zimmer, Preparation of Uranium Kernels by an External Gelation Process, Nuclear Technology. 42 (1979), p. 163-71.

TEXAS A&M ENGINEERING

References

- J.L. Collins, M.H. Lloyd, and R.L. Fellows, The Basic Chemistry Involved in theInternal-Gelation Method of Precipitating Uranium as Determined by pH Measurements, Radiochimica Acta. 42 (1987), p. 121-34.
- J.L. Collins, Experimental Methodology for Determining Optimum Process Parameters for Production of Hydrous Metal Oxides by Internal Gelation, ORNL/TM-2005/102 (2005).
- V.N. Vaidya, S.K. MukerJee, J.K. Joshi, R.V. Kamat, and D.D. Sood, A Study of Chemical Parameter of the Internal Gelation Based Sol-Gel Process for Uranium Dioxide, Journal of Nuclear Materials. 148 (1987), p. 324-31.
- P.A. Haas, J.M. Begovich, A.D. Ryon and J.S. Vavruska, Chemical Flowsheet Conditions for Preparing Urania Spheres by Internal Gelation, Ind. Eng. Chem. Prod. Res. Dev. 19 (1980), p. 459-67.
- R.D. Hunt and J.L. Collins, Uranium kernel formation via internal gelation, Radiochim. Acta. 92 (2004), p. 909-15.
- J.L. Collins and J.S. Watson, Economic Evaluation for the Production of Sorbents and Catalysts Derived from Hydrous Titanium Oxide Microspheres Prepared by the HMTA Internal Gelation Process, ORNL/TM-1999/212 (2000).
- J.C. Marra, A.D. Cozzi, R.A. Pierce, and J.M. Pareizs, Cerium as a Surrogate in the Plutonium Immobilized Form, DE-AC09-96SR18500.

Appendix E

Master of Engineering Report: Hydride System Development (91 Pages)

ESTABLISHING METHODS FOR RECYCLING SPENT ZIRCALOY CLADDING USING A HYDRIDE-DEHYDRIDE PROCESSING ROUTE

A Project Report

Submitted to the Faculty of Purdue University Nuclear Engineering

By

Dustin T. Kraemer

Requirement for the Degree of
Master of Science in Nuclear Engineering

August 2005

ESTABLISHING METHODS FOR RECYCLING SPENT ZIRCALOY CLADDING USING A HYDRIDE-DEHYDRIDE PROCESSING ROUTE

A Project Report

Submitted to the Faculty

of

Purdue University Nuclear Engineering

by

Dustin T. Kraemer

Requirement for the Degree

of

Master of Science in Nuclear Engineering

August 2005

"*Deep is the well of truth and long does it take to know what has fallen into its depths*"
- *Friedrich Nietzsche,* 1844-1900

ACKNOWLEDGEMENTS

I would like to thank Dr. Sean M. McDeavitt, my major professor, for accepting me as his graduate student and contributing the time and motivation to help me succeed. I would like to thank the faculty of Nuclear Engineering for their support and encouragement in my endeavors at Purdue University. I'd also like to thank Dr. S. Revankar, Dr. R. Taleyarkhan, and Dr. R. Trice for serving as members of my advisory committee. I would like to thank Paul Mews and Eric Howell for their help in building the glovebox. In addition, I would like to thank Adam Parkinson, who will be continuing this research, for his help in running recent experiments and evaluating some of the results.

I would like to acknowledge the U.S. Department of Energy's Nuclear Energy Research Initiative for the support of this research project (NERI ID NO. DE-FC07-05ID14656).

I want to thank the United States Navy for allowing me to pursue my master's degree prior to accepting my commission. I would especially like to thank my friends, who have come and gone, for their understanding while I chased my goals. Finally, I would like to thank my family for their continued support in all I do.

TABLE OF CONTENTS

ABSTRACT

Kraemer, Dustin T. MSNE., Purdue University, August 2005. Establishing Methods for Recycling Spent Zircaloy Cladding Using a Hydride-Dehydride Processing Route.
Major Professor: Sean M. McDeavitt.

Materials handling and processing equipment and early process development equipment were developed to recycle spent nuclear fuel cladding (i.e., Zircaloy) into a metal powder that may be used for advanced nuclear fuel fabrication. An inert atmosphere glove box for preparation and analyzing of specimens, a hydride process system, and a dehydride process system were designed and fabricated for the purpose of establishing feasibility of recycling Zircaloy cladding hulls from spent nuclear fuel. Initial experiment analysis established criteria for hydriding of tubular Zircaloy specimens. It was found that brittle hydrides can be formed from Zircaloy tubes and crushed to fine powder. The designed dehydride process was built to decompose the zirconium hydride powder formed through the hydride process. Initial analysis of the hydriding apparatus and design recommendations are made.

1. OVERVIEW

This project report describes the establishment of materials handling and processing equipment and early process development experiments. The ultimate goal of this activity is to develop a recycling approach that will convert spent nuclear fuel cladding from light water reactors (i.e., Zircaloy) into a metal powder that may be used for advanced nuclear fuel applications. More specifically, this activity is a component of a larger project that is developing a zirconium matrix cermet storage form as a possible transmutation fuel form for transuranic oxides; this research is sponsored by the United States Department of Energy's Nuclear Energy Research Initiative (NERI) under project DE-FC07-05ID14656[11].

The process being developed involves the vapor phase synthesis of zirconium hydride (hydriding), conversion of the hydride to powder, and the conversion of the hydride back to metallic powder (dehydriding). The object of this project was to assemble the requisite equipment to enable process development experiments followed by initial process demonstration experiments. This included the establishment of a controlled atmosphere tube furnace for the hydriding reaction, an inert atmosphere glovebox for powder handling, and a small heater/crucible system in the glovebox's airlock for the dehydriding reaction.

In the process demonstration experiments, Zirconium hydride was generated using Zircaloy tubes and cubic samples (mass < 10 g) at temperatures between 400^{o}C and

750°C. The demonstration experiments provided data to clarify coarsely-defined process variables for pressure, temperature, flowrate, and process time. Results show that heavily hydrided samples were produced when processed between 500 and 600°C, 23 to 28 inches of water, and 6 to 12 hours of exposure to hydrogen. The resulting product could be ground to fine powder via a mortar and pestle. This demonstrates the viability of this hydride process for Zircaloy recycle.

1.1 Justification for Research

The US Department of Energy's Advanced Fuel Cycle Initiative (AFCI) is developing processing methods to recycle transuranic (TRU) oxides from spent nuclear fuel [11]. The plan for the recycled TRU isotopes is to burn or transmute them in a yet to be determined nuclear system that could be a Generation IV nuclear reactor (fast or thermal) or an accelerator-driven transmutation device [11]. The TRU nuclear properties make the fast spectrum systems especially efficient for isotopic destruction; thermal nuclear systems will transmute the TRU isotopes, but they tend to produce as much TRUs as they destroy. On the other hand, near term engineering research programs are focused on TRU burning in thermal reactors because of the ready availability of these systems. These TRU isotopes have long half lives (> 20 years) and high alpha particle activities (>100 nCi/g) [12] [19].

The chief end of the parent NERI project that governs this present work is to place the TRU isotopes into an acceptable form for short-term storage. The proposed

storage form comprises TRU/REFP mixed oxide microspheres incorporated into a metal matrix cermet pin [11]. As a broad overview, the processes involved in the generation of a cermet pin will include the recycle of Zircaloy cladding to form the cermet matrix, the conversion of the TRU/REFP isotopes into oxide microspheres, and the final cermet fabrication process. The proposed Zircaloy recycle process is the hydride-dehydride process described in this report. The TRU/REFP conversion will be accomplished by a sol-gel microsphere generation process and cermet fabrication will combine the recovered Zircaloy powder with the TRU/REFP oxide microspheres to be accomplished by hot extrusion [11].

The metal matrix is the relevant issue in this current project since the recycled Zircaloy powder is designed to become feed material for the cermet fabrication process. The design goal of the storage form is to secure the extracted TRUs in a safe, proliferation resistant state until a TRU-burning fast reactor infrastructure is in place (50 to 60 years). The primary advantage of using a cermet storage form is that it may be inserted directly into a fast reactor for TRU burning with minimal post-storage processing (that is, assuming that the in-situ He gas generation from alpha decay is properly vented through a porous matrix).

Spent fuel from a Light Water Reactor (LWR) contains large amounts of Zircaloy waste. The key advantage of recycling the Zircaloy cladding alloy is that it is already of nuclear grade quality (i.e., the natural hafnium content of zirconium has been removed for neutronic purposes). In addition, the reduction in waste volume associated with spent Zircaloy hulls could have an economic benefit to the cost of radwaste disposal. An economic analysis is planned as part of the parent NERI project to evaluate the costs and

benefits. Some technical issues that may hinder the Zircaloy recycle process include 1) the surface oxide that forms on the Zircaloy cladding during LWR service, and 2) the elevated radiation levels associated with the spent hulls due to neutron activation and fuel-cladding chemical interactions[18]. Therefore, the ultimate goal of the Zircaloy recycle task project is to engineer a hydride-dehydride processing solution that overcomes or accommodates these complications. This present work has laid the foundation for this goal.

1.2. Present Work

The establishment of the hydride and dehydride processing equipment was accomplished to explore the feasibility of the individual operations involved in the proposed Zircaloy recycle process. An inert atmosphere glovebox (Section 3.2) was constructed to handle, load, and evaluate samples and powders before and after experiments; zirconium and zirconium hydride powders are pyrophoric and rapidly oxidize in air. The starting samples were Zircaloy tubes and solid pieces cut into rough cube shapes. An analytical balance was installed inside of the glovebox to enable the discernment reaction completion though mass change measurements; selected products powders were also analyzed using x-ray diffraction.

Inside of the glovebox, metal samples were sealed into an aluminum oxide tube (~6 cm diameter) with a stainless steel tube cap with inlet and exit lines for the process gas. This vessel was loaded and transferred through the vacuum airlock of the glovebox

and placed inside of a tubular furnace (Section 3.3). An Ar-5%H_2 gas mix was regulated and allowed to flow through the vessel for 6 to 24 hours.

The post-test hydride samples were unloaded inside of the glovebox and evaluated using an analytical balance to calculate the mass increase in the sample due to formation of hydrides and/or oxides. The results presented in Section 4 show that the hydride process is effective for forming brittle hydrides from the Zircaloy tubes at temperature between 500 and 600°C with pressures above 23 inches of water under flowing Ar-5%H_2. Inefficient hydriding was accomplished at other temperatures between 300°C and 800°C, but the process was quite slow at temperatures below 500°C and the formation of ZrH_2 is less favorable at temperature above 600°C.

Toward the end of this project, a simple dehydride apparatus was designed and built. This system is now operational but the dehydride process was not demonstrated for this report. The apparatus consists of a wire-style resistance heater with a maximum temperature near ~900°C wrapped around an alumina crucible that may contain the zirconium hydride powder. The apparatus is operated under vacuum inside the airlock of the glovebox (Section 3.4). This apparatus was not part of the original scope of this particular student project, but became evident during the hydride demonstration experiments and construction was completed quickly. Thus, the system description is included in this report to provide documentation for future researchers.

2. BACKGROUND

2.1. Zirconium Hydride

The primary reaction of interest is the ZrH_2 formation reaction that occurs between the zirconium in the Zircaloy cladding and the hydrogen in the Ar-5%H_2 process gas. This reaction is written as

$$Zr + H_2 \rightarrow ZrH_2 \ . \tag{2.1}$$

Slight hydriding of the Zircaloy will harden the metal, but extensive hydride formation will severely strain the lattice, thus embrittling the Zircaloy and ultimately causing a loss of structural integrity [1]. The hydride phase transformation takes the Zircaloy from a hexagonal close packed structure with a density of 6.5 g/cm^3 to a tetragonal structure with a density of 5.6 g/cm^3[1]. During this transition, a physical transformation occurs as the material becomes brittle and, under the right conditions, can be formed into a powder. Industrially produced (i.e., Ormet-Wah Chang) zirconium hydride powder is produced in a three part process (hydriding, milling, dehydriding). Milling is implemented while the

zirconium powder is highly brittle. This increases the ability for ZrH_2 to decompose fully to fine powder.

The partial molar (Gibb's) free energy of the hydride reaction (Eq. 2.1) provides a measure for the spontaneity of the reaction and the available work that can be done by the energy released[20]. The partial molar free energy (ΔG) is obtained from the Gibb's energy relation:

$$\Delta G = \Delta G^0 + RT \ln K \tag{2.2}$$

where R is the gas constant (8.314 J/mol·K), T is the temperature in Kelvin, and K is the equilibrium constant. ΔG^o is the standard free energy of the reaction, which is related to the reaction enthalpy and entropy by

$$\Delta G^0 = \Delta H^0 - T\Delta S^0 . \tag{2.3}$$

where ΔH^0 is the Enthalpy and ΔS^0 is the Entropy of the system under standard temperature and pressure. When the reaction is at equilibrium, the free energy, ΔG (Eq. 2.2) will be zero and the relationship between ΔG^o and the equilibrium constant can then be written as

$$\Delta G^0 = -RT \ln K \tag{2.4}$$

Further, the equilibrium constant for the hydride reaction is obtained by the relation:

$$K_{eq} = \frac{[Zr(s)] \times [H_2(g)]}{ZrH_2(s)} \tag{2.5}$$

The thermodynamic data for ZrH_2 formation is presented in Table 2.1. This table was generated using HSC Chemistry v5.1 software [16], which relies on published data from Knacke, et al [15]. The software was used to calculate values for ΔH, ΔS, ΔG and K for temperatures from 0 to 1200ºC in 50 degree increments. It is evident from the data in Table 2.1 that the free energy of formation is negative up to approximately 950ºC to 1000ºC so hydride formation should be spontaneous and does not require catalyzing or heat addition. However, it is also evident that the magnitude of ΔG is quite small for temperatures between 600ºC and 1200ºC such that the process environment may be manipulated through gas pressure and flowrate to manipulate the completion of the hydride reaction.

Further, there are some limiting phenomena that are relevant to the completion of the reaction. These issues include solid state diffusion, hydrogen solubility, and ZrH_2 disassociation at low pressure. Pure zirconium has two allotropic phases: 1) the hexagonal-close-packed α phase which is stable below 862ºC and 2) the body-centered-cubic β phase which is stable from 862ºC to the melting point at 1855ºC[1]. The Zr-H phase diagram presented in Figure 2.1 shows the equilibrium phases at STP, but the diagram also includes pressure isobars ranging from 0.1 to 1000 mmHg that indicate ZrH_2 decomposition at lower pressures. This diagram and the data in Table 2.1, taken

together, indicates that the formation of ZrH_2 is feasible in the presence of flowing hydrogen at 1 atm (760 mmHg) and the decomposition of ZrH_2 is feasible at pressures below ~0.01 atm at elevated temperatures. Therefore, the process engineering experiments will focus on enabling these phenomena with reasonably high reaction rates and minimal handling operations.

Table 2.1. Thermochemical Data for ZrH_2 Formation [15].

Temperature (^oC)	**ΔH (kcal/mol)**	**ΔS (cal/mol·K)**	**ΔG (kcal/mol)**	**K**
0	-40.3363	-30.6434	-31.9660	3.79E+25
50	-40.6437	-31.6806	-30.4061	3.68E+20
100	-40.8788	-32.3593	-28.8039	7.44E+16
150	-41.0612	-32.8193	-27.1737	1.09E+14
200	-41.2037	-33.1383	-25.5243	6.18E+11
250	-41.3142	-33.3608	-23.8615	9.31E+09
300	-41.3978	-33.5137	-22.1894	2.9E+08
350	-41.458	-33.6146	-20.5110	15637660
400	-41.4971	-33.6753	-18.8286	1298797
450	-41.5171	-33.7040	-17.1440	151942.1
500	-41.5190	-33.7068	-15.4586	23449.12
550	-41.5041	-33.6881	-13.7737	4542.296
600	-41.4729	-33.6514	-12.0901	1062.711
650	-41.4261	-33.5994	-10.4088	291.3536
700	-41.3640	-33.5340	-8.7304	91.37697
750	-41.2872	-33.4571	-7.0556	32.15386
800	-41.1959	-33.3700	-5.3849	12.49494
850	-41.0902	-33.2738	-3.7187	5.292694
900	-41.8998	-33.9857	-2.0294	2.388334
950	-41.6877	-33.8088	-0.3345	1.14756
1000	-41.4596	-33.6260	1.3514	0.586141
1050	-41.2156	-33.4381	3.0280	0.316091
1100	-40.9562	-33.2457	4.6951	0.178923
1150	-40.6815	-33.0492	6.3525	0.105774
1200	-40.3918	-32.8492	8.0000	0.065022

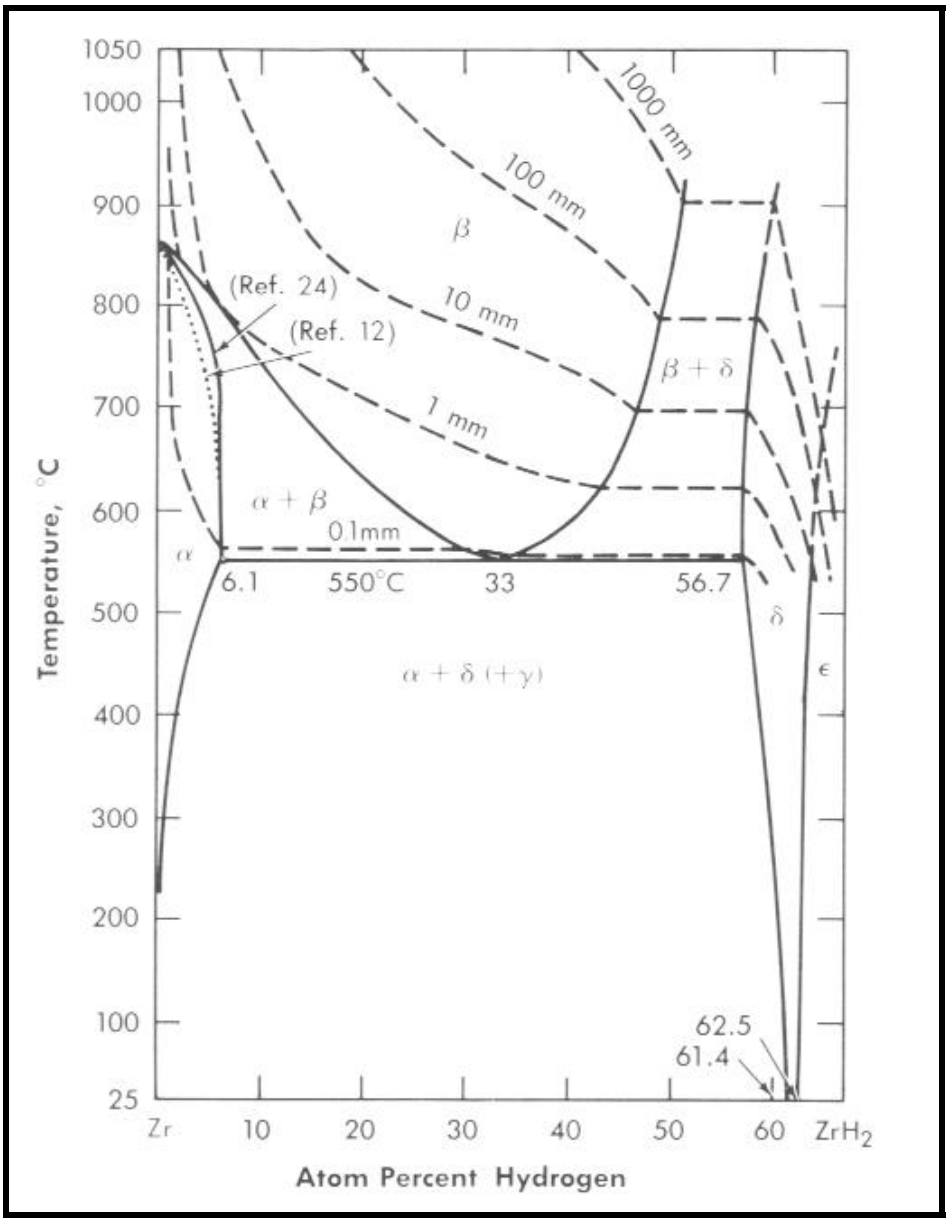

Figure 2.1. Zr-ZrH_2 Phase Diagram [1].

2.2. Zirconium Oxide

The possible presence of oxygen in the experimental system makes it imperative to understand the formation of oxides that will hinder the process efficiency of the Zircaloy recycle process. Specifically, zirconium oxide (ZrO_2) will be readily formed if the alloy samples are contacted with oxygen at the process temperatures. Because of this, it is relevant to understand the reaction and quantify the mass change associated with the reaction to account for error in the system. The oxide reaction is written as

$$Zr + O_2 \rightarrow ZrO_2 \quad . \tag{2.6}$$

The thermochemical data for this formation was generated using HSC Chemistry v5.1 software [16], which relies on published data from Barin [14]. The software was used to calculate values for ΔH, ΔS, ΔG and K for temperatures from 0 to 1200ºC in 100 degree increments. From this data, it is evident that free energy of formation is strongly negative (as seen in table 2.2) and, as expected, ZrO_2 is extremely stable, emphasizing the need for an inert atmosphere.

Table 2.2. ZrO_2 Thermochemical Properties [14].

Temperature (°C)	ΔH (kcal)	ΔS (cal/K)	ΔG (kcal)	K
0	-262.974	-46.3382	-250.317	2E+200
100	-262.920	-46.1844	-245.686	8.1E+143
200	-262.759	-45.8041	-241.087	2.3E+111
300	-262.560	-45.4240	-236.525	1.58E+90
400	-262.351	-45.0871	-232.000	2.13E+75
500	-262.141	-44.7963	-227.507	2.07E+64
600	-261.934	-44.5446	-223.040	6.79E+55
700	-261.731	-44.3247	-218.597	1.25E+49
800	-261.533	-44.1308	-214.174	4.18E+43
900	-262.268	-44.7741	-209.741	1.19E+39
1000	-261.919	-44.4886	-205.278	1.74E+35
1100	-261.565	-44.2211	-200.843	9.31E+31
1200	-259.220	-42.5942	-196.473	1.41E+29

2.3. Trace Element Interactions

There are minor elements in the Zircaloy alloy, so a cursory inspection was made to examine their potential interaction with hydrogen. These elements include Fe, Sn, and Cr [9]. Using HCS Chemistry v5.1 [16], it was noted that known hydride phases exist for the thermodynamic databases, but FeH(g), SnH(g), SnH_4(g), CrH(g), and CrH have positive free energies of formation at the temperatures between 100°C to 1200°C. Therefore, these compounds are not expected to form.

3. EXPERIMENTAL EQUIPMENT AND MATERIALS

As stated above, the ultimate goal of this project is to demonstrate an all-in-one hydride-grinding-dehydride process but the first step toward this is to establish the fundamental process variables for the separate process steps. To that end, the equipment constructed in this present project was designed with the intention of exploring the hydride and dehydride processes as separate operations. The central base of operations for these experiments is an inert atmosphere glovebox that enables the handling of pyrophoric powders and maintaining sample purity (Section 3.2). The hydriding system comprises a controlled atmosphere tube furnace with gas flow control, as described in Section 3.3. The dehydriding system comprises a simple electric heater wrapped around a ceramic crucible in the glovebox airlock, as described in Section 3.4

3.1. Experimental Materials and Specimen Preparation

The starting materials in this project include clean (i.e., non-oxidized and unirradiated) Zircaloy IV cladding tubes and a solid Zircaloy IV alloy cylinder provided by Argonne National Laboratory. Table 3.1 lists some characteristics of the materials used. The materials were sectioned using an oil-cooled diamond saw, cleaned using

ethanol and an ultrasonic cleaner, dried in air and then placed inside of the inert atmosphere glovebox. Zircaloy IV has a large zirconium (~98.2 wt %) content. It is used as a representative material for the commercial cladding alloys, which include Zircaloy 2, Zircaloy 4, and Zirlo, which are all high Zr alloys Pure zirconium exists in two stable phases (α and β) and the phase behavior of the Zr-based cladding alloys is only slightly modified by the alloying additions.

Table 3.1. Selected Properties for Zirconium, Zirconium Hydride, and Zircaloy IV

Pure Materials	**Density (g/cm^3)**	**Air Ignition Temperature***
Zirconium**	6.49	600ºC
Zirconium Hydride†	5.6	270ºC
Zircaloy IV	**Composition‡ (ppm)**	**Composition‡ (wt %)**
Zr	bal	97.81-98.43
Sn	9000-13000	1.2-1.7
Fe	3000-4000	0.18-0.24
Cr	1200-2300	0.7-0.13
O	6800	0.12
other	trace	*

* Ignition temperature for fine powders with -325 mesh (~44μm) particle size.
** data provided by Electronic Space Products International, Inc.[17]
† data provided by A.D. Mackay, Inc.[10]
‡ data provided by Oremet-Wah Chang, Inc.[9]

Samples were loaded into the hydriding chamber inside of an inert atmosphere glovebox, transferred out using an airlock, and then inserted into a tubular furnace where a hydrogen gas mix was forced into and out of the chamber. Temperatures were controlled using a variable transducer and the temperature profile for each test was recorded using thermocouples attached to a computer-based data acquisition system. The

samples were then reopened after transfer back into the inert atmosphere where the final samples were measured using an analytical balance to compare post experiment mass with pre experiment mass. The mass increase was then calculated to determine the amount of hydrogen picked up and percent hydrided.

3.2. Glovebox Design

An inert atmosphere glovebox was acquired from Purdue University's Chemistry Department and was stripped, redesigned, and extensively modified to accommodate current and future projects. Figure 3.1 shows a schematic of the glovebox setup used for this project and Figure 3.2 shows a photograph of the equipment in operation. The original glovebox consisted of stainless steel sheets, gasketed by clamps, bolted to a steel frame which had a large Plexiglas viewing window and two glove ports. The gasket material and gloves were changed to RTV silicon sealant and ambidextrous hypalon gloves. Additionally, the inner seams were sealed with RTV silicone rubber compound to further reduce leakage.

Small penetrations were capped or sealed and new threaded penetrations were welded to the rear panel. These penetrations accommodated the gas inlet tubing, gas exhaust, tubing leading to the photohelic pressure switch for atmosphere control, and the electrical power feedthrough. The inlet gas is 99.997% pure commercial grade argon and it passes into the glovebox via a solenoid valve. The inlet flowpath is channeled to the left side of the box where it is distributed through a perforated flow channel (Fig. 3.1). A

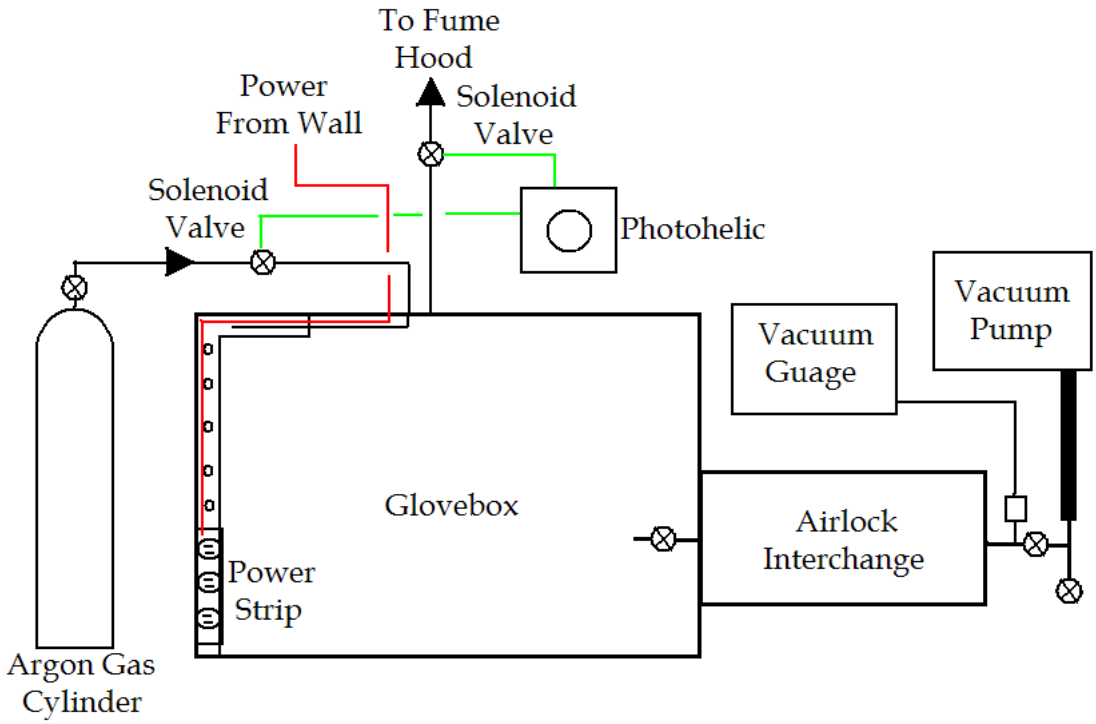

Figure 3.1. Schematic Diagram of the Controlled Atmosphere Glovebox.

Figure 3.2. Photo of the Controlled Atmosphere Glovebox and Support Equipment.

positive pressure is maintained to minimize oxygen leakage into the box. The Dwyer Photohelic pressure switch is coupled to the inlet and exhaust solenoids to maintain the box between 0.2 and 2.5 inches of water operating pressure. The argon gas passes through the box in a once-through scheme and is vented to the building exhaust duct.

The power feedthrough provides electricity to a power strip inside the box. This allows the user to operate the analytical balance, mounted fluorescent lighting, and other electrical devices within the box. An airlock chamber was recycled from a previously decontaminated glovebox and fitted to the glovebox. The airlock allows passage of objects into and out of the glovebox without contaminating the atmosphere with air. A vacuum pump is used to evacuate the chamber to 0.1 mm Hg before opening the inner lock door.

3.3. Hydride Process Design

Hydriding of samples was accomplished using a tube furnace and a controlled atmosphere aluminum oxide reaction vessel capped with a stainless steel tube seal (Figs. 3.3 and 3.4). The tube seal is a gasketed solid disk that was modified to enable the insertion of gas inlet and outlet tubes and a thermocouple feedthrough to enable process monitoring. Figure 3.4 is a detailed schematic of the reaction vessel. A series of stainless steel heat shields were conceived and built to reduce heat transfer from the furnace to the rubber gasket of the tube seal. Figure 3.3 displays a picture of the apparatus as it sits inside of the glovebox. The gas inlet passes through a coil of copper tubing inside of the

heated portion of the process vessel allowing the gas to reach process temperature prior to interacting with the sample. Inside the vessel is a stainless steel sample tray with handle to insert and remove the sample and crucible easily. The sample tray was designed to allow the stream of gas to pass under the tray and sample using the curved end of the alumina reaction vessel to reflect and distribute the flow evenly as it flowed over the sample. The crucibles used are alumina boats as seen later in Figure 4.1.

Argon – 5% hydrogen (Ar-5%H_2) is used as the process gas because the H_2 content is below the flammable gas limit. (Future iterations on this process may involve higher hydrogen concentrations with appropriate safety precautions.). The gas pressure and flowrate was controlled and monitored by a gas flow meter and a magnahelic pressure gage. The process gas travels into the vessel through the copper coil inlet and is therefore heated before contacting the specimen. The spent process gas exits the vessel and passes through a silicon oil bubbler designed to prevent the backflow of air into the system. The silicon oil bubbler and overflow trap were constructed from two Pyrex, 1000 mL Erlenmeyer flasks sealed by rubber stoppers and RTV sealant. Gas inlet and exit from each component was accomplished by tapping holes in the stoppers. The Pyrex flasks are the weakest structural component of the process. Therefore, a 1 psi pressure relief valve was added to the gas inlet stream prior to entering the reaction vessel. The gas was vented to the building exhaust. Figures 3.6 and 3.7 display a schematic and photograph, respectively, of the complete hydride process equipment.

The furnace temperature was controlled with a variable transformer. Real time monitoring and regulating of the temperature was accomplished using the Fieldpoint data acquisition system from National Instruments operated by Labview software. The

thermocouples were placed inside the furnace element and inside the reaction vessel next to the sample. Figure 3.3 is the temperature profile from experiment Zy14 detailed in section 4.14. Temperature was increased to 510^{o}C while flowing argon before hydrogen was introduced. The temperature continued to rise to a peak 564^{o}C before settling at a constant 538.5^{o}C. Hydrogen flow was shut off after 8 hours. At that point power was shut off and pure argon was flowed through the system during cooldown.

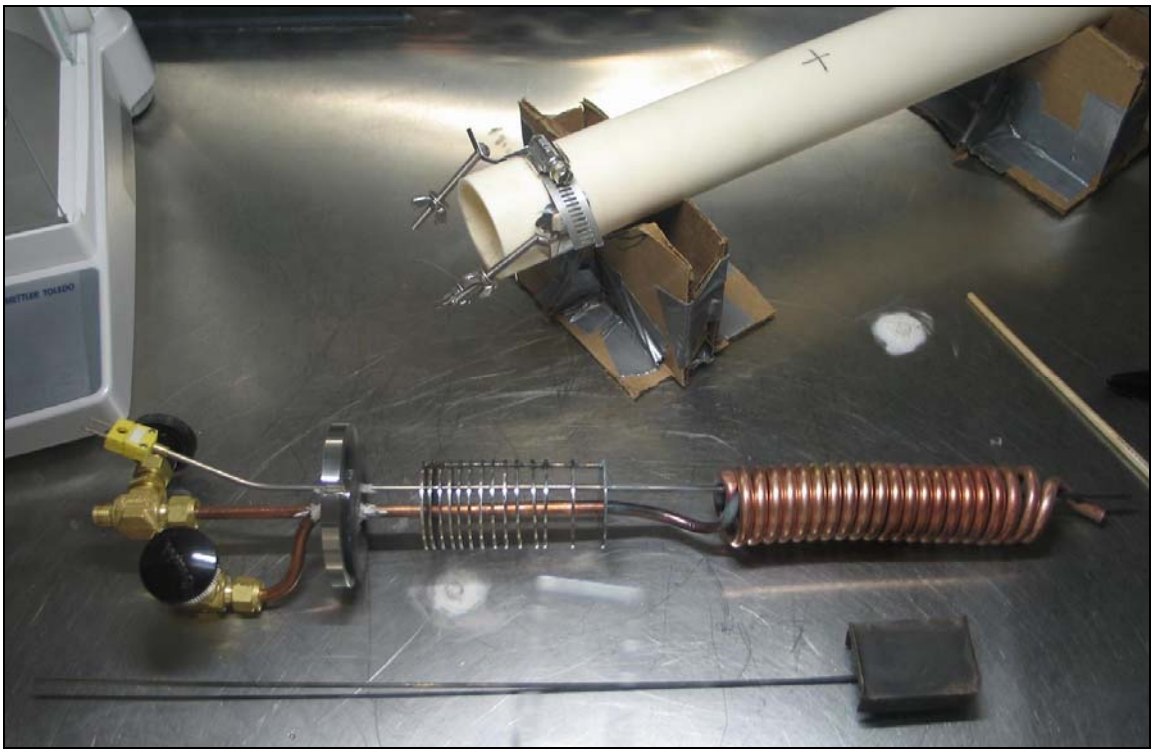

Figure 3.3. Photo of the Hydride Reaction Vessel Showing the Alumina Tube, the Tube Seal and the Sample Tray.

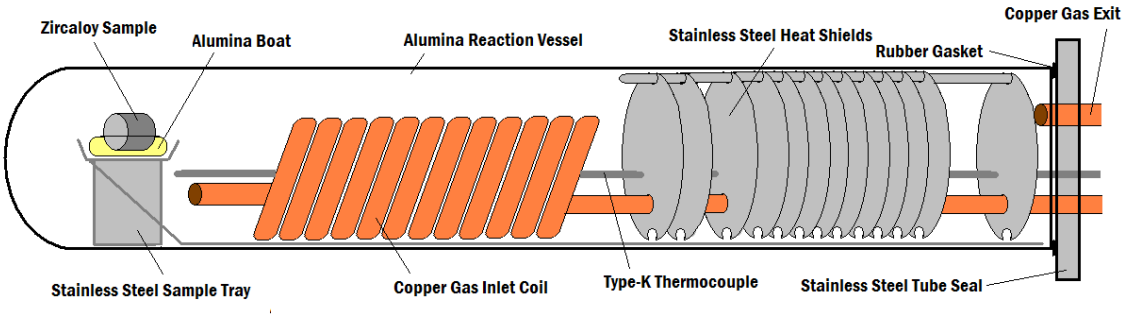

Figure 3.4. Schematic Diagram of Reaction Vessel, Heat Shields, Tube Seal, and Sample Tray.

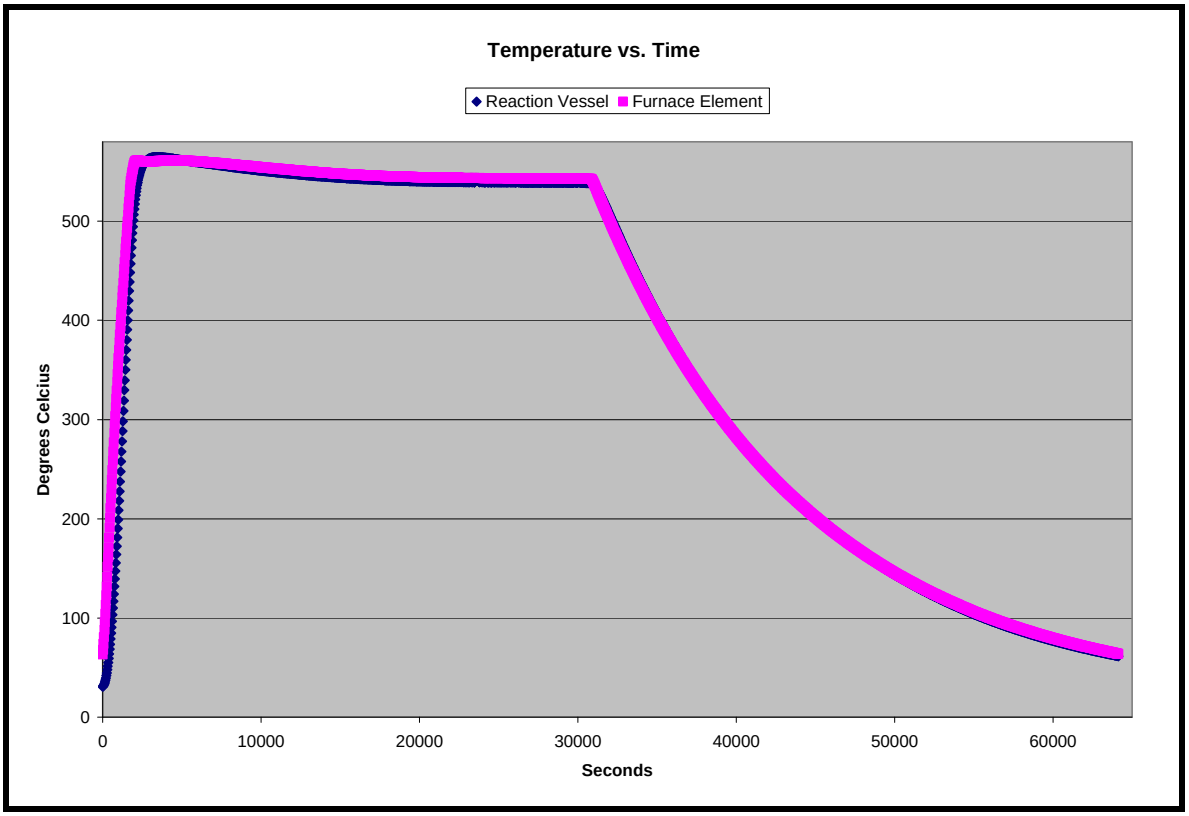

Figure 3.5. Temperature Profile of Experiment Zy14.

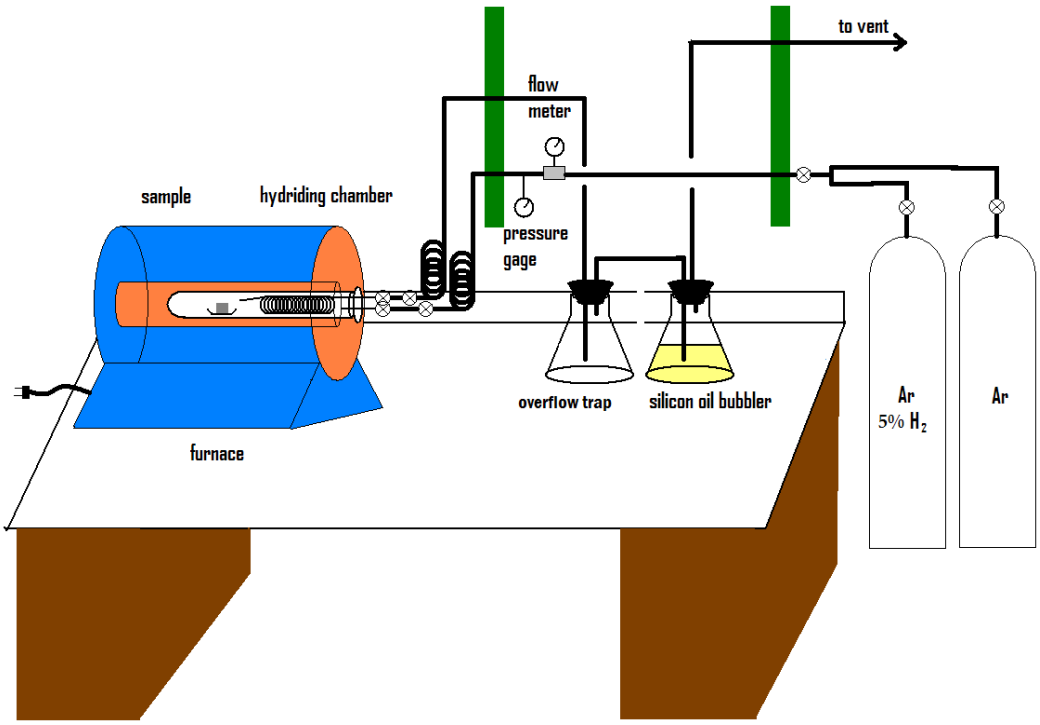

Figure 3.6. Schematic Diagram of the Hydride Process Equipment.

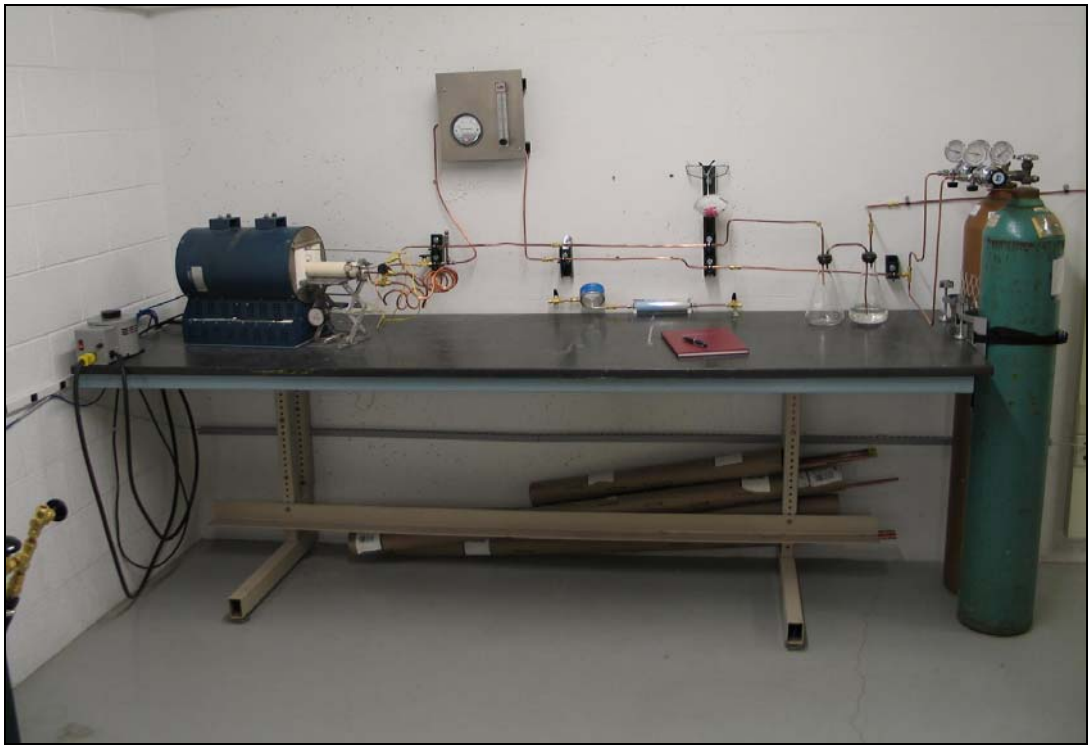

Figure 3.7. Photo of the Hydride Process Equipment.

3.4. Dehydride Process Design

The dehydride process will be carried out inside of the vacuum airlock chamber of the glovebox. The zirconium hydride samples will be pre-ground using a mortar and pestle inside of the glovebox to a fine powder. The powder is placed inside of a conical ceramic crucible that is wrapped with a thermocouple style ohmic heater (shown in Figure 3.8) purchased from ARi, Inc (Addison, IL). The heater and crucible are then placed inside of another ceramic cup style crucible and placed on a stainless steel stand. The stainless steel stand is made of small tubes to minimize the contact with the crucible, therefore minimizing heat transfer to the airlock walls. A circular disc with a small, centered whole is placed upon the crucible. This disc will help retain powder inside the crucible in case of an air pocket uprooting powder during evacuation. The small whole in the ceramic disc is used to feed a thermocouple next to the powder to monitor temperature using the data acquisition.

The airlock door will be replaced with a new airlock door, as seen in Figure 3.9, specifically designed for the dehydride process. The door has all the same components as the original door (vacuum connection, valves, and vacuum TC gauge), but with an added wire feed through gland. The gland will pass a power lead, to be connected to the heater, and two pairs of type-K thermocouples. One set of thermocouple wires are connected to the thermocouple measuring the powder temperature. The second pair of thermocouple wires is used to monitor the temperature drop across the airlock in a vacuum. Preliminary testing shows the temperature across the vacuum to be sufficient enough to

melt wiring. Therefore a single standing sheet of stainless steel is placed between the dehydride crucible and the wiring for the thermocouple and power leads.

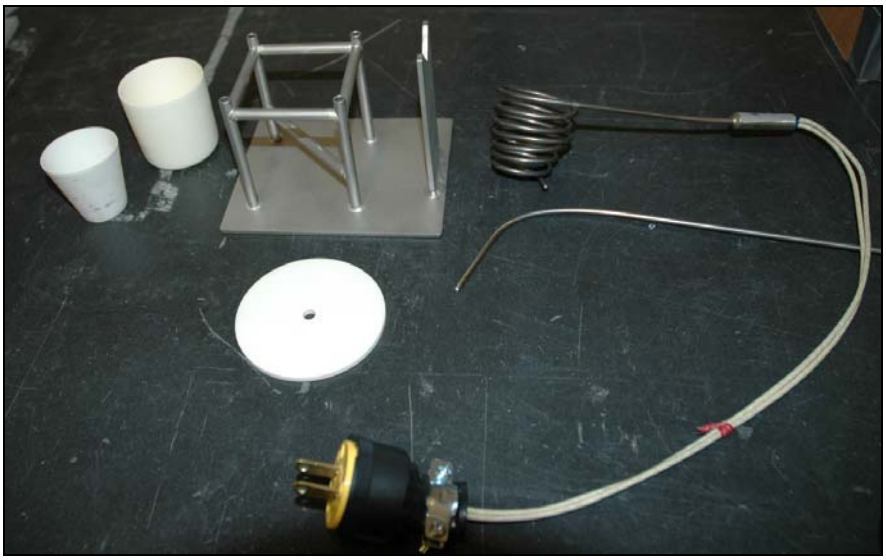

Figure 3.8. Photo of Dehydride Equipment.

Figure 3.9. Photo of Dehydride Airlock Door.

4. RESULTS

After the assembly of the experimental equipment, fourteen process development experiments were completed to define the process variables for hydriding and to provide a roadmap for follow-on research. Representative samples of the Zircaloy tubes and cubes used in these experiments are shown in Figures 4.1 and 4.2. The samples were exposed to hydrogen using the setup described in Section 3.3 under the conditions summarized in Table 4.1. An analytical balance (Mettler model no. AB-304-S) inside of the glovebox was used to record sample masses (error ±0.0001g) before and after hydriding to determine the mass change of the sample.

These mass measurements were used to evaluate the relative efficiency of hydride formation for each experiment according to the following calculation sequence. First, from the alloy data in Table 2.1, Zircaloy (Zy) contains nominally 98.2 wt% Zr. Therefore, the number of moles of zirconium in a known mass of Zircaloy may be calculated as follows:

$$Zr(mol) = \frac{Zy\ mass(g) \times 0.982}{M_{Zr}(g/mol)} \tag{4.1}$$

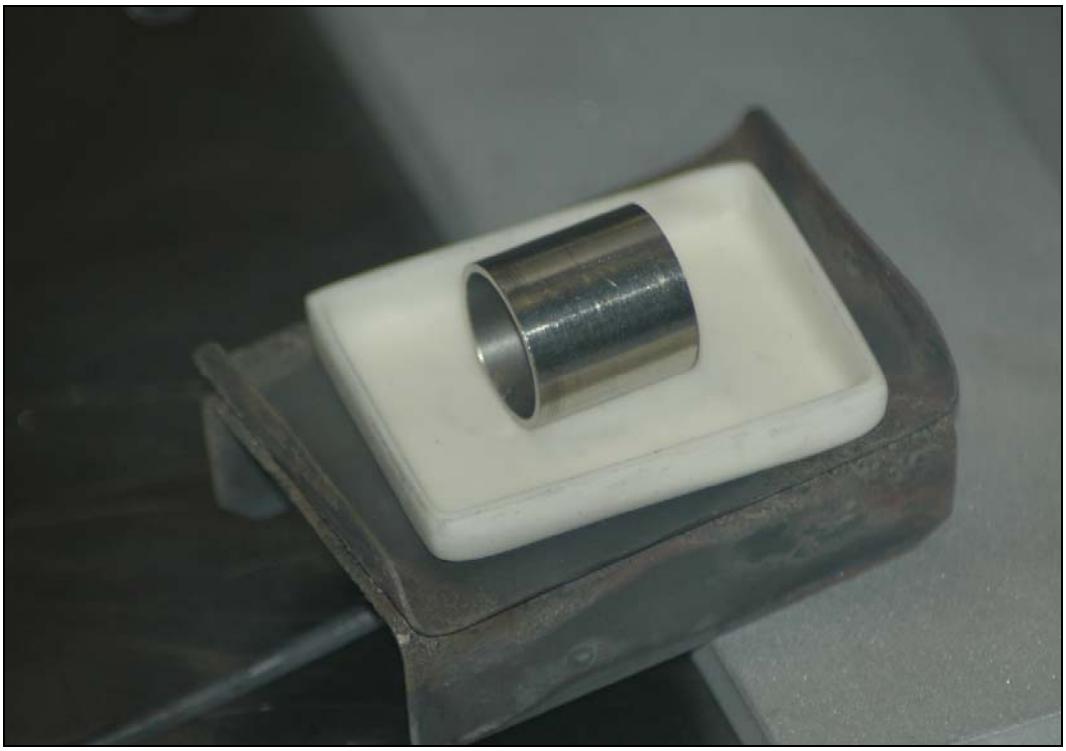

Figure 4.1. Photo of a Typical Zircaloy IV Tube Sample Before Hydriding.

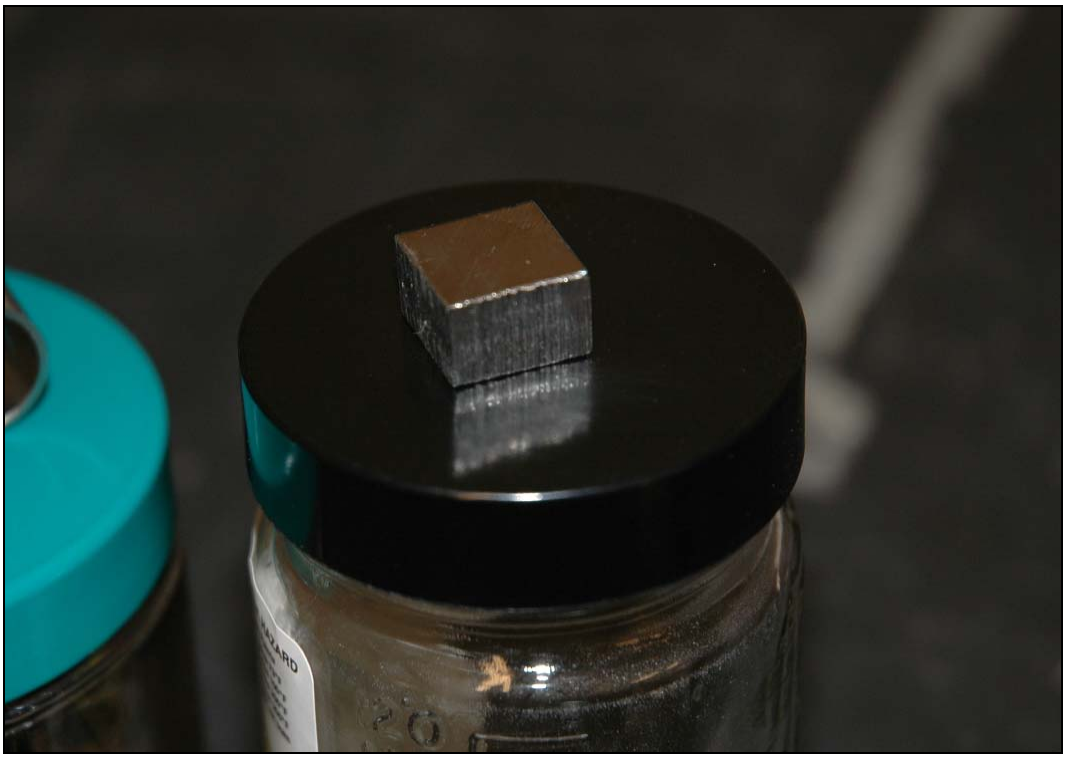

Figure 4.2. Photo of a Typical Zircaloy IV Cube Sample Before Hydriding.

Table 4.1 Table of Hydride Formation Experiment Conditions and Results.

Specimen	Sample Geometry	Process Gas	Temp. (°C)	Time (hr)	Flow Rate (SCFH) +/- 0.2	Pressure (Inches H20) +/- 0.2	Sample Mass (g)	Δ Mass (g)	mol H2 Supplied	Theoretical % Hydride*	%Hydride Less Oxide Error†	Comments
Zy1	Tube	Ar-4.83%H2	360	6.0	8.0	28.0	2.3805	**	7.50E+05	**	**	Small shards from ends of tube
Zy2	Tube	Ar-4.83%H2	733	6.0	3.0	12.0	3.5256	0.0534	2.81E+05	69.8%	67.2%	Shattered when tapped w/ wrench
Zy3	Tube	Ar-4.83%H2	518	6.0	7.0	25.0	4.1906	0.0676	6.56E+05	74.3%	72.1%	Unzipped to longitudinal shards
Zy4	Tube	Ar-4.83%H2	477	12.0	3.5	4.5	3.6519	0.0112	6.56E+05	14.1%	11.6%	Turned greyish-black, retained shape
Zy5	Tube	Ar-4.83%H2	503	12.0	7.0	24.0	3.7222	0.0739	1.31E+06	91.5%	89.0%	Unzipped to longitudinal shards
Zy6	Tube	Ar-4.83%H2	522	23.5	3.0	12.0	3.7565	0.0809	1.10E+06	99.2%	96.8%	Very brittle, broke off in square pieces
Zy7	Tube	Ar-5.02%H2	525	24.0	7.8	25.5	3.2810	0.0704	3.02E+06	98.9%	96.1%	Square pieces
Zy8	Tube	Ar (99.997%)	488	6.0	7.5	25.0	3.7812	0.0025	0.00E+00	3.0%	0.0%	Control Experiment
Zy9	Tube	Ar-5.02%H2	603	6.0	6.5	23.0	3.7473	0.0714	6.33E+05	87.8%	85.3%	Sample begain to flex and pull apart
Zy10	Tube	Ar-5.02%H2	543	8.0	8.0	26.5	4.0353	0.0438	1.04E+06	50.0%	47.7%	Blackened ends, greyish center, process done in temperature steps
Zy11	Tube	Ar (99.997%)	546	12.5	7.5	22.0	3.6570	0.0020	0.00E+00	2.5%	0.00%	Control experiment
Zy12	Tube	Ar-5.02%H2	755	5.2	7.5	25.5	3.1764	0.0308	6.33E+05	44.7%	41.8%	Golden color, shattered when hit
Zy13	Cube	Ar-4.97%H2	529	12.0	7.4	23.0	8.1227	0.0211	1.43E+06	12.0%	10.8%	Hydrided on exterior layer only
Zy14	Tube	Ar-4.97%H2	538	8.0	7.5	24.0	3.2039	0.0491	9.65E+05	70.6%	67.7%	Large cracking, ground to powder

* Relative to total zirconium mass being hydrided

† Assumed 0.002 g zirconium oxidizes

** Data not observed or calculated due to recovery loss

ZrH_2 and ZrO_2 contain one mole of zirconium to one mole of H_2 gas and O_2 gas. Therefore, the calculated moles of zirconium, *Zr(mol)*, is equivalent to the number of moles of hydrogen that would be present in the sample if it were completely hydrided, $H_2(mol,100\%)$. This value can then be used to calculate the expected mass increase to hydride the whole sample using the following:

$$H_2(g,100\%) = H_2(mol,100\%) \times M_{H_2}(g/mol) . \quad (4.2)$$

This quantity, coupled with the measured mass change, Δm, can then be used to determine the hydriding efficiency in the sample if it is assumed that ZrH_2 formation is responsible for the mass increase. This calculation was one using the following expression:

$$\%hydride_{th} = \frac{H_2(g,100\%)}{\Delta m(g)} \quad (4.3)$$

The Sections that follow describe each of the fourteen experiments and their results, which are also summarized in Table 4.1. Experiments Zy8 and Zy11 were performed as control experiments to determine an approximation for the mass of zirconium that will react with oxygen impurities in the hydride system and form ZrO_2. In Table 4.1, this approximate oxidation mass was subtracted from the measured Δm before the $\%hydride_{th}$ calculation was made using equation 4.3.

4.1. Experiment Zy1

The very first experiment was a demonstration to determine whether ZrH_2 would form and if the Zircaloy tube would indeed form a powder in the process vessel. Literature suggested temperatures between room temperature and 800^{o}C for hydriding would be most effective [6], so a low temperature experiment was planned at ~350°C. The experiment began under flowing hydrogen and Ar-5%H_2 was introduced at 100°C as the furnace was being heated. The furnace temperature rose to 460°C before being reduced to a steady 360^{o}C. Figures 4.3 and 4.4 document the condition of the sample after 6 hours at ~28 inches H_2O pressure. The Zircaloy tube was observed to have formed blisters on its' outer surface and the tube ends were frayed off radially in small platelets.

As this was the first experiment, there was some difficulty during the unloading process and a portion of the platelets were spilled inside the glovebox and lost. Therefore, the mass change measurement and subsequent calculations were not performed. This mishap did provide the impetus to design the stainless steel sample stage that worked effectively for the remaining experiments and is shown in Figure 3.3.

Figure 4.3. ZrH_2 Platelets from the Frayed Ends of Sample Zy1.

Figure 4.4. Sample Zy1 After Hydriding for 6 hours at ~360°C.

4.2. Experiment Zy2

In the second experiment, the Ar-5%H_2 flow was started at 23°C and the hold temperature was 733°C with a and lower pressure, 12 inches of water. Figure 4.5 shows the sample after is broke into pieces under a very slight mechanical force; the blackish grey coloration was consistent with zirconium hydride. After 6 hours of exposure the sample increased in mass by 0.0534 grams, which corresponds to 67.2% hydride formation. One interesting observation is that the bottom of the sample that was in contact with the aluminum oxide boat did not change color. The sample retained its cylindrical shape and appeared unaffected. Destructive analysis by light tapping with a wrench resulted in the sample shattering into equal halves on axis. A second strike to one half shattered the sample into many small pieces. This observation is consistent with the formation of a brittle hydride.

Figure 4.5. Sample Zy2 after Hydriding for 6 hours at ~733°C.

4.3. Experiment Zy3

In experiment Zy3, the Ar-5%H_2 flow was started at ambient temperature with a maximum hold temperature of 518^{o}C, just under the $\alpha+\delta$ transition border shown previously in Figure 2.1. The pressure was held at 25 inches of water. After 6 hours the sample mass increase corresponded to a sample of 72.1% hydride. The sample had almost completely crumbled longitudinally in long shards, as seen in Figure 4.6, which apparently followed a vertical orientation to the original tube structure. There was a trace amount of fine powder in the alumina boat, but the bottom of the sample was retained a recognizable shape (Figure 4.7). The color once again corresponded to that of zirconium hydride.

Figure 4.6. Long Shards from Sample Zy3.

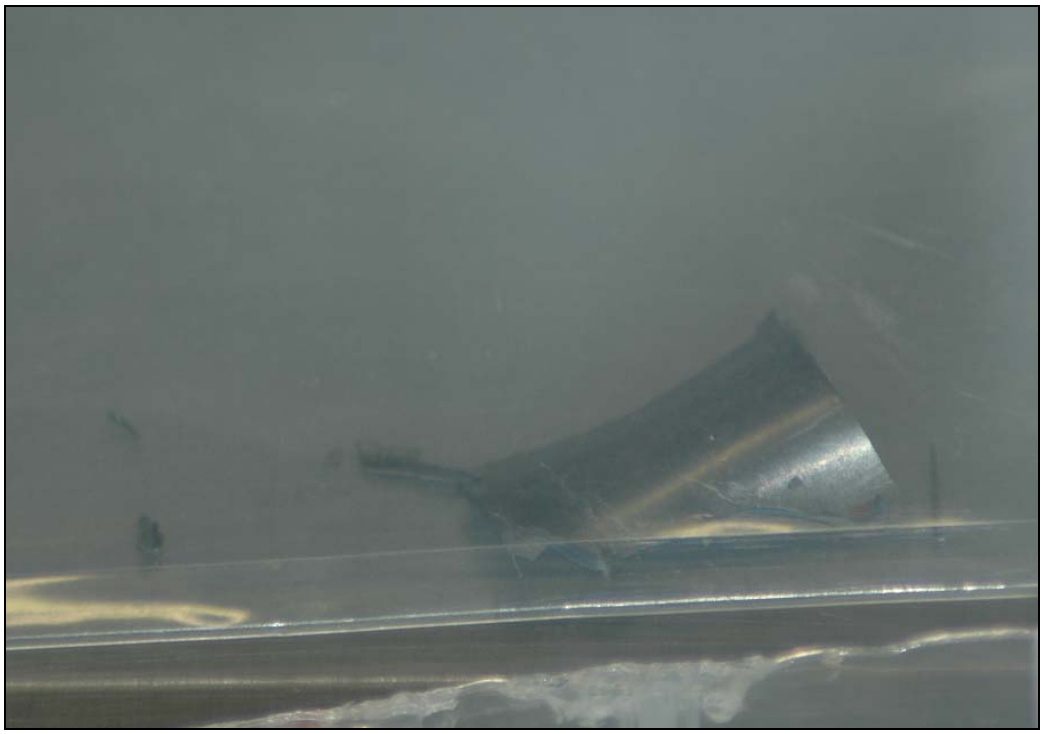

Figure 4.7. Bottom Solid Structure Left from Sample Zy3.

4.4. Experiment Zy4

Experiment 4 was conducted to examine low flow rote, low pressure conditions. Here the pressure was reduced to 4.5 inches of water inside the reaction vessel. The exposure time was lengthened to 12 hours while the hold temperature was reduced to 477^{o}C. This experiment began exposure at room temperature again before reaching the stable temperature. After 12 hours the sample was slightly discolored (grayish-black) and retained its full shape, as seen in Figure 4.8. The calculated mass increase reveals a poor hydrogen pickup (11.61% hydride).

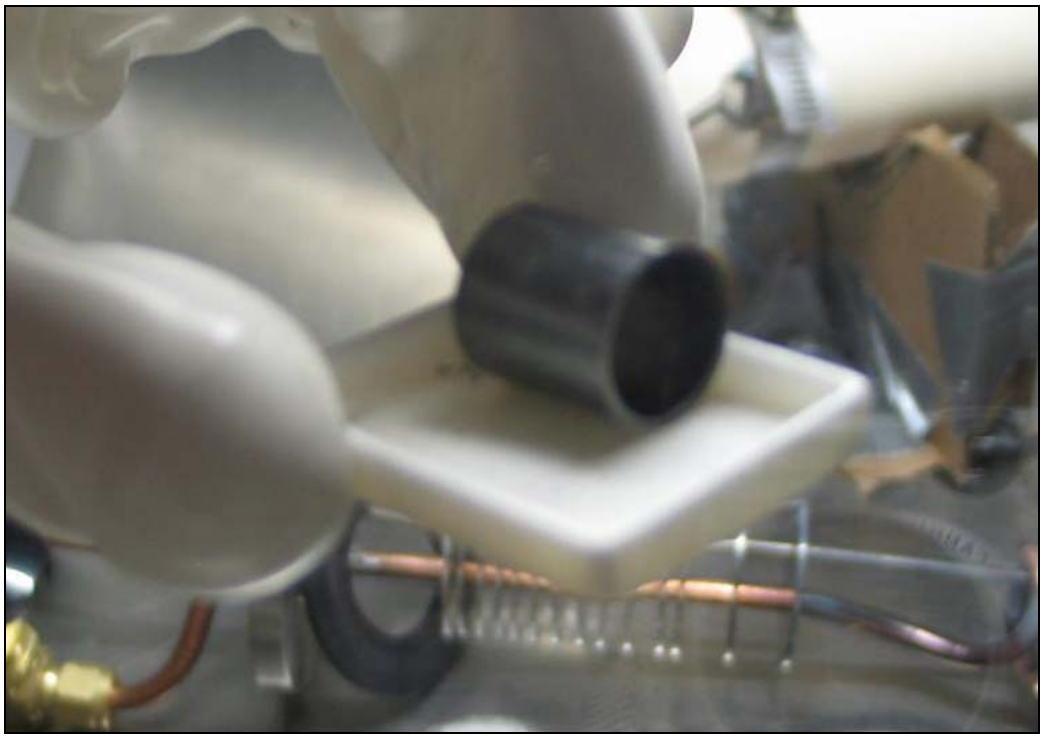

Figure 4.8. Sample Zy4 after Hydriding for 12 hours at ~477°C.

4.5. Experiment Zy5

Experiment Zy5 repeated the conditions used in experiment Zy3 with a longer duration. This experiment initiated a new procedure where the Ar-5%H_2 process gas was not introduced until the sample was within 30°C of the desired stable temperature. This experiment was conducted at 503°C. After 12 hours the sample was removed. Some fine powder was present but the bulk of the sample was shredded into long longitudinal shards (visibly larger than the shards observed in experiment Zy3), as seen in Figure 4.9. No recognizable section of the original tubular shape remained and a rich grayish-black color was present. The mass increase corresponded to an 89.0% hydride composition.

Figure 4.9. Sample Zy5 after Hydriding for 12 hours at ~503°C.

4.6. Experiment Zy6

Experiment Zy6 was intended as a 24 hour experiment using the conditions of experiments Zy3 and Zy5. The temperature was held constant at 522^{o}C. At some point after 7.5 hours and before 23.5 hours the hydrogen gas mix supply was depleted. A slight negative pressure was then established in the reaction vessel by the building exhaust. The sample remained at temperature under a very slight negative pressure for an indeterminate time and extensive oxygen contamination was possible. After 23.5 hours the sample was removed; a grayish-black color was observed but the sample was largely intact. A few moderately sized, irregular square-shaped pieces had separated from the sample and fallen off. When touched, the sample broke easily into smaller pieces as seen

in Figure 4.10. Mass calculations correlate to a 96.8% hydride composition, but data from this experiment are not considered reliable even though it matches experiment Zy7's conclusions using the same process variables.

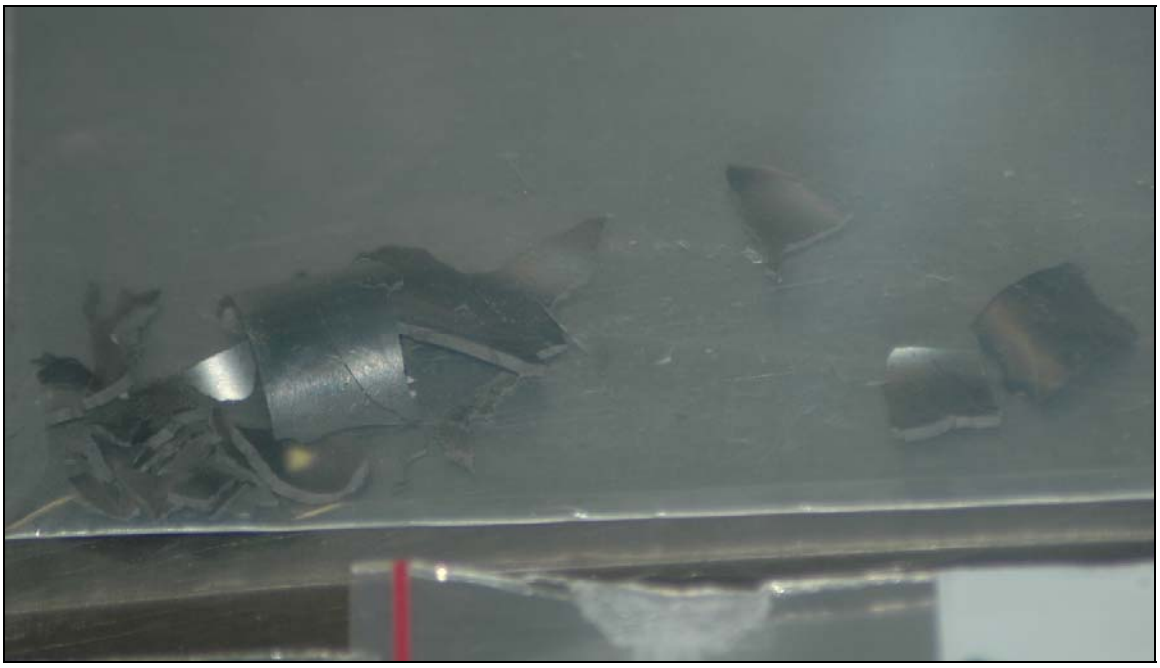

Figure 4.10. Sample Zy6 Sample Zy5 after Exposure for 23.5 hours at ~522°C.

4.7. Experiment Zy7

Experiment 7 was a repeat of experiment 6, but without the loss of gas. The sample was held at 525^{o}C for 24 hours before being removed. Color composition matched the prior experiments and the mass increase corresponded to a 96.1% hydride composition. The sample had fallen apart in square patterns again (Figure 4.11) and, when touched gently, would crumble easily.

Figure 4.11. Sample Zy7 after Hydriding for 24 hours at ~525°C.

4.8. Experiment Zy8

Experiment Zy8 was used as a control experiment. All procedures and measurements were carried out in the same manner as the previous hydride experiments. However, the process gas was pure argon. A tubular Zircaloy sample was held at 488°C for 6 hours. However, the argon gas depleted during cool down pulling a slight vacuum on the sample, thus discrediting the results of this experiment. It is important to note that a mass increase of 0.0025 grams of was observed. The distinguishing difference between this sample and the hydride samples is that this sample retained a grey-metallic shine, as seen in Figure 4.12, compared to the dark dullness of the hydrided samples.

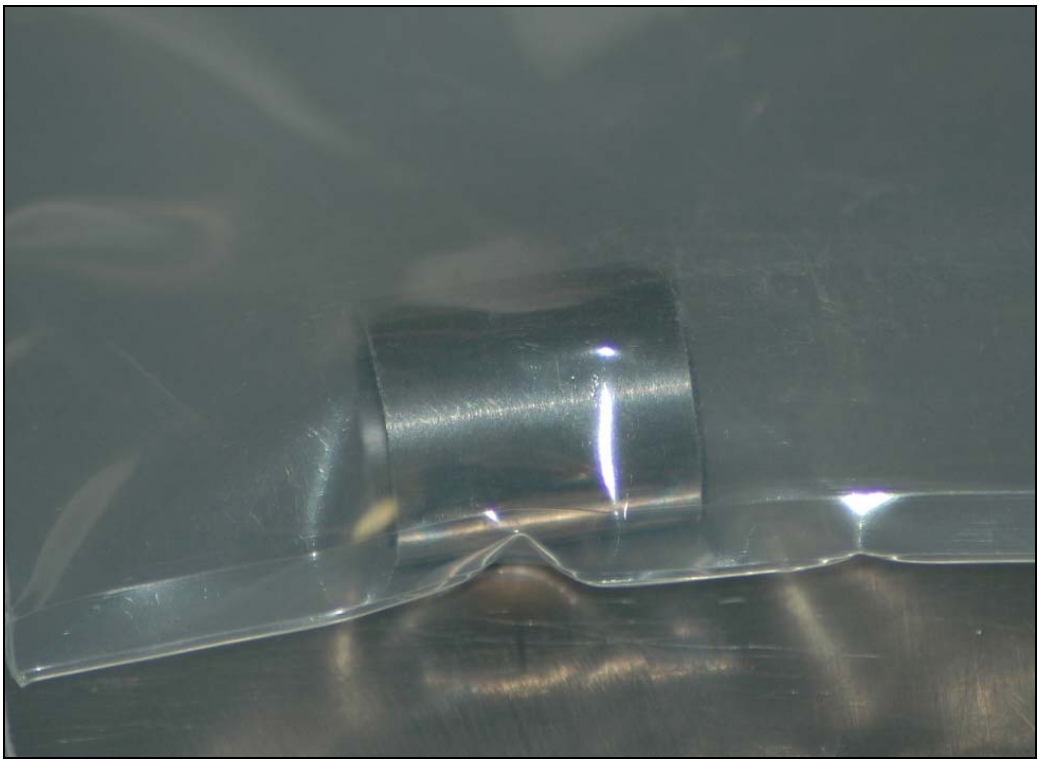

Figure 4.12. Control Experiment Sample Zy8 after 6 hours at ~488°C.

4.9. Experiment Zy9

Experiment Zy9 was designed to evaluate hydriding above the $\alpha+\delta$ phase field shown in Fig. 2.1. In this experiment the temperature was held constant at 603^{o}C for 6 h. The mass was still in a solid cylinder shape, but the top half began to pull off and "unzip" radially and longitudinally from the bottom half of the sample. The top half crumbled to smaller pieces when touched, as seen in Figure 4.13. The color was consistent with the other zirconium hydride experiments.

Figure 4.13. Sample Zy9 after Hydriding for 6 hours at ~603°C.

4.10. Experiment Zy10

Experiment Zy10 was a dynamic step experiment. The sample began hydriding near the $\alpha+\delta$ phase boundary (543^{o}C) for 3 hours then the temperature decreased to 383^{o}C for the remaining 5 hours. Complications with post test specimen handling and mass measuring discredit this data, but it is of important note that the solid mass recovered exhibited an apparent 47.7% hydride composition. Some small quantity of powder could have been lost. The sample was grayish-black, except in the center of the outer circumference, which remained slightly gray. The sample began to pull apart and unzip from the end closest to the hydrogen flow as seen in Figure 4.14.

Figure 4.14. Sample Zy10 after Hydriding for 3 hours at ~543°C and 3 hours at ~383°C.

4.11. Experiment Zy11

Experiment Zy11 was conducted a repeat control experiment since the previous experiment was compromised by a loss of gas flow. Conditions were similar to the experiment Zy8. The sample was heated to a stable temperature of 546°C for 12.5 hours prior to removal. The mass increase observed was 0.002 grams. The sample is shown in Figure 4.15 and it retained hardness and strength, even when struck violently with a small hand tool. The sample remained shiny, but there were some blackish-gray areas on the sides that didn't touch the aluminum oxide sample boat.

Figure 4.15. Control Sample Zy11 Heated for 12.5 hours at 546°C.

4.12. Experiment Zy12

Experiment Zy12 was a high temperature experiment. The sample was heated at a stable temperature of 755^{o}C for 5.2 hours. The sample only remained intact and was only "hydrided" to 41.7% from eq. 4.4. The material turned slightly golden in color with some areas of black, as seen in Figure 4.16, which could point to nitrogen contamination in the process vessel at this higher temperature. Destructive analysis by striking the sample confirmed the brittleness of the product, hence the pieces seen in Fig. 4.16.

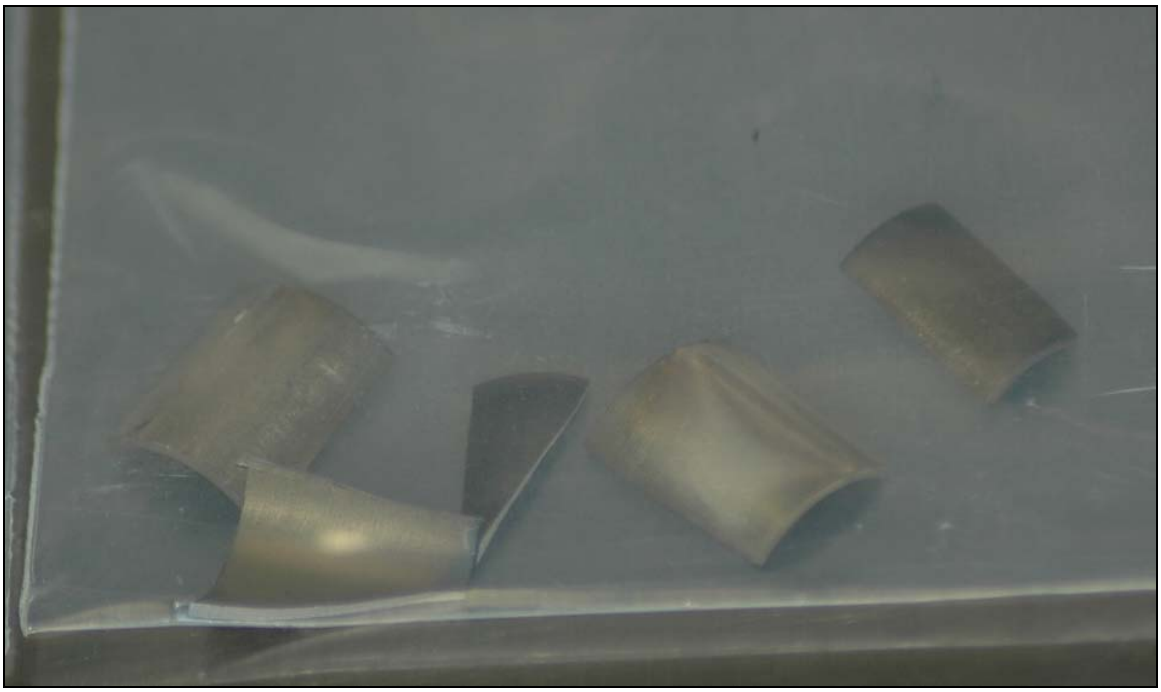

Figure 4.16. Sample Zy12 after Hydriding for 5.2 hours at ~755°C.

4.13. Experiment Zy13

Experiment Zy13 was designed to duplicate experiments Zy5 with a solid cubic sample (Fig 4.2) rather than a tubular piece of Zircaloy. The sample was twice as massive as the typical tubular samples. The cubic sample was heated at 529^{o}C for 12 hours. After the experiment, the sample remained intact and had turned grayish-black on all sides but the bottom (shown in Figures 4.17 and 4.18). The mass increase calculation indicates only a 10.8% hydride composition. The center portion of the sample seemed unaffected by the hydrogen.

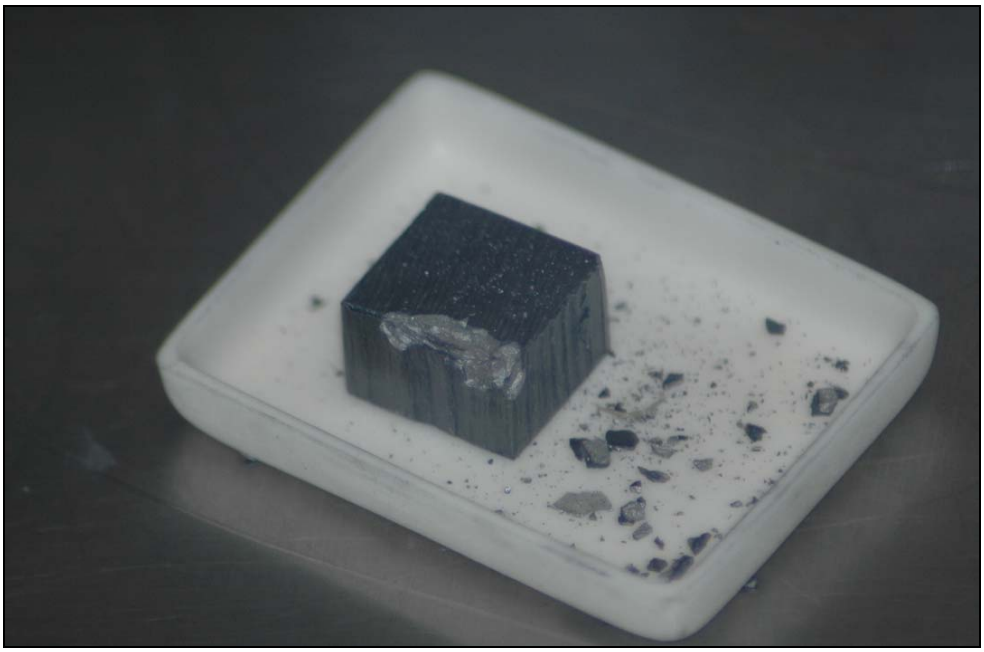

Figure 4.17. Sample Zy13 after Hydriding for 12 hours at ~529°C.

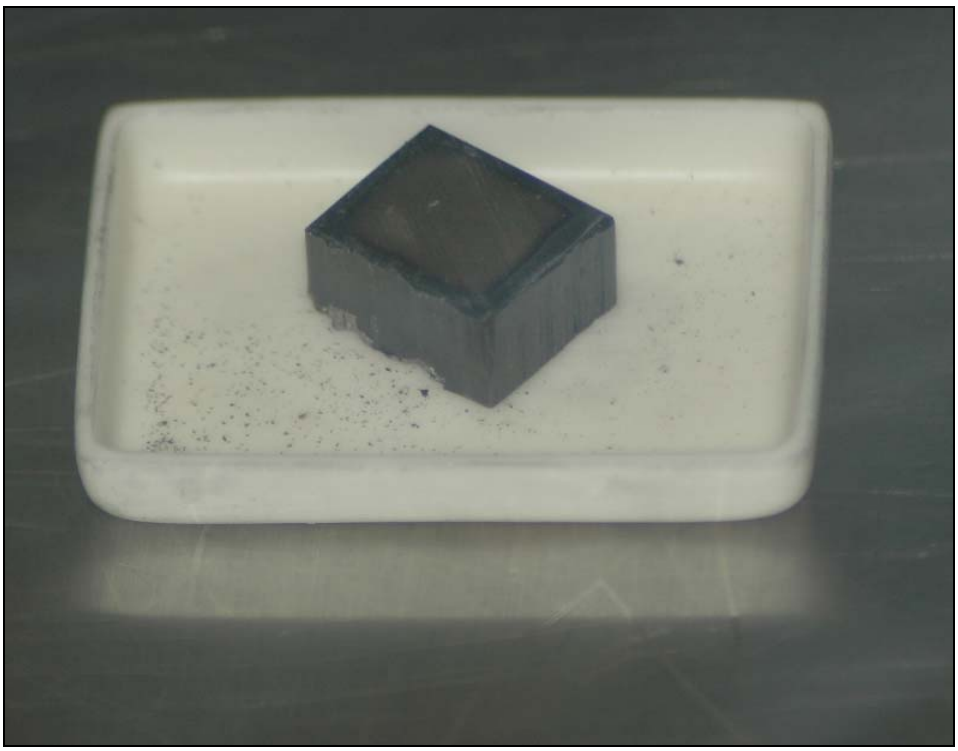

Figure 4.18. Bottom of Sample Zy13.

4.14. Experiment Zy14

Experiment Zy14 was designed to produce a high hydride percentage in a sample that would then be ground into fine powder. The tubular sample was heated at a constant 539°C for 8 hours. The mass increase calculated a 67.7% hydride composition. The sample unzipped in an irregular square shaped pattern, as observed in earlier experiments. The sample was grayish-black in color, as shown in Figure 4.19.

Figure 4.19. Sample Zy14 after Hydriding for 8 hours at ~539°C.

The sample was then ground to a powder using a mortar and pestle. The bottom surface of the sample that touched the crucible retained a near-metallic toughness was not

able to be ground. The top of the sample produced the finest powder while the middle produced larger pieces. Figure 4.20 shows the final powder product.

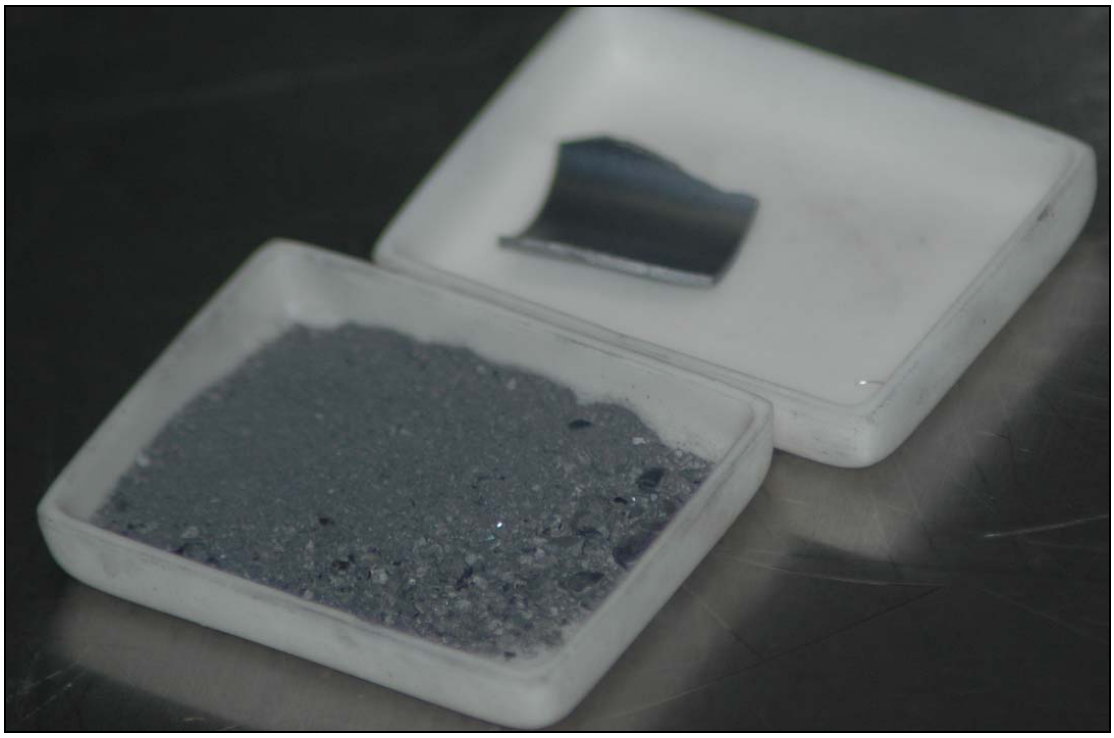

Figure 4.20. Sample Zy14 After Grinding.

A portion of the powder recovered from sample Zy14 and submitted for X-ray diffraction analysis[*]. Figure 4.21 shows the resulting diffraction pattern. Software analysis of the diffraction pattern reveals a close match with the $ZrH_{1.801}$ and ZrH_2 known data from the powder diffraction file. However, there are some unidentified peaks in the diffraction pattern. It has been confirmed that these peaks do not correspond to ZrO_2, Zr, Al_2O_3, CrH_2, Cu, CuH, CuO, CrO_2, Fe_2O_3, FeH, Sn, SnO_2, $ZrH_{1.66}$ (δ-phase), or $ZrH_{1.950}$

[*] Analysis performed by Dave Roberts and Adam Parkinson, Purdue University.

(ε-phase). The meaning of these peaks will be the subject of future investigation, but it is encouraging that the primary peaks in the pattern correspond directly to hydride formation and eliminate the residual presence of Zr and ZrO_2 within the resolution of the instrument.

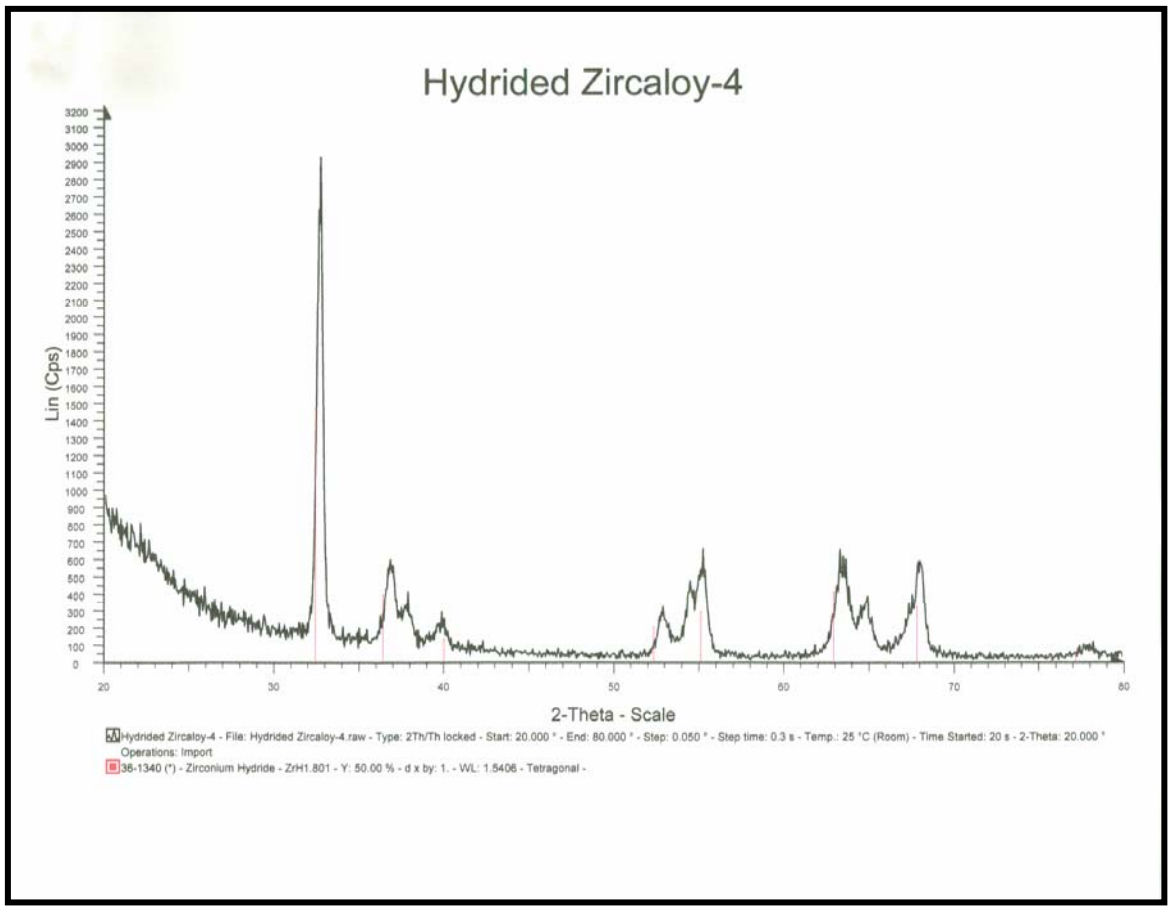

Figure 4.21. X-ray Diffraction Results from Pulverized Zy14 Powder.

4.15. Dehydride Apparatus Shakedown Test

The dehydride apparatus described in Section 3.4 was designed and built for this project, but it not operated for this report. The intention was to dehydride powder from experiment Zy14, but the heater malfunctioned during the shakedown test making that operation impossible in the scope of this project. Therefore, this section only describes the operational lessons learned from the heater failure to provide a record for future experimenters in this NERI project.

The initial temperature calibrations runs with the heater resulted in a redesign of the system due to excessive temperatures experienced on the airlock surface. During these calibrations, the heater temperature was slowly increased while the heater temperature, airlock wall temperature, and the temperature drop across the vacuum chamber were monitored. A temperature of 966°C was recorded as the peak temperature achieved by the heater. The maximum temperature 18 inches across the vacuum chamber was 130°C.

Unfortunately, the thermal energy within the vacuum chamber was too large for the wiring and the plastic components melted (Figure 4.23), cutting power to the heater. When the heater failed, the temperature dropped rapidly causing the ceramic disc covering crucible to shatter from thermal shock; the condition of the assembly is shown in Figure 4.24. Figure 4.25 shows the temperature profile of this calibration run. The time vs. temperature of the system and the sharp decrease in temperature indicates the point of failure.

There are some important features to note from this operation. First, the resistance heater was able to heat the process crucible above 900C in vacuum, which is well within the range needed to promote the dehydriding with a high process rate. Second, the fatal flaw in the first design was the lack of proper thermal shielding to protect the sensitive parts of the system. A redesign that includes a new heat shield assembly and removes the plastic from the airlock will easily overcome this failure mode.

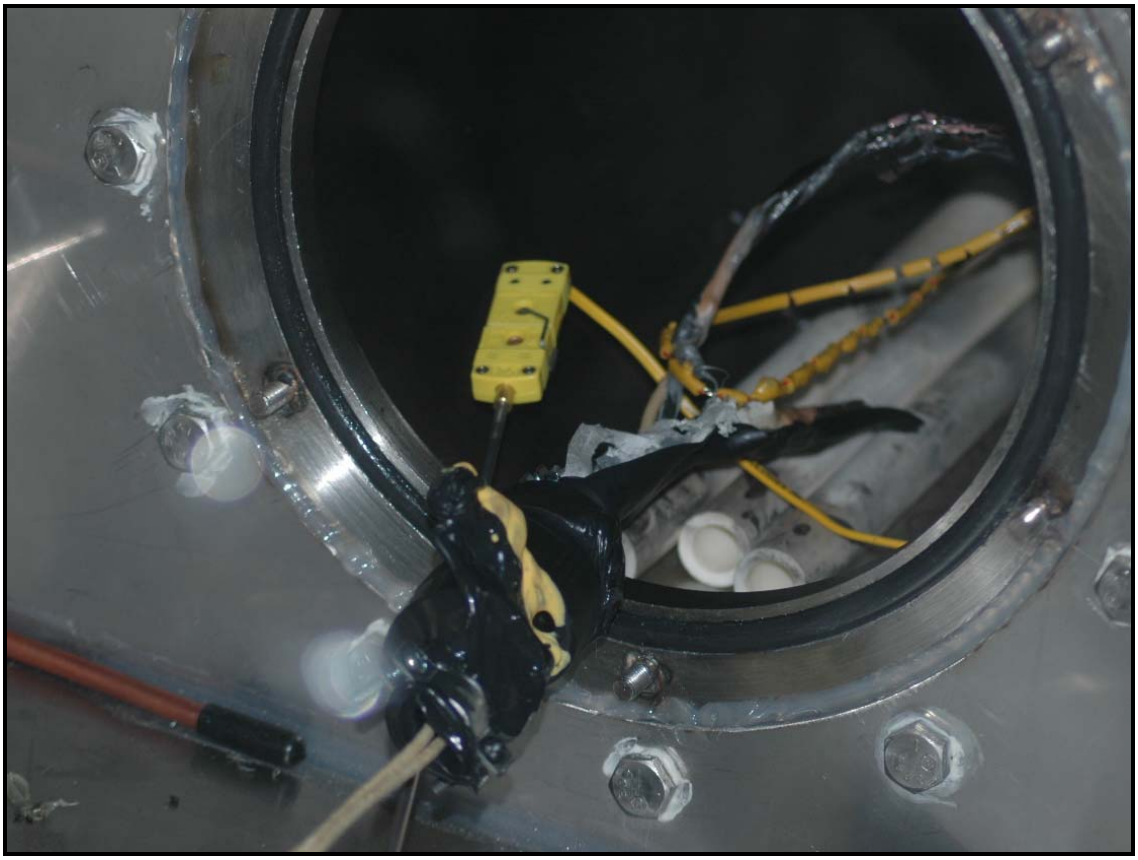

Figure 4.23. Dehydride Apparatus After Failure.

Figure 4.24. Dehydride Apparatus After the Calibration Run and Heater Failure.

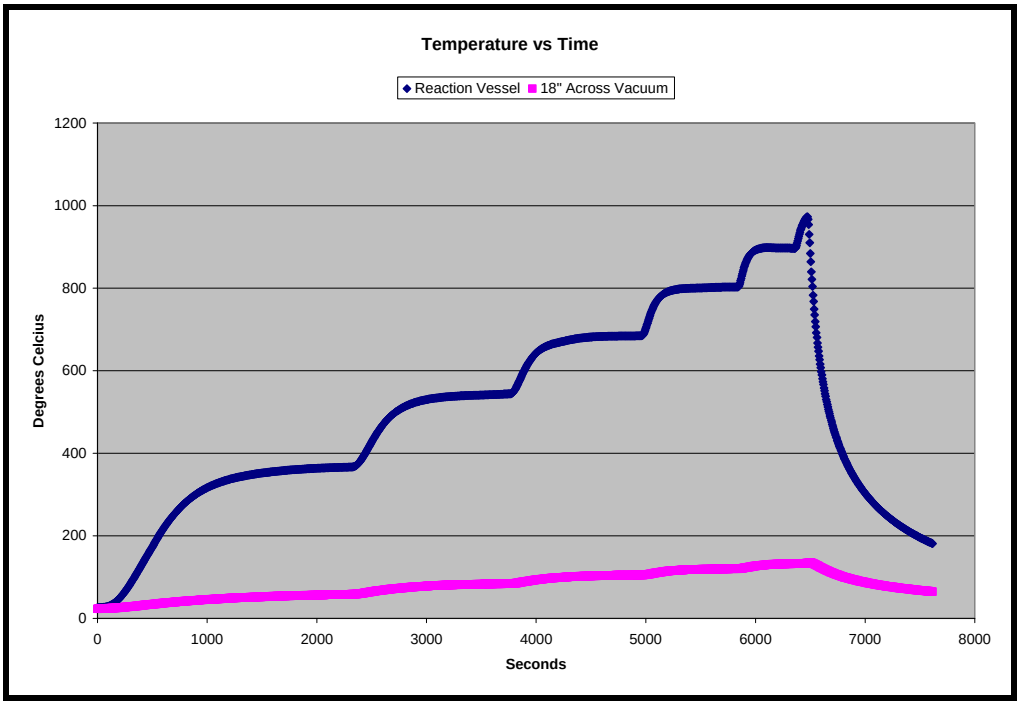

Figure 4.25. Temperature Profile from the Dehydride Apparatus Calibration Run.

5. DISCUSSION OF RESULTS

Overall, there are two accomplishments to highlight from this project. The first is the establishment of the inert atmosphere glovebox and process equipment described in Section 3. The second is the performance of the initial development tests described in Section 4. The first accomplishment is fully examined under the system descriptions in Section 3 so no further discussion will be presented. On the other hand, the experimental results in Section 4 merit further discussion to more completely understand the lessons learned from this project.

5.1. Hydride Experiments

The process development experiments provided insight into the hydride/dehydride process and enabled the coarse definition of process variables for zirconium hydride formation. The results are presented in Figure 5.1 in a summary format using the Zr-H binary phase diagram. Each experiment is displayed on the diagram showing the nominal test temperature and the calculated post-test hydrogen content.

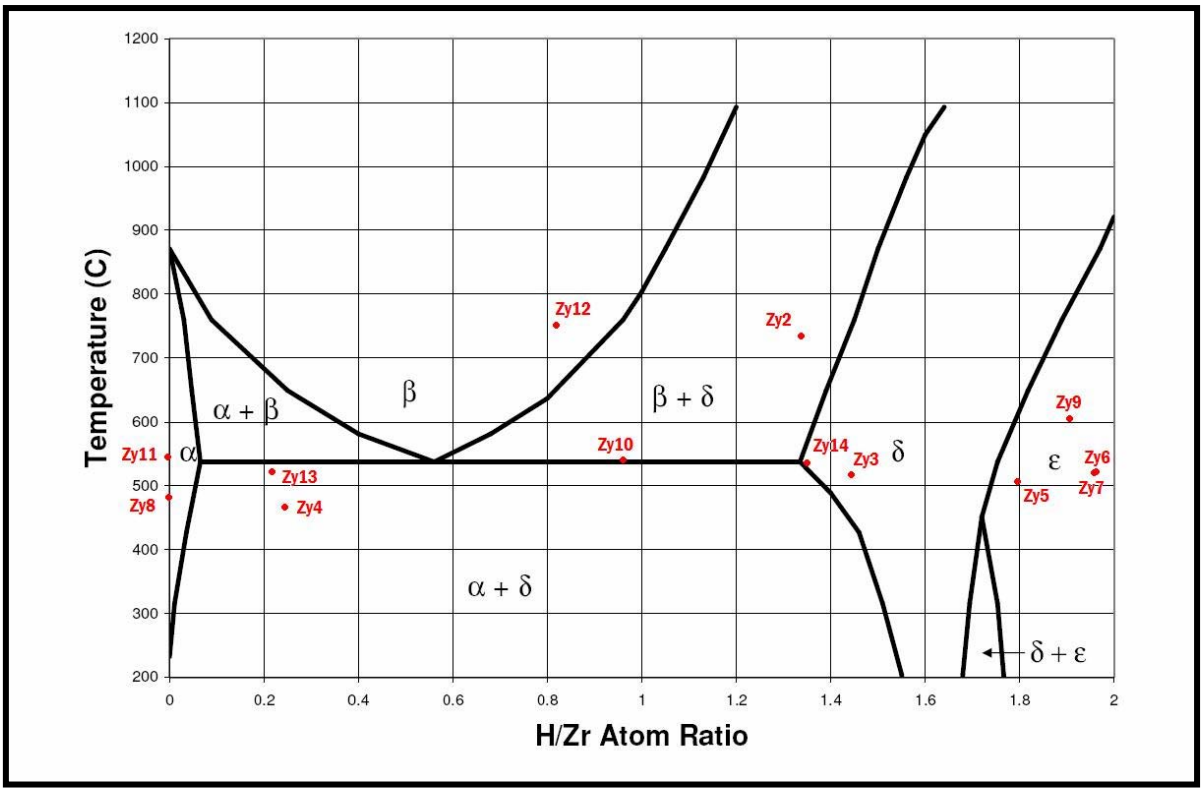

Figure 5.1. Zr-H binary phase diagram with experiment overlay

First inspection of the data indicates that the samples from Zy13 (the cubic sample) and Zy4 (very low pressure) were very poorly hydrided whereas the samples from Zy5, Zy6, Zy7, and Zy9 were heavily hydride and likely formed the ZrH_{2-x} ε phase. The samples from Zy3 and Zy14 were moderately hydrided and readily crumbled with modest mechanical force; from the diagram, these samples may have been in the $ZrH_{1.6\pm x}$ δ phase field. Samples Zy2 and Zy12 were low to moderate in their hydrogen content and they both maintained their original tube shape and were easily shattered with moderate force. Sample Zy10 was a singular experiment with shorter process times at two different

temperatures so the result may not represent “complete” hydriding. Samples Zy8 and Zy11 were the control experiments.

5.1.1. Control experiments

Experiments Zy8 and Zy11 both exhibited mass increases of ~0.002 grams in the absence of hydrogen. The most likely reason for this mass increase is due to contamination from air or other impurities. Table 2.1 shows large negative values of Gibb’s free energy for all prevalent temperatures, thus oxygen contamination would rapidly convert to form ZrO_2. The amount of oxide present in the Zircaloy sample only amounted to 0.16%. However, this amount could mimic a hydride error of 2.52%. Therefore, a standard value of 0.002 grams of the Δm should be considered as error in calculating percent hydride.

5.1.2. Pressure

Early experiments proved that the hydriding of Zircaloy could be accomplished. Comparing experiment Zy4 to Zy5 demonstrated the need for adequate pressure in the system. The hydride percentage for Zy5 was 8 times larger than Zy4 when all the other variables were relatively the same. A minimum of ~12 inches of water will facilitate adequate hydriding. However, pressures of 26 inches of water provide higher hydride percents. The system design inherently couples system pressure and flowrate. Therefore, higher pressures will supply more moles of hydrogen to the sample.

5.1.2. Temperature

The experimental results may be better understood with the assistance of the thermochemical data in Table 2.1. The table of free energies (ΔG) suggests that hydriding will occur from room temperature up to 975^{o}C. Experiments Zy2 and Zy12 demonstrate the need to keep the temperature low during the hydriding process. As the temperature rises the ΔG becomes less and less negative up to 975^{o}C, thus a lesser temperature would facilitate more hydriding. α-Zr has lesser solubility limit for H_2 than β-Zr.

Keeping the temperature below the $\alpha+\delta \rightarrow \beta$ or $\beta+\delta$ phase will cause the Zircaloy to become more embrittled at lower hydride percentage, thus easier to grind. However, the powder recovered would not be as fine. Therefore, grinding a sample of the highest hydride concentration will yield finer powder. To get the highest concentration, the pressure-composition isotherm graph (Figure 5.2) was used to determine which temperature would yield the highest hydrogen to zirconium atom ration. The experiments support the isotherms for 500, 550, and 600^{o}C.

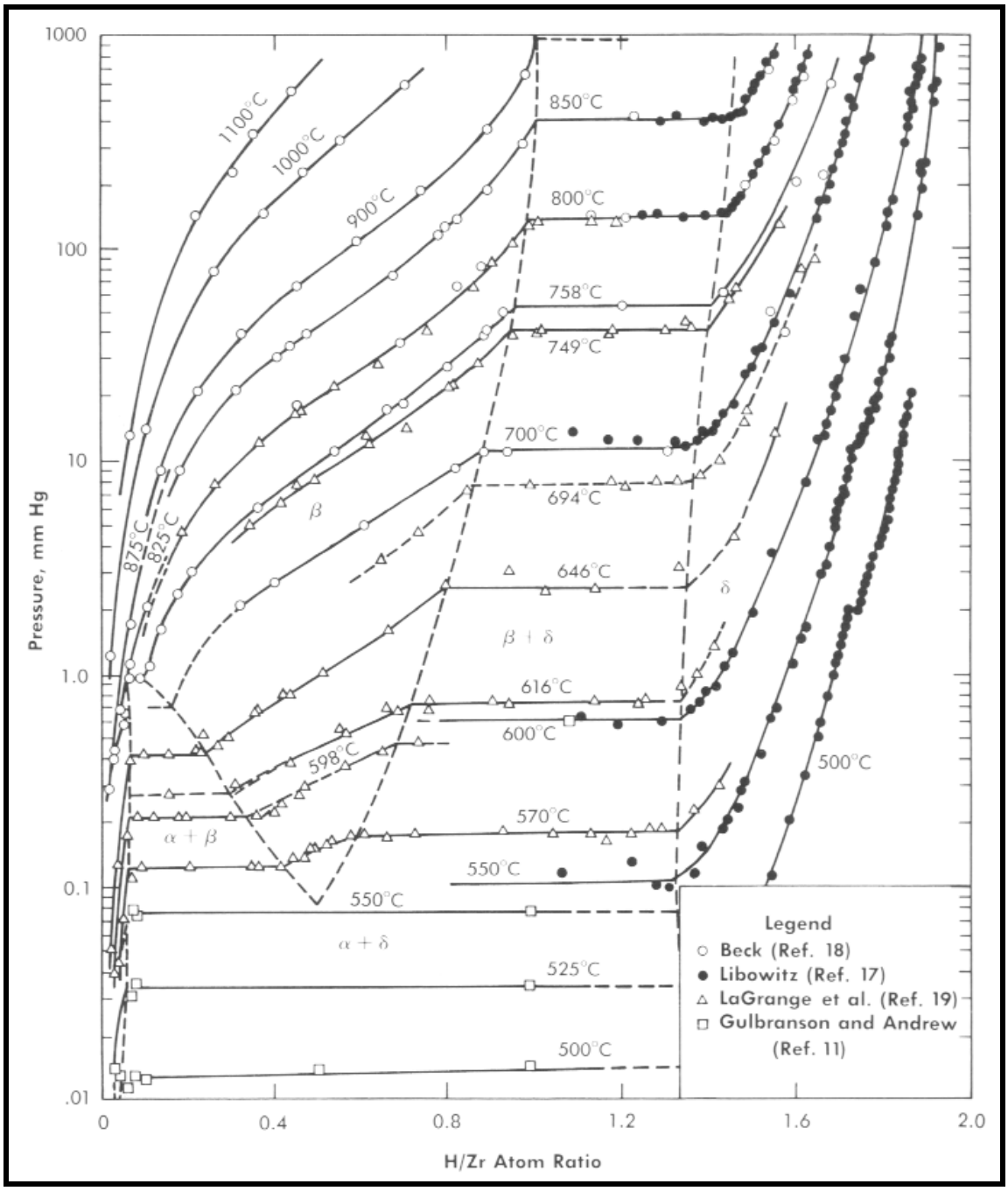

Figure 5.2. Pressure-composition isotherms[1]

5.1.3. Time

Comparing experiments of similar variables, such as Zy3 and Zy5 as well as Zy14 and Zy7 one can see that time has a dependence on the percent hydrided. However, this relationship is not linear. The relationship is logarithmic and therefore a threshold of 24 hours is adequate for hydriding most all the zirconium in the Zircaloy.

5.1.4. Geometry

At the time that cubic samples were introduced into the experiment matrix, the temperature, flowrate, and pressure variables were relatively understood. The cubic sample in experiment Zy13 did not hydride to the degree that was expected if tubular samples were used. This was likely do to the low surface area to volume ratio. The cubic samples developed a hydride layer on the surface of the cube. This layer retarded further hydriding of the sample.

There was an observed distribution of the hydride throughout the samples as well. The highest point of each sample accumulated the most hydrogen while the lowest piece (touching the crucible) exhibited low concentration. Experiments Zy10 and Zy14 exhibited this the most. This became most apparent when grinding sample Zy14 with the mortar and pestle.

5.2. Dehydride Test Apparatus Shakedown

The dehydride apparatus constructed performed as designed up to high temperature. Table 2.1 suggests that the decomposition of ZrH_2 to Zr and H_2 will begin

to spontaneously occur at 975^{o}C. However, with aid from a vacuum, the ΔG is sufficiently close enough to liberate hydrogen starting at 600^{o}C. Ideally the experiment should be carried out between 975 and 1150^{o}C to rapidly off gas the H_2 from the compound [4] [6]. To solve the heat transfer issue to the wiring regarding such high temperatures, a stainless steel heat shield was designed to fit between the heater and wiring. The dehydride apparatus will also sit on alumina tubes to minimize heat transfer to the airlock walls.

6. SUMMARY AND RECOMMENDATIONS

A new collection of process development equipment was established for the purpose of evaluating the feasibility of a hydride-dehydride method for recycling Zircaloy cladding from spent nuclear fuel. An inert atmosphere glovebox and a controlled atmosphere tube furnace were constructed and placed into operation. A third device designed for dehydriding experiments was designed, but a heater failure occurred and there is still some development left to be done for that system.

After this equipment was established, the formation of zirconium hydride from Zircaloy samples was evaluated and it was found that the Zircaloy could be hydrided up to 98% conversion. It was also found that the samples would crumble slightly into large chunks when hydride percentage began to reach 70% conversion. Experimentation determined that hydriding alone would not produce a fine zirconium powder, but the brittle product is easily ground with a mortar and pestle, indicating that milling is a viable process option. Experiments proved a distribution of the hydrogen in the sample with the top having the highest concentration and the base having the lowest due to decreased flow in that area. Specimen geometry, specifically thickness, was a large factor in the final hydride conversion result. Diffusion of hydrogen into the sample decreases further into the sample. It was observed that thin walled samples hydrided much faster than samples approaching 1cm in thickness.

Present work has concluded that zirconium will not crumble to fine powder when hydrided while static. Therefore, new apparatus should be constructed where the hydriding and grinding processes will be done in situ. Milling should be effective for creating a fine powder before the dehydriding process is initiated [5]. This will speed up hydride formation and the *in situ* process will help attain higher hydride percentages and finer zirconium hydride powder.

Further experimentation should be conducted using Zircaloy samples of varying geometry and oxidation levels to simulate the real spent cladding conditions. Experimentation should also be conducted to establish optimal conditions for dehydriding zirconium hydride powder to form metallic zirconium powder. Some test variables of interest include higher pressure, low temperature (table 2.1 suggests higher driving forces for low temperature), and low flowrate with higher temperature.

Further progress should include:

- Re-orientating Zircaloy samples inside of hydride system
- Developing new reaction vessel to hydride and grind Zircaloy samples using an in-situ process
- Characterize hydride distribution throughout samples
- Develop system parameters for producing fine zirconium hydride powder
- Characterize the transition between the phases of the zirconium-hydrogen system to determine desired path of hydrogen diffusion through phases and establishing desired product phase
- Determining hydride percentage needed to produce fine powder (100% hydriding may not be needed)

- Production and evaluation of fine, hydrided zirconium hydride powder
- Rebuilding and troubleshooting dehydride system inside airlock
- Production and evaluation of fine zirconium powder via hydride-dehydride process
- Incorporating gas purification apparatus and oxygen sensors to the hydride process and to the glovebox along with adding a HEPA filtration system and gas recycling system to the glovebox

LIST OF REFERENCES

LIST OF REFERENCES

[1] Mueller, W.M., Blackledge, J.P., and Libowitz, G.G., Metal Hydrides, Academic Press, New York, 1968.

[2] Handbook of Chemistry and Physics, 63rd ed., CRC Press, 1983.

[3] Hard, R.A. and Megy, J.A. (1987). *U.S. Patent No. 4,655,825*. Washington DC: U.S. Patent and Trademark Office.

[4] Speed, S.E. (1970). *U.S. Patent No. 3,676,071*. Washington DC: U.S. Patent and Trademark Office.

[5] Flükiger, R., Foner, S., McNiff Jr., E.J., Schwartz, B.B., Adams, J., Forman, S., Eagar, T., and Rose, R.M., IEEE Transaction on Magnetics, v. MAG-15, No. 1, 1979, 689.

[6] Hard, R.A. and Megy, J.A. (1984). *U.S. Patent No. 4,470,847*. Washington DC: U.S. Patent and Trademark Office.

[7] Megy, J.A (1978). *U.S. Patent No. 4,127,409*. Washington DC: U.S. Patent and Trademark Office.

[8] Megy, J.A (1978). *U.S. Patent No. 4,072,506*. Washington DC: U.S. Patent and Trademark Office.

[9] Haygarth, J.C. and Graham, R.A., Oremet-Wah Chang Presentation to Argonne National Laboratory

[10] McDeavitt, S.M. (1992). Hot Isostatic Pressing of U-10Zr Alloy Nuclear Fuel by Coupled Grain boundary Diffusion and Power-Law Creep. Doctoral Thesis, Purdue University, West Lafayette, IN.

[11] McDeavitt, S.M., Kraemer, D.T., Parkinson, A., Totemeier, A.R., and Wegener, J.J. (2005). Zirconium Matrix Cermet Storage Form and Transmutation Fuel for Transuranics. To be submitted to the American Nuclear Society.

[12] Human Health Fact Sheet: Transuranic Radionuclides. Argonne National Lab, July, 2002.

[13] Small, W.M., Root, J.H., Khatamian, D. (1998). Observation of Kinetics of γ Zirconium Hydride Formation in Zr-2.5Nb by Neutron Diffraction. AECL-11913.

[14] Barin I: Thermochemical Data of Pure Substances, Part I, VCH Verlags Gesellschaft, Weinheim, 1993.

[15] Knacke O., Kubaschewski O., Hesselman K., Thermochemical properties of inorganic substances, 2nd ed., Springer-Verlag, Berlin, pp.1-1113, 1991. (KKH 91).

[16] Outokumpu HSC Chemistry for Windows. Version 5.1Outokumpu Research Oy, P.O. Box 60 FIN – 28101 PORI, FINLAND. 2002

[17] Electronic Space Products International. Private communication via website: http://www.espi-metals.com/msds's/Zirconium.htm. September 2004.

[18] Anglin, J., Literature Study to Characterize the Behavior of Zircaloy Cladding, Purdue University, 2004.

[19] Huber, B., Research on the Management of Fuel Cladding Waste, Proceedings of International Symposium on the Conditioning of Radioactive Wastes for Storage and Disposal, IAEA, Commission of European Communities, Brussels.

[20] Kubaschewski, O., Alcock, C.B., Spencer, P.J., Materials Thermochemistry, Pergamon Press, Oxford, 1993.

APPENDICES

Appendix A: Variac calibration curves

Table A.1. Hydride process variac setting calibration data

Variac Setting	Degrees Celsius	Process Gas
23.5	360	Ar-4.83%H2
45	741	Ar-4.83%H2
34	528	Ar-4.83%H2
31	487	Ar-4.83%H2
33	511	Ar-4.83%H2
34	531	Ar-4.83%H2
34	535	Ar-5.02%H2
32	488	Ar 99.997%
38	604	Ar-5.02%H2
34.5	543	Ar-5.02%H2
27	383	Ar-5.02%H2
34.5	546	Ar 99.997%
46	755	Ar-5.02%H2
33	512	Ar-4.97%H2
34.5	530	Ar-4.97%H2
34.5	538.5	Ar-4.97%H2

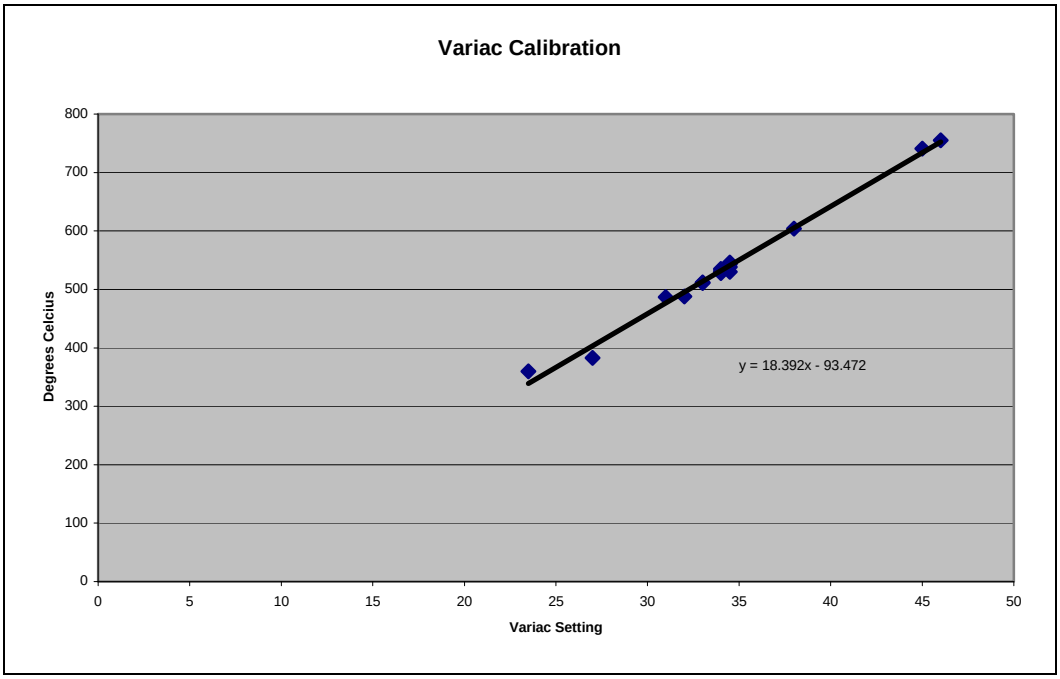

Figure A.1. Hydride process variac setting calibration plot

Table A.2. Dehydride process variac setting calibration data

Variac Setting	Crucible Degrees Celsius	Across Air-Lock Degrees Celsius	Outside w/ IR Degrees Celsius
20	367	58	40
30	545	84	65
40	686	105	102
50	805	120	135
60	897	132	170
70	975	135	

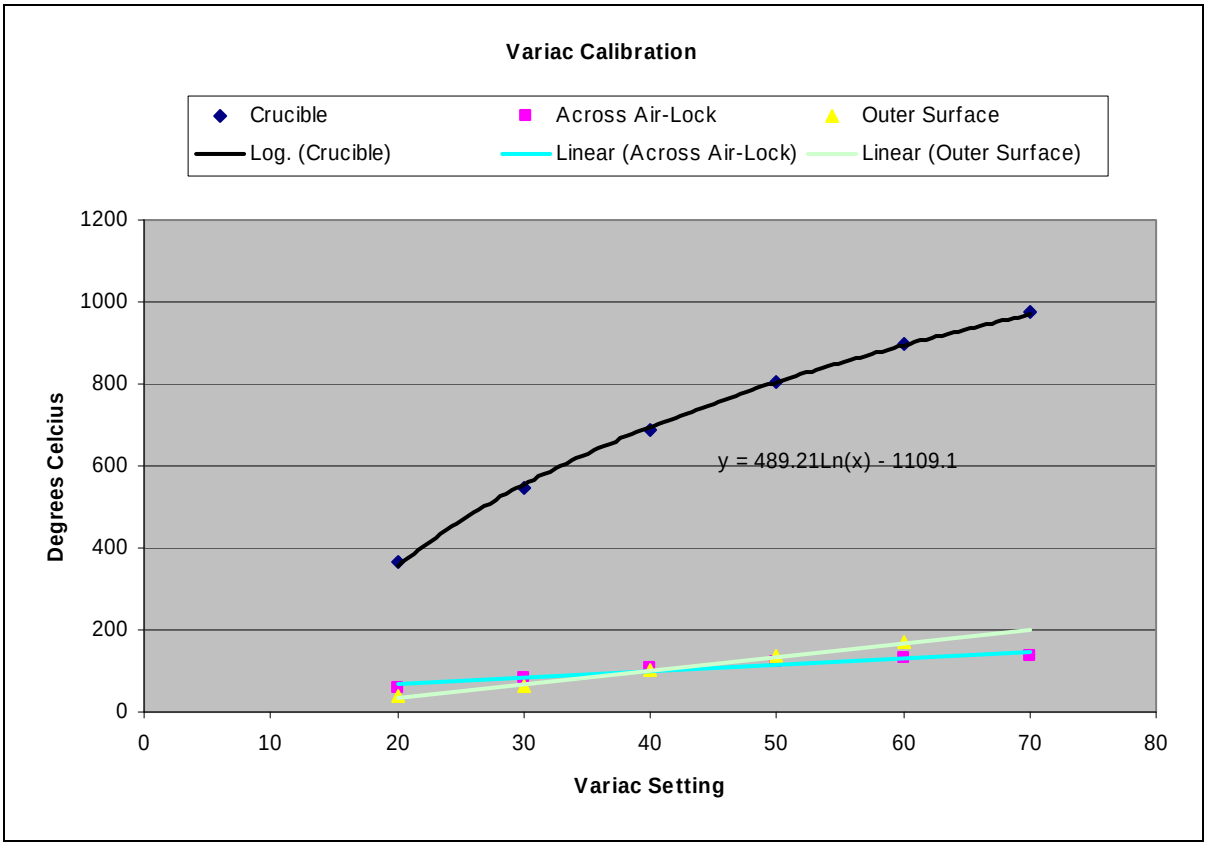

Figure A.2. Dehydride process variac setting calibration plot

Appendix B: Experiment temperature profiles

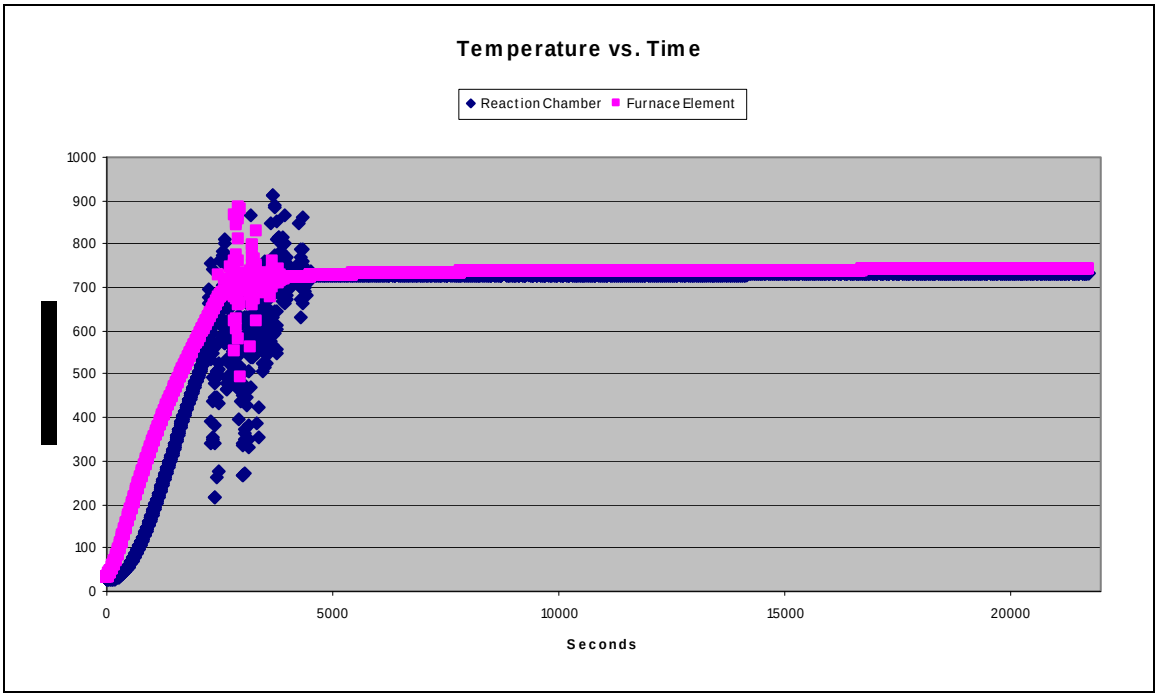

Figure B.1. Experiment Zy2 temperature profile

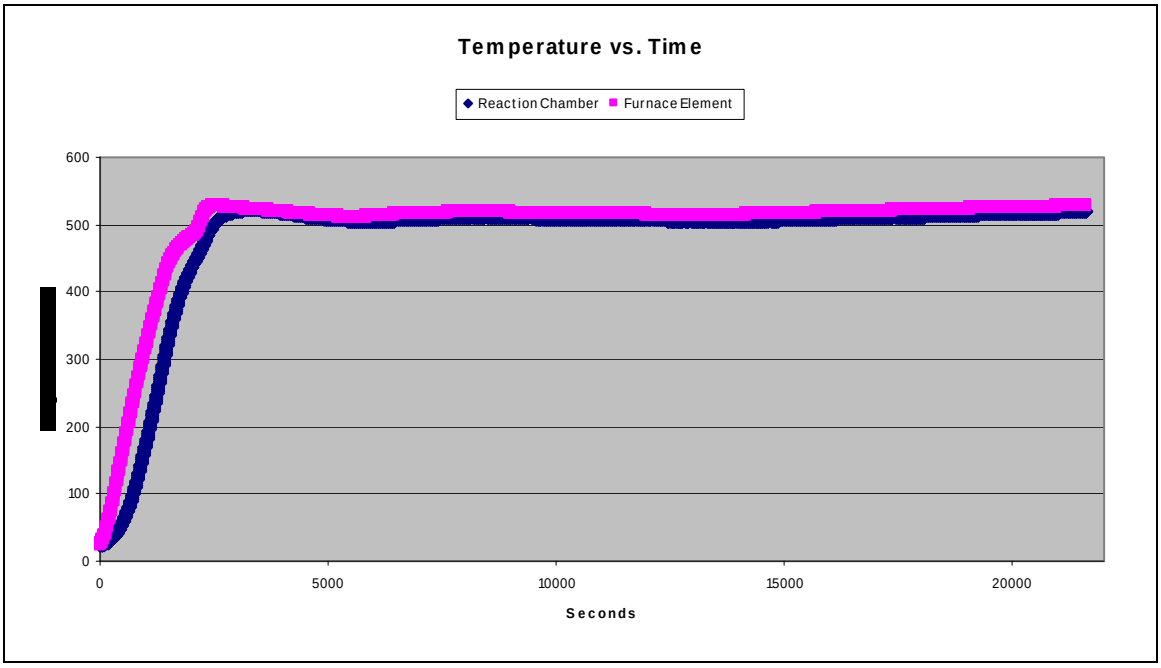

Figure B.2. Experiment Zy3 temperature profile

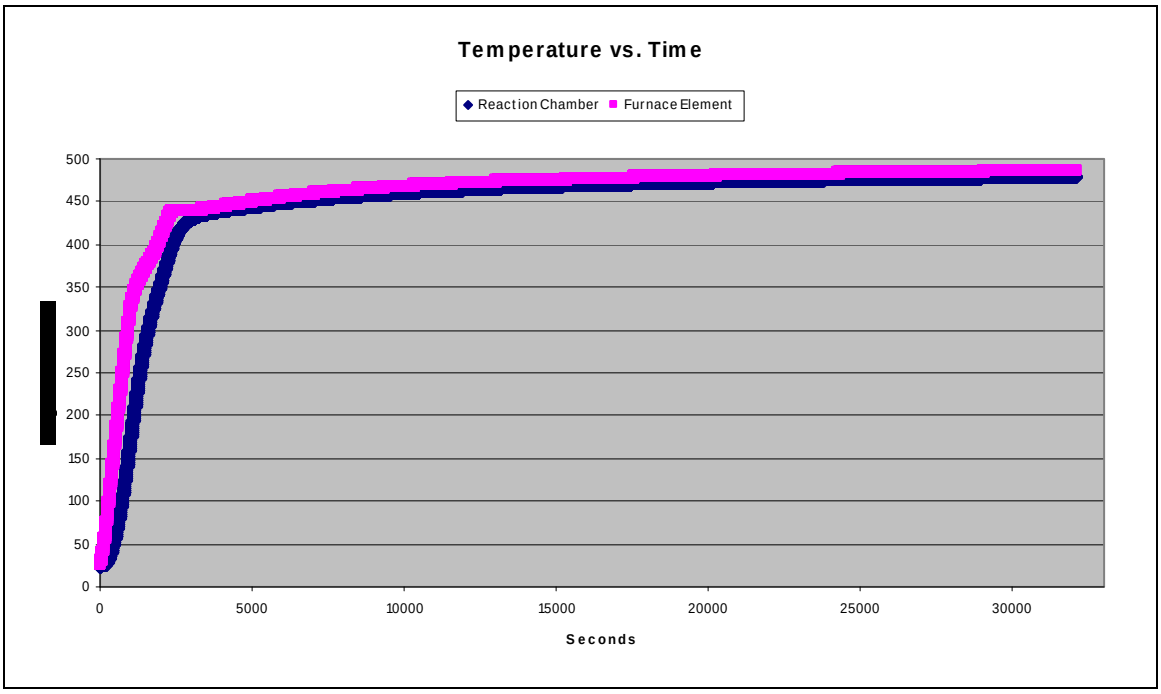

Figure B.3. Experiment Zy4 temperature profile

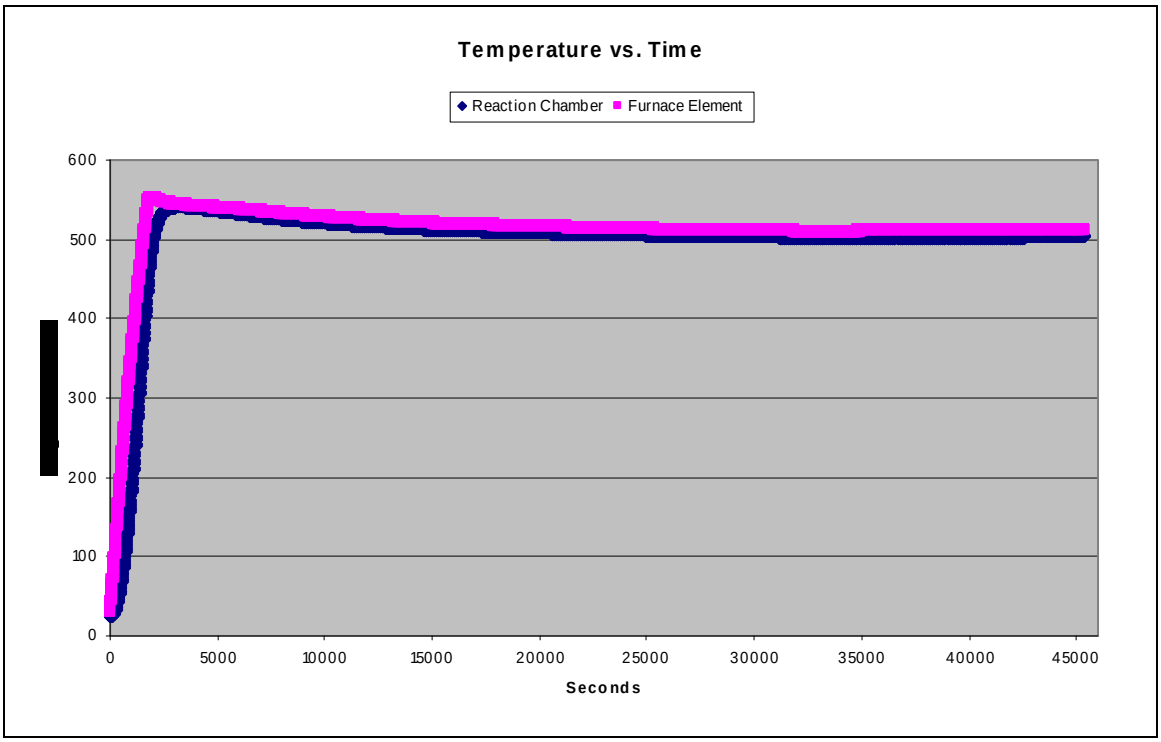

Figure B.4. Experiment Zy5 temperature profile

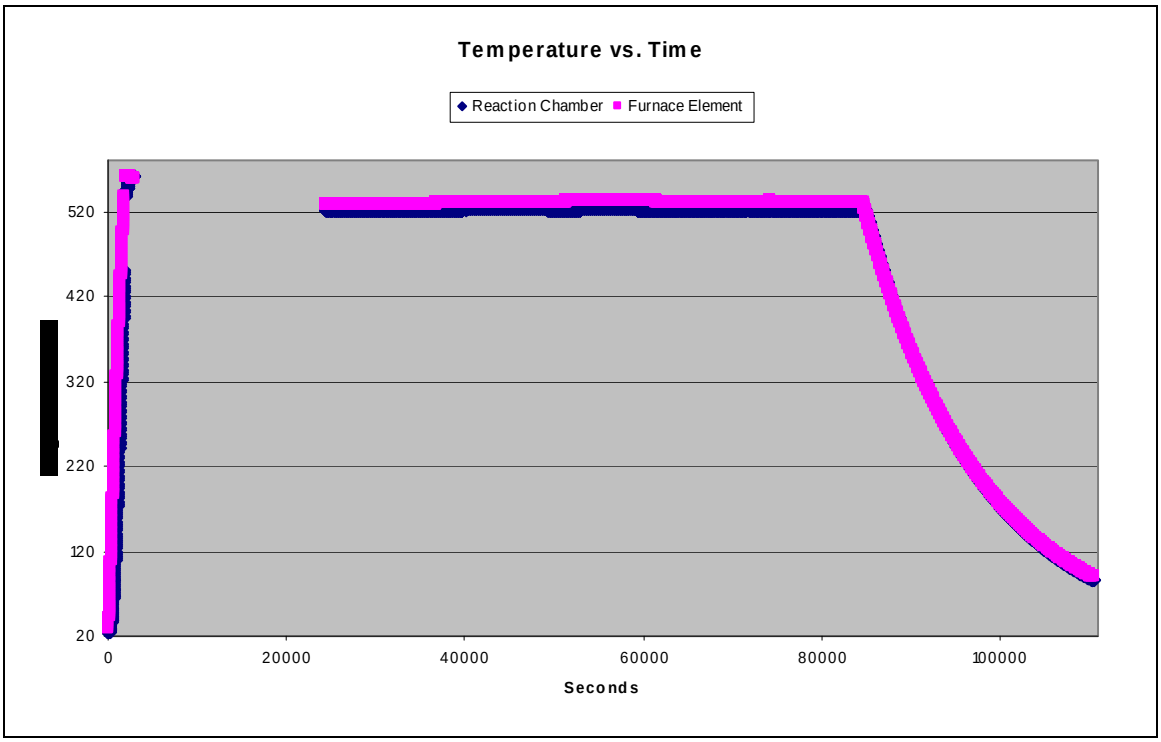

Figure B.5. Experiment Zy6 temperature profile

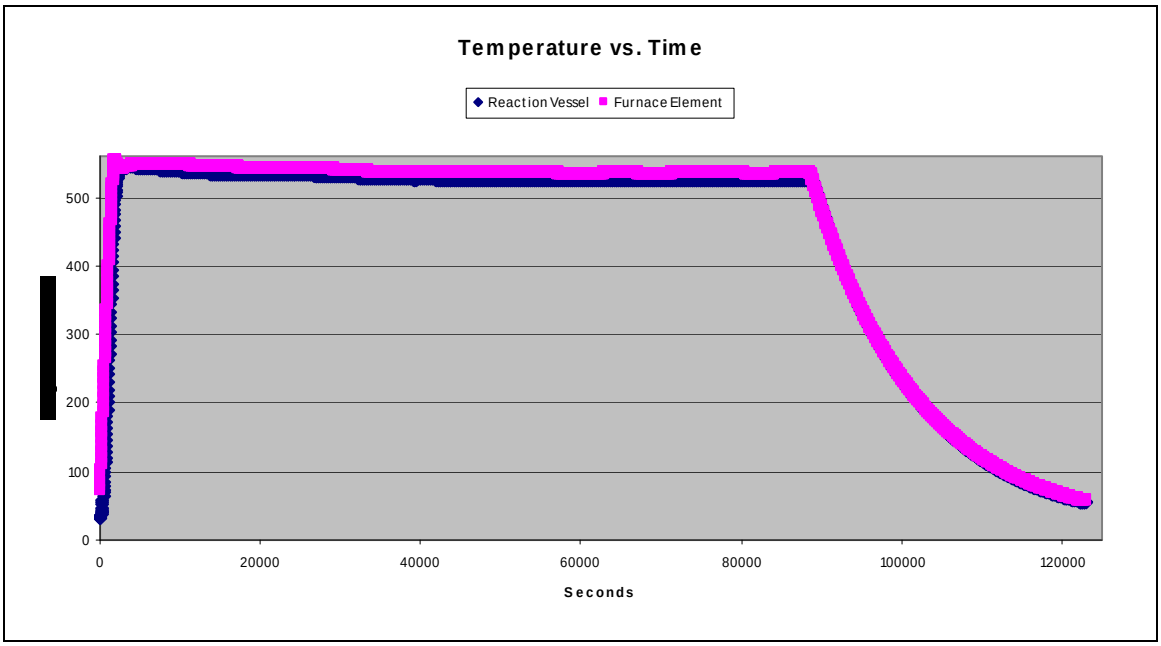

Figure B.6. Experiment Zy7 temperature profile

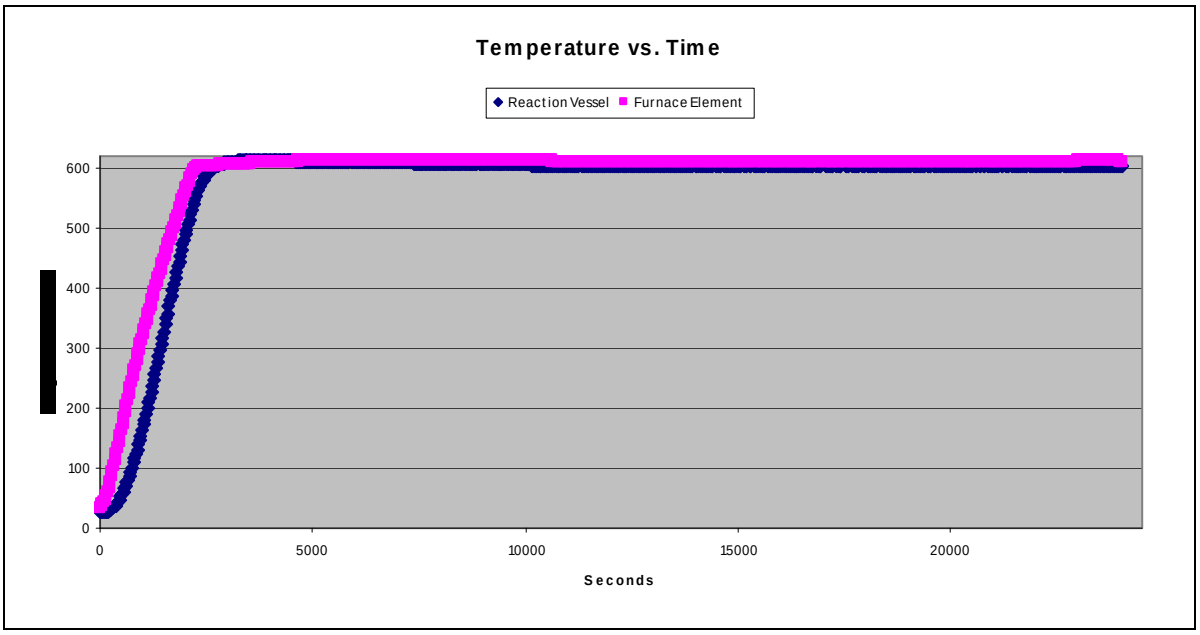

Figure B.7. Experiment Zy9 temperature profile

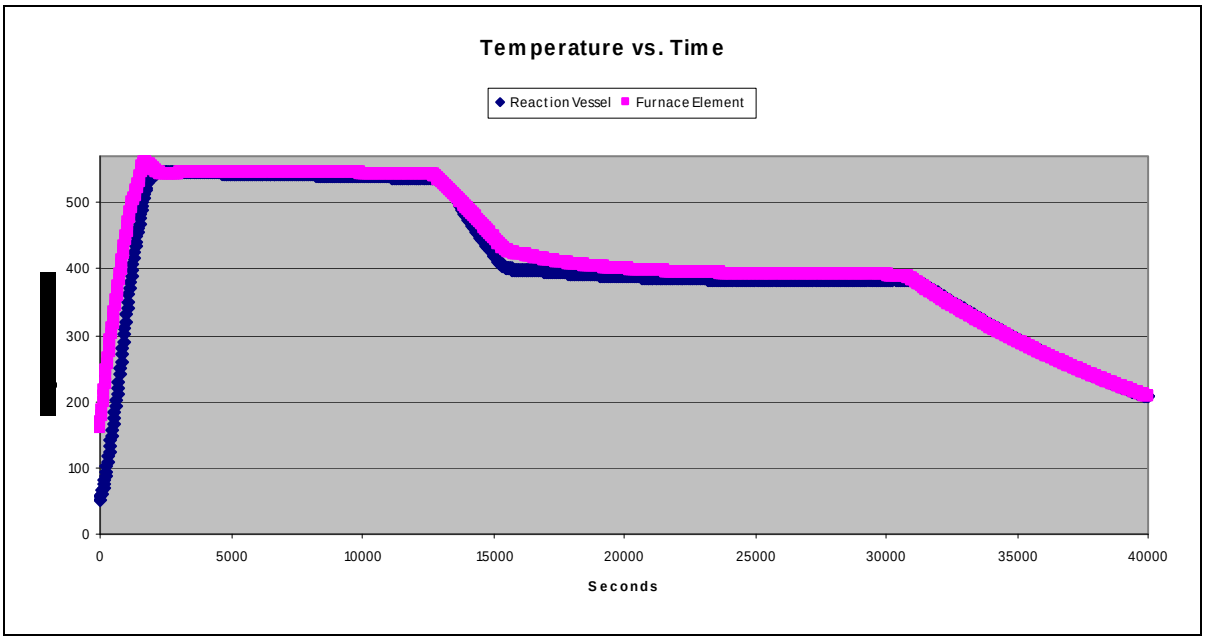

Figure B.8. Experiment Zy10 temperature profile

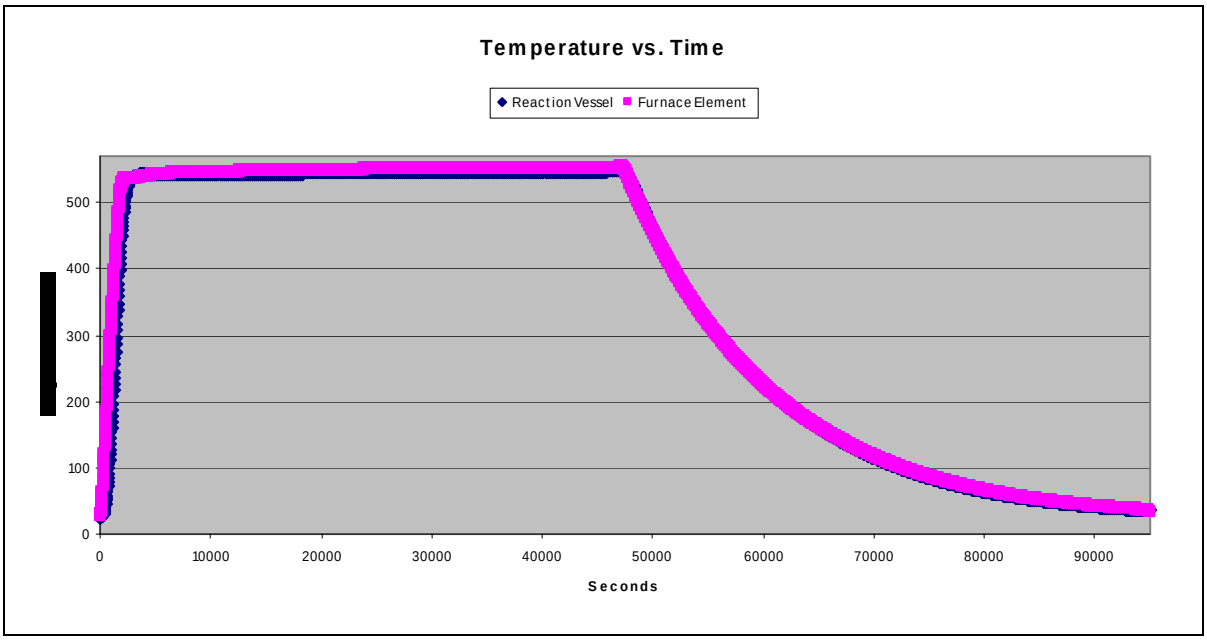

Figure B.9. Experiment Zy11 temperature profile

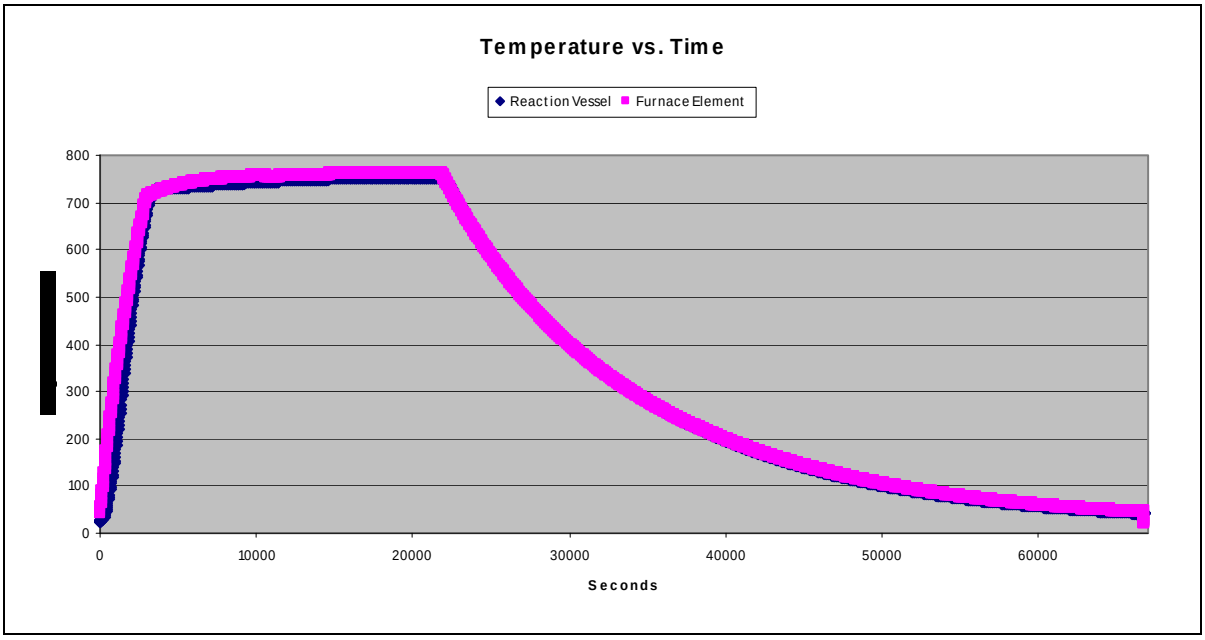

Figure B.10. Experiment Zy12 temperature profile

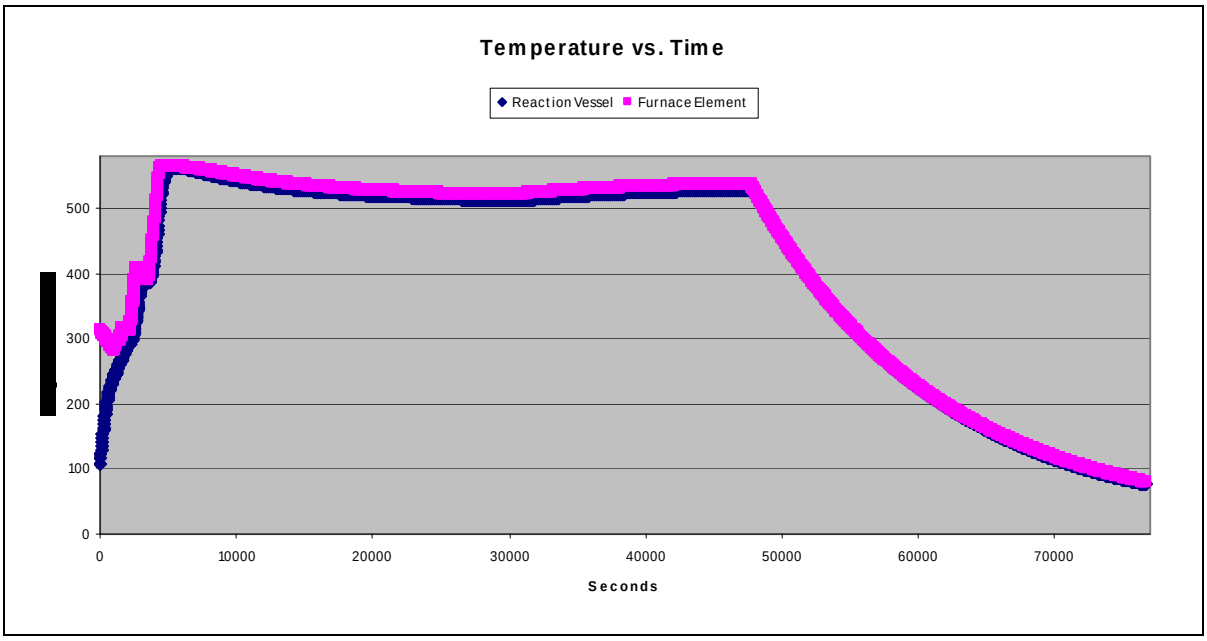

Figure B.11. Experiment Zy13 temperature profile

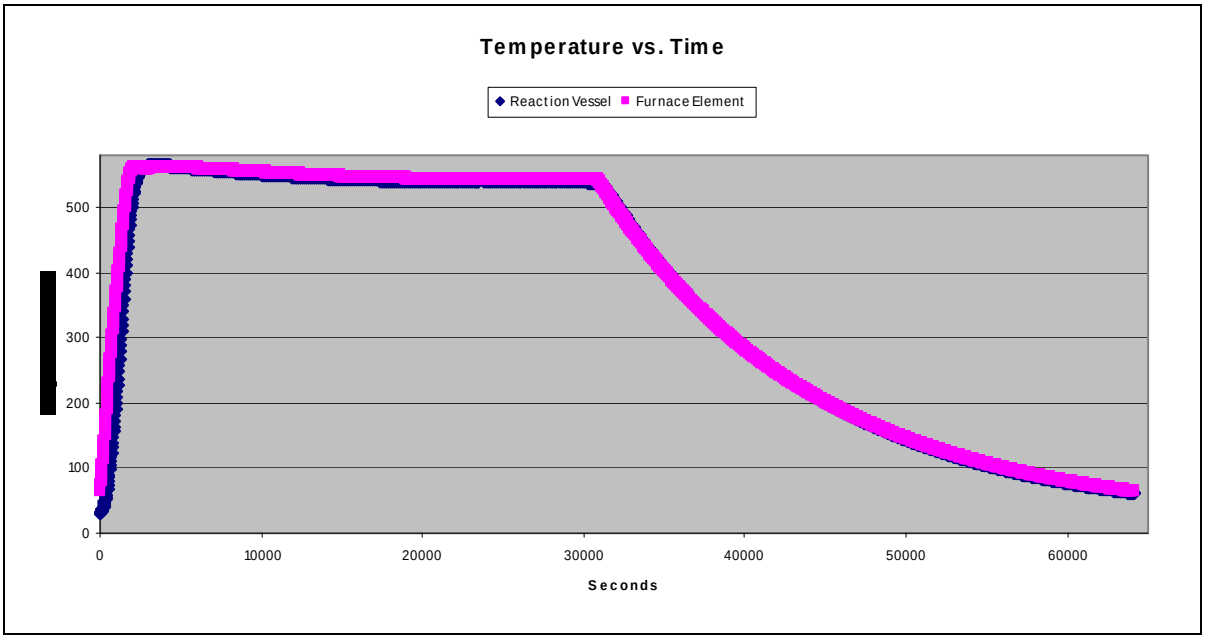

Figure B.12. Experiment Zy14 temperature profile

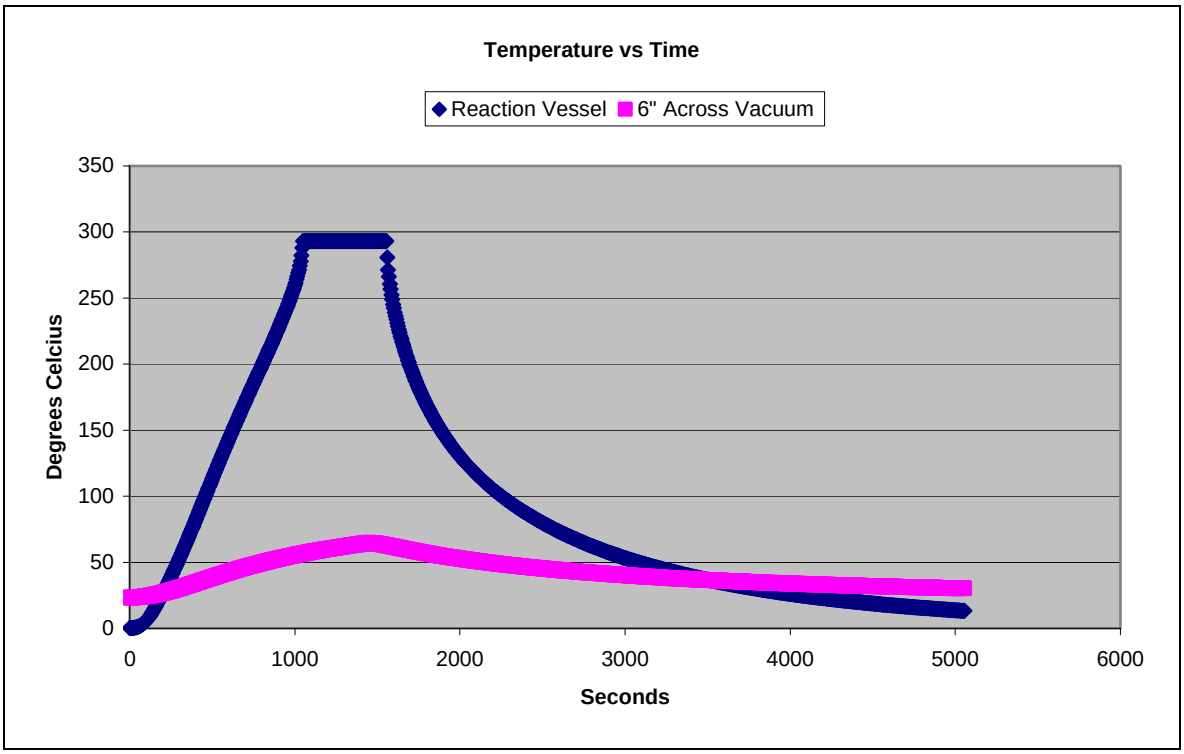

Figure B.13. Dehydride test1 temperature profile

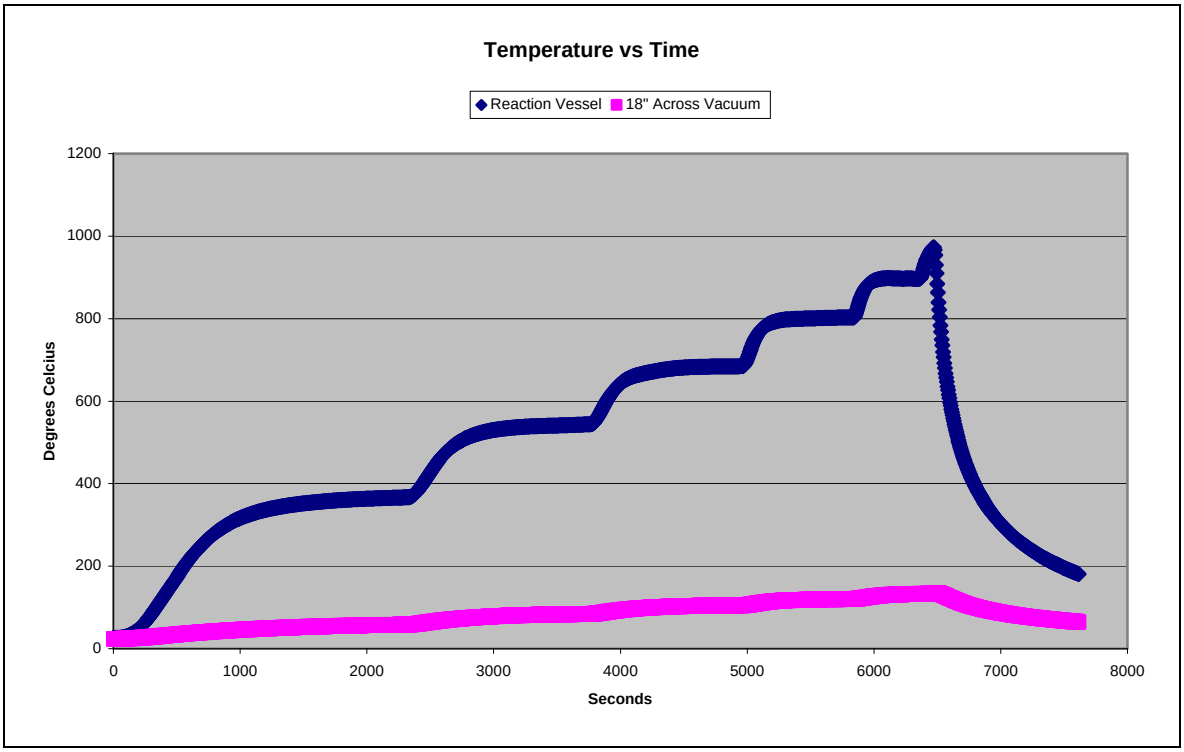

Figure B.14. Dehydride test2 temperature profile

Appendix C: Procedures

C.1. Transferring from open atmosphere through airlock into inert atmosphere

1) place equipment into airlock and seal it
2) close valve inside box and outer purge valve, open inner valve on outside
3) turn on vacuum pump
4) tighten wing nuts on outer door at ~1.5 mm Hg
5) pump down to ~0.1 mm Hg (100 microns) with vacuum pump
6) close inner valve on outside
7) remove inside wing nuts
8) backfill airlock with argon from the box using inside valve
9) open inner door and remove equipment into box

C.2. Transferring from inert atmosphere though airlock to open atmosphere

1) pump down and backfill the airlock if necessary
2) place equipment into airlock from inside box
3) close door and seal it
4) close inside valve and open inner valve on outside
5) pump down the airlock to ~2 mm Hg to tighten inner and loosen outer wing nuts
6) open outer purge valve to bring airlock to atmospheric pressure
7) open outer door and place on table
8) remove equipment, replace door, and seal door

C.3. Glovebox Operation

1) remove jewelry from hands and wrists
2) optional – wear long sleeves or powder arms with baby powder
3) insert arms into gloves slowly as to allow exhaust solenoid to evacuate box as needed
4) turn on overhead light
5) work slowly never allowing pressure to drop below -0.5 inches H^2O or above 3.5 inches H^2O
6) tare scale and measure samples at the same pressure by adjusting glove position
7) turn off overhead light and put back all samples and tools
8) remove hands slowly leaving gloves inside of box

C.4. Hydride Experiment

1) place reaction vessel inside of tube furnace, keeping valves closed on reaction chamber
2) attach thermocouple plugs
3) attach exhaust line to reaction vessel

4) open argon tank to 3 psi
5) release gas tank shut off valve, valve after pressure release valve, then valve prior to flowmeter to purge system. Allow system to purge for 5 minutes
6) attach inlet line to reaction vessel
7) open reaction chamber inlet line valve, then immediately open the reaction vessel exhaust valve
8) adjust flowmeter to 7 SCFM
9) turn on variable transformer and turn up to 80%
10) turn on data acquisition program and beginning recording data
11) once temperature reaches 15 degrees Celsius below desired operating temperature turn down the variac to estimated calibration setting
12) open hydrogen-argon mix tank valve to 3 psi and open shut off valve
13) shut argon tank shut off valve
14) adjust flowrate to less than 28 SCFM
15) begin active timing for experiment
16) after conclusion of experiment open argon tank shut off valve and close the hydrogen-argon mix tank
17) allow the reaction chamber to reach 80 degrees Celsius
18) shut reaction chamber inlet and exhaust valves
19) immediately shut argon tank shut off valve then intermediate valves in system
20) stop data acquisition
21) remove reaction chamber and place in airlock

C.5. Dehydride Experiment

Appendix D: Equipment photographs

Figure D.1. Glovebox plumbing

Figure D.2. Glovebox photohelic pressure sensor

Figure D.3. Glovebox vacuum pump and plumbing

Figure D.4. Glovebox exhaust vent and plumbing

Figure D.5. Data acquisition relay

Figure D.6. Hydride gas cylinders, overflow trap, and silicon oil bubbler

Figure D.7. Hydride system flowmeter and magnehelic pressure meter

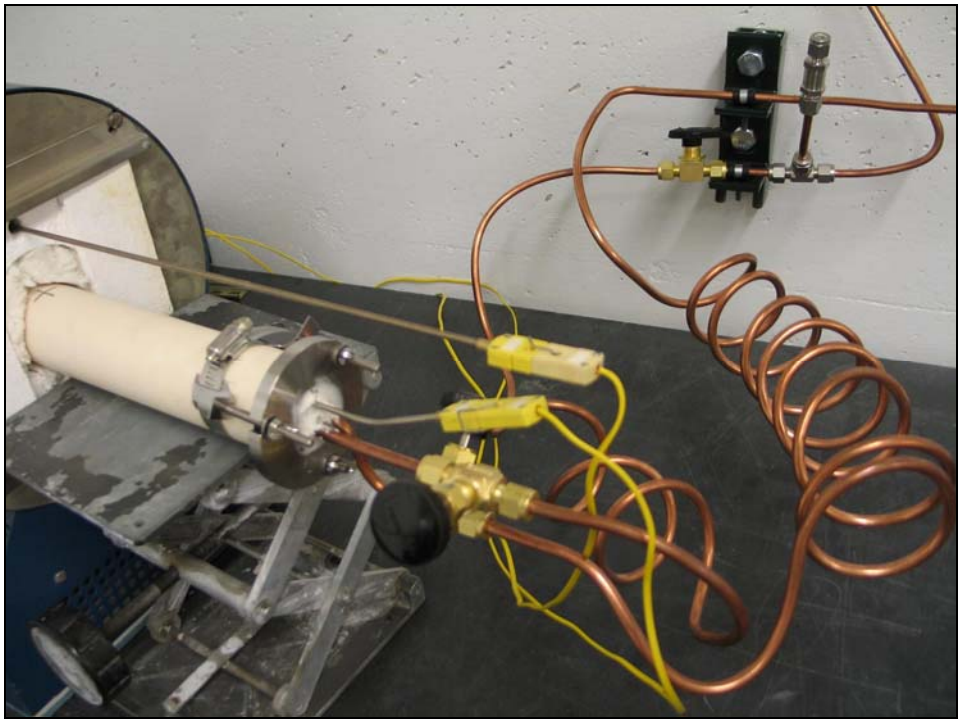

Figure D.8. Hydride system reaction chamber, inlet, exhaust, pressure relief valve, and thermocouples

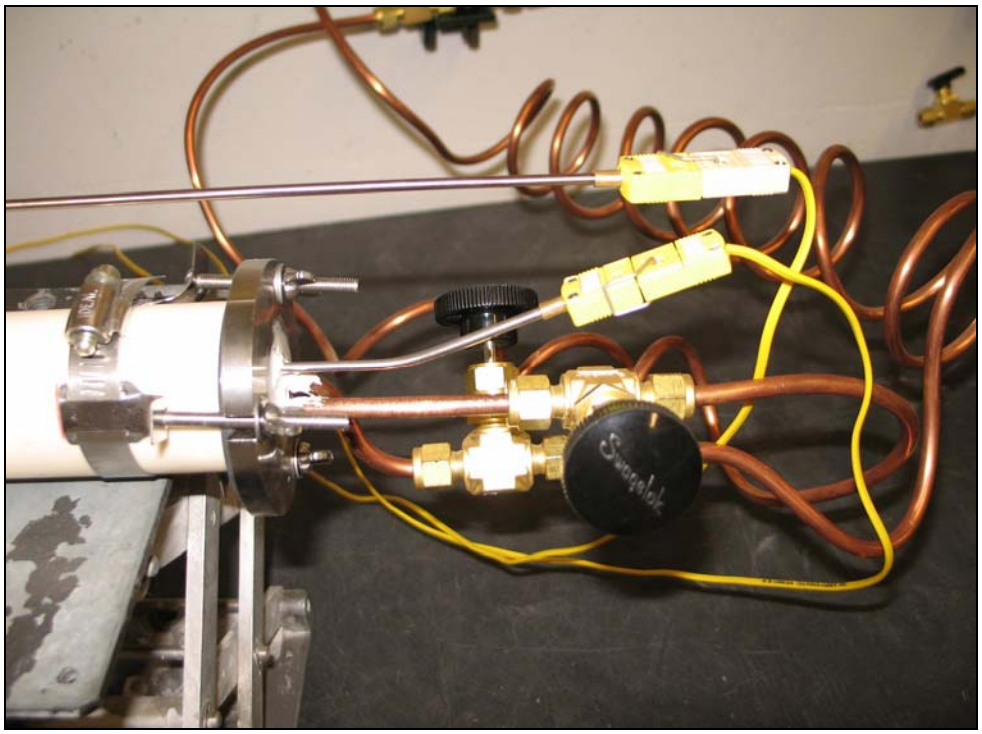

Figure D.8. Hydride system reaction chamber fittings

Figure D.9. Hydride system tube furnace and variable transformer

Figure D.10. Dehydride system door and attachments

Figure D.11. Glovebox Tools

Figure D.12. Glovebox vial holder and vials

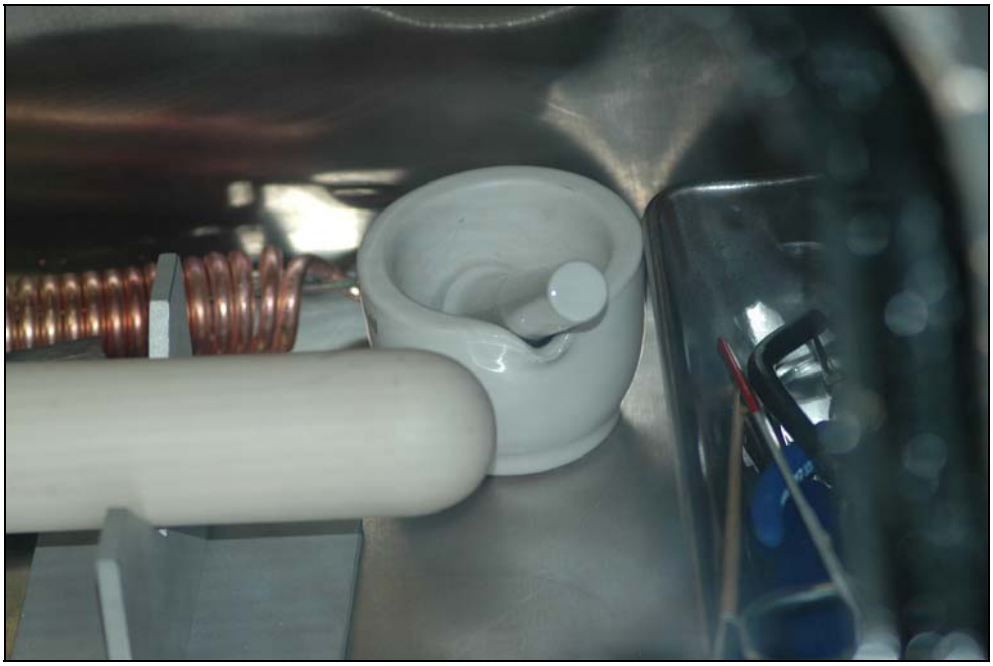

Figure D.13. Glovebox mortar and pestle

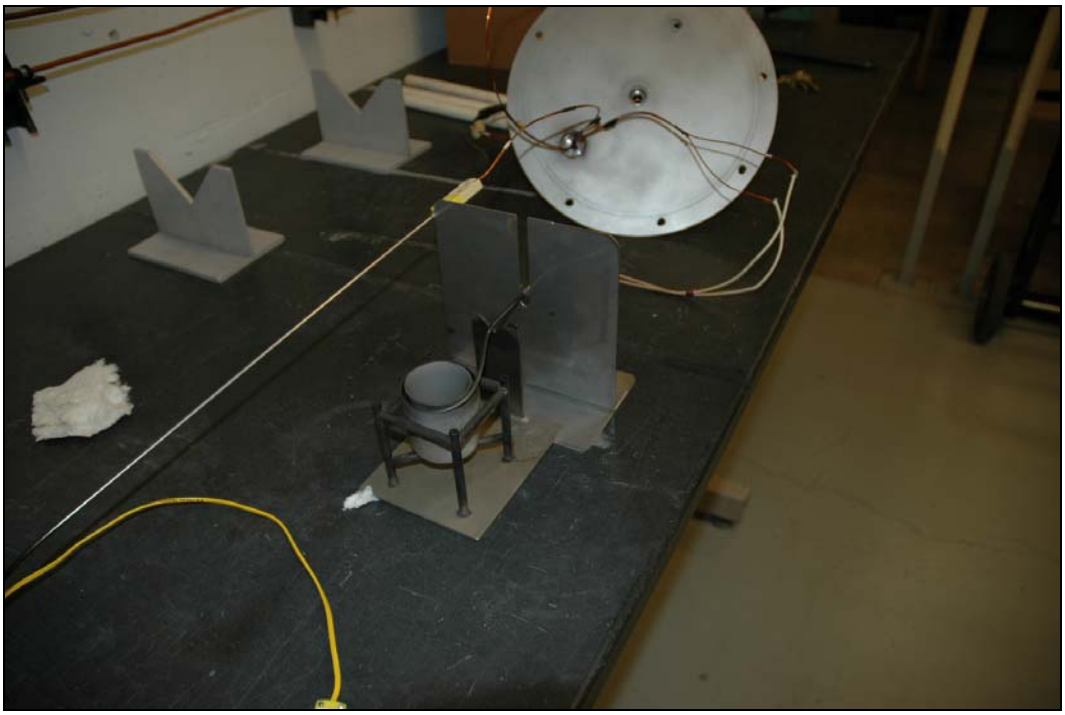

Figure D.14. Dehydride apparatus with heatshield

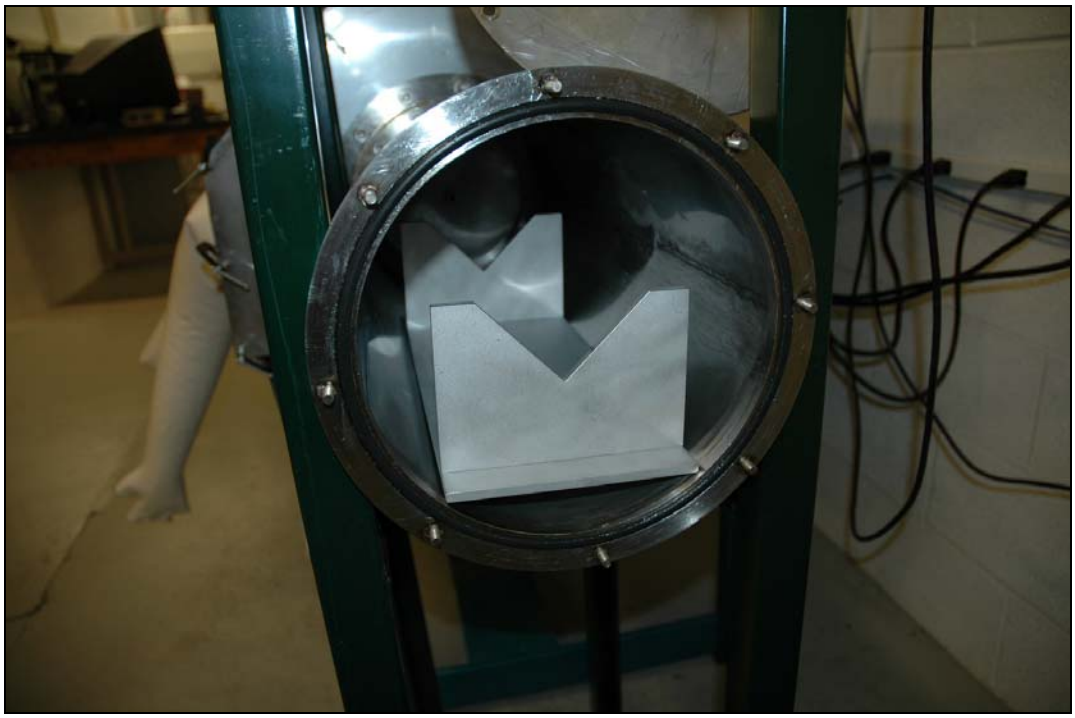

Figure D.15. Airlock transfer cradle

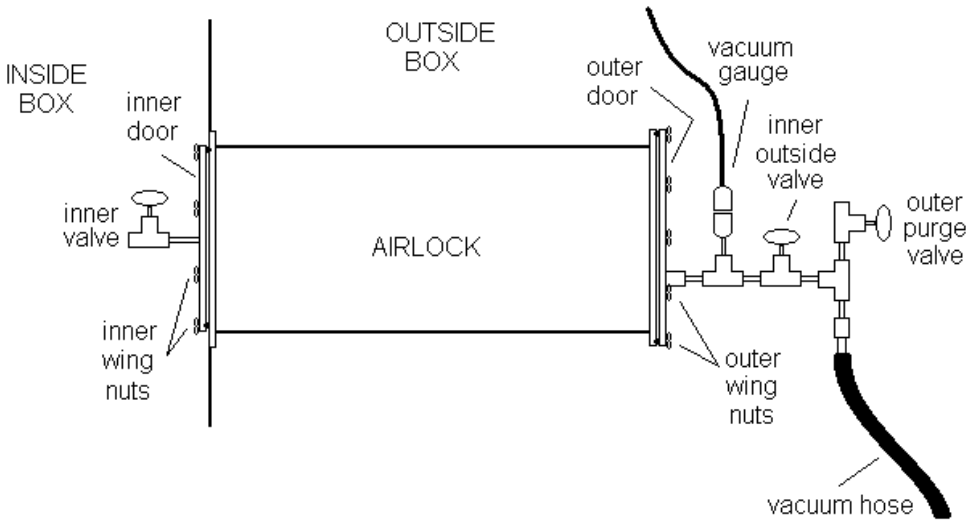

Figure D.16. Airlock schematic

VITA

VITA

Dustin Thomas Kraemer was born in 1980 in Wadsworth, OH, USA, but attended school in nearby Doylestown, Ohio. He has been a student at Purdue University since 1999 and has received the following degree: Bachelor of Science in Nuclear Engineering in December of 2003 while completing the Naval ROTC curriculum. He will receive his Master of Science in Nuclear Engineering degree in August of 2005. He was commissioned as an Ensign in the United States Navy in July of 2005. He will pursue his nuclear career as a naval submarine officer in the United States Navy.

Appendix F

Master of Science Thesis: Zircaloy Hydride Method (97 Pages)

HYDRIDE PRODUCTION IN ZIRCALOY-4 AS A FUNCTION OF TIME AND TEMPERATURE

A Thesis

By

ADAM JOSEPH PARKISON

Submitted to the Office of Graduate Studies of Texas A&M University
in partial fulfillment of the requirements for the degree of

MASTER OF SCIENCE

May 2008

HYDRIDE PRODUCTION IN ZIRCALOY-4 AS A FUNCTION OF TIME AND TEMPERATURE

A Thesis

by

ADAM JOSEPH PARKISON

Submitted to the Office of Graduate Studies of
Texas A&M University
in partial fulfillment of the requirements for the degree of

MASTER OF SCIENCE

May 2008

Major Subject: Nuclear Engineering

HYDRIDE PRODUCTION IN ZIRCALOY-4 AS A FUNCTION OF TIME AND TEMPERATURE

A Thesis

by

ADAM JOSEPH PARKISON

Submitted to the Office of Graduate Studies of
Texas A&M University
in partial fulfillment of the requirements for the degree of

MASTER OF SCIENCE

Approved by:

Chair of Committee,	Dr. Sean McDeavitt
Committee Members,	Dr. Lin Shao
	Dr. Haiyan Wang
Head of Department,	Dr. Raymond Juzaitis

May 2008

Major Subject: Nuclear Engineering

ABSTRACT

Hydride Production in Zircaloy-4 as a Function of Time and Temperature. (May 2008)

Adam Joseph Parkison, B.S., Purdue University

Chair of Advisory Committee: Dr. Sean M. McDeavitt

The experiments performed for this thesis were designed to define the primary process variables of time, temperature, and atmosphere for an engineering system that will produce metal powder from recycled nuclear fuel cladding. The proposed system will hydride and mill Zircaloy cladding tubes to produce fine hydride powder and then dehydride the powder to produce metal; this thesis is focused on the hydride formation reaction. These experiments were performed by hydriding nuclear grade Zircaloy-4 tubes under flowing argon-5% hydrogen for various times and temperatures. The result of these experiments is a correlation which relates the rate of zirconium hydride formation to the process temperature. This correlation may now be used to design a method to efficiently produce zirconium hydride powder.

It was observed that it is much more effective to hydride the Zircaloy-4 tubes at temperatures below the α-β-δ eutectoid temperature of 540°C. These samples tended to readily disassemble during the hydride formation reaction and were easily ground to powder. Hydrogen pickup was faster above this temperature but the samples were generally tougher and it was difficult to pulverize them into powder.

DEDICATION

This thesis is dedicated to my parents, Scott and Melanie Parkison, as well as my brothers, Brian and Alex Parkison.

ACKNOWLEDGEMENTS

I would like to specially thank my committee chair Dr. Sean M. McDeavitt as well as my committee members Dr. Lin Shao and Dr. Haiyan Wang for all the help and encouragement they have given me. I would also like to thank the faculty of Texas A&M University for providing me with a great education, and for always being available whenever I needed assistance. Additional thanks go to my friends and colleagues, Aaron Totemeier, Luis Ortega, and Matt Solmos for being willing to share ideas and to give me ideas regarding this research. I would like to acknowledge the U.S. Department of Energies Nuclear Energy Research Initiative for supporting this project (NERI ID NO. DE-FC07-05ID14656). Finally, I would like to thank my family for all of their support and encouragement.

NOMENCLATURE

BCC	Body Centered Cubic
FCCI	Fuel-Cladding Chemical Interaction
HCP	Hexagonal Close-Packed
RTV	Room Temperature Vulcanizing
SCFH	Standard Cubic Feet per Hour
TRU	TRansUranic
UHP	Ultra High Purity
VAC	Volts Alternating Current
XRD	X-Ray Diffraction

TABLE OF CONTENTS

LIST OF FIGURES

LIST OF TABLES

CHAPTER 1

INTRODUCTION: PRODUCTION OF ZIRCONIUM HYDRIDE POWDER

If nuclear energy is to maintain its status as a clean, safe, and reliable energy source, the nuclear waste issue must be addressed in an economic and responsible manner. The research described here is part of a larger project funded by the U.S. Department of Energy's Nuclear Energy Research Initiative that is developing a method to safely store and potentially recycle transuranic (TRU) isotopes from spent nuclear fuel. This will be accomplished by encapsulating the TRU oxides in a Zircaloy matrix cermet via powder metallurgy. [1] Therefore, the recovery of Zircaloy metal powder from spent fuel cladding is a required operation for the success of this concept.

Experiments were performed to define the fundamental mechanism and process variables of hydride formation in Zircaloy-4 in order to provide a basis for an engineering system that will ultimately produce metal powder from recycled nuclear cladding. The proposed Zircaloy recycle process will hydride and mill Zircaloy cladding tubes to produce fine hydride powder and then dehydride the powder to produce metal; the research described here is exclusively focused on understanding the hydride formation reaction. To this end, hydriding experiments were performed using nuclear grade Zircaloy-4 tubes exposed to flowing argon-5% hydrogen for various times and temperatures. Zircaloys are nominally ~98 wt. % zirconium and the composition of Zircaloy 4 cladding is shown in Table 1. [2]

This thesis follows the style of *Journal of Nuclear Materials*

Table 1: Composition of Zircaloy-4 (in wt %).

Element	Wt % in Zircaloy-4
Sn	1.2-1.7
Fe	0.18-0.24
Cr	0.07-0.13
O	0.12
Zr	Balance

The recycle of zirconium from spent nuclear fuel cladding is desirable, in part, because the cladding material already contains "nuclear grade" zirconium, which has a very low hafnium content. As a lesser point of interest, the Zircaloy cladding becomes radioactive in service due to neutron activation and ion implantation of radioactive isotopes from the fission process. The Zircaloy becomes further degraded and contaminated via fuel-cladding chemical interactions (FCCI). As a result, it is not clear that spent Zircaloy can be discarded as low level waste, so the partial recycle of the Zircaloy "waste" into a TRU storage form may reduce the ultimate volume of high level waste attributable to reprocessing.

As stated above, the research described here focuses on quantifying the process variables for the transformation of Zircaloy cladding hulls into a zirconium hydride powder. One of the advantageous phenomena inherent in the transformation of Zircaloy cladding into zirconium hydride is that the density changes from ~6.5 g/cm^3 (ρ_{Zr} = 6.49 g/cm^3 [3]) to ~5.6 g/cm^3. [4] This difference in density coupled with the brittle nature of

zirconium hydride results in an extremely brittle zirconium hydride product which can then be easily ground into a fine powder.

The hydride formation data from this research was quantified as the metal-to-hydride conversion percent (P_H) in Zircaloy-4 tubes as a function of time and temperature. These data were used to develop an understanding of how the hydride process effects embrittlement of the cladding. A correlation for P_H as a function of time and temperature is developed in Section 5.2 based on a parabolic equation for the a α-Zr phase and a linear equation for the β-Zr phase as seen in Equations 1 and 2.

$$\begin{aligned} &\text{For } 440^{o}\text{C} < T < 540^{o}C \\ &P_H = At^m \\ &A = 0.028T - 6.39 \\ &m = 1.74 \pm 0.05 \end{aligned} \qquad [1]$$

$$\begin{aligned} &\text{For } 540^{o}\text{C} < T < 640^{o}C \\ &P_H = At \\ &A = 0.085T - 20.5 \end{aligned} \qquad [2]$$

"P_H" is degree of reaction completion in % hydride
"t" is time in hours
"T" is temperature in Celsius

Where *A* and *m* are constants which were found experimentally. The rate of hydride formation with respect to temperature can then be used to engineer a pathway along the binary Zr-H phase diagram, Figure 1

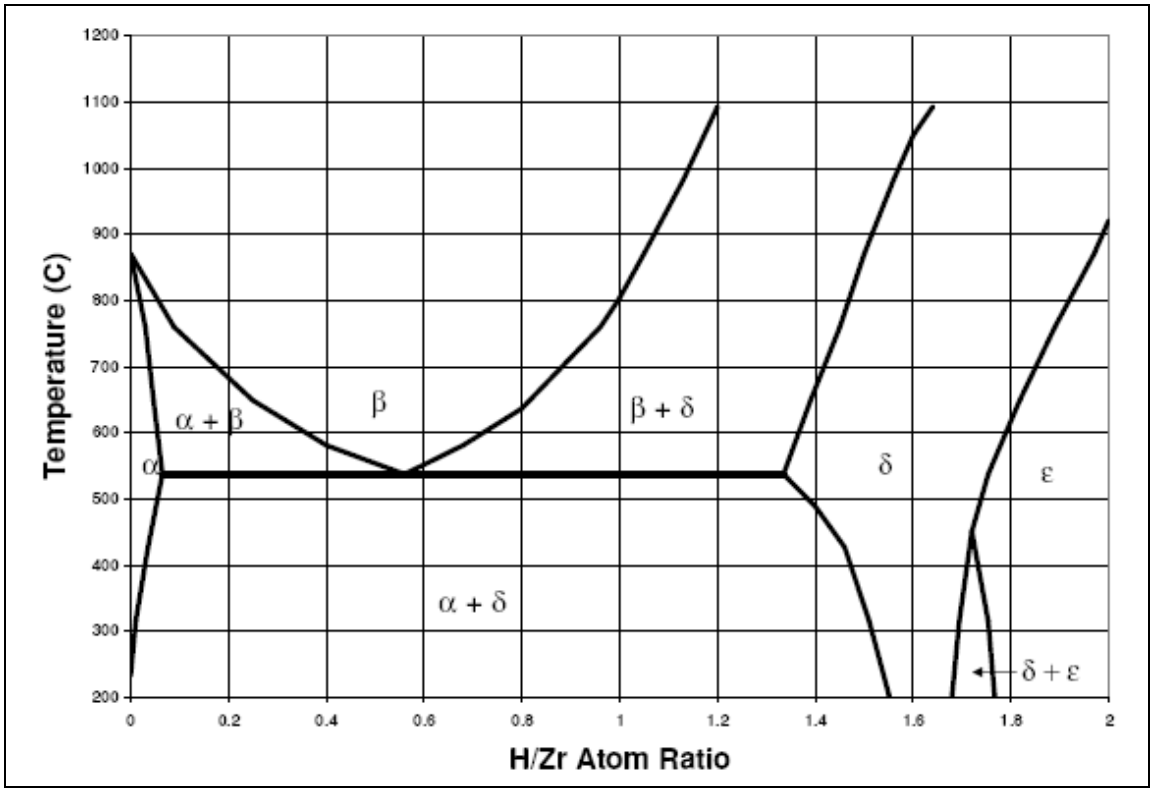

Figure 1. Hydrogen-zirconium phase diagram.

CHAPTER 2

PREVIOUS WORK

2.1 ZIRCONIUM PROCESSING

Industrial processes designed to produce and refine pure zirconium have been developed and implemented with varying degrees of success. These methods include, but are not limited to, sodium reduction of $ZrCl_4$, potassium reduction of ZrO_2, electrolysis of the fused salt K_2ZrF_6, the Kroll process, and the hydride/dehydride process. [5] The two reduction methods are known to both have purity issues, especially with respect to contaminating gasses such as nitrogen and oxygen. As with any electrolysis process, the fused salt method is limited for industrial use because it is expensive due to its high energy demand, and is a batch process technique. [6]

The Kroll process is by far the leading process for the production of zirconium. This process transforms zirconium ore to zirconium ingots by way of several chemical steps. The zirconium ore is processed prior to being reacted with chlorine gas to form $ZrCl_4$ along with other volatile chlorine compounds. The product is distilled and separated to generate a pure $ZrCl_4$ vapor stream. This gas is then passed over molten magnesium, resulting in the formation of $MgCl_2$ liquid and Zr sponge by the following reaction.

$$2Mg(l) + ZrCl_4(g) \rightarrow 2MgCl_2(l) + Zr(s) \qquad [3]$$

The magnesium and chlorine can later be recovered and recycled in the process. This process is useful in producing zirconium sponge as well as zirconium ingots, but is limited in its ability to produce zirconium powder. [7]

The hydride/dehydride process is known to produce a high purity zirconium powder, with a purity which is very similar to the initial purity of the zirconium to be transformed. This process is considered superior to all other methods with respect to the purity of the resulting zirconium powder. [6] Patent number 4,470,847 describes this process in detail. [8]

The hydride/dehydride process for zirconium powder production is based upon the concept that zirconium swells dramatically do to density changes as hydrogen is added to the material. It has been reported that this volume change is on the order of 8.2% to 15.4%. [7] This volume change combined with the brittle nature of zirconium hydride allows the resulting zirconium hydride to be ground to a fine powder. The zirconium hydride powder may then be dehydrided at temperatures above 800°C at low pressures, resulting in a fine zirconium powder. [6]

It is widely reported that the maximum hydrogen pickup occurs at temperatures near 300°C for all pressures. However, for the production of zirconium powder, the general practice is for the reaction to take place at 800°C. [6] This high temperature allows for rapid hydrogen absorption which is ideal for thick pieces of zirconium. The high temperature is required because the zirconium hydride reaction is a diffusion controlled process. Diffusion is known to be a temperature dependant phenomenon with a parabolic relation with respect to time. Therefore, the higher the temperature, the

faster the hydride reaction will progress through the bulk of the material. [7] It is also known that the rate of the hydride reaction is proportional to the surface area of the material. A result of this is that the rate of the hydride reaction within bulk material is dramatically lower than for a metal sponge or powder. [9] Regardless of the geometry, it has been found that the rate of hydrogen pickup within zirconium is proportional to the square root of the pressure. Given this dependence it is evident that slight differences in pressure are more important at lower pressures, while at higher pressures, variations in pressure will have less of an impact. [7]

It has been reported that it is necessary to have a concentration of 50 atom percent hydrogen within the zirconium matrix in order for the zirconium hydride sample to easily grind to powder. This is the recommended hydrogen concentration for zirconium hydride materials which have been produced at high temperatures such as 800°C. This corresponds to a regime where hydrogen is diffusing through the body-centered cubic (BCC) β-Zr phase, which is known to be a more stable phase than the hexagonal close-packed (HCP) α-Zr phase. [6]

Further, the reaction rate of hydrogen with zirconium is known to be dependent on surface effects. These surface effects may include films left from the processing of the material, as well as the oxide surface layer. It is therefore essential to thoroughly clean specimens which are to be reacted. It has been found that the oxide surface layer may be dissolved into the bulk Zr lattice by preheating it at 1050°C. This surface oxide layer plays an important role at low temperature. In fact, the hydride rate has been seen to be up to 7700 times higher for these heat treated materials than for the materials

which contain an oxide surface layer at 150°C. The heat treatment of zirconium has been seen to have an effect on the hydride reaction at heat treatment temperatures as low as 500°C. [7]

When hydrogen is reacted with zirconium, it occupies the tetrahedral positions of the HCP alpha and BCC beta phases. However, when elements such as oxygen or nitrogen react with zirconium, they occupy the octahedral positions of the HCP alpha and BCC beta phases. These oxygen or nitrogen atoms cause local distortions in the metal lattice making it impossible for hydrogen to locate itself in the nearby tetrahedral positions. This effect has been seen to cause a strong dependence of oxygen or nitrogen content within the metal on the hydride reaction rate. It is therefore of the utmost importance to have a clean, nitrogen and oxygen free system in order for the hydride reaction to progress quickly. Specifically, nitrogen is the element of most interest when considering this effect, and has the largest impact on decreases in the reaction rate of hydrogen and zirconium. [7]

2.2 PREVIOUS HYDRIDE PROCESS DEVELOPMENT EXPERIMENTS

This thesis is a continuation of work performed by Dustin Kraemer, the results of which can be seen in reference 3. The work performed by Kraemer focused on the design and construction of an experimental system which can be used to produce a zirconium hydride powder, using the hydride process. The original system which was designed and built by Kraemer was the foundation for the experimental setup used in this thesis. Kraemer performed 14 proof of concept experiments which gave a basic understanding of the behavior of the system for various temperatures, pressures, and

hydride times. It was observed that zirconium hydride produced in the alpha phase was more brittle than zirconium hydride produced in the beta phase. It was also observed that the hydride reaction proceeded more rapidly at higher pressures than for lower pressures. These results indicated that zirconium hydride could be produced and then turned to powder by grinding with a mortar and pestle.

CHAPTER 3

EXPERIMENTAL DESIGN AND PROCEDURE

The hydride formation experiments were performed on nuclear grade Zircaloy-4 tubes by exposing them to flowing argon - 5% hydrogen process gas, with time and temperature as process variables. The experimental setup is an improved version of the system described by Kraemer [3] and it consists of a controlled atmosphere reaction vessel containing a small sample of Zircaloy-4. The vessel is a sealed alumina tube with flowing Ar-H_2 gas and is inserted into a tube furnace. The system is loaded and unloaded inside of an inert argon atmosphere glovebox to minimize the contamination of the hydride product from contaminants in the air, most notably nitrogen, oxygen, and water. Following the scoping project reported by Kraemer, which included 14 proof of principle experiments, 87 experiments were carried out to fully define the hydride formation process. Appendix A shows a complete summary of these experiments, and the results are described in Chapter 4.

3.1 EXPERIMENTAL DESIGN

3.1.1 Process Gas Flow

Figure 2 shows the schematic of the gas delivery system. The process gas source comes from two separate gas cylinders. One cylinder contains ultra high purity (UHP) argon and the second cylinder contains Ar-5%H_2. The UHP argon was used during and after experiment 51. Previous to this, welder's grade argon was used, but it was found that welder's grade argon was not pure enough to get consistent results for this process

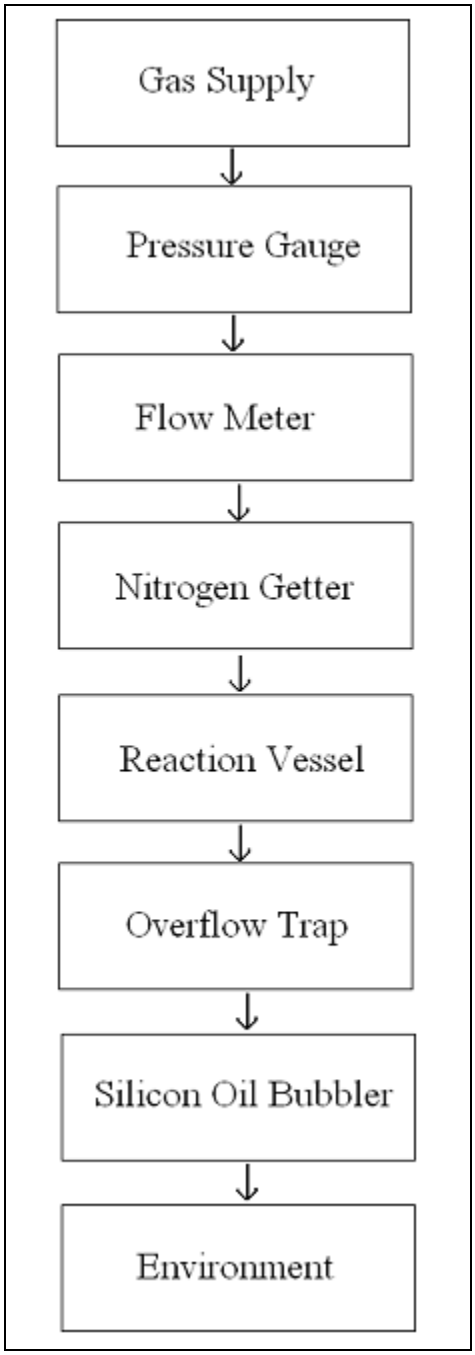

Figure 2. Schematic of process gas flow path.

(see Chapter 4). The gas supply is controlled via a gas flow meter (Dwyer model number RMB-50-SSV) and a pressure gage (Dwyer model number 2030). There is then an inline 5 psi relief valve (Swagelok model number SS-4C-5). This is to avoid over-pressurization of the system and is located immediately before the titanium sponge getter. The getter was designed, manufactured and installed in this position after experiment 57 as part of this project. For experiments 53-57, it was located between the gas cylinders and the flow meter. It was moved to its final downstream position to account for any leaks or sources of contamination introduced by the flow meter, pressure gage, or pressure relief valve.

Once the gas leaves the getter in this final configuration, it flows directly into the reaction vessel through an inlet valve. The process and purge gas is heated as it enters the reaction vessel through a copper coil inside of the reaction vessel. The gas exits the copper coil at the end of the vessel near the metal sample, passes over the sample, and then flows out of the reaction vessel through an outlet valve. After leaving the reaction vessel, the gas passes through an overflow trap followed by a silicon oil bubbler to prevent any contaminating gasses from entering the system. The gas then travels through a PVC tube to a fume hood, where it is vented to the atmosphere.

3.1.2 Reaction Vessel

The reaction vessel and its internal parts are shown in Figure 3. The reaction vessel is a 2-in outer diameter aluminum oxide tube, sealed with a stainless steel tube seal via rubber gasket. The tube seal, inlet gas line with the copper inlet coil, outlet gas line, stainless steel heat shields, and K-type thermocouple are all one unit that can be inserted and removed from the reaction vessel together. The interface of the inlet gas line, outlet gas line, and thermocouple with the tube seal, were all sealed using an epoxy designed for vacuum conditions. The samples are contained in an alumina crucible which is held in place within the reaction vessel by a stainless steel sample tray.

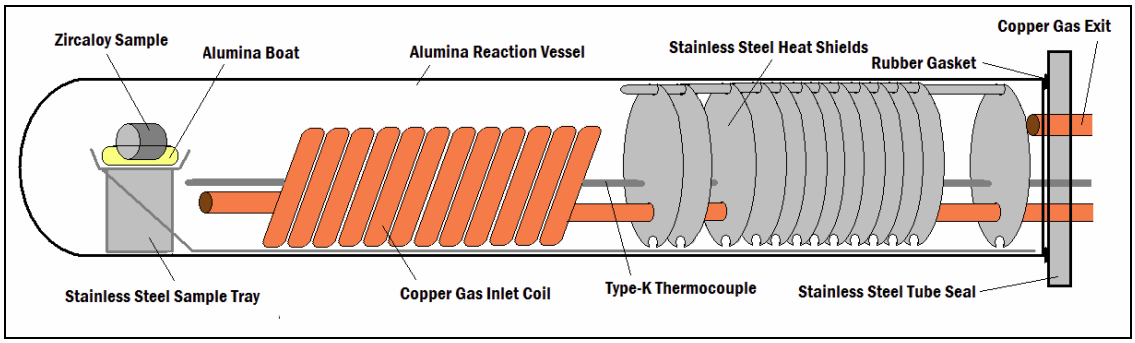

Figure 3. Schematic of reaction vessel. [3]

The gas enters the reaction vessel via the inlet tube, which then flows through a coil of copper tubing prior to being passed over the sample. This insures that the temperature of the process gas is at thermal equilibrium with the sample before the sample exposure to fresh hydrogen takes place.

3.1.3 Titanium Sponge Getter

The getter was added to the system after experiment 52 in order to remove contaminants, most notably nitrogen, oxygen, and water, from the gas source as well as contaminants introduced due to possible leaks in the system. The getter consists of a 1-5/8 inch outer diameter aluminum oxide tube with a 350 W furnace (Watlow model number VC401N06A) placed around it. The tube was filled with titanium sponge in such a way that the sponge is only in the heated region of the tube. It is important that the titanium sponge remain only in the heated region in order to avoid hydriding the titanium, which would reduce, or perhaps even eliminate, the hydrogen actually reaching the sample.

For this reason a titanium cage was created to contain the titanium sponge. The cage was created using three titanium rods to connect two custom-made perforated titanium plates. The rods were connected to the plates using titanium screws. The furnace around the getter is maintained to achieve an internal temperature of 1000°C to 1100°C. This prevented the titanium from reacting with the hydrogen, but allowed it to rapidly consume any oxygen, nitrogen, and water which might be in the system. It is essential that the getter remain at temperature with gas flow at all times, even when there is not a sample in the reaction vessel. This is because of the length of time it takes to heat up as well as the desire to maintain a pure getter system.

3.2 EXPERIMENTAL PROCEDURE

3.2.1 Sample Preparation and Loading

The first step in the experimental process is to prepare the samples. The samples began as nuclear grade Zircaloy-4 tubes 5-in long with an inner diameter of 0.515-in and an outer diameter of 0.580-in. The tubes were then sectioned into small cylinders of approximate length 0.6-in and approximate mass 3.5 grams, using a Leco diamond saw model number VC-50. The sectioned samples were then cleaned in ethanol in an ultrasonic cleaner.

A typical experiment begins by obtaining an accurate mass measurement of the sectioned Zircaloy-4 sample to within 0.0001 grams using a precision balance (Metler Toledo model number AB104-S) installed inside of an inert argon atmosphere glovebox. First, the sample is weighed along with the alumina crucible. Next, the sample is removed and the mass of the alumina crucible is obtained. Finally, the scale is zeroed with the alumina crucible on it, and the mass of the sample is measured directly. This method is used for two reasons. First, the separate masses of the sample and alumina crucible are compared to the mass of the masses of the two together. This is to insure that accurate masses are recorded. For quality control reasons the masses were not recorded unless they agreed to within 0.0003 grams. If they did not agree to 0.0003 grams, the mass measurements were repeated until this criterion was met. The other reason this weighing process was implemented is because the mass of the sample alone is needed in order to calculate the “percent hydride”, a term used to reflect the quantity of zirconium hydride formation after the experiment. The masses of the sample and the

alumina crucible together before and after the reaction are compared to compute the mass change (Δm). This Δm is then applied to the mass of the sample alone in order to determine the percent hydride (P_H) formed during the test by Equation 4.

$$P_H = \frac{\Delta m}{m_{Z-4}} \times \frac{M_{Z-4}}{M_H} \times \frac{1}{2} \times 100$$

P_H = Percent hydride
Δm = Mass difference before and after reactoin
$m_{Z\text{-}4}$ = Initial mass of sample
$M_{Z\text{-}4}$ = Effective atomic mass of Zircaloy - 4
M_H = Atomic mass of hydrogen [4]

The Zircaloy sample and alumina crucible are then placed on the stainless steel sample tray shown in Figure 3, and inserted into the reaction vessel. The stainless steel tube seal assembly with attached tubing, heat shields, and thermocouple is then carefully inserted into the aluminum oxide tube making sure that the sample remains upright during loading. The tube is then sealed by hand tightening three wing nuts and removed from the glovebox by way of the airlock.

3.2.2 Furnace Loading and Hydride Reaction

Once the sample has been weighed and loaded into the reaction vessel, it is then inserted into the furnace (Astro Industries model number A143S). The outlet tube is connected first, followed by the inlet line. When both the outlet and inlet lines are connected, the inlet valve is opened followed by the outlet valve. This seemingly tedious procedure is performed in order to avoid over-pressurization of the system, as well as to minimize any possible contaminates which may enter the system. Over-

pressurization was a concern because, as stated previously, the purge gas was never turned off once the titanium sponge getter was added.

The system is then brought to the approximate operating pressure and flow rate of 25-in of H_2O and 3 standard cubic feet per hour (SCFH) and the variable voltage transformer (Staco Energy transformer model number 3PN1510B) used to control the furnace is turned up to 80% (100% = 120VAC). The reason that the pressure and flow rate are brought to operational values during heating is because it was found that if they were not, the extra flow rate would have a cooling effect on the reaction vessel, causing temperature instability. The higher pressure also functions to minimize any gaseous impurities which may enter the system.

A calibration curve was produced using temperature data from the early experiments, which indicates when the transformer should be turned down from 80% to the desired operating value. This plot is shown as Figure 4. Once the temperature reaches the value determined from Figure 4, the transformer is turned down to the operating voltage. This was done in order to maximize temperature stability throughout the experiment. In order to maintain consistent temperature values from experiment to experiment, the transformer setting is set based on its output voltage in experiments including and after number 68 instead of visual inspection of the transformer dial as was performed in experiments prior to 68. The voltage settings were found by first visually setting the transformer to the desired setting and then recording the voltage. This insured that for any future experiments performed at this temperature, the transformer would be at a consistent voltage. This was done due to the difficulty in achieving

consistent transformer settings by visual means. It also allows for the possible use of a backup transformer which may not be calibrated exactly the same. This proved useful when the transformer used in this experiment failed and had to be replaced by an identical Staco Energy transformer with slight differences in calibration.

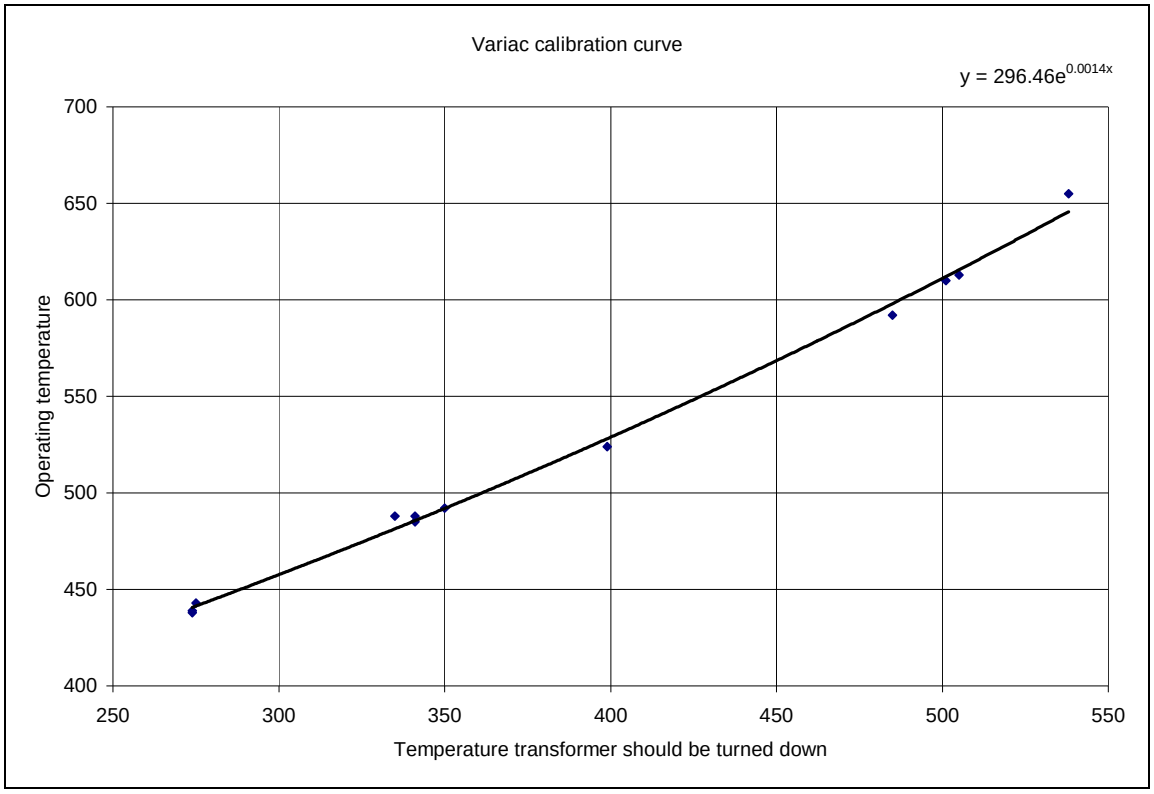

Figure 4. Plot showing when to set transformer to operating voltage.

Once the transformer is set to the desired setting, the temperature is allowed to come to a relatively steady state of +/- 0.2°C per minute. At this point the Ar-5%H_2 gas flow is started, the UHP argon flow is stopped, and the current time and temperature are noted. The flow rate is set to 3 SCFH and the pressure is set to 26.5-in H_2O. These

variables are set by adjusting the valve immediately after the regulator as well as the outlet valve of the reaction vessel. This gives control over both flow rate and pressure. The gage pressure of 26.5-in H_2O corresponds to a process pressure of 25-in H_2O because a 1.5" of H_2O pressure drop was measured across the titanium getter for a flow rate of 3 SCFH.

3.2.3 Process Shutdown and Furnace Unloading

After the desired reaction time has been accomplished, the furnace is shut down, Ar-5%H_2 gas flow is stopped, and UHP argon gas flow is started. It then becomes desirable to decrease the flow rate through the process vessel to conserve gas. The pressure is maintained at 26.5-in H_2O, but the flow rate is reduced to the point where ~4-5 bubbles per second are observed in the bubbler at the exhaust point. The pressure must remain high to minimize contaminants in the system, but at this point in the process the effect due to flow rate is minimal. The reaction chamber is then cooled until it reaches a temperature of no more than 40°C. The value of 40°C was chosen because it is below the temperature where any appreciable reactions with air should occur, and is at a point where the reaction vessel can be handled safely without a risk of being burned. The rate of cooling is approximated by Equation 5 and can last anywhere from 10 to 12 hours depending on the final process temperature. Where T is the system temperature, T_o is the temperature that the system was turned off, and t is the time after system shutdown in minutes.

$$T = T_o e^{-0.0038t} \qquad [5]$$

When the reaction chamber reaches an appropriately low temperature, the outlet valve is closed, followed by the inlet valve. The inlet tube is then disconnected followed by the outlet tube. Similar to the reasons stated above, the process is performed in this order to minimize contaminants as well as to avoid over-pressurizing the system.

3.2.4 Sample Analysis

The reaction vessel is removed from the furnace and placed into the glovebox, where it is opened and the sample is carefully removed. The alumina crucible which contains the sample is weighed on the scale and the combined mass is recorded. This combined mass is what is then compared to the pre-reaction mass in order to determine the percent hydride from Equation 4.

CHAPTER 4

RESULTS

As cited in Section 2.2, the basic setup for this hydride formation study experiment was established by D.T. Kraemer [3], who performed fourteen proof-of-concept experiments using the original system configuration at Purdue University. The original experiments did not lay out a systematic test matrix to evaluate hydride formation, but rather they scoped out the behavioral boundaries for several process variables. The work reported here picks up where that work ended and another eighty seven experiments have been carried out. Appendix A provides a detailed summary table for all 101 experiments. Experiments 15 to 19 (Section 4.1) established the impact of pressure and sample orientation on hydride formation in Zircaloy-4. Experiments 20 to 24 (Section 4.2.1) studied the temperature dependence of hydride formation. Experiments 26 to 29 (Section 4.2.2) attempted to show the effect of the physical integrity of zirconium hydride near the alpha-beta eutectoid temperature. Experiments 30 to 57 (Section 4.2.3) focused on determining the source of nitrogen contamination, and to demonstrate that the nitrogen contamination had been minimized. Experiments 32, 45, and 96 (Section 4.2.3) were control experiments performed in an effort to quantify the amount of contamination in the system. Experiments 58 to 101 (Section 4.3) were performed to study the temperature and time dependence on the rate of hydrogen pickup in Zircaloy-4 tubes. The results for each of these tests are reviewed in the following sections.

(Experiments 15 to 47 were performed at Purdue University when the author was enrolled as a dual-status graduate-undergraduate student. The author and his advisor moved this project to Texas A&M University where the system was rebuilt and experiments 47 to 101 were performed.)

4.1 EFFECTS OF SYSTEM PRESSURE ON THE HYDRIDE OF ZIRCALOY-4

The process gas pressure in Kraemer's experiments (samples 1 to 14) ranged from 4.5 to 28-in H_2O. In an effort to eliminate pressure as a process variable, experiments 15 to 19 were performed to determine what effect, if any, the cover gas pressure might have on the zirconium hydride formation reaction. It is known that near atmospheric pressure the solubility of hydrogen in zirconium is nearly independent of pressure for the temperatures of interest, and can be seen in Figure 5. [7] However, very few of the experiments performed for this thesis were allowed to go to completion. While the theoretical hydrogen content may be independent of pressure, the reaction rate may still be pressure dependent.

This was found to be the case and data supporting this conclusion are tabulated in Table 2 and illustrated in Figure 6. Experiment 16 was excluded from this plot because it was dropped on the glovebox floor prior to weighing, so the P_H measurement was not reliable. The experiments were performed at 10.5 and 25-in H_2O and held at ~520ºC for ~6 hours. The results clearly revealed that the rate of hydride formation was more rapid for higher cover gas pressures. Due to the strong direct correlation between pressure and the hydride formation rate, it was decided to standardize the system pressure to 25-in H_2O for all remaining experiments. The higher pressure was chosen for all experiments

after Exp. 19 for the simple fact that the reaction rates will be higher, thus decreasing the amount of time required for each experiment.

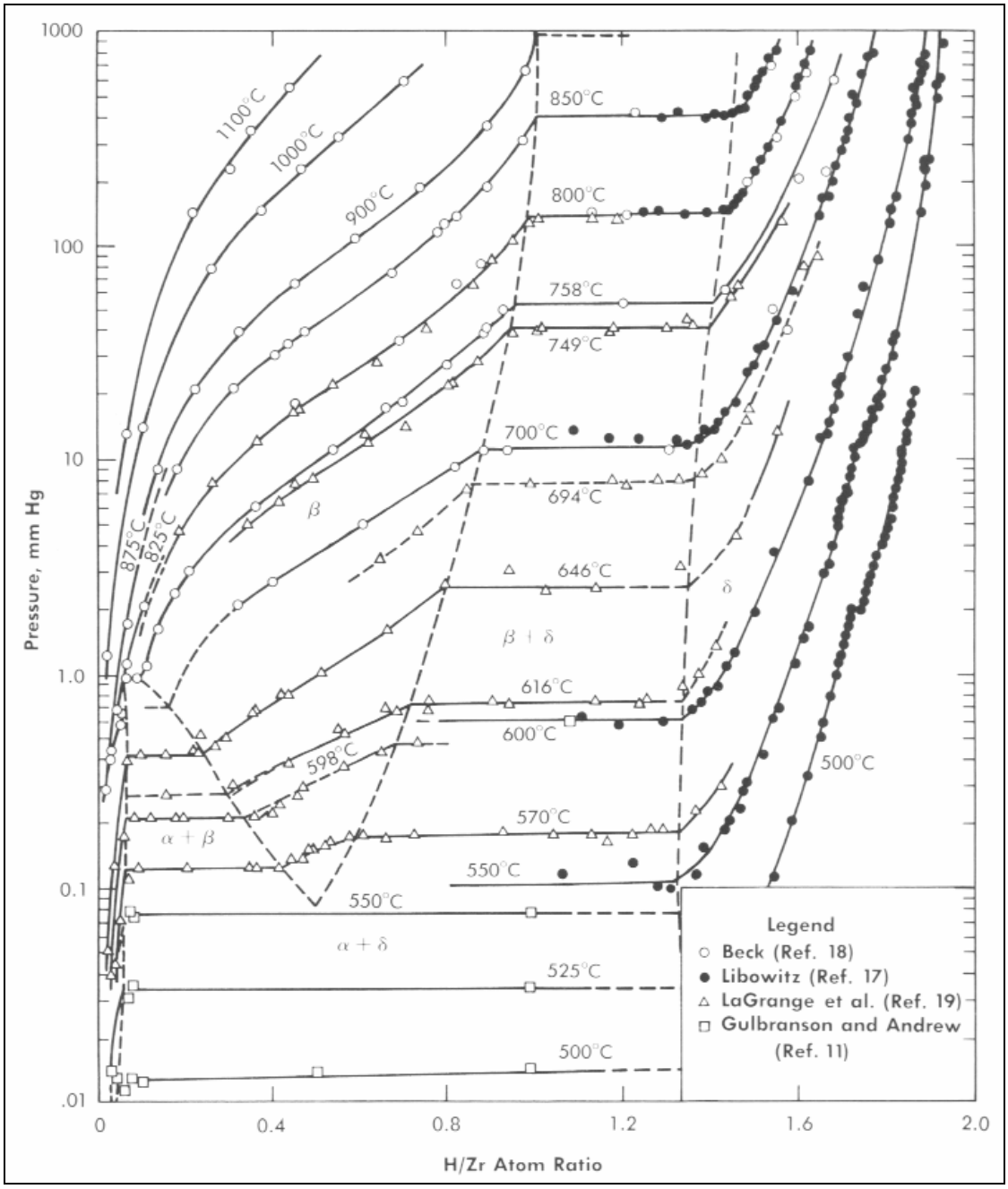

Figure 5. Hydrogen pickup as a function of temperature and pressure. [11]

In addition to the pressure differences, the sample orientation was briefly studied. In other words, the orientation of the Zircaloy tube was varied from horizontal (i.e., on its side) to vertical (i.e., upright). The reasoning for the variation was suggested by the results from Kraemer's tests that showed an asymmetric distribution of hydride formation in the horizontal orientation; that is, the top wall of the tube hydrides more rapidly than the bottom. The results from experiments 15 to 19 are also highlighted in Figure 6. While the results seem to indicate a slightly higher hydrogen pickup for the upright orientation, this brief study was not sufficient to come to any conclusion based on sample orientation. Even so, every sample after experiment 19 was loaded into the process vessel in an upright position.

Table 2. Tabulated results of orientation/pressure study.

Exp.	Orientation	Pressure in-H_2O	P_H
15	upright	10.5	18
16	side	10.5	11
17	upright	24.75	92
18	side	24.75	65
19	side	10.5	11

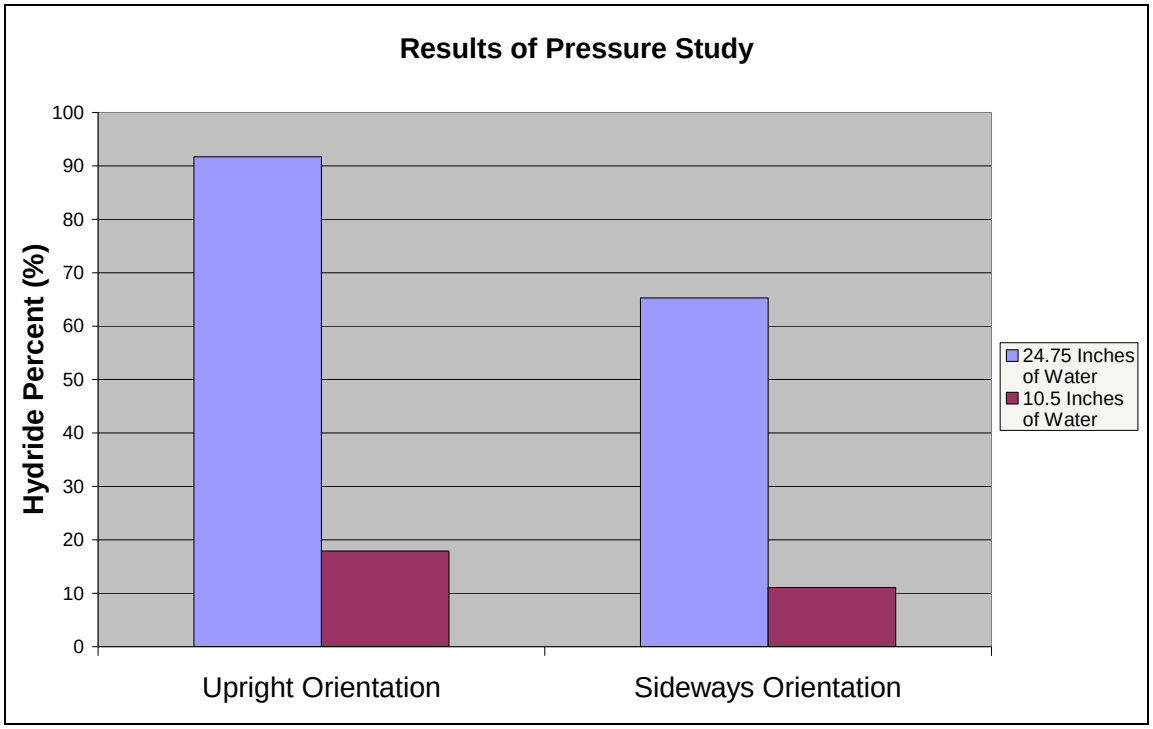

Figure 6. Plot indicating effect of pressure on hydride rate.

Prior to experiment 53 (before the getter system was added) the system pressure would remain very nearly constant during experimental runs with very little fluctuation. However, during and after experiment 53 the pressure would fluctuate. The observed fluctuation was manifested as a slow increase in pressure corresponding to when the gas flowing through the system was switched from argon to the Ar-5%H_2 mixture as discussed in section 3.2.2. This seems to imply that there is some sort of flow restriction being created when the Ar-5%H_2 gas mixture enters the getter. It is hypothesized that the flow restriction might be caused by hydride formation in the titanium sponge, but this was never verified because it was outside of the scope of this project.

This issue was handled by manually adjusting the pressure as needed in order to maintain a pressure of 25-in H_2O. It is recommended that if this experiment is to be repeated, a precise low pressure regulator be installed in the system. This would make the process much less labor intensive, but more importantly, increase the reliability of the data. The process of manually adjusting the pressure caused variations of +/- 3-in H_2O or +/- 0.1% absolute pressure.

4.2 DISCOVERY AND REMOVAL OF PROCESS GAS CONTAMINATION

4.2.1 Dependence of Hydride Formation on Temperature

Experiments 20 to 24 were designed to gain preliminary understanding on hydride formation as a function of temperature. Each sample was hydrided for six hours with the exception of experiment 24 which was hydrided for 7 hours, and the temperatures varied from 353°C to 747°C. The results from these tests are summarized in Table 3 and are plotted in Figure 7.

Table 3. Tabulated results of temperature study at six hours.

Exp.	°C	P_H
20	353	6
21	451	6
22	541	5
23	647	15
24	747	48

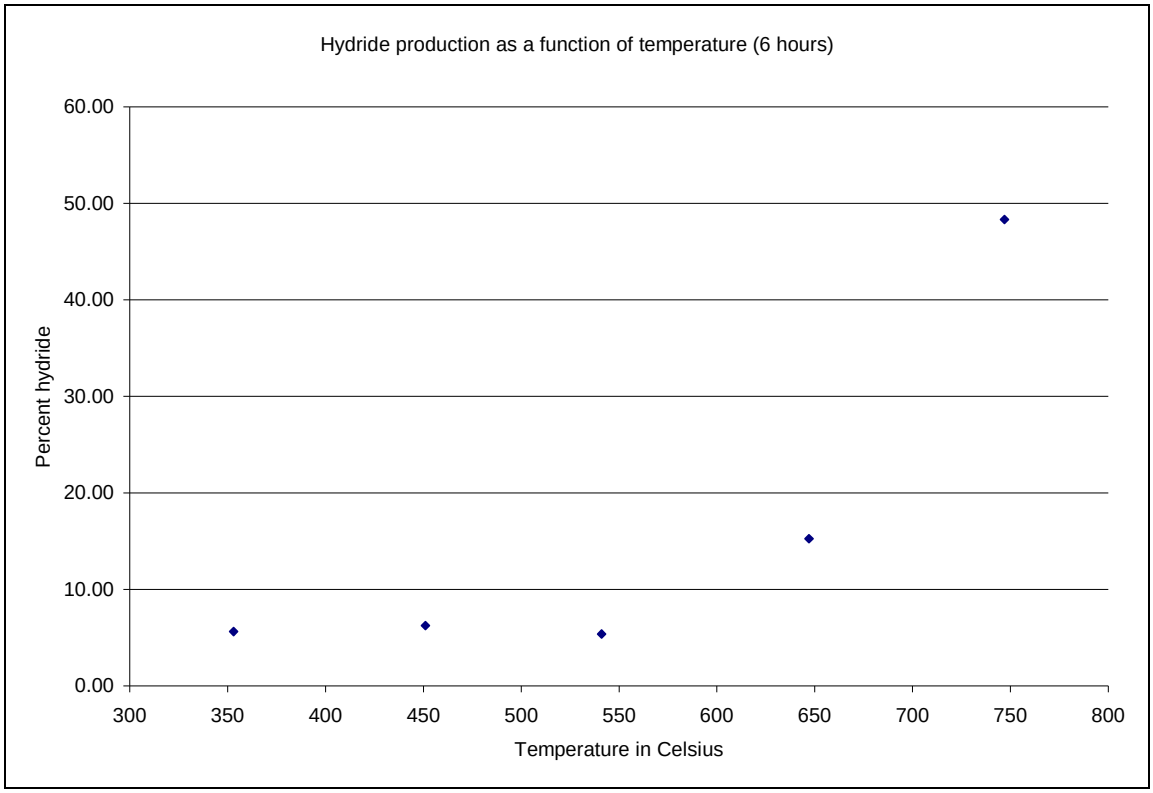

Figure 7. Results from 6 hour temperature study.

The above data was initially puzzling because of the inconsistent results, especially when compared to later experiments. Experiments 20 to 22 showed abnormally low hydride percentages that were within the same range as the control experiments (discussed in section 4.2.3). However the most important discovery from this data came from experiment 24. The sample was removed from the process vessel and was observed to have a significant gold color. Pictures of experiment 24 are show in Figure 8. There is very good reason to believe that this gold color was due to reaction with nitrogen impurities in the cover gas, thus creating zirconium nitride. It is known that the rate at which nitrogen is absorbed in zirconium greatly increases at temperatures

above 700°C. [7] This would explain why experiment 24 showed a strong indication (i.e., gold discoloration) of the presence of zirconium nitride while the samples from experiments 20 to 23 did not. Based on this hypothesis it was determined that the system gas supply was not as pristine as once thought. Due to the probability of nitrogen contamination in the system, these experiments are not included in the final rate study.

Figure 8. Golden color of experiment 24 indicating nitride contamination.

4.2.2 Hydride Formation at Temperatures near α-β-δ Eutectoid Temperature

The next five experiments (nos. 26 to 29) were designed to study the effects of hydride formation at temperatures near the α-β-δ eutectoid temperature. These experiments were all performed for six hours. It was postulated that if the temperature was held near the α-β-δ eutectoid temperature, the material would more easily turn to powder due to the phase change between the alpha and beta phases. While the concept of phase changes within the material turning it to powder remains just as true, the results

from experiments 26 to 29 were wildly inconsistent, in part because of the system contamination noted in the previous section. The data from these experiments is shown in Table 4.

Table 4. Results of study for temperatures near α-β-δ eutectoid temperature at six hours.

Exp.	°C	P_H
26	547	85
27	543	59
28	543	44
29	542	24

These experiments showed that the system was not at a point where reproducible data could be obtained. This is apparent due to the fact that these four experiments varied in temperature by only 5°C, yet varied in hydride percent by up to 60%. This gave a clear indication that either the experimental setup or the experimental process needed to be changed.

4.2.3 Discovery of Sources of Nitrogen Contamination and Their Removal

The data from experiments 26 to 29 made it clear that more work needed to be done to increase the reliability of the data produced by the system. Experiments 30 to 52 represent a sequence of troubleshooting experiments designed to discover the cause of the inconsistencies in the data due to nitrogen contamination. One interesting result from these experiments came in experiment 31. This experiment showed a mass gain which corresponded to a theoretical percent hydride of $P_H = 107.4\%$. This result could indicate that the sample contained pure ZrH_2 with excess hydrogen in solution, but that

is unlikely. The more likely scenario however is that this data represents a false hydrogen pickup and that contaminating elements such as nitrogen, oxygen, and water are responsible for such a high apparent hydride. The reason that this appeared to be the more likely scenario is because nitrogen contamination was suspected based on the results described above and because the P_H is determined by a change in mass. For each contaminating atom of oxygen or nitrogen, a false hydrogen pickup of 16 or 14 atoms respectively is observed. This illustrates that it is absolutely necessary to eliminate any contamination from the system.

Experiments 32, 45, and 96 were control experiments intended to give a quantitative measure of contamination within the system. The control experiments were performed in exactly the same manner as the hydride experiments, with the exception that a flow of Ar-5%H_2 gas is never passed over the samples. A summary of these experiments is given in Table 5. The results from experiments 32 and 45 show a high false hydrogen pickup due to contamination. Experiment 96 is shown here for comparison, but it was run after the contamination was eliminated from the process gas, as described later in this section. A fundamental flaw in performing control experiments for this particular setup is that during the hydride formation, the samples crumble and a high surface area is created. This greatly increased surface area increases the rate of hydrogen pickup, but it also should increase the pickup of any impurities which may be in the system. The control experiments lack this increase in surface area, so any indicated false hydrogen pickup is not conservative, but instead should under predict the

actual level of contamination. This is the reason that control experiments did not play a larger role in this project.

Table 5. Tabulated results for control experiments.

Exp.	°C	Time in hours	P_H
32	519	26	4
45	567	21	6
96	440	4	0

As stated previously experiments 30 to 36 were performed to determine the reason that the hydride results were inconsistent. During these experiments the purity of the Ar-5%H_2 gas supply was called into question but it was not until after experiment 36 that the true cause of contamination was discovered. After experiment 36 it was discovered that the one psi relief valve installed in the system was leaking. This valve is designed to allow gas flow in one direction and only when the pressure of the system exceeds one psi. It was found that this valve was allowing a small amount of gas through even when the pressure was under one psi. This indicated that the valve was faulty and pointed to the very real possibility that if the valve let gas out at pressures less than one psi, it was also allowing air into the system. This explained the appearance of gold nitride in the samples, and hence a major cause of inconsistencies within the experimental results. This one psi valve was replaced with a functioning five psi relief valve.

Because the relief valve had been replaces and was known to be one of the sources of nitrogen contamination, experiments 37 to 57 were performed in an effort to

acquire valid reproducible data. However, the data from experiments 37 to 39 were questionable to various degrees and for various reasons. Experiment 37 showed an abnormally low hydrogen pickup, experiment 38 had an anomalous temperature instability such that the temperature was allowed to cross the alpha-beta eutectoid temperature in a poorly controlled manner, and Ar-5%H_2 gas flow stopped an hour prior to the completion of experiment 39. The errors in experiments 37 to 39 were due to operator error instead of error caused by nitrogen contamination.

Therefore, the data from experiments 40 to 57 represent the first step toward a systematic study of the hydride formation process and the results were generally very good. They displayed very high values of P_H and more importantly were consistent with expected results as shown in Table 6. The data shows that times on the order of 6 to 24 hours are not necessary for the samples used in this study, and in fact are not even desirable. This is because high P_H values (approaching 90 to 100%) were routinely produced beyond six hours.

While these experiments showed predictability in the data, there was still some visual observation of slight nitrogen contamination. Perhaps the most peculiar result from experiments 40 to 57 was the appearance of experiment 46 (Fig. 9). When the specimen was removed from the reaction vessel, it was found to be completely deteriorated into shards and small pieces and it had a brown coloration. This deterioration and discoloration gave the sample an appearance similar to dried tobacco. The result of experiment 46 which was performed at 310 ºC for 24 hours, is shown in Figure 9 and can be compared to a picture of experiment 47 which was performed for 24

hours as well at 432ºC in Figure 10. It is possible that the appearance of experiment 46 is the result of the low temperature, but this was never reproduced. While experiment 46 was brown in color, it did not have the same luster as the experiments which showed a clear indication of nitrogen contamination. The brown color was also considerably different from the gold color indicative of zirconium nitride which gives the impression that this may not be a nitrogen contaminated specimen. This conclusion is supported by the fact that the zirconium-nitrogen reaction is very slow at 310 ºC.

All experiments up to experiment 47 were performed at Purdue University. After this the entire experimental apparatus was relocated to Texas A&M University where experiments were continued. The entire system was broken down, cleaned with alcohol, resealed, and then rebuilt (with some improvements) after its relocation.

Table 6. Results for experiments 40-57.

Exp.	°C	Time in hours	P_H
40	582	24	90
41	556	24	97
42	570	6	84
43	570	18	97
44	563	12	91
45	567	21	6
46	310	24	57
47	432	24	86
48	572	6	72
49	566	6	78
50	566	6	53
51	565	6	17
52	571	6	21
53	574	6	90
54	575	6	92
55	567	4	35
56	576	4	72
57	579	4	46

*Exp. 45 was a control experiment

Figure 9. Experiment 46 showing tobacco-like appearance.

Figure 10. Experiment 47 for comparison with experiment 46.

While experiments 40 to 50 seemed to show reliable results, there was still a slight visual indication of nitrogen contamination. For this reason, UHP argon was used as the purge gas for all experiments after experiment 51 and it was decided that the system would further benefit from the addition of a nitrogen getter. This titanium sponge getter as described in section 3.1.3 was put into place after experiment 52. The purpose of adding a getter to the system was to remove impurities from the process gas. It was eventually determined (after experiment 57) that the system performs better if the getter were relocated to a position in the gas flow path which was immediately before the reaction vessel. This would guarantee that any contaminates which may leak into the system through the various seals and instruments are removed prior to entering the reaction vessel. All seals and connection fittings were either wrapped in Teflon tape or sealed with Room Temperature Vulcanizing (RTV) silicon. The combination of using UHP argon, installation of the nitrogen getter, and improving the seals, completely eliminated any observable trace of nitrogen or oxygen contamination. It can be concluded from these results that the hydride reaction is strongly affected by nitrogen, oxygen, and water contamination which may be in the system.

4.3 X-Ray Diffraction Analysis

An X-Ray Diffraction (XRD) analysis was performed on samples 31, 40, 43, and 46, as shown in Figures 11, 12, 13, and 14 respectively. The analysis of sample number 31 agrees very well to epsilon phase zirconium hydride meaning that it is very probable that the actual composition is at least 85% zirconium hydride with the remaining weight gain caused by impurities. This is the sample which had a calculated P_H value of

107.4%. In the figures below, there is often a slight shift in the higher angle spectral peaks, which is typically accompanied with irregular sample preparation and "out-of-plane" powder loading. These shifts were acceptable in this study since there was no need to optimize the powder loading for analytical results; sample identification is all that was sought.

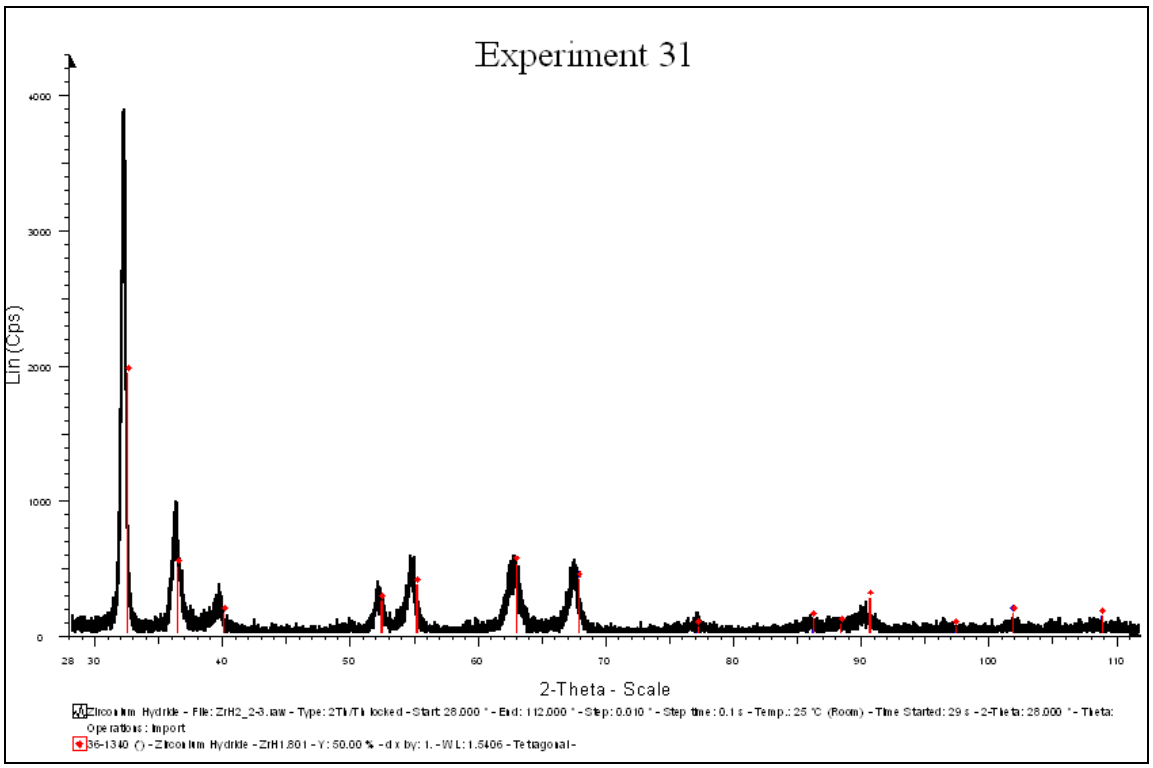

Figure 11. XRD analysis of experiment 31 showing clear indication of epsilon phase zirconium hydride.

The XRD peaks for experiment 40 also showed a clear indication of the presence of zirconium hydride (Figure 12). The spectrum produced was very clean but showed

some small peaks which were unaccounted for. These peaks could be due to the presence of tin or tin compounds because Zircaloy-4 is composed of 1.2-1.7% tin as shown in Table 1. Another possible cause might be from nitride formation within the material. They could also be caused by the presence of various phases of zirconium hydride coupled with the somewhat low confidence level of the XRD software's fitting program due to its limited data set. This is the more likely scenario because it is difficult to produce visible results for species with low concentrations such as tin in Zircaloy-4 using XRD.

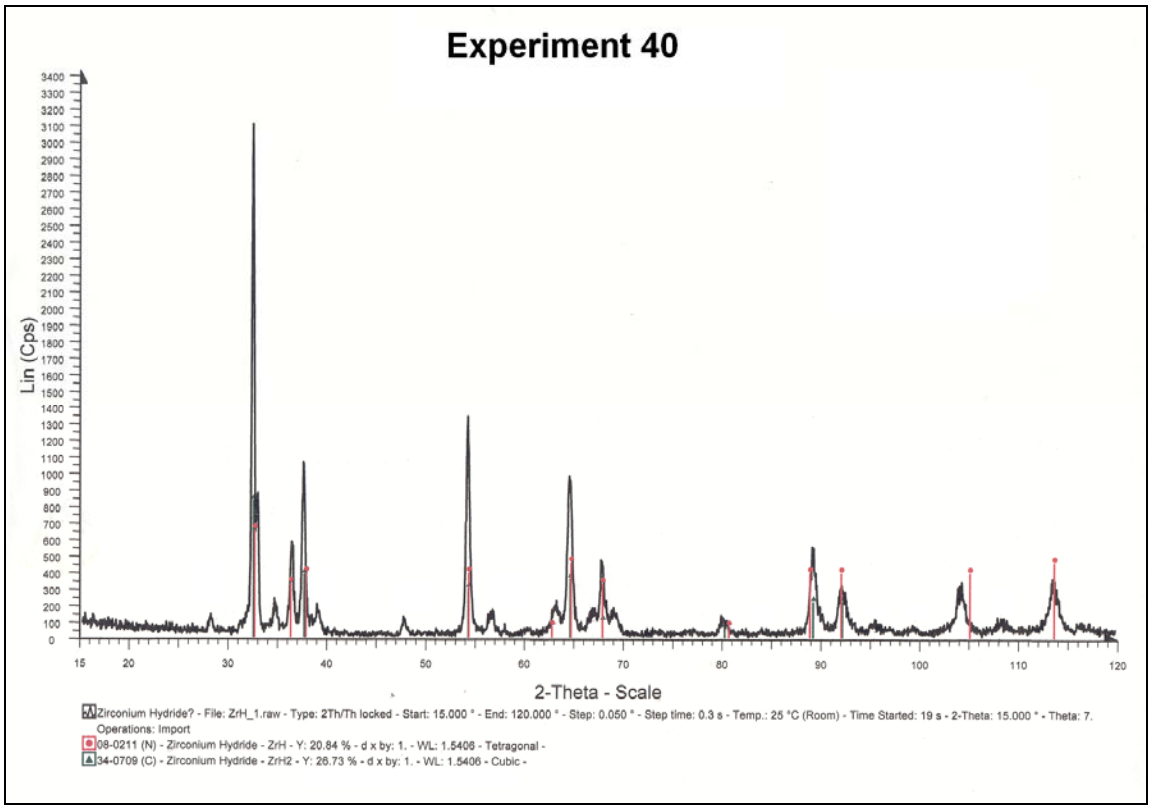

Figure 12. XRD analysis of experiment 40 showing indication of zirconium hydride.

The plot for experiment 43 showed results that indicated the presence of zirconium hydride, but was very noisy as shown in Figure 13. The major peaks corresponded to the presence of zirconium hydride but it was very difficult to get any usable results from any smaller peaks. The reason that the spectrum was so noisy is because of the low number of counts collected by the XRD machine. These low counts were not enough to clearly distinguish some of the smaller peaks from the background.

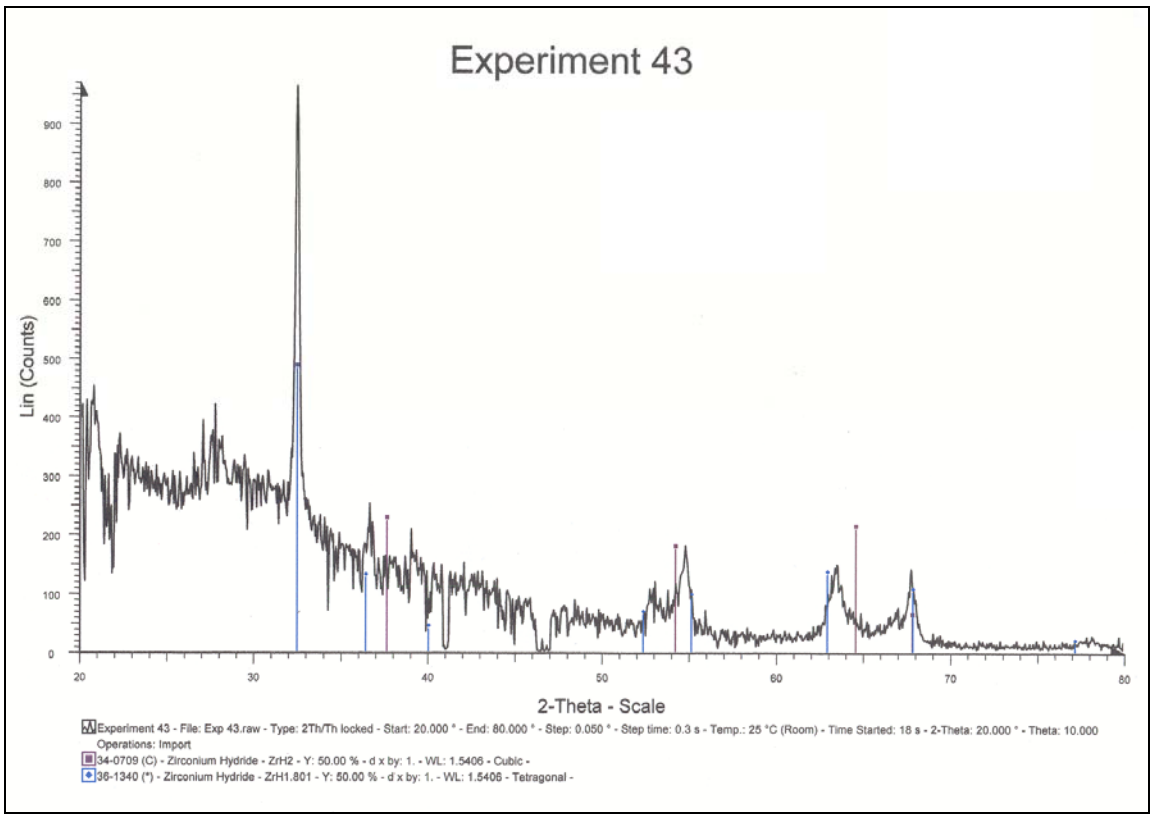

Figure 13. XRD analysis of experiment 43 showing indication of zirconium hydride.

The spectrum shown in Figure 14 shows the results of the XRD analysis of experiment 46. This spectrum indicates the presence of zirconium hydride. As with the

previous patterns it is difficult to determine anything else about the composition of the samples simply because it is difficult to see the presence of species which have low concentrations in the sample using XRD.

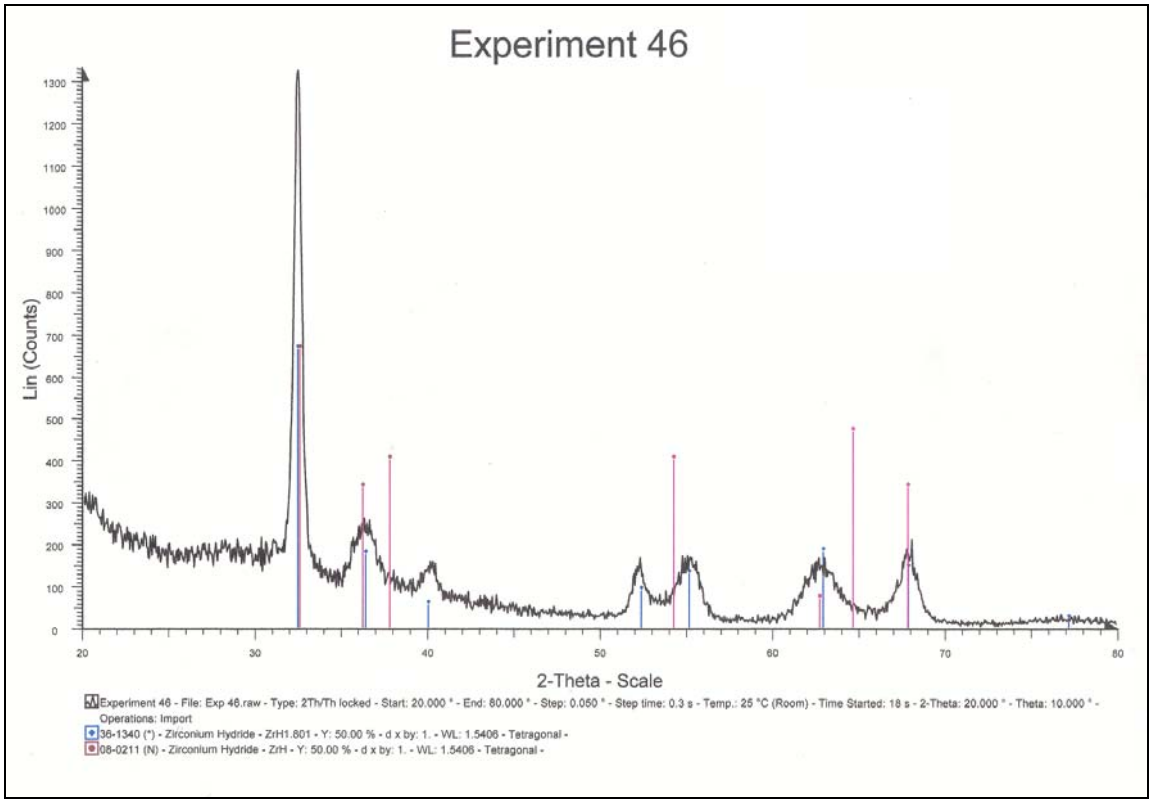

Figure 14. XRD analysis of experiment 46 showing indication of zirconium hydride.

It was determined from the XRD analyses that zirconium hydride was in fact being produced. It was also observed, as expected, that XRD is not necessarily a useful tool for determining the presence of any other chemical species. For this reason, XRD analysis was no longer performed after experiment 46.

4.3 RATE STUDY ON THE FORMATION OF ZIRCONIUM HYDRIDE AS A FUNCTION OF TIME AND TEMPERATURE

The results obtained from experiments 15 to 57 gave an indication as to how the system needed to be changed in order to achieve reproducible data. The most notable of these results was the elimination of contaminating gasses such as nitrogen from the process gas. At this point, it finally became possible to acquire the desired data to evaluate the time and temperature dependence of hydride formation in Zircaloy-4.

This rate study was performed using three times (1, 2, and 4 hours) and six temperatures (440, 480, 520, 560, 600, and 640ºC). The three times were chosen largely based on the results from experiments 40 to 57, which showed that hydride times beyond six hours would produce P_H levels above 90%. Therefore, these short time periods were chosen so that a broad range of P_H data would be obtained to quantify the formation process as it progresses instead of only at high P_H levels. The six temperatures were chosen such that three of them were above the α-β-δ eutectoid temperature (540ºC) and three were below this point.

Duplicate experiments from this text matrix (plus a few repeat experiments) were completed with experiments 58 to 101, with experiment 96 being a control sample. Table 7 shows a summary of the data from these tests and the results are presented graphically in Figure 15. Duplicate experiments were performed to show systematic reproducibility and to better approximate the true behavior. In theory, multiple experiments (five or more) at each time-temperature combination would improve the

data statistics, but the selection of two experiments each was reasonable to show reproducibility and to assure the timely completion of the project.

As expected, the rate of hydride formation varies strongly with temperature in the first four hours of the process. The only exceptions to this observation can be seen in the four hour tests. These four hour experiments displayed a slight decrease in hydrogen pickup for temperatures of 600 and 640ºC. This is presumed to be caused by the samples reaching their maximum hydrogen content and this actually indicates a leveling off of the hydrogen pickup. This would also indicate that Zircaloy-4 rapidly reaches its maximum hydrogen content at temperatures around 450ºC.

It was expected that the hydride formation data would behave differently when the sample was held above and below the α-β-δ eutectoid temperature and this was indeed the case. It was observed that samples which were hydrided at temperatures below 540ºC became highly embrittled and were often reduced to shards after the hydride reaction. At temperatures above 540ºC, the samples were often entirely intact after the experiment, even though the P_H values were high. All experiments produced an embrittled sample which could be ground to a powder. The difference is that for temperatures below the eutectoid line, the sample had already begun disassembling itself and was dramatically easier to grind into a very fine powder. Experiments performed at temperatures above the eutectoid line, for the most part remained intact upon the completion of the hydride reaction and the samples required much more effort to grind into a powder.

Table 7. Experimental results from rate study.

Exp.	ºC	Time in hours	P_H
58	568	4	94
59	568	4	95
60	519	4	92
61	520	4	93
62	481	4	78
63	485	4	80
64	481	4	94
65	569	1	43
66	579	1	21
67	600	1	30
68	479	4	78
69	435	4	79
70	436	1	1
71	522	1	8
72	440	4	42
73	526	2	26
74	422	1	12
75	441	1	2
76	436	2	1
77	530	2	33
78	611	4	88
79	616	1	36
80	614	4	83
81	576	2	49
82	654	4	86
83	648	4	87
84	578	2	49
85	665	2	87
86	643	2	71
87	613	2	72
88	615	2	57
89	537	1	7
90	635	1	34
91	487	1	4
92	636	1	31
93	477	2	62
94	475	2	64
95	482	1	14
96	440	4	0

97	429	2	14
98	558	1	31
99	483	2	25
100	427	2	31
101	474	2	15

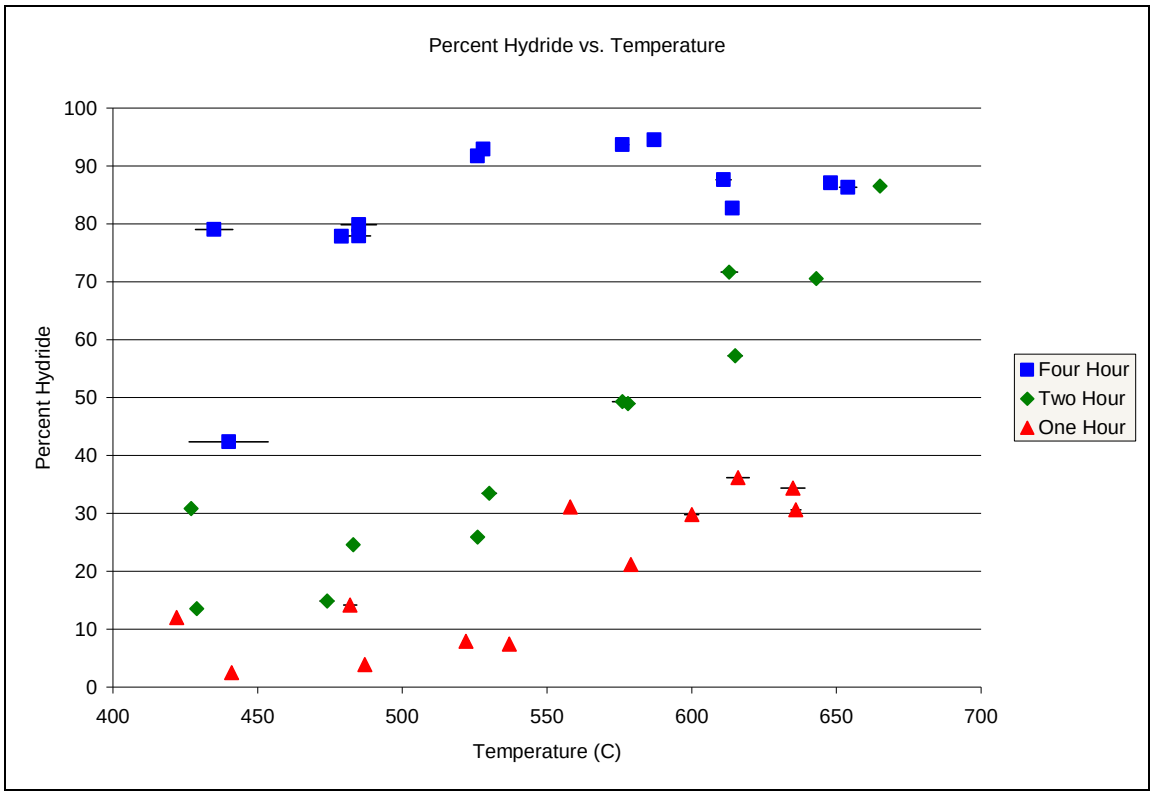

Figure 15. Formation of zirconium hydride as a function of temperature.

The results of this rate study were consistent with the expected behavior of hydrogen formation in Zircaloy-4. It can be seen from Figure 15 that the data displays a general trend of increasing P_H with increasing temperature, which is expected from a

thermally-activated process. It can also be seen that P_H is greater for longer reaction times, as would be expected

CHAPTER 5

DISCUSSION OF EXPERIMENTAL RESULTS

In the previous chapter, results were presented for 87 experiments completed to evaluate hydride formation in Zircaloy-4 tubes; the final 44 of these experiments were completed to quantify the rate of hydride formation. This rate study was intended to be composed of 36 data points, but 7 experiments were repeated for various reasons. These reasons included pressure fluctuations, improper analysis, and obvious disagreement with expected trends.

5.1 EXPERIMENTAL OBSERVATIONS

The experiments performed prior to the rate study (Nos. 15 to 57) were focused on establishing methods and procedures to generate reliable data. These tests were plagued by nitrogen contamination which was eventually minimized by replacing a leaking relief valve, creating better seals on the gas supply, and most importantly, installing a nitrogen getter. Contamination from nitrogen (in air) is believed to cause an under prediction in the achievable P_H for a given time and temperature. While nitrogen causes a false indicated hydrogen pickup of 14 times the measured value by mass, it is also likely that nitrogen absorbed on the surface of the specimen greatly decreases the diffusion rate of hydrogen within the cladding. This effect is believed to be so limiting that it negates the over prediction caused by the difference in atomic masses resulting in an under prediction of P_H. This diffusion limiting characteristic is due to the fact that nitrogen occupies the octahedral positions, putting strain on the crystal lattice. [7] This

has the effect of limiting the diffusion of hydrogen because the lattice strain makes it energetically unfavorable for hydrogen atoms to occupy the tetrahedral sites in the immediate vicinity of any dissolved nitrogen atoms.

This effect should, at least in theory, hold true for oxygen contamination as well for the same reasons stated above. This was observable in the rate study tests because it was found to be difficult to acquire reproducibility for low temperatures and short hydride times. The data generated from the one hour tests generally had more scatter than the data from longer experiments. It is reasonable and consistent to speculate that this is related to the zirconium oxide surface layer present on all samples. This effect should be of concern if this process is to be used on an industrial scale, especially when considering spent fuel cladding. Spent fuel cladding is of special concern because it contains a thick outer oxide layer as well as an inner crud layer both of which were nonexistent for these experiments. These two features may be the Achilles heel of this process if it is to be used on an industrial scale for spent fuel cladding. A possible fix to this issue could be to remove as much of the crud layer as possible. The oxide layer can then be dissolved into the zirconium lattice by heat treatment at near 1100°C. This has been shown to greatly increase the hydride rate, especially for the initial stages of the hydride reaction. [7]

It was found that if this material is to be pulverized, it is much more desirable to produce zirconium hydride in the presence of alpha phase zirconium as opposed to beta phase zirconium. The α-Zr phase was seen to be dramatically more brittle after hydriding than the β-Zr phase, often disassembling itself into course, jagged particles

during the reaction process. This is believed to be because the α-Zr solubility for hydrogen is far lower than that of β-Zr, resulting in the earlier formation of significant quantities of the brittle δ-$ZrH_{1.6}$ phase. This transformation induces volumetric strains due to density changes associated with δ phase formation and the δ phase is fairly brittle. It can be seen from the phase diagram (Fig. 1) that at temperatures below the α-β-δ eutectoid temperature, the δ phase begins precipitating with very low hydrogen pickup. This is in contrast to temperatures above the eutectoid temperature in which delta phase does not begin to form until a P_H of 28% has been achieved. Another advantage to hydriding α-Zr is that the process may be completed at lower temperatures, which is important because nitrogen pickup is strongly temperature dependent and greatly increases at temperatures above 700°C. [7] A downside to the alpha phase pathway is that the hydrogen pickup rate is directly dependent on temperature. This means that it will take longer to produce materials with high hydrogen concentrations when operating in the alpha phase. However, for the sake of pulverization, this lower hydrogen pickup rate was seen to be insignificant. In fact, since hydriding α-Zr forms δ-$ZrH_{1.6}$ earlier in the process than when hydriding β-Zr, the low temperature process is more amenable to acceleration by *in situ* mechanical milling than the higher temperature scenario. It may therefore be possible to completely negate the rate limitations caused by low processing temperatures.

5.2 HYDRIDE FORMATION RATE

Because it was observed that the reaction pathway of the hydride formation reaction has a strong impact on the brittleness of the material, it is desirable to develop a

set of equations to predict hydrogen formation, and thus phase morphology, at any given time. The data obtained in the rate study allows for the creation of a correlation which describes the time dependent behavior of hydride formation as a function of temperature. To this end, three possible formulations were explored. The first is the Avrami equation which is commonly applied to phase formation in metastable supersaturated solid solutions. The second was a parabolic rate law, which would be consistent with a diffusion-controlled process. The third was a simple linear fit of the data. There is no data-driven reason to select one of these fits over another, but the efficacy and applicability of each is discussed below.

A correlation was first formulated using the Avrami equation which is given by:

$$P_H = 1 - K * \exp(-t^n) \quad [6]$$

The hydride formation data from the rate study in Chapter 4 is plotted verses time in Figure 16 and the functional fit based on the Avrami form is also shown. The development of this correlation was accomplished by linearizing the Avrami equation such that it takes the form below.

$$\ln[-\ln(1 - P_H)] = \ln(K) + n \times \ln(t) \quad [7]$$

Where P_H is the time dependent fraction of completion of the hydride reaction, t is time, and both K and n are constants to be determined. The data was plotted using Equation 7, and a linear fit was created for each temperature series performed in the rate study. From these linear fits, the constants K and n in the Avrami equation were determined at each temperature, as summarized in Table 8 and Appendix B.

Table 8. Results of rate study using Avrami equation.

°C	K	n
440	0.047	2.077
480	0.104	2.099
520	0.073	2.506
560	0.334	1.437
600	0.424	1.126
640	0.471	1.181

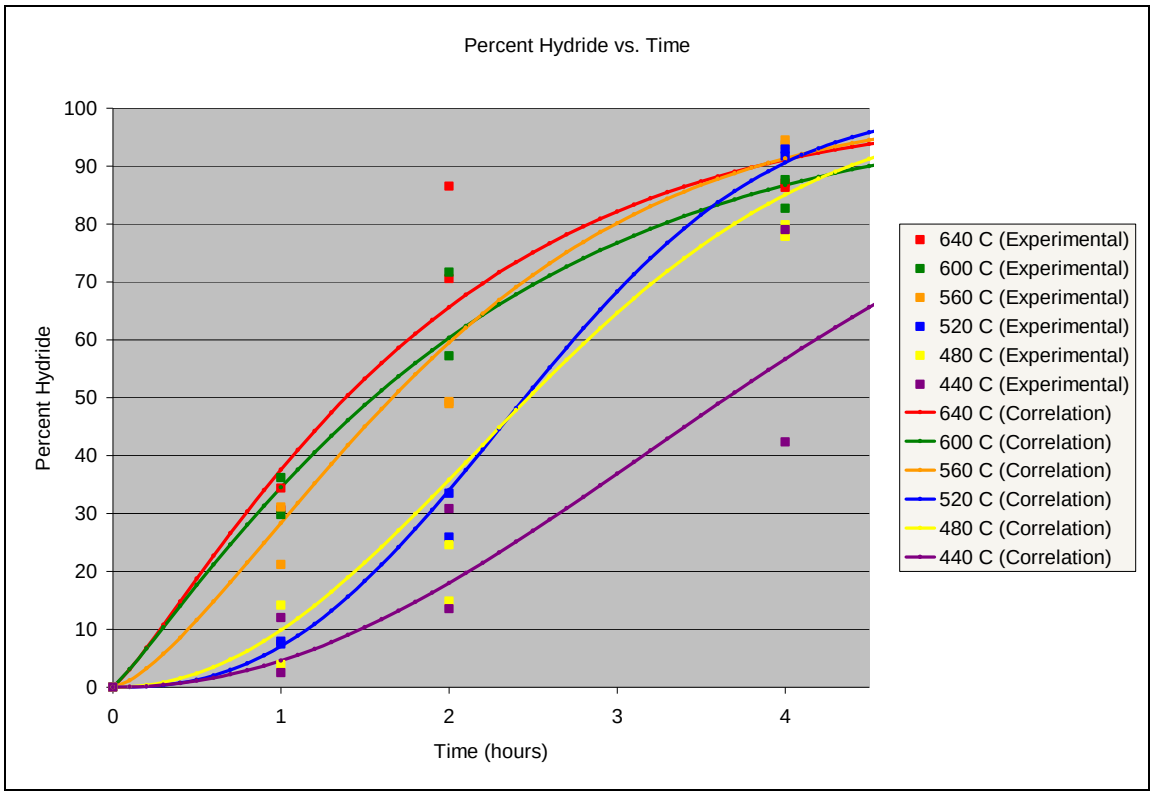

Figure 16. Time dependence of hydrogen pickup with Avrami correlation.

The fit from the Avrami equation is not satisfactory. This equation applies to chemical reactions and phase changes, which both apply to this series of experiments. However, it is also true that the equation is applicable for metastable phase transitions.

The experimental scenario provides hydrogen to the samples and it is expected that the hydrogen formation reaction proceeds at a rapid rate. Therefore, the hydride formation rate is limited by the transport of hydrogen from the process gas into the zirconium material and the Avrami supersaturation condition is never achieved. This correlation was therefore rejected but the above discussion is included here for completeness.

Because the hydride reaction is transport controlled, a parabolic formulation consistent with hydrogen diffusion in zirconium was considered next. [6] The parabolic correlation has the form given by Equation 1, shown below:

$$P_H = At^m \qquad [1]$$

Where P_H is the degree of completion of the reaction in percent ZrH_2, t is the time in hours, and A and m are constants to be determined. The data was plotted as a function of time for each temperature of interest and these constants were found by linearizing Equation 1 resulting in Equation 8.

$$\ln P_H = \ln A + m \ln t \qquad [8]$$

It was observed that for times of four hours and for temperatures of 600 ºC and 640ºC, the material had apparently already achieved saturation, so the curve fit was produced using only the data generated at one and two hours. The constants are tabulated in Table 9 and shown in Appendix C, and the experimental data is re-plotted with the parabolic correlation in Figure 17.

Table 9. Constants for parabolic hydride rate.

ºC	A	m
440	5.7	1.70
480	6.8	1.72
520	7.9	1.80
560	26	0.94
600	33	0.96
640	32	1.27

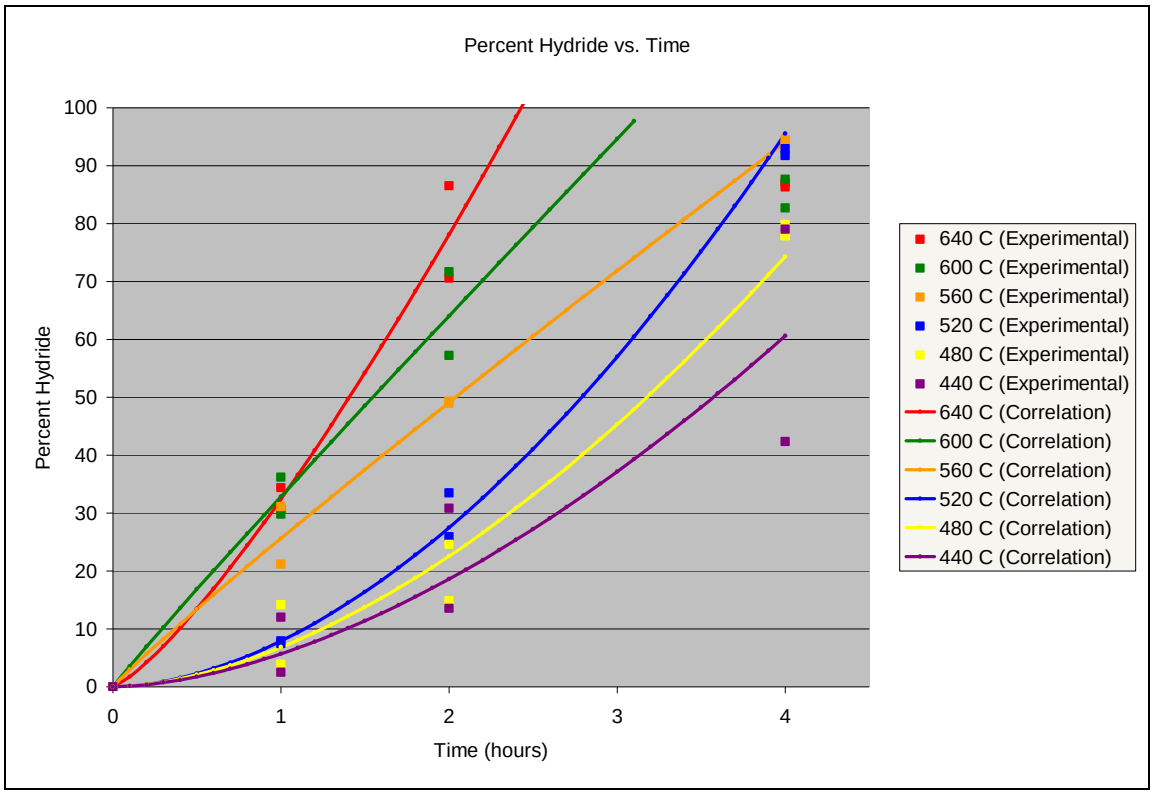

Figure 17. Time dependence of hydrogen pickup with parabolic correlation.

The data in Table 9 can then be used to predict the completion of the hydride reaction. It can also be useful to solve Equation 1 for the reaction time so that one may

determine the length of time the hydride reaction should progress in order to achieve the desired hydrogen content. Equations were developed for the constants A and m and are plotted in Figures 18-19 and shown in Equations 1 and 11.

$$\text{For } 440^{o}\text{C} < T < 540^{o}C$$
$$P_H = At^m$$
$$A = 0.028T - 6.39 \qquad [1]$$
$$m = 1.74 \pm 0.05$$

$$\text{For } 540^{o}C < T < 640^{o}C$$
$$P_H = At^m$$
$$A = 0.085T - 20.5 \qquad [11]$$
$$\text{m} = 1.1 \pm 0.2$$

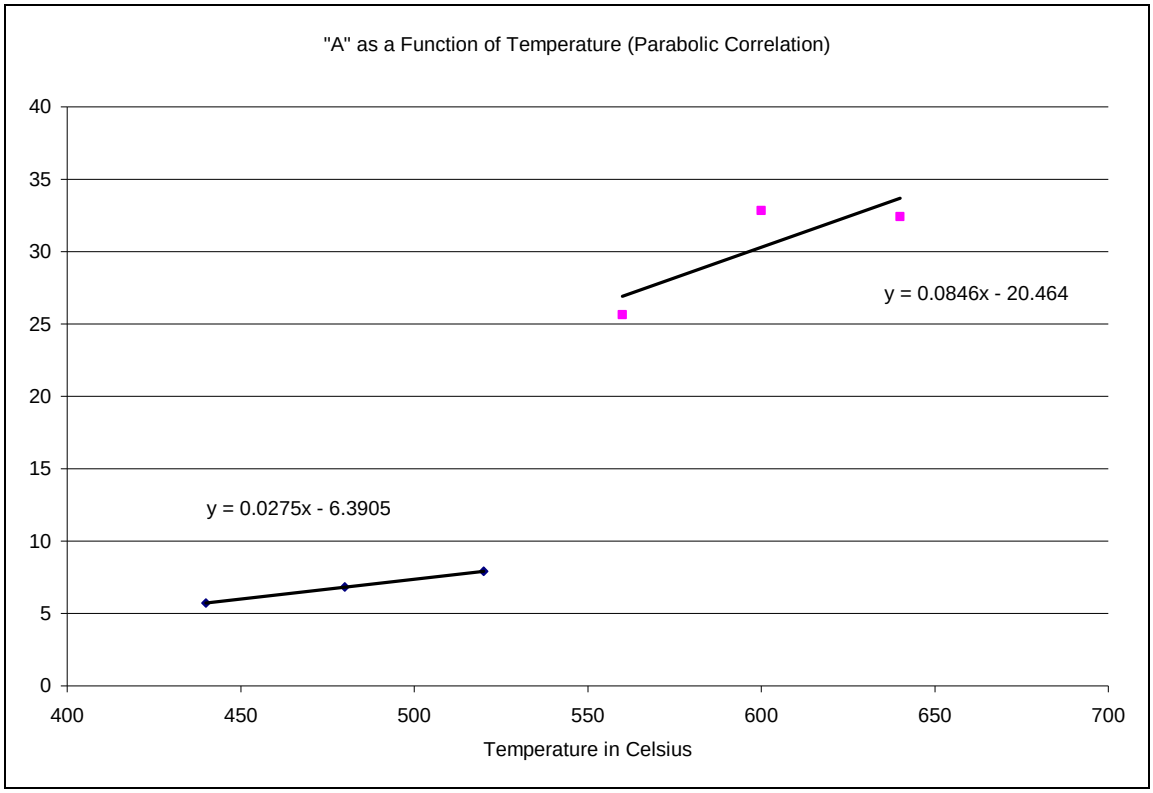

Figure 18. Plot showing step change in *A* at 540°C phase transition.

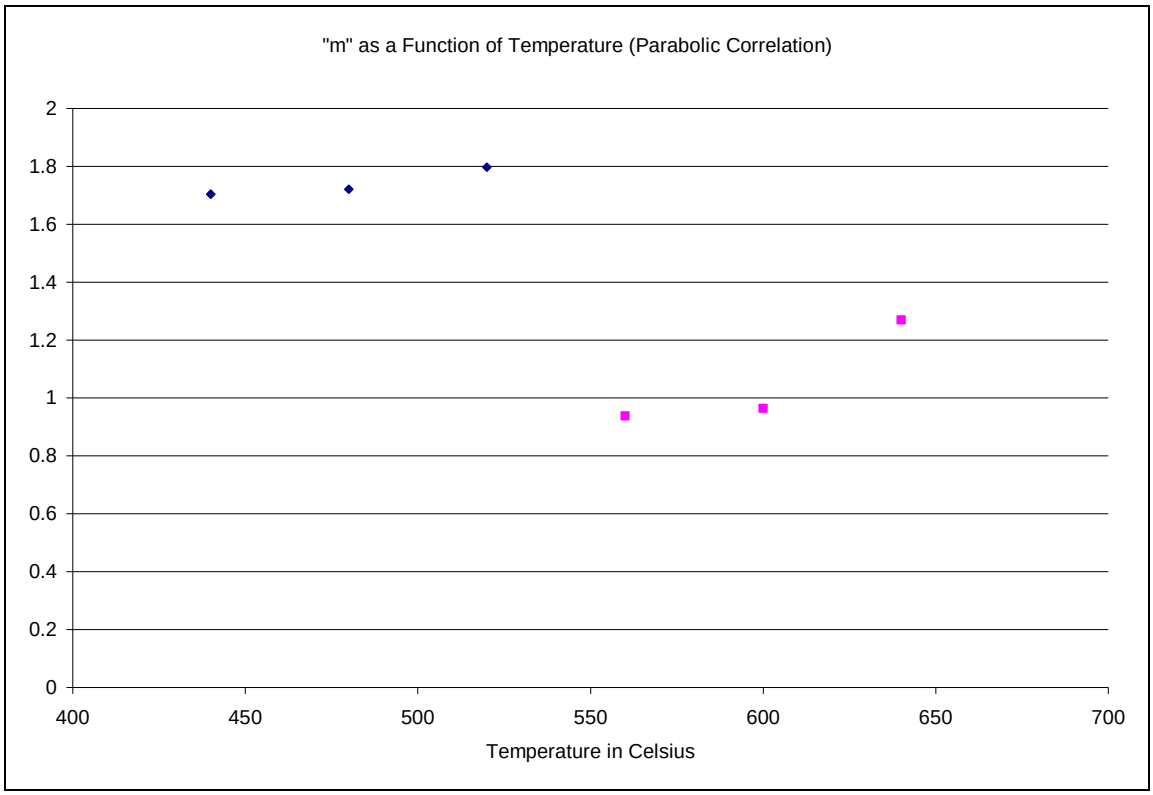

Figure 19. Plot showing step change in m at 540°C phase transition.

The correlation produced from the rate study is applicable at temperatures from 440°C to 640°C and times between one and four hours. Care should be taken if it is to be extrapolated to times less than one hour and for temperatures lower than 440°C due to issues regarding diffusion through the oxide layer as stated previously. This phenomenon is believed to be as important as the diffusion of hydrogen through the bulk of the material for low hydrogen concentrations. This correlation should be grossly predictive for times longer than four hours and for higher temperatures up until the samples reach P_H values approaching the saturation level, which occurs quite rapidly, but

this extrapolation has not been demonstrated. It can be seen from the correlation that the constants *A* and *m* exhibit a step change at the alpha beta phase transition. This step change is consistent with the α-Zr to β-Zr phase change.

This parabolic fit represents the data reasonably well, but it still has limitations as a physical representation of the hydride formation process. A textbook-style parabolic rate law for diffusion-controlled reaction (e.g., case hardening of steel) would have an exponent of m=0.5 and represent the diffusion of hydrogen through a surface reaction zone to measurable penetration depth before the formation reaction would occur. In the current experiments, the Zircaloy material crumbles under hydrogen exposure, typically within the first hour of the test, thus rapidly changing the amount of exposed surface area. Therefore, it is not a surprise that the m-values are not equal to 0.5. On the other hand, the calculated values of m (1.7±0.1 for α-Zr and 1.1±0.2 for β-Zr) indicate that a linear fit may be just as appropriate for the data.

A linear fit was produced (Appendix D) by fitting a line to the data for one and two hours as well as the point corresponding to a time and P_H equal to zero for each temperature. This linear fit agrees well with the data for the β-Zr phase, as would be expected based on the results from the parabolic correlation. However, the data obtained for the α-Zr phase seems to better fit the parabolic correlation. The parabolic fit with an "m" value greater than one implies that the reaction rate increases as a function of time for the α-Zr phase. This makes sense physically due to the time dependence of the material's surface area caused by the samples fracturing during the reaction. The data can be seen plotted with these two functional forms in Figure 20.

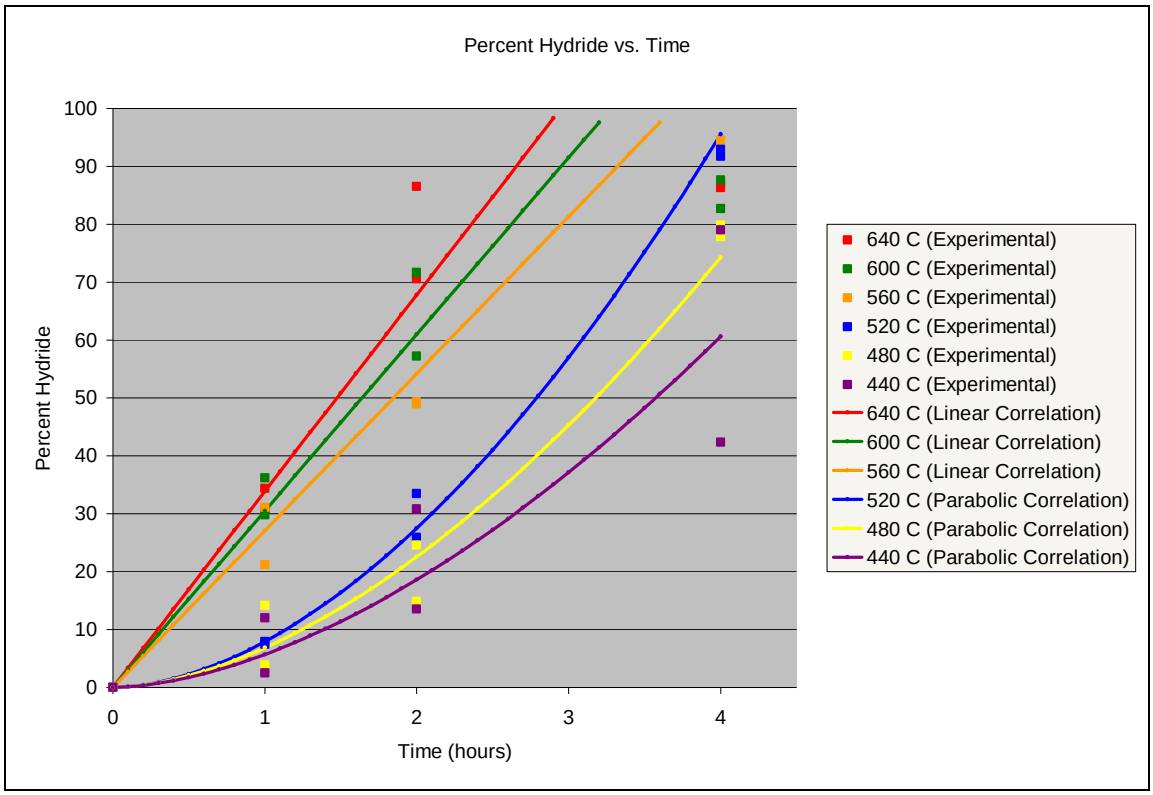

Figure 20. Data plotted with final correlation.

5.3 APPARENT ACTIVATION ENERGY FOR HYDRIDE FORMATION

An apparent activation energy of hydride formation in Zircaloy can be estimated using the calculated results from the previous section. This can be performed by assuming that the rate of change in P_H is a thermally activated phenomenon following an Arrhenius-style behavior, as represented by Equation 9. By linearizing this equation as shown in Equation 10, the apparent activation energy may be estimated.

$$R = R_o e^{-Q/kT}$$

"R" is the reaction rate or $\frac{dP_H}{dt}$ [9]
"Q" is the activation energy
"k" is the gas constant
"T" is the temperature in $^{\circ}C$

$$\ln R = \ln R_o - Q/kT \quad [10]$$

The Avrami correlation has been excluded from the activation energy analysis because there was not a physical basis for its use, nor did it accurately fit the data. It was determined from the preceding discussion that P_H along the β-Zr pathway expressed a linear relationship with respect to time, and P_H along the α-Zr pathway displayed a parabolic relationship. For the sake of this analysis, the reaction rates for the parabolic correlation were determined at a time equal to two hours. This is because at times near and below one hour, the data obtained was not as reliable. It was also apparent from the data that the samples often would reach saturation before four hours had expired, therefore two hours was chosen as the time for the sake of determining the activation energy. The activation energy obtained from the linear correlation for the β-Zr pathway was found to be 40 ±4 kJ/mol which roughly agrees with tabulated values of hydrogen diffusion in zirconium: 42 kJ/mol and 65.5 kJ/mol. [10] The activation energy for the α-Zr pathway was determined using the parabolic correlation, and was found to be 26 ±3 kJ/mol. This lower activation energy is believed to be due to the samples disassembling themselves during the reaction, which increases the surface area of the material, and would express itself as a decrease in activation energy. This time dependence of the

surface area makes it extremely difficult to obtain activation energies which are consistent with hydrogen diffusion in zirconium.

It should be noted that the activation energies produced from these correlations are not true activation energies, but rather apparent activation energies which are specific to this process. It was difficult to get true activation energies for diffusion of hydrogen in α-Zr because the samples had the tendency to disassemble during the reaction. If true diffusion activation energies are to be obtained, the change in surface area with respect to time needs to be taken into account.

CHAPTER 6

SUMMARY AND RECOMMENDATIONS

Small tube samples of nuclear grade Zircaloy-4 were exposed to flowing argon-5% hydrogen to quantify the first step in a processing concept proposed for the recycle of spent nuclear fuel cladding. The procedures developed by this research and the resulting data can be used to efficiently produce a zirconium hydride powder. The proposed Zircaloy recycle process will hydride and mill Zircaloy cladding tubes to produce fine hydride powder and then dehydride the powder to produce metal; the research described above is exclusively focused on understanding the hydride formation reaction.

The principal outcomes and observations from this work may be summarized as follows:

1. The hydride formation experimental system was perfected and the procedures described in Section 3.2 were used to perform a systematic study of the reaction vs. time and temperature.
2. One of the most significant obstacles to the generation of reliable data was nitrogen contamination in the process gas. Great efforts were made in the purification of the process gas by way of better seals and the addition of a high temperature titanium sponge nitrogen getter. These efforts were seen to dramatically increase the reproducibility and predictability of the data obtained.

3. Hydride formation was observed to proceed rapidly in the absence of nitrogen contamination in the gas. For temperature ranging from 480°C to 640°C, the reaction was typically complete in less than 4 hours.
4. It was observed that the P_H measurements were easier to reproduce at higher temperatures and when the reaction was allowed to proceed for longer periods of time. This is believed to be caused by the oxide boundary layer inhibiting hydrogen diffusion.
5. It was observed that for temperatures above the α-β-δ eutectoid the samples maintained a relative toughness. It was also found that at temperatures below this eutectoid the samples readily ground to a powder, and often times would disassemble during the reaction process resulting in small shards of zirconium hydride. This is believed to be due to the precipitation of the brittle δ-Zr phase at low hydrogen concentrations along the α-Zr phase pathway.
6. A correlation was produced for a temperature range of 440-640°C and hydride times of 1-4 hours. It was found that for temperatures above the α-β-δ eutectoid the P_H data were well represented by a linear dependence with respect to time, while for temperatures below this eutectoid the P_H data were well represented by a parabolic trend with respect to time. The equations are given below.

$$\begin{aligned} &\text{For } 440^{o}\text{C} < T < 540^{o}C \\ &P_H = At^m \\ &A = 0.028T - 6.39 \\ &m = 1.74 \pm 0.05 \end{aligned} \qquad [1]$$

For $540^{o}\,\mathrm{C} < T < 640^{o}\,C$

$$P_H = At \qquad [2]$$

$$A = 0.085T - 20.5$$

7. Apparent activation energy was extracted from these correlations. For the parabolic correlation the activation energy was found by calculating the rate of hydride formation from the slope of the function at a time equal to two hours, while the rate of hydride formation is simply equal to the value of *A* for the linear correlation. The activation energies for these respective correlations were found from the Arrhenius equation shown below. The apparent activation energy for the β-Zr pathway was found to be 40 ± 4 kJ/mol, and 26 ± 3 kJ/mol for the α-Zr pathway.

$$R = R_o e^{-Q/kT} \qquad [9]$$

The following observations and recommendations are presented to assist further research in this area.

1. It is strongly recommended that any nitrogen contamination from the air be removed by thoroughly sealing the system and by the addition of a nitrogen getter device.
2. This research proved that the hydride method can be used to produce a zirconium hydride powder. However, the hydride reaction by itself is not sufficient to producing a powder on its own and subsequent milling or grinding must be performed.

3. A systematic study of the reaction kinetics is recommended to gain understanding into the apparent activation energy. The activation energies presented in this thesis are merely apparent activation energies based on the measured results. While hydride formation in zirconium is known to be diffusion controlled, it becomes difficult to quantify this effect on Zircaloy-4 tubes. This is due to the presence of an oxide passivation layer, as well as an observed increase in surface area resulting from the material disassembling itself during the hydride reaction.
4. *In situ* observation of the reaction progress could be monitored using hot stage crystallography to better understand the effect of precipitation of the brittle δ-phase.

REFERENCES

[1] S.M. McDeavitt, A. Parkison, A.R. Totemeier and J.J. Wegener "Fabrication of Cermet Nuclear Fuels Designed for the Transmutation of Transuranic Isotopes," Materials Science Forum, 561-565: 1733-1736 (2007).

[2] Haygarth, J.C. and Graham, R.A., Oremet-Wah Chang Presentation to Argonne National Laboratory.

[3] Kraemer, D.T. (2005). Establishing Methods for Recycling Spent Zircaloy Cladding Using a Hydride-Dehydride Processing Route. Masters Thesis, Purdue University, West Lafayette, IN.

[4] McDeavitt, S.M. (1992). Hot Isostatic Pressing of U-10Zr Alloy Nuclear Fuel by Coupled Grain boundary Diffusion and Power-Law Creep. Doctoral Thesis, Purdue University, West Lafayette, IN.

[5] eds. J.J. McKetta and G.E. Weismantel, Encyclopedia of Chemical Processing and Design, v. 58, "Thorium and Thorium Compounds Supply-Demand Relationships" (Marcel Dekker, Inc. NY, 1997) pp.78-85.

[6] Lustman, B and Kerze, F, Jr. The Metallurgy of Zirconium, McGraw-Hill Book Company, Inc, New York, 1955.

[7] Miller, G.L. Metallurgy of the Rarer Metals-2: Zirconium, 2nd edition, Academic Press Inc., Publishers, New York, 1957.

[8] Hard, R.A. and Megy, J.A. (1984). U.S. Patent No. 4,470,847. Washington DC: U.S. Patent and Trademark Office.

[9] Kalish, H. S. “The Preparation of Zirconium Powder.” Zirconium and Zirconium Alloys: American Society for Metals (1953): 5-36.

[10] Rashid, Y.R., Sunderland, D.J., and Montgomery, R.O. “Creep as the Limiting Mechanism for Spent Fuel Dry Storage”, EPRI, Palo Alto, CA: 2000. 1001207.

[11] Mueller, W.M., Blackledge, J.P., and Libowitz, G.G., Metal Hydrides, Academic Press, New York, 1968.

APPENDIX A: RAW DATA FROM HYDRIDE EXPERIMENTS

Experiment number	% Hydrogen used	Flow rate at end of experiment (SCFH)	Pressure (" H20)	Temperature (degrees Celcius)	Time (hrs)	sample mass (g)	actual % if all hydride
1	4.83	8	28	360	6	2.3805	#VALUE!
2	4.83	3	12	733	6	3.5256	69.7977
3	4.83	7	25	518	6	4.1906	74.3367
4	4.83	3.5	4.5	477	12	3.6519	14.1329
5	4.83	7	24	503	12	3.7222	91.4909
6	4.83	3	12	522	23.5	3.7565	99.2426
7	5.02	7.75	25.5	525	24	3.281	98.8779
8	0	7.5	25	488	6	3.7812	3.0468
9	5.02	6.5	23	603	6	3.7473	87.8037
10	5.02	8	26.5	543	8	4.0353	50.0186
11	0	7.5	22	546	12.5	3.657	2.5202
12	5.02	7.5	25.5	755	5.2	3.1764	44.6836
13	4.97	7.4	23	529	12	8.1227	11.9706
14	4.97	7.5	24	539	8	3.2039	70.6213
15	4.97	5	10.75	521	6	2.676	17.9094
16	4.97	5	10.75	517	6	2.7359	11.2852
17	4.97	5	24.75	534	6.3	2.8495	91.6954
18	4.97	5	24.75	529	6.3	2.9652	65.2722
19	4.97	5	10.25	518	6	3.1677	11.0561
20	4.97	5	24.25	353	6	3.5114	5.6431
21	5.1	5	23.25	451	6	3.5418	6.2453
22	5.1	5	25	541	6	3.5194	5.3684
23	5.1	5	25	647	6	3.5042	15.2546
24	5.1	5	25	747	7	3.5464	48.3379
25	5.1	5	25	344	12	3.5213	0.7852
26	4.97	5	25	547	6	3.5291	84.8755
27	5.1	5	25	543	6	3.5555	58.9717
28	4.97	5	23.5	543	6	3.5118	43.8278
29	4.97	4.5	27	542	6	3.5481	24.1574
30	4.97	5	23.25	544	24	3.4936	61.2037
31	4.97	4.75	25.5	519	24	3.5085	107.4397
32	0	5	25	519	26	3.5395	4.2964
33	5.1	5	25	517	24	3.5761	12.7573
34	5.5	4.75	23.5	532	24	3.5226	20.2769
35	5.5	4.8	25.5	501	24	3.5094	13.1311
36	5.5	5	25	522	24	3.482	24.3513
37	5.1	5	25	510	24	3.5748	18.4339
38	5.1	5	24.5	525	24	3.5143	47.3371
39	5.1	5	25	572	21	3.486	36.2206
40	4.94	5	25	582	24	3.566	89.6832

mass increase (g)	mol H2 supplied	Zr (g)	mol Zr	100% hydride (g)	100% oxide (g)	actual % if all oxide	% hydride if .002g oxide	grams Zr converted to hydride
?	750032	2.3377	0.02563	0.0517	0.8200	#VALUE!	#VALUE!	#VALUE!
0.0534	281262	3.4621	0.03795	0.0765	1.2144	0.0440	0.6718	2.3260
0.0676	656278	4.1152	0.04511	0.0909	1.4435	0.0468	0.7214	2.9686
0.0112	656278	3.5862	0.03931	0.0792	1.2579	0.0089	0.1161	0.4163
0.0739	1312556	3.6552	0.04007	0.0808	1.2821	0.0576	0.8901	3.2537
0.0809	1101609	3.6889	0.04044	0.0815	1.2940	0.0625	0.9679	3.5704
0.0704	3020703	3.2219	0.03532	0.0712	1.1302	0.0623	0.9607	3.0953
0.0025	0	3.7131	0.04070	0.0821	1.3025	0.0019	0.0000	0.0000
0.0714	633373	3.6798	0.04034	0.0813	1.2908	0.0553	0.8534	
0.0438	1039382	3.9627	0.04344	0.0876	1.3900	0.0315	0.4773	1.8916
0.0020	0	3.5912	0.03937	0.0794	1.2597	0.0016	0.0000	0.0000
0.0308	633373	3.1192	0.03419	0.0689	1.0941	0.0282	0.4178	1.3033
0.0211	1427778	7.9765	0.08744	0.1763	2.7979	0.0075	0.1084	0.8643
0.0491	964715	3.1462	0.03449	0.0695	1.1036	0.0445	0.6774	2.1314
0.0104	482358	2.6278	0.02881	0.0581	0.9218	0.0113	0.1447	0.3801
0.0067	482358	2.6867	0.02945	0.0594	0.9424	0.0071	0.0792	0.2127
0.0567	506475	2.7982	0.03067	0.0618	0.9815	0.0578	0.8846	2.4753
0.0420	506475	2.9118	0.03192	0.0643	1.0214	0.0411	0.6216	1.8101
0.0076	482358	3.1107	0.03410	0.0687	1.0911	0.0070	0.0815	0.2534
0.0043	482358	3.4482	0.03780	0.0762	1.2095	0.0036	0.0302	0.1041
0.0048	494975	3.4780	0.03813	0.0769	1.2200	0.0039	0.0364	0.1267
0.0041	494975	3.4561	0.03789	0.0764	1.2123	0.0034	0.0275	0.0950
0.0116	494975	3.4411	0.03772	0.0760	1.2070	0.0096	0.1262	0.4344
0.0372	577470	3.4826	0.03818	0.0770	1.2216	0.0305	0.4574	1.5929
0.0006	989949	3.4579	0.03791	0.0764	1.2129	0.0005	-0.0183	-0.0634
0.0650	482358	3.4656	0.03799	0.0766	1.2156	0.0535	0.8226	2.8509
0.0455	494975	3.4915	0.03827	0.0772	1.2247	0.0372	0.5638	1.9685
0.0334	482358	3.4486	0.03780	0.0762	1.2097	0.0276	0.4120	1.4209
0.0186	434122	3.4842	0.03819	0.0770	1.2222	0.0152	0.2156	0.7512
0.0464	1929430	3.4307	0.03761	0.0758	1.2034	0.0386	0.5857	2.0092
0.0818	1832959	3.4453	0.03777	0.0761	1.2085	0.0677	1.0481	3.6112
0.0033	0	3.4758	0.03810	0.0768	1.2192	0.0027	0.0169	0.0588
0.0099	1979898	3.5117	0.03850	0.0776	1.2318	0.0080	0.1018	0.3575
0.0155	2028425	3.4592	0.03792	0.0764	1.2134	0.0128	0.1766	0.6109
0.0100	2049777	3.4462	0.03778	0.0762	1.2088	0.0083	0.1050	0.3620
0.0184	2135184	3.4193	0.03748	0.0756	1.1994	0.0153	0.2170	0.7421
0.0143	1979898	3.5105	0.03848	0.0776	1.2314	0.0116	0.1586	0.5566
0.0361	1979898	3.4510	0.03783	0.0763	1.2105	0.0298	0.4471	1.5431
0.0274	1732411	3.4233	0.03753	0.0756	1.2008	0.0228	0.3358	1.1494
0.0694	1917784	3.5018	0.03839	0.0774	1.2283	0.0565	0.8710	3.0500

41	4.94	5	25	556	24	3.532	96.8091
42	4.94	5	25.5	570	6	3.5776	84.4977
43	4.94	5	23.75	570	18	3.5606	96.9374
44	4.94	4.5	22	563	12	3.4639	91.3954
45	0	5	25	567	21	3.5054	5.9157
46	4.94	5	24	310	24	3.5144	56.6455
47	4.94	5	25.75	432	24	3.5994	85.9064
48	5	5	24.5	572	6	3.56	71.5827
49	5	5	25	566	6	3.5821	77.7020
50	5	5	25	566	6	3.5644	53.2652
51	5	5	25	565	6	3.5419	17.3041
52	5	1	25	571	6	3.5641	21.4630
53	5	3	25	574	6	3.4982	90.2358
54	5	3.2	26	575	6	3.5348	92.0392
55	5	3	25	567	4	3.6144	34.6789
56	5	3	25	576	4	3.6108	72.2347
57	5	3	25	579	4	3.6114	45.6815
58	5	3	25	568	4	3.6014	93.6640
59	5	3	24	568	4	3.5544	94.5136
60	5	3	25	519	4	3.5864	91.7429
61	5	3	25	520	4	3.5254	92.9382
62	5	3	25	481	4	3.6004	77.9470
63	5	2.9	27	485	4	3.5205	79.8470
64	5	2.4	30	481	4	3.5453	93.9763
65	5	3	25	569	1	3.5505	42.8309
66	5	3	25	579	1	3.6361	21.1648
67	5	3	25	600	1	3.5888	29.7901
68	5	2.9	30	479	4	3.5632	77.8555
69	5	0.1	30	435	4	3.5464	79.0040
70	5	3	25	436	1	3.4028	0.8125
71	5	3	25	522	1	3.6209	7.8906
72	5	3	25	440	4	3.5572	42.3616
73	5	3	25	526	2	3.5905	25.9256
74	5	3	25	422	1	3.5592	12.0410
75	5	3	25	441	1	3.5388	2.4742
76	5	3	25	436	2	3.5991	0.8963
77	5	3	25	530	2	3.5389	33.4655
78	5	3	25	611	4	3.5504	87.6112
79	5	3	25	616	1	3.5507	36.2096
80	5	3	25	614	4	3.5706	82.7275

0.0742	1917784	3.4684	0.03802	0.0766	1.2166	0.0610	0.9420	3.2672
0.0656	479446	3.5132	0.03851	0.0776	1.2323	0.0532	0.8192	2.8781
0.0749	1438338	3.4965	0.03833	0.0773	1.2265	0.0611	0.9435	3.2989
0.0687	863003	3.4015	0.03729	0.0752	1.1932	0.0576	0.8873	3.0184
0.0045	0	3.4423	0.03773	0.0761	1.2075	0.0037	0.0329	0.1131
0.0432	1917784	3.4511	0.03783	0.0763	1.2106	0.0357	0.5402	1.8644
0.0671	1917784	3.5346	0.03875	0.0781	1.2398	0.0541	0.8335	2.9460
0.0553	485269	3.4959	0.03832	0.0773	1.2263	0.0451	0.6899	2.4120
0.0604	485269	3.5176	0.03856	0.0777	1.2339	0.0490	0.7513	2.6428
0.0412	485269	3.5002	0.03837	0.0773	1.2278	0.0336	0.5068	1.7739
0.0133	485269	3.4781	0.03813	0.0769	1.2200	0.0109	0.1470	0.5114
0.0166	97053.8	3.4999	0.03837	0.0773	1.2277	0.0135	0.1888	0.6607
0.0685	291161	3.4352	0.03766	0.0759	1.2050	0.0568	0.8760	3.0093
0.0706	310572	3.4712	0.03805	0.0767	1.2176	0.0580	0.8943	3.1043
0.0272	194108	3.5493	0.03891	0.0784	1.2450	0.0218	0.3213	1.1404
0.0566	194108	3.5458	0.03887	0.0784	1.2438	0.0455	0.6968	2.4708
0.0358	194108	3.5464	0.03888	0.0784	1.2440	0.0288	0.4313	1.5295
0.0732	194108	3.5366	0.03877	0.0782	1.2405	0.0590	0.9110	3.2220
0.0729	194108	3.4904	0.03826	0.0771	1.2243	0.0595	0.9192	3.2084
0.0714	194108	3.5218	0.03861	0.0778	1.2354	0.0578	0.8917	3.1405
0.0711	194108	3.4619	0.03795	0.0765	1.2144	0.0585	0.9032	3.1270
0.0609	194108	3.5356	0.03876	0.0781	1.2402	0.0491	0.7539	2.6654
0.0610	187637	3.4571	0.03790	0.0764	1.2127	0.0503	0.7723	2.6699
0.0723	155286	3.4815	0.03816	0.0769	1.2212	0.0592	0.9138	3.1813
0.0330	48526.9	3.4866	0.03822	0.0770	1.2230	0.0270	0.4024	1.4028
0.0167	48526.9	3.5707	0.03914	0.0789	1.2525	0.0133	0.1863	0.6652
0.0232	48526.9	3.5242	0.03863	0.0779	1.2362	0.0188	0.2722	0.9594
0.0602	187637	3.4991	0.03836	0.0773	1.2274	0.0490	0.7527	2.6337
0.0608	6470.25	3.4826	0.03818	0.0770	1.2216	0.0498	0.7641	2.6609
0.0006	48526.9	3.3415	0.03663	0.0738	1.1721	0.0005	-0.0190	-0.0634
0.0062	48526.9	3.5557	0.03898	0.0786	1.2472	0.0050	0.0535	0.1901
0.0327	194108	3.4932	0.03829	0.0772	1.2253	0.0267	0.3977	1.3893
0.0202	97053.8	3.5259	0.03865	0.0779	1.2368	0.0163	0.2336	0.8236
0.0093	48526.9	3.4951	0.03831	0.0772	1.2260	0.0076	0.0945	0.3303
0.0019	48526.9	3.4751	0.03809	0.0768	1.2190	0.0016	-0.0013	-0.0045
0.0007	97053.8	3.5343	0.03874	0.0781	1.2397	0.0006	-0.0166	-0.0588
0.0257	97053.8	3.4752	0.03810	0.0768	1.2190	0.0211	0.3086	1.0725
0.0675	194108	3.4865	0.03822	0.0770	1.2230	0.0552	0.8502	2.9641
0.0279	48526.9	3.4868	0.03822	0.0771	1.2231	0.0228	0.3361	1.1720
0.0641	194108	3.5063	0.03844	0.0775	1.2299	0.0521	0.8015	2.8102

81	5	3	25	576	2	3.571	49.2954
82	5	3	25	654	4	3.5448	86.3196
83	5	3	25	648	4	3.5822	87.0907
84	5	3	25	578	2	3.5553	48.9946
85	5	3	25	665	2	3.5585	86.5052
86	5	3	25	643	2	3.5459	70.5678
87	5	3	25	613	2	3.5877	71.6722
88	5	3	25	615	2	3.5675	57.2233
89	5	3	25	537	1	3.5392	7.4217
90	5	3	25	635	1	3.5684	34.3511
91	5	3	25	487	1	3.5441	3.9008
92	5	3	25	636	1	3.6143	30.5999
93	5	3	25	477	2	3.543	61.5209
94	5	3	25	475	2	3.5891	63.6838
95	5	3	25	482	1	3.5756	14.1768
96	5	0	25	440	4	3.5649	0.1293
97	5	3	25	429	2	3.5674	13.5635
98	5	3	25	558	1	3.6021	31.0873
99	5	3	25	483	2	3.6343	24.5988
100	5	3	25	427	2	3.5719	30.8341
101	5	3	25	474	2	3.5672	14.8560

0.0382	97053.8	3.5067	0.03844	0.0775	1.2301	0.0311	0.4671	1.6381
0.0664	194108	3.4810	0.03816	0.0769	1.2210	0.0544	0.8372	2.9143
0.0677	194108	3.5177	0.03856	0.0777	1.2339	0.0549	0.8452	2.9731
0.0378	97053.8	3.4913	0.03827	0.0772	1.2247	0.0309	0.4640	1.6200
0.0668	97053.8	3.4944	0.03831	0.0772	1.2258	0.0545	0.8392	2.9324
0.0543	97053.8	3.4821	0.03817	0.0769	1.2214	0.0445	0.6797	2.3667
0.0558	97053.8	3.5231	0.03862	0.0779	1.2358	0.0452	0.6910	2.4346
0.0443	97053.8	3.5033	0.03840	0.0774	1.2289	0.0360	0.5464	1.9142
0.0057	48526.9	3.4755	0.03810	0.0768	1.2191	0.0047	0.0482	0.1674
0.0266	48526.9	3.5042	0.03841	0.0774	1.2292	0.0216	0.3177	1.1132
0.0030	48526.9	3.4803	0.03815	0.0769	1.2208	0.0025	0.0130	0.0453
0.0240	48526.9	3.5492	0.03891	0.0784	1.2450	0.0193	0.2805	0.9956
0.0473	97053.8	3.4792	0.03814	0.0769	1.2204	0.0388	0.5892	2.0499
0.0496	97053.8	3.5245	0.03864	0.0779	1.2363	0.0401	0.6112	2.1540
0.0110	48526.9	3.5112	0.03849	0.0776	1.2316	0.0089	0.1160	0.4073
0.0001	0	3.5007	0.03838	0.0774	1.2280	0.0001	-0.0246	-0.0860
0.0105	97053.8	3.5032	0.03840	0.0774	1.2288	0.0085	0.1098	0.3846
0.0243	48526.9	3.5373	0.03878	0.0782	1.2408	0.0196	0.2853	1.0091
0.0194	97053.8	3.5689	0.03912	0.0789	1.2519	0.0155	0.2206	0.7874
0.0239	97053.8	3.5076	0.03845	0.0775	1.2304	0.0194	0.2825	0.9910
0.0115	97053.8	3.5030	0.03840	0.0774	1.2287	0.0094	0.1227	0.4299

APPENDIX B: CONSTANTS FROM AVRAMI CORRELATION

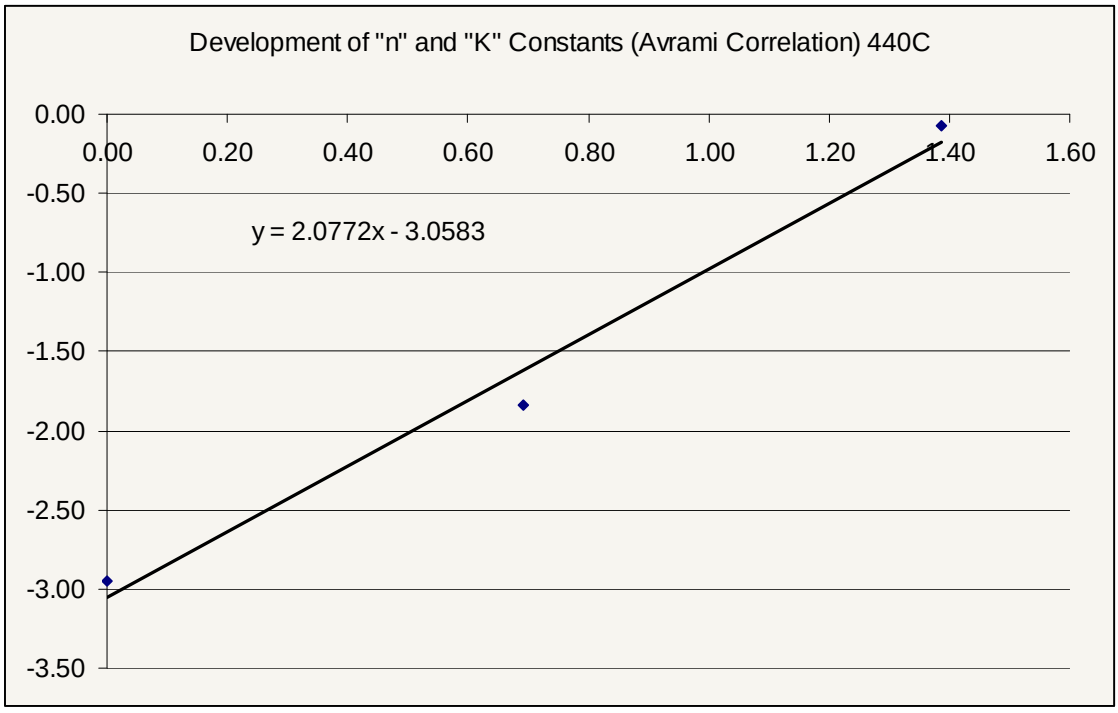

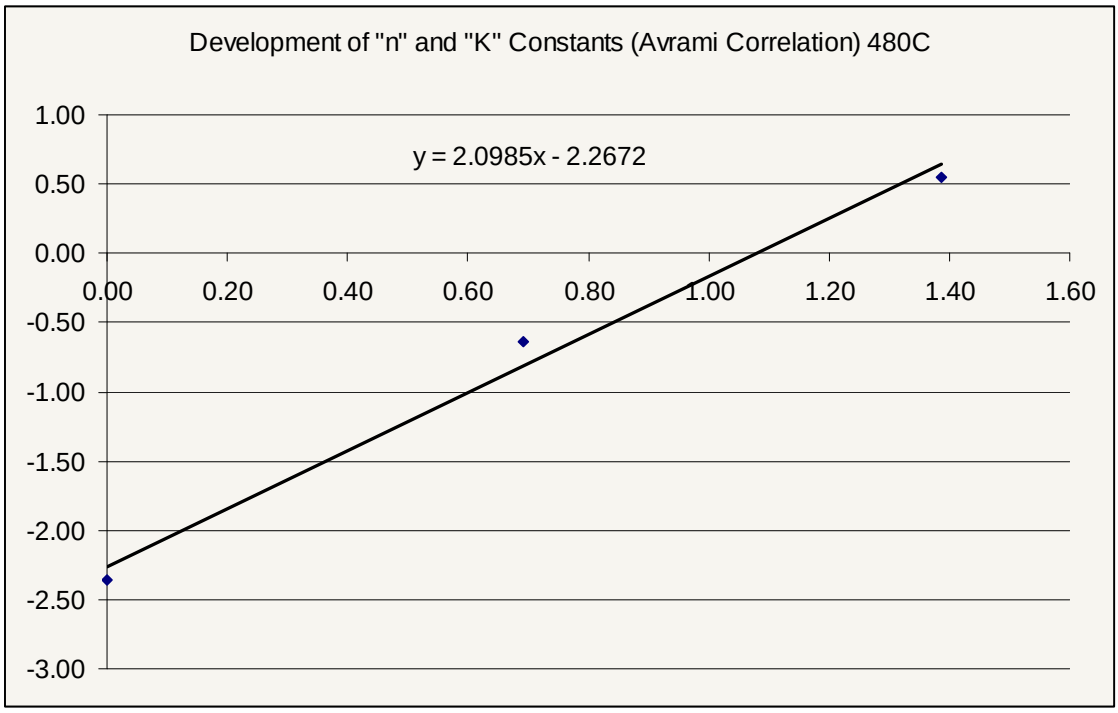

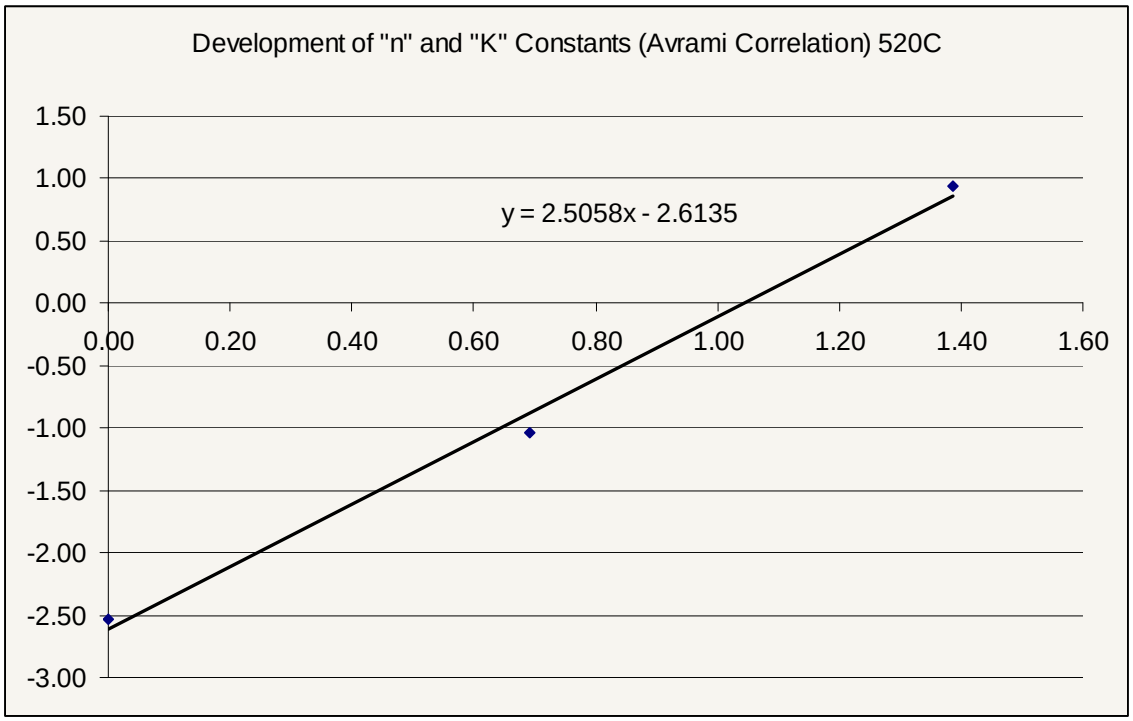
Development of "n" and "K" Constants (Avrami Correlation) 520C
y = 2.5058x - 2.6135
1.50
1.00
0.50
0.00
-0.50
-1.00
-1.50
-2.00
-2.50
-3.00
0.00
0.20
0.40
0.60
0.80
1.00
1.20
1.40
1.60

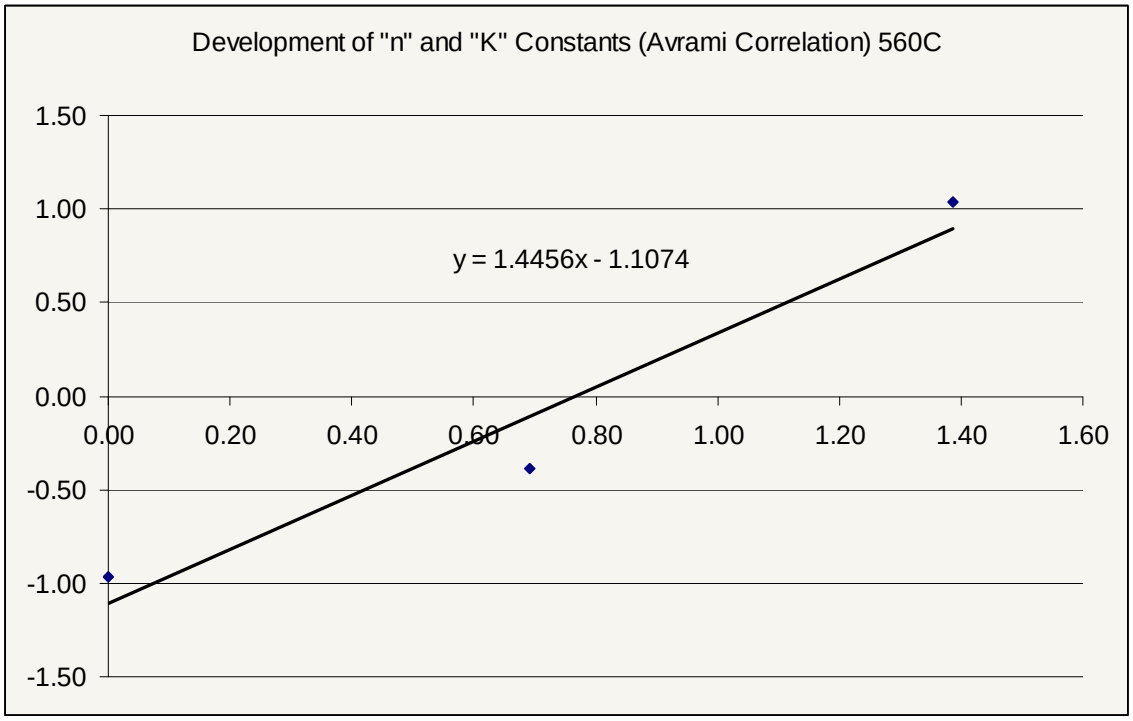
Development of "n" and "K" Constants (Avrami Correlation) 560C
y = 1.4456x - 1.1074
1.50
1.00
0.50
0.00
-0.50
-1.00
-1.50
0.00
0.20
0.40
0.60
0.80
1.00
1.20
1.40
1.60

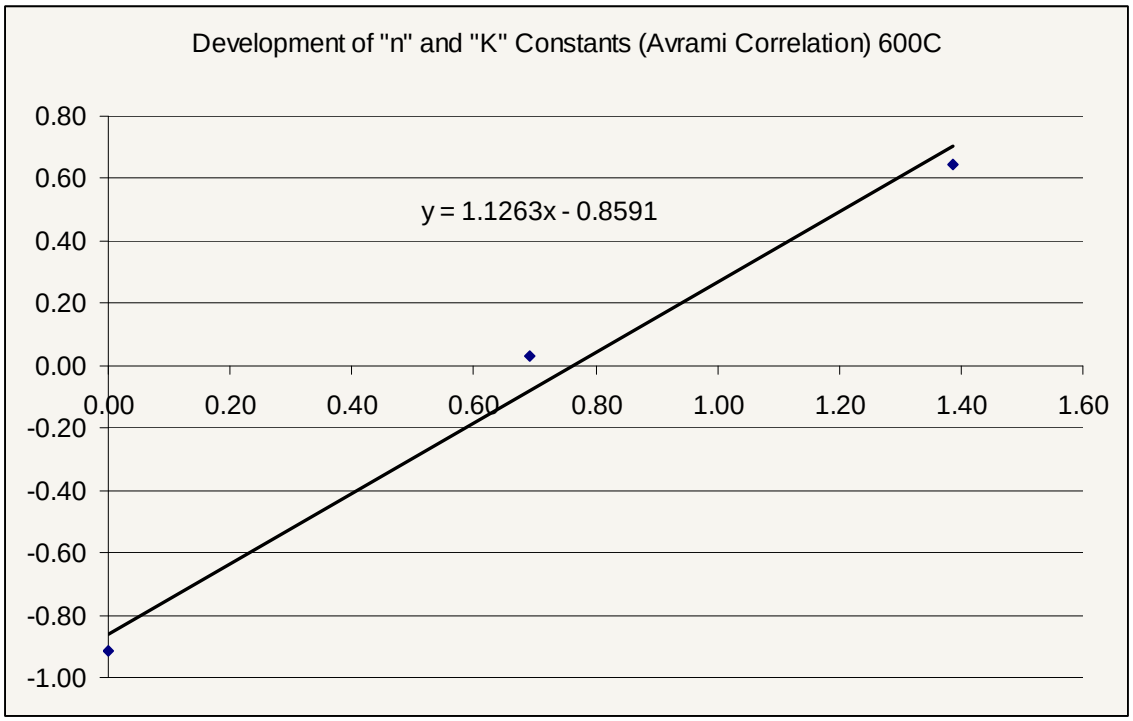
Development of "n" and "K" Constants (Avrami Correlation) 600C
y = 1.1263x - 0.8591
0.80
0.60
0.40
0.20
0.00
-0.20
-0.40
-0.60
-0.80
-1.00
0.00
0.20
0.40
0.60
0.80
1.00
1.20
1.40
1.60

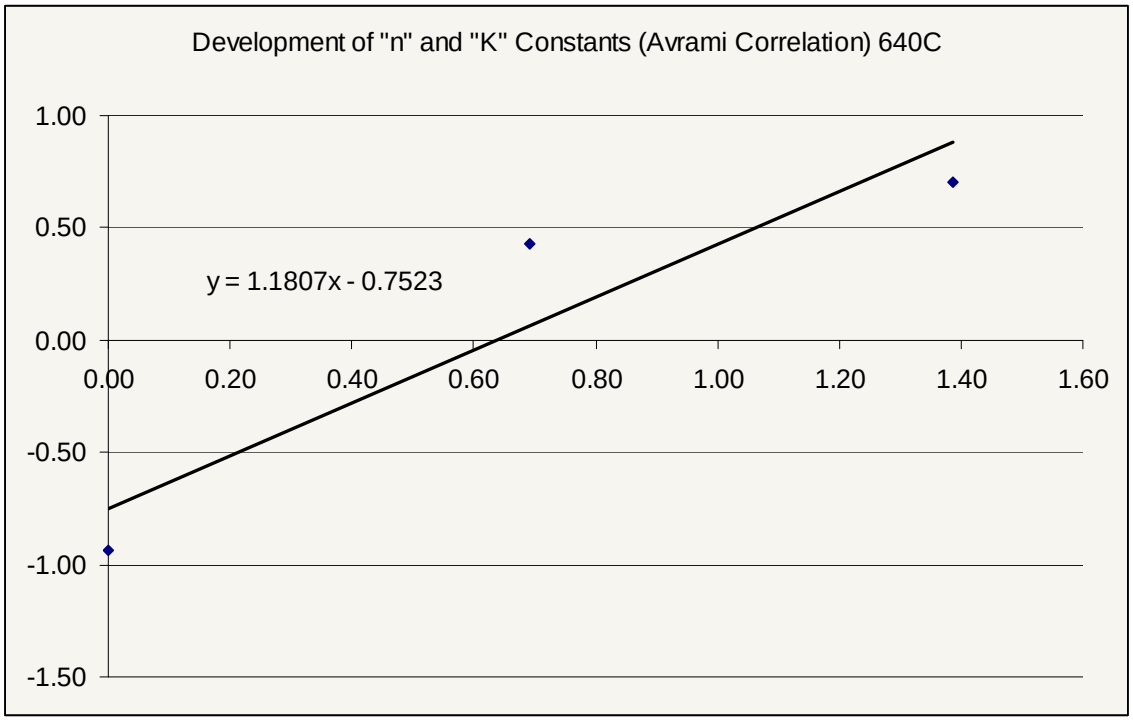
Development of "n" and "K" Constants (Avrami Correlation) 640C
y = 1.1807x - 0.7523
1.00
0.50
0.00
-0.50
-1.00
-1.50
0.00
0.20
0.40
0.60
0.80
1.00
1.20
1.40
1.60

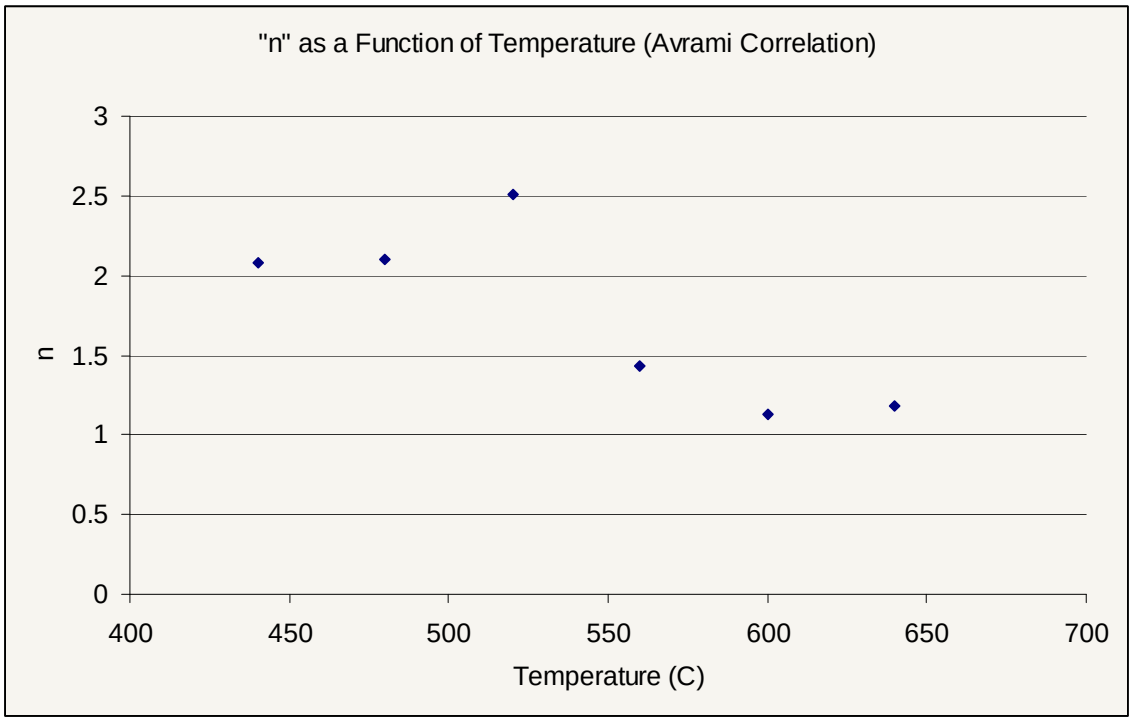
"n" as a Function of Temperature (Avrami Correlation)
n
3
2.5
2
1.5
1
0.5
0
400
450
500
550
600
650
700
Temperature (C)

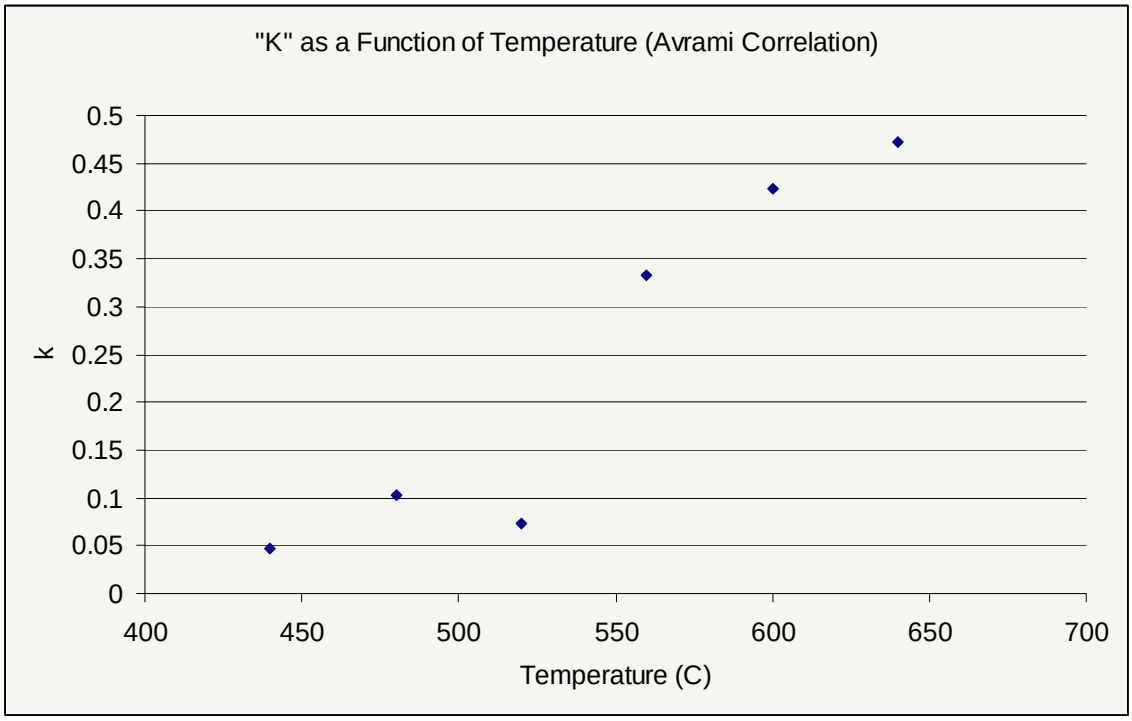
"K" as a Function of Temperature (Avrami Correlation)
k
0.5
0.45
0.4
0.35
0.3
0.25
0.2
0.15
0.1
0.05
0
400
450
500
550
600
650
700
Temperature (C)

APPENDIX C: CONSTANTS AND Q VALUE FROM PARABOLIC CORRELATION

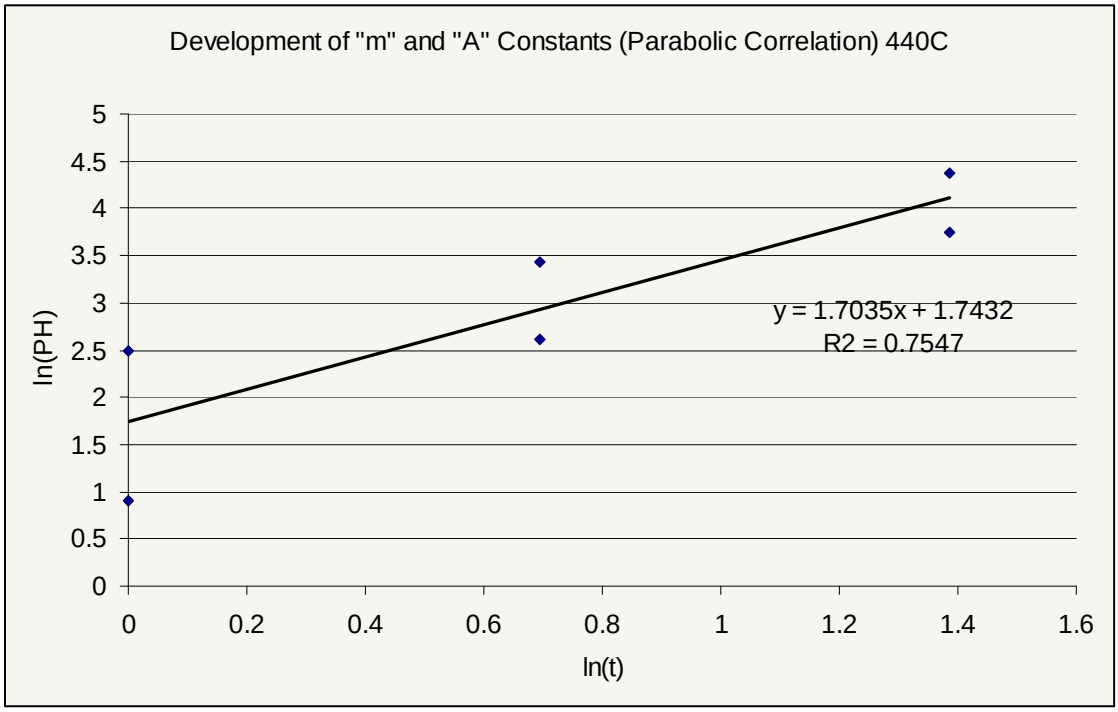

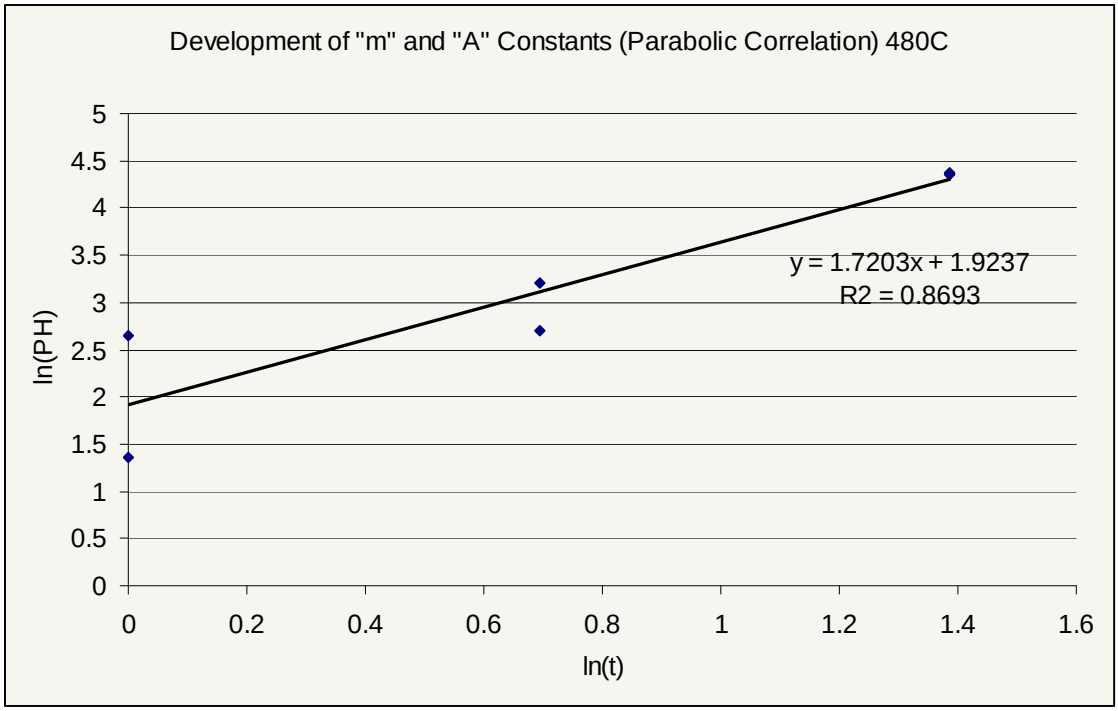

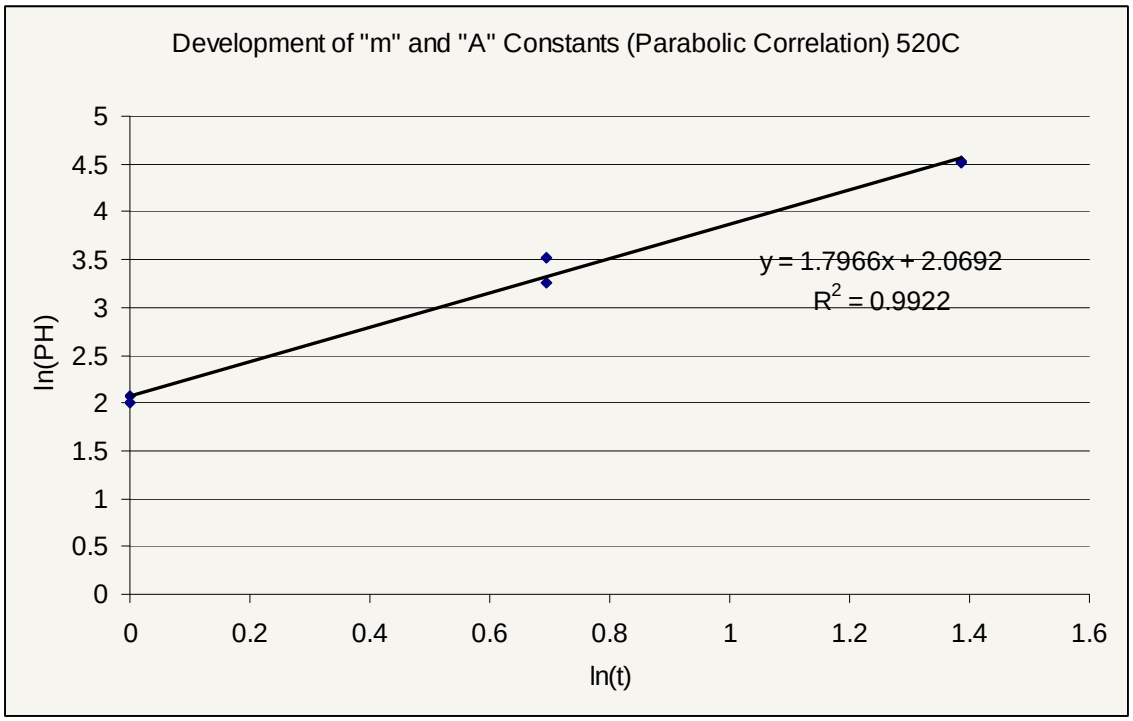
Development of "m" and "A" Constants (Parabolic Correlation) 520C
ln(PH)
ln(t)
y = 1.7966x + 2.0692
R2 = 0.9922
0
0.5
1
1.5
2
2.5
3
3.5
4
4.5
5
0
0.2
0.4
0.6
0.8
1
1.2
1.4
1.6

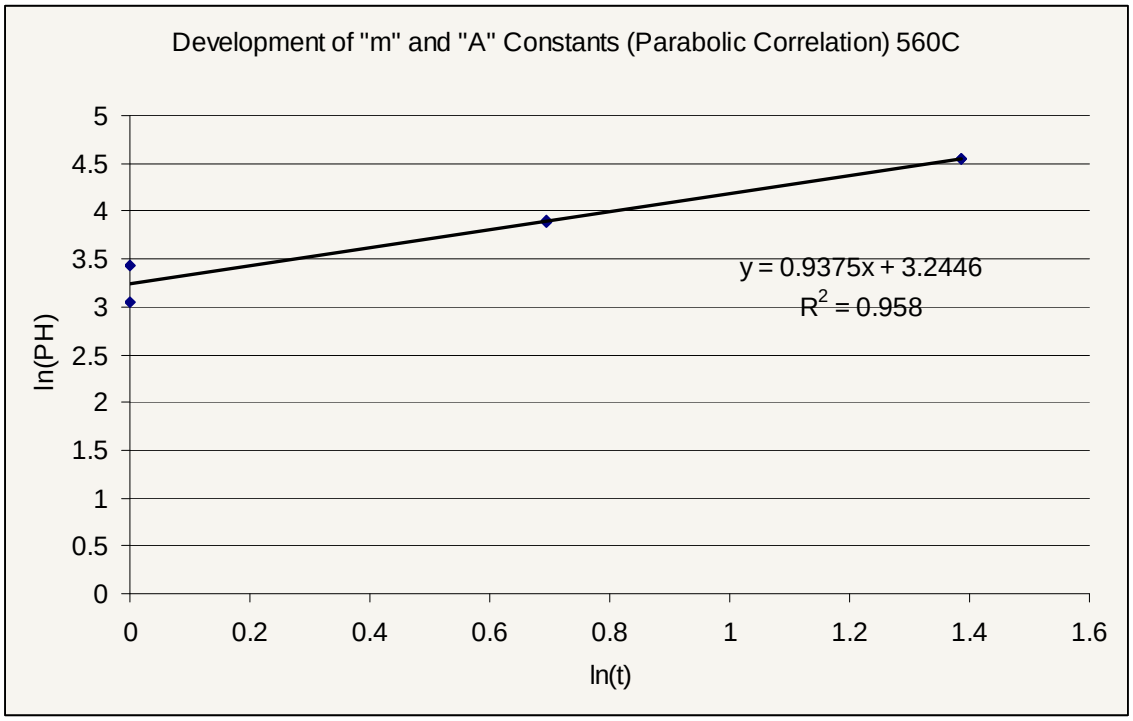
Development of "m" and "A" Constants (Parabolic Correlation) 560C
ln(PH)
ln(t)
y = 0.9375x + 3.2446
R2 = 0.958
0
0.5
1
1.5
2
2.5
3
3.5
4
4.5
5
0
0.2
0.4
0.6
0.8
1
1.2
1.4
1.6

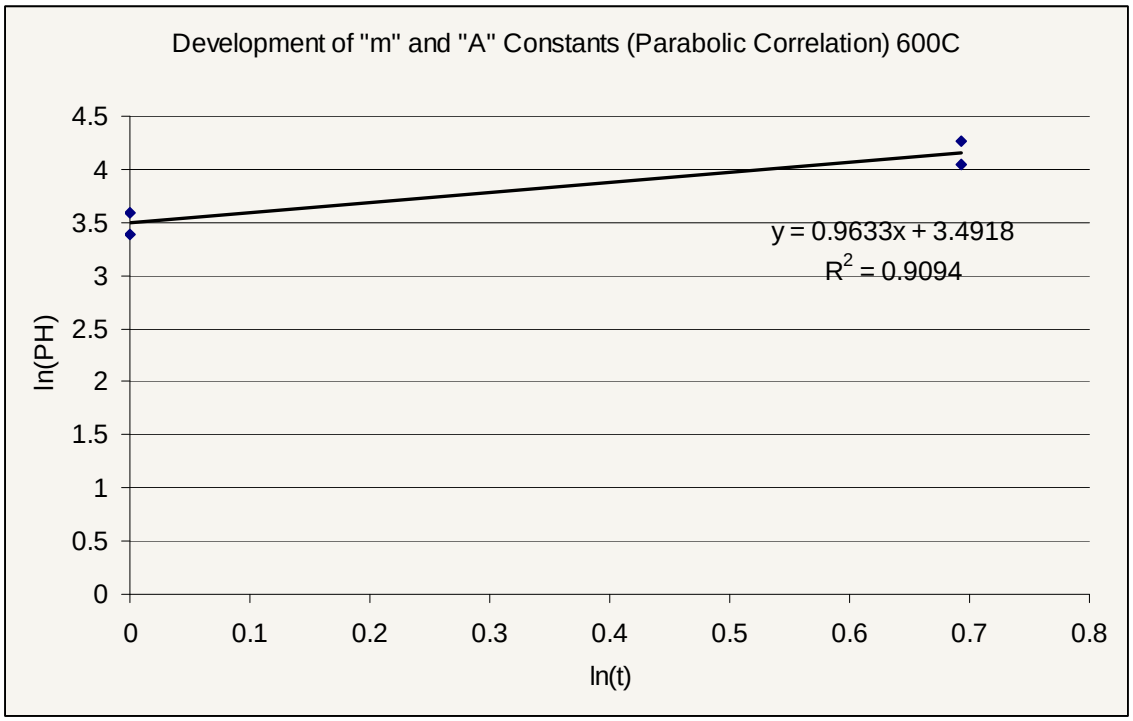
Development of "m" and "A" Constants (Parabolic Correlation) 600C
y = 0.9633x + 3.4918
R2 = 0.9094
ln(PH)
ln(t)
4.5
4
3.5
3
2.5
2
1.5
1
0.5
0
0
0.1
0.2
0.3
0.4
0.5
0.6
0.7
0.8

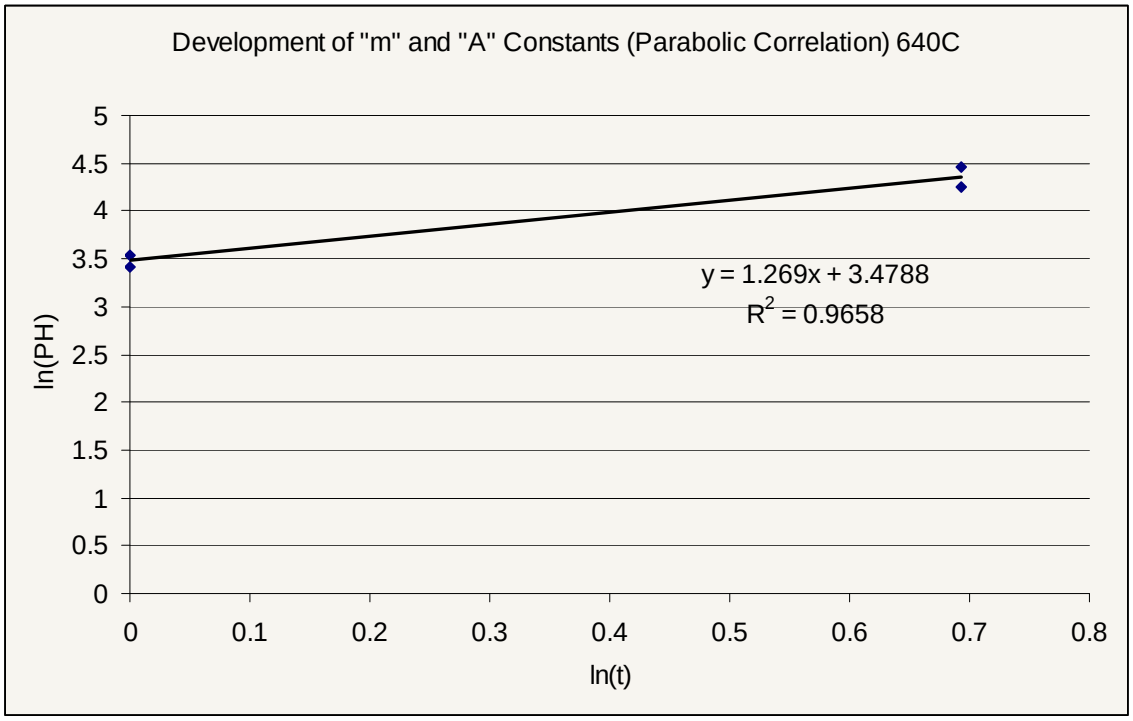
Development of "m" and "A" Constants (Parabolic Correlation) 640C
y = 1.269x + 3.4788
R2 = 0.9658
ln(PH)
ln(t)
5
4.5
4
3.5
3
2.5
2
1.5
1
0.5
0
0
0.1
0.2
0.3
0.4
0.5
0.6
0.7
0.8

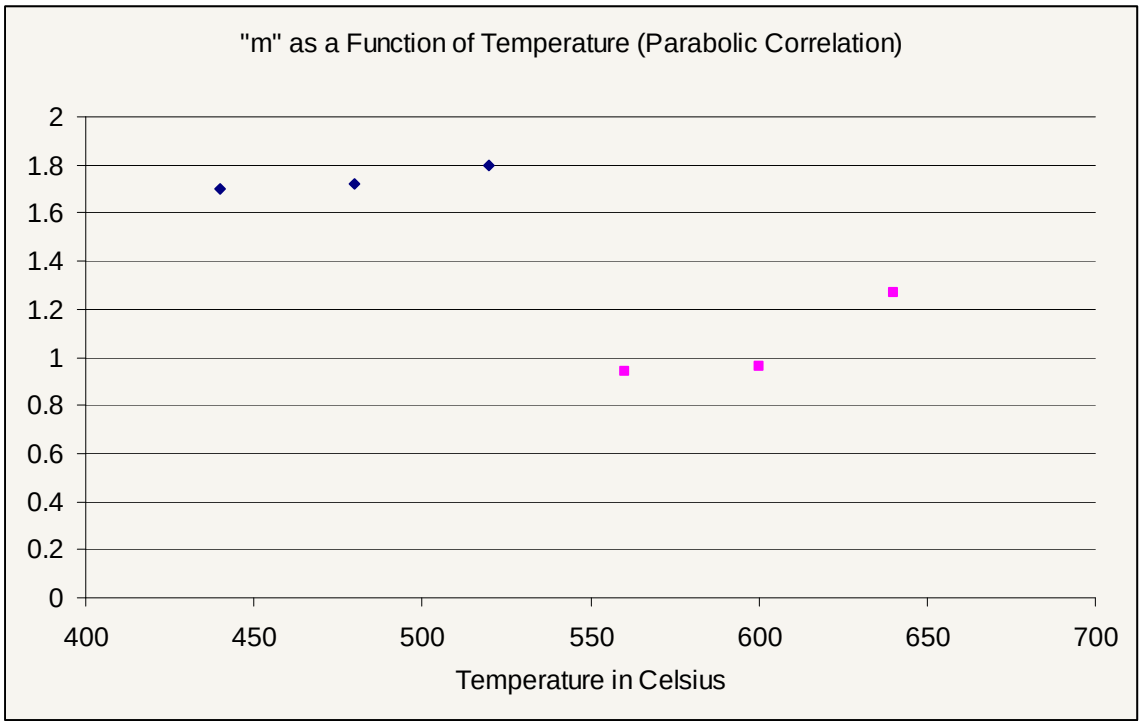
"m" as a Function of Temperature (Parabolic Correlation)
2
1.8
1.6
1.4
1.2
1
0.8
0.6
0.4
0.2
0
400
450
500
550
600
650
700
Temperature in Celsius

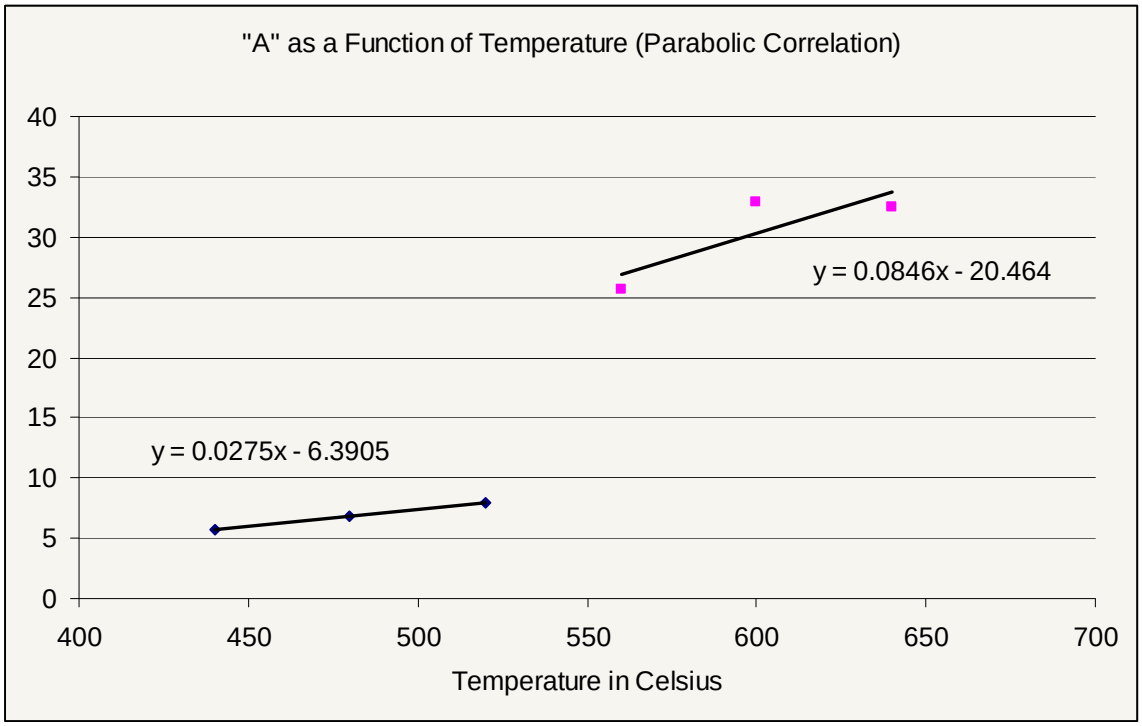
"A" as a Function of Temperature (Parabolic Correlation)
40
35
30
25
20
15
10
5
0
y = 0.0846x - 20.464
y = 0.0275x - 6.3905
400
450
500
550
600
650
700
Temperature in Celsius

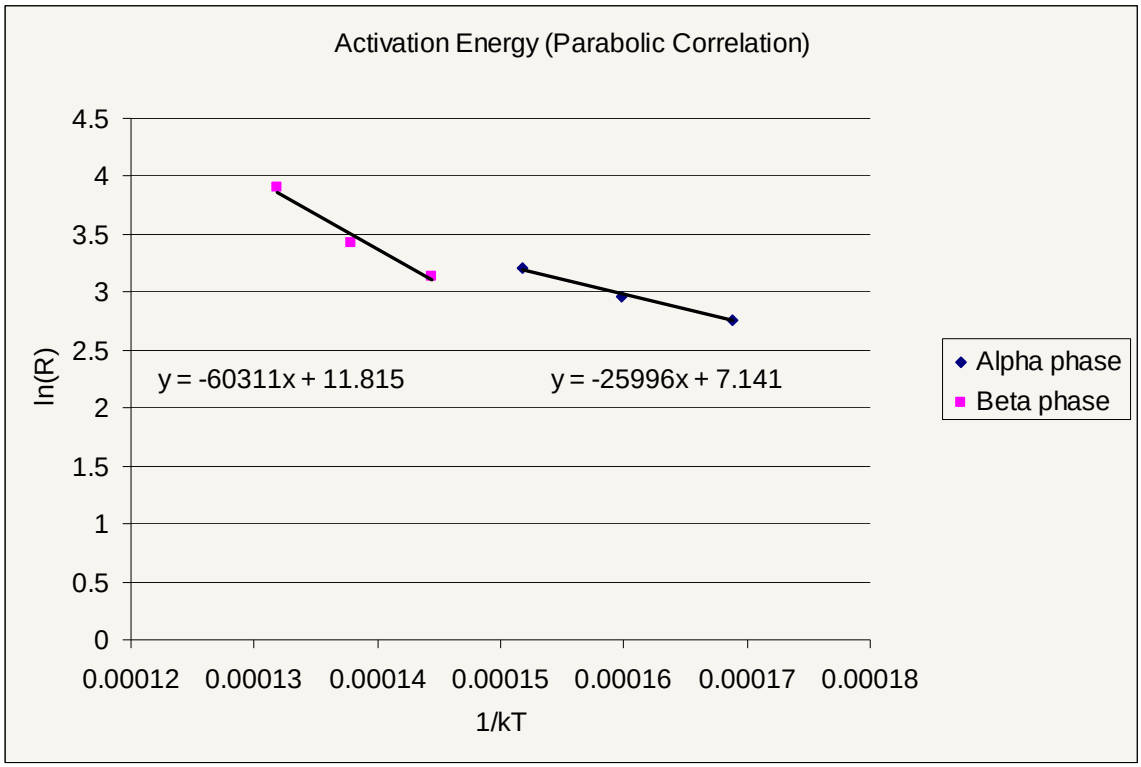
Activation Energy (Parabolic Correlation)
4.5
4
3.5
3
2.5
2
1.5
1
0.5
0
ln(R)
y = -60311x + 11.815
y = -25996x + 7.141
0.00012
0.00013
0.00014
0.00015
0.00016
0.00017
0.00018
1/kT
Alpha phase
Beta phase

APPENDIX D: CONSTANTS AND Q VALUE FROM LINEAR CORRELATION

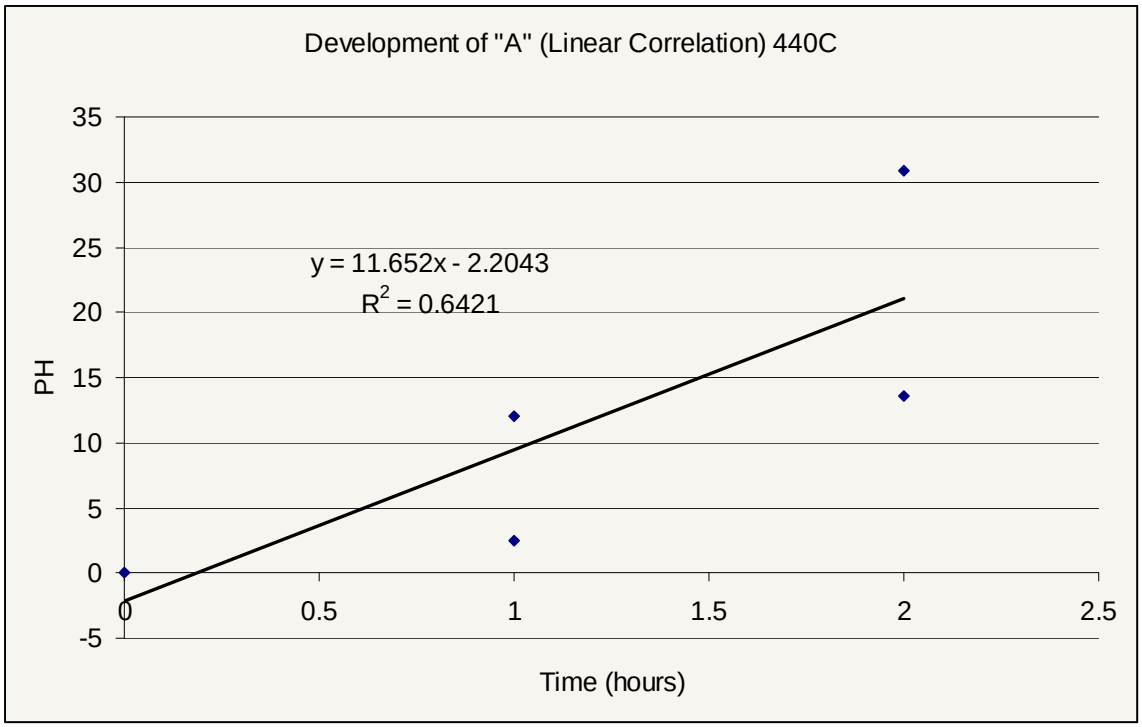

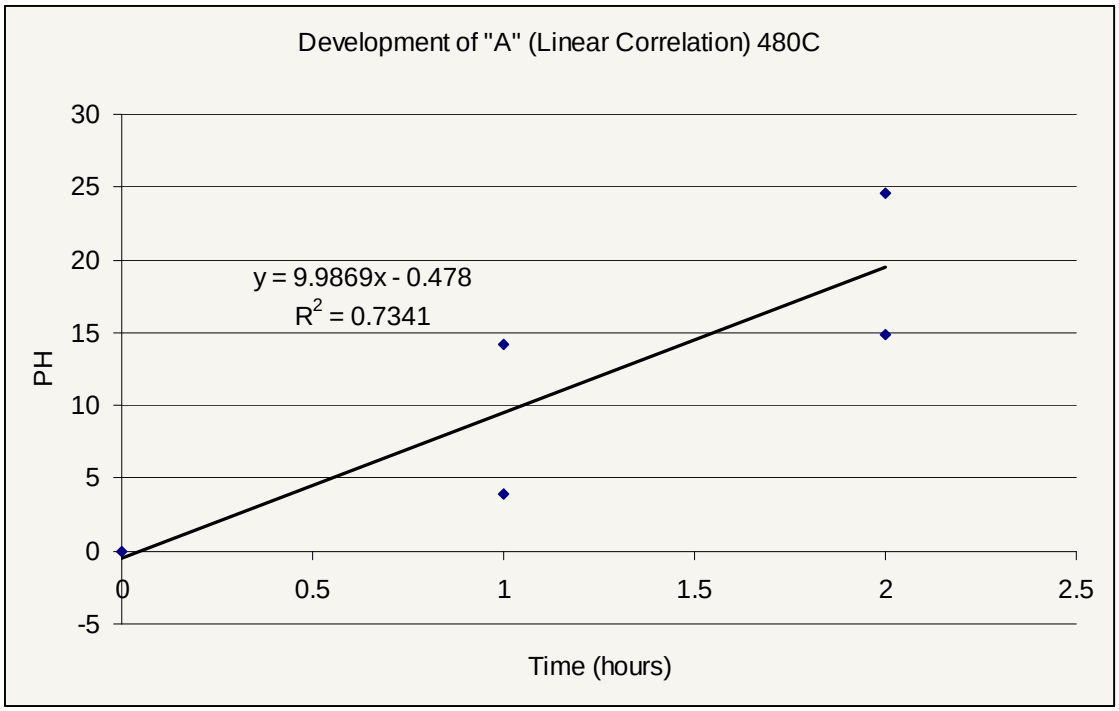

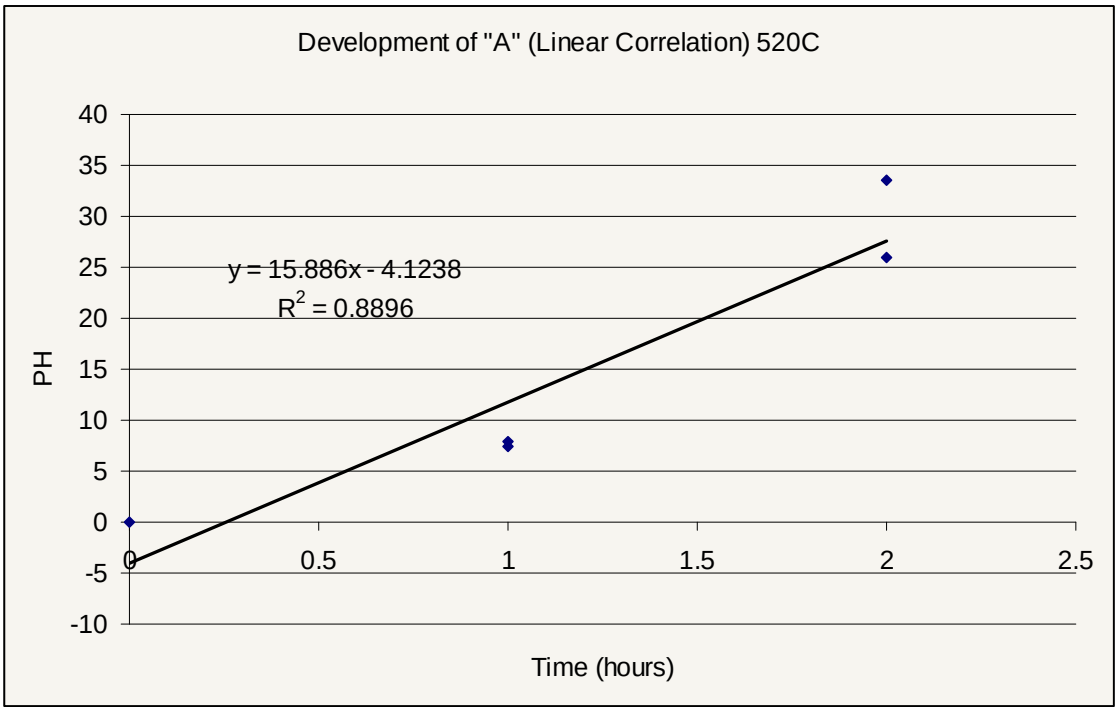
Development of "A" (Linear Correlation) 520C
y = 15.886x - 4.1238
R2 = 0.8896
PH
Time (hours)
40
35
30
25
20
15
10
5
0
-5
-10
0
0.5
1
1.5
2
2.5

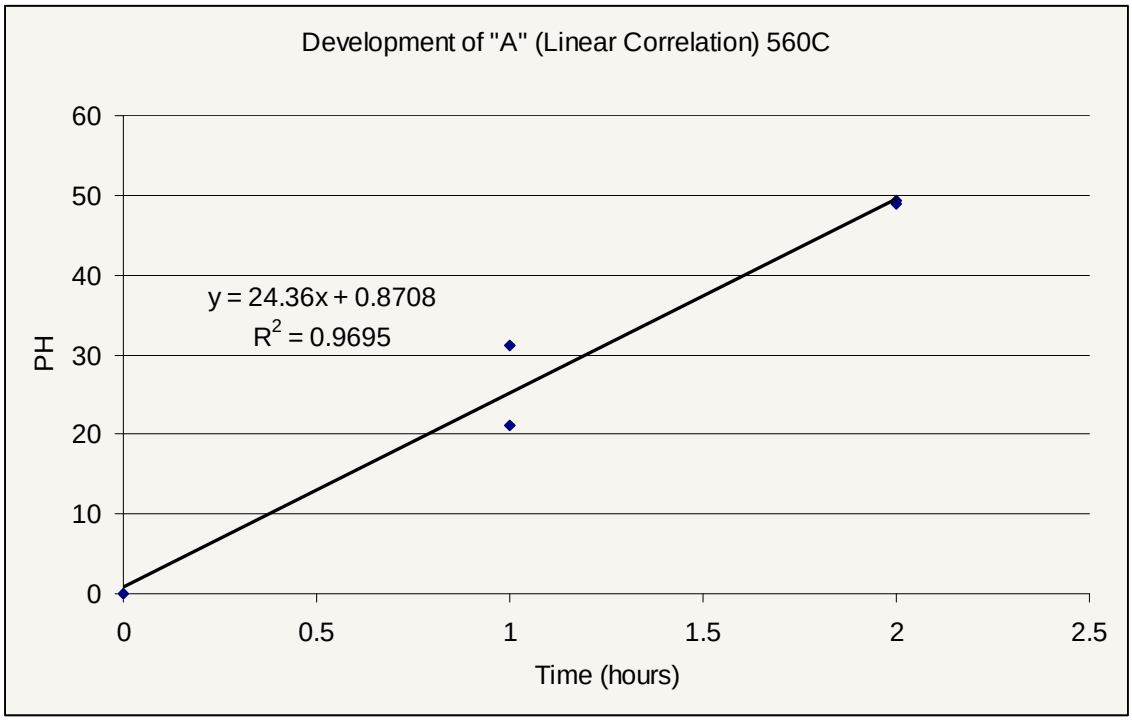
Development of "A" (Linear Correlation) 560C
y = 24.36x + 0.8708
R2 = 0.9695
PH
Time (hours)
60
50
40
30
20
10
0
0
0.5
1
1.5
2
2.5

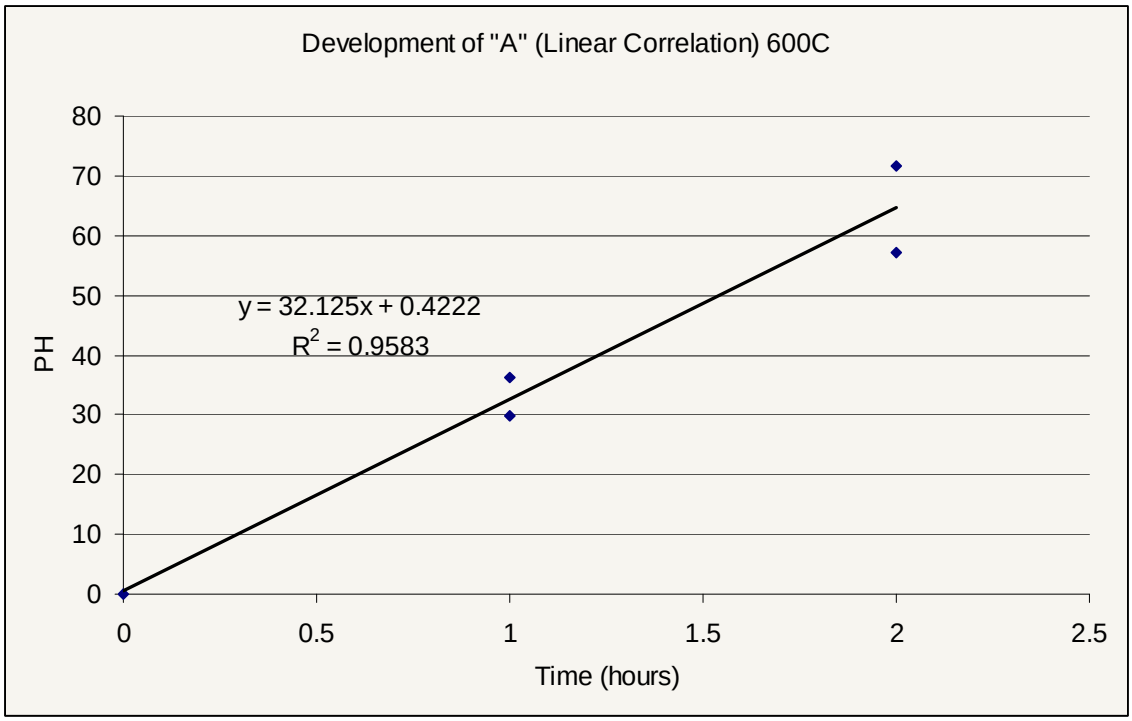
Development of "A" (Linear Correlation) 600C
PH
Time (hours)
y = 32.125x + 0.4222
R2 = 0.9583
0
10
20
30
40
50
60
70
80
0
0.5
1
1.5
2
2.5

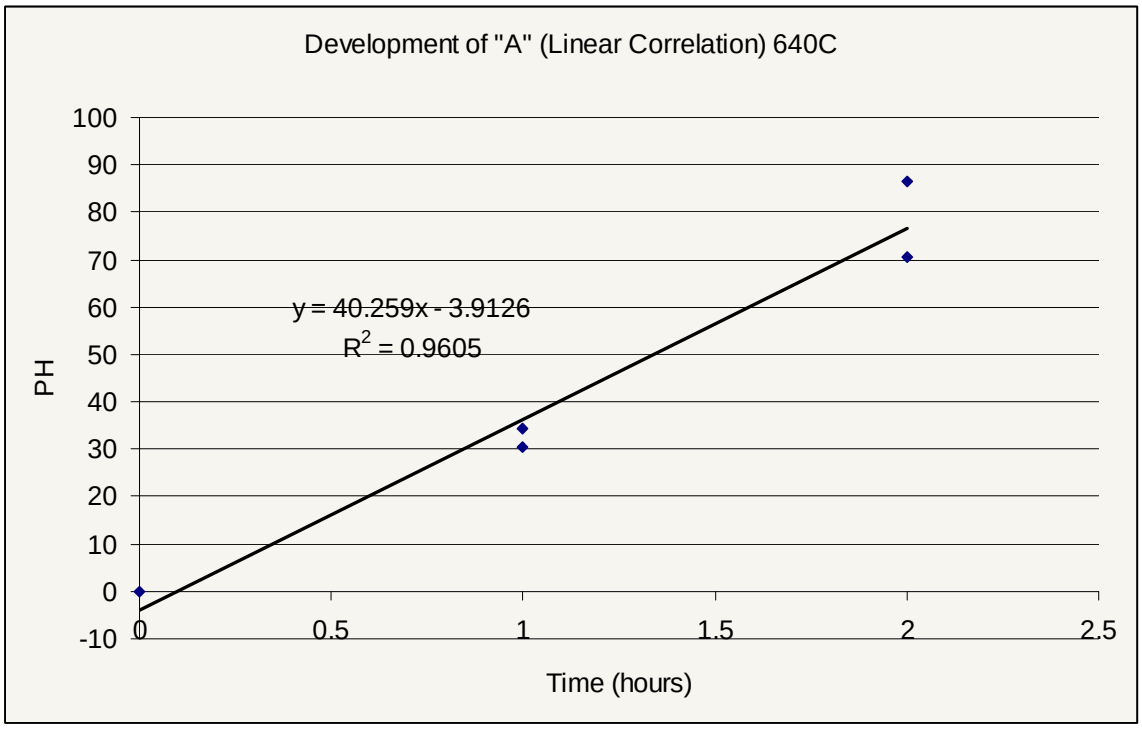
Development of "A" (Linear Correlation) 640C
PH
Time (hours)
y = 40.259x - 3.9126
R2 = 0.9605
-10
0
10
20
30
40
50
60
70
80
90
100
0
0.5
1
1.5
2
2.5

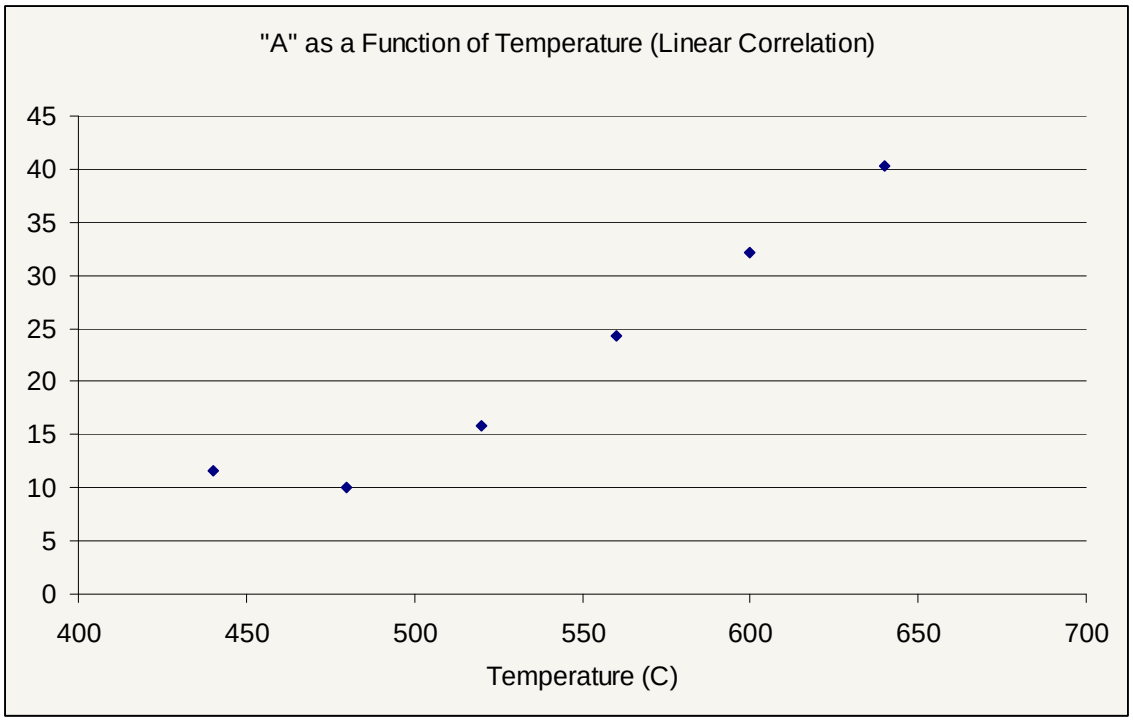
"A" as a Function of Temperature (Linear Correlation)
45
40
35
30
25
20
15
10
5
0
400
450
500
550
600
650
700
Temperature (C)

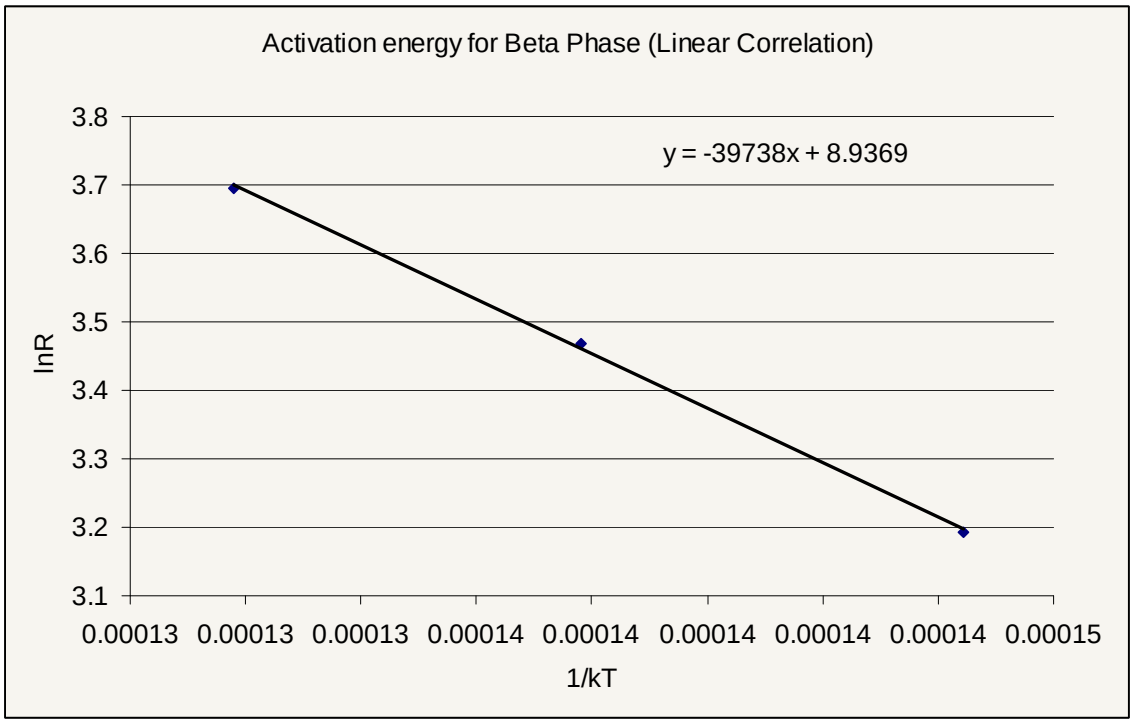
Activation energy for Beta Phase (Linear Correlation)
y = -39738x + 8.9369
3.8
3.7
3.6
3.5
3.4
3.3
3.2
3.1
lnR
0.00013
0.00013
0.00013
0.00014
0.00014
0.00014
0.00014
0.00014
0.00015
1/kT

VITA

Adam Joseph Parkison received his Bachelor of Science degree in nuclear engineering from Purdue University in 2006. He came to Texas A&M University in the Fall of 2006 and graduated with a Master of Science degree in May 2008. His research interests include nuclear materials with an emphasis on new nuclear fuel forms, as well as the recycling of spent nuclear fuel.

Adam Parkison can be reached at Department of Nuclear Engineering Texas A&M University, 3133 TAMU College Station, TX 77843-3133. His email address is ajparkison@tamu.edu.

Publications:

S.M. McDeavitt, A.R. Totemeier, **A. Parkison**, J.J. Wegener and R.D. Kelley, "A Zirconium Matrix Cermet for Storage and Transmutation of Transuranic Isotopes Separated from Spent Nuclear Fuel," 136th TMS Annual Meeting & Exhibition, Symposium on Materials Issues for Advanced Nuclear Systems, Orlando, FL, Feb. 25-Mar. 1, 2007.

S.M. McDeavitt, **A. Parkison**, A.R. Totemeier and J.J. Wegener "Fabrication of Cermet Nuclear Fuels Designed for the Transmutation of Transuranic Isotopes," Accepted to the 6th Pacific Rim International Conference on Advanced Materials and Processing (PRICM-6), Jeju Island, Korea, November 5-9 (2007). Invited international paper

S.M. McDeavitt, **A. Parkison**, A.R. Totemeier and J.J. Wegener "Fabrication of Cermet Nuclear Fuels Designed for the Transmutation of Transuranic Isotopes," Materials Science Forum, 561-565: 1733-1736 (2007).

A.J. Parkison and S.M. McDeavitt, "Hydride/Dehydride of Zircaloy for Use in Fast Reactors," American Nuclear Society Student Conference, Troy, NY, Mar. 30 - April 1, 2006.

S.M. McDeavitt, D.T. Kraemer, **A. Parkinson**, A.R. Totemeier and J.J. Wegener, "Zirconium Matrix Cermet Storage Form and Transmutation Fuel for Transuranics," Proc. of the Am. Nucl. Soc. Winter Meeting, Washington D.C., Nov. 13–17, 2005, ANS Transactions, 93:743 (2005).

Appendix G

Argonne National Laboratory Data Review: Thermophysical Properties of Zirconium Hydride (21 Pages)

Data Review by J. Fink and L. Leibowitz, Argonne National Laboratory

2005 to 2006

Review of Zirconium Hydride Enthalpy Data

(J. .K. Fink and L. Leibowitz, Argonne National Laboratory)

Data Review

Table 1 summarizes the available zirconium hydride enthalpy data [1.2]. These measurements were made relative to zero enthalpy at 273.15 K. Douglas and Victor provided tabulated enthalpy data and average enthalpies used to calculate heat capacities. The enthalpy data of Douglas and Victor are shown as a function of temperature in Figure 1. This figure shows an increase in enthalpy with increasing hydrogen content at the higher temperatures but little or no variation with hydrogen content at low temperatures. Beck reported enthalpy data only in graphical form and showed smoothed curves of calculated heat capacities but not the derivations of the heat capacities from the enthalpy data. The Beck data and smoothed curves, which were obtained by digitizing the published graph via computer, are shown in Figure 2. The three compositions of the measurements by Beck have similar enthalpy increments at low temperature but at high temperature, these data have a different behavior as a function of hydrogen content than the data of Douglas and Victor.

Table 1 Measurements of Enthalpy of ZrHy

Reference	Year	y	T, K	#	Comments
T. B. Douglas & A, C. Victor [1]	1958	0	373-1173	16	H(T)-H(0^oC) measured cal/g; tabulated data – gives individual runs & mean for each temperature – number of mean values (#)listed in column 5
		0.324	373-1173	14	
		0.556	373-1173	15	
		0.701	373-1173	15	
		0.999	373-1173	17	
		1.071	373-1173	13	
R. L. Beck [2]	1962	1.01	532-1060	18	H(T)-H(0^oC) measured in cal/gm; graphical data
		1.33	542-1040	8	
		1.78	547-886	11-	

In their 1968 review of zirconium hydrides, Mueller, Blackledge, and Libowitz [3] concluded that the heat capacities reported by Douglas and Victor were not reliable because of large peaks in heat capacity at the eutectoid temperature. Mueller et al. hypothesize that the samples of Douglas and Victor had not been kept at the eutectoid temperature (see Fig. 4) sufficiently long for the phase transformation to go to completion because no peaks were observed in the heat capacity data reported by Beck at higher H/Zr ratios. However, Figure 3 shows that the enthalpy data reported by Douglas and Victor at H/Zr = 0.999 and 1.071 show good agreement with the graphical data reported by Beck at H/Zr = 1.01. Because the $ZrH_{0.999}$ Douglas and Victor data and the $ZrH_{1.01}$ data of Beck are in reasonable agreement, data from both sets of experiments have been included in this analysis.

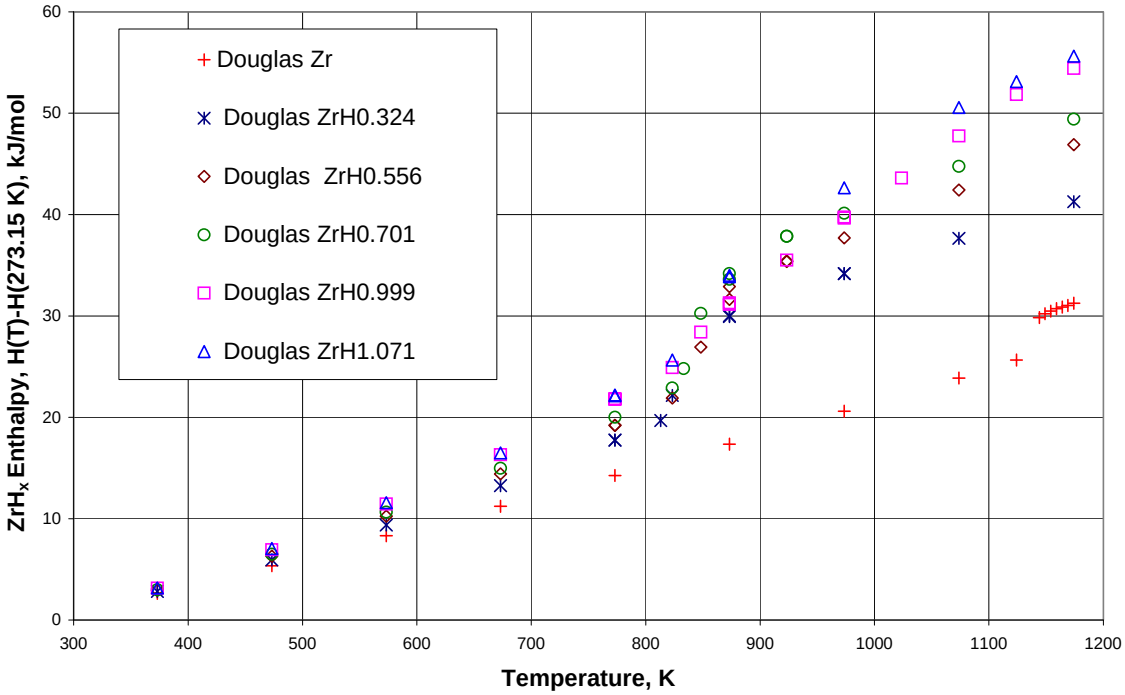

Figure 1 Enthalpy measurements of Douglas and Victor

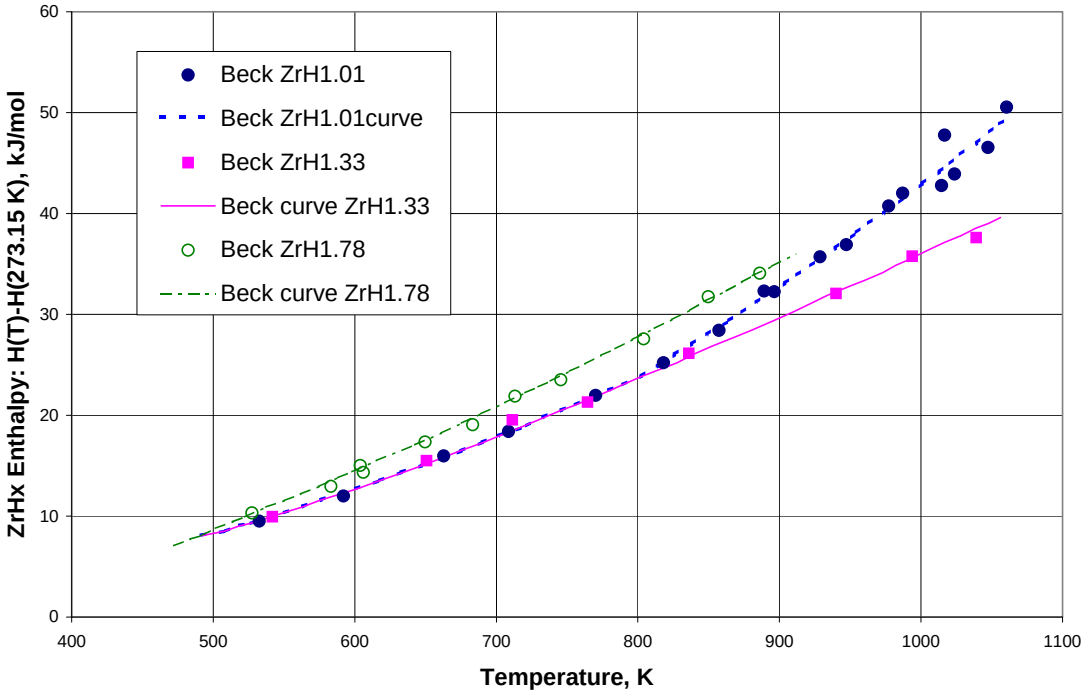

Figure 2 Enthalpy measurements of Beck with Beck's smoothed curves.

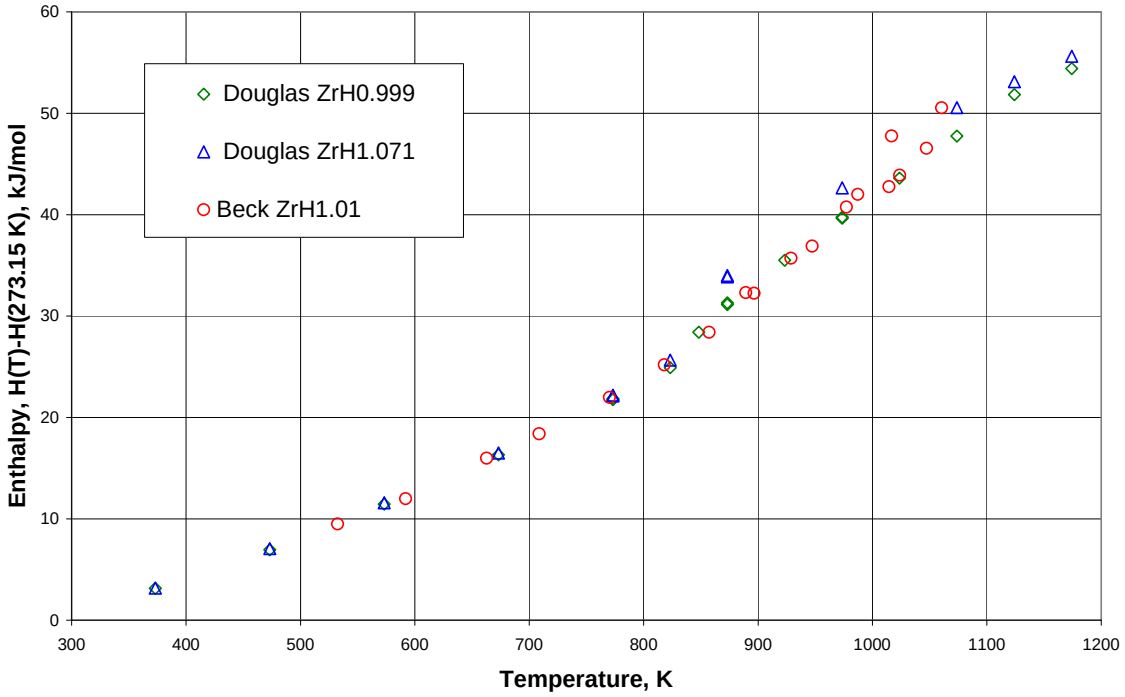

Figure 3 Comparison of the enthalpy data of Douglas and Victor with that of Beck.

Data Analysis

The data were analyzed relative to zero enthalpy at 273.15K because all the enthalpy measurements were made on this basis. After equations were obtained to represent the data, the enthalpy difference H(298.15) – H(273.15K) was determined for each composition from the low temperature fitting equation. Then the constants of all equations were adjusted to obtain equations for H(T) - H(298.15 K). The enthalpy difference was also used to adjust the data to H(T) - H(298.15K).

All the measurements were made prior to 1968 using the 1948 International Practical Temperature Scale (ITPS). Thus, in theory, all temperatures required correction to the 1968 ITPS and then to the 1990 ITPS. However the correction from 1968 ITPS to 1990 ITPS is so small in the temperature range of these data, that it is not significant. The correlations for correction from 1948 ITS to 1968 ITPS, given by Douglas [4], were applied to the data. The corrections were less than 1 K below 1000K and only 1 K from 1000 to 1174K. Because the data of Beck were obtained from their graph, the errors in digitizing these data are on the same order as the temperature correction.

The phase diagram of Dupin et al.[5] has been used to obtain temperatures of the phase transitions for the H-Zr system. Their phase diagram from Figure 3 in Reference 5 has been reproduced with permission in Figure 4.

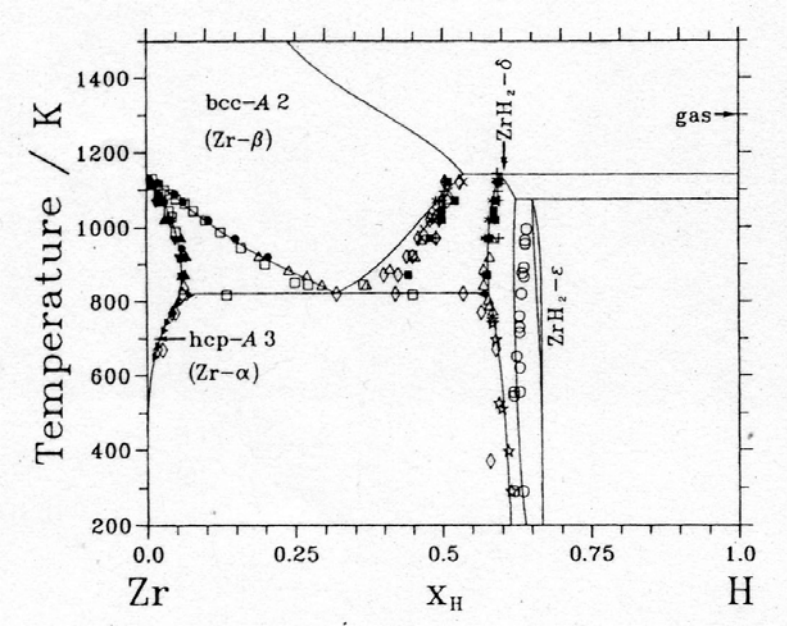

Figure 4 Zr-H phase diagram of Dupin et al. [5], reproduced with permission.

Phase transition temperatures used in this analysis for each ZrH_y composition for which data are available are shown in Table 2. In obtaining phase transition temperatures, the compositions $ZrH_{0.999}$, $ZrH_{1.01}$, and $ZrH_{1.071}$ have all been represented by ZrH because the small composition differences are less than can be determined from the digitized phase diagram. The H/Zr ratio (y) is related to X_H by

$$X_H = y/(1+y).$$

Table 2 Phase Transition Temperatures for ZrH_y

H/Zr (y)	X_H	Temperature, K	
0.324	0.24	821.9	873.6
0.556	0.36	821.9	850
0.701	0.41	821.9	~873[a]
1.0	0.5	821.9	1086
1.33	0.57	821.9	1140.6
1.78	0.64		1074

[a] The value 873 K is based on the data curve in the phase diagram, not the calculated line, which gives ~930 K.

The eutectoid temperature, 821.9 K and the reaction temperatures 1040.6K, 1074 K are the temperatures given for these phase boundaries in Table I "Invariant Reactions" on their web site: www.inpg.fr/ltpcm/base/zircobase. The temperature 873K for the phase

change to the bcc-A2 phase is based on the experimental data shown in Figure 4. This value was used in the data analysis instead of the higher value (930 K) given by the thermodynamically consistent calculated line given in the Dupin et al. web site because the enthalpy measurements are consistent with this lower temperature. The data were first analyzed by us using 930 K for the transition temperature but this analysis gave unrealistically high values for the heat capacity of the intermediate phase and showed that data from 873 K to 930 K were consistent with the linear equation for the higher-temperature phase. The enthalpy data were consistent with a phase change around 873 K, which is the value given by the experimental data shown in Figure 4. This apparent inconsistency between the experimental enthalpy data and the thermodynamically optimized phase diagram needs further study.

Analysis of the Douglas and Victor Data for $ZrH_{0.324}$, $ZrH_{0.556}$, $ZrH_{0.701}$,

In the analysis of the data from 273.15 K to 821.9 K, the regression equations were constrained to give an enthalpy change of zero at 273.15K. Quadratic equations were used to fit the data from 273.15 K to 821.9 K. Both quadratic and linear equations were considered for the high-temperature phases (above 873 K or 850 K) but statistical F tests indicated that the higher order quadratic equations were not justified. Thus, linear equations were selected for the high-temperature range for all compositions.

Attempts were made to fit the data in the intermediate phase using a linear regression analysis. However, little data existed for this phase (3 data points for $ZrH_{0.324,}$ 2 data points for $ZrH_{0.556,}$ 4 data points for $ZrH_{0.701}$) and the resulting equations had unrealistically high slopes. Thus these regression equations are not recommended. Instead linear equations for this phase were estimated assuming the same slope as the higher-temperature phase. Because similar enthalpy changes at the eutectioid boundary 821.9 K may be expected for all compositions along this phase transformation, a constant term based on the enthalpy change for ZrH at this transition was considered. However this gave equations that were too low for the data available for $ZrH_{0.556}$ and $ZrH_{0.701.}$ The constant term was estimated by assuming the line at the mid temperature was half way between the enthalpy increments at the ends of the phase. Note that this line is an estimate not a recommendation. This analysis indicates that enthalpy measurements are needed for all compositions from 821.9 K to 873 K.

Equations for the enthalpy increment relative to zero at 273.15 K were converted to equations relative to zero at 298.15 K by subtracting the enthalpy increment between the enthalpy at 298.15 K and the enthalpy at 273.15 K. For $ZrH_{0.324}$, $ZrH_{0.556}$ and $ZrH_{0.701}$, these enthalpy differences are, respectively, 0.640, 0.693, and 0.714 kJ/mol. The equations for the enthalpy increment, H(T)-H(298.15K). are given below where the enthalpy increment is in kJ/mol and the temperature, T, is in K. The multiple R value for each equation obtained from the Microsoft EXCEL® regression analysis is given after each recommended equation. Graphs showing the data and the fits are given in Figures 5 through 7.

$ZrH_{0.324}$

298.15 K to 821.9 K

$H(T)- H(298.15K) = - 5.99 + 0.01395\ T + 2.06 \times 10^{-5}\ T^2$ (R=0.9993)

821.9 K to 873.6 K

$H(T)- H(298.15K) = - 4.97+ 0.035\ T$ (estimated)

873.6K to 1174 K

$H(T)- H(298.15K) = - 0.863+ 0.0353\ T$ (R= 0.9995)

$ZrH_{0.556}$

27 3.15 K to 821.9 K

$H(T)- H(298.15K) = - 6.46 + 0.0150\ T + 2.24 \times 10^{-5}\ T^2$ (R=0.9998)

821.9 K to 850 K

$H(T)- H(298.15K) = - 14.2+ 0.048\ T$ (estimated)

850 K to 1174 K

$H(T)- H(289.15K) = - 10.18+ 0.04825T$ (R= 0.996)

$ZrH_{0.701}$

27 3.15 K to 821.9 K

$H(T)- H(298.15K) = - 6.56 + 0.01486\ T + 2.40 \times 10^{-5}\ T^2$ (R=0.9996)

821.9 K to 873K

$H(T)- H(298.15K) = - 12.6+ 0.048\ T$ (estimated)

873 K to 1174 K

$H(T)- H(298.15K) = - 8.12+ 0.0486\ T$ (R= 0.996)

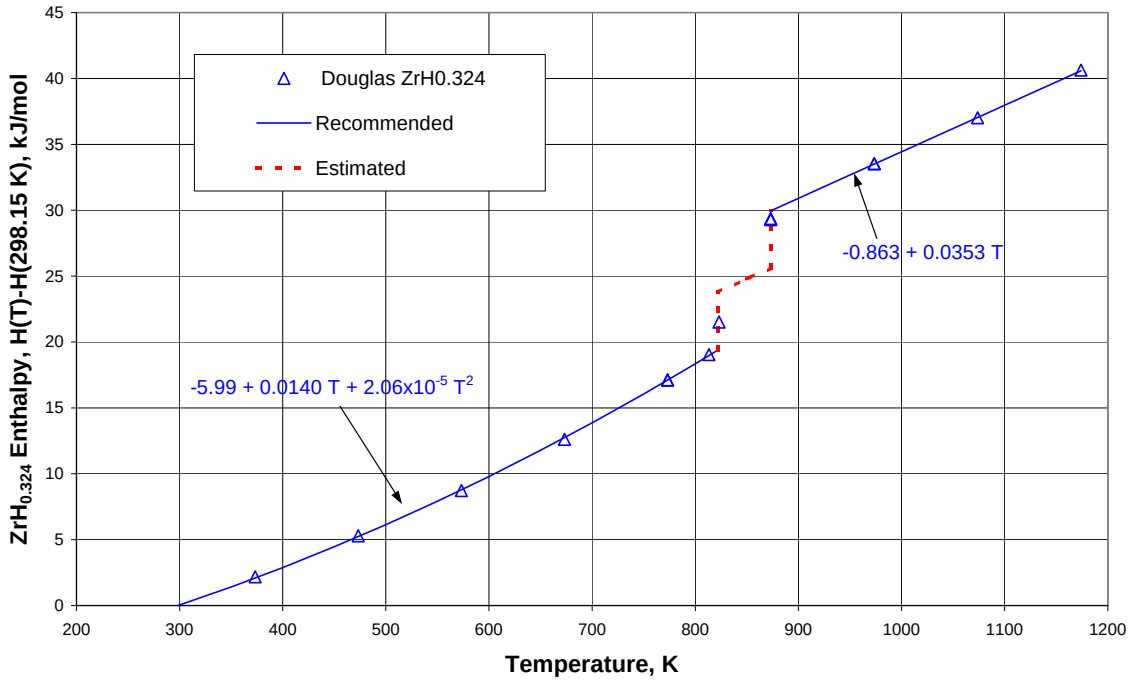

Figure 5 Fits to $ZrH_{0.324}$ Enthalpy Data of Douglas and Victor.

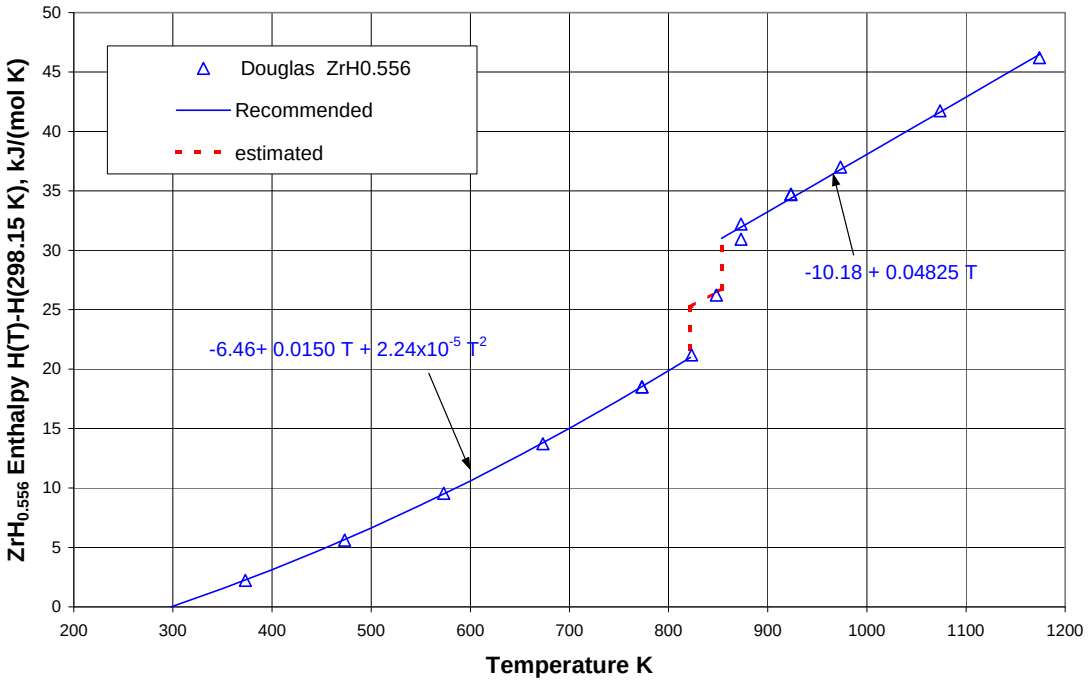

Figure 6 Fits to $ZrH_{0.556}$ Enthalpy Data of Douglas and Victor.

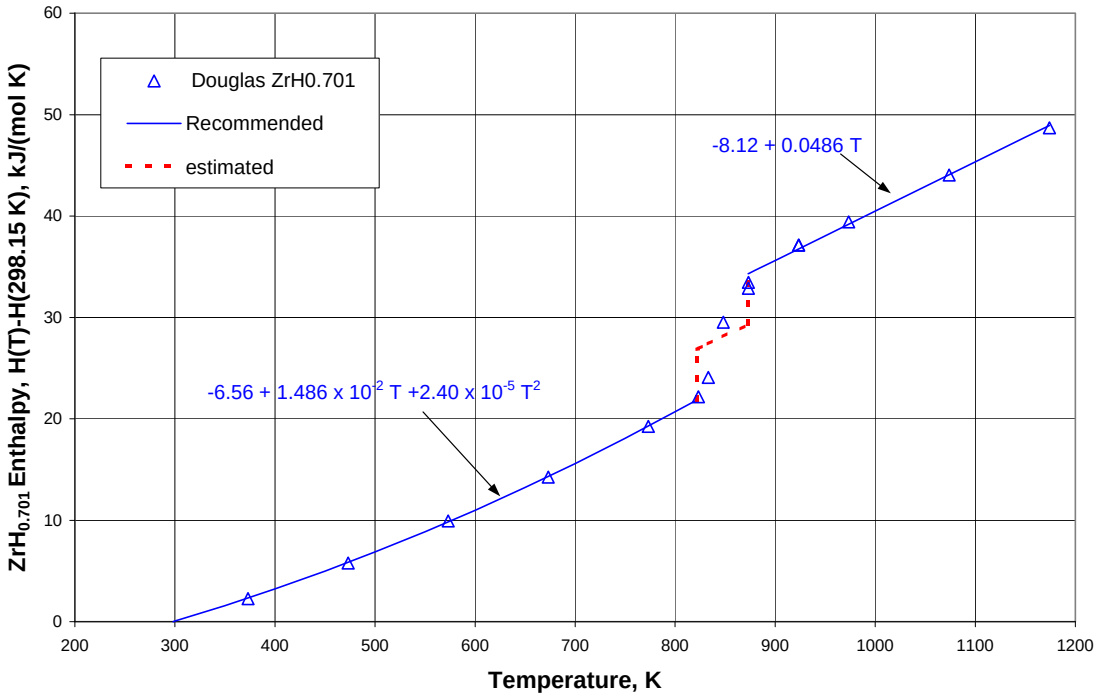

Figure 7 Fits to $ZrH_{0.701}$ Enthalpy Data of Douglas and Victor.

Analysis of Data for $ZrH_{0.999}$, $ZrH_{1.01}$, and $ZrH_{1.071}$

Figure 3 showed reasonable agreement between the $ZrH_{1.01}$enthalpy measurements of Beck[2] and the Douglas and Victor[1]enthalpy measurements of $ZrH_{0.999}$ and $ZrH_{1.071}$. In analysis of these data, a number of different ways to fit them were considered. First, all the three sets of data were fit together to three equations for the three temperature ranges. Secondly, the $ZrH_{1.071}$data of Douglas and Victor was fit separately from the $ZrH_{0.999}$ data and $ZrH_{1.01}$ data because the $ZrH_{1.071}$ data seem high at higher temperatures. Examination of the resulting equations showed that the equations for $ZrH_{1.01}$ alone did not differ significantly from the fits to the $ZrH_{0.999}$ data and $ZrH_{1.01}$ data. This may be because some $ZrH_{1.01}$ data of Beck are of similar magnitude to the $ZrH_{1.071}$ data. Thus, the equations obtained from the combined fits to the three compositions are recommended for representing the enthalpy increment of ZrH.

The 18 data from 273.15 K to 821.9 K were fit to a quadratic equation using Microsoft EXCEL® regression analysis with the constraint that the enthalpy increment at 273.15K is zero. Both quadratic and linear equations were considered for the 26 data in the temperature range 821.9 K to 1086 K. These two fits were almost identical with similar R values indicating that the quadratic equation is not justified statistically. However, the quadratic equation gave a lower value at the phase transition temperature 1086K. A linear equation was used to fit the 4 data above 1086 K. The value of the high-temperature linear equation at the phase transition was 0.05 kJ/mol higher than the value from the quadratic fit but 0.34 kJ/mol lower than the value from the linear equation.

These small variations at the phase transition indicates that the phase transition enthalpy change is small. An attempt was made to fit all the data in both phases to a quadratic equation but this was rejected because the data above 1086K clearly have a different slope that could not be reproduced using a quadratic equation. Because only 4 data are available above 1086 K and these analyses indicate a very small if any change at the phase transition, the data above 1086 K were refit to a linear equation with the constraint that the value at 1086 was equal or greater than the value obtained at the phase transition from the 821.9K-1086K linear equation. The resulting equation gave zero for the enthalpy change at 1086K.

The enthalpy increment from 273.15 K to 298.15 K (0.733 kJ/mol) was used to convert the equations to enthalpy relative to zero enthalpy at 298.15 K. The recommended equations for the ZrH enthalpy increments H(T)-H(298.15 K) in kJ/mol and temperature, T, in K are given below and shown with the data in Figure 8.

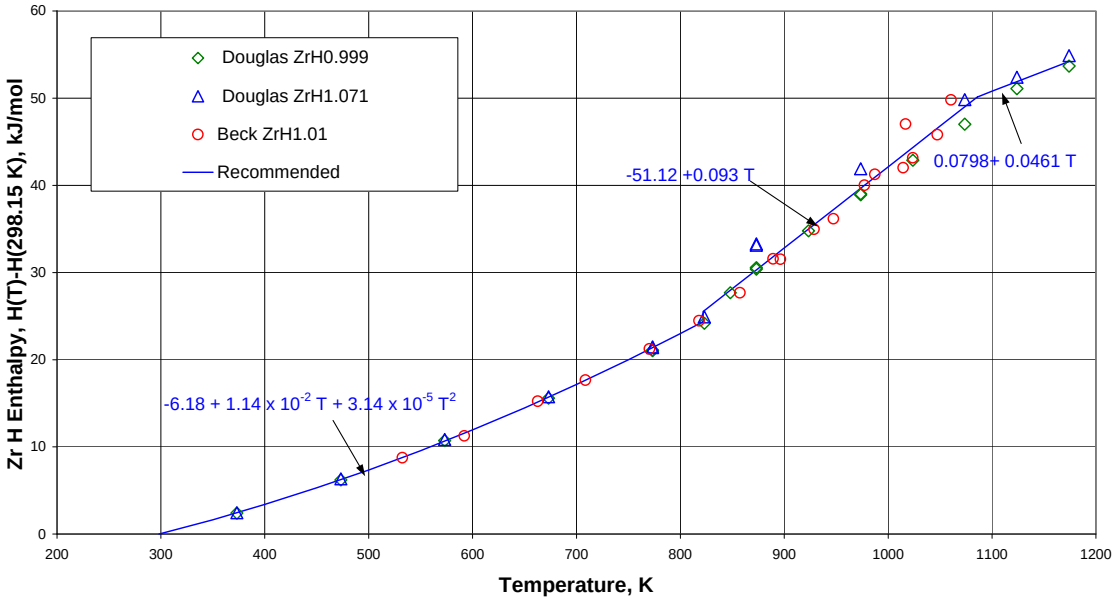

Figure 8 Fits to the $ZrH_{0.999}$, $ZrH_{1.071}$ and $ZrH_{1.01}$ enthalpy data.

ZrH

27 3.15 K to 821.9 K

$H(T)- H(298.15K) = - 6.18+ 0.01136\ T + 3.14x10^{-5}\ T^2$ (R=0.9997)

821.9K to 1086K

$H(T)- H(273.15K) = - 51.12 + 0.09326\ T$ (R=0.9803)

1086K to 1174 K

$H(T)- H(273.15K) = 0.798+ 0.04611T$ (R=0.89)

Analysis of the Beck Data for $ZrH_{1.33}$

The smooth curve through Beck's $ZrH_{1.33}$ enthalpy data (Figure 2) and the curve suggested by Beck to represent the heat capacity [2] are consistent with a single quadratic plus 1/T equation throughout the measurement range. It appears that the curve shown by Beck was not obtained with a constraint to give zero at 273.15 K.

Only 4 data are available from 273.15 to 821.9 K and 4 data are available for the higher phase. The 4 low temperature data were fit to a quadratic equation constrained to give zero at 273.15 K. The high-temperature data were fit to a linear equation. These equations gave a 0.13 kJ/mol for the enthalpy change at the phase transition, which is within the uncertainty in the data. Because the enthalpy increment at the phase transition is so small and Beck selected a single equation for the entire temperature range, a single quadratic equation for the entire temperature range was considered. The data for the entire temperature range were fit using a quadratic equation constrained to zero at 273.15K. Comparison of the variances from the two-equation representation and the single-equation fit indicated that two equations are not statistically justified. Thus, a single equation is recommended for the entire temperature range of data. The enthalpy increment, H(298.15 K)-H(273.15 K) =0.861 kJ/mol was used to express the equation relative to zero enthalpy at 298.15 K. The equation shown in Figure 9 and given below is recommended for the $ZrH_{1.33}$ enthalpy increments H(T)-H(298.15 K) in kJ/mol and temperature, T, in K.

$ZrH_{1.33}$

298.15 K to 1050 K

$$H(T)- H(273.15K) = - 8.48 + 0.02208T + 2.13x10^{-5} T^2 \quad (R=0.9986)$$

Analysis of the Beck Data for $ZrH_{1.78}$

The 11 data of Beck are in a single phase. They were fit to a quadratic equation constrained to give zero at 273.15 K. Because the heat capacity curves given by Beck are consistent with an enthalpy equation that included both quadratic and 1/T terms, this form of equation was also considered. However, statistical analysis indicated that the additional 1/T term is not justified by the enthalpy data. The enthalpy increment between 273.15 K and 298.15 K, 0.768 kJ/mol, was used to obtain an equation relative to zero enthalpy at 298.15 K. Figure 10 shows the data and fit. The recommended equation for the enthalpy increment H(T)-H(298.15 K) in kJ/mol with temperature, T, in K is

$ZrH_{1.78}$

298.15 K to 900 K

$$H(T)- H(298.15K) = - -5.67+ 6.22x10^{-3} T + 4.29x10^{-5} T^2 \quad (R=0.9990)$$

A graph of the data and fit is shown in Figure 10.

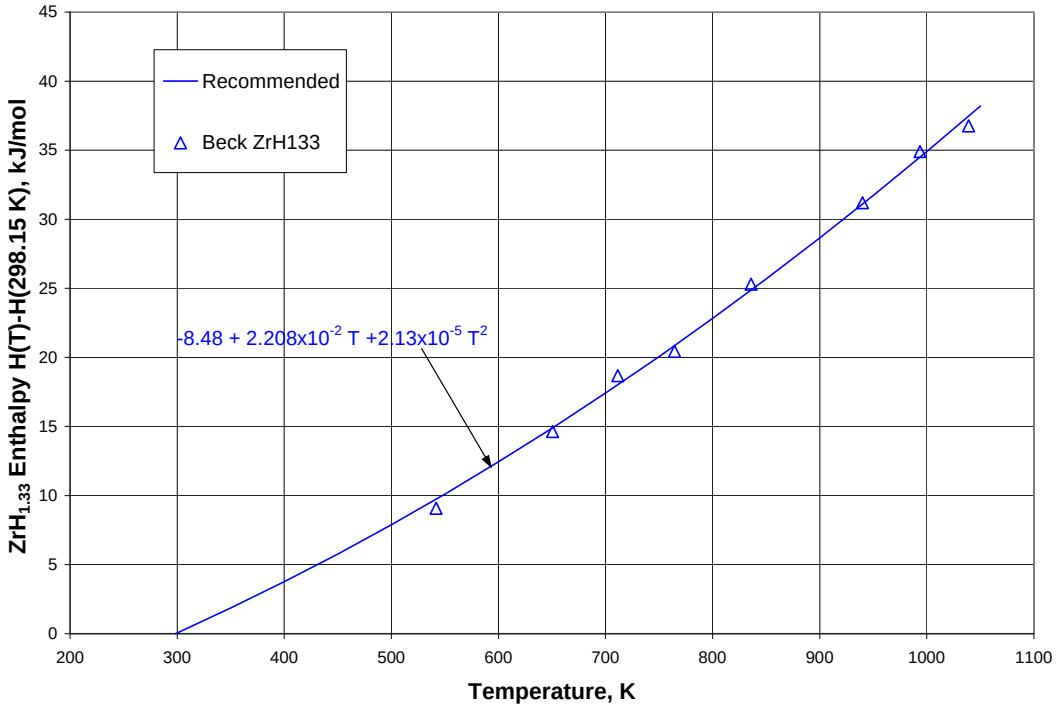

Figure 9 Fit to $ZrH_{1.33}$ enthalpy data of Beck

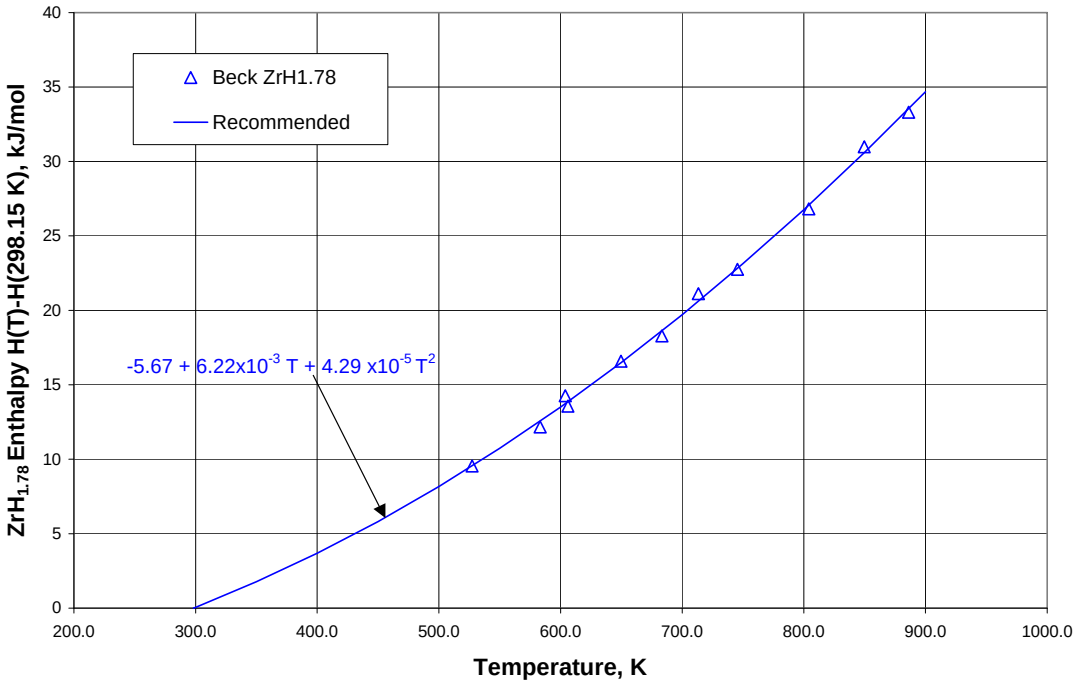

Figure 10 Fit to $ZrH_{1.78}$ enthalpy data of Beck

Summary of Recommendations

The ZrH_y enthalpy data of Douglas and Victor[1] and of Beck[2] have been analyzed to obtain equations to represent the enthalpy increments. Quadratic equations provide a good representation of enthalpy increments of $ZrH_{0.324}$, $ZrH_{0.556}$, $ZrH_{0.701}$ and ZrH in the low-temperature phase. In the intermediate-temperature phase, insufficient data are available for $ZrH_{0.324}$, $ZrH_{0.556}$, and $ZrH_{0.70}$ data to determine a reliable equation. Statistical analysis indicated that the ZrH data in the intermediate-temperature phase are best represented by a linear equation. Linear equations also provide the best representation of the enthalpy increments of $ZrH_{0.324}$, $ZrH_{0.556}$, $ZrH_{0.70}$, and ZrH in the high-temperature phase. Quadratic equations provide good representation of the enthalpy increments of $ZrH_{1.33}$, and $ZrH_{1.78}$ for the entire temperature range of data.

Recommended values for the enthalpy increments for ZrH_y calculated from these equations relative to zero at 298.15 K are given in Table 3. This analysis indicates enthalpy measurements are needed from 821.9 to 900 K for H/Zr <1

Table 3 Recommended ZrH_y Enthalpy Increments Relative to298.15 K,

T, K	H(T,K) –H(298.15 K), kJ/mol					
y	0.324	0.556	0.701	1	1.33	1.78
298.15	0.00	0.00	0.00	0.00	0.00	0.00
300	0.05	0.06	0.06	0.05	0.06	0.06
350	1.4	1.5	1.6	1.6	1.9	1.8
400	2.9	3.1	3.2	3.4	3.8	3.7
450	4.5	4.8	5.0	5.3	5.8	5.8
500	6.1	6.6	6.9	7.4	7.9	8.2
550	7.9	8.6	8.9	9.6	10.1	10.7
600	9.8	10.6	11.0	11.9	12.4	13.5
650	11.8	12.8	13.2	14.5	14.9	16.5
700	13.9	15.0	15.6	17.2	17.4	19.7
750	16.1	17.4	18.1	20.0	20.1	23.1
800	18.4	19.9	20.7	23.0	22.8	26.8
821.9	19.4	21.0	21.9	24.4	24.1	28.4
821.9				25.5	24.1	28.4
850				28.2	25.7	30.6
853.5		31.0		28.5	25.9	30.9
873		31.9	34.3	30.3	27.0	32.5
873.6	30.0	32.0	34.3	30.4	27.1	32.5
900	30.9	33.2	35.6	32.8	28.6	34.7
950	32.7	35.7	38.1	37.5	31.7	
1000	34.4	38.1	40.5	42.1	34.9	
1050	36.2	40.5	42.9	46.8	38.2	
1086	37.5	42.2	44.7	50.2		
1086	37.5	42.2	44.7	50.2		
1100	38.0	42.9	45.3	50.8		
1150	39.7	45.3	47.8	53.1		
1174	40.6	46.5	49.0	54.2		

References

1. T. B. Douglas and A. C. Victor, “Heat content of zirconium and of five compositions of zirconium hydride from 0^{o} to 900^{o} C,” J. Res. Nat. Bureau of Standards, 61 (1958), 13-23.

2. R. L. Beck, “Thermophysical properties of zirconium hydride,” Trans. ASM 55 (1962) 556-563.

3. William M. Mueller, James P. Blackledge, and George G. Libowitz, “Metal Hydrides,” Academic Press, New York (1968) 241-330.

4. T. B. Douglas, “Conversion of Existing Calorimetrically Determined Thermodynamic Properties to the Basis of the International Practical Temperature Scale of 1968,” J. Research NBS-A, 73A (1969) 451-470.

5. N. Dupin, I. Ansara, C. Servant, C. Toffolon, C. Lemaignan, and J. C. Brachet, “A thermodynamic database for zirconium alloys, J. Nucl. Mat. 275 (1999) 287-295.

ANL 2005 Report

A literature search on the thermophysical properties of zirconium hydride has been completed. Search results are summarized in Tables 1- 9. Data tabulated in the papers have been entered into the computer for analysis. Graphs with data have been scanned and the data extracted by a digitization program for analysis.

Table 1 Heat Capacity of ZrH_x

Reference	Year	x	T, K	#	Comments
Flowtow & Osbourne	1961	2.0	6.5-345.4	65	tabulated data, low T eq, 5 series of measurements
W. J Tomasch	1961	1.58	282-768	8	gives error bars for data
R. L. Beck (ref 3)	1962	1.33	825-1054	-	cal/mol Zr; curves no data, H-H(0) measured
		1.78	473-921	-	
C. C. Weeks	1967	1.58	273-1173		Snap Fuel, 4% U, curves no data
		1.65	273-1173		
		1.7	273-1173		
		1.81	273-1173		
F. Ducastelle	1970	1.55	1.84-8.04	38	Cp/T vs T^2
		1.96	1.74-8.34	43	
		1.84	2.07-8.36-	48	
S. Yamanaka et al	2001	0.0	366-700	7	Read from graph
		1.53	366-700	7	
		1.58	366-700	7	
Uno	2004	0.0	366-700	6	Read from graph – same group as Yamanaka – note changes in H/Zr ratio
		1.53	366-700	6	
		1.57	366-700	3	
		1.57	396-648	-	scanning - line

Table 2 Enthalpyof ZrH_x

Reference	Year	x	T, K	#	Comments
T. B. Douglas & A, C. Victor	1958	0	373-1173	16	H-H(0) measured cal/g; tabulated data –gives individual runs & mean for each temperature - # of mean values listed in column 5
		0.324	373-1173	14	
		0.556	373-1173	15	
		0.701	373-1173	15	
		0.999	373-1173	17	
		1.071	373-1173	13	
R. L. Beck (ref 3)	1962	1.01	532-1060	18	H-H(0) measured, cal/gm
		1.33	542-1040	8	
		1.78	547-886	11-	

Table 3 Thermal Diffusivity of ZrH_x

Reference	Year	x	T, K	#	Comments
C. C. Weeks	1967	1.58	273-1173	-	Snap Fuel, 4% U, curves no data
		1.65	273-1173	-	
		1.7	273-1173	-	
		1.81	273-1173	-	
S. Yamanaka et al.	2001	0.0	290-573	7	Read from graph
		1.49	292-621	15	
		1.56	287-665	16	
		1.59	288-670	16	
		1.66	285-663	15	
B. Tsuchiya et al.	2001	1.76	294-607	37	Read from graph – heating & cooling cycles separate
		1.83	293-627	27	
		1.90	293-620	32	
		1.94	294-613	39	

Table 4 Thermal Conductivity of ZrH_x

Reference	Year	x	T, K	#	Comments
R. L. Beck (ref 3)	1962	0.83	485-1180	31	read from graph, cal/(cm-s-C) comparative method
		1.33	520-1100	35	
		1.78	573-997	32	
S. Yamanaka et al	2001	0.0	288-573	7	Read from graph
		1.49	292-672	17	
		1.56	287-664	15	
		1.59	287-670	16	
		1.66	285-662	13	
B. Tsuchiya et al.	2001	1.6	300-620	-	curves calculated from thermal diffusivity & literature Cp & density
		1.76			
		1.83			
		1.90			
		1.94			

Table 5 Thermal Expansion of ZrH_x

Reference	Year	x	T, K	#	Comments
R. L. Beck (ref 3)	1962	0.69	330-1115	-	curves – no data; micro in/in
		1.01	330-1170	-	
		1.54	330-1145		
		1.83	330-850	-	
R. L. Beck (ref 3)	1962				Average expansion coefficient for each phase reported
S. Yamanaka et al (ref 9)	1999	1.56 to 1.68	-	6	Coefficient as function of H/Zr, points read from graph, equation

Table 6 Density of ZrH_x

Reference	Year	x	T, K	#	Comments
M. T. Simnad	1981		room temp	-	2 eqs as funct of H/Zr. H/Zr <1.6, H/Zr >1.6
		0-1.93	room temp	16	data attributed to Beck
		1.7-2	room temp	11	data attributed to Korst

Table 7 Lattice Parameters for ZrH_x

Reference	Year	x	T, K	#	Comments
R. L. Beck (ref 3)	1962	0.69	330-1115	-	curves – no data; micro in/in
		1.01	330-1170	-	
		1.54	330-1145		
		1.83	330-850	-	
R. L. Beck (ref 13)	1962	1.47-1.92	room temp	12	room temperature, a for each phase as function of %H
		1.66-1.92	room temp	7	room temperature c for epsilon phase as fnc %H
Moore & Young	1968	1.64	297-1033	6	a, fcc
		1.67	297-573	6	a. fcc; a,c fct at 297
		1.70	297-977	10	a fcc; a, c fct (6 values)
		1.73	297-889	9	3 a fcc 6 a,c fct
		1.76	297-866	4	a fcc at 866 3a, c fct
		1.81	297-977	11	2 a fcc;at 955, 977; a, c fct
F. Ducastelle et al.	1970	1.55 to 1.96	room temp	7	lattice parameters, a, c
J. S. Cantrell et al.	1984	1.99 to 1.70	108-293	21	a, c, epsilon phase fct delta l/l delta t; V as H/Zr
		1.7 to 1.5	108-293	8	a in delta phase fcc delta l/l delta t; V as H/Zr
R. C. Bowman et al	1985	1.99-1.7	293	10	unannealed, a, c, epsilon phase – some of Cantrell data reanalyzed
		1.7-1.5	293	6	unannealed, a, delta phase – some of Cantrell data reanalyzed
		1.99-1.71.	293	9	after annealing at 525 C, epsilon phase
		1.7-1.5	293	6	after annealing at 525 C, epsilon phase
S. Yamanaka et al. (ref 16)	1999	1.56 to 1.68	-room temp	6	lattice parameter a (nm); equation

Table 8 Compressibility of ZrH_x

Reference	Year	x	T, K	#	Comments
S. Yamanaka et al	2001	0	room temp	1	Points read from graph
		1.47		1	
		1.54		1	
		1.64		1	
		1.66		1	

Table 9 Electrical Conductivity & Electrical Resistivity of ZrH_x

Reference	Year	x	T, K	#	Comments
P. W. Bickel and T G. Berlincourt	1970	1.54	1.1-300	4	tabulated data, hall coefficients & structure from x-ray diffraction
		1.59	1.1-300	3	
		1.62	1.1-300	3	
		1.63	1.1-300	3	
		1.64	1.1-300	4	
		1.74	1.1-300	3	
		1.81	1.1-300	4	
		1.87	1.1-300	3	
		1.90	1.1-300	3	
		1.96	1.1-300	4	
S. Yamanaka et al	2002	0	293-673	9	Conductivity data read from graph; curve through Zr data; curve through combined ZrHx data
		1.56		9	
		1.61		9	
		1.66		9	
M. Uno et al.	2004	0	293-673	9	Resistivity data read from graph - same data + 3 points graphed as resisitivity; curve through combined ZrHx data
		1.56		9	
		1.61		10	
		1.66		11	

Initial comparisons of enthalpy and heat capacity data indicate reasonable agreement from measurements by different groups. Figure 1 shows a comparison of the enthalpy measurements by Douglas and Victor [8] for $ZrH_{0.999}$ and $ZrH_{1.071}$ with those of Beck [3] for $ZrH_{1.01}$. Figure 2 compares $ZrH_{1.58}$ heat capacity data from two investigators with an empirical equation given by Yamanaka et al. [10].

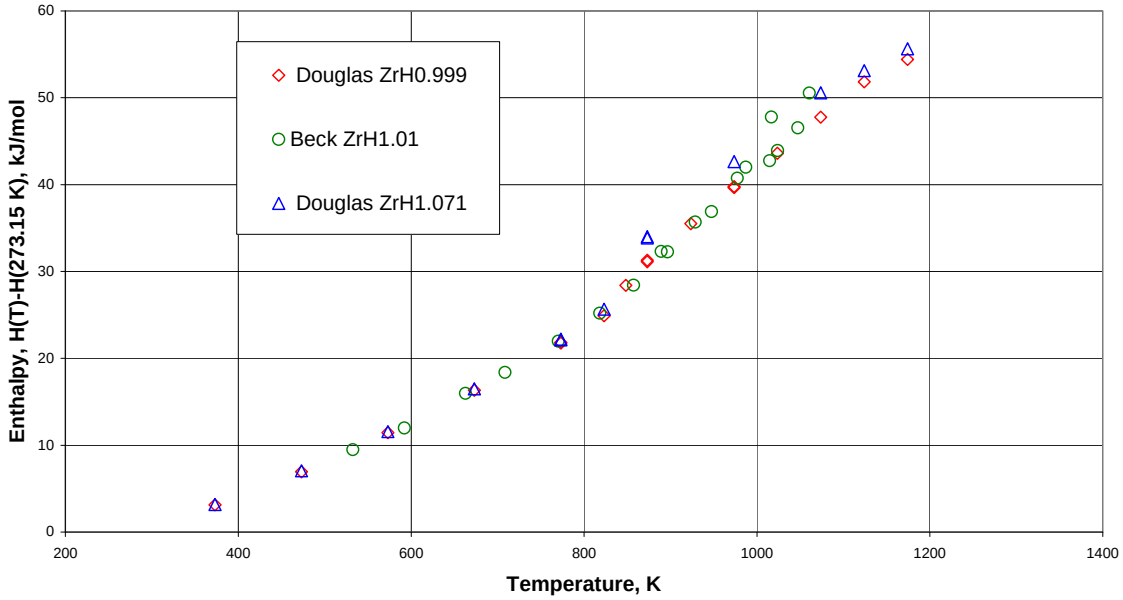

Figure 1 Enthalpy of ZrH_x as a function of temperature.

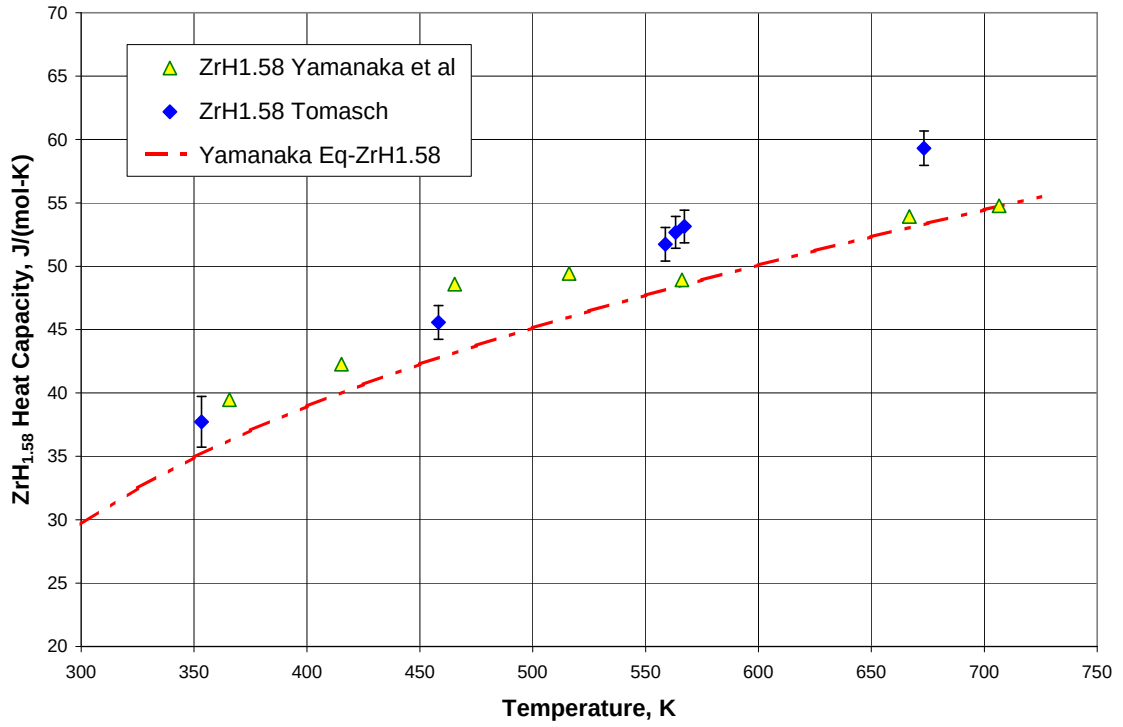

Figure 2 Heat capacity of $ZrH_{1.58}$ compared with empirical equation.

References

1. H. E. Flotow and D. W. Osborne, "Heat capacities and thermodynamic functions of ZrH_2 and ZrD_2 from 5 to 350 K and the hydrogen vibration frequency in ZrH_2," J. Chem Phys. 34 (1961) 1418-1425.

2. W. J Tomasch, "Specific heats of delta-phase Zr-H and Zr-D," Phys. Rev. 123 (1961), 510-514.

3. R. L. Beck, "Thermophysical properties of zirconium hydride," Trans. ASM 55 (1962) . 556-563.

4. C. C. Weeks, M. M. Nakata, and C. A. smith, "Thermal properties of SNAP Fuels", Proceedings of the Seventh Conference on Thermal Conductivity, (1967) 387-398.

5. F. Ducastelle, R. Caudron, and P. Costa, "Proprietes electroniques des hydrures," Le J. de Phys. 31 (1970) 57-64.

6. S. Yamanaka, K. Yamada, K. Kurosaki, M. Uno, K. Takeda, H. Anada, T. Matsuda, and S. Kobayashi, "Thermal properties of zirconium hydride," J. Nucl. Mater. 294 (2001) 94-98.

7. M. Uno, K. Yamada, T. Maruyama, H. Muta, and S. Yamanaka, "Thermophysical properties of zirconium hydride and deuteride,"J. Alloys Comp. 366 (2004) 101-106.

8. T. B. Douglas and A. C. Victor, "Heat content of zirconium and of five compositions of zirconium hydride from 0^o to 900^o C," J. Res. Nat. Bureau of Standards, 61 (1958), 13-23.

9. B. Tsuchiya, J. Huang, K. Konashi, M. Teshigawara, and M. Yamawaki, "Thermophysical properties of zirconium hydride and uranium-zirconium hydride," J. Nucl. Mater. 289 (2001) 329-333.

10. S. Yamanaka, K. Yoshioka, M. Uno, M. Katusra, H. Anada, T. Matsuda, and S. Kobayashi, "Thermal and Mechanical properties of zirconium hydride," J. Alloys Comp. 293-295 (1999) 23-29.

11. M. T. Simnad, "The U-ZrH_x alloy: Its properties and use in TRIGA fuel," Nucl. Eng. Des. 64 (1981) 403-422.

12. K. E. Moore and W. A. Young, "Phase studies of the Zr-H system at high hydrogen concentrations," J. Nucl. Mater. 27 (1968) 316-324.

13. R. L. Beck, "Zirconium-hydrogen phase system," Trans. ASM 55 (1962) 542-555.

14. J. S. Cantrell, R. C. Bowman, Jr., and D. B. Sullenger, “X-ray diffraction and nuclear magnetic resonance studies of the relationship between electronic structure and the tetragonal distortion in ZrH_x,”J. Phys. Chem. 88 (1984) 918-923.

15. R. C. Bowman, Jr., B. D. Craft, J. S. Cantrell, and E. L. Venturini, “Effects of thermal treatments on the lattice properties and electronic structure of ZrHx,” Phys. Rev. B 31 (1985) 5604-5614.

16. S. Yamanaka, K. Yoshioka, M. Uno, M. Katsura, H. Anada, T. Matsuda, and S. Kobayashi, “Isotope effects on the physiochemical proerties of zirconium hydride,” J. Alloys Comp. 293-295 (1999) 908-914.

17. P. W. Bickel and T. G. Berlincourt, “Electrical properties of hydrides and deuterides of zirconium,” Phys. Rev B 2 (1970) 4807-4813

18. S. Yamanaka, K. Yamada, K. Kurosaki, M. Uno, K. Takeda, H. Anada, T. Matsuda, and S. Kobayashi, “Characteristics of zirconium hydride and deuteride,” J. Alloys Comp. 330-332 (2002) 99-104.

Appendix H

Master of Science Thesis: Hot Extrusion Method (95 Pages)

EVALUATION OF A ZIRCONIUM-MATRIX CERMET FOR THE STORAGE AND TRANSMUTATION OF TRANSURANIC ISOTOPES

A Thesis

Submitted to the Faculty of
Purdue University

By

Aaron Robert Totemeier

In Partial Fulfillment of the Requirements for the Degreeof
Master of Science Nuclear Engineering

August 2006

EVALUATION OF A ZIRCONIUM-MATRIX CERMET FOR THE STORAGE AND TRANSMUTATION OF TRANSURANIC ISOTOPES

A Thesis

Submitted to the Faculty

of

Purdue University

by

Aaron Robert Totemeier

In Partial Fulfillment of the

Requirements for the Degree

of

Master of Science Nuclear Engineering

August 2006

Purdue University

West Lafayette, Indiana

This thesis is decidated to my mother and father, Debbie and John Totemeier.
Without their unwavering love and support, none of this would have been achieved.
Thank you both.

ACKNOWLEDGMENTS

The author gratefully acknowledges the support of the U.S. Department of Energy (DOE) under contract number: DE-FC07-05ID14656. Also, many thanks go to Edward Merrit and David Regan for their help with the electronic and hydraulic systems and to Paul Mews and Adam Parkison for their assistance with the experimentation. I would like to thank Dr. Dayanada and Dr. Revankar for being on my thesis committee and Dr. McDeavitt for advising me through this work.

PREFACE

This research was born from the U.S. DOE Advanced Fuel Cycle Initiative (AFCI) and the desire to reduce the waste volume load on a geologic repository such as Yucca Mountain, NV. In no way does it remove the current and future need for such a repository. Instead, the intention is to extend the life and storage capabilities by removing plutonium and minor actinides.

The overall concept is to remove transuranic elements from spent nuclear fuel through the UREX+ process and separate the zirconium from fuel cladding through a zirconium hydride-dehydride process currently under development. This recycled Zr will then be used as the matrix of a cermet storage form for transuranic oxides with the possibility of conversion to a transmutation target or fast reactor burner pin. Within this larger project design, the focus of this thesis is an evaluation of the necessary concepts and theories for fabricating and utilizing such a storage form.

TABLE OF CONTENTS

Page

Page

LIST OF TABLES

LIST OF FIGURES

ABSTRACT

Totemeier, Aaron Robert M.S.N.E., Purdue University, August, 2006. Evaluation of a Zirconium-Matrix Cermet for the Storage and Transmutation of Transuranic Isotopes. Major Professor: Sean M. McDeavitt.

Reduction of the radiotoxic inventory of spent nuclear fuel (SNF) in the United States has lead to an interest in the development of a zirconium matrix cermet storage form for transuranic (TRU) isotopes. A hot extrusion process has been developed for fabrication of the proposed cermet.

A 90 t hydraulic press has been outfitted with ceramic fiber heaters to heat the extrusion tooling and billet. Eight extrusion development tests were performed to determine the initial response of the hot extrusion process to temperature, billet green density, and particle loading. Zirconium powder (-325 mesh) is used as the matrix phase and yttria-stabilized zirconia (YSZ) (400 μm diameter) as the TRU oxide simulant. It has been confirmed that below temperatures of 700 °C the extrusion of powder zirconium will not proceed. In two experiments, low green density of the pre-extruded billet is believed to have caused fracture of the extruded rod by allowing gases to be trapped in the extrusion canister. A large amount of particle damage was observed for a reduction ratio (A_o/A_f) of 9 and 2.6, though less damage is seen in the smaller reduction. High particle loading causes particle fracture by impact during deformation. A lower particle loading and method to maintain interparticle spacing during extrusion are suggested to relieve this contact fracture.

The SRIM code package has been used to determine He ion ranges in Zr and UO_2 as a TRU oxide simulant. From this information the amount of undamaged Zr matrix as a function of particle size and volume loading has been calculated, suggesting a smaller particle size may be used in future work. Matrix damage is caused by energetic

alpha particles and fission products emitted from the oxide particles, it does not consider damage from the neutron environment in the reactor.

Metallography of the extruded cermet samples was performed to visualize particle distribution and damage. Microstructural analysis is discussed in Chapter 5. Detailed microscopic analysis on porosity and oxygen gettering in the matrix has not been performed at this time.

This work is the beginning of an ongoing project to perform parametric studies of the hot extrusion process for Zr cermet fabrication. Future work will include analysis of the reduction ratio, particle loading, and matrix density and their effect on oxide particle damage in the extruded rod.

1. INTRODUCTION

The production of high level nuclear waste is a necessary consequence of fission reactors. The current waste disposal plan for the U.S. is to bury the waste in a geologic repository such as Yucca Mountain, NV. After 300 years of observation, the facility will be closed and our current engineering ability will have to maintain a safe storage facility for thousands of years. In the short term (300-500 yr), a large amount of radioactive material will be transmuted into stable isotopes through natural decay. However, many of the transuranic (TRU) elements (i.e. Am, Cu, Np, Pu) have isotopes with half-lives in the range of 10^4-10^7 years. These materials generate a large of amount radiation and will exist long after our engineering ability can maintain the repository. One solution to this problem is to burn the material in a suitable reactor; either a fast reactor or an accelerator driven system. Because such systems are currently unavailable, the issue of storing the TRU waste needs to be addressed.

Spent nuclear fuel (SNF) reprocessing methods are currently being developed by the U.S. Dept. of Energy's (DOE) Advanced Fuel Cycle Initiative (AFCI) to address these issues [1]. The UREX+ process is a system of separation methods that may be manipulated to isolate uranium, technetium, cesium, strontium, and all of the TRU isotopes. The TRU isotopes are extracted during one of the last steps of the process known as TRUEX, a chemical separation process that isolates the TRU isotopes in a nitrate solution. A technically feasible and economically inexpensive storage method is to convert the TRU into oxide powder and store the powder in canisters. However, due to the high radiotoxicity and mobility of the powder, this method could produce a hazard if the canister fails and the powder is dispersed. It is desired to have a storage system that is economical, versatile in loading components, and steadfast against

corrosion and failure. In addition, the TRU storage method should be amenable to future recovery for burnup in advanced nuclear energy systems.

Many proven waste immobilization materials exist, including glass, mineral, and metal matrix storage [2]. Glass and mineral forms involve complicated fabrication and are fragile with respect to the type and amount of waste they hold. Metal alloys are well-known and sturdy but very susceptible to radiation damage from the fuel. Retrieval of waste from these forms is also difficult, if not impossible.

Because of the significant energy content of the TRU isotopes, the desire to recycle exists. This transforms a long-term waste liability into a new energy resource. Therefore, the design concept for the TRU-bearing form developed in this thesis is twofold. First the product will act as a storage form, providing safe, reliable storage of the TRU isotopes until the necessary transmutation systems are available. Second, the storage form may be converted into a fuel form for burnup in a fast reactor or accelerator driven system. To this end, a simple process for conversion from storage form to fuel form is desired. By simple, it is meant that the conversion will involve no major chemical processes or risk of TRU release.

A zirconium matrix cermet has been chosen for this dual purpose storage/fuel form. The formability and durability of metals far outweighs those of glasses and minerals, as does their performance in the harsh environment of a fast reactor system. Zirconium was chosen as the matrix metal because of its strength, corrosion resistance, and nuclear properties, as well as its long history in the nuclear industry and abundance in Zircaloy cladding in SNF. A different project related to this design but not germane to this thesis involves the extraction of the Zr from SNF cladding and conversion to its powder form for reuse as the matrix for the cermet [3].

The chosen fabrication method for the cermet storage form is powder metallurgical hot extrusion. This thesis is the beginning of an ongoing project to evaluate the fabrication parameters and behavior of the Zr matrix storage form. Several extrusion development tests have been performed to develop the process and identify initial parameters of concern for future study.

2. BACKGROUND

The following provide background reviews of the disparate set of technologies that converge in this project. These sections cover the use of dispersion fuels in nuclear energy systems, powder metallurgy for cermet fabrication, hot extrusion, and the impact of helium generation.

2.1 Cermet Dispersions: Theory & Fabrication

A cermet is a multiphase system with a *cer*amic dispersant in a continuous *met*al matrix. This is in contrast to a cercer in which both dispersant and matrix are ceramic. Dispersion fuels have been around in the U.S. since the beginning of the nuclear era. Many combinations of dispersant/matrix have been studied over the years and the theory is well-developed [4]. Although sintered UO_2 pellets have been used as the primary reactor fuel for commercial nuclear power, cermet dispersions have been used in research reactors and specialty sytsems for many years. The first commercial power reactor to use dispersion fuel was the Vallecitos BWR in California using fully-enriched UO_2 at 20 wt% in stainless steel [4].

Transmutation of actinides will most likely take place in a fast reactor or accelerator driven system (ADS). Fast reactor operating temperatures are higher than current LWRs. Also, to achieve a high transmutation efficiency, longer burn times will be required, leading to an increase in fissions and related damage. This harsher environment will require advanced materials that are capable of maintaining their thermal, chemical, and mechanical properties during exposure. An important property of a cermet fuel/transmutation target is the *inertness*, or neutron transparency of the matrix phase. If neutrons lose energy through interactions with the metal matrix they may not have the necessary energy to induce fission in the fuel. Inert matrices

have been designed using ceramic oxides, carbides, nitrides, and metals at different institutions around the world.

A key benefit of dispersion fuels is the localization of the damage zones produced under irradiation. In a solid solution fuel the damage produced from fission and the subsequent radiation and gas buildup can damage the entire structure, altering the macroscopic properties of the fuel. In a dispersion fuel, the damage caused by these phenomena is localized and the fabrication may be customized to ensure that a desired amount of undamaged matrix always exists. Other benefits of the cermet dispersion include fission gas retention, solid fission product containment, and high thermal conductivity [5, 6].

2.1.1 Matrix Damage in Dispersion Fuels

Damage in a dispersion fuel matrix is caused by the release of fission products, helium buildup from alpha decay and (n,α) reactions, and radiation damage from the intense neutron and radiation environment. Fission products are large, high energy ions that may create many lattice point defects as they travel through the matrix. In a cermet dispersion, these products will initiate within the fuel particle and the majority of their damage will be concentrated therein. Some fission products, especially those emitted near the particle surface, may escape the particle and travel into the matrix.

The same applies to alpha particles from both decay and (n,α) reactions. Though the alpha particles are smaller in size and energy than fission products, alphas from decay may travel with a kinetic energy measured in megaelectronvolts, enough to create many defects in a metal lattice where atomic binding energy is on the order of 25 eV. The collisional damage produced by fission products and alpha particles is compounded when the resultant gases migrate and agglomerate in the cermet. This gas buildup may lead to swelling and cracking in the matrix.

To understand the damage from gases, the region around the dispersed particle may be split into four zones [7]. Figure 2.1 is a graphical representation of these

damage zones. Zone i is the fuel particle, in this case, the TRU oxide. This region will have a high concentration of displacement damage, gaseous fission products, and helium gas from TRU decay. Zone ii is a shell $\sim$ 5 μm around the particle which receives damage from recoil implantations and energetic alpha particles. It is possible that He gas will accumulate at the metal/oxide interface. Zone iii stretches approximately 15 μm away from the particle and is damaged primarily by alpha particle implantation. The undamaged host material is zone iv. It is important to note that all regions will receive damage from the radiation environment in the reactor, but the model described here is only related to material damage by specific radiation sources from within the TRU particles. The aforementioned distances are a function of the range of fission fragments and He ions in the matrix and are given as a reference.

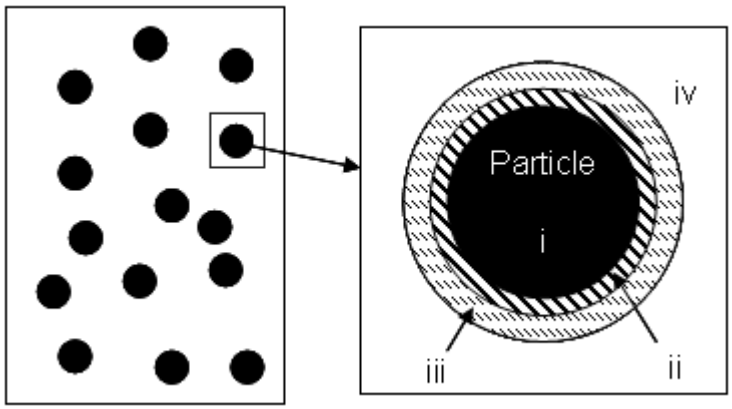

Figure 2.1. Damage zones around a dispersion fuel particle.

As mentioned above, one benefit of dispersion fuels is the ability to control where this kind of damage occurs. Knowing the range of the damage-inducing species, the size of the particle inclusions and their amount in the matrix, a dispersion fuel may be fabricated with a designed amount of matrix damage. Figure 2.2.a shows the ideal case of a continuous ligament network of undamaged matrix. Note the clear separation of damage zones in the figure. This scenario allows the matrix metal to

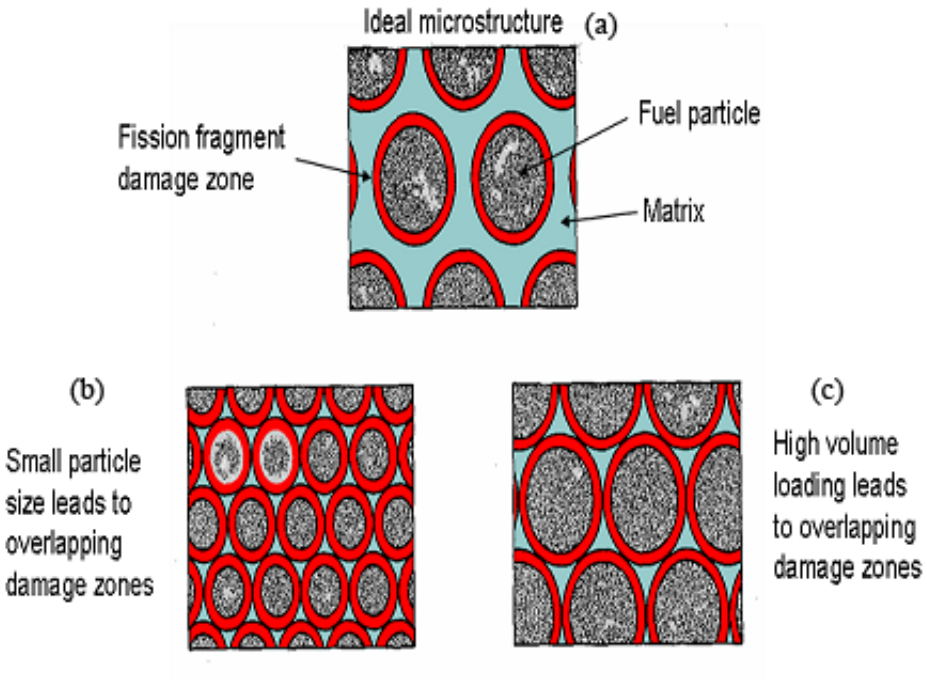

Figure 2.2. Overlapping damage zones in dispersion fuels. [8]

retain its macroscopic properties, unlike the case when the damage zones touch, or worse, overlap. Two cases where zone overlap occurs are shown in the figure. Figure 2.2.b shows a case when volume loading is held constant and particle size is decreased. The addition of more particles increases the amount of damaged matrix and can lead to overlap. Figure 2.2.c. shows a second case where the particle size remains constant and the volume loading is increased until the damage zones overlap.

In order to determine how much damage will occur in a dispersion fuel, and subsequently how much matrix remains intact, a few simple assumptions are made. The first is that all particles are perfect spheres of equal diameter. A fabrication method that has shown excellent uniformity in sphere size is the rotating electrode atomization process [8], wherein the feedstock is rotated in an electric arc and the spheres are *thrown* off of with near uniform diameter. Another fabrication route that has shown good sphericity and uniformity is sol-gel processing with a vibrating nozzle [9].

The second, and largest, assumption in dispersion fuel theory is that the particles are arranged in a face-centered cubic (FCC) array in the matrix. Although this greatly simplifies the theory for calculations, it is unfeasible in a fabrication sense. Real cermets have a random distribution of particles and this FCC assumption can fall apart at high loadings. Loadings as high as 60% can be achieved with non-spherical or bi-modal particle distributions. However, with this assumption, the maximum volume loading attainable with spherical particles is 0.74.

Based on the aforementioned assumptions, dispersion theory allows the calculation of the amount of matrix damage produced by the species that escape the particles. The following values must be known for these calculations:

$$\begin{aligned} \lambda_p &= \text{range of ion or } \alpha\text{-particle in the fuel particle} \\ \lambda_m &= \text{range of ion or } \alpha\text{-particle in matrix} \\ D &= \text{fuel particle diameter} \\ V_f &= \text{volume loading of particles} \end{aligned}$$

The dimensionless number $D/2\lambda_{m,p}$ occurs in all of the equations of dispersion fuel theory and relates the particle diameter to the species range [4, 10]. For $D/2\lambda_p \leq 1$, the radioactive species can escape the fuel particle from any point of origin. As the value increases, species originating from the inner regions of the fuel particle will become trapped in the fuel.

The first step in determining the amount of matrix damage is to calculate the fraction of the species that will escape the particle, P_a. This equation doesn't use the FCC array assumption because it is based solely on a single particle and the species range within it [4].

$$P_a = \frac{3}{4}\Big(\frac{2\lambda_p}{D}\Big) - \frac{1}{16}\Big(\frac{2\lambda_p}{D}\Big)^3 \tag{2.1}$$

Equation 2.1 is valid for all particles where $D \geq \lambda_p$. For $D/2\lambda_p$ <1.5, nearly 50% of the species will escape the particle. As the particle becomes much larger than the species range fewer species escape and only the region around the particle surface (λ_p

thick) will emit species into the matrix. The depletion of species in this region, P_f, can be calculated from the total escape fraction, P_a, as:

$$P_f = \frac{P_a}{1 - [1 - (2\lambda_p/D)]}. \tag{2.2}$$

Equations 2.1 and 2.2 may be used to determine how effective a particle will be at containing damage species. From equation 2.2, the fraction of particles escaping the depleted zone around the particle surface levels off at 30% for $D/2\lambda_p \geq 5$.

The equations for calculating damage in the cermet involve the FCC array assumption. The percent of undamaged matrix, V_m, is calculated by:

$$V_m = 1 - \frac{V_f}{1 - V_f}\left[\left(1 + \frac{1}{\frac{D}{2\lambda_m}}\right)^3 - 1\right]. \tag{2.3}$$

Defining the undamaged distance between particles by d', a relation between fuel loading, particle size, and species range in the matrix can be used to determine when the undamaged distance between particles becomes zero and matrix continuity is diminished,

$$\frac{d'}{2\lambda_m} = \frac{D}{2\lambda_m}\left[\left(\frac{0.74}{V_f}\right)^{\frac{1}{3}} - 1\right)\right] - 1. \tag{2.4}$$

Figure 2.3 was made using equations 2.3 and 2.4. It shows the percent of undamaged matrix as a function of $D/2\lambda_m$ and fuel loading. The separate lines refer to a specific volumetric fuel loading in the cermet. The line representing $d' = 0$ is the limit of separate damage zones; left of this line the zones will overlap, increasing matrix deterioration from radiation damage. From this figure, if a cermet with 30 vol.% fuel loading of particles with $D/2\lambda_m = 5$ is fabricated, ~68% of the matrix material will not be damaged by the emitted α-particles and fission products.

These calculations are fundamental to the design of a dispersion fuel. Though they do not consider diffusion of species within the matrix after emission, they can give a good approximation of how much damage will be caused in the matrix from nuclear processes within the fuel. The assumptions of sphericity and an ordered particle array are made. Uniform spherical particles can be achieved if tight controls are held during

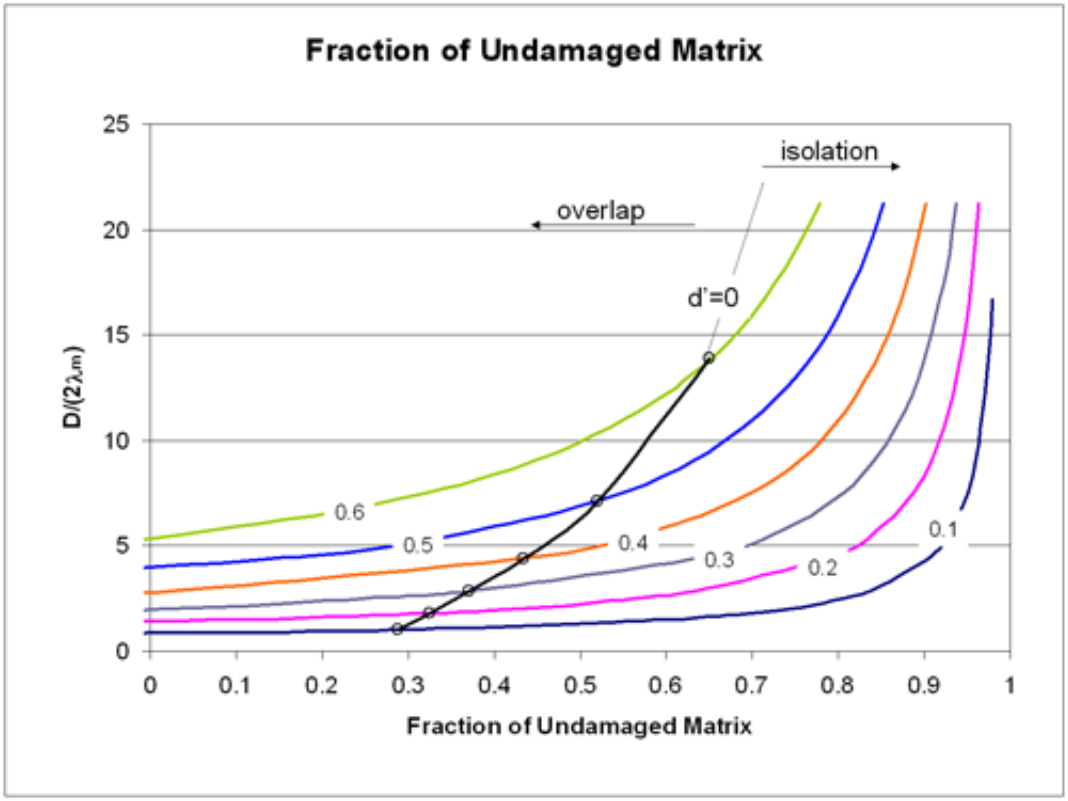

Figure 2.3. Fraction of Undamaged Matrix

fabrication. However the ordered array of particles is not economically achievable; the closest approach being a random arrangement.

2.1.2 Previous & Current Research in Cermet Fuels

Cermet fuels are an active research topic in today's nuclear community, due in no small part to the worldwide desire to reduce Pu inventories. Buffe et al. [11] describe a Zr-PuO_2 cermet for multi-recycling in pressurized water reactors (PWR). After thermodynamic, thermo-chemical, and thermo-mechanical calculations, the authors conclude that when using an oxide particle in a Zr matrix the particle must be coated with a chemically inert material to inhibit oxygen gettering. Also when using particles greater than 100 μm in diameter the PuO_2 particles should be porous to accommodate

fission products. The authors also present calculations to determine the effects of particle shape and size on the elastic moduli and thermal expansion of the cermet.

Bhatnagar [12] studied the fabrication and mechanical properties of ThO_2 cermets with a stainless steel (SS) matrix. The thoria powder was crushed from pre-sintered compacts to -100 to +170 mesh and coated with Ni in a salt bath. The powered thoria was then mixed with SS powder to varying weight percent and hot pressed at 1030 °C at a pressure of 213 kg/cm^2. The authors found that the density of the cermet decreased with increasing weight percent thoria down to 86.41% TD for a 60 wt% loading. The authors report an increase in 0.2% offset yeild strenth with increased loading due to increased resistance to plasitc flow and shared load bearing of the dispersed phase. These same factors cause a decrease in the ductility of the cermet as compared to the pure metal phase. The authors explain a decrease in Brinnell Hardness with increased dispersant as a result of residual thermal stresses due to the difference in thermal expansion of the two phases. Excellent bonding of the nickel coating to the thoria powders was achieved by the salt bath method.

Cold rolling of Al/Al_2O_3 cermets was investigated by Lee et al. [13]. Aluminum powder was prepared by nitrogen gas atomization, yielding spherical particles with a mean diameter of 36 μm. Alumina powder of 5 μm was used as the dispersed phase. Several loadings and reduction ratios were examined. The authors conclude that with a loading of less than 10 vol.% the dispersed phase is uniformly distributed throughout the cermet, however at loadings greater than 15 vol.% the Al_2O_3 began to cluster. Cermet densities near the true limit were achieved for Al_2O_3 concentrations less than 20 vol.%. Using these low volume loadings and small particles show no particle damage from the rolling process, however it would be interesting to see if this holds true with particles on the order of 100 μm diameter.

The Experimental Feasibility of Targets for Transmutation of Actinides (EFTTRA) project in Switzerland is designed to look at transmutation of americium and other long-lived fission products. The EFFTRA-T4 experiment analyzed the production and irradiation of an americium transmutation target [14]. The specimen

was prepared by infiltration of an americium nitrate solution into a $MgAl_2O_4$ pellet with 49% porosity. The pellets were calcined at 700 °C for 4 hours and sintered at 1650 °C in an Ar/H_2 atmosphere. The sintered pellets had a density of 96.5% TD and had mean Am content of 11.1 wt%. One pellet was cut axially to evaluate the Am distribution with α-radiography. A cylindrical shell, roughly 200 μm thick was noticed to contain a higher Am concentration (14 wt%) than the remaining pellet (9 wt%). This inhomogeniety was also seen in an optical micrograph and is believed to have been caused by non-uniform porosity in the spinel pellets or a diffusion process during thermal treatment. The pellets were irradiated for 358 full power days in the HFR Petten reactor prior to both non-destructive and destructive PIE tests were performed on the pellets.

Murray and Williams [15] describe the hot extrusion of a UO_2/Fe cermet using iron powders less than 60 μm and stoichiometric UO_2 particles of $76 - 150$ μm. The powders were mixed and cold compacted at 20 tons/in^2 in a steel can then hot extruded at 1200 °C. Up to 30% volume loading the extrusion pressure was nearly constant, the pressure increased linearly up to 50% volume loading. No information could be found about particle damage during these experiments.

Pouchon [16] describes a *sphere-pac* concept for cermet production. In this concept the spherical particles are produced by internal gelation. Multi-modal packing of the matrix and dispersed phase allowed green densities greater than 80%. The product ws densified by sintering. This method differs from the vipac concept which uses vibratory packing to achieve a high green density [17].

Dispersion fuels are widely used in research reactors around the world. Purdue University's PUR-1 reactor uses a plate type U/Al dispersion. Other reactors of note that use dispersion fuel include the HFIR reactor at Oak Ridge National Laboratory which provides the highest reactor-based neutron flux in the United States. Idaho National Laboratory's ATR reactor, which is a key source of iridium-192 for industrial radiography also uses dispersion fuel.

2.2 Powder Metallurgy in Cermet Fabrication

Powder metallurgy techniques are used throughout many manufacturing and fabrication industries besides nuclear; including polymers, pharmaceuticals, and catalyst production. Powder metallurgical processes allow a great deal of control over the finished product. Besides the amount of each component in the product, the microstructure, finished shape, and composite structures can be controlled.

In most cases, the forming process used for cermets is the same as with solid materials. The difference lies in the mixture of powder material at the start of the process. Because of this, some type of container is used to keep the powder in a desired shape. For extrusion and drawing a canister is used, whereas in rolling, the powder is contained in a "window". Though forging and swaging processes can be used in powder metallurgy, it is believed that the repetitive impact will cause failure of the ceramic particles in cermets. This concern has lead to the use of hot forming processes wherein the metallic phase is sufficiently plastic to move with the oxide inclusions. Extrusion and drawing are similar processes whereby an area reduction is achieved by forcing a billet through a reducing die. In drawing, the material is pulled through the die face, whereas extrusion pushes the billet.

A cold-drawing process has been investigated at Argonne National Laboratory [18]. The goal of this work was to produce a cermet nuclear fuel containing $(Th,U)O_2$ as the dispersed phase in a Zr matrix. The process involved several incrementally increasing reduction passes with an annealing step after two passes to remove work hardening. Although the process can be time consuming for large scale fabrication due to the many passes, it allows the matrix porosity to be controlled by proper selection of the number of reduction passes. A large amount of damage was seen in the oxide microspheres in this work, leading to an interest in hot extrusion for a "single-pass" forming process.

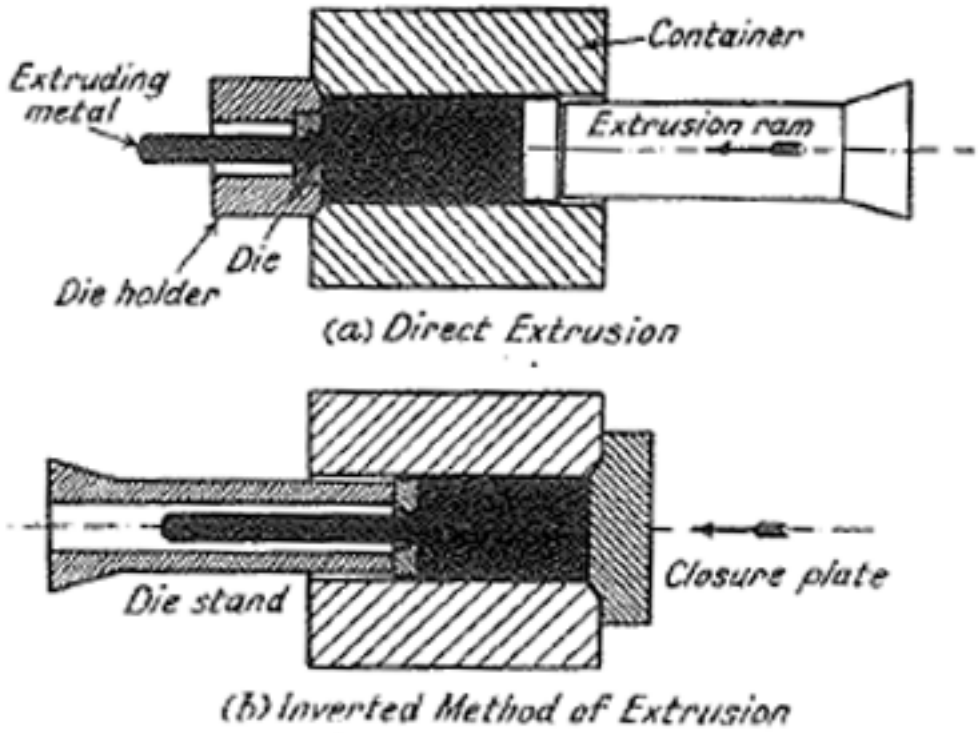

Figure 2.4. Direct and Indirect extrusion presses [19].

2.2.1 Extrusion

Two types of extrusion exist, direct and indirect. Figure 2.4 is a schematic showing the difference in these two methods. The main difference is where the extrusion force is applied. In the direct process, the billet is pushed through the die; indirect extrusion pushes the die into the billet.

In direct extrusion, the billet is pushed through the die by a force, usually applied by a ram or hydrostatic force. Figure 2.5 shows typical pressure profiles for both direct and indirect extrusion. In direct extrusion the sharp rise at the beginning of the press is the densification of the billet and deformation to fill out any space between the billet and the tooling. As the billet is extruded, the pressure drops nearly linearly as the friction between the billet and holder is reduced. When only a small amount of the billet remains, the pressure rises sharply as this material resists flow toward the

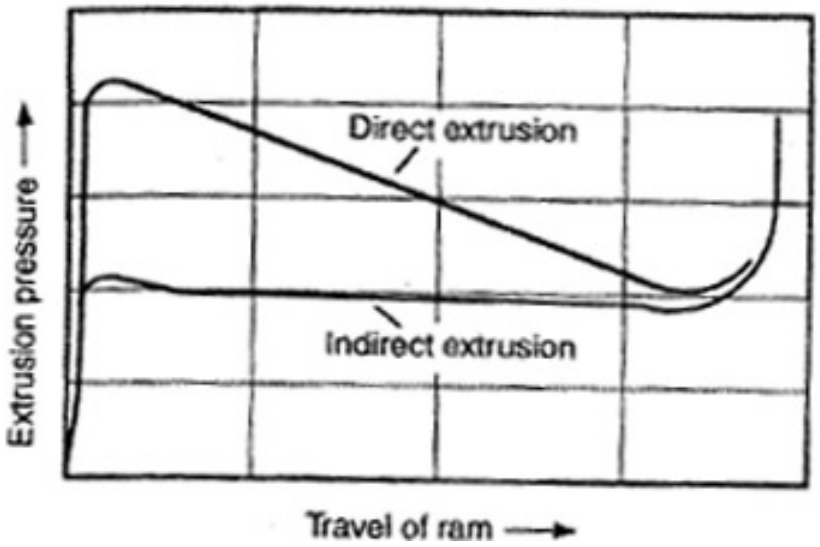

Figure 2.5. Extrusion pressure for direct and indirect method [20].

center of the die. Direct extrusion has the ability to be a continuous process when connected with a proper feed system such as a screw loader. Direct extrusion is the process used in this thesis.

With indirect extrusion the billet is held steady and the die is forced into it. This removes the friction force of the billet and holder because there is no motion between them. After compaction of the billet, the only pressure needed is to create the deformation zone at the die entrance. The pressure remains relatively constant throughout the process until only a thin section of billet is left.

The pressure required by extrusion can be calculated by a simple equation relating it to the reduction in area of the billet [19].

$$P = k \cdot \ln\left(\frac{\mathrm{A}}{\mathrm{A_o}}\right) \tag{2.5}$$

where k refers to the resistance to deformation of the setup. Although k is related to the rheology of the metal, it is also dependent on the temperature, speed of extrusion, and friction. It is theoretically independent of the extent of plastic deformation because the deformation is by hot working, which requires that resistance remain constant throughout the process [19]. This contrasts with cold working where work

hardening can rapidly increase the resistance to deformation. Extrusion pressure is greatly affected by the selection of tooling material, die shape, and lubrication [21].

The extrusion rate and pressure are directly related. Extrusion rate can be important when billet cooling is a concern. If the billet is much hotter than the holder, time in the holder should be minimized (speed increased). However, a very high rate of extrusion can lead to defect formation and bending of the extruded billet.

A certain threshold pressure must be overcome to induce flow. At low temperatures this threshold pressure is much larger than high temperature extrusions. For most soft metals under working conditions, variations in speed have a minor effect on extrusion pressure. Zirconium extrusion is a high temperature process and billet cooling will be a concern in this design.

Extrusion temperature is mostly a characteristic of the material to be extruded. A high temperature will decrease the resistance to deformation of the workpiece, leading to lower pressures. However, if the temperature is too high, hot shortness may ensue. This phenomenon involves a loss of ductility at high temperatures and may lead to cracking of the billet. The onset of hot shortness usually involves an impurity in the metal, such as sulfur in iron forming FeS. The lower temperature boundary is the point at which deformation resistance cannot be easily overcome.

Extrusion and drawing dies are quite similar. Any piece with a reduction in area or change in shape can be a die. A lot of early work in metal extrusion involved flat dies, with no lead-in angle, α, or radiused edges. Though these dies perform well for solid metals, a powder billet in a container would undergo gross deformation. Therefore a conical reduction die has been chosen for this project. Intuitively, a gradual reduction in area would lead one to think that the extrusion pressure for such a die would be less than for its flat counterpart. However, the decrease in deformation work with a conical die is often offset, if not overcome, by the increase in friction at the larger die face [19].

During extrusion of powders, the yield strength of the billet changes as it deforms through the die. To accommodate for this phenomenon equation 2.6 is used for the pressure of powder extrusion:

$$P = a' + b' ln\left(\frac{A_0}{A_f}\right) \tag{2.6}$$

where a' and b' refer to the redundant and homogeneous work, respectively [20]. Redundant work refers to the formation of cold welds between the particles and the breaking and reforming of these welds during deformation. It has been proposed that the large amount of redundant work in powder extrusion creates sound particle bonds and removes the need for post-extrusion sintering [20]. The use of fine powders can increase the extrusion pressure because of the increased formation of cold welds in the powder. Homogeneous work refers to the work necessary to push the billet through the die.

2.2.2 Metal Flow in Direct Extrusion

Three classifications exist for describing the flow of metal through an extrusion die. They are simply termed Type A, Type B, and Type C flow. Several methods for flow visualization exist, however they are not discussed here due to the difficulty in analyzing a powder billet in this manner.

Figure 2.6(a) shows flow of Type A in a flat die. It can be seen that the metal undergoes no deformation until entering the die face, and the billet front sees very little deformation. In the die, the central portion of the billet travels faster than the outer edges. It can be seen that the outer portion of the first region to pass through the die has remained at the die entrance and formed a small dead zone. Also, the central portion of the billet undergoes very little deformation compared to the outer edges which are stretched back along the sides of the rod. It should also be noted that the further along the extrusion, the more deformation the central region sees. Type A flow is a "best case" that is rarely seen in actual metal working. Figure 2.6(b) is flow of type B, which is much more common than Type A. Essentially, the same flow pattern

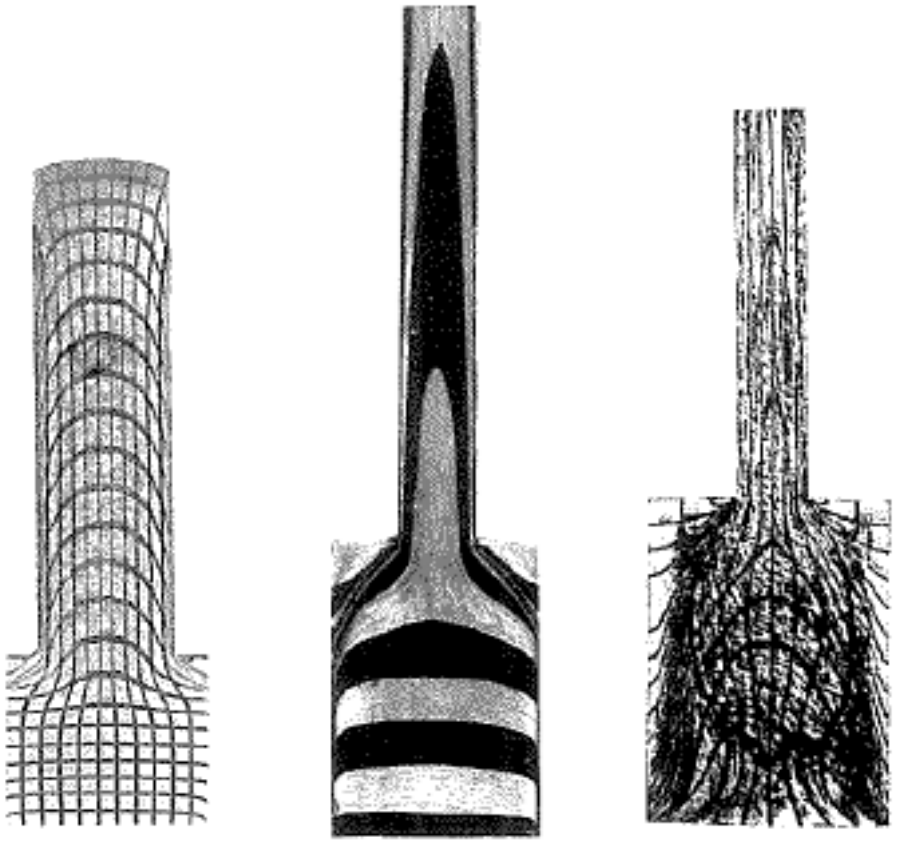

(a) Type A (b) Type B (c) Type C

Figure 2.6. Metal flow regimes in extrusion. [19]

is seen as that in Type A except the shearing of the outer regions is to a greater extent. This is caused by increased friction between the die and billet. The effect of this larger shear increases the size of the dead zone and causes the central region to travel much further than the outer region. Extreme deformation of the outer regions of the rod can be seen. As the extrusion progresses this buildup of sheared material can decrease the plastic flow region of the billet and interfere with the extrusion shape as in Type C flow, (Figure 2.6(c). The main difference in C flow is that the dead zone which is usually near the die face, stretches back along the length of the billet into the holder. As the extrusion progresses this material begins to move inward to take the place of the central region. This material can become enfolded and intrude into the

extrusion path causing defects such as piping and central burst. Avitzur [21] presents several treatments for the solution of required pressure and work of extrusion through converging, or conical, dies. As seen in figure 2.7, the velocity and flow fields in such a die are a complicated system, understood best when described in three distinct zones. Zone I is the undeformed billet, experiencing friction from motion against the holder if direct extrusion is employed, but not friction from the die. Zone II is the deformation zone bounded by the die face. Zone III is the deformed billet exiting the die. In Zone I and III the velocity of the billet is in the axial direction only and can be related by conservation of mass as:

$$v_o = v_f \cdot \left(\frac{R_f}{R_o}\right)^2 \tag{2.7}$$

In Zone II, the velocity is described in cylindrical coordinates and is directed at the apex of the conical die. Using this flow description, several theories of extrusion work and deformation energy have been developed [21]. These theories have lead to the formulation of the optimum die angle α_{opt} for reducing the work required as:

$$\alpha_{opt} \approx \sqrt{\frac{3}{2} m \cdot \ln \frac{\mathrm{R_o}}{\mathrm{R_f}}} \tag{2.8}$$

where m is a constant shear friction term, $\tau = m\frac{\sigma_o}{\sqrt{3}}$.

Die angle not only affects the required extrusion pressure, but is also responsible for many extrusion defects such as the formation of a *dead zone*. A dead zone is a region of material in the billet, near the die, that does not flow (see Figure 2.6). Buildup of this material can cause a reduction in the flow region available and lead to defect formation.

Central burst, or chevroning, is a defect that involves the formation of a repetitive central cavity in the extruded billet. Figure 2.8 shows this phenomenon. Central burst occurs when the zone of deformation (Zone II) becomes an annulus and Zones I and III have a common boundary on the axis of the extrusion. These phenomena occur for a unique combination of the reduction ratio, rheology, die angle, and friction of the process.

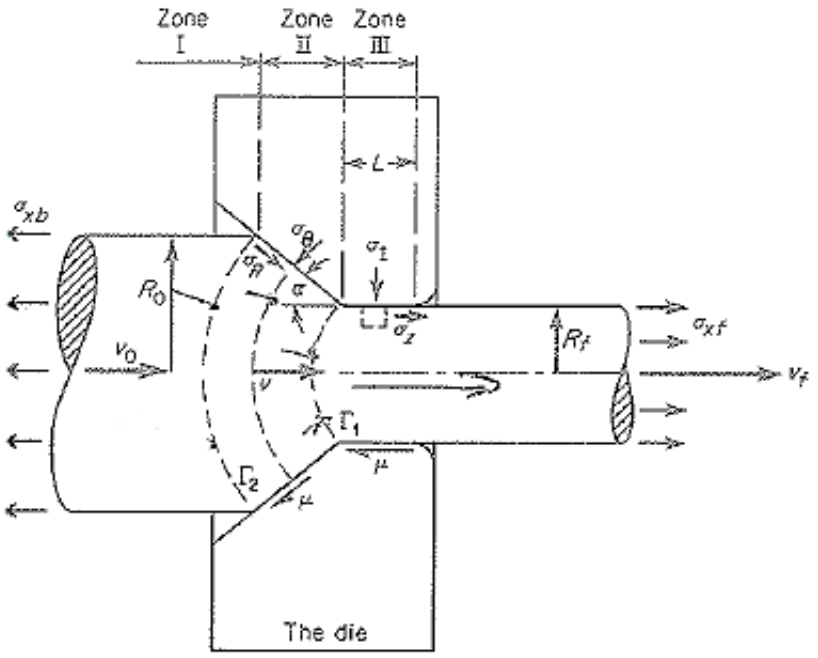

(a) Flow Field

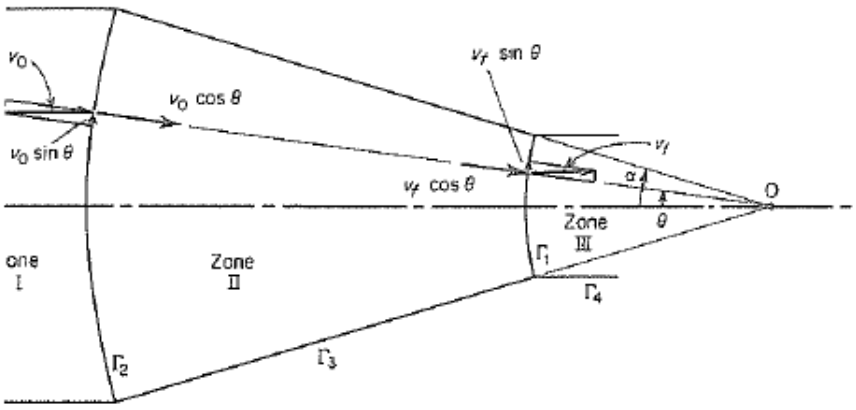

(b) Velocity Field

Figure 2.7. Flow and velocity fields in a conical die. [21]

2.2.3 Previous Work in Zirconium Extrusion

Due to its use as a fuel in Naval reactors, recent information on zirconium extrusion is scarce. Lustman [22] presents extrusion constants, K, for some early experiments, listed in Table 2.1.

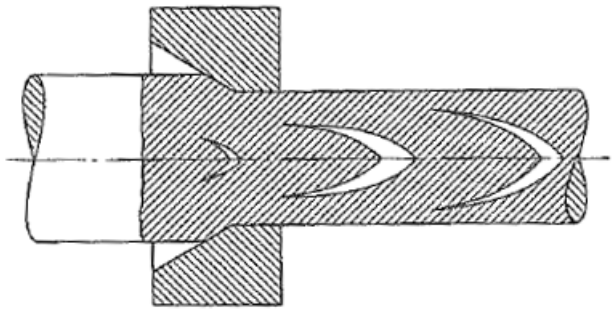

Figure 2.8. Central burst defect. [21]

Table 2.1
Extrusion Constants for Zirconium [22].

Billet Diameter (in)	Temperature (°C)	Press Capacity (t)	K† (psi)
2 †	1130	300	30,000
3.5	700 - 850	500	20,000 - 25,000
4.5	750	1600	29,000

†Billet sheathed in copper.

No information given about actual pressures or reduction ratios.

Because of the lack of knowledge about the information listed in Table 2.1, all that can be inferred is that a similar extrusion constant will be necessary for the proposed process design. Assuming the constant has a value of 30,000 psi and the billet undergoes an area reduction (A_o/A_f) of 9, a pressure of 450 MPa should be required. The hydraulic press used for this thesis has a capacity of 90 t which correlates to nearly 3 GPa when applied to a 0.75 in diameter billet.

Lustman [22] gives no information about temperature relations to K, except to say that the information gives little variation between $700 - 850$ °C, evident from Table 2.1. Extrusion speeds as high as 5 in/sec have been successfully used in Zr extrusion. The lower limit is bound by the cooling of the billet in the holder.

Work at Knolls Atomic Power Laboratory has shown that extrusion of powder zirconium with a reduction ratio of 11 at 800 °C formed a fully dense matrix around UO_2 particles [23]. Other research notes a reduction ratio of 15 is needed to achieve full density [15]

2.3 Helium and Fission Product Gas Considerations

Helium plays an important role in the development of most nuclear materials due to the strong source that results from α-decay and (n,α) reactions. Even at very low concentrations, inert gases can cause drastic changes in the performance of metals. During the early years of reactor development inert gases in nuclear fuels received a lot of attention, it wasn't until later when controlled thermonuclear fusion devices came about that helium was studied in great detail due to the high helium production rates in these reactors. The 1982 International Symposium on "Fundamental Aspects of Helium in Metals" [24] divides the issue into three main topics [24]: (1) single helium atoms and small vacancy clusters (HeV), (2) formation and kinetics of He bubbles, and (3) He-induced changes of properties in metals.

The α-decay of TRU isotopes in the cermet storage form will lead to a buildup of He gas, which is insoluble in most materials. This will lead to the precipitation of He bubbles which subsequently may cause swelling and cracking of the material. In a TRU storage form, the formation and behavior of these helium bubbles is of great importance, especially in the current design because the storage form is subsequently used for transmutation. It may be necessary to process the storage form by annealing to remove trapped helium before irradiation. Another option is to use a porous matrix during the storage stage that will allow He gas release, unless the He is trapped in the TRU inclusions. The ability to control porosity in the extrusion process needs to be determined. During this stage of the design process, He will not be analyzed experimentally. Yttrium-stabilized zirconia microspheres are used as a TRU simulant and no He will be produced.

One primary concern is the He behavior in the metal matrix and what requirements this will put on the fabrication of the form. It is currently unknown where the He will reside in the cermet. Helium could migrate and gather within the TRU particles, at the matrix/inclusion interface, in grain boundaries within the matrix, at damage sites, or some combination of these. If a sufficient amount of He is re-

tained in the matrix, a degassing process may be necessary prior to transmutation. Studies show that large helium-vacancy complexes can degas from metals at elevated temperatures ($T \geq \sim$1000 °C) [25], but bubble induced swelling must be avoided.

The α-particles ejected from the TRU isotopes have energies in the $4 - 5$ MeV range. This energy is orders of magnitude above the binding energy of metal atoms in the matrix which is measured in electronvolts. Therefore, each α will create a large zone of radiation damage in the matrix (e.g. Frenkel pairs and displacement cascades). The SRIM/TRIM [26] code has been used to determine He ion ranges and damage production in zirconium and will be presented in section 4.8.

Atomistic theories dealing with the interaction of single He atoms and small clusters of atoms and vacancies (HeV) have become "easy" to analyze with the availability of high-powered computers. These theories involve interatomic potentials which account for the pair-wise forces that atoms and vacancies exert on each other and the surrounding lattice sites. These potentials can be developed either *ab initio* or empircally [27, 28]. At the present time, concern lies with the growth and interaction of He bubbles in the cermet and although atomistic theory will be a necessity at a future time, it will be left out of this discussion.

Consider a single α-particle emitted by natural decay from a TRU nucleus. The α-particle causes a cascade of damage and then picks up two electrons from the surrounding material to become a stable He atom. Helium gas is formed when two He atoms meet within the solid and form a diatomic nucleus; this meeting is referred to as the nucleation step. This gas nucleus will strain the surrounding lattice until a vacancy moves nearby and they combine. The nucleus may grow and become a bubble as more He atoms and vacancies migrate to the nucleation site. Equilibrium is achieved when the internal pressure p is equal to the surface energy γ of the matrix by $p = 2\gamma/r$, where r is the bubble radius.

The nucleation of gas bubbles is strongly temperature-dependent, hence in a thermal gradient, heterogeneous nucleation will occur [29]. The difference in thermal conductivity of the ceramic particles and metal matrix will cause a strong tempera-

ture gradient within the particle, though the surrounding matrix will keep the overall gradient much lower. This may not be a concern during storage, but its effect will be much greater at fast reactor temperatures. It has also been shown that He bubbles tend to migrate up a gradient, which may lead to void formation in the center of the particle [29].

After nucleation, the bubbles will grow in size. There are several mechanisms by which this can occur, including single gas atom absorption, vacancy absorption, coalescence and Ostwald Ripening [30]. In the case of absorbing a single gas atom, the new bubble is not in equilibrium unless the absorbed gas atom has a vacancy associated with it. If this is not the case, a new vacancy must flow to the bubble or a Frenkel pair must be created at the bubble-matrix interface [31]. Bubble growth by vacancy absorption is typically a concern at high temperatures (or high irradiation damage) since vacancy motion at low temperatures is low.

Coalescence is a collisional process whereby two bubbles combine to form a larger bubble. In order for a bubble to move through a solid material, atoms from the "front" edge of the bubble must move the "back" edge. This can occur through three processes: (1) vapor diffusion through the bubble, (2) surface diffusion around the inner surface of the bubble, and (3) vacancy diffusion through the lattice near the bubble. A fourth method which occurs with faceted bubbles is ledge diffusion, whereby one of the bubble faces undergoes a step migration into the matrix. Bubbles can also migrate to and diffuse along grain boundaries. After two bubbles combine, they are not in equilibrium with the surface until enough vacancies flow to the bubble.

Trinkaus [30] gives an excellent discussion on the energetics and kinetics of formation for He bubbles. Two key parameters involved in He interaction theory are the temperature of the matrix and helium production rate. At high production rates and low temperatures, thermally activated vacancy sites are low in number and do not contribute to He bubble formation. Under these conditions, bubbles form by Frenkel pair production, metal interstitial atom ejection, or by the loop punching mechanism [30]. This condition is usually found during low-temperature He ion im-

plantation, a common method for introducing He into a specimen for study. The first stage of growth is a clustering of interstitial He atoms. When this cluster becomes large enough (5-7 atoms) [30] a Frenkel pair is formed. A process termed *trap mutation* occurs when additional He atoms join the cluster and create more Frenkel pairs near the cluster. Loop punching is a phenomena whereby metal interstitials are emitted in clusters as opposed to individually. Small clusters tend to form 3-D structures and as the number of interstital atoms in the cluster increases they tend to form 2-D platelets which may evolve into disolocation loops.

The other scenario occurs at low He production rates and high temperatures. At elevated temperatures the thermal vacancy population is large enough that when HeV complexes are formed the internal pressure of the He cavity can maintain equilibrium without creating Frenkel pairs and dislocation loops. Under these conditions, with continuous He supply, the gas bubble undergoes two different stages: a gas-driven early stage and a vacancy supersaturation-driven late stage. This will be facilitated by the increased number of vacancies created by the ejected α-particles.

2.4 Zirconium: History & Metallurgy

Martin Henrich Klaproth, a German chemist, discovered zirconium in 1789 in the natural mineral zircon [32]. Thirty-five years later, Berzelius became the first to isolate the pure metal by reducing K_2ZrF_6 with potassium metal; the product metal was so impure that no attractive properties were found. In 1924 van Arkel and de Boer used their iodine process to refine Zr. This process involved the decomposition of zirconium tetraiodide onto a hot filament producing rods of high purity metal, known as "crystal bar" [22]. Initially, the pure metal was used primarily in the electronics industry until it was found that Zr is highly corrosion resistant. This led the U.S. Bureau of Mines to develop a process, under the direction of W.J. Kroll, to produce large quantities of high-purity Zr metal. The Kroll process heats Zr and its impurities (primarily Hf) with carbon in a chlorine atmosphere, producing metal chlorides and CO/CO_2 gas. The $ZrCl_4$ is then reacted with molten Mg in a He atmosphere. This produces Zr sponge which undergoes a vacuum distillation to remove magnesium chloride and any excess Mg in the sponge [22, 32].

Removal of hafnium is of great importance for zirconium in the nuclear industry. Hf is present at 2-3 wt% in most zirconium minerals. Besides corrosion resistance, zirconium is used in the nuclear industry because of its low neutron cross sections. Hafnium's thermal neutron cross section is an order of magnitude higher than Zr, as seen in Figure 2.9, and is used as a control rod component in today's reactors. Of note, Baldi [33] calls for a need to reduce the uncertainties of Zr cross sections in the epithermal region if it is to be used in fast reactor systems, citing a large variation in k_∞ and void coefficient for a PuO_2/Zr cermet using several cross section libraries.

In 1949, zirconium became a hot topic in the nuclear industry. Joint research initiatives were started on property measurement, production/separation technologies, and fabrication techniques. Some of the key institutes in this development were Oak Ridge National Laboratory, Bureau of Mines, Westinghouse Atomic Power Division and Argonne National Laboratory [22]. Much work continues on zirconium and the

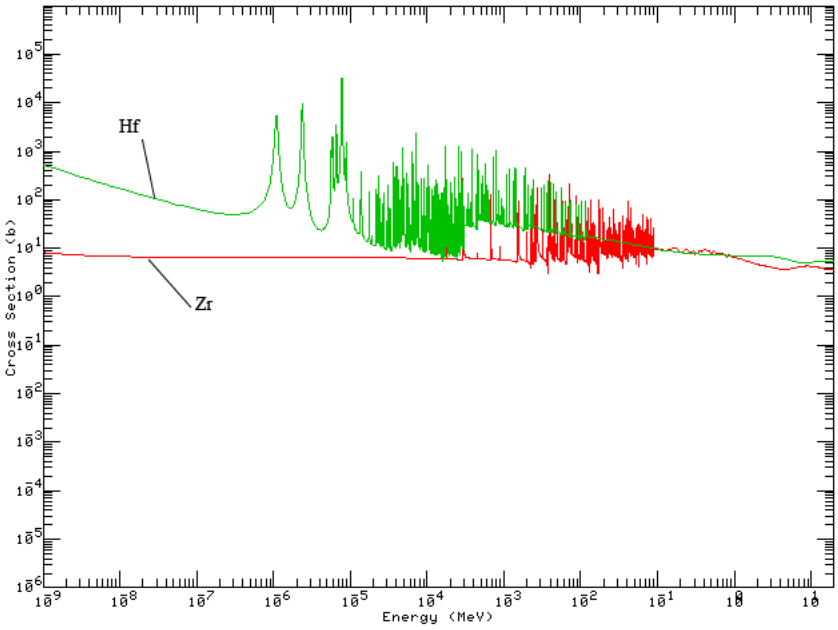

Figure 2.9. Absorption cross section for Zr and Hf. From KAERI website.

effects of the reactor environment on its properties, including the International Symposium on Zirconium in the Nuclear Industry [34] and others [35]. However, due to its use in naval reactors, much information about processing and forming is not openly available today.

Zirconium has two phases, a low-temperature alpha phase with an hexagonal close-pack (HCP) structure and a high temperature beta phase that is body-centered cubic (BCC). The lattice parameters of each phase and the transition temperature are listed in Table 2.2. Impurities such as oxygen and hafnium can change the lattice parameters of both phases, making true measurement difficult unless care is taken to remove all impurities. An impurity concentration of just 1 at.% can change the lattice parameters in the alpha phase by nearly a tenth of a percent [22]. Table 2.2 lists several parameters of zirconium structure, including thermal and mechanical properties.

According to the free energy of formation of Zr/ZrO_2, the metal will reduce oxygen from most TRU oxides. It may be necessary to coat the oxide particles with an inert

Table 2.2
Zirconium Properties

Property	Value	Property	Value
α phase (HCP)		Young's Modulus	68 GPa
a_o	3.232 Å	Shear Modulus (298 K)	33 GPa
c_o	5.147 Å	Poisson Ration (298 K)	0.34
c_o/a_o	1.593 Å	Density (298 K)	
β phase (BCC)		Thermal Conductivity (300 K)	22.6 $\frac{W}{m \cdot K}$
a_o	3.61 Å	Thermal Expansion (298 K)	5.7 $\frac{\mu m}{m \cdot K}$
$\alpha \rightarrow \beta$ Transistion	865 °C	Density	6.511 $\frac{g}{cm^3}$
Melting Point, T_m	1845 °C	Electrical Resistivity (293 K)	421 n$\Omega \cdot$m
Boiling Point, T_B	$\sim$ 4400 °C		

metal to inhibit gettering. Oxygen reduction of the TRU oxides could lead to the formation of metallic TRU, which may lead to localized melting within the cermet at reactor temperatures. Another concern with the formation of zirconia around the dispersed fuel particles is the lower thermal conductivity of the oxide, leading to delays in the thermal response of the fuel.

Figure 2.10 shows the Zr-O binary phase diagram. Oxygen is soluble up to 30 at.% in α-Zr which explains why the metal is used as an oxygen getter in some systems. Oxygen migrates as a negative ion in Zr.

Figure 2.11 is the Zr-Cu phase diagram. Copper is only soluble in α-Zr to 0.2 wt.%, increasing slightly for the beta phase. For this design, copper will be used as the billet canister and as a sacrificial lubrication during extrusion. After the solid cermet is formed the copper layer will need to be removed either by machining or electrochemical corrosion. Lustman [22] recommends using Cu as a sheath material for Zr extrusion at temperatures below 750 °C and iron at higher temperatures. Copper has been chosen as the sheath material for these experiments based on its

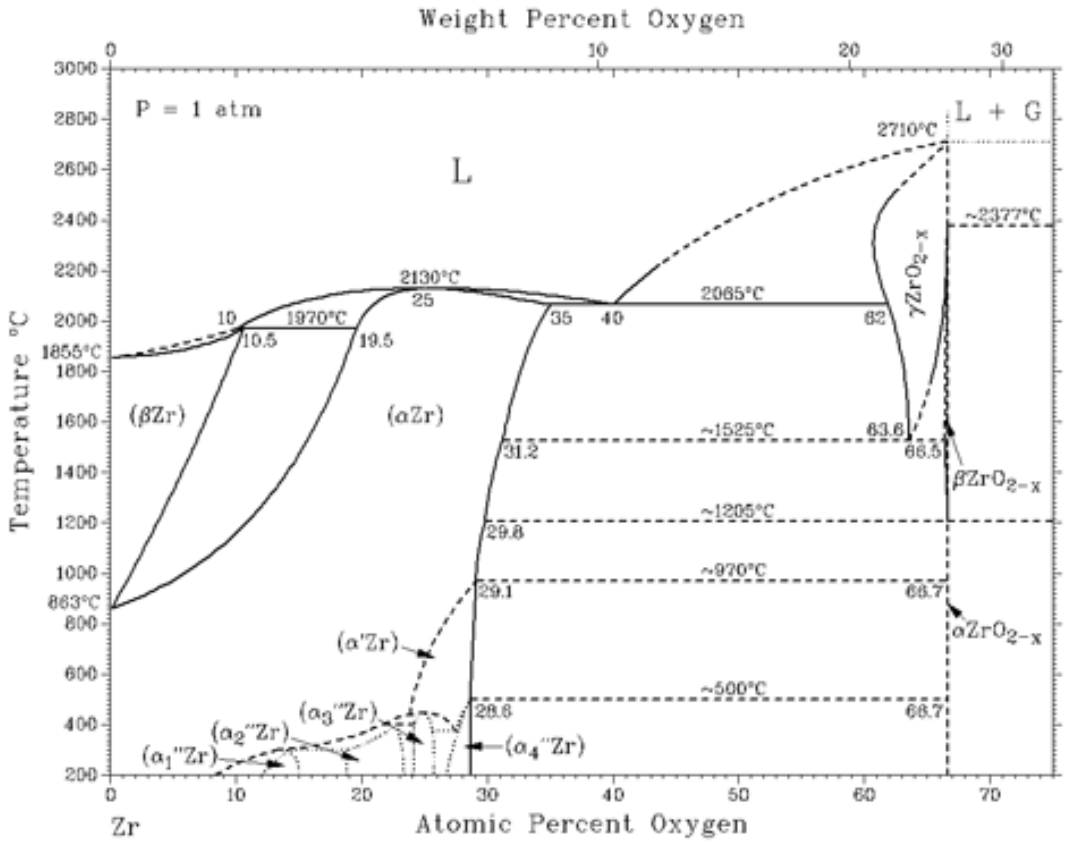

Figure 2.10. Zr-O system [36]

successful use at Idaho National Laboratory [8]. The main concern with using copper is the Cu-Zr eutectic temperature of 885 °C AND 38.2 at.% Zr. The billet will not be heated above this temperature in order to avoid a eutectic reaction.

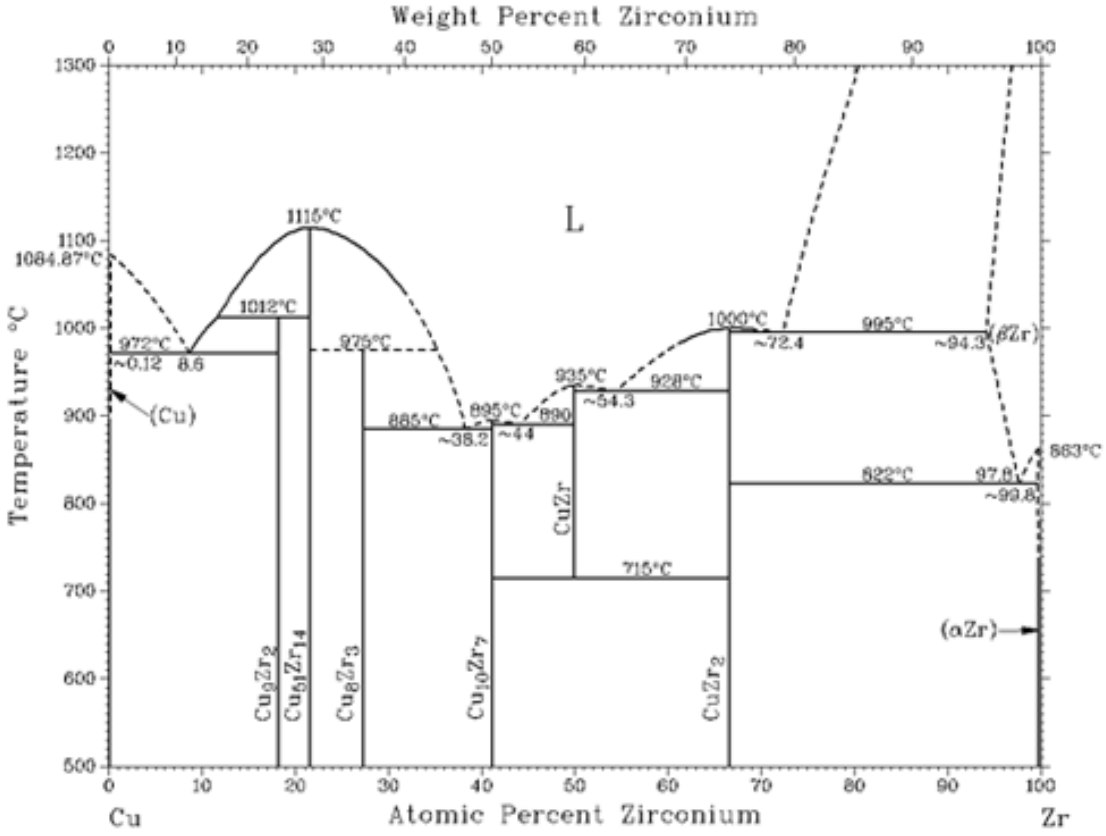

Figure 2.11. Zr-Cu system [36].

3. EXPERIMENTAL SETUP

3.1 Equipment

3.1.1 Hydraulic Presses

A direct extrusion process was established using a 90 t hydraulic press and cylindrical ceramic fiber heaters. The press had been in storage and unused for a number of years. Previously it was used as a cold-isostatic press, having the press cylinder mounted on top of a 4-leg stand with a movable pedestal at the botom. A separate control box containing an Enerpac modular air hydraulic pump with a Gibbons electric motor and the required high pressure tubing accompanied the press. The control box also contains a digital pressure controller, without the pressure transducer. Table 3.1 contains the product information about the units in this system.

Figure 3.1(a) shows the dual-action cylinder above the pedestal. Figure 3.1(b) shows the control box with a view of the hydraulic pump and the gauges and electronics on the front.

The system was originally built by PSIKA Pressure Systems Ltd., unfortunately this company went out of business at the end of 2004 when the owners retired. No documentation was available from them. On the pump is a label for A&B Hydraulics in Indianapolis, IN but this company was no longer available either.

The system was inoperable upon receipt. Our laboratory did not have an available 240V power supply near the press. During the wait for electricity, several hydraulic supply retailers were contacted about information for the press components. The units weren't identifiable from the Enerpac website due to their age. Several local companies were contacted and a supplier in Indianapolis was able to recognize the components. From their information it was determined that the system was originally

Table 3.1
Unit Information for PSIKA Press.

Unit	Manufactuer	Part No.	Description
Ram Cylinder	Enerpac	*unknown*	Dual-action hydraulic ram
Hydraulic Pump	Enerpac	*unknown*	Modular Air Hydraulic pump
Electric Motor	Gibbons Electric		Electronic motor
Load Cell	Omega	LCDW20K	Washer type load cell, 0-20000 pounds
Bridge Conditioner	Fylde Electronics	FE-492-BBS	Combination bridge balance and dc power supply
DC Amplifier	Fylde Electronics	FE-254-GA	Differential DC amplifier
Trip Unit	Fylde Electronics	FE-285-DTU	Dual (low and high) trip unit

built in the mid-1970's. This would prove to be another difficulty in repairing the system.

The hydraulic pump was started after the 240 V power supply was installed, but pressure would not build up. The pump and high pressure tubing were disassembled and cleaned. The gasket on the hydraulic reservoir also needed replacing. After cleaning and rebuilding the system, it was able to provide a small amount of pressure. A secondary relief valve was located and adjusted, allowing full pressurization. Only one hydraulic line came with the system to connect the pump to the dual-action cylinder. This would only allow pressurizing one side of the ram without repositioning the hose at pressure. A new hose was added to the system and it enabled the cylinder to extend and retract.

(a) Ram cylinder (b) Control Box

Figure 3.1. Press system with ram cylinder and control box

In the control box is an electronics box containing equipment to control the pressure of the system. The electronics box contains a digital readout, a differential dc-amplifier, a bridge conditioner, dual-trip unit, and a manual/automatic operation switch. The units were produced by Fylde Electronics Ltd. in the United Kingdom. Initially the unit would allow manual operation through a hand-held control. Switching to automatic control would pull the ram into the cylinder. Many failed attempts were made to configure the system for automatic control, usually ending in a blown fuse. Finally the unit was sent to the manufacturer for analysis. Fylde confirmed that the unit was functioning properly and returned it with operations manuals for the amplifier, trip unit, and bridge.

Using the manuals and the notes from Fylde , control of the direction of the press cylinder was achieved in automatic mode. However there was no load cell in the system to allow it to control the pressure. The load cell has since been purchased and will be installed for future work. The control box also has a data recording plug that will record the pressure of the system.

A manual Carver Laboratory press was also used (Fig. 3.2). This press uses a hand operated hydraulic system to apply pressure between a hydraulic ram at the bottom of the press and a static plate at the top. The Carver press has a maximum capacity of 12 t. This press system was used while the Enerpac press was not functioning.

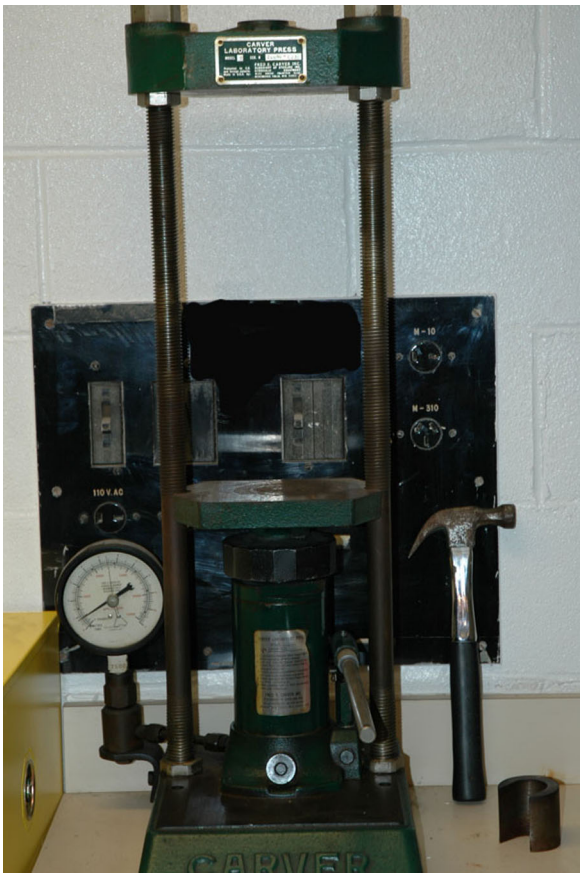

Figure 3.2. Carver Laboratory manual hand press.

3.1.2 Extrusion Tooling

The extrusion tooling for this experiment is made of NuDie V (AISI H-13) tool steel. This steel was chosen for its low cost, high temperature toughness, and the proof of principle work performed at Idaho National Laboratory (INL) [8]. The tools were designed using CAD software and manufactured by the Purdue Nuclear/Aeronautics department machine shop and Peerless Pattern of Lafayette, IN. The tooling design was kept simple, using only three components: billet holder, die, and ram. Figure 3.3 is a schematic of the tooling and the billet.

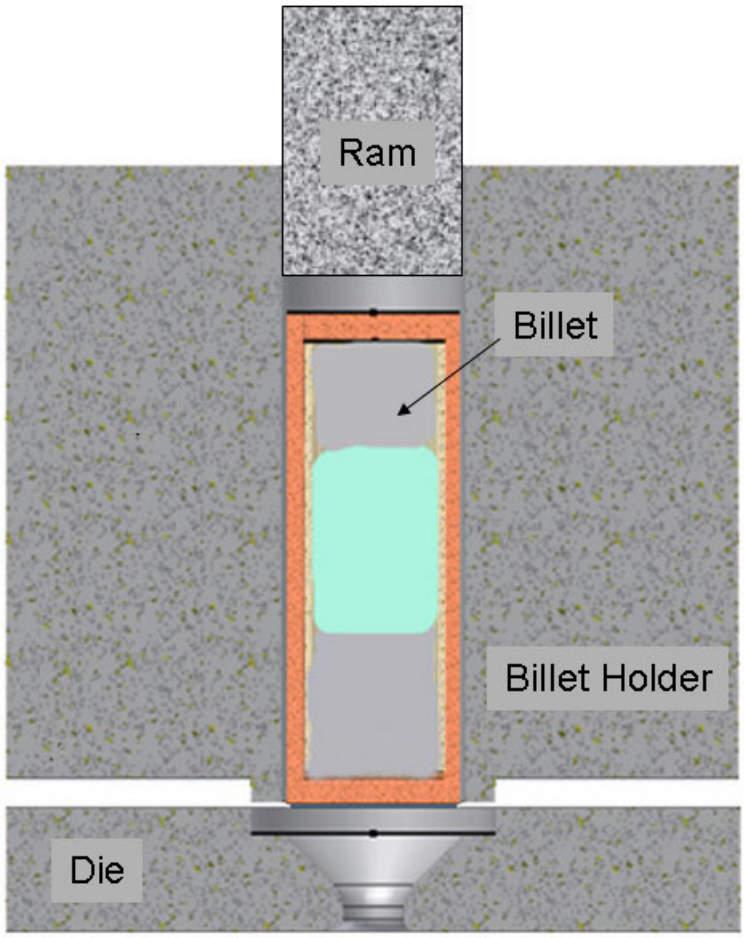

Figure 3.3. Die assembly with billet. Die and billet faces are flush during extrusion, separated here for visual purposes.

Following the specifications provided by the manufacturer, all tool steel components were heat treated. First the steel is preheated to austenitize at 1025 °C, holding at 650 °C and 830 °C to equilibrate. The time at the austenitizing temperature was 45 minutes. The component was then air quenched from 1025 °C under forced convection to maintain a quench rate of at least 25 °C/min. After cooling to room temperature, the components are tempered twice at 540 °C for at least two hours with an air cool to room temperature between tempers. Tempering at this temperature maximizes the hardness of the metal.

The first heat treatment always results in highly oxidized surfaces with a large amount of scaling. These components were returned to the machine shop for polishing. The subsequent pieces were wrapped in stainless steel foil packets that had been filled with discarded newsprint to consume oxygen in the package. Although the units came out discolored, no major oxidation or surface defects were incurred and post-heat treatment machining was avoided.

The billet holder is essentially an H-13 cylindrical tube. The purpose of the billet holder is to align the billet with the die and to keep the billet from expanding radially during the extrusion. The billet holder dimensions are 7.62 cm (3 in) O.D. x 6.35 cm (2.5 in) high with a 1.9 cm (0.75 in) axial hole in the center. At the bottom of the holder is a mating lip, 0.25 cm thick and 0.25 cm deep that locks into the die. This two-piece die configuration allows simplified machining and separation of the die and holder after the extrusion. It was found that a one-piece die/billet holder unit was expensive to manufacture and could only be used once [8].

Several dies were made for this project, all attaching to the billet holder as shown in Figure 3.3. The opening of the die is 1.9 cm (0.75 in), corresponding to the billet diameter. The importance of die angle and friction was discussed in section 2.2.1. It was requested that all faces in contact with the billet be machined as smooth as possible. No modeling calculations were performed to optimize the work required to deform the billet, therefore the initial die angle (α) was 90° as a best guess for optimization.

The billet for this extrusion is an open-ended copper canister containing a blend of zirconium and yttrium-stabilized zirconia (YSZ) powders. The open end of the canister is sealed with a copper lid. The diameter of the copper was kept at 1.9 cm (0.75 in) and its height varied when necessary. The plug for the open end of the canister is .254 cm (0.1 in) thick and 1.907 cm (0.751 in) in diameter to fit tightly and keep the Zr from spilling out or air from getting in.

Several extrusion methods have been used in this project, beginning with a setup developed from the literature review and discussion with advisor and R. Fielding of INL [8].

4. RESULTS, AND THEORETICAL ESTIMATES

The objective of these experiments was to develop a working extrusion process in the laboratory and define the initial parameters of interest for future work. Table 4.1 is an overview of the extrusion experiments run during this project.

4.1 Extrusion Development Test HX-1

4.1.1 Procedure

The first of the extrusion experiments was designed to test the system setup and make any necessary changes. Table 4.2 lists the system parameters for this experiment. The billet was prepared in the Ar atmosphere glovebox. The copper canister was fabricated to tightly hold the Zircaloy tube inside, the O.D. of the tube was 1.65 cm. The tube was cut to leave 0.1 in at the top of the canister for the copper lid. The tube was inserted into the canister and the bottom layer of the canister was covered with -325 mesh MgO powder. The Zr powder was weighed out and about half of it was poured into the canister with a funnel. The YSZ powder was then weighed and poured on top of the Zr powder. The remaining Zr powder filled in the top of the canister. The two powders were mixed in the can with a laboratory spoon. Some powder was lost during the mixing as the spoon was larger than necessary. The spoon was held to keep it from touching the bottom of the canister and mix as little of the MgO powder as possible. Mixing continued for approximately 10 minutes until the powders appeared well mixed. The canister was tapped on the floor of the glovebox to pack the powders. This left a small gap at the top of the canister, below the Zircaloy tube. This gap was filled with MgO powder and the copper lid was hand pressed into the billet.

Table 4.1
Overview of Extrusion Experiments

	Mixing Method	A_o/A_f	V_f	Temp. (°C)	Comments
HX-1	stir	9	20 †	700 §	tooling destroyed
HX-2	stir	9	40 †	700 §	ram destroyed, press malfunction
HX-3	shake	9	15 †	800 §	billet cooled before extrusion, 23.1 kpsi applied
HX-4	shake	9	‡	805 §	35.3 kpsi applied, no extrusion
HX-5	shake	9	20	800	Tooling heated to 760 °C, tooling failure
HX-6	shake	9	20	830	extrusion of 0.5" of cermet, rod burst
HX-7	shake	9	30	845	high strain rate, extrusion of full billet, rod burst
HX-8	shake	2.66	10	850	full billet extrusion

†HX-1, HX-2, & HX-3 are weight percent.

‡Billet from HX-3 was reused in HX-4.

§Temperature not well defined due to billet transfer.

Table 4.2
HX-1 Description

Cu Canister		Powders	
Volume (cm^3)	6.6	Loading (wt.%)	20
I.D. (cm)	1.65	Zr (g)	10
O.D. (cm)	1.91	YSZ (g)	2.5
Mass (g)	29.5		
Cu Lid		Temperature (°C)	
Thickness (cm)	0.261		
Mass (g)	5.0	700 °C	
O.D. (cm)	1.651		

The billet and tooling were assembled and put into a furnace. The tooling included the die, billet holder, and the extrusion ram. The die had a reduction ratio of 9, with a final diameter of 0.25 in. The die angle was supposed to be 90°, however it appeared to be much larger than this. Miscommunication with the machine shop had caused the wrong angle to be used. The die was still used as it was the only one on hand. The assembly was heated to 700 °C for 30 minutes before being removed from the furnace and placed on a mobile cart with fire-resistant blocks layered on the surface. The cart was moved to the press and the assembly placed on the pedestal.

There was no end cap for the press cylinder as it was forgotten during preparation. A piece of 1/4 in thick steel was placed between the press cylinder and the extrusion ram.

4.1.2 Observations

The press was powered up and pressurized. As there was no working load cell with the unit, pressure was measured from the oil pressure at the reservoir. As the pressure increased, the steel plate between the two rams deformed and the extrusion

ram became lodged in the press cylinder. It appeared to be extruding because the visible portion of the ram was decreasing, however this was the ram going further into the cylinder locking mechanism. When this was realized the press was immediately unloaded and powered down.

4.1.3 Outcomes of HX-1

The billet holder, die, and billet were fused to the extrusion ram which was jammed into the press cylinder. The die was easily removed from the billet holder, leaving the billet exposed. Slight deformation of the bottom of the billet showed that it did compress into the die face, however no extrusion occurred. The billet holder, extrusion ram, and billet assembly was hanging from the cylinder and unmovable. The tooling was allowed to cool overnight as no quench method was available. Several minutes of prying and hammering were involved in separating the assembly from the press cylinder.

Upon closer examination it was found that the cylinder locking mechanism had been damaged, as seen in Figure 4.1. The locking mechanism is an attachment for cold-isostatic pressing and would not be needed during these experiments. No other damage occurred to the press and the tooling was taken to the Carver press to try and separate the components. The assembly was loaded to 8 t and no movement occurred. At this point the tooling in this assembly was considered lost and new components would be needed, except the die. The tool assembly was taken to the machine shop and cut radially though the billet. Figure 4.2 shows the sectioned billet.

4.1.4 Procedure Modifications

A tool steel cap was fabricated for the press cylinder. The cap was designed to hang freely from the cylinder, via the locking mechanism, until loading. The bottom of the cap is 0.5 in thick. No other modifications were made at this time.

Figure 4.1. Press ram locking mechanism, damaged after HX-1.

Figure 4.2. Sectioned HX-1 billet, unextruded. Copper canister, Zircaloy sheath, and cermet mixture visible.

4.2 Extrusion Development Test HX-2

4.2.1 Preparation

This experiment was run prior to the analysis of the HX-1 billet. Table 4.3 lists the experiment parameters. The main difference is the YSZ loading was increased to 40

wt.% . A new billet holder and extrusion ram were fabricated and heat treated. The die from HX-1 was reused, having taken no damage during the previous experiment. The billet preparation for HX-2 follows the method used in HX-1. The copper lid

Table 4.3
HX-2 Description

Cu Canister		Powders	
Volume (cm^3)	6.6	Loading (wt.%)	40
I.D. (cm)	1.65	Zr (g)	6.5
O.D. (cm)	1.91	YSZ (g)	4
Mass (g)	29.5		
Cu Lid		Temperature (°C)	
Thickness (cm)	0.261		
Mass (g)	5.0	700 °C	
O.D. (cm)	1.71		

was slightly larger than designed and caused the top of the billet to expand. The expansion kept the billet from easily going into the billet holder and the Carver press was used to press it into the holder.

Again, the tooling and billet were assembled and heated in a furnace to 700 °C for 45 minutes. The press was powered up prior to removing the tooling from the furnace.

4.2.2 Observations

The press was loaded with a small amount of pressure and the cap was inspected to ensure a good fit. The press was then loaded to an oil pressure of 7500 psi. The maximum pressure listed on the press control box is 10,000 psi. The view to the press was obstructed for safety. Visual confirmation of ram displacement did not occur, however a creaking noise could be heard coming from the tooling. This continued for

~30 seconds, at which time it was thought that some extrusion had occurred and the press was unloaded.

4.2.3 Outcomes of HX-2

Figure 4.3. H-13 tool steel extrusion ram destruction after HX-2.

Upon retraction of the press cylinder it could be seen that the extrusion ram had been deformed. The assembly was removed from the press and placed on the fire resistant brick. Inspection of the cylinder cap showed no signs of damage. No material passed through the die and it was easily removed from the billet holder. The exposed billet showed signs of deformation into the die. As in HX-1, the ram, billet,and billet holder were fused together. After pressing the assembly on the Carver press the ram moved about 0.1 in out of the billet holder (see Figure 4.3). Further removal wasn't possible with the Carver press. The tooling was allowed to cool overnight and then placed on the Enerpac press to force the billet and ram out of the holder. The assembly was separated and the billet holder was salvaged.

Figure 4.4 is the cross sectioned billet from HX-2. It can be seen that there is a large quantity of YSZ in the billet. The loading for this experiment was 40 wt.% , however this appears to be too high. Most of the particles are in contact with each

other and this is not desirable. Also, it became evident from Fig. 4.4 that there was too much copper in the canister.

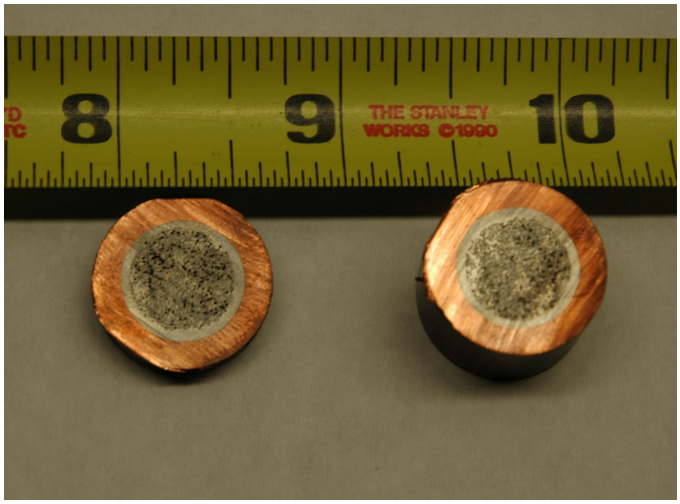

Figure 4.4. Sectioned billet from HX-2, unextruded. Copper canister, Zircaloy tube, and cermet powders visible

4.2.4 Procedure Modifications

The copper canister is a sacrificial element of the billet, used as a lubricant for extrusion and protection for the Zircaloy tube. The canister O.D. was set at 0.75 in because that is a standard copper bar diameter and the internal diameter was set to be flush with the Zircaloy tube. It was decided that there was too much copper in the billet and it needed to be removed. The copper canisters could be fabricated much quicker than the tool steel components so the outer diameter was left. This required the removal of the Zircaloy tube because it would no longer fit inside the new canister. This change was acceptable at this stage of development because it was felt that the extra resistance to deformation of the tube may be keeping the billet from extruding. The MgO powder was also removed. No evidence of Zr/Cu interaction had been seen from the billets and the MgO was felt to be an unnecessary component in the billet.

A new die was fabricated with a computer-operated lathe to ensure the 90° die angle in an attempt to reduce the extrusion threshold pressure of the billet. A smaller angle was not chosen because of the possibility of increasing the surface friction at the die face. A boron nitride aerosol lubrication would be applied to the billet and all tool surfaces it contacts during the extrusion. This die was not available in time for use with HX-3 so the original die was used again.

Communication with R. Fielding at INL confirmed that Zr extrusion was very difficult at temperatures less than 700 °C [8]. Originally, billet cooling during transfer wasn't anticipated as a problem due to the large thermal mass of the billet holder surrounding it. It was now felt that this issue also needed to be addressed. A new furnace would be used to heat the billet separately from the tooling, so a higher billet temperature could be achieved. The extrusion ram would no longer be heated with the tooling and would be used cold.

The powder preparation mixing method was also changed to achieve a more homogeneous distribution of YSZ. After weighing, the powders were combined in a sealed glass vial, the volume of the vial was about 1.5 times that of the copper canister. The vial was then shaken vigorously by hand. Shaking continued until the powders appeared well mixed, usually 6-8 minutes. The powders were then loaded into the canister and it was tapped for several minutes to pack the particles. After HX-2 the Enerpac press stopped functioning. It was decided to use the Carver press for the next experiments until the Enerpac press was repaired.

4.3 Extrusion Development Test HX-3 & HX-4

HX-3 was a test of the Carver press. Complications during the initialization of the extrusion of HX-3 led to a failure to extrude. The billet was slightly compacted but no other deformation was seen and it was reused for HX-4.

Table 4.4
HX-3 & 4 Description

Cu Canister		Powders	
Volume (cm^3)	6.6	Loading (wt.%)	15
I.D. (cm)	1.65	Zr (g)	16.55
O.D. (cm)	1.91	YSZ (g)	2.95
Mass (g)	29.5		
Cu Lid		Temperature (°C)	
Thickness (cm)	0.261		
Mass (g)	5.0	800 – 820 °C	
O.D. (cm)	1.65		

4.3.1 Preparation

The die and billet holder were coated with the BN spray and placed in a furnace at 600 °C. The powders were weighed out to give a 15 wt.% loading and shaken in the glass vial. The cermet mixture appeared much better mixed than with the in-can stirring method. The billet was sealed and placed in a furnace. The new furnace is controlled by a variac. This made precise temperature control difficult, with the temperature varying by up to 20 °C. The tooling was held at temperature for 2 h and the billet for $\sim$ 1.5 h with the variac set near 48.5%. The tooling was removed from the furnace and placed on the Carver press. The billet was placed in an insulation-lined pan and taken to the press. The billet furnace and Carver press were across the lab from each other ($\sim$60 ft.). Assembly took place on the Carver press pedestal. This assembly method proved to be flawed because the press pedestal was not rigidly attached to the ram. During assembly the billet fell off the pedestal and the tooling was moved out of position while trying to secure the billet. Reassembly took a couple minutes and it was believed that the billet had cooled well below the desired temperature.

4.3.2 Observations

The experiment proceeded, loading the billet to 5.1 t, achieving a pressure of 159.1 MPa. At this point, increased pressure was difficult even with the use of an extension bar for the hydraulic ram. No deformation was observed and the assembly was quickly disassembled. It was assumed that the billet had cooled below the extrusion temperature and another attempt should be made with assembly taking place on a sturdy surface. The billet had become compressed, having a reduction in height of ~ 5 mm. The tooling and billet were re-coated with BN and reheated in the same way as before. Assembly during HX-4 took place on the fire resistant brick which went much smoother than the pedestal assembly of HX-3. The billet was loaded into the holder and the entire assembly was placed on the die. The cold ram was placed in the top of the billet holder and the press was loaded.

4.3.3 Outcome of HX-3&4

The billet was loaded to 243 MPa and no extrusion occurred. From the literature, it was expected that a pressure greater than 300 MPa would be needed. This was outside the capacity of the Carver press setup. The billet was sectioned using a diamond saw and mounted for polishing. Figure 4.5 is the resulting billet from these experiments. The sectioned billet again shows no extrusion. The missing copper from the top and bottom of the billet was removed during cutting to allow the billet to fit in the polishing mold. The YSZ powder is homogeneously distributed throughout the matrix, suggesting that the new mixing method was successful. At the top of the billet (right side of figure) a discoloration of the matrix metal can be seen. This is believed to be the corrosion of the Zr metal due to a poor canister lid fit.

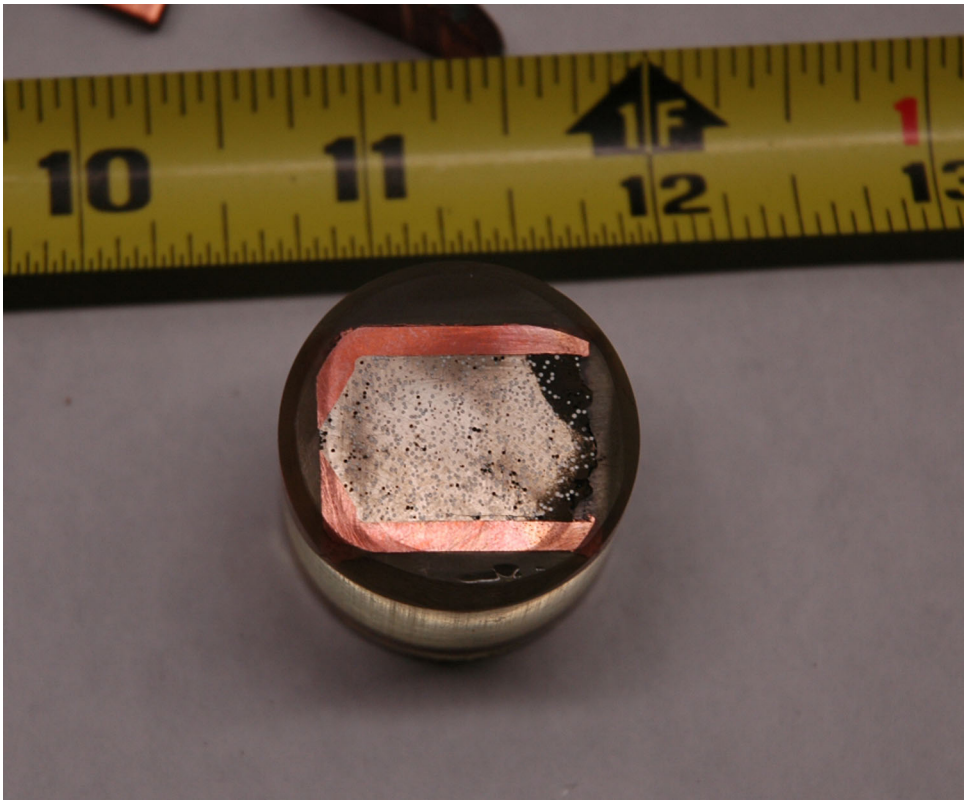

Figure 4.5. Sectioned billet from HX-3&4, unextruded, mounted. The discoloration at the top of the billet (right side) is corrosion from a loose lid fit during heating.

.

4.3.4 Procedure Modifications

During HX-3&4 the Enerpac press was repaired and a new procedure was developed. In order to reduce the room temperature exposure time of the components, an *in situ* heating process was designed using ceramic fiber heaters purchased from Watlow, in St. Louis, MO. The heaters were chosen for their high temperature capability and ability to fit into the Enerpac press system. The heaters are positioned on the press pedestal so that exposure to room temperature is limited to a few seconds while the billet is transferred into the billet holder. Figure 4.6 is a schematic representation of this setup on the Enerpac press pedestal, with the pedestal pulled out from under the ram. The tooling heater has an ID of 10 cm (4 in) and a height of 20 cm

(8 in) The billet heater's ID is 3.8 cm (1.5 in) and is also 20 cm tall. These heaters use resistive heating elements to radiantly heat the component. Contact with the inside wall of the heater is not recommended because of the possibility of damaging or shorting the elements. This was not a concern for the tooling heater because it would not be moved during extrusion. However, the billet heater would be used to position the billet over the tooling for transfer. Therefore, the billet was contained in an Al_2O_3 crucible inside the heater

The ceramic board between the two heaters provides support for the billet heater. It has a hole in the top large enough for the billet to fall through for transfer. The hole is also used as a thermocouple port during heating. The ceramic board on top of the billet heater is used as insulation and provides a rigid thermocouple port. The lower heater is wrapped in fabric insulation for the duration of the process. Two thermocouples are used; one in the billet heater and on in the tooling heater.

Two 120V, 12Amp variacs are used to power the heaters. A control panel was fabricated using 1.3 cm (1/2 in) thick plexiglass and attached to the side of the press stand (Fig. 4.7). The backside of the panel (nearest the heaters) has a set of banana clips that allow quick removal of the wires connected to the heater terminals.

When the desired temperatures are reached, the press is powered up and the thermocouples are removed. The billet heater is positioned over the hole in the lower ceramic board until the billet drops into the bore hole of the billet holder. Beneath the tooling is a tool steel *spacer* to keep the billet holder at the top of the heater. The spacer is 7.6 cm (3 in) long with a 2.5 cm (1 in) diameter bore hole. This leaves 0.64 cm (0.25 in) of space at the top of the tooling heater. The billet heater and lower ceramic board are removed and the extrusion ram inserted. The pedestal is then moved under the press ram and the extrusion begins.

The powder mass calculation was changed to a volume percent calculation for the new billets. The equation involved the canister volume, V_T, loading percent, L, and powder density, ρ.

$$m_{\mathrm{YSZ}} = L \cdot V_T \cdot \rho_{\mathrm{YSZ}}$$

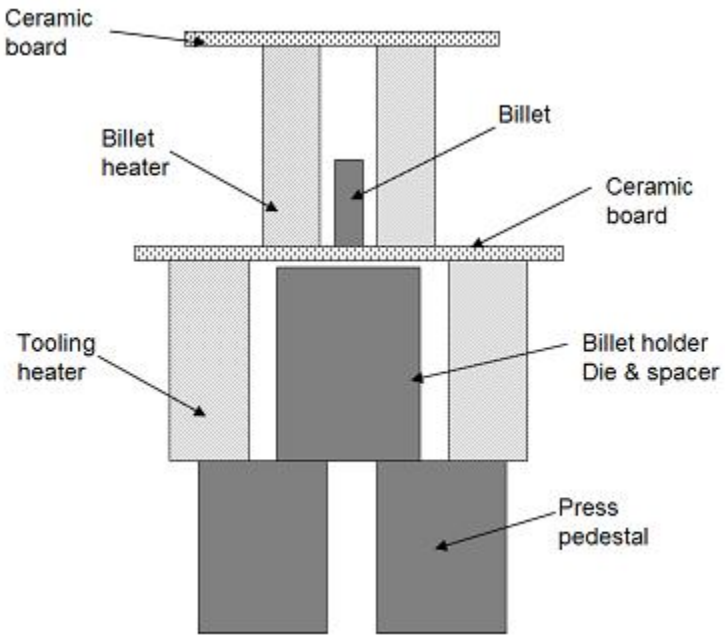

(a) Schematic

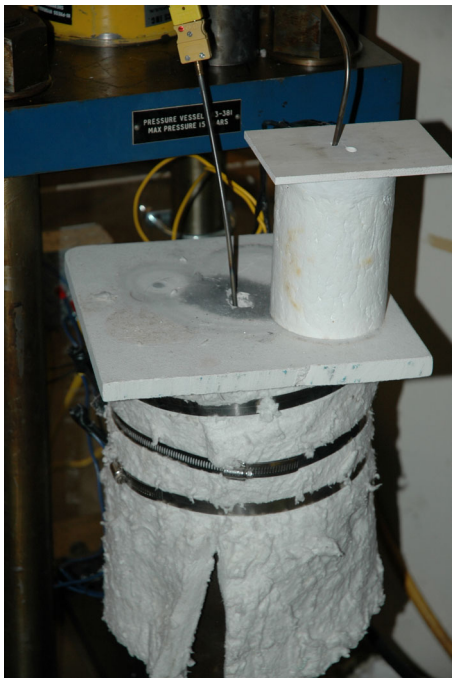

(b) Equipment

Figure 4.6. *In situ* heating setup, schematic (a) not to scale.

Figure 4.7. Heater control panel for *in situ* method.

$$m_{\mathrm{Zr}} \quad = \quad (V_T - L \cdot V_T) \cdot \rho_{\mathrm{Zr}}$$

The canister volume, V_T, is adjusted for particle packing by a packing factor, PF. If the true canister volume was 6 mL, the volume used in the above equations would be $6 \cdot$ PF. After weighing the powders they were again combined in the glass vial and shaken as in HX-3.

4.4 Extrusion Development Test HX-5

This experiment was the first run using the *in situ* heating setup. Due to a misplaced thermocouple, the temperature of the tooling was taken to 760 °C and subsequently deformed on loading. The bottom of the copper canister extruded prior to tooling failure. In Figure 4.8(a) it can be seen that a cavity was formed in the

(a) HX-5 Billet (b) HX-5 Die

Figure 4.8. HX-5 die and billet, post experiment. Billet and die deformation match. Also shows $\sim$ 3 cm of copper extrusion with formation of a cavity near cermet/canister interface.

copper piece that extruded. This cavity is due to the different rheologies of the copper and cermet; copper deforming more easily than the cermet. This was good evidence for use of Cu as a sacrificial lubricant even with the temperature restraint.

The billet holder was also ruined from deformation. The pressure caused the bottom of the bore hole to expand to 2.6 cm. The extrusion ram underwent no deformation. The billet information has been repeated in HX-6.

4.4.1 Procedure Modifications

A third thermocouple was added to the system to allow measurement of the temperature at the die face and the external tooling temperature.

4.5 Extrusion Development Test HX-6

4.5.1 Preparation

Table 4.5
HX-6 Description

Cu Canister		Powders	
Volume (cm^3)	5.1	Loading (vol)%	20
I.D. (cm)	1.65	Zr (g)	10.62
O.D. (cm)	1.91	YSZ (g)	2.32
Mass (g)	24.8	PF (%)	40
Cu Lid		**Temperature (°C)**	
Thickness (cm)	0.259	Billet	850 †
Mass (g)	5.0	Die/Tooling	549
O.D. (cm)	1.651		

†Temperature held at 830 °C, flashed to 850 °C before removing furnace.

Table 4.5 describes the conditions of HX-6. Prior to billet assembly, the Cu canister was modified by removing the 90° edge from the bottom with a grinding wheel. Although this left an uneven surface on the copper, it wasn't expected to adversely affect the outcome. The powders were prepared by the shake mixing method. The PF value of 40% was found to slightly underestimate the actual packing achieved with the tapping method, leaving a small gap at the top of the canister. A higher PF value would be used in the next experiment.

The components were coated with BN and placed in their respective heaters. The tooling was heated prior to billet preparation, taking almost two hours to achieve a flat temperature profile at 540 °C. The billet heater reached operating temperature in approximately 30 minutes. The billet was held at this temperature for 20 minutes

to achieve equilibrate. The overtemperature denoted by † in Table 4.5 was used to counter the slight cooling that occurs after removal of the insulation from the billet heater, prior to insertion. After sitting at temperature for 20 minutes, the billet heater was taken to 850 °C for a few minutes and removed.

4.5.2 Observations

Like HX-5, the billet transfer was very quick, taking only a few seconds. The billet had expanded slightly during heating and was forced into the bottom of the holder. The press was powered up prior to transfer and was ready to go when the press pedestal was positioned.

The press was initially loaded to an oil pressure of 17.2 MPa. The ram slowly displaced and the pressure relaxed to a value of 10.3 MPa. The load was increased to 20.7 MPa (oil pressure) and again allowed to relax. The relaxation stopped near 13.8 MPa. The pressure was increased to 27.6 MPa and very little movement of the ram occurred. At this point it was determined that either the billet had cooled below the extrusion temperature or not enough pressure was being applied. Not wanting to damage any of the components and noting the displacement of the ram, the experiment was stopped. The tooling heater was removed and the assembly was quenched in room temperature water.

4.5.3 Outcomes of HX-6

The product of HX-6 had an extruded section about 5 cm in length. The initial 3.5 cm was the bottom of the copper plug. This section had a bend in it, most likely caused by too rapid of extrusion for the copper. After the copper there was a straight section approximately 2 cm long of extruded Zr/YSZ cermet. Near the die exit there was a tear in the extruded rod prior to quenching. After removing from the quench, the tear burst the remaining rod open and broke it into two pieces (Fig. 4.9). It is possible that some of this damage was caused by the fall of the assembly during the

quench. However, the burst section is most likely related to the tear. The tear could have been caused by surface damage in passing through the die. Dead zone formation could have inhibited cermet flow and allowed the powder to be extruded without the copper canister. Another possibility is pressurization of gas in the canister during deformation. Because the cermet powders are not fully dense prior to extrusion, a large amount of gas from the glovebox was be present in the canister. During deformation this gas would become pressurized and possibly accumulate in pockets. After passing through the die, the pressure keeping the gas pocket from expanding would be removed and a rapid expansion could cause a rupture in the side of the extruded rod. This burst section is more prevalent in HX-7 and will be discussed further.

Figure 4.9. Remnants of HX-6, showing copper extrusion, burst, and remaining billet. Smaller sections

The extruded cermet of HX-6 was separated and mounted in Leco quick drying epoxy for microscopic analysis. A portion of the leading edge was cut radially and

the remainder was cut axially. Figure 4.10 is a view of the radial cross section taken from the leading edge of the billet, the diameter of the section is 0.635 cm. Notice the gap at the cermet/Cu interface showing that the bond is not well-formed in this region. Also visible are some porous regions, and depressions from oxide particle *pull out* during sample polishing.

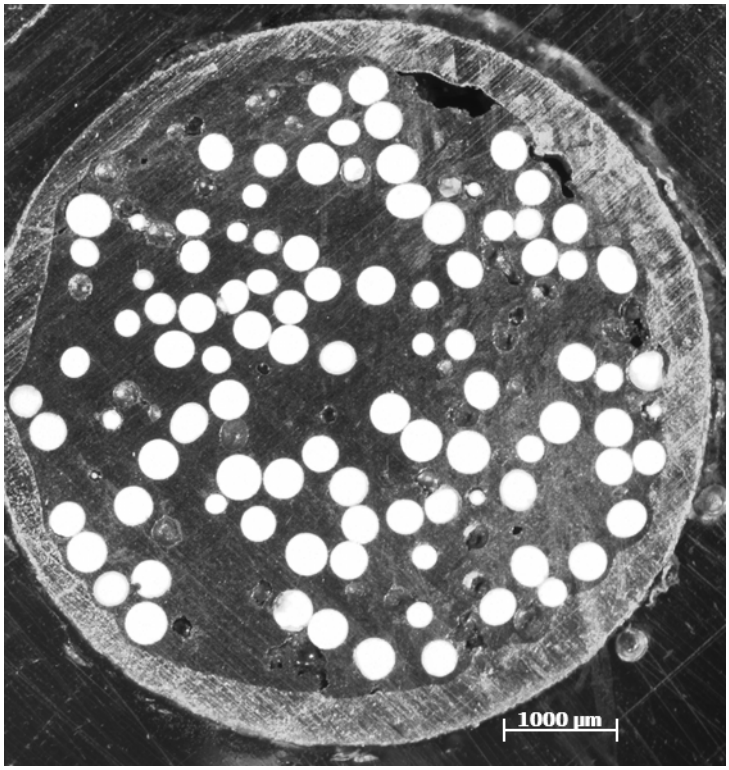

Figure 4.10. HX-6 radial cross section taken from cermet/Cu interface (bottom of billet) Diameter=0.635 cm. Cu sheath visible around cermet powders, Zr matrix = dark phase, YSZ = white particles.

Figure 4.11 is the axial cut of the specimen. The left side of the figure is the end that was extruded first, corresponding to Figure 4.10. A large amount of particle damage can be seen. It was expected that the damage concentration would be higher near the edge of the cermet, but as can be seen in the figure, no immediate spatial correlation exists. Of note, most damaged particles are fractured perpendicular to the extrusion direction. This suggests that the stress field in the deformation zone,

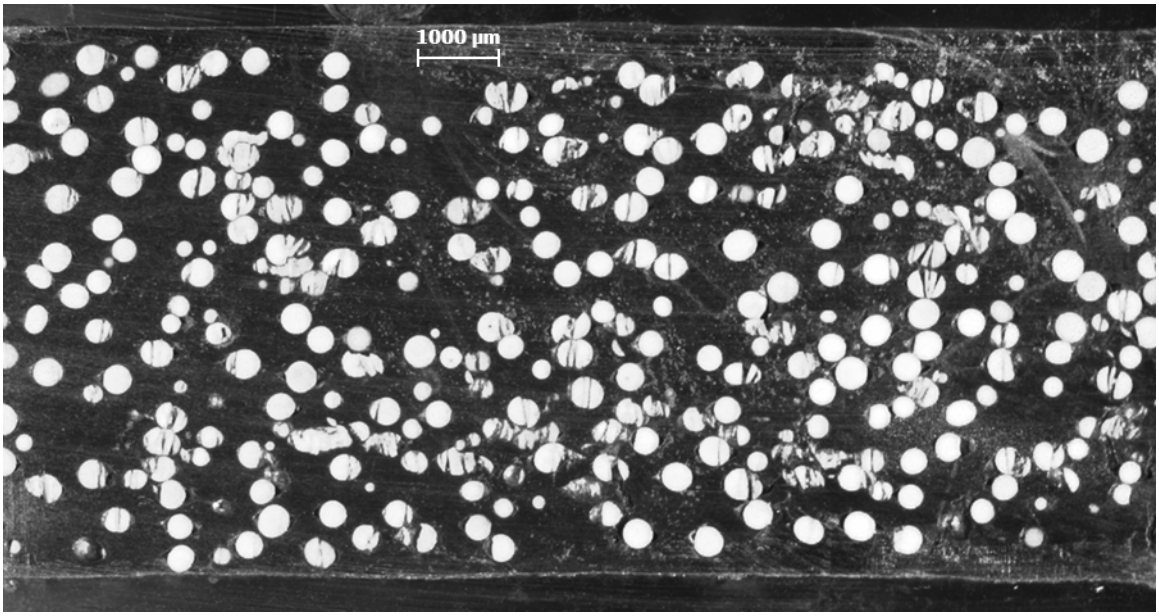

Figure 4.11. Results from HX-6, left side of figure is "front" of rod. Zr metal phase around white YSZ particles. Diameter=0.635 cm.

where flow is toward the axis, is too high for these particles. Particles that are in contact with each other show fracture occurring at the point of contact. As mentioned above, particle integrity in the cermet is of great importance. Cracking and fracture of the inclusions needs to be kept to a minimum, especially during fabrication. It can be seen in Figure 4.11 that some particles have been completely pulverized during deformation.

It was desired to do a grain size analysis on this specimen. The reason this has not been completed is due to the difficulty in etching Zr metal, usually requiring the use of HF [37]. The specimen was sent to Buehler Analysis Ltd., in Lake Bluff, IL. They were unable to etch the specimen, however, they provided a well-polished sample and were able to do a porosity measurement on the matrix. Using their in-house image analysis software Buehler measured less than 5% porosity in the matrix. This information strengthens the gas bubble burst theory mentioned earlier. It is believed that during deformation the gas in the canister was forced into pressurized bubbles.

Upon exiting the die, the release of deformation pressure could have caused the rod to burst.

Figure 4.5.3 was used to verify the loading calculation used during billet preparation, Eq. 4.1. Using the Scion Image software, the area ratio of YSZ particles to total area was calculated as 20-23%. This corresponds to a volume ratio of the same value. The volume loading of the pre-extruded powders was 20 vol.% .

4.5.4 Modifications to Procedure

HX-6 was considered a successful experiment. Although the entire billet did not extrude, it showed that the system would work for extrusion. The next test would load the billet to the maximum press capability.

4.6 Extrusion Development Test HX-7

4.6.1 Preparation

The particle loading was changed to 30 vol.% in this experiment.

Table 4.6
HX-7 Description

Cu Canister		Powders	
Volume (cm^3)	5.2	Loading (vol.%)	30
I.D. (cm)	1.65	Zr (g)	11.85
O.D. (cm)	1.91	YSZ (g)	4.43
Mass (g)	24.7	PF (%)	50
Cu Lid		Temperature (°C)	
Thickness (cm)	0.259	Billet	845
Mass (g)	5	Die/Tooling	545
O.D. (cm)	1.651		

Table 4.6 lists the parameters of HX-7. A PF value of 50% was used because in HX-6 it was found that a value of 40% underestimated the actual green density. The billet temperature was slightly higher than HX-6 as well. The ceramic fiber heaters have excellent temperature control with the variacs used and approaching the Zr/Cu eutectic was not a concern. Also as in HX-6, the bottom edge of the canister had been ground smooth using a grinding wheel.

The procedure is the same for this experiment as was used in HX-6. The billet was easily loaded into the holder. The time from billet heater removal to press loading was less than 30 s.

4.6.2 Observations

Upon loading, the ram displaced almost immediately, at an oil pressure of $\sim$ 6.9 MPa. The press cylinder was extended as quickly as it would go. The ram displaced more smoothly than in HX-6, becoming fully inserted into the billet holder within 30 seconds.

4.6.3 Outcomes of HX-7

Figure 4.12. Damage in HX-7. Left: full rod, showing break at beginning and end of cermet. Right: closeup of rod burst.

Initially, with the ease of deformation seen, it was hoped that the full rod had extruded. This was confirmed after removal of the tooling. Although the portion of the billet protruding from the die was highly deformed, two extruded sections were found at the bottom of the pedestal. The two sections of the extruded cermet had broken near the center. At the end of the piece that was nearest the die was a highly disfigured section seen in Figure 4.12. This damage is similar to that seen in the remaining billet protruding from the die. The damage seen in this figure is believed to have been caused by trapped gases in the canister. No damage or excessive porosity was seen in the extruded rod and it is believed that the majority of the gas accumulated at the top of the billet.

Figure 4.13(a) is an axial cut of the back end of the extruded piece ($\sim$2 in. into rod). The concentration of particle damage is much higher at the edges of the rod than the center. This corresponds to the metal flow theory discussed in section 2.2.2 where it was seen that the outer regions of the extruded rod undergo a much greater deformation than the central regions. Figure 4.13(b) is a close up of a completely destroyed particle in this outer region. Notice the elongation of the destroyed particle due to the higher deformation in this region. Particle damage does exist in the central regions of this rod, however most of these particles appear to be damaged by contact with other particles.

Also of interest in Figure 4.13(a) is the Cu/cermet interface. Copper will deform much easier than the cermet, as evidenced from previous runs, and appears to flow around the cermet in areas of high deformation resistance, usually involving a YSZ particle. This suggests that mechanical removal of the copper would most likely destroy some of the cermet. Originally the Zr-IV sheath was included to separate the copper from the cermet powder and facilitate removal. It is evident that some type of barrier is necessary or bare-powder extrusion.

Image analysis suggests the volume loading in the section seen in Figure 4.13 is slightly higher than expected, 37 vol.% instead of 30 vol.% . This is most likely caused by the buildup of YSZ at the outer edges of the extruded billet.

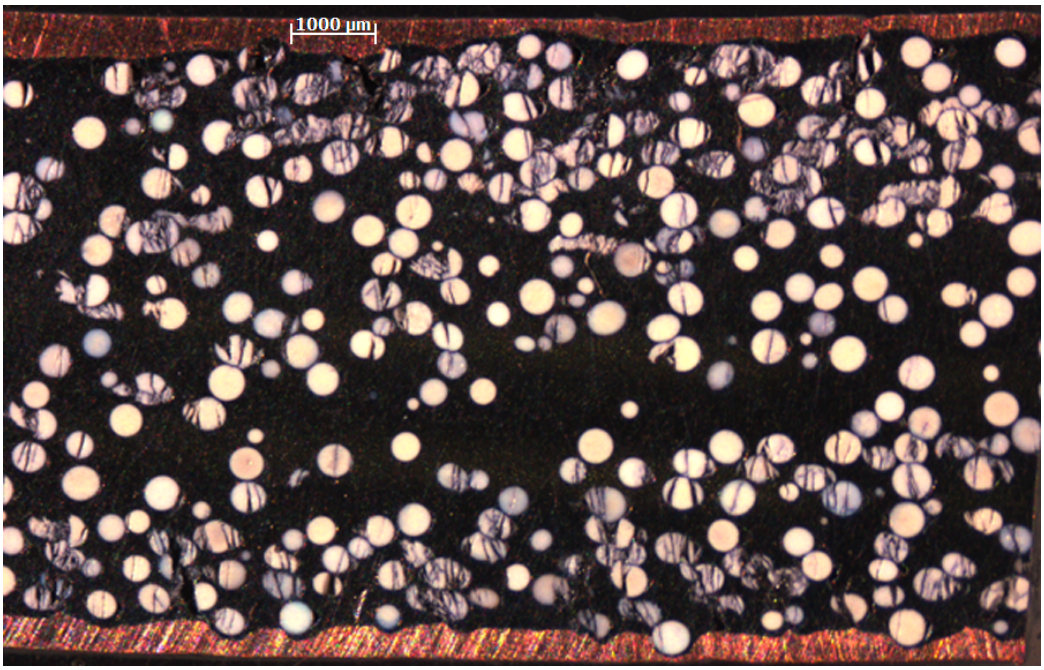

(a) Damage Profile

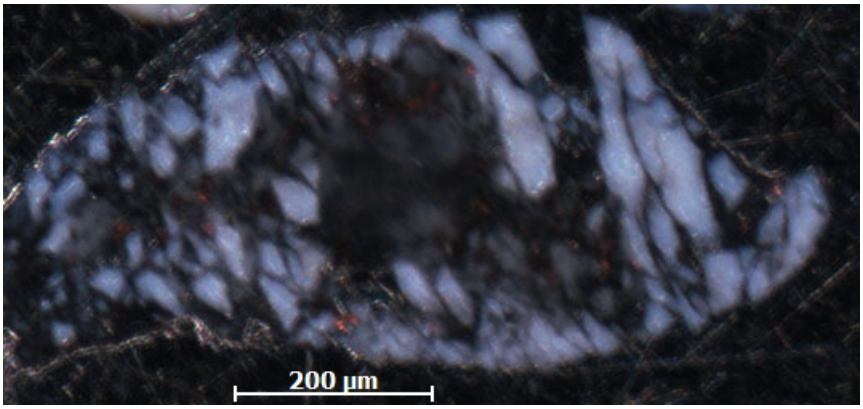

(b) Destroyed Particle

Figure 4.13. (a)Axial cut of extruded rod from HX-7. Notice damage concentration is much higher at outer regions of rod where deformation is greater. Contact fracture exists throughout specimen. Zr matrix with dispersed YSZ phase.(b) Completely destroyed YSZ particle showing elongation due to deformation.

4.6.4 Modifications to Procedure

The results of HX-6&7 show that extrusion will occur with the *in situ* setup. The bursting seen in the extruded rod is believed to be caused by trapped gases in the billet. In the next experiment the billet powders will be loaded as fully as possible and tap-packed into the canister to achieve a higher green density. To reduce particle damage a die has been made with a smaller reduction ratio (A_o/A_f=2.66). From the literature it is possible that this reduction will not form a well-bonded matrix cermet, however, evidence from the previous experiments suggests that is not the case. Specifically HX-3&4 in which only hot pressing occurred and a well-bonded matrix was formed. A new canister has been fabricated with a 45° chamfer on the bottom edge to remove excess copper.

4.7 Extrusion Development Test HX-8

4.7.1 Preparation

Table 4.7
HX-8 Description

Cu Canister		Powders	
Volume (cm^3)	5.7	Loading (vol.%)	10
I.D. (cm)	1.65	Zr (g)	17.72
O.D. (cm)	1.91	YSZ (g)	1.82
Mass (g)	26.9	PF (%)	55
Cu Lid		Temperature (°C)	
Thickness (cm)	0.259	Billet	850
Mass (g)	4.9	Die/Tooling	543
O.D. (cm)	1.648		

Experiment HX-8 was the first to use a canister with a chamfered bottom edge. To reduce the amount of particle damage seen in previous runs this billet is the lowest volume loading used thus far at 10 vol.% . Also, a die with a smaller area reduction was fabricated, A_o/A_f=2.66. The die was machined to a thickness of 0.406 cm which may be too thin for the die to survive the extrusion pressure. The die temperature was kept near 540 °C to provide as much strength as possible during extrusion.

The billet powders were weighed and blended as in experiment HX-6. The powders were then slowly added to the canister and it was tapped on the table. After tapping the canister, a metal rod was used to pack the powders more fully. A PF of 55 was used in this experiment in an attempt to get as much powder as possible into the billet and avoid excess gas buildup. The powders were added in eight segments, each time being tapped and packed with the rod. With the exception of a small amount of Zr dust escaping during packing, all powders were loaded into the billet. The canister lid was loaded into the top and also tapped with the metal rod. The top of the lid was seated 0.13 cm below the top of the canister.

The die, billet holder, and billet were coated with BN spray. The tooling and billet were heated with the *in situ* method to the temperatures listed in Table 4.7.

4.7.2 Observations

The billet was loaded into the holder and the extrusion ram loaded in about 30 seconds. The oil pressure never rose above 10.3 MPa and the ram displaced smoothly to full insertion, at which point the pressure rose and the ram was unloaded.

The tooling heater was removed and the assembly was removed from the pedestal. There was no extruded billet attached to the die but it was evident that the material had extruded from the full insertion of the ram and the material at the die face was deformed and cracked. Powder particles were falling out of the die face and burning in air, suggesting poor densification of the billet. The assembly was quenched in room temperature water and disassembled.

4.7.3 Outcomes of HX-8

Figure 4.14. Extrusion experiment HX-8 results showing die, extruded billet, and sectioned billet.

Figure 4.14 shows the die and billet after the extrusion. The thin die did not fail as seen in HX-5, however it did deform a small amount, though this deformation is not visible in Figure 4.14. Due to the small degree of deformation and the low pressures during extrusion, it is believed that this deformation occurred at the end of the extrusion when only a then amount of the billet remained in the holder. From the literature this remaining billet will cause an increase in extrusion pressure because of its resistance to flow inward to the die. A small portion of extruded billet (~ 0.635 cm) protruded from the die exit. This material was primarily copper with a thin coating of cermet powder at the bottom. Only copper was left in the face of the die, showing full cermet extrusion.

The extruded billet had fallen into the press pedestal. After retrieval it was observed to have a large crack near the bottom cermet/canister interface. The billet was cut along this crack and both pieces were sectioned axially for observation. The full and sectioned billet can be seen in Figure 4.14. A very large gap has formed between the bottom of the canister and the cermet. Also, the matrix has undergone some cracking at the tip and near the break in the billet. Figure 4.15 is a low

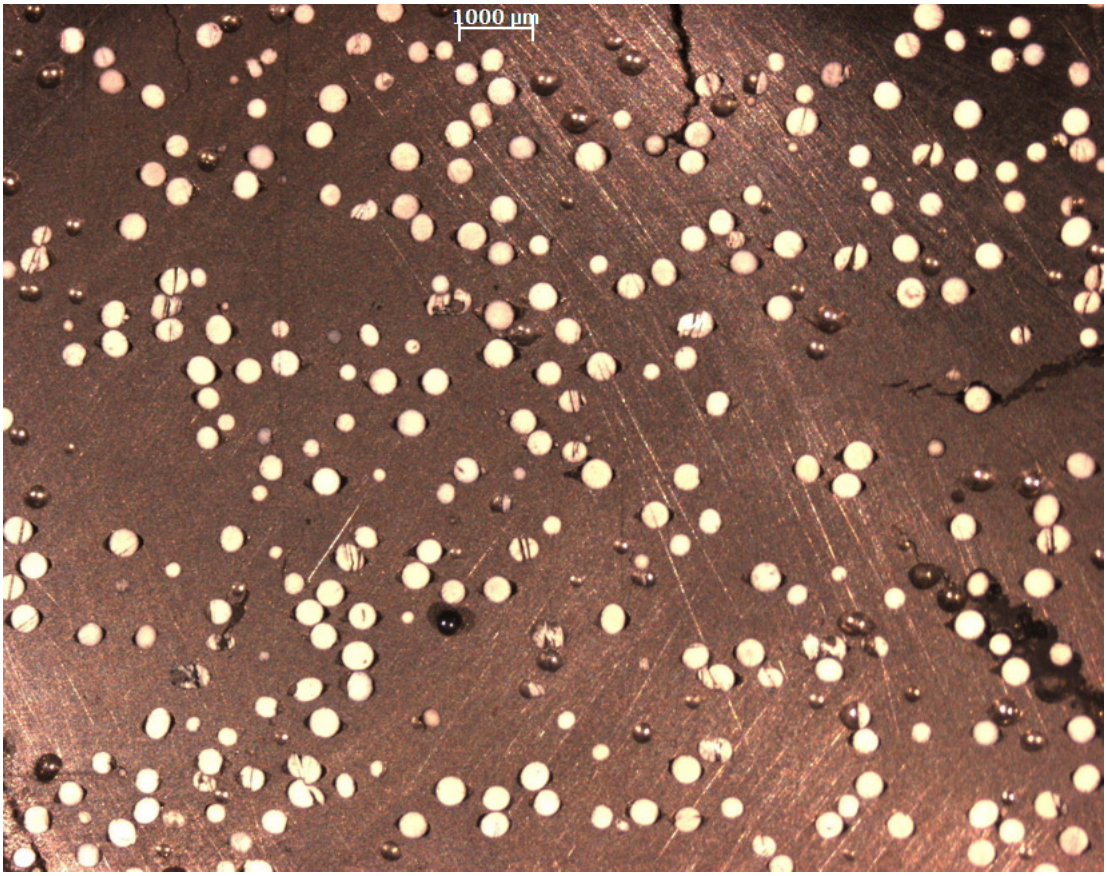

Figure 4.15. Low magnification optical image of HX-8 billet, trailing section. Right side of image corresponds to the front of the billet. Zr matrix with YSZ dispersed particles.

magnification view of the trailing section of the billet (after the break). Though some particle fracture can be seen, the concentration is much lower than in previous experiments with the larger area reduction. Some matrix damage has occurred in the form of cracking. The right side of the image is the front of the billet, near the cracked

section. These cracks travel approximately 1 mm into the billet. Matrix cracking can also be seen at the top of the image and in the lower corner. These suggest that the matrix is not well-formed due to the small area reduction.

Matrix irregularities can be seen near the particles as well. A gap has formed around the particles that is elongated in the extrusion direction. A closeup of this phenomena can be seen in Figure 4.16.

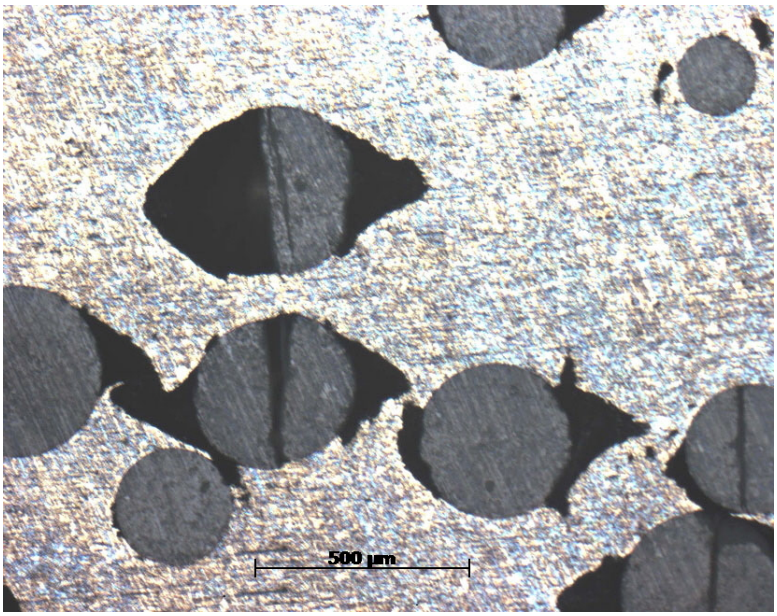

Figure 4.16. Zr matrix flow around YSZ particles in HX-8 showing gap formation along extrusion direction, 5X.

.

Figure 4.16 suggests that with the lower reduction ratio, matrix flow around the YSZ particles is poor. This may be beneficial as it will provide a pocket for He gas accumulation around the particle, though this gap will have to be removed before conversion to a fuel form.

4.8 SRIM Calculation of He Ion Ranges

The SRIM code was used to assist in making a hypothesis about He activity in the cermet. SRIM calculates the stopping ranges of ions in matter, while TRIM

calculates damage production caused by the transport of ions [26]. SRIM stopping powers are calculated with the Projected RAnge aLgorithm (PRAL).

SRIM was used to calculated the distance of He ions in Zr metal and UO_2. Urania was chosen to simulate the TRU oxides because the code does not have data for them. The data has been calculated for a 5.5 MeV He ion in both materials. This will provide an upper bound to the ion range in the material as most α-particles emitted from natural TRU isotope decay are below this range. Table 4.8 shows the results of the SRIM code.

Table 4.8
Hi Ion Ranges in Zr and UO_2

He Ion Energy	Ion Range in Material (μm)	
(MeV)	Zr (6.511 g/cm^3)	UO_2 (19.22 g/cm^3)
0.5	1.26	0.77
1	2.15	1.34
2	4.26	2.69
3	7.01	4.37
4	10.39	6.34
5	14.35	8.56
5.5	**16.52**	**9.75**

From Table 4.8 it can be seen that He ions travel further in Zr metal than UO_2, almost 7 μm further at 5.5 MeV. These ranges were used to calculate the amount of He that would escape from a UO_2 particle and the fraction of undamaged Zr matrix for the proposed cermet. From literature, fission products travel a shorter distance in both Zr and UO_2 ($\sim$ 9 μm). Therefore only He was used in the calculation of matrix damage.

5. DISCUSSION

The extrusion development tests in this thesis have been used to identify initial parameters of concern with hot extrusion of a zirconium-matrix cermet. The tests began with a "best-guess" estimate for fabrication and have been modified throughout the process.

The first discussion point is the temperature dependence of the hot extrusion. From the literature, the extrusion temperature is limited by billet cooling and the onset of hot shortness. In tests HX-1 through HX-4 the billet did not extrude due to cooling during transfer from the furnace to the press. The billet was heated to ∼700 °C in the furnace and transferred to the press in room temperature air. Although attempts were made to limit this exposure, such as wrapping the billet in insulation during HX-3&4, the time in air was measured in minutes and the billet cooled below the extrusion temperature. In later tests, the billet temperature was maintained above 800 °C and extrusion was observed.

The temperature of the billet may also be a reason for some of the damage seen in the tests using the *in situ* heating setup. The billet is heated to ∼800 °C and placed in the billet holder which is at 540 °C. This large thermal gradient may lead to rapid cooling near the billet edges, which could increase the resistance to deformation seen in this region. As evidenced from HX-2, the H-13 tooling cannot withstand a temperature of 700 °C which would reduce the driving force of the cooling. Initially a low-cost tooling option was desired, however it is now evident that a material with a higher operating temperature is necessary. A possible replacement for H-13 is the molybdenum alloy TZM. This alloy has high strength and high temperature resistance to deformation with 99.4% Mo, 0.5% Ti, and 0.1% Zr. Use of this material

may require a redesign of the tooling heating method to minimize oxygen contact with the TZM at high temperatures. Table 5.1 lists a few TZM properties.

Table 5.1
TZM Properties

Conductivity (W/cmK)	Specific Heat (J/gK)	Density (gcm^3)
1.4615	0.272	10.242

Oxide particle fracture in the cermet is a major concern from the results of these experiments. Particle cracking was seen in all extruded billets. Particle fracture appears to occur in two distinct modes: deformation fracture and contact fracture. Deformation fracture is seen in particles that have developed cracks perpendicular to the extrusion direction, this occurs as the particles pass through the die and the surrounding matrix flow is radially inward (Fig. 2.7). These particles appear isolated in the matrix, although "invisible" particles below the sectioning plane may be causing contact fracture in some cases. Particles damaged by contact with another particle show fracture patterns beginning at the point of contact and "spidering" out through the particle. Evidence of contact fracture can be seen in Figure 5.1. Also seen in HX-6 and HX-7 are particles that have been completely pulverized during deformation. The majority of these particles are near groups of other particles or in the outer region of the extruded rod where deformation is highest. Particle integrity is a goal of this fabrication method and these pulverized particles can not be present in the finished form.

To alleviate particle damage, experiment HX-8 used a die with a reduction ratio of 2.66, and a lower volume loading than the previous runs. This was done to reduce billet deformation and increase interparticle spacing. Particle damage in HX-8 (Fig. 4.15) is much less than in the larger reduction extrusions. Although damage still occurred by both modes, few pulverized particles are seen in the sectioned billet and damage at the outer edges of the extruded rod is no more severe than in the central

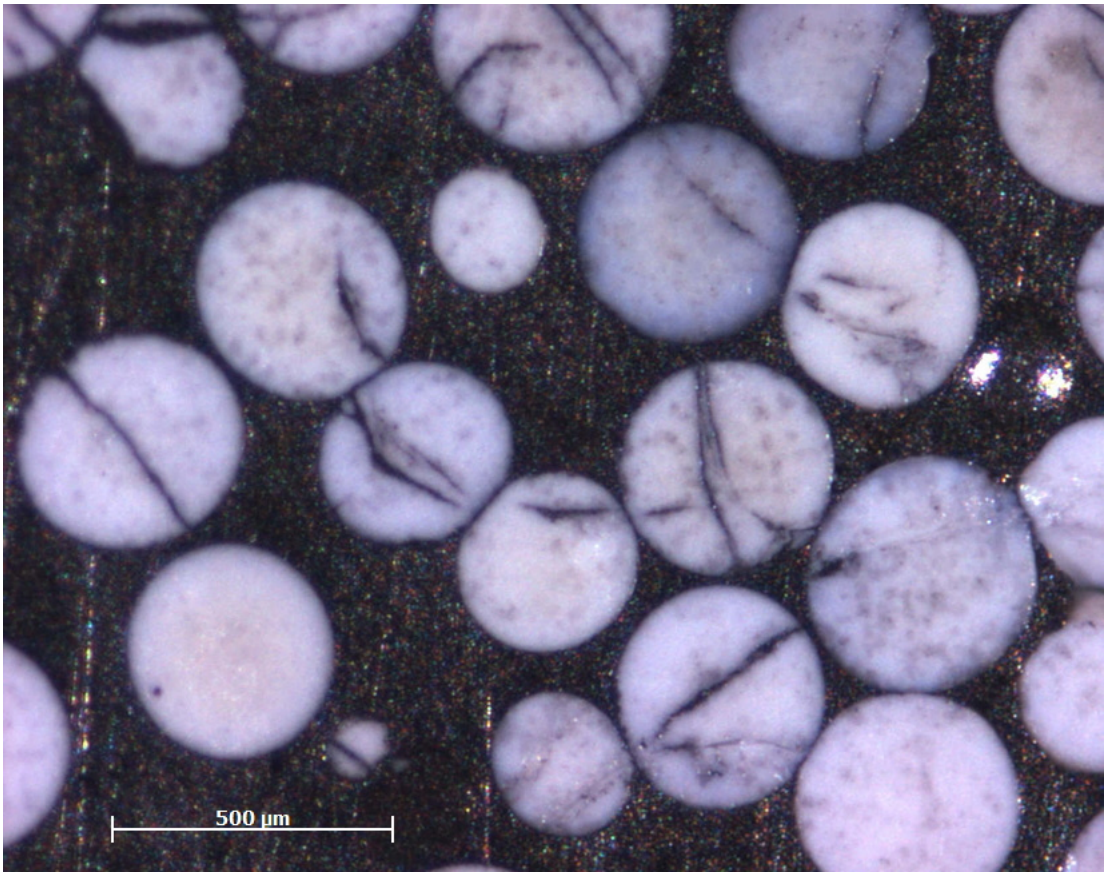

Figure 5.1. Evidence of contact damage in YSZ particles. Note the fracture line traveling through the particles embedded in the Zr matrix.

region. Another result of the smaller reduction was the formation of gaps around the particles, elongated in the extrusion direction. This suggests that the radial flow at the die was not significant enough to fill in the area around the particle. These gaps may be a beneficial attribute of this smaller reduction, providing a "pockets" for trapped He gases to accumulate during storage. These gaps would have to be removed prior to fuel element burning to rigidly contain the fuel particles. Literature suggests that a reduction ratio of 11 will produce a fully dense Zr matrix with hot extrusion, however no information is given on particle damage. Future analysis will include a detailed look at matrix density and the formation of these gaps as a function of matrix and ceramic particle size and the reduction ratio.

The micrographs of the sectioned billets have been analyzed to calculate information about the specimens in extrusion tests HX-3 through HX-8. The calculations were performed using lineal analysis according to the theories described by Underwood [38]. The number of oxide particles per unit length of matrix, N_L, and per unit area, N_A were measured for each specimen, the following values were calculated from this information:

- N_V: number of particles per unit volume of billet
- V_V: volume fraction of oxide particles
- S_V: surface area of oxide particles per unit volume
- r: oxide particle radius
- λ: mean interparticle spacing of oxide particles

Table 5.2
Microstructural Analysis of Cermets

	HX-3	HX-6	HX-7	HX-8
N_L (cm^{-1})	7.64 ±1.77	9.85 ±2.91	12.74 ±3.0	5.43 ±1.58
N_A (cm^{-2})	251	283	264	153
N_V (cm^{-3})†	6079	7838	10138	4321
V_V (cm^{-3})	0.197	0.291	0.521	0.164
r (μm)	193.1	221.5	306.9	225.9
S_V (cm^{-1})	30	39	51	22
λ (μm)	1051	720	376	1540
χ		0.286	.474	0.116

†: Calculated value assumes r = 200 μm

In Table 5.2 it can be seen that most values change accordingly with particle loading. Of note, the interparticle spacing, λ, is a strong indicator of particle damage.

This value averages the measured spacing over the entire specimen, not taking into account any specific grouping. The data suggest that an average λ value higher than $\sim$900 μm is needed to minimize particle damage in the matrix.

The particle radius, r, is included from the calculations as a measure of how accurate the calculated value is to the assumed value of 200 μm. Note HX-3,6,8 are withing 30 μm of the assumed value. However HX-7 is quite large compared to the actual particles. A large part of this difference stems from the high damage concentration seen in HX-7. The likelihood that some of these damaged particles were counted multiple times during the lineal analysis is high. This can also be seen in the standard deviation of HX-6 & HX-7 compared to HX-3 & HX-8 where particle integrity allowed easy counting.

The parameter χ in Table 5.2 is the ratio of N_A of the damaged particles to the total N_A, counting damaged particles as those particles that have been fractured into more than two separate pieces. It is seen that in specimen HX-7 nearly half of the oxide particles were severely damaged. HX-7 did have the highest particle density, N_V, and used a larger reduction ratio than HX-8. This confirms that the lower particle loading and extrusion ratio of experiment HX-8 led to a lower percentage of damaged particles.

Another type of damage seen during these experiments is breaking of the extruded rod. Experiments HX-6 through HX-8 all show some type of rod damage after passing though the die, either in the form of a crack through the rod, or a complete destruction of the rod as seen in HX-6 and HX-7. The cause of these cracks is still unclear, though the damage seen in HX-7 is believed to have been caused by gases trapped in the billet canister during preparation. As the billet compacts, prior to the onset of extrusion, these trapped gases may accumulate in the billet and form a large void. This void will become highly pressurized during deformation and the release of this pressure upon exiting the die may cause rapid expansion of the void, fracturing the rod. This damage was seen in HX-6 in the form of a split rod, however in HX-7 the damage was to a larger extent.

Reduction of particle damage by contact may be achieved by including a "sacrifical" matrix coating around the oxide particles. This would involve coating the particles with a layer of Zr powder prior to blending with the matrix Zr. This will increase particle isolation during the extrusion and may reduce damage from particle contact. Reducing particle damage by deformation may be achieved by decreasing the size difference between matrix and oxide powders.

Table 5.3
Green Density of Zr Matrix in Extrusion Development Tests

Billet	Matrix % T.D.
HX-1	24.8
HX-2	16.8
HX-3&4	41.6
HX-6	34.6
HX-7	40.8
HX-8	59.3

The billets used in these tests were not compacted with much force as hand packing was used. The green density of the billets could be improved by cold-pressing prior to extrusion. Table 5.3 lists the green density of the Zr matrix, assuming the ceramic particles are 100% dense. No attempt was made to evacuate trapped gases in the billet canisters. From Table 5.3, extrusions HX-6 and HX-7 could have as much as 60% of the matrix volume occupied by gas from the glove box. This is a strong argument for the damage seen in these extrusions being caused by this trapped gas. An evacuation method needs to be developed for future tests. One method to accomplish this is the inclusion of a tube in the top of the canister than can be connected to a vacuum pump and crimped after evacuation.

From Table 5.3 the green density of the matrix in HX-8 is near 60%. This billet was prepared in a similar manner to the previous billets with the addition of forced

packing after the addition of the powders. This method shows near 20% increase in green density of the matrix.

The effect of matrix green density on extrusion pressure is minimal. Prior to extrusion the matrix is compacted while the pressure increases to the extrusion threshold. Although onset of extrusion may occur with less ram displacement, the pressure profile during extrusion will not change. The primary effect of matrix green density is seen during particle rearrangement during compaction, prior to extrusion. Particles in a dense matrix will undergo less relative motion during this densification step. This is important with a cermet of this kind (large particle size difference) because the motion of the smaller matrix particles is higher than the large ceramic inclusions. This can lead to a "bunching" of ceramic particles, causing them to contact each other prior to extrusion which may lead to contact fracture during deformation.

The SRIM code was used to calculate He ion ranges in the Zr matrix and in a UO_2 particle (TRU simulant), see Table 4.8. This information was used to calculate He escape and damage zones in the proposed cermet. Because He travels further in Zr than fission fragments (16.5 μm v. 14 μm), only He was used to calculate the volumetric damage in the Zr matrix. From the SRIM output, an interparticle spacing greater than 33 μm will be needed to prevent overlap of He and fission product damage zones.

Figure 5.2 shows the fraction of He that will escape from UO_2 particles of varying diameter. It can be seen that for $D/2\lambda \geq 5$ (100 μm diameter), less than 20% of the He will escape the particle.

Figure 5.3 shows the calculation of the damage zones created by 5.5 MeV He ions in Zr metal. The black dots represent the location of experiments HX-3 through HX-8. From the figure it can be seen that for all loadings and particle sizes used, more than 80% of the matrix will remain intact. This is important because matrix integrity determines the macroscopic response of the cermet. One of primary reasons cermets are of interest is the retention of metallic properties in the macroscopic body. If the cermet loading or matrix damage becomes too high, this quality will not hold.

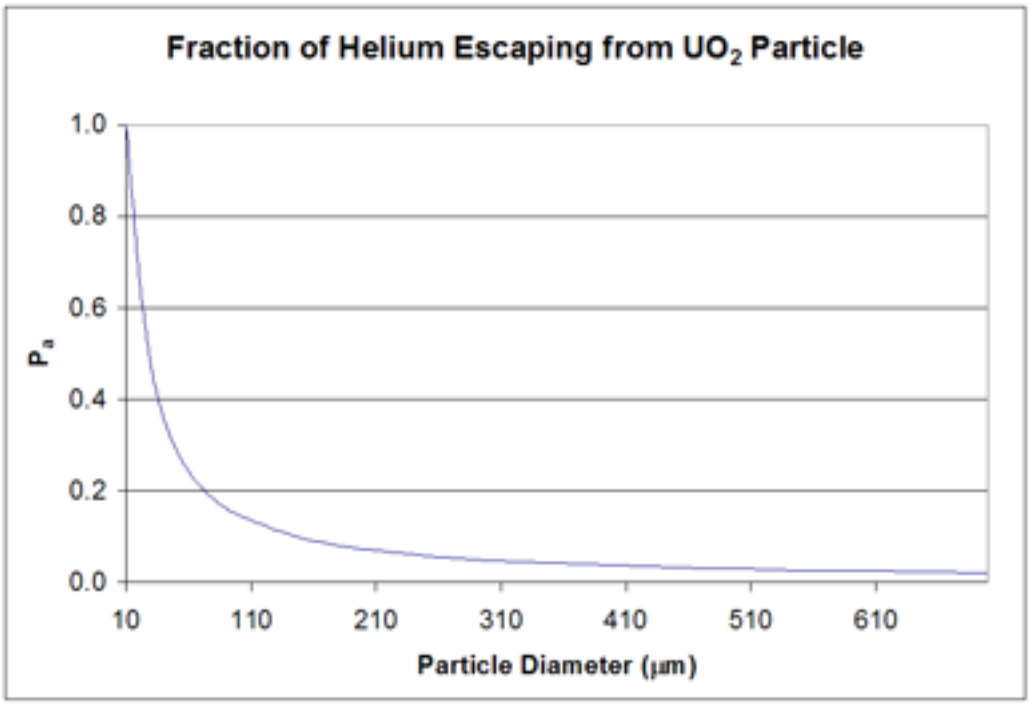

Figure 5.2. Escape fraction, P_a, for 5.5 MeV He ions in spherical UO_2 particles.

The figure also includes the regions of overlapping and isoloated damage zones in the cermet.

Figures 5.2 and 5.3 suggest that a smaller particle size may be used in the proposed cermet. The current YSZ particles are 400 μm in diameter and show a large amount of fracture during fabrication at volume loadings of 20 - 30%. Figure 5.3 suggests that particles with half the diameter could be used at the same loading without detriment to matrix integrity. Initial results from a separate neutronic study of the cermet suggest that a volume loading of 30% TRU particles may be too large for reactor stability [39]. Therefore, if a TRU loading of less than 30 vol.% is assumed, particles of 150 μm diameter or larger could be used in the cermet and 60% of the matrix would remain undamaged from He and fission products. If it is found that the limit is 10 vol.% , 100 μm particles would damage less than 20% of the matrix.

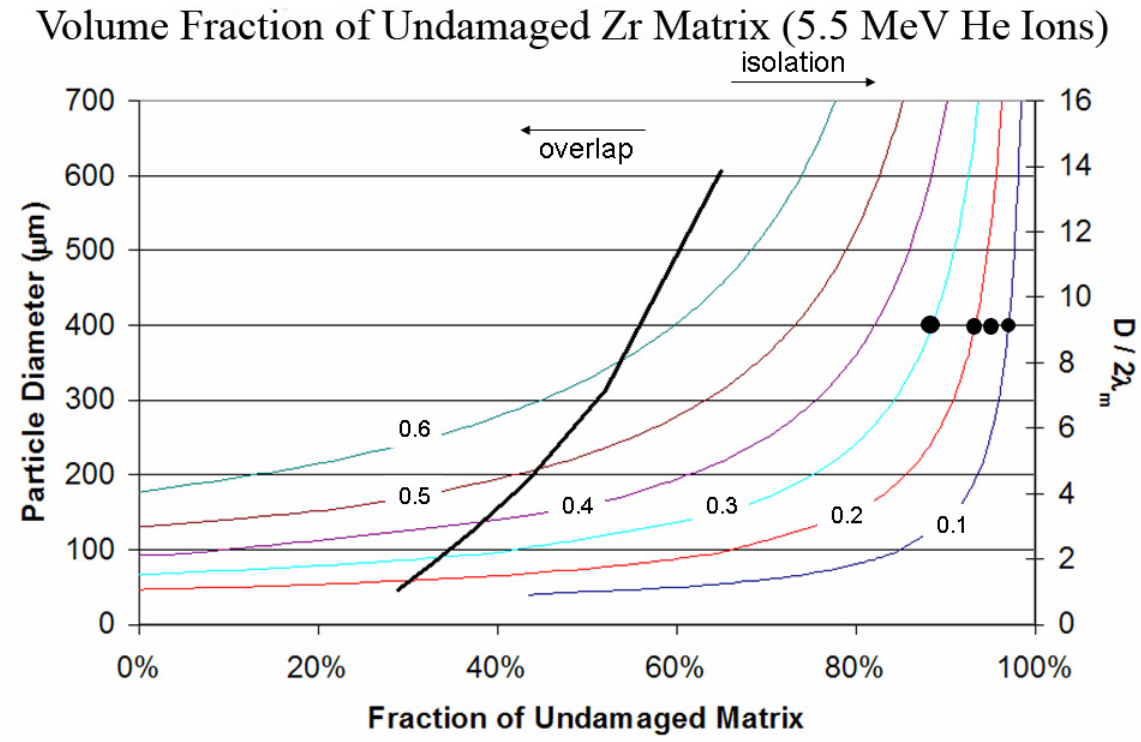

Figure 5.3. Undamaged Zr matrix v. fuel volume loading for 5.5 MeV He ions with a range of 16.5 μm

6. SUMMARY & FUTURE WORK

In conclusion, this goal of this project was to evaluate the fabrication parameters necessary for fabrication of a dual purpose zirconium matrix cermet by hot extrusion. The extrusion process was established through a series of experiments and modifications, resulting in an *in situ* heating method for temperature control of the billet and tooling. The billet preparation tests have shown that a shake-mixing method of powder blending and vibratory packing with forced compaction can yield matrix green densities near 60%, which may have a large impact on particle damage in the extruded cermet. Trapped gases in the pre-extruded billet may be causing a rupture in the extruded rod and should be removed. A starting point for parametric studies has been developed based on the extrusion development tests and calculation of cermaic particle size effects.

Future work in the development of the proposed cermet should include:

- Cermet metallography study.

  The extruded cermets from this study should used to determine the necessary polishing steps to obtain a "clean" microstructure in the specimen. Also, from the comments by Buehler analysis, typical HF acid concentrations in the proposed etchants are too aggressive for this cermet. This may be due to a lack of sound particle bonds between the matrix powder. An examination should be performed to determine a more appropriate HF concentration for etching of these cermets.

- Analsysis of reduction ratio effects on extruded matrix density.

  To develop a relationship between matrix porosity and extrusion ratio, several sizes of zirconium powder should be extruded, free of oxide particles, with sev-

eral reduction ratios and the final matrix porosity calculated. This examination should also include a study of green density effects on final porosity.

- Optimization of particle contact damage by pre-blending isolation.

  Extended pre-mixing of the cermet powders should include the use of a tumbler to mix the powders for several hours prior to loading. A Zr metal powder coating on the oxide particles could be used to increase the interparticle spacing of the oxide particles prior to extrusion.

- Optimization of particle deformation damage by reduction ratio and particle size ratio.

  Oxide particle deformation damage should be studied with several reduction ratios, and metal/oxide powder size ratios to develop criteria for reducing this type of damage.

- Evacuation of trapped gases in pre-extruded billet.

  A method for pumping gases out of the loaded billet should be developed. A possible method is to place a stem through the canister lid that can be attached to a vacuum pump and crimped shut after evacuation.

- Inclusion of Zircaloy cladding tube around cermet powders.

  The Zircaloy tube should be co-extruded with the cermet powders to provide an outer protective layer, separating any oxide particles from the outer surface of the rod.

- Bare-powder extrusion

  The need for a billet canister could be avoided if a bare-powder extrusion process is used. This would require a new system for applying "back-pressure" to the billet during the powder densification step. This could be achieved by placing a cold-pressed plate of cermet in the die face that will extrude after the billet has been compressed.

LIST OF REFERENCES

LIST OF REFERENCES

[1] U.S. D.O.E. Advanced Fuel Cycle Initiative 2003 Annual Report. Technical report, 2003.

[2] Robert E. Berlin and Catherine C. Stanton. *Radioactive Waste Management*. Wiley, New York, 1989.

[3] Sean M. McDeavitt, D.T. Kraemer, A. Parkison, A.R. Totemeier, and J.J Wegener. Zirconium Matrix Cermet Storage Form and Transmutation Fuel for Transuranics, 2005.

[4] A.N. Holden. *Dispersion Fuel Elements*. Gordon and Breach Science Publishers, New York, 1967.

[5] A. Fernandez, R. J. M. Konings, and J. Somers. Design and Fabrication of Specific Ceramic-Metallic Fuels and Targets. volume 319 of *Journal of Nuclear Materials*, pages 44–50, Tokai, Japan, 2003.

[6] S. Baldi and J. Porta. Elements of Comparison Between Different Inert Matrix Fuels as Regards Plutonium Utilisation and Safety Coefficients. *Progress in Nuclear Energy*, 38(3-4):375–378, 2001.

[7] A. van Veen, R.J.M Konings, and A.V.Fedorov. Helium in Inert Matrix Dispersion Fuels. *Journal of Nuclear Materials*, 320:77–84, 2003.

[8] Randall Fielding. Idaho National Laboratory, private communication., 2005.

[9] Jack Collins, R.D. Hunt, G.D. Del Cul, and D.F Williams. Production of Depleted UO_2 Kernels for the Advanced Gas-Cooled Reactor Program for US in Triso Coating Development. Technical Report ORNL/TM-2004/123, Nuclear Science and Technology Division, ORNL., 2004 2004.

[10] A.G. Samoilov, A.I. Kashtanov, and V.S. Volkov. *Dispersion-Fuel Nuclear Reactor Elements*. Israel Program for Scientific Tranlations Ltd., Jerusalem, 1968.

[11] L. Buffe, S. Dubois, J. M. Gatt, and S. Valin. Advanced Plutonium CERMET Fuels: Elaboration on Process and Thermo-Mechanical Modeling. Global 2003., pages 1980–1988, New Orleans, LA, United States, 2003. American Nuclear Society.

[12] R. Bhatnagar, A. R. Das, and M. L. Vaidya. Fabrication and Mechanical Property Studies of Thoria Stainless Steel Cermets. *Transactions of the Indian Ceramic Society*, 48(2):32–35, 1989.

[13] Seong-Hee Lee, Tetsuo Sakai, and Yoshihiro Saito. Fabrication of Al/Al_2O_3 Particle Reinforced Metal Matrix Composite by Sheath Rolling of Powder Mixture. *Materials Transactions, JIM*, 39(12):1206–1213, 1998.

[14] R.J.M Konings et al. The EFTTRA-T4 Experiment on Americium Transmutation. *Journal of Nuclear Materials*, 282:159–170, 2000.

[15] H. M. Finniston and John Perry Howe. *Metallurgy and Fuels*. McGraw-Hill, New York,, 1956.

[16] M. A. Pouchon, M. Nakamura, Ch Hellwig, F. Ingold, and C. Degueldre. Cermet Sphere-Pac Concept for Inert Matrix Fuel. volume 319 of *Journal of Nuclear Materials*, pages 37–43, Tokai, Japan, 2003. Elsevier.

[17] Y. Shigetome, S. Kono, Ch Hellwig, and P. Heimgartner. Vipac Fuel Fabrication for Irradiation Tests of the FUJI Project. Global 2003: Atoms for Prosperity: Updating Eisenhower's Global Vision for Nuclear Energy, pages 1342–1347, New Orleans, LA, United States, 2003. American Nuclear Society.

[18] Sean M. McDeavitt, T. J. Downar, A. A. Solomon, S. T. Revankar, M. C. Hash, and A. S. Hebden. Thoria-Based Cermet Nuclear Fuel: Cermet Fabrication and Behavior Estimates. volume 4 of *International Conference on Nuclear Engineering, Proceedings, ICONE*, pages 59–67, Arlington, VA, United States, 2002. American Society of Mechanical Engineers.

[19] Claude Edmund Pearson. *The Extrusion of Metals*. Wiley, New York, 1953.

[20] P. R. Roberts and B. L. Ferguson. Extrusion of Metal Powders. *International Materials Reviews*, 36(2):62–79, 1991.

[21] Betzalel Avitzur. Study of Flow Through Conical Converging Dies. In *Proceedings of a Symposium on the Relation Between Theory and Practice of Metal Forming*, pages 1–46, New York, 1970. Plenum Press.

[22] Benjamin Lustman and Frank Kerze. *The Metallurgy of Zirconium*. McGraw-Hill, New York,, 1st edition, 1955.

[23] H. H. Hirsch. Fabrication of Zirconium by Powder Metallurgy Techniques. *Metal Progress*, 68(6):81–85, 1955.

[24] H. Ullmaier. Proceedings of the International Symposium on Fundamental Aspects of Helium in Metals. volume 78 of *Radiation Effects*, page 426, Juelich, W Ger, 1983.

[25] A. Van Veen, J. H. Evans, W. Th M. Buters, and L. M. Caspers. Precipitation in Low-Energy Helium Irradiated Molybdenum. *Radiation Effects*, 78(1-4):53–66, 1982.

[26] James F. Ziegler. SRIM-2003. volume 219-220 of *Nuclear Instruments and Methods in Physics Research, Section B: Beam Interactions with Materials and Atoms*, pages 1027–1036, Albuquerque, NM., United States, 2004.

[27] J. Th M. De Hosson, L. Caspers, and A. Van Veen. Atomistic Studies of Helium Trapping in Metals. *Radiation Effects*, 78(1-4):25–36, 1982.

[28] S. E. Donnelly, J. H. Evans, and North Atlantic Treaty Organization. Scientific Affairs Division. *Fundamental Aspects of Inert Gases in Solids*. Plenum Press, New York, 1991.

[29] B. R. T. Frost. Theories of Swelling and Gas Retention in Ceramic Fuels. *Nuclear Applications & Technology*, 9(2):128–41, 1970.

[30] H. Trinkaus. Energetics and Formation Kinetics of Helium Bubbles in Metals. *Radiation Effects*, 78(1-4):189–211, 1982.

[31] D. Kaletta. The Growth of Gas Bubbles in Solids Under Irradiation at Elevated Temperatures Around 0.5 Tm. *Radiation Effects*, 78:245–259, 1983.

[32] A.W. Schlechten. *Zirconium*. Rare Metals Handbook. Reinhold Publishing Corp., New York, 1954.

[33] S. Baldi, J. Porta, Y. Peneleau, S. Pelloni, J. M. Paratte, and R. Chawla. Importance of Zirconium Cross Sections in Calculating Reactivity Effects for Inert Matrix Fuels. *Progress in Nuclear Energy*, 38(3-4):351–354, 2001.

[34] Gerry D. Moan, Peter Rudling, ASTM Committee B-10 on Reactive, Refractory Metals, and Alloys. *Zirconium in the Nuclear Industry: Thirteenth International Symposium*. ASTM, West Conshohocken, Pa., 2002.

[35] J. H. Schemel, American Society for Testing and Materials., American Institute of Mining Metallurgical, and Petroleum Engineers. *Zirconium in Nuclear Applications : A Symposium Co-Sponsored by the American Society for Testing and Materials and the American Institute of Mining, Metallurgical, and Petroleum Engineers*. American Society for Testing and Materials, Philadelphia, 1974. ASTM Special Technical Publication ; 551.

[36] ASM International. Binary Alloy Phase Diagrams, 1996.

[37] Gregory Choczaj. Lab Analyst, Buehler Analsys Ltd. , private communication., 2006.

[38] Ervin E. Underwood. *Quantitative Stereology*. Addison-Wesley Series in Metallurgy and Materials. Addison-Wesley Pub. Co., Reading, Mass., 1970.

[39] Volkan Seker. Purdue University, School of Nuclear Engineering, private communication., 2006.

Appendix I

Global 2007 Summary: Hot Extrusion Method (2 pages)

A.R. Totemeier and S.M. McDeavitt, "A Zirconium Cermet for Transuranic Isotope Storage and Burning," Presented at Global 2007: Advanced Nuclear Fuel Cycles and Systems, Boise, ID, September 9-13 (2007).

A Zirconium Cermet for Transuranic Isotope Storage and Burning

Aaron R. Totemeier and Sean M. McDeavitt

Fuel Cycle and Materials Laboratory, Texas A&M University, College Station, TX 77843
artoteme@tamu.edu and *mcdeavitt@tamu.edu*

INTRODUCTION

The development of UREX+ processes to recycle spent fuel has led to the development of a zirconium matrix cermet storage form for transuranic (TRU) isotopes. In UREX+, radioactive isotopes are separated into aqueous solutions; the TRU isotopes are converted into oxide powder or microspheres [1]. As part of the cermet development option described here, hot extrusion has been established as the primary fabrication route for the zirconium cermet. Powder metallurgy offers many benefits over other fabrication methods and enables incorporation of TRU oxide powder.

EXPERIMENTAL SETUP

Zirconia microspheres were used to simulate the TRU oxides and green billets were formed by mixing the oxide with zirconium metal powder (nominal diameter = 44μm) and the mixture was sealed in a copper canister for handling and extrusion. The powders were weighed and blended in an argon atmosphere glovebox. A 90 ton dual-acting hydraulic press was used to apply the extrusion pressure; the extrusion die and other tooling parts were fabricated from precipitation hardened H13 tool steel. Ceramic fiber heaters were used to heat the tooling (~540ºC) and the powder-filled billet (~800ºC) to their respective process temperatures.

RESULTS

Initial experiments used extrusion tooling with a die reduction ratio of R= 9 (R is the ratio of the entrance and exit cross sectional areas) and moderately high oxide powder loadings (20 to 40 volume %). In these tests, significant oxide particle damage was observed. This damage was apparently caused by two mechanisms: 1) contact with other oxide particles leading to cracking through stress concentration and 2) complete crushing of individual particles undergoing shear failure. The damage profile at the outer edge of the product cermets was higher than in the central zones. This is consistent with the metal flow regimes observed in conical die extrusions [2].

Further, the R=9 trials had a destructive radial crack in each of the finished rods that caused the extruded rods to fracture into two lengths. For high strain rate extrusion tests, the destruction was catastrophic and the finished rods shattered into several smaller pieces. This observation is consistent with examples where process gas becomes trapped in the cermet matrix leading to failure. In this case, the argon cover gas in the glovebox may have been sealed in the cermet structure, causing failure.

To minimize this damage, the reduction ratio (R=2.66) and the oxide particle loading (10 to 15 vol %) were reduced. This was done to lower the internal stresses experienced during extrusion. The damage observed in the product cermet was evenly distributed, suggesting the flow stress in the outer regions of the billet had been reduced. This specimen did not exhibit a large radial crack, however several smaller, randomly oriented cracks were observed. Small cavities were present around the oxide particles stretching along the extrusion axis, suggesting the reduction ratio was too small.

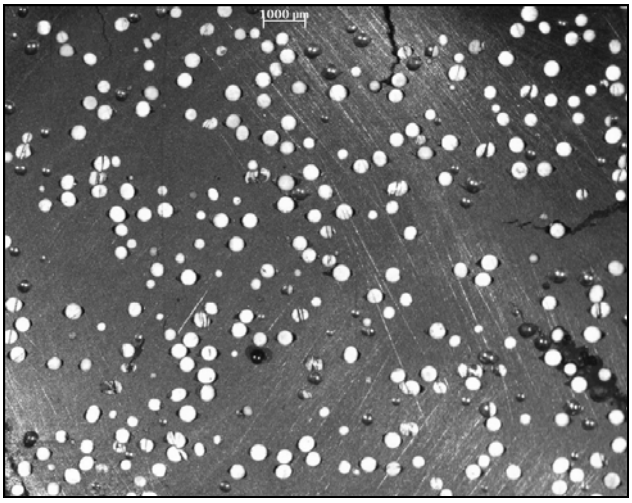

Figure 1. Low magnification structure of an extruded cermet (R=2.66) [3].

DISCUSSION

The hot extrusion of zirconium matrix cermets has been demonstrated at temperatures above 500ºC, but there are notable issues with the methods used and the product morphologies. In these initial studies, the extrusion tooling and powder compacts were heated separately to temperatures of ~540ºC and ~800ºC, respectively. This enabled the use of a die material rated for lower temperature operation (<600ºC), but it allowed for rapid cooling in the billet that complicated the extrusion process.

The experiments enabled the identification of critical process variables such as areal reduction (R), oxide

volume fraction, extrusion strain rate, and temperature. The damage observed in the R=9 tests led to modifications that produced less damage. Further modifications are underway to improve the fabrication methods and determine functional ranges for the critical process variables.

The principal modification includes changing the extrusion die assembly to use high temperature die materials (e.g., W-Mo alloys) such that the powder and die may be preheated together. Further, the copper powder container is being eliminated and a bare extrusion setup with an inert cover gas is being established to eliminate gas trapping during extrusion. To facilitate bare powder extrusion, the necessary back-pressure will be provided by a pre-compacted disk of Zr metal at the die face.

Oxide particle damage is undesirable and may be reduced through increasing the pre-extrusion interparticle spacing and reducing the flow stress in the deformation region of the die. In the new extrusion design, this will be evaluated through the manipulation of four process variables: 1) the extrusion die angle, 2) the areal reduction ratio, 3) the extrusion temperature, and 4) the oxide volume fraction.

REFERENCES

1. U.S. DOE, Advanced Fuel Cycle Initiative Annual Report, 2003
2. C.E. PEARSON. *The Extrusion of Metals*, Wiley, New York (1953).
3.. A. Totemeier, *Evaluation of a Zirconium Matrix Cermet for Storage and Transmutation of Transuranic Isotopes.* M.S.N.E. Thesis, Purdue University (2006)

Appendix J

Global 2007 Presentation: Hot Extrusion Method (10 pages)

A.R. Totemeier and S.M. McDeavitt, "A Zirconium Cermet for Transuranic Isotope Storage and Burning," Presented at Global 2007: Advanced Nuclear Fuel Cycles and Systems, Boise, ID, September 9-13 (2007).

A Zirconium Matrix Cermet for Transuranic Isotope Storage and Burning

Aaron R. Totemeier and Sean M. McDeavitt
Texas A&M University
Fuel Cycle and Materials Laboratory

Global 2007
Boise, ID
September 9-13, 2007

U.S. DOE NERI Project #: 05-067

Fuel Cycle & Materials Laboratory

NERI

Introduction

- Advanced Fuel Cycle Goal
  - Develop advanced fuel cycle technologies to recycle spent nuclear fuel without separating pure Pu.
  - UREX+ family of solvent extraction processes
    - +1a leaves Pu intimately mixed with minor actinides
- What do we do with the recovered TRU?
  - Reduce waste load for YM repository and recover a potentially valuable fission energy source.
  - Removal of 97% of Cs & Eu, and 99.9% of TRU will greatly increase linear drift load in YM
  - Fast reactor transmutation of TRU isotopes will convert a long-term waste liability into a short-term issue and generate electricity!

Possible TRU/Zr Recycle Scheme

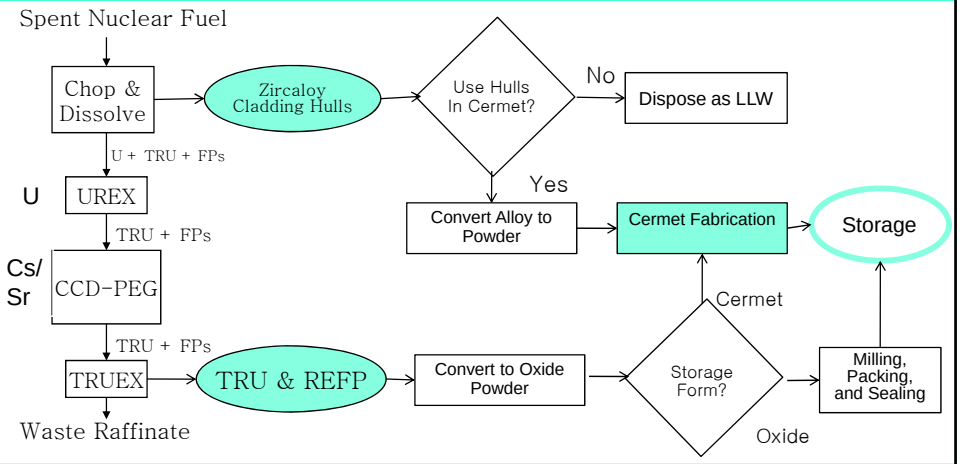

Cermet Dispersion Fuel

- Cermet: dispersion of ceramic particles in a metal matrix
  - Retains beneficial metallic properties: strength, thermal performance
  - TRU in stable oxide form
  - High fission gas retention and damage localization
- Long history in nuclear industry
  - Research reactors
- Why Zr cermet for transmutation?
  - FR Environment
    - High temperature
    - Long burn time
    - Fast neutrons

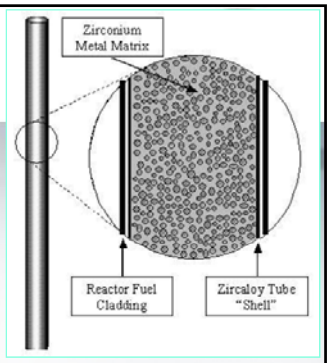

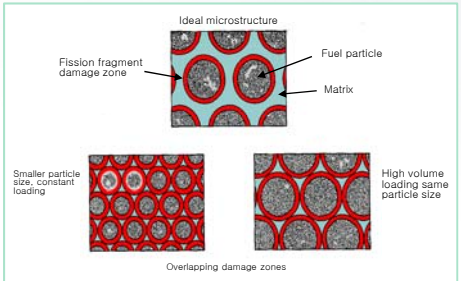

Process Development

- Process Guidelines:
  - High metal matrix density
  - Well-bonded oxide particles
  - Amenable to full-scale production
  - Low cost implementation
- Initial studies designed to develop process knowledge, study cermet behavior during processing, evaluate finished product microstructure.

Powder Metallurgical Hot Extrusion

- Powder metallurgy provides good control over final product
  - Microstructure, porosity, component mixing, shape
  - Powders are easily combined
- Hot Extrusion
  - Previous work cold drawing work at ANL
  - Well-known industrial process
  - Plastic flow of metal matrix at high temperature
  - Possible porosity control for He venting during storage
- Literature on Zr extrusion is vague and prone to dead-ends

Experimental Setup

Argon Atmosphere Glovebox

Enerpac Hydraulic Press

- Dual-action hydraulic press, 100 t capacity
  - Enerpac modular air hydraulic pump powered by Gibbons electric motor

Materials

- Zirconium metal powder
  - -325 mesh (44 μm)
- ZrO_2 microspheres used as TRU simulant
  - 500 μm diameter
- Cu canister for powder encapsulation
- H-13 Tool Steel
- No radioactive materials used in this study

Extrusion Tooling – Bare Powder

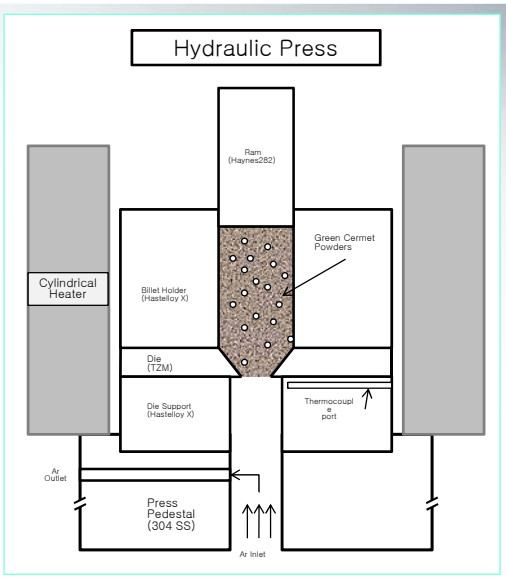

Experimental Results

T = 850°C, R=9, V_f=20%, ~95% TD

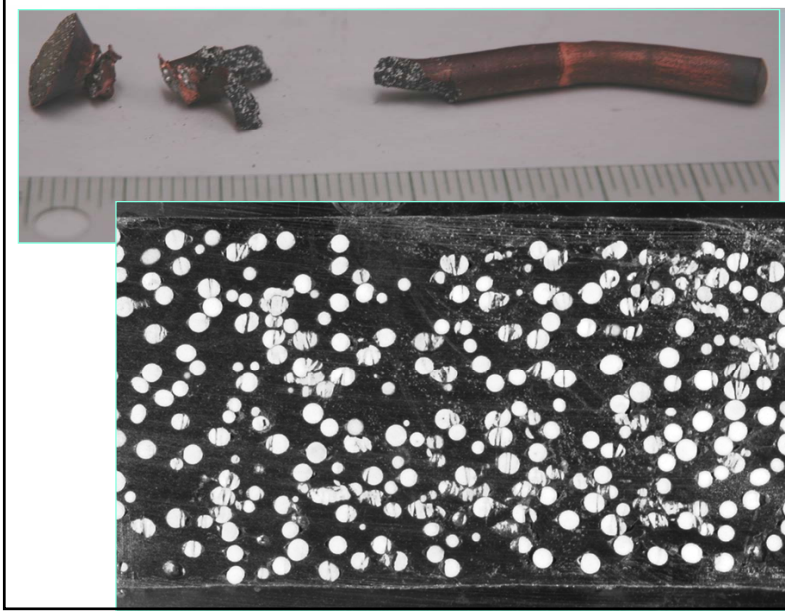

Particle Cracking

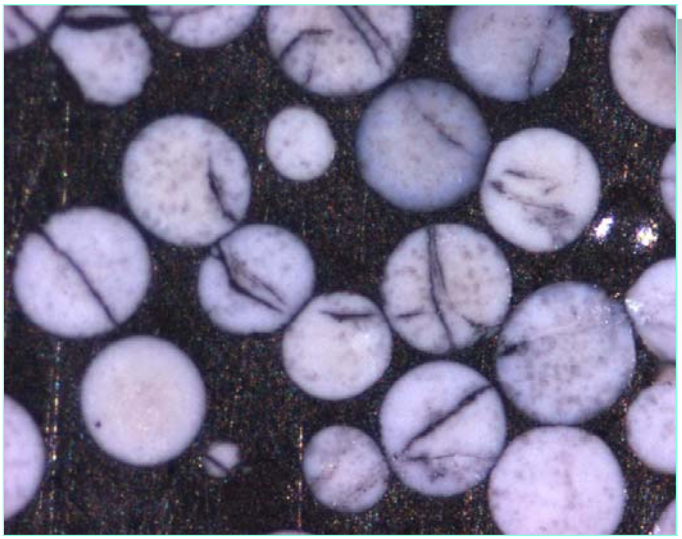

V_f = 40%
Hot Pressed

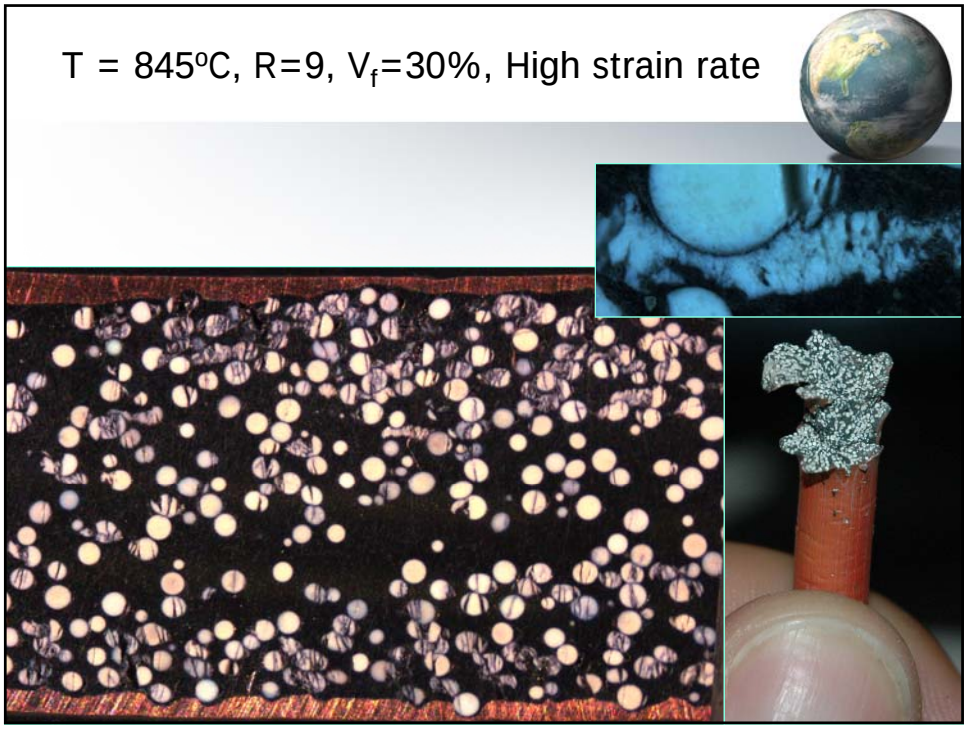
T = 845ºC, R=9, V_f=30%, High strain rate

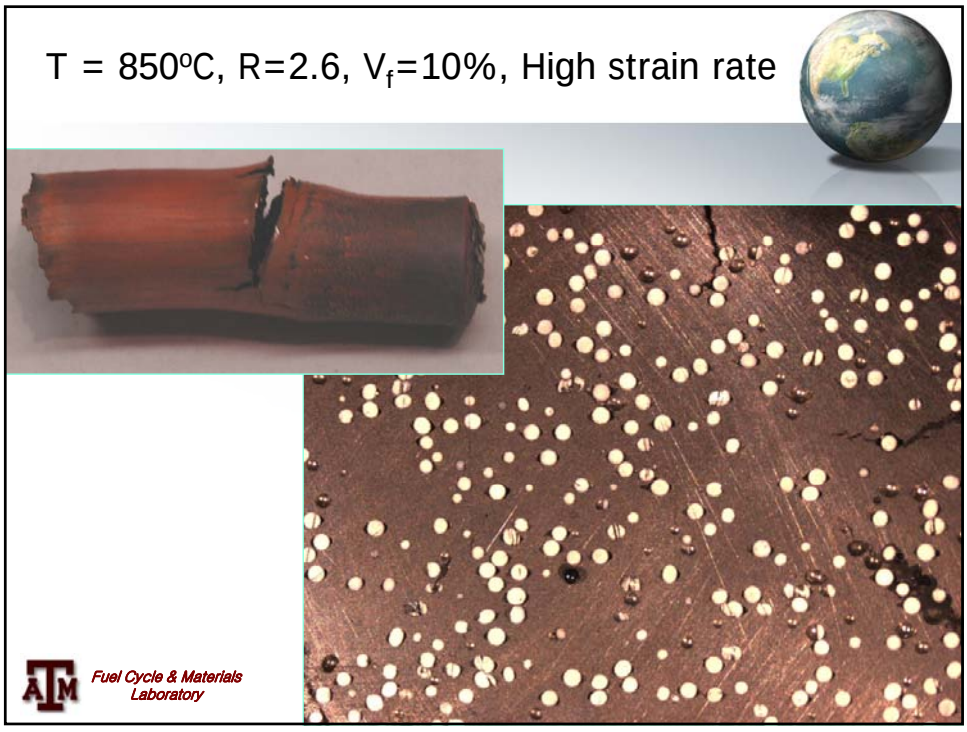
T = 850ºC, R=2.6, V_f=10%, High strain rate
Fuel Cycle & Materials Laboratory

Porosity in R=2.6 specimen

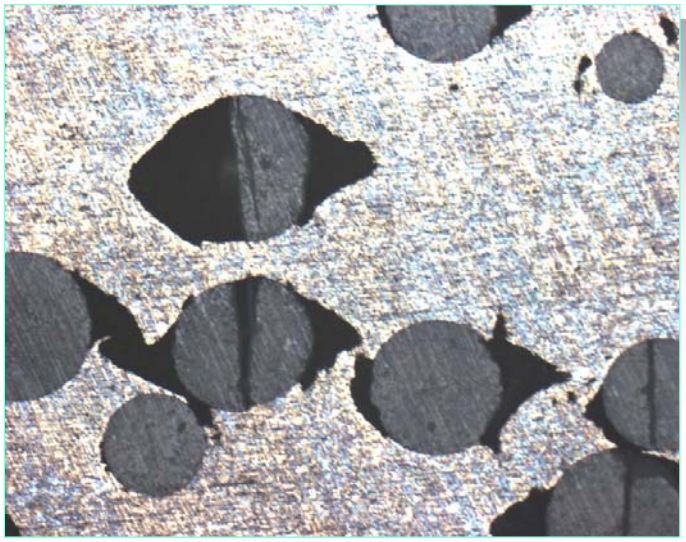

Results of Initial Experiments

- T < 800 ^{o}C would not extrude
- Extrusion did occur with a reduction ratio of 9.
  - Good matrix density
  - High particle damage concentration with V_f > 20%
- R=2.6 extrusion yielded low density matrix, however particle gaps could allow for gas trapping around high density oxides.
- Upper temperature limited to < 870 ^{0}C due to Zr-Cu eutectic
- H-13 tool steel performed well at T < 550 ^{0}C
- Gas trapping in canister could be causing rod burst

Current Status

- Bare extrusion of β-phase cermet
  - Removed copper canister
  - 200,000 lb load cell placed in-line for data recording
  - Extrusion temperature raised to >870 ^{0}C
  - TZM die material, high nickel alloys for other tooling
- Fabrication of cermet specimens for further analysis
  - Ion beam implantation studying radiation damage and fission gas behavior in the matrix

Acknowledgments

The authors would like to thank:

- INL
  - Randal Fielding
- Haynes International
  - Paul Manning and Steve Matthews
- US DOE NERI

Fuel Cycle & Materials Laboratory
Global 2007:
September 9–13, 2007
NERI

Appendix K

PhD Preliminary Dissertation Proposal - Paper (12 Pages)

Radiation Damage in an Extruded Zirconium Matrix Cermet
A Thesis Proposal

By

Aaron R. Totemeier

Texas A&M University

January 7, 2009

Radiation Damage in an Extruded Zirconium Matrix Cermet

A

Thesis Proposal

By:

Aaron R. Totemeier

from the:

Nuclear Engineering Department

at

Texas A&M University

January 7, 2009

1. Introduction

The proposed dissertation involves the investigation of the radiation damage response of an extruded zirconium matrix cermet that has been developed for the storage and burning of transuranic (TRU) elements extracted from used nuclear fuel. The cermet is designed to be a viable storage form for up to 500 years, though it is envisioned that the necessary fast reactor economy will be in place to burn these elements before this time. It is desired to have the cermet storage form be fully capable of insertion into a fast reactor core as a fuel element with minimal to no post-storage processing. The accumulation of helium gas from alpha decay of the transuranics poses the primary concern regarding the long-term stability of the fuel form.

2. Motivation

The long-term (>300 y) radioactivity and heat load generation in spent nuclear fuel is produced by transuranic elements which are generated via neutron reactions with uranium during nuclear electricity generation. These isotopes constitute a small (~1 wt. %) fraction of the spent fuel, but represent a significant portion of the long-term radiotoxic inventory of spent fuel. Removal of these isotopes, via various reprocessing technologies, can significantly increase the capacity of a long-term storage facility as heat generation is the limiting factor[1]. Fission energy can be recovered from the transuranic elements in a fast neutron flux. After separation, these isotopes must be isolated in a thermodynamically stable configuration and stored in a suitable device until such time as a decision (political) regarding their use is made. The proposed cermet allows for the conversion of a long-term radiotoxic waste liability into a recoverable electricity generation source.

Zirconium (and its alloys) is extensively used in the nuclear industry as it has many beneficial properties, including a high resistance to corrosion, high strength, high thermal conductivity, and it is nearly transparent to thermal neutrons. The response of zirconium to neutron radiation environments has been widely studied both in regards to changes in atomic configuration and its physical properties[2-6]. Pure zirconium, though rarely used in commercial reactors, is generally irradiated in crystal bar form to analyze atomistic processes (point defect behavior) and further the knowledge of how the base material contributes to the performance of the various alloys. Alloy compositions, such as the Zircaloys, are generally irradiated to high neutron fluence to determine their behavior, though atomistic studies are performed as well.

The proposed cermet uses zirconium metal powder recovered from spent fuel cladding via hydride/dehydride processing[7]. The powder lends itself to use in powder metallurgical processes such as extrusion which are generally cost-effective and easily scalable from lab- to full-scale production. The transuranic material is in the form of oxide microspheres with a diameter most likely below 500 μm. These microspheres can be fabricated from the TRU-nitrate stream produced during the UREX+ family of processes. The nitrate solution can be processed, via sol-gel processing, to produce oxide microspheres of various diameters [7].

Previous work on the fabrication of the cermet has been published in a Master's Thesis [8] and conference proceedings[7, 9, 10].

Thesis Statement

An extruded zirconium-based cermet will provide an adequate storage form for encapsulated transuranic oxide microspheres and the radiation damage imposed by alpha decay will not damage the cermet beyond its ability to perform as a fuel in a potential fast reactor.

3. Background

3.1. Zirconium-Based Cermet Dispersion Fuel

A cermet is a multiphase system consisting of a dispersed ceramic phase in a metal matrix. In the proposed cermet, transuranic oxide microspheres constitute the dispersed fuel phase and zirconium metal forms a continuous matrix phase. A cermet combines the preferred thermophysical properties of the metal phase with the more thermodynamically stable oxide. Cermets have many applications including bioceramics, friction materials, machine cutting tools, and oxide dispersion strengthened alloys.

A fast reactor will likely be used for transmutation of transuranic elements as high energy neutrons are required to fission these isotopes. Fast reactors operate at higher temperatures and have a harder neutron spectrum than the current commercial LWR fleet. Also, to achieve high transmutation efficiency, high burnups are necessary. These issues require a robust fuel design, capable of withstanding the harsh environment associated with hard neutron spectrums at elevated temperatures without affecting the incident neutron energies. Zirconium is a good candidate material as it has high thermal conductivity, low coefficient of linear expansion, high corrosion resistance, high mechanical strength, and low neutron interaction probabilities[11, 12].

A cermet composite was chosen for the proposed storage/fuel form because the macroscopic properties will more closely resemble those of zirconium metal and the transuranic elements will be maintained in a thermodynamically stable oxide phase. The *dispersion* fuel concept is being employed to further improve the macroscopic properties and reduce the effect of radiation damage on the fuel properties. Depending on the oxide loading (likely to be ~30 vol. %), the properties of the fuel will be suitable for use in a reactor environment. Another reason for the desire to have *near*-zirconium properties is that the properties of the transuranic oxides, and their response to radiation environments, are relatively unknown.

3.1.1.Radiation Damage in Dispersion Fuels

Radiation damage from the reactor neutron flux will affect the entire fuel form and zirconium has been shown to withstand very high neutron fluence with little radiation induced property change. One of the major benefits associated with dispersion fuels is the localization of radiation-induced damage in the fuel[13-16]. Radiation damage associated with the fission process (fission fragments, gamma, alpha, and beta particles) and nuclear decay of the transuranic isotopes (primarily alpha-decay) will only damage the matrix region immediately surrounding the oxide microspheres. Figure 1 schematically represents this phenomenon. The following list details the damage regions that will be created in the cermet during reactor operation, corresponding to Figure 1:

- Zone i (fuel particle): fission fragment and alpha particle damage from decay and (n,α) reactions; high He concentration
- Zone ii: recoil implantations and energetic alpha particles, ~ 5 μm thick
- Zone iii: energetic alpha particles, ~ 10 μm thick

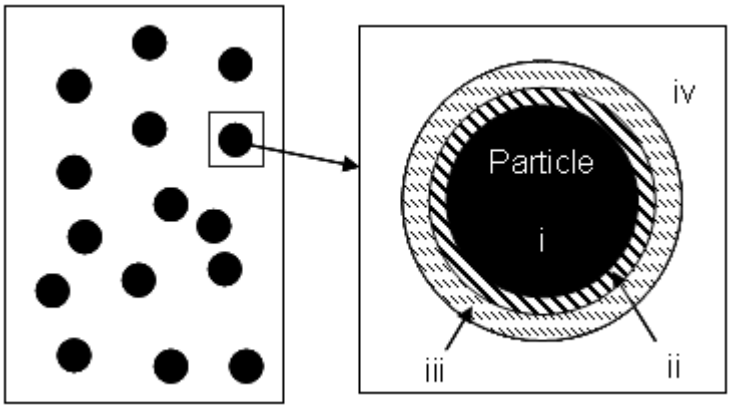

Figure 1. Zones of varying microstructural damage in a dispersion fuel.

During the storage phase, only energetic alpha particles will damage the matrix. Therefore a uniform damage shell should be present prior to reactor insertion. The thickness of the shell depends on several factors but it will be less than the mean penetration depth of the alphas in the matrix (~ 15 μm). The effect of this damage localization depends on the size of the oxide microspheres, the oxide volume loading, and the depth of penetration of the fission fragments and alpha particles in the two phases. It is possible to have overlapping damage zones in the matrix resulting in more rapid deterioration of the macrostructural properties. This situation occurs when the interparticle spacing of the oxide is too small (ie. the volume loading is too high or the particle size is too large for a given type of radiation). It is currently not known how these damage zones will affect the overall fuel performance and no estimates for property degradation as a function of this type of matrix damage have been found. Due to the complexity of modeling these systems[14], experimental investigation of each specific cermet composition (phases, microsphere size and shape, volume loading) will be required to fully determine its performance and operational limits. Preliminary neutronics studies (not performed in this work) suggest that the proposed cermet should have an oxide particle loading of approximately 30 volume percent. At this loading, if oxide particles of 400 mm are used, the percent of undamaged matrix should remain above 80% and minimal overlapping damage zones are expected, though zone overlap is highly dependent on powder mixing method.

3.2. Radiation Damage in Zirconium

Zirconium has been extensively studied with regards to in-reactor performance and radiation damage mechanisms [2-4, 6, 11, 17]. The majority of the work presented in literature details neutron and electron radiations aimed at understanding both the atomistic processes and their macrostructural effects. Ion bombardment studies have focused on the modification of the corrosion properties of various zirconium alloys used in nuclear fuel cladding. No detailed investigations involving He ion bombardment have been found, except to investigate the critical dose for blistering in zirconium alloys[18]. As an hcp metal, zirconium's response to radiation damage is more complex than bcc metals, however, arguments have been made that zirconium is more complex than other hcp metals as well[19]. These arguments could be due, in part, to a lack of similarly extensive research in these other metals.

Dislocation loops in zirconium, as with other metals, can take the form of so-called <a>-type loops and <c>-component loops. The <**a**>-type loops have a Burger's vector of **b**=1/3<11$\underline{2}$0>, while various <**c**>-component loops have been observed depending on the composition and microstructure of the material and the incident radiation[3].

3.2.1.Neutron Irradiation in Single Crystals

Early low temperature (< 350 K) irradiations showed that growth in zirconium single crystals is a volume-conserving process at neutron fluences up to 10^{23} n/m^2. A model for irradiation growth in zirconium was first developed by Buckley and closely followed the experimentally observed a-axis expansion and c-axis contraction. This was consistent with the formation of interstitial dislocation loops on the prism planes and the collapse of vacancy loops on the basal planes. Investigations to higher fluence became warranted when it was found that polycrystalline material did not agree with the accepted model. Carpenter et al began a series of single crystal irradiations to high fluence in 1981, irradiating crystals of various orientation and purity to fluences of up 2 x 10^{25} n/m^2. These initial irradiations showed, after an initial growth transient, saturation in the growth strains of both a-axis and c-axis crystals. Upon further irradiation to higher fluence (7 x 10^{25}n/m^2) it was found that this saturation was actually temporary [2].

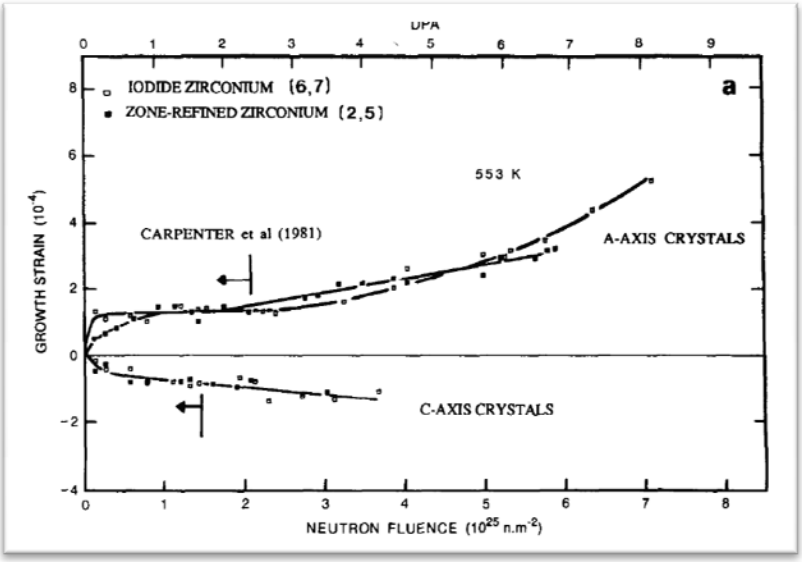

Figure 2. Irradiation growth of zirconium single crystals irradiated to high fluence. [2]

At a fluence of approximately 3 x 10^{25}n/m^2 an increase in irradiation growth, termed breakaway growth, occurs in well-annealed single crystals. It has been determined that breakaway growth occurs due to the formation of <c>-component vacancy loops. Figure 2 is taken from Carpenter et al and shows the results of their extensive series of irradiations on crystal bar zirconium.

3.2.2.Neutron Irradiation in Polycrystalline Specimens

Growth studies of neutron irradiated polycrystalline zirconium show that growth is consistent with interstitials being annihilated at <a>-type dislocations and vacancies to <c>-component loops and twin

boundaries. Annealing deformed crystals causes a reduction in growth rate associated with a reduction in dislocation density[6].

Texture appears to be very important in the stable growth rate observed in polycrystalline zirconium. Figure 3 compares polycrystalline samples of the same purity irradiated at 353 K and 553 K. The main difference between the two materials shown in Figure 3 is the texture. The *present study* investigated zirconium rods while the *Rogerson* work used sheet material, both materials underwent a similar heat treatment.

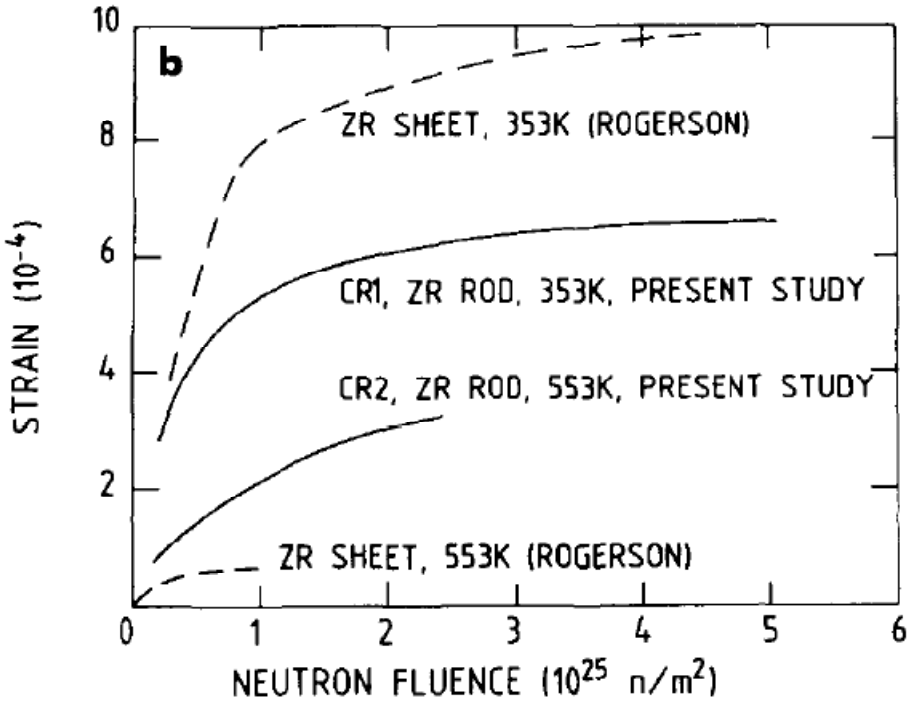

Figure 3.Neutron irradiated polycrystalline zirconium samples of rod texture (present study) and sheet texture (Rogerson) at 353 K and 553 K[6].

3.2.3.Neutron Irradiated Zircalloy-2

Figure 4 contains data of annealed and 25% cold-worked Zircaloy-2 at 353 K and 553 K. All alloys, like the pure material, show an initial rapid growth transient at low fluence. The annealed specimen irradiated at 353 K shows growth saturation at low fluence with a slight increase to another saturation level while the 553 K specimen shows an onset of breakaway growth at ~ 3 x 10^{25}n/cm^2. The increase in growth rate observed in the annealed specimen at 553 K at ~ 5 x 10^{25}n/cm^2 is consistent with the appearance of <c>-component dislocations and subsequent vacancy absorption at these dislocations[4].

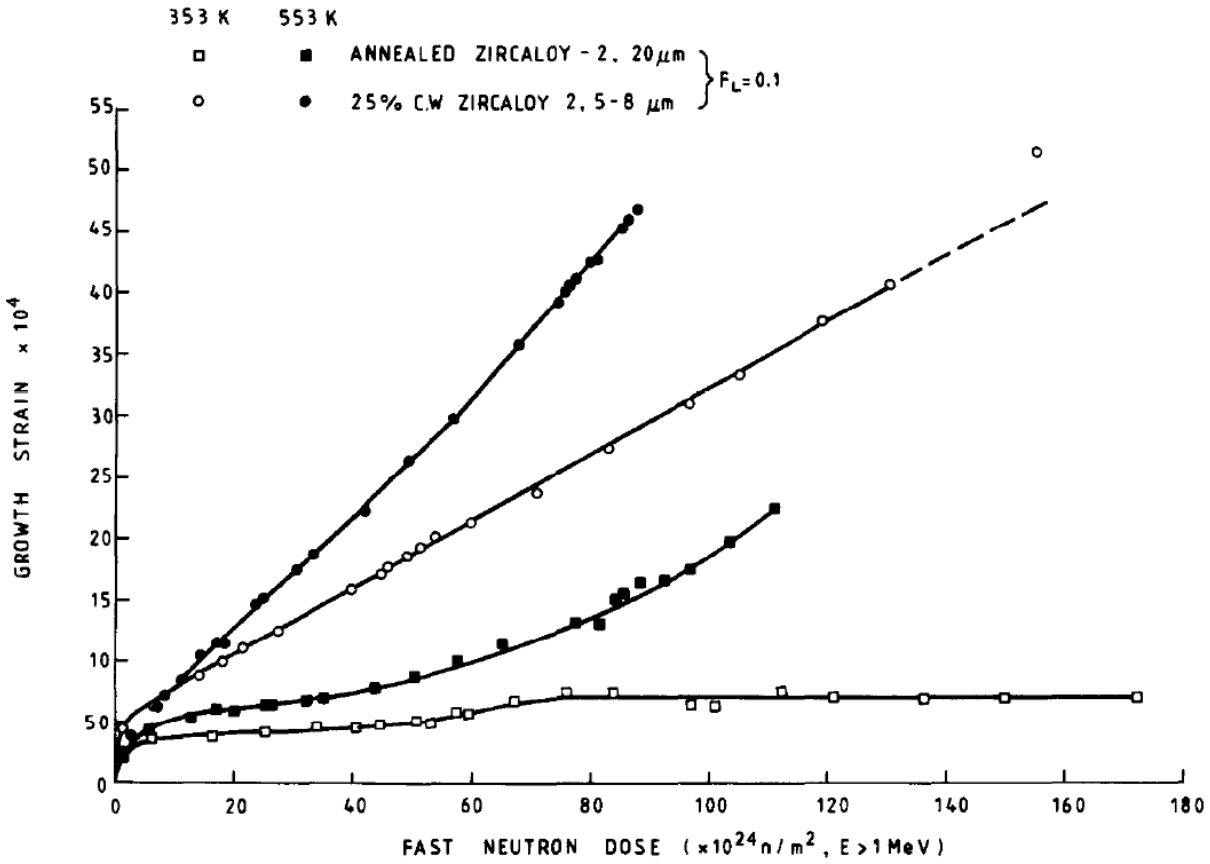

Figure 4. Neutron irradiated Zircaloy-2 at 353 K and 553 K, annealed and 25% CW specimens [4].

3.2.4.Cavity Formation

Void stability in zirconium has been found to be highly dependent on the concentration of insoluble gases in the metal, for example helium. Many common gases are soluble to some degree in zirconium and therefore are unable to stabilize vacancy clusters even to very high dpa. Void stability has been observed in both electron and neutron irradiated material at temperatures between 625 and 775 K. The concentration of stabilized voids increases with impurity content in electron irradiation material while the opposite is true for neutron irradiation material.

4. Proposed Investigation

4.1. Methodology:

The purpose of the proposed work is to, as near as possible, simulate the conditions imposed on the matrix material of a transuranic-bearing cermet during storage. As such, room temperature implantations of He ions will be the first implantations performed. Self-ion implantations will be performed to investigate the effect of increased matrix damage while maintaining a constant gas atom concentration. Xenon implantations may be used to study the effect of large gas atom implantation and the increased damage associated with them.

4.2. Transuranic-bearing Cermet Estimates

The ceramic phase of the proposed cermet is a mixture of transuranic oxides. The specific composition of the oxides depends on the power history of the used nuclear fuel and the partitioning route utilized and its efficiency. Using a *standard* LWR fuel assembly after a five year cool down in a spent fuel pool and the efficiencies of the UREX separations process, calculation of the isotopic concentration of TRU isotopes can be performed. Table 1 shows the concentration [20] and specific alpha activity for Pu, Am, and Cm isotopes. The table also shows the specific alpha particle production of each isotope. (Note: other isotopes are present in the TRUEX product stream; however, only alpha emitters are included in the table.) Table 1 shows two primary contributors to the alpha population from such a TRU composition over a 1000 year storage time, ^{244}Cm and ^{241}Am. Together, these isotopes produce over 94% of the alpha particles from the TRU mixture. The other isotopes, due to their low mass fraction, alpha branching ratio, or long half-life, will not have an appreciable effect on the matrix in the time frame being considered.

Table 1. LWR Fuel Assembly (5 yr decay) TRUEX product alpha generation.

Element	Isotope	decay energy (MeV)	TRUEX Product 5yr decay (curies/liter)	Specific Alpha Generation Over Time (α/g)			
				50 y	200 y	500 y	1000 y
PU	236	5.867	1.0134E-17	1.100E-03	1.100E-03	1.100E-03	1.100E-03
PU	237	5.75	7.8130E-30	3.502E-20	3.502E-20	3.502E-20	3.502E-20
PU	238	5.593	5.3877E-12	1.885E+02	4.586E+02	5.664E+02	5.773E+02
PU	239	5.245	6.4964E-11	9.969E+00	3.979E+01	9.905E+01	1.967E+02
PU	240	5.256	3.6467E-11	2.047E+01	8.124E+01	1.999E+02	3.896E+02
PU	241	5.14	1.1607E-11	2.781E-02	3.053E-02	3.054E-02	3.054E-02
PU	242	4.984	8.2894E-12	7.825E-02	3.129E-01	7.821E-01	1.564E+00
PU	244	4.666	1.6111E-15	7.055E-08	2.822E-07	7.055E-07	1.411E-06
AM	**241**	**5.638**	**3.2395E-01**	**2.643E+12**	**9.413E+12**	**1.892E+13**	**2.741E+13**
AM	243	5.438	2.5886E-01	1.272E+11	5.052E+11	1.245E+12	2.434E+12
CM	241	6.185	1.1671E-24	1.126E-12	1.126E-12	1.126E-12	1.126E-12
CM	242	6.216	1.5038E-05	1.578E+09	1.578E+09	1.578E+09	1.578E+09
CM	243	6.169	1.0325E-03	7.673E+10	1.093E+11	1.102E+11	1.102E+11
CM	**244**	**5.902**	**1.4888E-01**	**1.324E+13**	**1.552E+13**	**1.553E+13**	**1.553E+13**
CM	245	5.623	1.0923E-02	4.633E+09	1.842E+10	4.549E+10	8.916E+10
CM	246	5.475	2.4689E-03	1.865E+09	7.381E+09	1.806E+10	3.484E+10
CM	247	5.353	4.7433E-05	1.088E+04	4.352E+04	1.088E+05	2.176E+05

CM	248	5.162	5.4765E-06	5.279E+04	2.111E+05	5.277E+05	1.055E+06
Total				**2.558E+13**	**3.587E+13**	**4.561E+13**	**1.609E+13**

As mentioned, energetic alpha particles will create a shell of damaged matrix material around each oxide particle. The extent of this damage depends on the number and energy of particles that escape the oxide microspheres. As most of the alphas will be generated within the body of the microsphere, only a small percentage will escape the oxide and cause damage in the matrix. The escape fraction, P_a, depends on the diameter of the microsphere, D, and the mean penetration length of the alphas in the oxide, λ_p [14].

$$P_a = \frac{3}{4}\left(\frac{2\lambda_p}{D}\right) - \frac{1}{16}\left(\frac{2\lambda_P}{D}\right)^3$$

Obviously, a large diameter microsphere will retain more alpha particles than a smaller one. Conversely, if the particle diameter is smaller than λ_p, all alpha particles can escape.

The mean penetration length for 5.5 MeV alpha particles in UO_2 was calculated using SRIM[21]. Data for UO_2 was used because, again, transuranic oxides data is not available. Estimates of the alpha fluence experienced by the matrix material surrounding the microspheres (various diameters) were obtained using the alpha activity of the ^{244}Cm and ^{241}Am. The results of the calculation are shown in Table 2 for different microsphere diameters and storage times.

Table2. Alpha particle fluence for various TRU oxide microsphere diameters

Diameter (um)	Escape Fraction P_a	Fluence (α/cm^2)		
		200 y	500 y	1000 y
50	0.385404	2.362E+10	3.312E+10	4.211E+10
100	0.196113	2.403E+10	3.371E+10	4.286E+10
200	0.098483	2.414E+10	3.385E+10	4.304E+10
300	0.065708	2.416E+10	3.388E+10	4.308E+10
500	0.039441	2.417E+10	3.389E+10	4.309E+10
1000	0.019724	2.417E+10	3.390E+10	4.310E+10

4.3. Proposed Testing

Using the 140 keV beam line at the Ion Beam Laboratory (IBL) at Texas A&M the three materials will be subjected to a variety of implantations. Helium implantation fluences on the order of 1x10^{16}cm^{-2} are obtainable with this beam line. This is higher than the estimated alpha fluence shown in Table 2.

The implantation species will include helium, xenon, and self-ion implantation. Helium and xenon will be used to compare the effect of noble gas concentration on the materials. Self-ion implantation will be used to investigate the effect of increased radiation damage without increasing the gas concentration.

Self-ion implantation can be used to achieve a damage microstructure equivalent to what would be created in a neutron flux.

Oxygen is an efficient helium atom trap in zirconium and the concentration of dissolved oxygen and thickness of the surface oxide may play an important role in the proposed analysis. Oxygen concentration in the matrix may require further investigation involving pre-implantation of oxygen.

Transmission electron microscopy will be performed on the specimens to characterize the damage profile and gas atom behavior.

4.3.1.Samples

The zirconium samples to be investigated include: 1) crystal bar (c-axis), 2) Zircaloy-2, 3) extruded (low oxygen content) , 4) extruded (high oxygen content), and potentially one or two other extruded specimens if the comparison of the two extruded specimens warrants further investigation of oxygen concentration.

4.3.2.Sample Preparation and Characterization

Thin foil specimens of each material will be prepared using crystal bar zirconium, Zircaloy-2, and extruded zirconium (~44 um pre-extruded nominal grain size). The oxygen content of the extruded matrix material is currently unknown as the powdered material was transported in water. A separate supplier will be used to obtain material stored in argon.

Samples will be sectioned and thinned for TEM analysis prior to implantation using a diamond saw and both mechanical and electrochemical polishing. The final electrochemical polish will be performed within an hour of implantation as this has been shown to reduce the surface oxide concentration by an order of magnitude.

Specimens of each material will be analyzed via TEM and SEM to determine pre-implantation characteristics and textures. The extruded material will be analyzed via EDS/WDS to determine oxygen concentration.

4.3.3.Correlation with Neutron Data

As the body of knowledge concerning helium implantation in zirconium specimens is relatively small, especially compared to neutron and electron irradiations, a method of comparison between the neutron data may be useful. Such a method has been described by Was and Allen[22] wherein equivalent damage structures created via neutron irradiation can be created with light and heavy ion irradiations. This technique may prove worthwhile to compare the data generated in this work with the extensive database that exists for previous zirconium irradiations.

References

1. Wigeland, R.A., et al., *Separations and transmutation criteria to improve utilization of a geologic repository.* Nuclear Technology, 2006. **154**(1): p. 95-106.
2. Carpenter, G.J.C., R.H. Zee, and A. Rogerson, *Irradiation growth of zirconium single crystals: A review.* Journal of Nuclear Materials, 1988. **159**: p. 86-100.
3. Griffiths, M., *A Review of Microstructure Evolution in Zirconium Alloys.* Journal of Nuclear Materials, 1988. **159**: p. 190-218.
4. Rogerson, A., *Irradiation growth in zirconium and its alloys.* Journal of Nuclear Materials, 1988. **159**: p. 43-61.
5. Schemel, J.H., *Zirconium in nuclear applications : a symposium co-sponsored by ASTM and the American Institute of Mining, Metallurgical, and Petroleum Engineers.* 1974, Philadelphia: American Society for Testing and Materials. 526 p.
6. Zee, R.H., et al., *Irradiation growth in deformed zirconium.* Journal of Nuclear Materials, 1987. **150**(3): p. 319-330.
7. McDeavitt, S.M., et al. *Zirconium matrix cermet storage form and transmutation fuel for transuranics*. American Nuclear Society Winter Conference, 2005. Washington, D.C., United States.
8. Totemeier, A.R., *Evaluation of a Zirconium-Based Cermet for Transuranic Isotope Storage and Transmutation*, M.S. in *Nuclear Engineering*. 2006, Purdue University, W. Lafayette.
9. Totemeier, A. *A Zirconium Cermet for Transuranic Isotope Storage and Burning*. *Global 2007:*Advanced Nuclear Fuel Cycles and Systems. 2007. Boise, ID.
10. McDeavitt, S.M., et al. *Thoria-based cermet nuclear fuel: Cermet fabrication and behavior estimates*. International Conference on Nuclear Engineering, 2002. Arlington, VA, United States.
11. Lustman, B. and F. Kerze, *The metallurgy of zirconium*. 1st ed. 1955, New York,: McGraw-Hill. 776 p.
12. Schlechten, A.W., *Zirconium*. Rare Metals Handbook, ed. C.A. Hampel. 1954, New York: Reinhold Publishing Corp.
13. Fernandez, A., R.J.M. Konings, and J. Somers. *Design and fabrication of specific ceramic-metallic fuels and targets*. 2003. Tokai, Japan: Elsevier.
14. Holden, A.N., *Dispersion Fuel Elements*. 1967, New York: Gordon and Breach Science Publishers.
15. Samoilov, A.G., A.I. Kashtanov, and V.S. Volkov, *Dispersion-Fuel Nuclear Reactor Elements*. 1968, Jerusalem: Israel Program for Scientific Tranlations Ltd.
16. Veen, A.v., R.J.M. Konings, and A.V.Fedorov, *Helium in Inert Matrix Dispersion Fuels.* Journal of Nuclear Materials, 2003. **320**: p. 77-84.
17. Moan, G.D., P. Rudling, and ASTM Committee B-10 on Reactive and Refractory Metals and Alloys., *Zirconium in the nuclear industry : thirteenth international symposium*. 2002, West Conshohocken, Pa.: ASTM. xii, 893 p.
18. Zee, R.H., *On the Critical Dose for Blistering in Helium Irradiated Zirconium and Zr-Nb.* Journal of Nuclear Materials, 1983. **115**: p. 131-133.
19. Griffiths, M., *Evolution of microstructure in hcp metals during irradiation.* Journal of Nuclear Materials, 1993. **205**: p. 225-241.
20. Regalbuto, M. Personal communication. 2004.
21. Ziegler, J.F. *SRIM-2003*. 2004. Albuquerque, NM., United States: Elsevier.
22. G. Was, T.A., *Radiation Damage from Different Particle Types*, in *Radiation Effects in Solids*, K.E.e.a. Sickafus, Editor. 2007, Springer. p. 65-98.

Appendix L

PhD Preliminary Dissertation Proposal - Presentation (19 Pages)

Ion Implantation Studies in an Extruded Zirconium Matrix Cermet

Dissertation Proposal Presentation by:

Aaron Totemeier

January 29, 2009

Ion Implantation Studies in an Extruded Zirconium Matrix Cermet

A Dissertation Proposal By:

Aaron Totemeier

January 29, 2009

Overview

- Introduction
- Motivation
- Zr-TRU Cermet Dispersion
- Radiation Damage in Zirconium
- Proposed Investigation
  - Ion implantation
  - Correlation with neutron data
- Conclusion

Introduction

- The proposed dissertation investigates the ability of a zirconium-transuranic oxide cermet to withstand radiation damage and helium gas buildup over a designed 500 year storage lifetime.
- The work intends to determine whether the cermet can be utilized as a viable fuel form at the end of this 500 years or if the radiation damage and gas buildup necessitate further processing.

Introduction: Cermet

- Cermet: ceramic phase in a metal matrix
  - Retains beneficial metallic properties: strength, thermal performance
  - Oxide phase provides added features to the material, e.g. strength
  - e.g. bioceramics, friction materials, ODS steels, WC cutting tools
- Have been used as fuel for research reactors (e.g. TRIGAs) and specialty systems (e.g. space reactors).

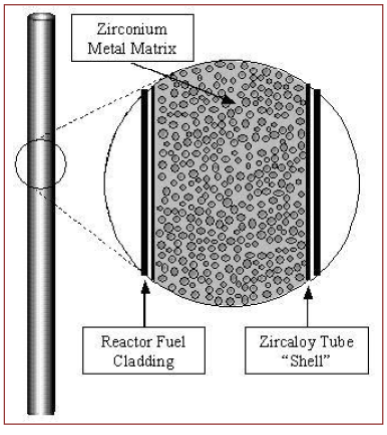

Motivation

Used Nuclear Fuel (UNF?)

- AFCI goal is to reduce long-term radiotoxicity and recover energy from UNF.
- The long-term (>300 y) heat load & radiotoxicity from UNF is provided by transuranic (TRU) isotopes.
  - Removal of 99.9% of Cs,Sr,Er, and TRUs would increase YM capacity by order of magnitude.
- TRU isotopes have fission energy that can be recovered in fast reactors or accelerator driven systems.

How is it done?

- *UR*anium *EX*traction aqueous chemical separation methods.
  - UREX, FPEX,NPEX,TRUEX,TALSPEAK

Process	Product						
UREX+1	U	Tc	Cs/Sr	TRU+Ln	FP		
UREX+1a	U	Tc	Cs/Sr	TRU	All FP		
UREX+2	U	Tc	Cs/Sr	Pu+Np	Am+Cm+Ln	Fp	
UREX+3	U	Tc	Cs/Sr	Pu+Np	Am+Cm	All FP	
UREX+4	U	Tc	Cs/Sr	Pu+Np	Am	Cm	All Fp

Notes:
(1) in all cases, iodine is removed as an off-gas from the dissolution process.
(2) processes are designed for the generation of no liquid high-level wastes

U: uranium (removed to reduce the mass and volume of high-level waste)
Tc: technetium (long-lived fission product, prime contributor to long-term dose at Yucca Mountain)
Cs/Sr: cesium and strontium (primary short-term heat generators; repository impact)
TRU: transuranic elements (Pu: plutonium, Np: neptunium, Am: americium, Cm: curium)
Ln: lanthanide (rare earth) fission products
FP: fission products other than cesium, strontium, technetium, iodine, and the lanthanides

Original content by Dr. James Laidler, ANL

Possible Recycle Scheme to TRU Storage

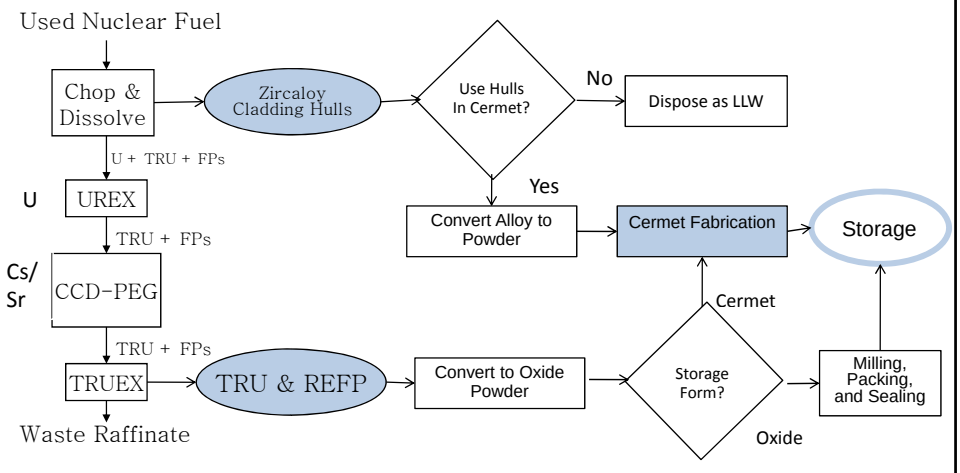

Zirconium Recovery – Hydride/Dehydride

UNF cladding hulls can be processed via hydride-dehydride to provide nuclear-grade Zr powder.

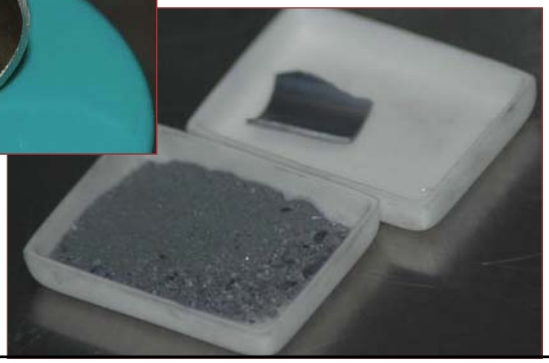

TRU Recovery – Sol-Gel Processing

Transuranic isotopes are separated in nitrate streams from the UREX process. This nitrate stream can be processed via sol-gel to form transuranic oxide microspheres.

Zr-TRU Cermet Dispersion

Storage form or Fuel form?

- After separation the TRU material must be immobilized and protected from mankind and vice versa.
- The proposed cermet provides a high strength, corrosion resistant, thermodynamically stable storage form.
  - Design lifetime as storage form = 500 years
- The cermet could also provide a fuel form for recovery of fission energy from the TRU isotopes.
  - Best case scenario: no costly post-storage processing required to perform as fuel
  - Have to answer the question, “What happens during storage?”

Why Zr Cermet?

- Recovery of fission energy from TRU isotopes will likely occur in a fast reactor.
  - Hard spectrum
  - High temperature
  - High burnup
- Conventional oxide fuels will not provide an adequate fuel matrix
  - High oxygen content will increase neutron moderation
  - Higher operating temperatures require higher thermal conductivity and lower thermal expansion in the fuel, metal fuels will have a higher safety margin.
- Zirconium is a well-known material in the nuclear industry and has many beneficial properties where transmutation of TRU is concerned.
  - High strength, low corrosion, excellent thermal properties, low neutron cross section
- Very little information exists on the physical characteristics of TRU material.
  - Nearly impossible to understand how a fuel pellet of TRU oxide would perform.
  - Would require a costly (years & $M) battery of tests that may ultimately prove useless.
- The cermet combines the benefits of zirconium metal and TRU oxides to form a good fuel candidate for recovery of fission energy from UNF.
  - Raw materials are readily available after reprocessing and are easily combined into a cermet with powder metallurgy techniques.

Dispersion Fuels

- The proposed cermet has a heterogeneous composition of oxide microspheres embedded in a continuous metal matrix.
- Each microsphere (ideally) is separated from its neighbors by such a distance that the response of the material to radiation damage is different compared to a solid solution or homogeneous fuel form.

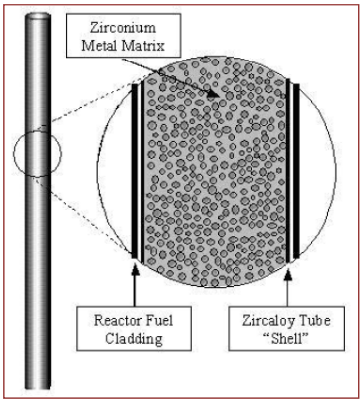

Dispersion Fuels

- Dispersion fuels have several inherent benefits that make them an excellent addition to the proposed cermet.

Benefit	Primary Contributor
Localized radiation damage	Microsphere isolation
Tailored thermophysical properties	Continuous matrix phase
Enhanced fission gas retention and lower f.g. induced swelling	Microsphere porosity accommodates fission gases
Improved property retention with burnup	Decreased radiation damage to the fuel

Localized Radiation Damage

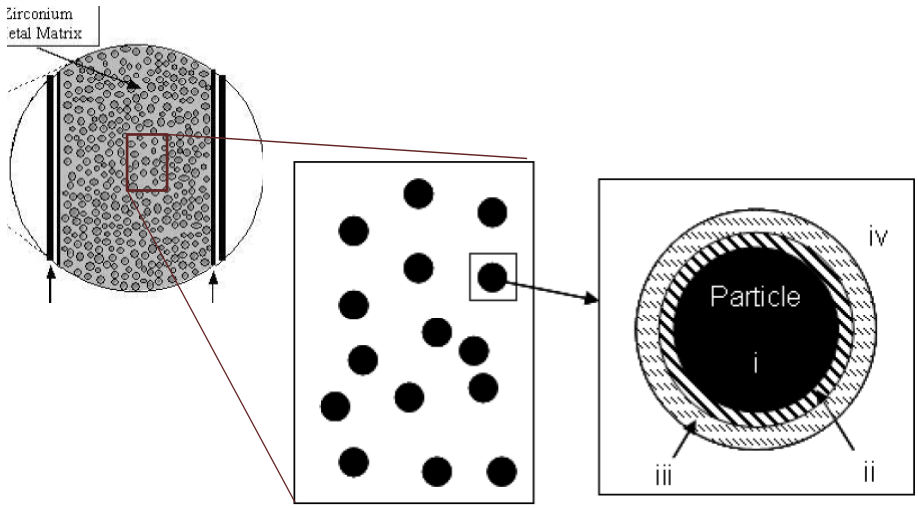

Localized Radiation Damage

Radiation originating from the oxide microspheres will only damage the matrix material around the microsphere. Unlike a solid solution or homogeneous mixture fuel wherein the entire fuel form is damaged by radioactive particles.

- Zone i: fuel particle, high concentration of fission fragment and α decay damage, high He concentration
- Zone ii (~5 μm): recoil implantations and energetic α particles
- Zone iii (~10 μm): energetic α particles
- Zone iv: undamaged matrix material

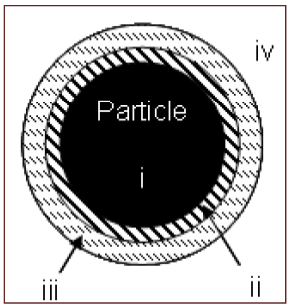

Matrix Damage in Proposed Cermet

- Damage zones can overlap, causing increased property degradation.
- Assuming spherical oxide inclusions and an FCC array of microspheres allows for calculation of the fraction of undamaged matrix in the cermet.
- Cumulative effects are unknown and must be experimentally determined for each cermet.

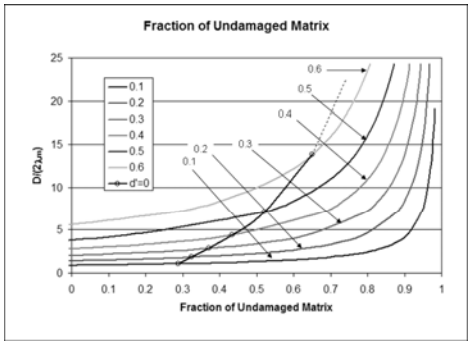

$Zr\text{-}ZrO_2$ Cermet

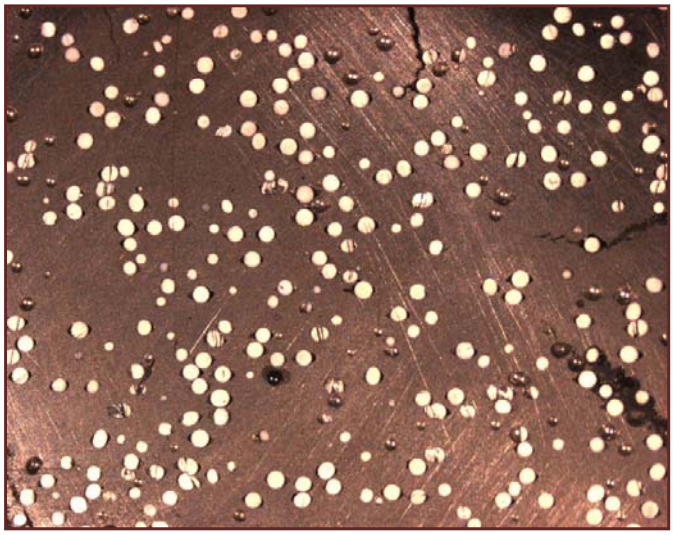

Introduction … again.

- The proposed dissertation investigates the ability of a zirconium-transuranic oxide cermet to withstand radiation damage and helium gas buildup over a designed 500 year storage lifetime.
- The work intends to determine whether the cermet can be utilized as a viable fuel form at the end of this 500 years or if the radiation damage and gas buildup necessitate further processing.

Radiation Damage in Zirconium

Radiation Damage in Zr

- Zirconium is one of the most widely studied metals in terms of radiation damage, however little evidence of previous ion implantation work has been found.
  - Majority of work performed has been with neutron and electron radiations; up to high fluences (~$8E^{25}$ n/m^2)
  - Most ion implantations have focused on Zr alloy corrosion
- Zr radiation response is considered more complex than other metals (even other hcp)
  - This could be due a lack of extensive research in other metals

<a>-type Dislocation Loops

- **b** = 1/3 <11$\underline{2}$0>
- Unlike bcc & fcc metals (and some hcp), Zr can accommodate both vacancy and interstitial <a>-type loops simultaneously
- <a> -type loops align in regular rows or layers parallel to the basal plane.
  - Observed as "corduroy" in TEM; light-dark bands due to local stress relaxation
- i- and v-loops form in alternating rows
- <a>-type loops do contribute to irradiation growth but their contribution tends to saturate at relatively low fluence
- Alloying with substitutional (e.g. Sn) elements reduces size/ increases density of <a> loops

<c>-component Dislocation Loops

- **b**= many varieties
- <c>-component loops are very sensitive to interstitial impurities and the specimen microstructure
- Difficult to analyze due to thin foil artifacts (e.g. surface hyrdides/oxides) usu. requires stereo-microscopy
- Loop clustering:
  - In neutron irradiated material, loops are uniformly distributed with no apparent dependence on g.b. proximity
  - Precipitate clusters can cause nonuniformity
  - In electron irradiated material, loops are generally found between <a> layers; size controlled by <a> layer spacing
- "Breakway" growth

Irradiation growth

- Growth is typically higher at lower temperatures;
  - creep compliance at higher temperatures could lead to earlier onset of relaxation; or possibly, only i-loops form at the lower temperature
- At low (T<553K) temperatures, growth is a volume conserving process ($1\text{-}3F_L$) in pure specimens
  - Typically: a-axis expansion; c-axis contraction
  - Consistent with biased migration and interstitial absorption at <a>-loops and vacancies at <c>-loops, g.b., and twin bound.
- Sn-atom trapping causes non volume conservative growth in Zr-2
- It has been argued that in the presence of a high network dislocation density, v-loops could form if there is a high interstitial bias at dislocations though there is no experimental data to support this.

Void Stability

- Most pure metals will form voids when irradiated in the 0.3 T_m to 0.5 T_m range.
- Zirconium does not form voids easily; most likely attributable to a lack of insoluble gas (He)
- HVEM irradiations:
  - No voids in specimens with 3,10,15 appm He even to 16dpa in 570-870K range
  - Voids readily nucleated in specimens with 100 appm irradiated in 670-780K range
- Impurities assist with void stabilization, likely due to interstitial bias, generally the more pure the specimen, the more difficult it is to form voids
- He diffusion is high even at temperatures below 750K. Therefore, assuming no trapping, it is quite possible for the majority of near-surface helium to escape a thin foil implantation. (Even the 100 appm specimen suggests this could have been the case).

Neutron Irradiation of Single Xtals

- At low temperatures (< 350 K) irradiation growth is a volume conserving process.
- Typically a-axis expansion and c-axis contraction
- "Breakaway" growth occurs around $3E^{25}$ n/m^2 and is associated with <c>-component vacancy loops

Neutron Irradiation of Single Xtals

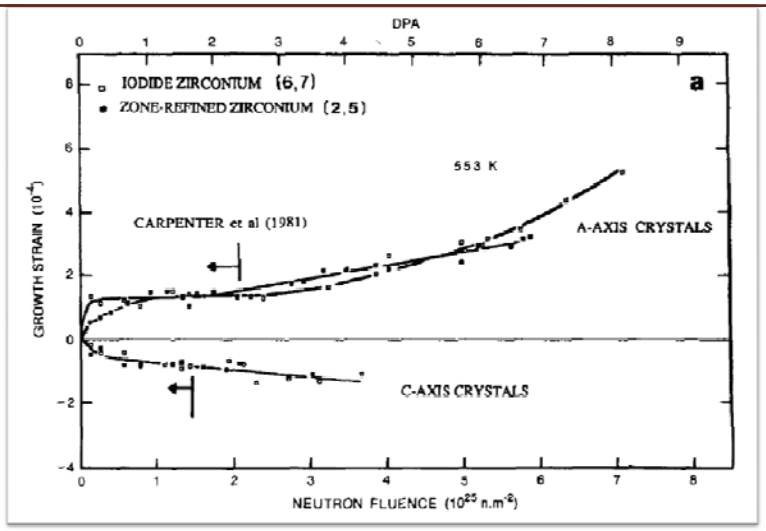

Carpenter, Zee, and Rogerson. *Irradiation growth of zirconium single crystals: a review.* JNM, 159

Neutron Irradiation of Poly-Xtals

Neutron irradiated polycrystalline specimens follow similar growth model to single crystals. However, polycrystalline material is much more susceptible to impurity atoms (type and concentration)

Also, texture plays a critical role in Zr growth, as seen in the graph at the right of the same purity material with different geometries.

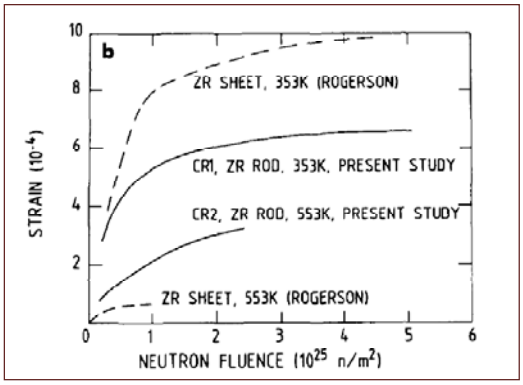

Zee, et al. *Irradiation growth in deformed zirconium*. JNM, 150.

Neutron Irradiated Zircaloy-2

- All Zr alloys show similar initial growth transients at low fluence.
- Irradiations at 353K exhibit lower growth strains compared to 553K.
  - Likely due to defect trapping at solute atoms
  - Evidence exists to suggest v-defects can migrate at near ambient temperatures in Zr
- The effect of cold-work is to increase the growth strain obtained in Zr-2. This is likely due to the formation of <c>-component loops during cold work and their subsequent contribution to breakaway growth.

Neutron Irradiated Zircaloy-2

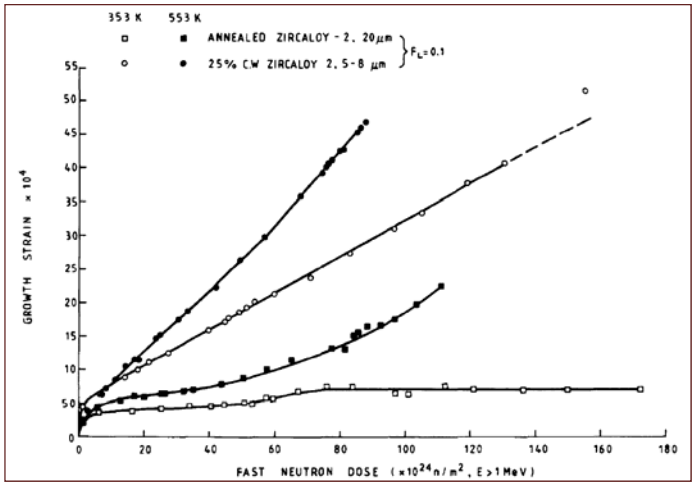

Proposed Investigation

- The purpose of the proposed work is to simulate the conditions experienced by the matrix material during the storage phase.
- The investigation will use the ion beam lines in Dr. Shao's Ion Beam Lab.
  - He implantation
    - Alpha particle effects
  - Zr implantation
    - Increase radiation damage while maintaining gas concentration
  - Xe implantation
    - Heavy gas atom implantation

Alpha production from TRU oxide microspheres

Element	Isotope	decay energy (MeV)	TRUEX Product 5yr decay (curies/liter)	Specific Alpha Generation Over Time (α/g)			
				50 y	200 y	500 y	1000 y
PU	236	5.867	1.0134E-17	1.100E-03	1.100E-03	1.100E-03	1.100E-03
PU	237	5.75	7.8130E-30	3.502E-20	3.502E-20	3.502E-20	3.502E-20
PU	238	5.593	5.3877E-12	1.885E+02	4.586E+02	5.664E+02	5.773E+02
PU	239	5.245	6.4964E-11	9.969E+00	3.979E+01	9.905E+01	1.967E+02
PU	240	5.256	3.6467E-11	2.047E+01	8.124E+01	1.999E+02	3.896E+02
PU	241	5.14	1.1607E-11	2.781E-02	3.053E-02	3.054E-02	3.054E-02
PU	242	4.984	8.2894E-12	7.825E-02	3.129E-01	7.821E-01	1.564E+00
PU	244	4.666	1.6111E-15	7.055E-08	2.822E-07	7.055E-07	1.411E-06
AM	**241**	**5.638**	**3.2395E-01**	**2.643E+12**	**9.413E+12**	**1.892E+13**	**2.741E+13**
AM	243	5.438	2.5886E-01	1.272E+11	5.052E+11	1.245E+12	2.434E+12
CM	241	6.185	1.1671E-24	1.126E-12	1.126E-12	1.126E-12	1.126E-12
CM	242	6.216	1.5038E-05	1.578E+09	1.578E+09	1.578E+09	1.578E+09
CM	243	6.169	1.0325E-03	7.673E+10	1.093E+11	1.102E+11	1.102E+11
CM	**244**	**5.902**	**1.4888E-01**	**1.324E+13**	**1.552E+13**	**1.553E+13**	**1.553E+13**
CM	245	5.623	1.0923E-02	4.633E+09	1.842E+10	4.549E+10	8.916E+10
CM	246	5.475	2.4689E-03	1.865E+09	7.381E+09	1.806E+10	3.484E+10
CM	247	5.353	4.7433E-05	1.088E+04	4.352E+04	1.088E+05	2.176E+05
CM	248	5.162	5.4765E-06	5.279E+04	2.111E+05	5.277E+05	1.055E+06
Total				**2.558E+13**	**3.587E+13**	**4.561E+13**	**1.609E+13**

Alpha Fluence to Matrix

$$P_a = \frac{3}{4}\left(\frac{2\lambda_p}{D}\right) - \frac{1}{16}\left(\frac{2\lambda_p}{D}\right)^3$$

Diameter (um)	Escape Fraction P_a	Fluence (α/cm²)		
		200 y	500 y	1000 y
50	0.385404	2.362E+10	3.312E+10	**4.211E+10**
100	0.196113	2.403E+10	3.371E+10	**4.286E+10**
200	0.098483	2.414E+10	3.385E+10	**4.304E+10**
300	0.065708	2.416E+10	3.388E+10	**4.308E+10**
500	0.039441	2.417E+10	3.389E+10	**4.309E+10**
1000	0.019724	2.417E+10	3.390E+10	**4.310E+10**

5.5 MeV alpha particles in UO2 used for λ_p

Proposed Testing

- Materials: Crystal Bar, Zr-2, Extruded Zr
  - Two start materials are used for the extruded Zr
    - Powder in H20, powder in Ar
- Initial implantations will use the 140 keV beam line to implant He, Xe, and Zr ions with fluence on the order of $1E^{16}$ cm^{-2}.
- Further implantations will be determined after investigation of these initial specimens.

Preparation and Characterization

- Thin foils specimens will be prepared by sectioning with a diamond saw, mechanical polishing, and electrochemical polishing.
- Oxygen plays an important role in Zr implantations (He trapping) and it has been shown that polishing within 1 hour of implantation can reduce surface oxygen concentration by an order of magnitude.
- SEM & TEM will be used to analyze specimens for defect concentration and specimen characterization.

Correlation with Neutron Data

- Was & Allen have suggested a method for comparing radiation damage from different particle types .
- Their theory and calculations will be applied to the data generated in this dissertation to determine its effectiveness with zirconium.
- If effective, this could allow future research to be done at a greatly reduced cost compared to neutron irradiation.

Conclusion

This dissertation is focused on the effects of ion implantation in Zr. Specifically to determine the ability of the proposed TRU-bearing cermet to be transitioned from storage form to fuel form with minimal cost.

Zirconium is a very complex material and extensive research has been done in the area of radiation damage. It is believed that the data generated in this work will confirm the previous findings concerning crystal bar and Zr-2 material, and provide a new data set for the extruded polycrystalline material.

Appendix M

Project Meeting Presentation: Criticality Calculations (15 Pages)

AFCI: Decay Heat and Criticality Calculations

Internal Group Meeting Presentation by:

V. Seker and T.J. Downar

January, 2006

AFCI: Decay Heat and Criticality Calculations

V. Seker
T. Downar S. McDeavit
January, 2006

Outline

- Introduction
- Methods Benchmarking
  - SCALE 5
  - MCNP
- Composition Specification
- Decay Heat Calculations
- Criticality Calculations
- Ongoing Work

Decay Heat Calculations

- Benchmarking:
  - Decay heat value for CORAIL-TRU assembly reproduced as a first step
    - All data on CORAIL-TRU taken from ANL publication
      - Document Number: ANL-AAA-020
      - Date: 8/14/2002
      - Title: Assessment of TRU Stabilization in PWRs
      - Authors: Taek K. Kim, John A. Stillman, Temitope A. Taiwo
  - CORAIL-TRU replaced with our isotopics (PURDUE-TRU) in identical assembly
  - Decay heat value for pure TRU in both cases was then computed
- All calculations performed with SCALE4.4

CORAIL-TRU Assembly
Assembly Parameters

Assembly Geometry	**17x17**
No of Rods (UO_2/MOX)	**180 / 84**
Mass of heavy metal, kg (UO_2/MOX)	**365 / 170**
Assembly pitch, cm	**21.6112**
Active height, cm	**427.0**
Assembly gap, cm	**0.1559**
Fuel pitch	**1.262082**
Cladding outer radius, cm	**0.474364**
Pellet radius, cm	**0.41266**
Cladding density, g/cm^3	**6.49012**
Pellet density, g/cm^3 (UO_2/MOX)	**10.02 / 10.02**
Power, MW (thermal/electric)	**3800 / 1300**
No of fuel assemblies	**193**
Specific power density, W/g	**36.0548**

CORAIL-TRU Assembly
Fuel Properties

Uranium Enrichment, %		5.04
TRU content in MOX, %		12.74
Initial TRU Vector	AM241	5.56
	AM242m	0.05
	AM243	3.88
	CM243	0.03
	CM244	3.48
	CM245	0.91
	NP237	2.95
	PU238	9.13
	PU239	29.64
	PU240	22.29
	PU241	8.29
	PU242	13.63
	U234	0.15

CORAIL-TRU Assembly
Analysis Methods

- Initial TRU vector compositions were placed in the sample assembly
- Assembly isotopics were then homogenized and normalized to 1.0 MT
- Decay heat was then computed and compared to the value reported by ANL

CORAIL-TRU Assembly
Homogenized Assembly Isotopics

Isotope	Initial Vector	Assembly Fraction
U238	--	91.111%
U235	--	4.836%
AM241	5.56%	0.225%
AM242m	0.05%	0.002%
AM243	3.88%	0.157%
CM243	0.03%	0.001%
CM244	3.48%	0.141%
CM245	0.91%	0.037%
NP237	2.95%	0.120%
PU238	9.13%	0.370%
PU239	29.64%	1.201%
PU240	22.29%	0.904%
PU241	8.29%	0.336%
PU242	13.63%	0.553%
U234	0.15%	0.006%

CORAIL-TRU Assembly
Decay Heat Results

Calculated Total = 6490 W / MT Published Total = 6950 W / MT

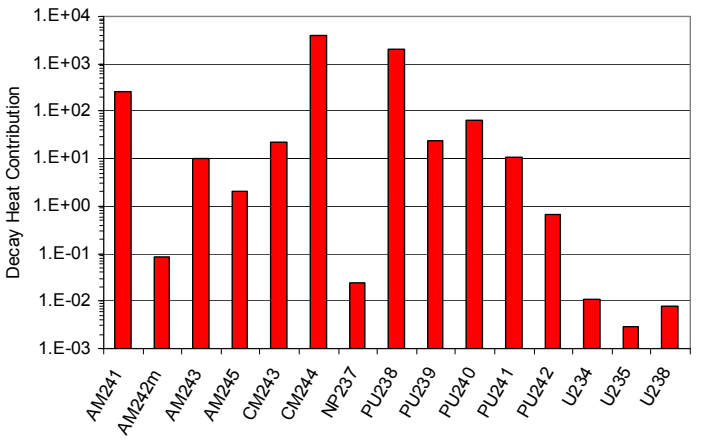

Common TRU Isotopes Properties

	Half-life (yr)	Decay Energy (MeV)
AM241	4.33E+02	5.63
AM242m	1.41E+02	0.07
AM243	7.37E+03	5.43
CM243	2.85E+01	6.18
CM244	1.81E+01	5.90
CM245	8.50E+03	5.62
CM246	4.73E+03	5.53
NP237	2.14E+06	4.81
PU238	8.77E+01	5.59
PU239	2.41E+04	5.24
PU240	6.56E+03	5.25
PU241	1.44E+01	0.01
PU242	3.74E+05	4.98
U234	2.46E+05	4.86

PURDUE-TRU Assembly Fuel Properties

Uranium Enrichment, %		5.04
TRU content in MOX, %		12.74
Initial TRU Vector	AM241	5.52
	AM242m	0.04
	AM243	4.41
	CM243	0.02
	CM244	2.54
	CM245	0.19
	CM246	0.04
	NP237	6.20
	PU238	3.45
	PU239	41.55
	PU240	23.32
	PU241	7.42
	PU242	5.30

Isotopic Comparison with ANL CORAIL Results

	PURDUE, %	CORAIL, %
AM241	5.52	5.56
AM242M	0.04	0.05
AM243	4.41	3.88
CM243	0.02	0.03
CM244	2.54	3.48
CM245	0.19	0.91
CM246	0.04	
NP237	6.20	2.95
PU238	3.45	9.13
PU239	41.55	29.64
PU240	23.32	22.29
PU241	7.42	8.29
PU242	5.30	13.63
U234		0.15

Isotopic Comparison with ANL CORAIL Results

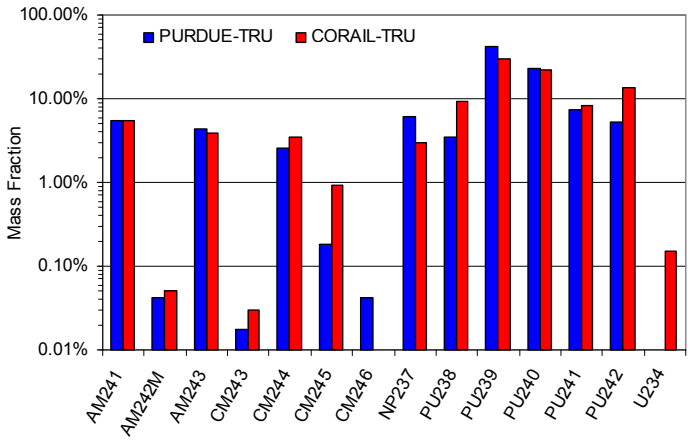

Decay Heat Results

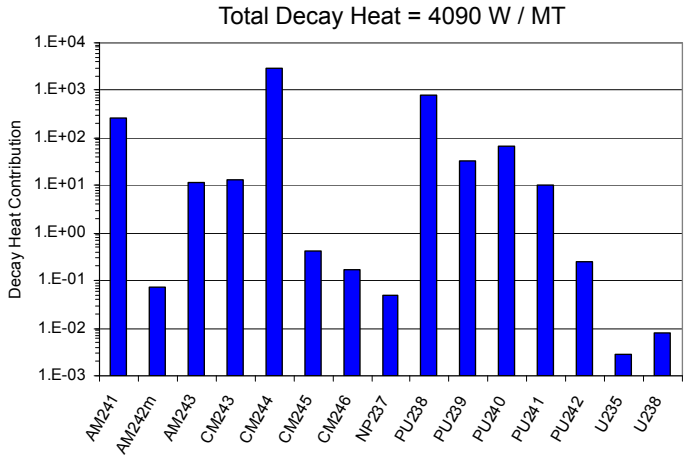

Pure TRU Products
Decay Heat Analysis

- Previous results provide an “apples-to-apples” comparison of the two different TRU compositions
- Our goal is to establish a storage form consisting of pure TRU products
- The following analysis reflect the presence of homogenized TRU at the given isotopic ratios
- CORAIL-TRU was included in this analysis as a reference value

Pure TRU Products
Decay Heat Comparison

PURDUE-TRU Total = 101 kW / MT CORAIL-TRU Total = 160 kW / MT

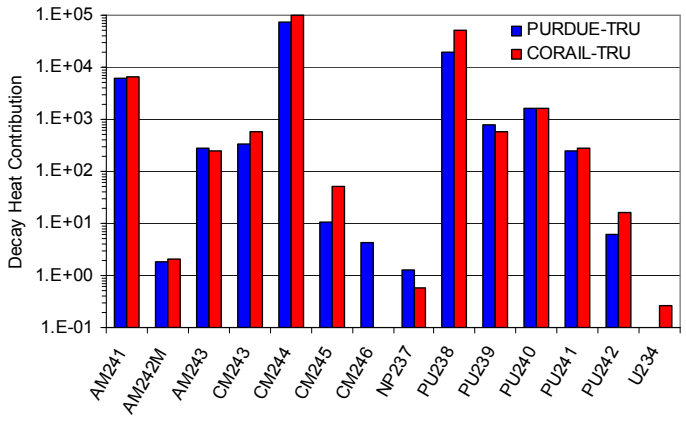

Summary of Decay Calculations

Configuration	Decay Heat (kW / MT)	Diff, %
CORAIL-TRU Assembly	6.49	--
PURDUE-TRU Assembly	4.09	-36.97
Pure CORAIL-TRU	160.0	--
Pure PURDUE-TRU	101.0	-36.88

- Decay heat from PURDUE-TRU is consistently 37% less than CORAIL-TRU
- Decay heat from pure PURDUE-TRU is determined to be 101 kW / MT

Criticality Calculations: Step 1 (Composition Specification):

- $TRUO_2$ powder, 10 g/cm^3 density (0.95*TD is used)
  - Zr metal, 6.5 g/cm^3 density
  - $TRUO_2$+Zr mixture
    - Volume fraction 0% - 50% $TRUO_2$
    - Porosity of Zr matrix 0% - 60%
- Neutronics Calculations
  - Parametric study on k_∞ (Calculations performed using MCNP4c with 10^6 neutron histories).
  - Assumption: All elements in TRU (Np, Pu, Am, Cm) are assumed to form oxide with 2 oxygen atoms.
- **DECISION** on the fractions of TRUoxide – Zr mixture and porosity of the Zr matrix.

Material Compositions in $TRUO_2$

Element	MW	ZAID	TrU Out w/Pu,Np (g/L)	Oxygen	Mass Fraction
NP	235	93235	1.69188E-10	2.30383E-11	2.54167E-11
NP	236	93236	3.8718E-07	5.2499E-08	5.81651E-08
NP	237	93237	0.364404607	0.04920231	0.054743657
NP	238	93238	2.04002E-10	2.74288E-11	3.06467E-11
NP	239	93239	9.66323E-08	1.29382E-08	1.45168E-08
NP(240M)	240	93240	1.01187E-17	1.34916E-18	1.52011E-18
PU	236	94236	3.80673E-07	5.16166E-08	5.71876E-08
PU	237	94237	2.93476E-19	3.96254E-20	4.40882E-20
PU	238	94238	0.202374702	0.027210044	0.030402281
PU	239	94239	2.440209424	0.326722601	0.366586986
PU	240	94240	1.36977089	0.182636119	0.205777495
PU	241	94241	0.435984084	0.057890003	0.065496875
PU	242	94242	0.311370722	0.041172988	0.046776499
PU	243	94243	7.35316E-16	9.68318E-17	1.10465E-16
PU	244	94244	6.05172E-05	7.93668E-06	9.09136E-06
AM	241	95241	0.323954346	0.043014685	0.048666908
AM	242	95242	2.99265E-08	3.95722E-09	4.49579E-09
AM (242M)	242	95242	0.002498863	0.000330428	0.000375398
AM	243	95243	0.258864212	0.034089114	0.038888569
AM	244	95244	1.94522E-19	2.55111E-20	2.92226E-20
CM	241	96241	1.16712E-24	1.54971E-25	1.75334E-25
CM	242	96242	1.50379E-05	1.98849E-06	2.25911E-06
CM	243	96243	0.001032454	0.000135961	0.000155103
CM	244	96244	0.148882889	0.019525625	0.02236633
CM	245	96245	0.010923066	0.001426686	0.001640947
CM	246	96246	0.002468912	0.000321159	0.000370899
CM	247	96247	4.7433E-05	6.14517E-06	7.12576E-06
CM	248	96248	5.4765E-06	7.06645E-07	8.22721E-07
oxygen			5.87286853	0.783694621	0.11773262

$TRUO_2$-Zr Powder density with varying volume fraction and porosity

		vol. %					
	dnsty(g/cm3)	1	2	3	4	5	6
TRU-O2	10	**0.05**	**0.1**	**0.15**	**0.2**	**0.25**	**0.3**
Zr	6.511	**0.95**	**0.9**	**0.85**	**0.8**	**0.75**	**0.7**
Porosity							
a	**0**	6.66045	6.8099	6.95935	7.1088	7.25825	7.4077
b	**0.05**	6.35118	6.51691	6.68263	6.84836	7.01409	7.17982
c	**0.1**	6.04191	6.22391	6.40592	6.58792	6.76993	6.95193
d	**0.15**	5.73263	5.93092	6.1292	6.32748	6.52576	6.72405
e	**0.2**	5.42336	5.63792	5.85248	6.06704	6.2816	6.49616
f	**0.25**	5.11409	5.34493	5.57576	5.8066	6.03744	6.26828
g	**0.3**	4.80482	5.05193	5.29905	5.54616	5.79328	6.04039
h	**0.35**	4.49554	4.75894	5.02233	5.28572	5.54911	5.81251
i	**0.4**	4.18627	4.46594	4.74561	5.02528	5.30495	5.58462
j	**0.45**	3.877	4.17295	4.46889	4.76484	5.06079	5.35674
k	**0.5**	3.56773	3.87995	4.19218	4.5044	4.81663	5.12885
l	**0.55**	3.25845	3.58696	3.91546	4.24396	4.57246	4.90097
m	**0.6**	2.94918	3.29396	3.63874	3.98352	4.3283	4.67308

$TRUO_2$-Zr Powder density with varying volume fraction and porosity

		vol. %					
	dnsty(g/cm3)	1	2	3	4	5	6
TRU-O2	10	**0.05**	**0.1**	**0.15**	**0.2**	**0.25**	**0.3**
Zr	6.511	**0.95**	**0.9**	**0.85**	**0.8**	**0.75**	**0.7**
Porosity							
a	**0**	6.66045	6.8099	6.95935	7.1088	7.25825	7.4077
b	**0.05**	6.35118	6.51691	6.68263	6.84836	7.01409	7.17982
c	**0.1**	6.04191	6.22391	6.40592	6.58792	6.76993	6.95193
d	**0.15**	5.73263	5.93092	6.1292	6.32748	6.52576	6.72405
e	**0.2**	5.42336	5.63792	5.85248	6.06704	6.2816	6.49616
f	**0.25**	5.11409	5.34493	5.57576	5.8066	6.03744	6.26828
g	**0.3**	4.80482	5.05193	5.29905	5.54616	5.79328	6.04039
h	**0.35**	4.49554	4.75894	5.02233	5.28572	5.54911	5.81251
i	**0.4**	4.18627	4.46594	4.74561	5.02528	5.30495	5.58462
j	**0.45**	3.877	4.17295	4.46889	4.76484	5.06079	5.35674
k	**0.5**	3.56773	3.87995	4.19218	4.5044	4.81663	5.12885
l	**0.55**	3.25845	3.58696	3.91546	4.24396	4.57246	4.90097
m	**0.6**	2.94918	3.29396	3.63874	3.98352	4.3283	4.67308

k_∞ with varying volume fraction and porosity

		vol. %					
	dnsty(g/cm3)	1	2	3	4	5	6
TRU-O2	10	0.05	0.1	0.15	0.2	0.25	0.3
Zr	6.511	0.95	0.9	0.85	0.8	0.75	0.7
Porosity							
0		1.27974	1.67884	1.90943	2.05953	2.16572	2.24558
0.05		1.30712	1.7065	1.93314	2.08157	2.18315	2.25901
0.1		1.33369	1.73354	1.95634	2.09946	2.19904	2.27379
0.15		1.36172	1.75936	1.9789	2.11874	2.2153	2.28716
0.2		1.3892	1.78538	2.00101	2.13636	2.2315	2.30024
0.25		1.41669	1.81075	2.0218	2.15562	2.24701	2.31318
0.3		1.44391	1.83515	2.04412	2.17333	2.26152	2.32516
0.35		1.47166	1.86139	2.06388	2.18994	2.27487	2.33725
0.4		1.49984	1.88482	2.08397	2.20478	2.28807	2.34938
0.45		1.52767	1.90861	2.10432	2.22168	2.3029	2.35993
0.5		1.55451	1.93266	2.1222	2.2362	2.31414	2.36868
0.55		1.58317	1.95542	2.14209	2.25334	2.32648	2.38073
0.6		1.61052	1.97745	2.159	2.26641	2.33811	2.38858

k_∞ with varying volume fraction and porosity

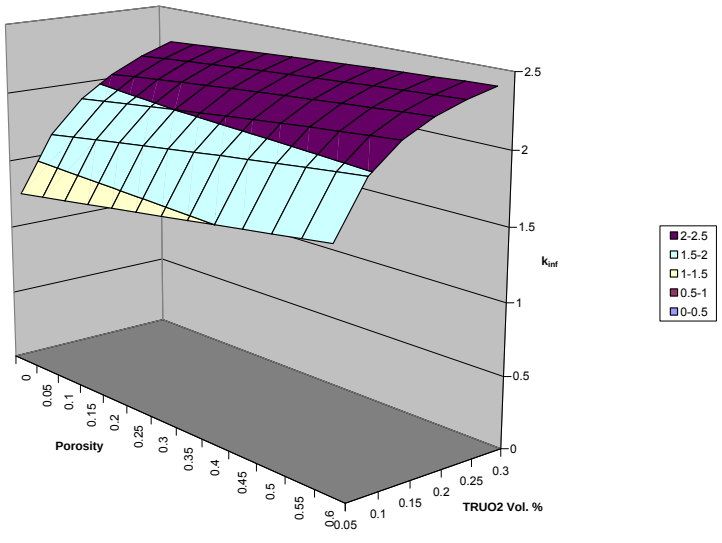

Analysis of Impact of Porosity and Volume Fraction on Criticality: Neutron Spectrum

Case I: 0% Porosity -$TRUO_2$ 5% vol.+ Zr %95 vol.

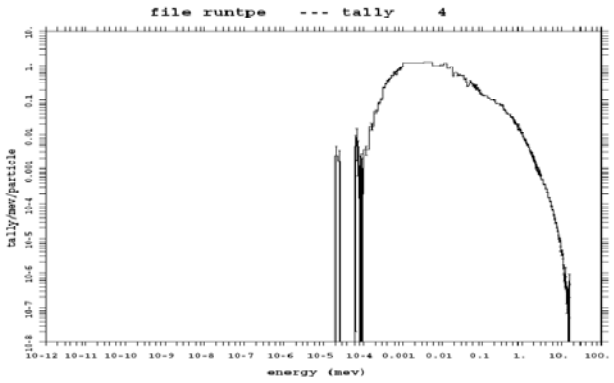

Analysis of Impact of Porosity and Volume Fraction on Criticality

CASE II: 60% Porosity -$TRUO_2$ 5% vol.+ Zr %95 vol.

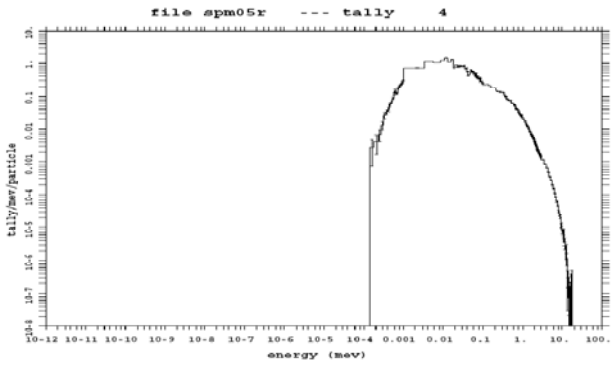

Analysis of Impact of Porosity and Volume Fraction on Criticality

Case III: 60% Porosity -$TRUO_2$ 30% vol.+ Zr %70 vol.

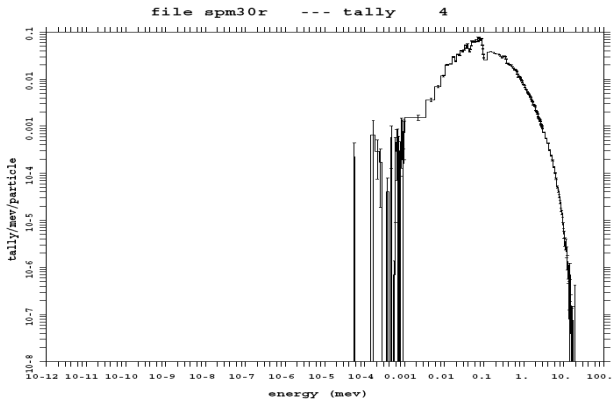

Analysis of Impact of Porosity and Volume Fraction on Criticality: Conclusions

- As porosity is increased the neutron spectrum hardens. Also as the porosity is increased there is reduced Zr absorption
- As the density of TRU is increased the neutron spectrum also hardens
- Both these effects increase the k-inf (criticality) of the mixture

After storage (decay)

	Initial	5 years	25 years	50 years
he_4	0.00E+00	1.07E+02	4.36E+02	7.13E+02
th230	0.00E+00	9.16E-03	2.17E-01	8.17E-01
pa233	0.00E+00	2.12E-03	2.22E-03	2.37E-03
u233	0.00E+00	9.69E-02	5.03E-01	1.04E+00
u234	0.00E+00	1.31E+03	6.08E+03	1.11E+04
u235	0.00E+00	5.88E+01	2.94E+02	5.87E+02
u236	0.00E+00	1.22E+02	6.27E+02	1.28E+03
u238	0.00E+00	4.83E-01	2.42E+00	4.83E+00
np237	6.20E+04	6.25E+04	6.53E+04	6.97E+04
np239	0.00E+00	3.79E-02	3.79E-02	3.78E-02
pu238	3.45E+04	3.32E+04	2.84E+04	2.33E+04
pu239	4.16E+05	4.16E+05	4.16E+05	4.16E+05
pu240	2.33E+05	2.37E+05	2.48E+05	2.53E+05
pu241	7.42E+04	5.83E+04	2.22E+04	6.64E+03
pu242	5.30E+04	5.30E+04	5.30E+04	5.30E+04
am241	5.52E+04	7.06E+04	1.04E+05	1.15E+05
am242m	4.25E+02	4.15E+02	3.76E+02	3.32E+02
am242	0.00E+00	5.35E-03	4.85E-03	4.29E-03
am243	4.41E+04	4.41E+04	4.40E+04	4.39E+04
cm242	0.00E+00	1.08E+00	9.79E-01	8.66E-01
cm243	1.76E+02	1.56E+02	9.59E+01	5.22E+01
cm244	2.54E+04	2.10E+04	9.76E+03	3.75E+03
cm245	1.86E+03	1.86E+03	1.86E+03	1.85E+03
cm246	4.20E+02	4.20E+02	4.18E+02	4.17E+02
total	1.00E+06	1.00E+06	1.00E+06	1.00E+06

Red color: initially zero produced through the decay of TRU

Effect of Storage Time on k_∞

Porosity		TRU-O2	0.05	PCM		0.15	
0		Zr	0.95	DIFF.		0.85	
	storage period						
	(year)						
	0		1.27974			1.90943	
	5		1.24107	-3867		1.87154	-3789
	25		1.23596	-511		1.86357	-797
	50		1.23094	-502		1.85608	-749
				-4880			-5335
Porosity							
0.3		TRU-O2	0.05			0.15	
		Zr	0.95			0.85	
	storage period						
	(year)						
	0		1.44391			2.04412	
	5		1.40433	-3958		2.00734	-3678
	25		1.40006	-427		2.00034	-700
	50		1.39328	-678		1.9907	-964
				-5063			-5342

Remarks and comments

- Throughout the decay of TRU, new elements are produced, and amount of initial ones changes, which causes variations in k_∞ as time passes.
- The total Δk_∞ after 50 yrs is about -5000 pcm, about -4000 pcm of it occurs after 5 yrs.
- The decrease in k_∞ should be taken into account in selection of the fractions of $TRUO_2$-Zr mixture.

Step 2 (Ongoing Work)

- Design of the storage fuel form
  - Rod Specifications (Initial Design)
    - Diameter ~ ¼ inch
    - Height ~ 5 inch
    - Cladding; zircaloy with no gap 1mm
  - Calculation Sequence
- Evaluate the TRU burning performance of the cermet storage/fuel pin in a simulated GenIV reactor system

Appendix N

November 2007 ANS Summary: MCNP Methods (3 Pages)

"The Design and Analysis of TRU Burning Sodium Cooled Fast Reactor,"
Volkan Seker, Christopher Glass, Kevin Kramer, Thomas J. Downar

November 2007

The Design and Analysis of TRU Burning Sodium Cooled Fast Reactor

[1]Volkan Seker, [1]Christopher Glass, [2]Kevin Kramer, [1]Thomas J. Downar

[1] 400 Central Drive,Nuclear Engineering Building,
W. Lafayette, Indiana, 47907,
vseker@purdue.edu , crglass@purdue.edu , downar@purdue.edu
[2] LLNL

INTRODUCTION

Sodium-cooled fast reactors have been proposed to be used as transuranics burning systems as part of the AFCI project. These systems have the advantage of being able to operate under passively safe conditions while consuming nearly 99% of current spent fuel actinides. Current systems are designed to run on recycled LWR discharge fuel with continuing operation using its own recycled discharge fuel.

COMPUTATIONAL MODELS

In the study presented here, the computer codes MONTEBURNS, MCNP5 and NJOY were utilized to evaluate the reactor neutronic characteristics. MONTEBURNS was used to obtain the equilibrium core compositions and to perform depletion. Neutronics parameters were calculated by the standalone MCNP and cross-sections for MCNP calculation were generated by NJOY at reactor operational temperatures.

MONTEBURNS is a computer code which utilizes a FORTRAN code and a PERL script to link Monte Carlo transport code MCNP with the depletion code ORIGEN2. The main function of the code is to transfer one-group cross-sections and fluxes obtained from MCNP to ORIGEN and then transfer back the material composition obtained after the specified depletion time step to MCNP in a repeated way until the specified total depletion time is reached [1]. Some modifications on the code were done to make it compatible with MCNP5 and run it on the parallel clusters.

MCNP5 is a Monte Carlo transport code that uses pointwise cross-section data. It is capable of producing several neutronic parameters such as; criticality, reaction rates, fluxes etc. [2]. MCNP5 becomes more flexible when it is used in conjunction with NJOY which can generates cross-section data file to be used with MCNP.

DESCRIPTION OF THE ACTUAL WORK

In the work here, the effect of several parameters on the calculation of equilibrium core compositions was investigated. These parameters were the number of depletion regions, the depletion time step size, the control rod insertion depth, and the temperature at which the cross-sections are generated.

The core model used in this study based on the compact core model proposed by the Argonne National Laboratory [5]. The geometry of the fuel and control assemblies and the one sixth of the core are depicted in Fig. 1 and 2, respectively. The detailed information about the core and fuel geometry, fuel and other structural material compositions can been found in the referenced ANL report [5].

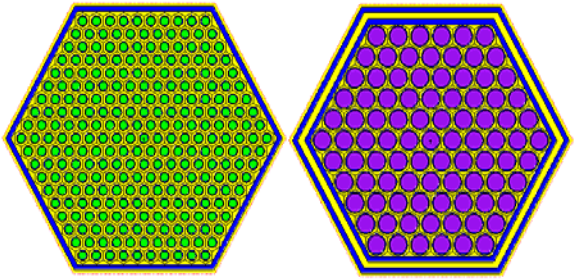

Fuel Assembly Control Assembly

Fig. 1 Fuel and control assemblies

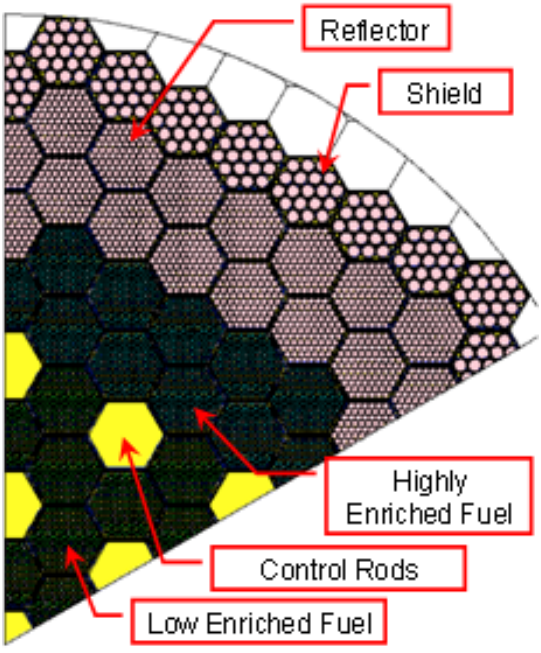

Fig. 2 One sixth of the core

In order to reach an equilibrium condition in the core, a seven batch reloading scheme was applied and 45 cycles were performed to ensure the convergence of the equilibrium. Prior to the final equilibrium core calculation, first the effect of the depletion region is investigated. Calculations were performed with 2 and 25 depletion regions. In the 2 depletion region model, the low and high enriched fuel regions are considered as depletion regions. On the other hand, 25 depletion regions is examined to take into account the axial and radial flux profiles, shown in Fig. 3, which resulted in 5 axial and radial regions as grouped in Fig. 3.

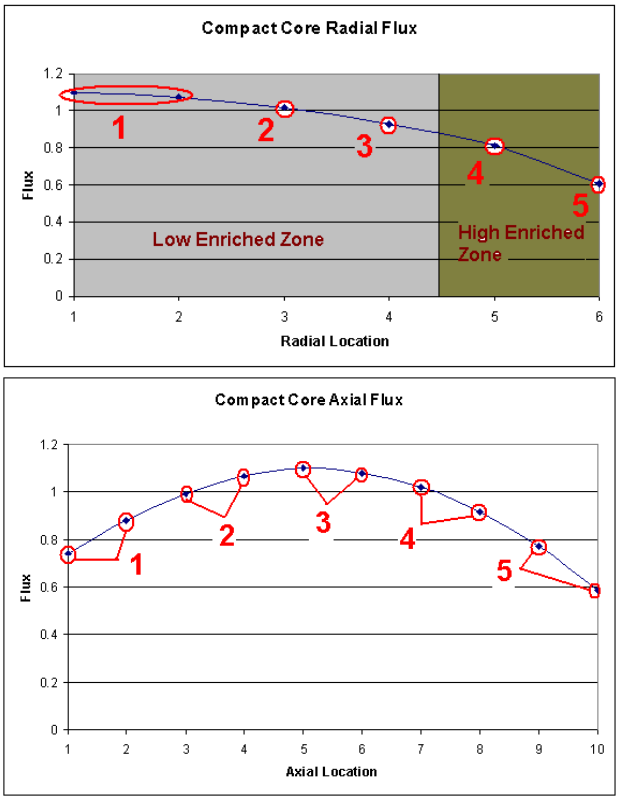

Fig. 3 Radial and axial flux profiles

The parametric on the depletion time step size is performed by varying the number of outer depletion steps for one cycle which has a length of 155.1 days. In order to see the effect of the position of the control rods, same depletion calculation is repeated at various control rod insertion depths. Finally the equilibrium search is done with cross-section generated at hot and cold core conditions.

RESULTS

The result of the first parametric study, number of depletion regions, is shown in Fig. 4. The difference of the BOC eigenvalues for two different models is about 750pcm which shows that two depletion region is not sufficient for the analysis.

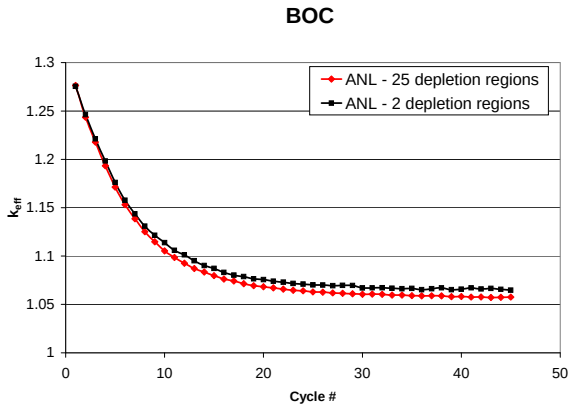

Fig. 4 Equilibrium with 2 and 25 depletion regions

Secondly, if we look at the effect of depletion time step size as shown in Fig. 5, we can see that time step size does not effect the depletion calculation, which gives us the flexibility to use large time steps to perform the equilibrium core composition calculation.

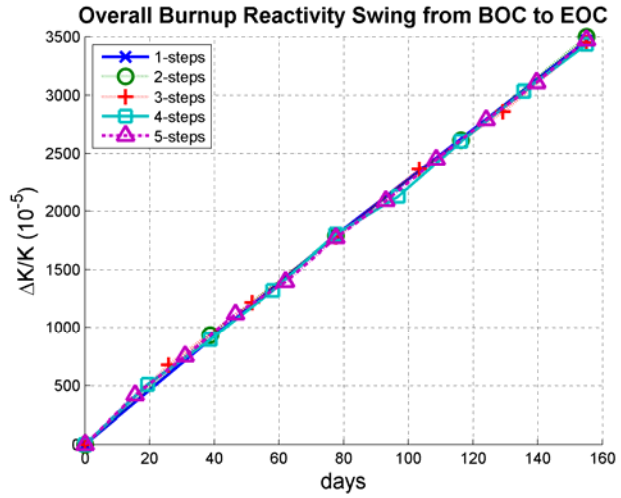

Fig. 5 Depletion time steps

As depicted in Fig. 6, control rod insertion depth causes about 400 pcm difference in the calculations between the fully inserted and fully withdrawn rod conditions. As the core nears equilibrium, the control rods will always be nearly fully withdrawn. The control rod can therefore be assumed to be at a fixed position nearly fully withdrawn for the entire calculation.

Finally, the use cross-section generated at the operating temperatures causes around 1000pcm difference at the equilibrium BOC condition and must be considered as an important parameter in the depletion calculations.

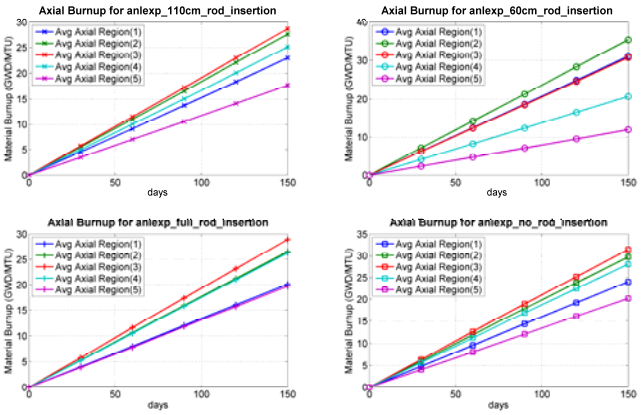

Fig. 6 Control rod insertion depths

Hot and Cold cross sections

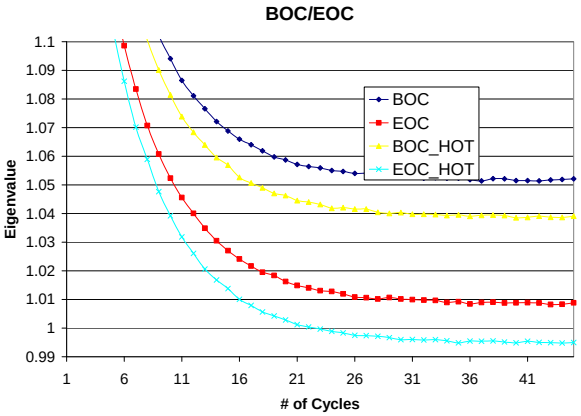

Fig. 7 Equilibrium at hot and cold cross-sections

REFERENCES

1. W.G. GRAY, K. O'NEILL " On the General Equations for Flow in Porous Media and Their Reduction to Darcy's Law", Water Resources Research, **12,** *2* 148-154 (1976).
2. B. STOCKER, H. F. NIESSEN, "Data Sets of the SANA Experiment 1994-1996" , Forschungszentrum Julich, Institute for Safety Research and Reactor Technology
3. F. REITSMA, "OECD/NEA/NSC PBMR Coupled Neutronics/Thermalhydraulics Benchmark" (2005).
4. T. J. DOWNAR, et. al., "PARCS: Purdue Advanced Reactor Core Simulator," PHYSOR 2002, Seoul, Korea, October (2002).
5. M. A. Smith and R. N. Hill, "Development and Analysis of a Compact Low-Conversion Ration Fast Burner Reactor," Argonne National Laboratory (ANL), ANL-AFCI-084, June 2003.
6. M. A. Smith, W. S. Yang, and R. N. Hill, "Preliminary Studies of a Nitride-Fueled Fast Burner Reactor," Argonne National Laboratory (ANL), ANL-AFCI-167, April 2006.

Appendix O

November 2007 ANS Presentation: MCNP Methods (14 Pages)

"The Design and Analysis of TRU Burning Sodium Cooled Fast Reactor,"
Volkan Seker, Christopher Glass, Kevin Kramer, Thomas J. Downar

November 2007

Monte Carlo Depletion Analysis of a Sodium Cooled Fast Reactor

Chris Glass, Volkan Seker, Thomas J. Downar
Purdue University

Kevin Kramer
U.C. Berkeley

November 2007

Outline

- Objective
- SFR Depletion Analysis
  - Monteburn model
  - Important factors to consider for depletion
- Parametric Comparison to deterministic methods for equilibrium core
- Summary / Continuing Work

Objective

- Develop methods to accurately model a large fast reactor system using MCNP5.
- Demonstrate the practicability of using Monte Carlo for hot, full power core depletion analysis.

Monteburns Depletion Method

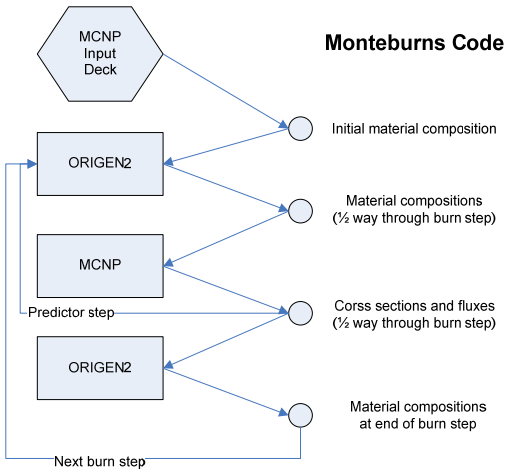

ABR Calculation with Metal Fuel

- A metal fuel core design proposed as part of the AFCI program was used as the basis for the core depletion model.
- Objective:
  - To demonstrate the applicability of Monteburn in Fast Reactor depletion calculation.

Fuel and Core Specification

- Fuel (550K)
  - 25% w/o Zirc + 75% w/o U-TRU
  - Low enrichment = 46% w/o TRU + 54% w/o U
  - High Enriched = 58% w/o TRU + 42% w/o U
- Pin
  - 0.295 cm fuel radius
  - 0.06 cm cladding thickness
- Core
  - Compact core configuration

ABR Core

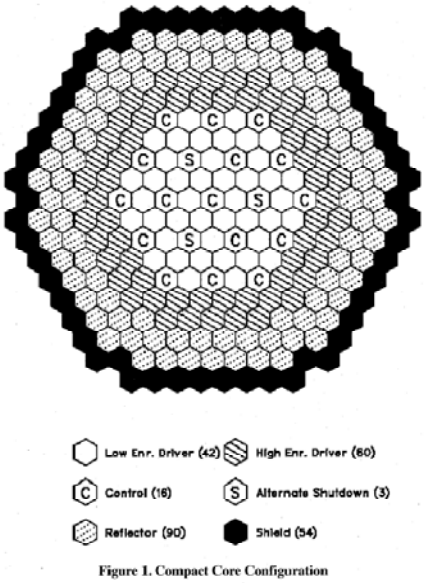

Figure 1. Compact Core Configuration

- 2.76m diameter
- 1.86m diameter fuel region
- 16.14cm Assembly Pitch
- 271 fuel pins/Assembly
- 840MWt
- 1/6 core symmetry
- AFCI-084

Axial Configuration

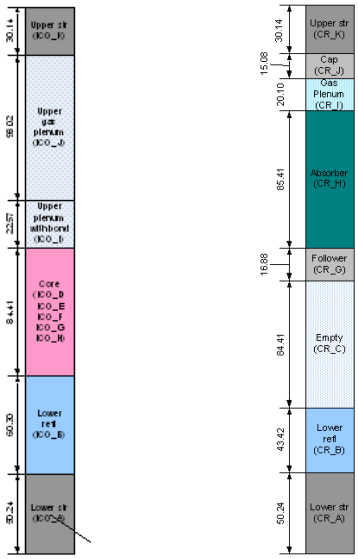

MCNP model

- 1/6 core model
- Explicitly model control rods, reflector, shield, and fuel assemblies
- Hot XS at assumed 550K were generated in NJOY using the ENDF-VI library

MCNP Explicit Model

1/6 Core Model

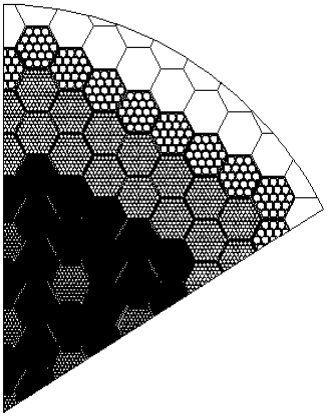

Fuel Assembly

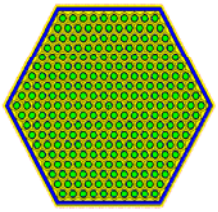

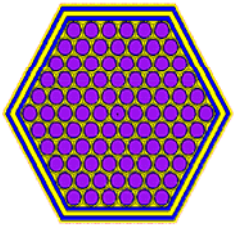

Control Assembly

Burnup Considerations

- In order to obtain parameters important to understanding core performance an equilibrium burnup distribution was obtained.
- Several effects must be considered when computing an equilibrium burnup distribution for example:
  - Burnup time step
  - Rod insertion depth
  - Number, size, and location of depletion zones

Effect of control rod insertion depth during depletion

Beginning of cycle (BOC) to end of cycle (EOC) is the calculated as (k_0-$k_{current}$)

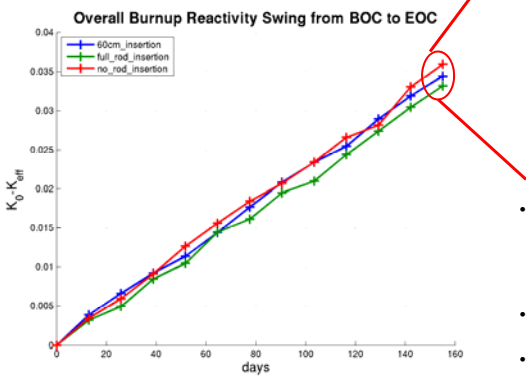

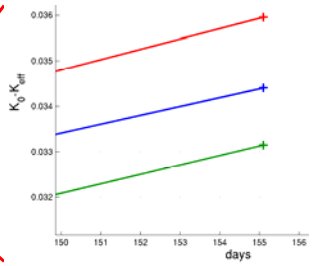

- Note the inverting of delta k for the full rod insertion vs. no rod insertion relative to burnup reactivity swing. This is the result of different initial k_0 for each case
- Results show more Δk change when control rods are not inserted.
- Control rod insertion dilutes Δk but overall has a higher $\Delta k/k$ due to k_0 being significantly lower

Effect of burnup step size

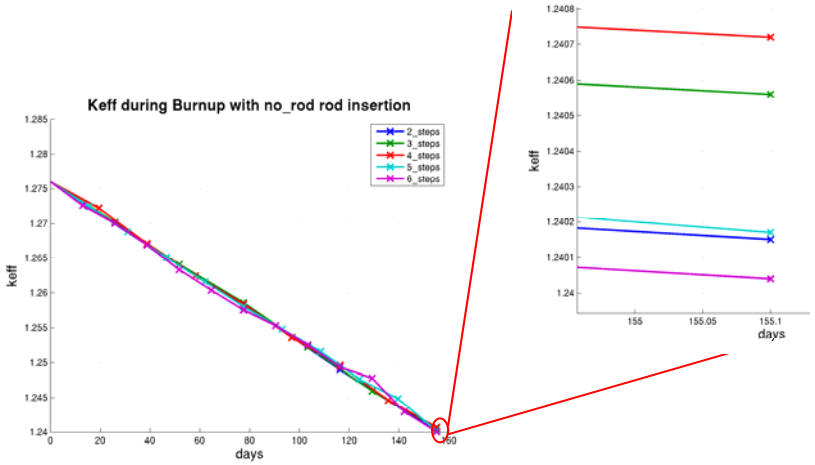

Core Axial Flux Distribution

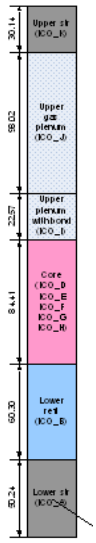

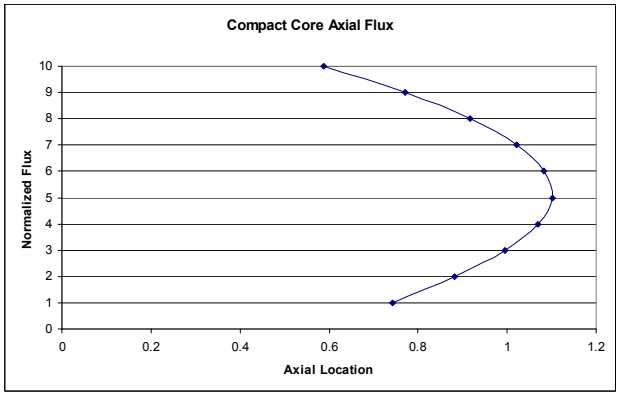

Radial Flux Distribution

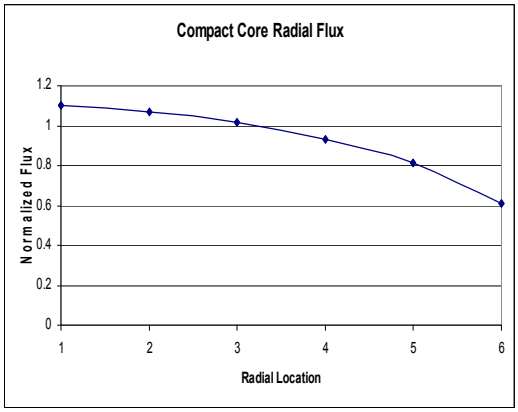

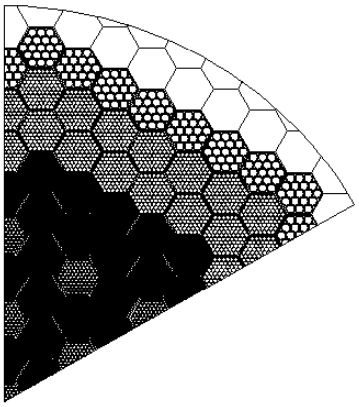

Depletion Regions

- The spatial variation in the flux distribution necessitates refining the axial and radial depletion mesh
  - 5 radial rings
  - 5 axial planes
- The grouping is depicted in the next 4 slides

Radial Discretization

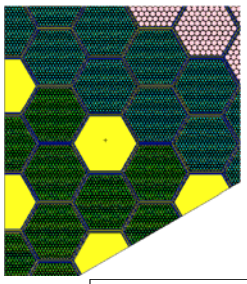

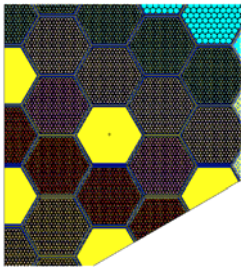

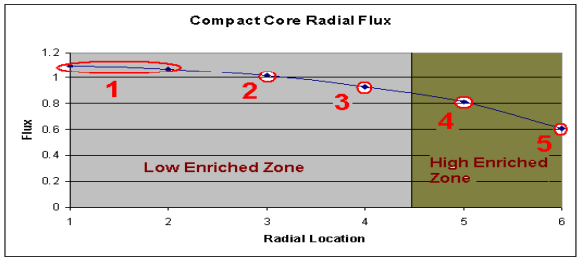

Axial Discretization

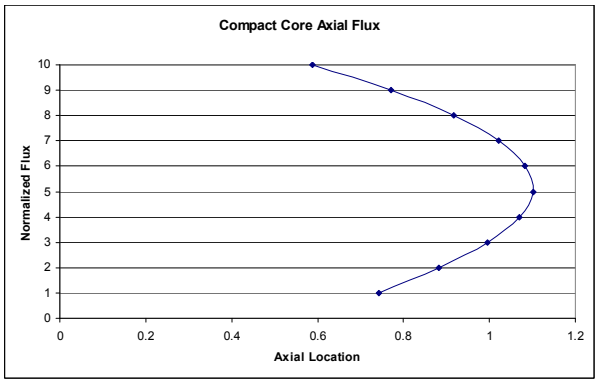

Equilibrium Search

- To obtain the equilibrium fuel composition the fresh core is burned considering;
  - 155.1 days of burn-up cycles
  - 7 batches
    - 1/7th of the burned fuel in each depletion region is replaced by fresh fuel after each cycles.
  - 45 total cycles are performed.
- Calculations were performed for two different numbers of depletion regions.
  - 2 radial – 1 axial region
  - 5 radial – 5 axial region

Equilibrium Search w/ 25 regions

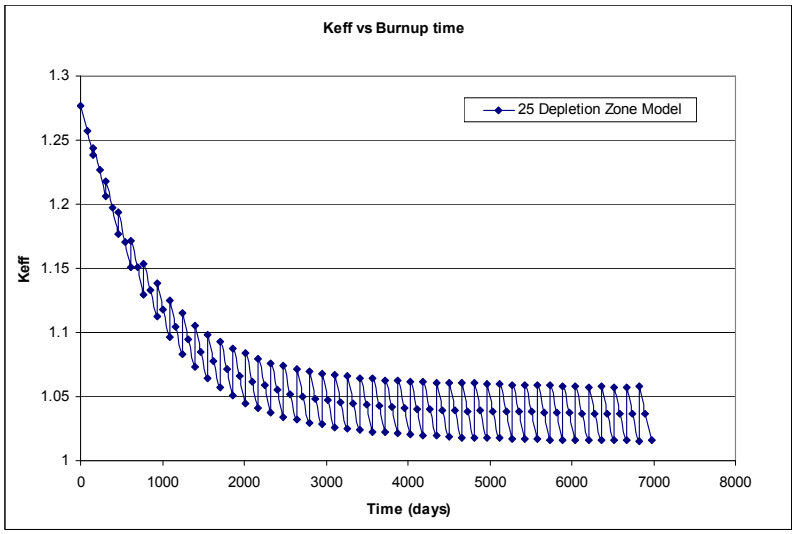

Beginning of Cycle Comparison

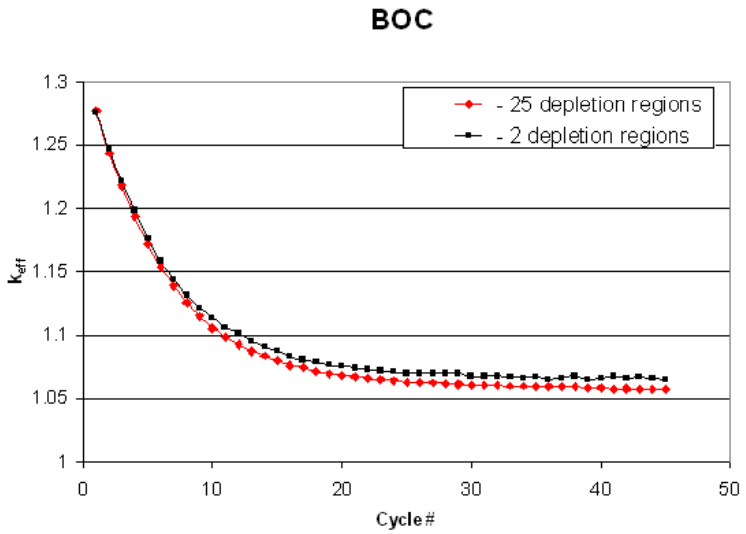

Comparison of k-eff

	2-zone	25-zone	Δk (pcm)
BOC	1.06469	1.05762	707
MOC	1.04495	1.03668	827
EOC	1.02366	1.01563	803

The Axial and Radial Discretization has a noticeable impact on the equilibrium core material number densities which in turn has a non-negligible impact on the k-effective.

Calculation Methods for Parametrics

- Delayed Neutron Fraction
  - MCNP has an option to turn off the contribution of delayed neutrons to compute the core eigenvalue.
  - Beta can be defined as:
    - $1-k_{no\text{-}delayed}/k$
- Sodium Density Worth
  - Core is uniformly voided of sodium
  - Linear Curve fit of k vs. sodium void will give ρ/%void.
- Sodium Void Worth
  - Core will be completely voided of sodium.

Methods Continued

- Radial Expansion Worth
  - Uniform 1% expansion of all surfaces. i.e. pin diameter, pitch, assembly wall, assembly pitch, etc.
- Axial Expansion Coefficient
  - 1% Uniform expansion in axial Direction
- Doppler
  - Fuel temperature is doubled by modifying XS using NJOY and cell temperatures in MCNP.

BOC Sodium Void Worth

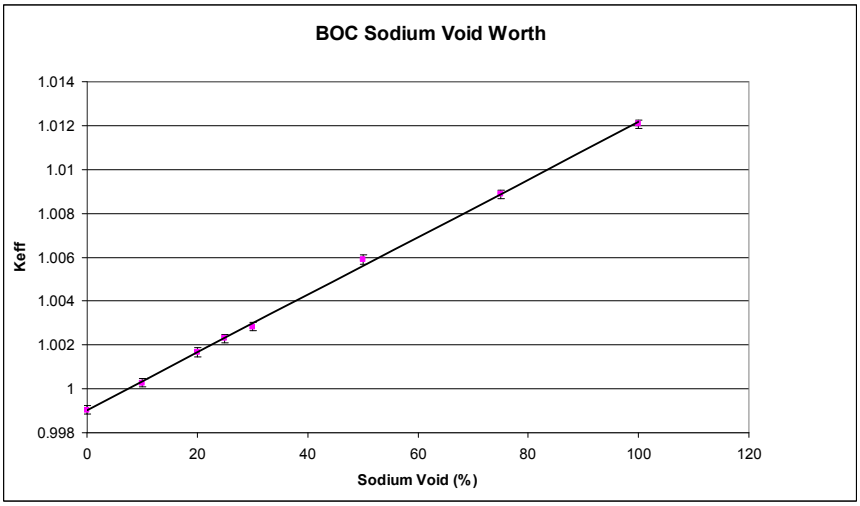

Note: Slope is about 10 pcm/% void

Calculated Reactor Parameters

	MONTEBURN
BOC HM Loading (kg)	4202
EOC HM Loading (kg)	4067
Burned Heavy Metal (kg)	135
BOC TRU Loading	1992
Net TRU consumption (kg/yr)	189.3

*Upper bound for uncertainty in all fuel masses is ~6.5%

Reactivity Worth Coefficients

	MONTEBURN	Std Dev*
Beta (BOC)	0.002633	**0.00001**
(EOC)	0.002567	**0.00001**
Burnup reactivity loss (% dk)	4.257	**0.107**
Axial expansion coefficient (cents/K)	-0.35	**0.001**
Doppler (cents/K) (BOC)	-0.067	**0.008**
Sodium Void Worth($) (BOC)	3.97	**0.107**
(EOC)	5.05	**0.11**

*Calculated assuming no uncertainty in isotopics

Conclusions

- Monte Carlo depletion methods are capable of providing sufficient accuracy for preliminary design and analysis of a SFR.
- Further modifications are required to the Monteburns code structure in order to allow more depletion regions which would improve the accuracy of the solution.

Appendix P

Master of Science Thesis: MCNP Methods (71 pages)

MONTE CARLO METHODS FOR DEPLETION AND DESIGN OF AN ADVANCED BURNER REACTOR

A Thesis

Submitted to the Faculty of
Purdue University

By

Christopher R. Glass

In Partial Fulfillment of the Requirements for the Degree
of
Master of Science in Nuclear Engineering

December 2007

MONTE CARLO METHODS FOR DEPLETION AND DESIGN OF AN ADVANCED BURNER REACTOR

A Thesis

Submitted to the Faculty

of

Purdue University

by

Christopher R. Glass

In Partial Fulfillment of the

Requirements for the Degree

of

Master of Science in Nuclear Engineering

December 2007

DEDICATION

To all those out there who didn’t think I had what it would take, but more importantly, to the few out there who knew that I could do it.

ACKNOWLEDGMENTS

The author would like to thank Dr Thomas Downar for his support and guidance over the last year. The author would also like to thank Mr. Volkan Seker for his help in the more difficult aspects of the work. Finally the author would like to thank all of the members of the PARCS research group, Andy, Volkan, Brendan, Mathieu, Zenja, Ben, and Yunlin for the fun work environment over the last year and a half.

TABLE OF CONTENTS

LIST OF TABLES

LIST OF FIGURES

LIST OF ABBREVIATIONS

ABR – Advanced Burner Reactor

ABTR – Advanced Burner Test Reactor

AFCI – Advanced Fuel Cycle Initiative

ARI – All control rods fully inserted

ARO – All control rods fully withdrawn

BOC – Beginning of Cycle

DOE – Department of Energy

EOC – End of Cycle

GNEP – Global Nuclear Energy Partnership

LWR – Light water reactor

SFR – Sodium Fast Reactor

TRU – Transuranics, any element with an atomic number greater than Uranium

U-TRU – Mixed Uranium and Transuranic

ABSTRACT

Glass, Christopher R. MS, Purdue University, December, 2007. Monte Carlo Methods for Depletion and Design of an Advanced Burner Reactor.
. Major Professor: Thomas J. Downar.

Monte Carlo depletion has long been criticized as being too computationally intensive to be feasible for all but the simplest of cases. The objective of this thesis was to investigate whether recent advances in high performance computing have made it possible for Monte Carlo depletion codes to be used for design and analysis of a practical, large scale reactor system. A sensitivity study was performed to analyze the effect of various parameters such as control rod insertion depth, depletion region size, and flux update time. These calculations show that only the depletion region size is of significant importance to provide an accurate equilibrium depletion calculation. After a homogenous reload equilibrium core calculation is completed, various key core parameters are calculated to benchmark the depletion methods which have been developed. The calculated parameters include equilibrium core mass, TRU consumption, sodium void worth, delayed neutron fraction, doppler, and axial expansion coefficient. These calculations show that the calculated parameters without a large statistical uncertainty compare very well to the reference values. However, the parameters with large statistical uncertainty, doppler and core mass, do not compare as well and further quantification and reduction of this error is suggested as future work.

Using the methods developed here, a new TRU-cermet fuel type was designed for operation within the sodium fast reactor. A final fuel design of 38% w/o TRU with a pin radius of 0.32 cm was found to display similar operating characteristics to its metal fueled counterpart. The same parameters calculated to benchmark the methods developed for the metal fueled core are again calculated to compare the cermet fueled core to the metal fueled core. It is found that the TRU-cermet fueled core has a smaller sodium void worth, but also a less negative axial expansion coefficient. These effects result in a core with safety characteristics similar to the metal fuel design, however, the TRU consumption rate of the TRU-cermet fueled core is found to be significantly higher than that of the metal fueled core.

CHAPTER 1. INTRODUCTION

1.1. Objectives

The overall goal of this research was to investigate the applicability of using MCNP to deplete and design a large sodium cooled fast reactor. The specific objectives are to:

1. Build a 1/6 symmetric model of a sodium cooled fast reactor in MCNP.
2. Develop the necessary methods to deplete this model accurately and time efficiently.
3. Verify these methods by benchmarking the results against current modeling techniques.
4. Develop a new TRU-cermet fuel type to operate in the given reactor geometry.
5. Compare TRU-cermet fueled performance to reference metal fuel.

1.2. Background

As part of a global initiative to increase the use of nuclear power throughout the world, the U.S. Department of Energy has produced a technology roadmap for next generation (Generation IV) nuclear reactors [1]. An important part of that roadmap includes the development of various advanced reactor designs. The current frontrunner of these advanced reactor designs is the sodium cooled fast reactor (SFR). The primary purpose of the SFR is to address the issue of growing spent fuel from current Light Water Reactors (LWR) while at the same time providing economical electricity generation. The SFR will close the nuclear fuel

cycle, utilizing the 99% of current reactor fuel energy that is currently wasted. As much as 99.9% of spent fuel actinides could be recovered and recycled, which will reduce the amount of fissile material in waste repositories to trace amounts[1]. Using this reactor design, current Yucca Mountain designs would be sufficient to store all of the United States' nuclear waste for generations. Another desirable trait of the SFR is that the plutonium is never separated into its pure state during reprocessing. This is very desirable for non-proliferation reasons. The SFR is also the nearest-term actinide management system of the "Generation IV" reactor designs with an estimated commercial deployment by 2020 [2]. Some SFR's are currently operating, and demonstration plants have been built and operated in France, Japan, Germany, the United Kingdom, Russia, and the United States with powers ranging from 1.1 to 1200 MWe [1].

SFR's are radically different from LWR's and thus have very different operational characteristics. One such difference is the SFR's use of "fast," or high energy neutrons as opposed to "thermal," or low energy neutrons to maintain criticality during operation. This results in very different fuel burnup, depletion, and reactivity feedback characteristics. Likewise, the SFR uses liquid sodium, instead of water, as a coolant. Liquid sodium burns in air and necessitates a more complicated coolant system. Thus, the SFR must overcome certain cost reduction issues to become commercially competitive. In addition, more study is needed regarding the SFR's passive safety response to all anticipated transients. Even with these technology gaps, the SFR is the most technologically developed of the Generation IV reactors.

An example of the SFR design can be seen in Figure 1.1. More detailed design descriptions are beyond the scope of this document, but can be found in the references [3]. Since the SFR is designed as an advanced fuel cycle reactor, we must understand the detailed fuel burnup. We must also understand how the reactor will respond under certain accident scenarios. The response of the reactor is estimated by certain reactivity feedback coefficients. These coefficients

characterize how the reactor will respond to various parameters such as temperature increases caused by a reduction in coolant flow, or to changes in the coolant density caused by a break in a main coolant line.

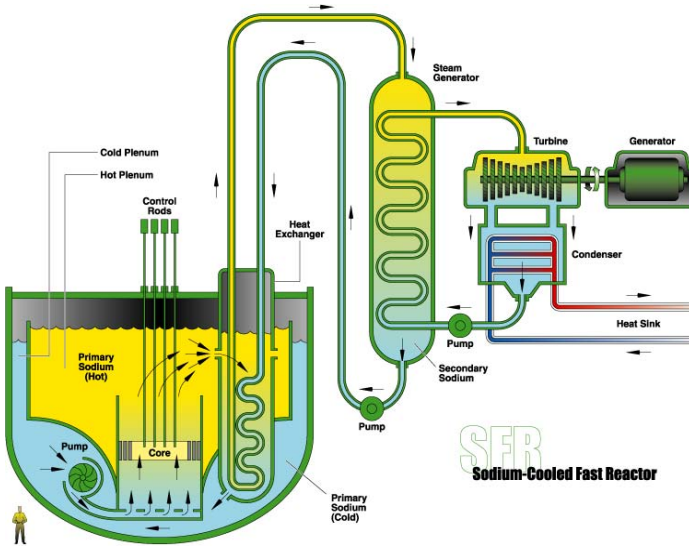

Figure 1.1 Sketch of SFR design [1]

CHAPTER 2. SIMULATION DESCRIPTION

The tools available today for simulating reactor core depletion were developed in the 1980's and have remained the standard tools utilized by the Department of Energy and Industry. There are a wide variety of tools in existence for virtually every type of analysis needed for a nuclear plant. Most of these tools are currently deterministic due to the high computational requirements of the alternative Monte Carlo codes. This paper will focus on investigating the applicability of using Monte Carlo for the depletion and design of a sodium-cooled fast reactor system.

2.1. Code Suite Description

The code suite used to perform the burnup simulations is: MCNP v5.0, ORIGEN v2.2 and *Monteburns* v1.0. MCNP (Monte Carlo N Particle code) is a Monte Carlo neutron transport code developed and maintained by the Los Alamos National Laboratory (LANL) [5]. ORIGEN is a radioactive decay and burnup code developed by the Oak Ridge National Laboratory [6]. Lastly, *Monteburns* is a fully automated tool, developed by LANL, to link MCNP to ORIGEN2[7].

MCNP is primarily used to calculate one-group cross-sections, fluxes, criticality and neutron economy for use during burnup. ORIGEN2 uses these cross-sections and fluxes to perform burnup calculations and returns the resulting material isotopic concentrations, for updating of the MCNP deck.

Monteburns was developed to address the issue of coupling Monte Carlo based transport calculations to a radioactive decay and depletion package. The program consists of perl scripts and a FORTRAN executable. It processes both input and output from MCNP and ORIGEN2 successively as the code executes. It transfers one-group cross-section and flux values from MCNP to ORIGEN2 for depletion

calculations, and then transfers the new material compositions from ORIGEN2 back to MCNP. The code works in a cyclic fashion, repeating until the desired burnup time is reached (usually days to months). It should be noted that the interaction between all three codes is file-based. I.E. no data exchange takes place in memory, which limits the types of calculations that can be performed. If the input or output decks format changes for either MCNP or ORIGEN2, the code system breaks. Hence, limits are placed on the versions of each code available for use. For this reason, MCNP v5.0 is incompatible with *Monteburns Version 2.0*. However, since we were interested in performing parallel neutron transport calculations to reduce wall clock time, modifications to the *Monteburns* scripts and executables were made to make it compatible with MCNP v5.0.

Full documentation of each of the code packages is beyond the scope of this document, but can be found in the manuals. For completeness, a general description of the code flow is provided instead.

The primary interaction between MCNP and ORIGEN2, facilitated by *Monteburns*, is through the modification of input files. MCNP is first run using a starting material composition. *Monteburns* then reads the MCNP output cross-sections and fluxes and writes an input deck for ORIGEN2. ORIGEN2 is next executed to deplete and decay the material compositions. This output is then used to update the MCNP input deck with new material isotopes and densities. This cycle is repeated for a user specified number of steps called the outer burn steps. The outer burn steps equate to the number of times the ORIGEN2 cross-section data is updated from MCNP and can affect the solution accuracy if the material and neutron flux are varying quickly relative to a time step. As a means of increasing accuracy, *Monteburns* incorporates a predictor-corrector strategy in which ORIGEN2 is first run half way through its burn step. MCNP is then used to calculate the one-group cross-sections at this point. Assuming the isotopics have not changed much over the course of the burn step, ORIGEN2 is then executed using the new one-group cross-sections. This process is illustrated in Figure 2.1. It should be noted that

although *Monteburns* facilitates multiple modifications of cross-sections, it does not perform temperature dependent calculations of the cross-sections. Instead, cross-sections must be pre-generated at a given temperature using a code such as NJOY [8].

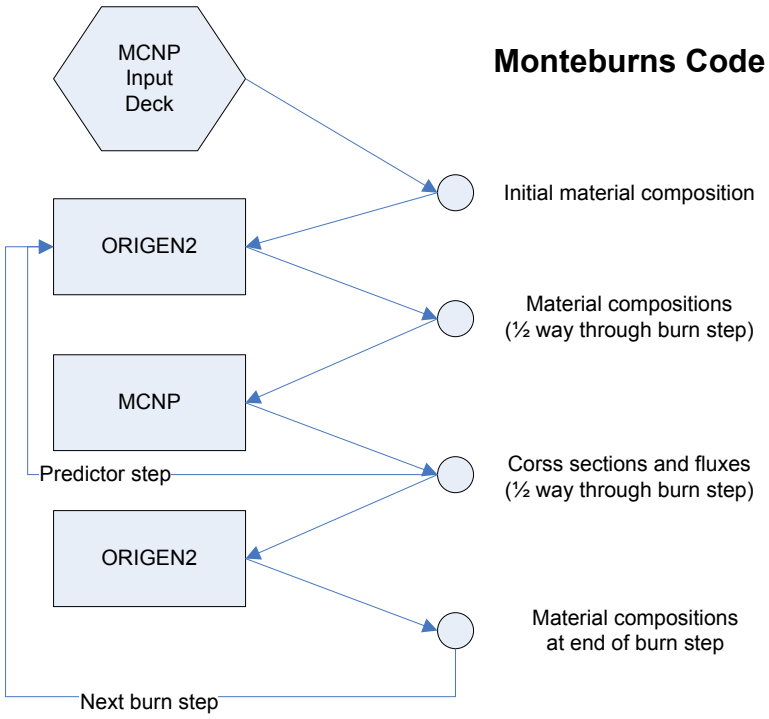

Figure 2.1 Program Structure of Monteburns Code

2.2. Limitations of Monteburns

Monteburns has a number of limitations imposed upon it due to the coupling of Origen2 and MCNP5. For one, *Monteburns* was does not take advantage of modern code practices or hardware. The interface mechanism is a serial file interchange, which leads to performance bottlenecks when writing and transferring these files on any modern high performance computer. Second, the use of MCNP5 sets hard limits on the number of cells that can be defined and the number of materials that can be burned in any given simulation. This sets a hard limit on the number of different depletion regions in a calculation to 40. This is due to the

fact that MCNP5 enforces a limit of 99 same type tallies in a problem. *Monteburns* uses two MCNP5 F4 flux tallies per material to be burned. Further inefficiencies in coding lower the number of materials that can be burned to 40. This means that a user may not be able to exactly specify the problem that he or she desires. It is these limitations, and others, have led multiple DOE labs to begin developing their own burnup codes (Shiva at LLNL, CINDER90 at LANL, ORIGEN-S at ORNL and MCB at CEA [9, 10]). For the purposes of this study though, *Monteburns* is sufficient in providing the necessary accuracy across the material regions of interest.

2.3. Model Description

2.3.1. Compact Core

The reactor core model is of a 840MWt compact core SFR as shown in Figure 2.2. It is 2.76m in diameter, with a 1.86m diameter fuel region [2]. The core is modeled using a symmetric configuration containing 14 full and 12 half for an effective total of 20 fuel assemblies as shown. Each fuel assembly contains 271 fuel pins composed of 25% Zircaloy and 75% Uranium. Fuel pins are 0.295cm in radius with a 0.06cm cladding thickness. They are either low enriched (46% TRU + 54% U) or highly enriched (58% TRU + 42% U). Further information on the core design chosen can be found in the references [11].

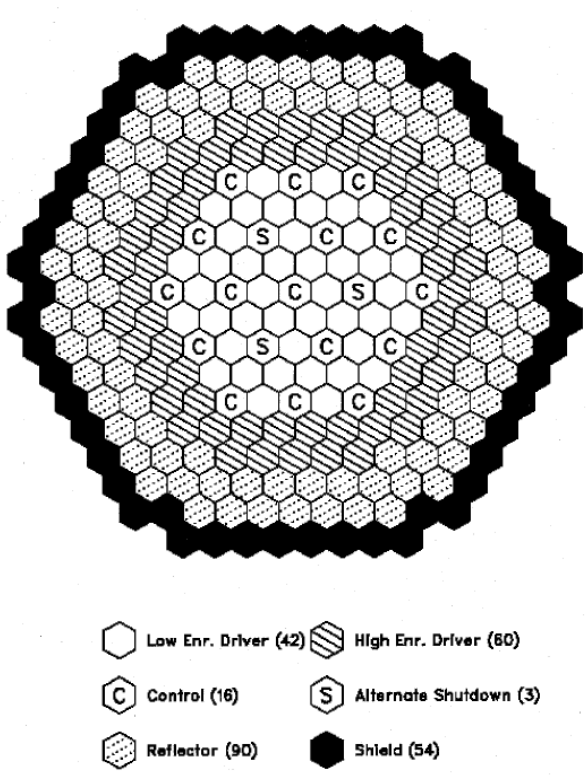

Figure 2.2 - Compact Core Configuration for SFR [ANL-AFCI-084]

2.3.2. MCNP Model

As discussed earlier, MCNP requires a working input deck to execute properly within the *Monteburns* code system. The input deck for the core design used can be seen in Appendix B. We begin with a 1/6 symmetric core model using 20 explicitly defined fuel assemblies instead of modeling the whole core at once. This is done to reduce the computational time required to determine the one-group cross-sections, fluxes and criticality eigenvalue for the core at each burn step. A picture of the core can be seen in

Figure 2.7. The fuel pins and cladding, as well as absorber and reflector pins in the control and reflector assemblies are explicitly modeled to accurately capture the flux throughout the assembly. It should be noted, however, that after an MCNP

execution the cross-sections associated with the fuel assembly are collapsed down to a single one-group cross-section for use in ORIGEN2. This is a limitation imposed by the use of ORIGEN2, but is acceptable for this study because we are interested in isolating burnup specific parameters without adding the complexity of dealing with variable cross-sections during depletion and decay.

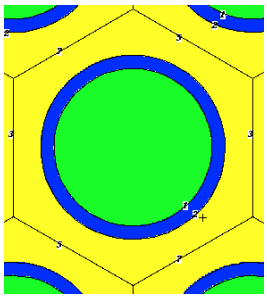

Figure 2.3 Low Enriched Fuel Pin

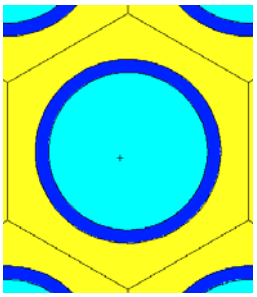

Figure 2.4 Highly Enriched Fuel Pin

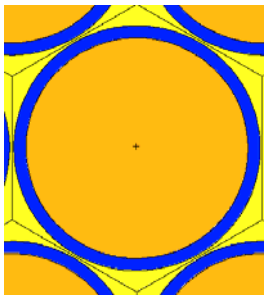

Figure 2.5 Control Rod Pin

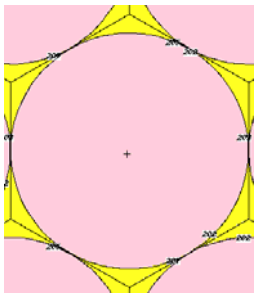

Figure 2.6 Reflector Pin

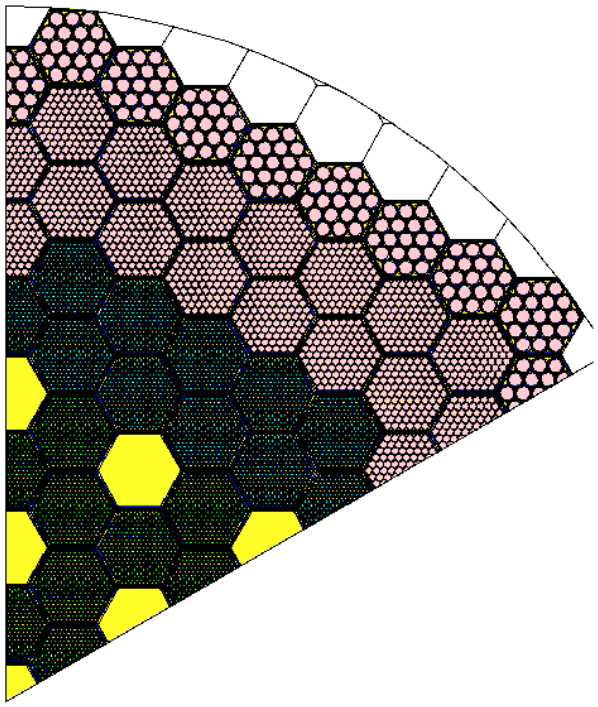

Figure 2.7 1/6 symmetric MCNP model of Compact Core

During a neutron transport step, the neutrons are sourced into the problem using the MCNP kcode source. For most runs, 15,000 to 20,000 particle histories per cycle are used. Early results showed that this number of histories is sufficient to accurately model the neutron flux. Later runs were done with 150,000 to 200,000 histories per cycle to reduce the statistical uncertainty in the eigenvalue calculation. For each cycle, the neutron distribution is converged upon and a criticality eigenvalue (k_{eff}) is found. A total of 200 cycles, skipping the first 50, are used to ensure full convergence of the solution. Further details on how MCNP calculates the k_{eff} and converges on the neutron distribution can be found in the MCNP manual.

The control rods, reflector and shielding assembly are explicitly modeled. The material compositions for non-fuel materials are taken from past experience with the proposed ABTR design. For completeness, the individual pin design for the fuel, absorber and reflector pins are shown in Figure 2.3 through Figure 2.6. The two fuel pin types are essentially the same geometry with different materials. The absorber pins differ from the reflector pins with a cladding material [11].

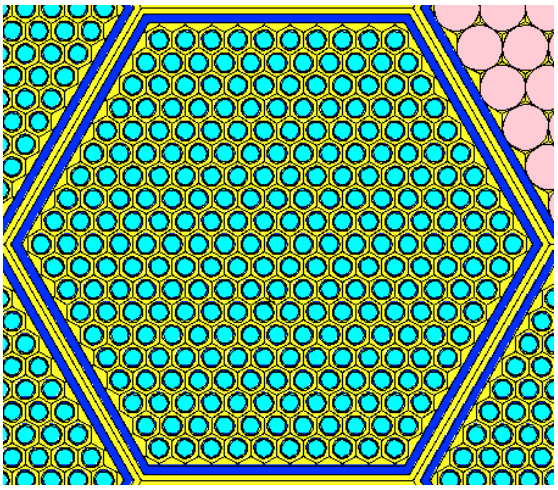

Figure 2.8 MCNP Highly Enriched Fuel Assembly

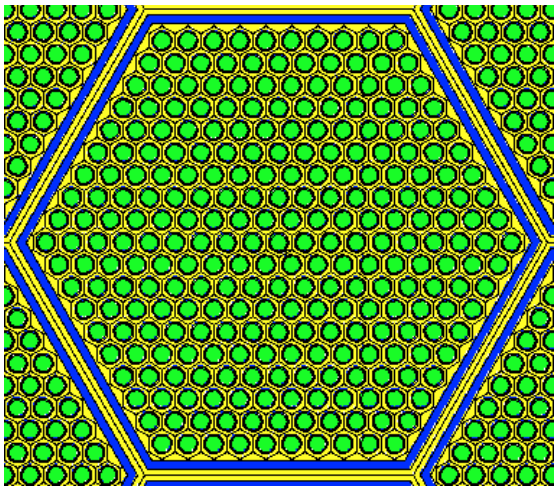

Figure 2.9 Low enriched Fuel Assembly

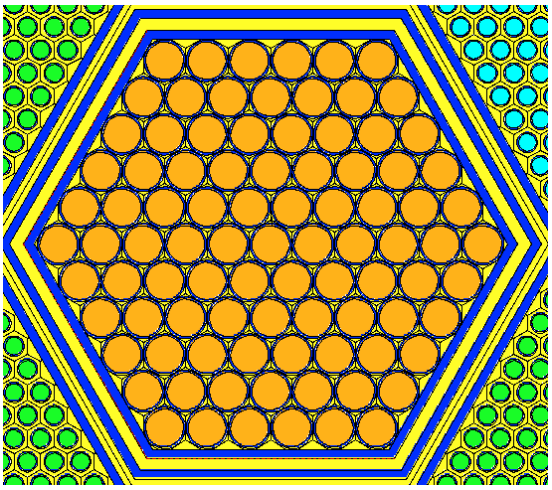

Figure 2.10 MCNP Control Rod Assembly

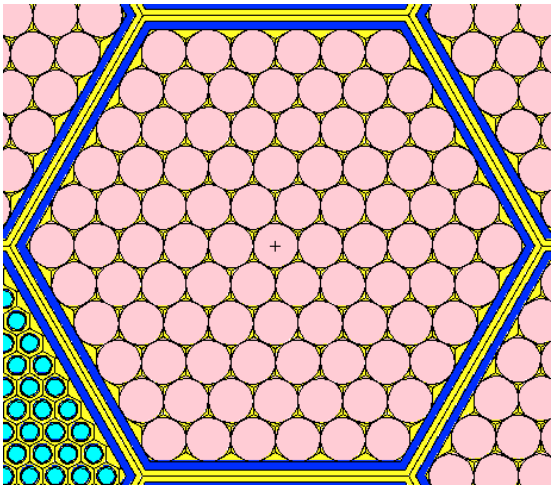

Figure 2.11 Reflector Assembly

2.3.3. Monteburns Model

The *Monteburns* model utilizes the aforementioned MCNP model with additional input parameters such as core power and burn time required for the ORIGEN2 burnup calculation. The model be found in Appendix A. The core power is modeled as 140MW (840 MW * 1/6 core) for a total of 155.1 days (180 day cycle at a capacity factor of 85%). This burnup time is sufficient to simulate a typical fuel cycle within a reactor. A total of six outer burn steps are used over the 155.1 days, which results in a time step of 25 days and 20.4 hours. Choosing the number of outer burn steps involves a balance between solution accuracy and computational time. For each additional burn step, MCNP and ORIGEN2 are executed twice. As will be show later, six outer burn steps is more than sufficient to accurately model the system. The number of internal burn steps (ORIGEN2 internal time steps) used is 40 per outer burn step. Again, more steps equates to more accuracy in the ORIGEN2 calculation. 40 internal steps is the default used by *Monteburns* and gives approximately 15 hours between internal steps and is more than sufficient to capture the isotopic variations over the given outer burn time step. Correspondingly, the neutron flux is not updated during the inner burn step. This forces the user to choose the number of outer burn steps so that this approximation will not adversely affect the neutronic solution.

Given the model description and assumptions, the focus of this work is to study how varying key parameters affect the simulation, then how these methods can be applied to the design and analysis of a new fuel type for this reactor.

2.4. Parametric Study

This section focuses on the study of certain parameters associated with the simulation models. The parameters studied were the control rod insertion depth, the number of outer burnup steps and the refinement of the axial and radial burnup mesh.

Each study is independent of each other as to isolate the effects of the individual parameters on the simulation results. I.E. control rods were inserted at various depths without changing the number of outer burn steps or mesh refinement. Then, using a subset of control rod insertion depths, the number of outer burn steps was varied to ascertain this effect. Lastly, the mesh was refined using 5 outer burn steps and control rod insertion depths of: no insertion, inserted halfway, inserted to maintain criticality above 1.0 and fully inserted.

2.4.1. Control Rod Insertion Depth

As part of this study, we are interested in determining what control rod insertion depth will result in an exactly critical reactor core. As stated earlier, the control rods act as neutron absorbers to reduce core criticality. The control rods were varied from fully removed, to ½ way inserted, to fully inserted. Figure 2.12 shows the results on criticality of the reactor core. It can be seen from the figure that the core configuration is such that even with the control rods fully inserted, the reactor is always above critical. This is because the initial core configuration considered is made up entirely of fresh fuel. This is not representative of actual operating conditions. An eigenvalue greater than 1 is of no importance for the purpose of the parametric study because the objective of the study is to determine how sensitive the burnup distribution is to control rod insertion, not what the actual operating conditions of a fresh core will be.

For the purposes of the control rod insertion depth study, the Monteburns model was depleted for the full cycle length at each of four different control rod heights. K-effective was determined and plotted at each burn step for each of the four control rod heights as shown in Figure 2.12. It appears that from Figure 2.12 each of the keff plots has approximately the same slope. It is however inconclusive so instead a plot of the change in k-effective vs time is made as seen in Figure 2.13.

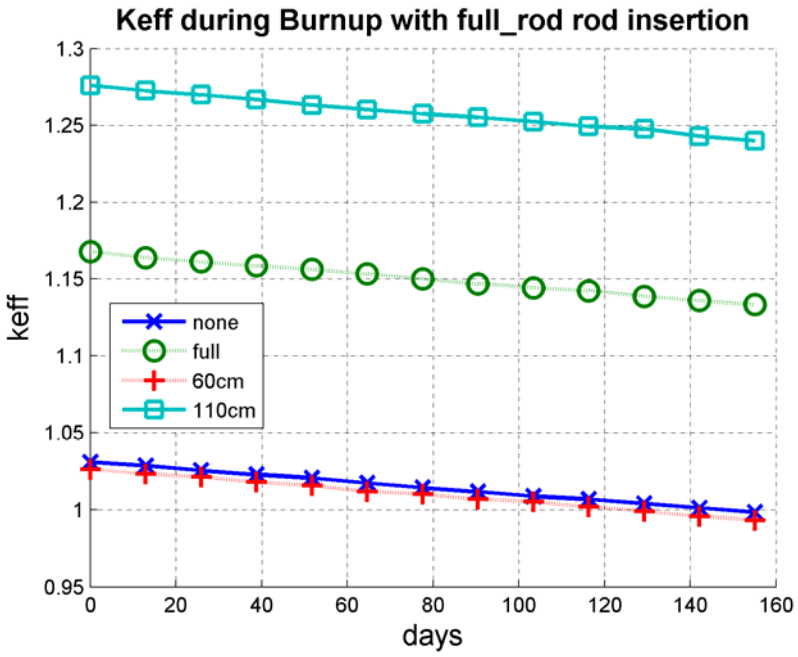

Figure 2.12 Keff for different control rod insertion depths

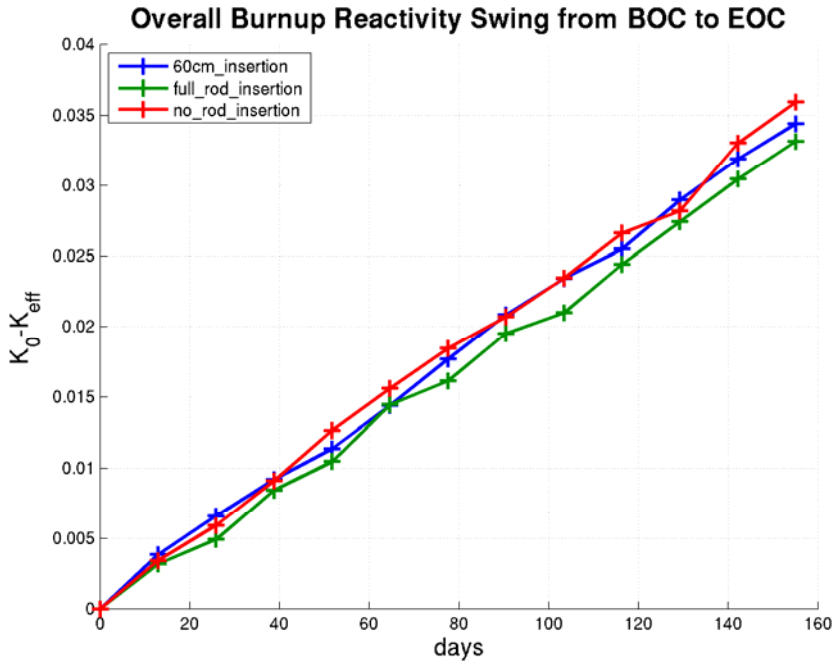

Figure 2.13 dK for various control insertion depth

Another way to investigate the control rod behavior, besides change in k_{eff}, to determine the effect of a parameter change is burnup reactivity swing. It is the change in reactivity of the system divided by the initial k_{eff} as shown in Equation 2-1. It is usually quoted in percent change per million (pcm) which requires multiplying the percentage by 10^5.

$$\frac{\Delta k}{k} = \frac{k_0 - k_{eff}}{k_0}(10^5\, pcm)$$

Equation 2-1

The burnup reactivity swing associated with three control rod configurations is shown in Figure 2.14. The resulting burnup reactivity from the beginning of cycle (BOC) to end of cycle (EOC) changes by approximately 400 pcm between the fully rodded and unrodded cases. This effect is exaggerated by the very different initial k_0's for each of the control rod heights as can be seen above in Figure 2.12. It is thus more practical to look at only k_0-k_{eff} when investigating this effect. From Figure 2.13 above it becomes more apparent that the change in eigenvalue for full insertion and no insertion becomes approximately 200 pcm. Thus for a core where the control rods must be inserted a significant amount, the control rod pattern during depletion must be considered. For this core, future calculations will show that even at BOC for an equilibrium core, the control rod is never inserted more than 40 cm. Thus the effect of the control rod insertion for this core is less than 100 pcm and can be assumed to be inconsequential. Next, we examine the number of outer burn steps used during the calculation.

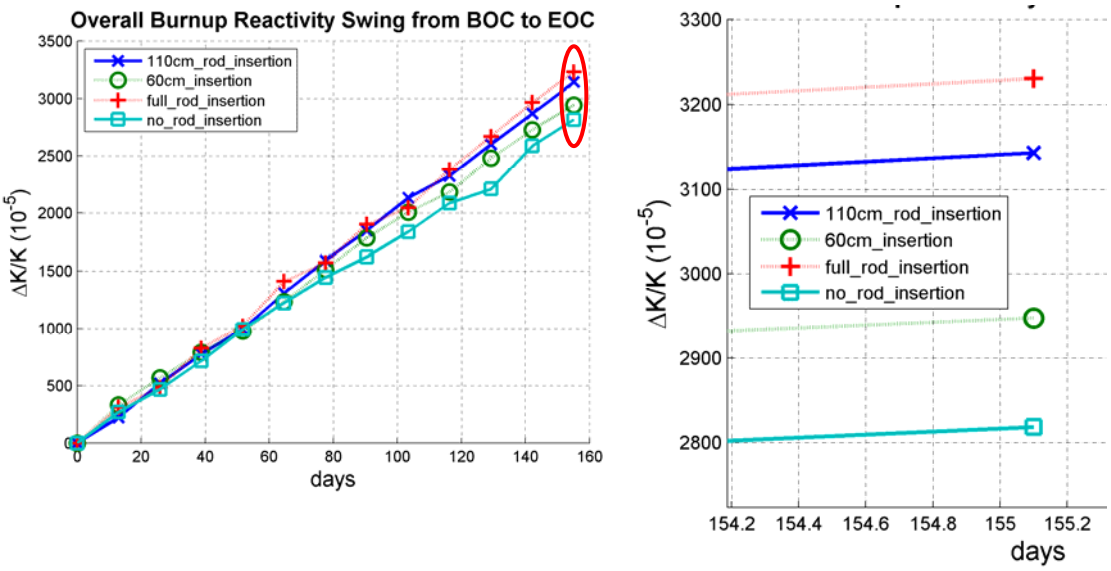

Figure 2.14 - Burnup Reactivity for 3 Control Rod Configurations

2.4.2. Outter Burn Step Size

The number of outer burn steps used in *Monteburns* directly controls the number of times a neutron transport calculation is performed. This in turn controls the number of times that the fluxes and collapsed cross-sections are updated and used in ORIGEN2. It is necessary to know the effect of reducing the number of steps. To do this, the number of outer burn steps was varied from 1 to 6 for 3 separate control rod configurations (rods fully removed, ½ way inserted and fully inserted). Figure 2.15 shows the reactivity swing associated with varying the number of outer burn steps. The reactivity swing for the fully inserted case envelops all others and ranges by approximately 80 pcm. This equates to about 2.5% of the overall burnup reactivity swing from BOC to EOC.

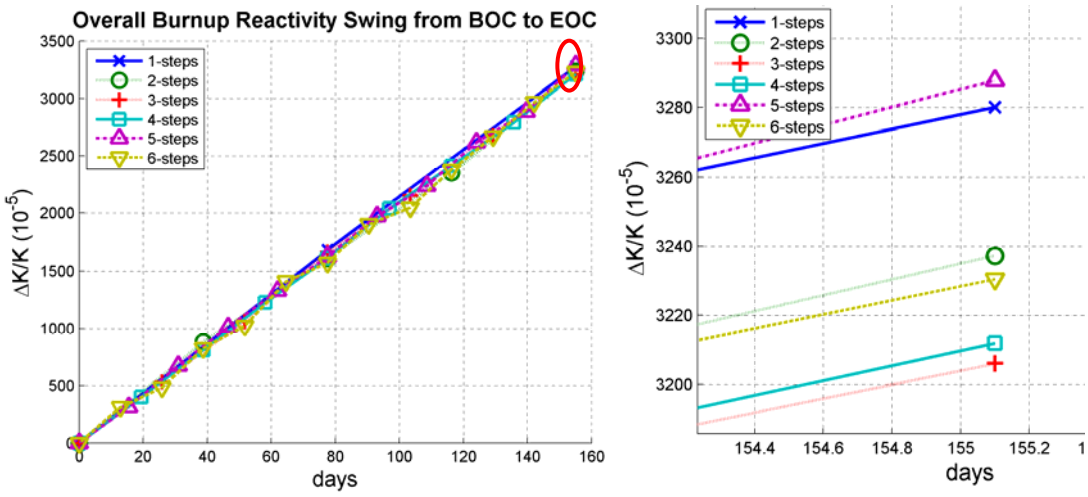

Figure 2.15 - Burnup Reactivity Swing for various numbers of outer burn steps

Since the burnup reactivity swing is a percentage in parts per million, we can compare this value with the overall uncertainties in k_{eff}. Table 2.1 shows the associated uncertainties with the k_{eff} calculated by MCNP. They are all on the order of 3.0-4.0 x 10^{-4} and when computing the root sum squared error associated with this variability in k_{eff}, one can quickly deduce that the 80 pcm difference in burnup reactivity swing between each of the 6 cases is due to the statistical uncertainties in k_{eff}. We can thus conclude that the number of outer burn steps for each cycle of this simulation does not have a noticeable effect on either material compositions or eigenvalue for this type of reactor. This is most evident from the observation that using only 1 outer burn step is statistically equivalent to using 5 outer burn steps. Even though it is shown to not have a large effect, the 6 outer burn step case is assumed to be the most physical, and is thus used for all of other parametric calculations in this section.

Table 2.1 - Comparison of Keff and Burnup Reactivity Swing

Control Rods Configuration									
	No insertion			*60cm insertion*			*Fully inserted*		
Number of Outer Burnup Steps	*Final Keff*	*Error*	*Burnup Reactivity Swing*	*Final Keff*	*Error*	*Burnup Reactivity Swing*	*Final Keff*	*Error*	*Burnup Reactivity Swing*
1	1.24060	3.40E-04	2776	1.13330	3.80E-04	2945	0.99253	3.10E-04	3280
2	1.24015	3.20E-04	2809	1.13329	3.20E-04	2945	0.99297	3.30E-04	3237
3	1.24056	3.70E-04	2777	1.13320	3.00E-04	2953	0.99329	3.30E-04	3206
4	1.24072	3.20E-04	2764	1.13279	3.40E-04	2988	0.99323	3.00E-04	3211
5	1.24017	3.50E-04	2807	1.13363	3.30E-04	2916	0.99245	2.80E-04	3287
6	1.24004	3.90E-04	2818	1.13328	3.40E-04	2946	0.99304	2.90E-04	3230
Relative Difference	**0.05%**	**17.95%**	**1.92%**	**0.07%**	**21.05%**	**2.41%**	**0.08%**	**15.15%**	**2.46%**

2.4.3. Radial and Axial Mesh Size

When investigating a model's validity, the refinement of the mesh immediately comes to mind as a parameter of potentially significant importance. In the previous simulations, it was assumed that the neutron flux would be flat across the reactor geometry out to the reflector assemblies. This assumption allowed the analysis to be simplified by using only two material regions during the burnup sequence. These regions consisted of only 1 zone axially throughout the whole core and two radial fuel regions. The two regions were defined out of necessity, due to the different initial isotopics caused by the reactor design's use of a low enriched fuel and high enriched fuel region. This assumption could result in very inaccurate burnup results if the flux profile is not uniform in both the axial and radial directions throughout the burnup regions. Normalized flux plots in both the radial and axial directions were created with the stand alone MCNP model to test the validity of the 2 zone approximation. These flux plots can be seen in Figure 2.16 and Figure 2.17. It can be seen that the flux is not flat as is assumed in the 2 depletion region model. Thus a refined depletion zone model must be created and the effect analyzed to determine the importance.

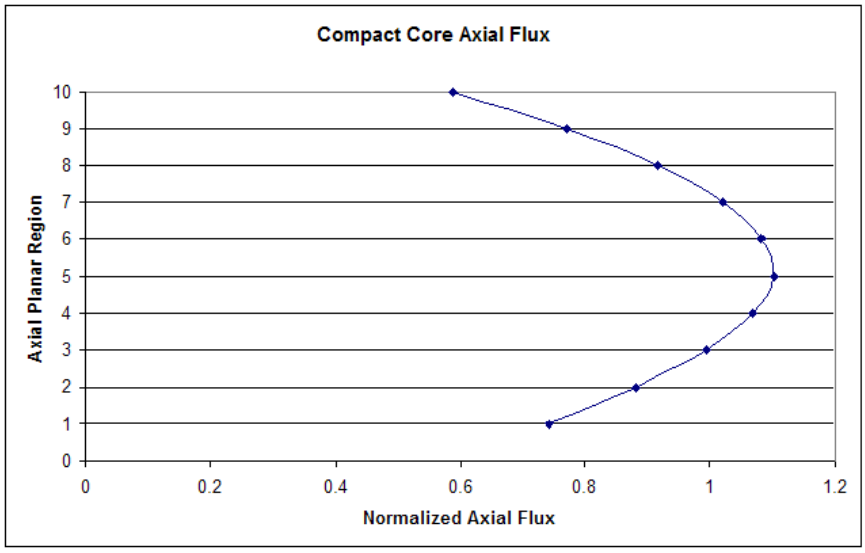

Figure 2.16 Axial Flux Profile

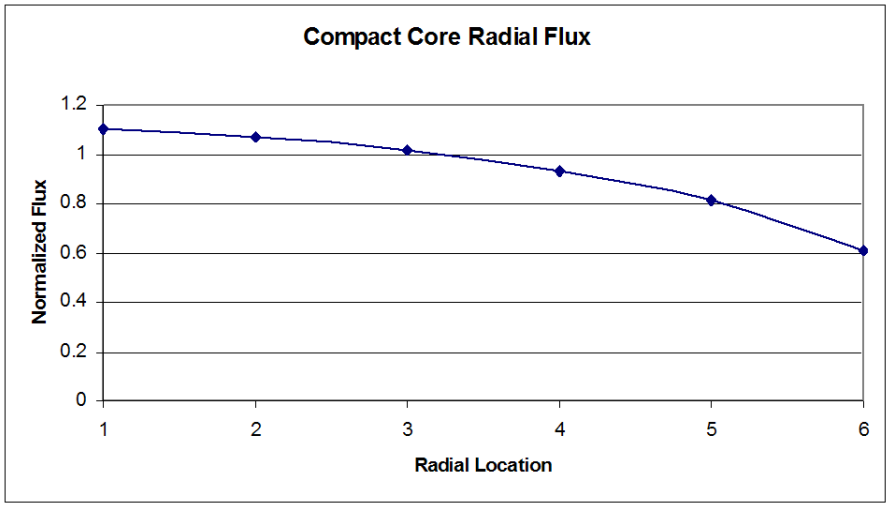

Figure 2.17 Normalized Radial Flux Profile\

It could be argued that the variation in the radial flux profile is low enough to justify the use of only two burnup zones. This reduces the computational time for *Monteburns*. On the other hand, one depletion zone in the axial direction is obviously insufficient. It is clear that the flux profile varies significantly in the axial

direction. The variation in flux will result in different material depletion throughout each outer burn step.

To check determine the impact this uneven flux distribution has on the depletion characteristics of the core, the *Monteburns* model was refined to burnup the fuel assemblies in 5 axial zones and 5 radial zones. Figure 2.18, Figure 2.19, and Figure 2.20 show this refined zoning relative to the original 2 radial, 1axial zone scheme. The red circles on each figure encompass a representative fuel assembly showing a separate material. In the case of two radial zones, the low enriched fuel zone is a different color than the highly enriched fuel zone. For the 5 radial zone case, there are still only two fuel types, but they are defined as different materials so *Monteburns* can burn them separately, preserving the spatial flux history. This zoning scheme is more complex, but the primary basis of comparison, k_{eff} and $\Delta k/k$, remain the same. The increased axial zoning is also show as different colors down the length of the core. Each of the three red circles in Figure 2.20 shows 5 different material zones contained within it. The refined model now has 25 material burnup zones.

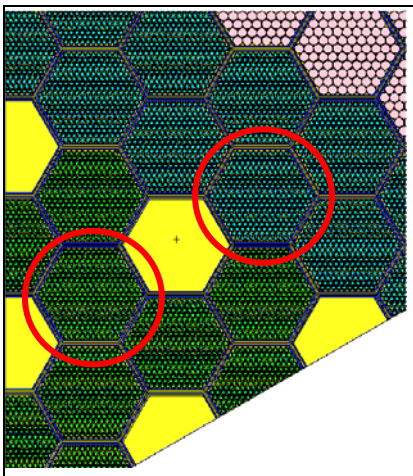

Figure 2.18 - Radial Zoning Scheme (2 Zones)

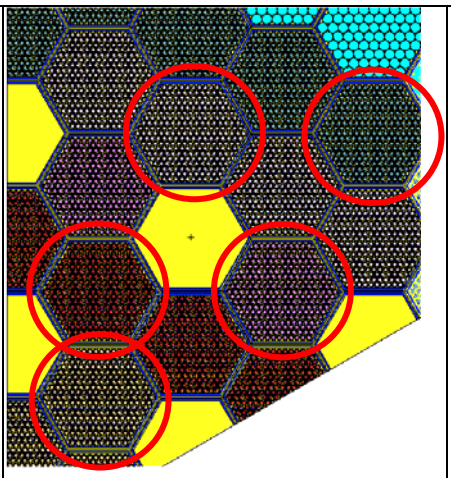

Figure 2.19 - 5 Radial Zone Mes

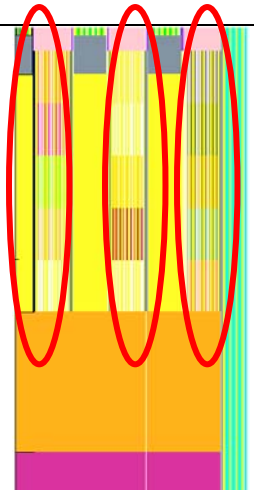

Figure 2.20 - 5 Zone in Axial Direction

With this new refined model, the final set of parametric calculations performed prior to equilibrium depletion is essentially a repeat of the control rod insertion study and time step study for the refined mesh. We then compare the results to that of the 2 radial/1 axial zone calculations.

The control rod configurations are the same as previously explored: no insertion, 60 cm insertion, 110 cm insertion, and full insertion. The end result is that by increasing the radial and axial zones for burnup, the final k_{eff} changes by a max of 0.08%. Examining the burnup reactivity swing associated with the new zoning scheme, shown in Figure 2.21, we can see that the new zoning does make a significant difference relative to the 2 radial, 1 axial zones. The burnup reactivity is now around 3400-3500 pcm, up from 2800 pcm using the simplified zoning scheme. Like in the 2 depletion zone model, we again see a significant difference in reactivity swing between the full and no rod insertion cases. Again this is insignificant because the maximum actual rod insertion during operation will be less than 60cm inserted. At this point, a further refinement of the axial zones is

warranted, but is left as future work due to the need to modify the *Monteburns* and MCNP5 code structure to allow for more depletion regions.

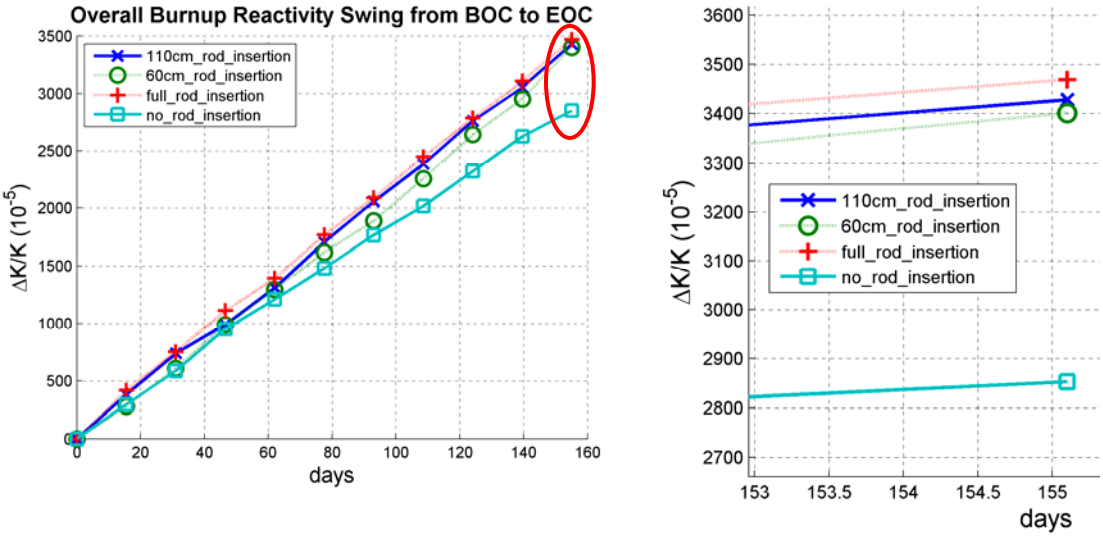

Figure 2.21 - Burnup Reactivity Swing for refined zoning

Examining the number of outer burn steps again, Figure 2.22, shows that the variations in reactivity swing are minimal (~80 pcm). This result was expected because the materials being burned in the ORIGEN2 calculation appear to be depleting in a linear fashion. The linearity of isotopic depletion, coupled with a predictor-corrector scheme, results in a fairly accurate solution no matter how long the time steps are for this reactor design. Each simulation is different though and it is better to resolve the material burnup in time to avoid extrapolation errors associated with non-linearities.

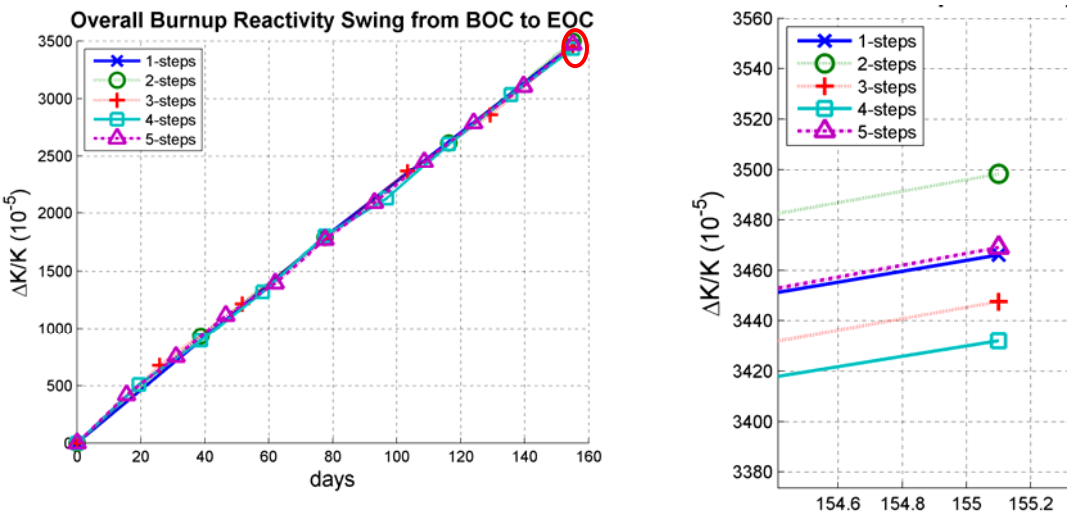

Figure 2.22 – Burnup Reactivity Swing for multiple time steps

Results for three control rod configurations and multiple burn steps are given in Table 2.2. Comparing to Table 2.1, we see a decrease in the variablilty of final k_{eff} for each time step size, but an increase in variability of the burnup reactivity swing for the unrodded and 60cm insertion depths. These changes could be attributed to the better resolution, implying that we are better capturing the flux profile and corresponding material burnup along the axis.

Table 2.2 Burnup Results from Refined Mesh

Control Rods Configuration									
	No insertion			*60cm insertion*			*Fully inserted*		
Number of Outer Burnup Steps	*Final Keff*	*Error*	*Burnup Reactivity Swing*	*Final Keff*	*Error*	*Burnup Reactivity Swing*	*Final Keff*	*Error*	*Burnup Reactivity Swing*
1	1.23864	3.40E-04	2916	1.12773	3.40E-04	3298	0.99120	2.90E-04	3466
2	1.23835	3.80E-04	2938	1.12710	3.20E-04	3352	0.99090	3.20E-04	3498
3	1.23837	3.50E-04	2937	1.12722	3.30E-04	3342	0.99139	3.00E-04	3448
4	1.23844	3.70E-04	2931	1.12758	2.90E-04	3311	0.99155	3.30E-04	3432
5	1.23944	3.40E-04	2853	1.12653	3.50E-04	3401	0.99117	3.10E-04	3469
6	na	na	na	na	na	na	na	na	na
Relative Difference	**0.09%**	**10.53%**	**2.91%**	**0.11%**	**17.14%**	**3.03%**	**0.07%**	**12.12%**	**1.89%**

2.5. Equilibrium Core Calculations

Up until now, all calculations had been done assuming a fresh fuel core loading. Once operational, this reactor will utilize a seven batch reloading scheme. The isotopics within the fuel will change drastically between the time the reactor first goes into operation with its fresh fuel loading, and the time it reaches an equilibrium core state. An equilibrium core state is one in which the beginning of cycle isotopics are equal to those of the previous cycle's.

In order to reach this equilibrium state, the core is depleted in *Monteburn* for a number of operating cycles, removing old fuel and adding new fuel at the end of each cycle. One significant approximation had to be made because an exact shuffling pattern for the core is not known. Instead of shuffling assemblies, removing a burned assembly and adding a new one, each burnup region had $1/7^{th}$ of its depleted fuel mass removed and $1/7^{th}$ of the total fresh fuel mass was added at the end of each burnup cycle. This was deemed a reasonable approximation because the flux in the radial direction is relatively flat, decreasing the need for explicit assembly shuffling.

Another simplification to the model which was necessary to make was the placement of the control rod during these calculations. As was seen above in

Figure 2.21, the depth of control rod insertion has a significant effect on the reactivity swing during burnup when the rod is varied between fully inserted, half inserted, and fully withdrawn. However, once this core reaches equilibrium, the control rods will never need to be inserted to the halfway point. For this reason it was assumed to be a reasonable approximation to reach an equilibrium core with the rod fully withdrawn. Further studies could find the critical rod position of this equilibrium core and repeat these calculations to find a new equilibrium state, however the effect of doing so is predicted to be negligible due to the results seen in Figure 2.21.

Finally, the equilibrium states of both the 2 depletion region and 25 depletion region models previously described were analyzed to determine the long term effects of the refined depletion zone modeling. The results can be seen below in Figure 2.23 and Figure 2.24. It can be seen that there is a noticeable difference between the 2 region and 25 region eigenvalues. The exact change for the final equilibrium core is highlighted in Table 2.3. It can be seen that there is a slightly higher reactivity swing between the two different models, approximately 100 pcm. It is also noted that the eigenvalue of the 25 depletion zone case is consistently lower than that of the 2 zone case. These effects can be attributed to the axial and radial discretization having a higher burnup in the more important center region of the core.

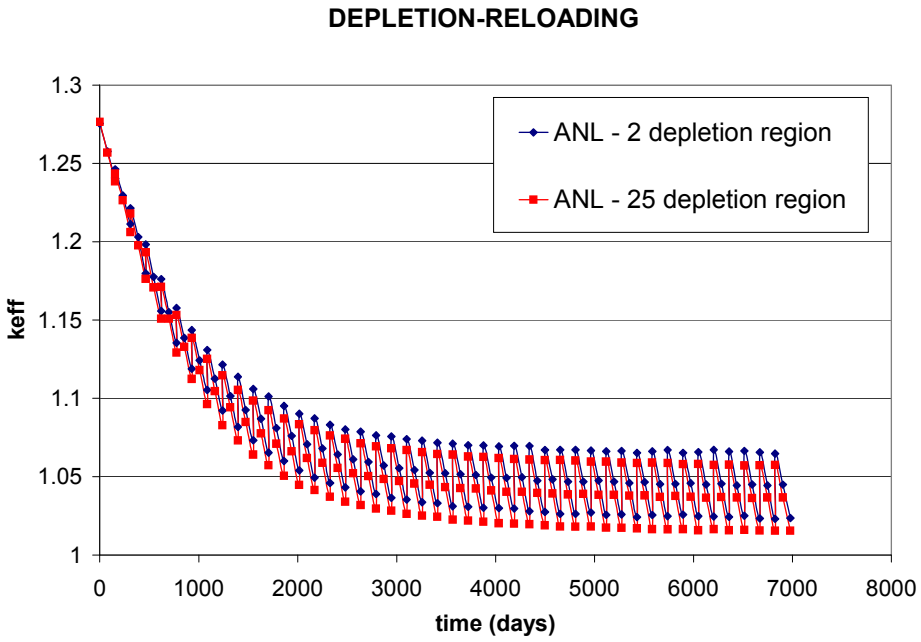

Figure 2.23: Keff vs Time for Equilibrium Core Calculation

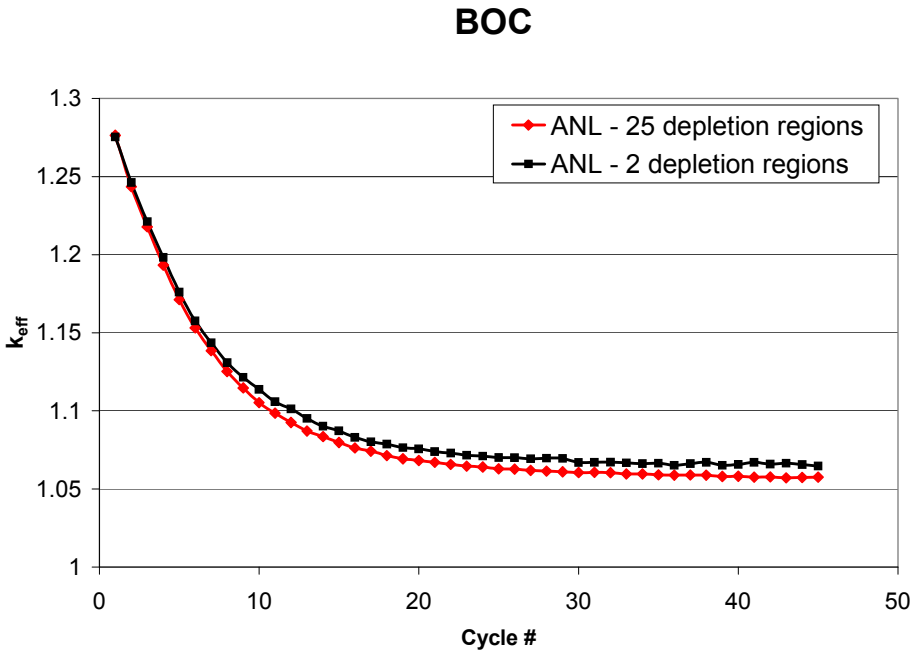

Figure 2.24 - BOC Eigenvalue for Equilibrium Calculation

Table 2.3 - Final Eigenvalue for Equilibrium Core

	2-zone	**25-zone**	**Δk (pcm)**
BOC	1.06469	1.05762	707
MOC	1.04495	1.03668	827
EOC	1.02366	1.01563	803

2.6. Method Verification

With the completion of the sensitivity study and equilibrium core composition search, it is now necessary to compare the results of the methods outlined above. To do this, various characteristics of the core depicted by the MCNP model are compared to those from reference material found in Ref 3. The parameters compared include various core loading masses, rate at which TRU is consumed, and many reactivity coefficients.

2.6.1. Core Mass

The first basis for verification of the final equilibrium core model is the composition of the core. The specific values used for comparison are total mass of heavy metal and TRU. The value for comparison in the reference is for the total core mass, so to make for a consistant comparison the mass of each depletion region outputted by Monteburns is summed up, and then multiplied by six to turn the one-sixth fuel mass into full core fuel mass. The comparison of these values is found in

Table 2.4. What we find is there is about a 10% difference in both the heavy metal and the TRU loadings between the Monteburns model and the reference. At first glance this difference may seem significant. However, it is important to note that Monteburns does not track uncertainties in isotopics. The uncertainty in depletion isotopics is not dependant on the global eigenvalue uncertainty, but rather the local flux uncertainty. Although these values were not tracked by Monteburns during the equilibrium search, a conservative estimate of the uncertainty can be made from the uncertainty of similar calculations. Similar calculations have shown the uncertainty in the local flux solution to be less than 1%. To be conservative, a 1% uncertainty is propagated across all 45 cycles which were performed in the equilibrium search. When this is done we get a conservative estimate for the final core isotopic uncertainty to be ~6.5%. This uncertainty, coupled with other assumptions which were made concerning the axial core geometry, could be significant enough to explain the 10% difference seen in fuel mass loadings between the two models. Further verification and validation in isotopic uncertainty is left as future work.

Table 2.4 - Core Fuel Mass Comparison

	Ref	**MONTEBURN**	**Δ%**
BOC HM Loading (kg)	4571	4202	**8.1**
EOC HM Loading (kg)	4437	4067	**8.3**
Burned Heavy Metal (kg)	134	135	**0.7**
BOC TRU Loading	2250	1992	**11.5**
Net TRU consumption (kg/yr)	193	189.3	**1.9**

2.6.2. Burnup Characteristics

The next value compared between the two cores is TRU consumption rate and mass of heavy metal burned. Here the difference in masses for the isotopes between BOC and EOC for each region are again summed up and multiplied by six to make for a consistent comparison. Again the results can be seen in Table 2.4. What we find is very good agreement between the Monte Carlo method and the reference core: less than 1%. The small difference between the two values adds much needed confidence in the accuracy of the depletion methods.

2.6.3. Delayed Neutron Fraction

The next value which was compared between the reference core and the Monteburns core is the effective delayed neutron fraction. MCNP5 has a feature in which the contribution of delayed neutrons to the eigenvalue problem can be shut off. This gives the eigenvalue due only to prompt neutrons. Subtracting the ratio of prompt eigenvalue to total eigenvalue from 1 can give the fraction of delayed neutrons within the core. It is important to note that this calculation method gives the effective delayed neutron fraction, not the actual physical fraction of delayed neutrons. Delayed neutrons are emitted from parent nuclei at a lower energy, 0.45 MeV on average, than prompt neutrons, 2 MeV on average. For a fast reactor where the majority of fissions happen at an energy above 0.45 MeV, the lower energy of delayed neutrons have less of an impact on eigenvalue than their prompt counterparts. This causes the effective delayed neutron fraction for fast reactors to be slightly smaller than the actual delayed neutron fraction. Calculations performed in MCNP predict an effective delayed neutron fraction of 0.002633 and 0.002567 for BOC and EOC respectively. Indeed these values are slightly lower than the Beta actual reference values of 0.00276 and 0.00277. However, the difference between the reference and Monteburns values are still less than 10% and give confidence in the calculation methods for these values as well as the final core composition.

Table 2.5 - Reactivity Coefficient Comparison

	Ref	MONTEBURN	Δ%
Beta (BOC)	0.00276	0.002633	**4.6**
(EOC)	0.00277	0.002567	**7.3**
Burnup reactivity loss (% dk)	4.261	4.257	**0.01**
Axial expansion coefficient (cents/K)	-0.34	-0.35	**2.9**
Doppler (cents/K) (BOC)	-0.047	-0.067	**42**
Sodium Void Worth($) (BOC)	3.83	3.97	**3.6**
(EOC)	4.85	5.05	**4.1**

2.6.4. Reactivity Feedback Coefficients

Further validation of the Monte Carlo model was accomplished by comparing various reactivity feedback coefficients. These values characterize the response of the core in the event of a transient and as such are of critical importance for safety analysis. It is thus of critical importance that a model be able to accurately predict these values. The reactivity feedback coefficients compared include: sodium void worth, axial and radial expansion feedback coefficients, and doppler. The manner in which each of these values was calculated in MCNP and the comparison of the Monte Carlo values to literature can be found in this section.

Before any of these calculations can be performed for the BOC equilibrium core, the critical rod position must be calculated. Multiple control bank configurations were not considered, instead only the critical banked rod configuration was considered. For BOC the critical rod insertion depth is 25 cm. A plot of eigenvalue vs. rod height is seen in Figure 2.25. Reactivity feedback coefficients can now be computed for BOC.

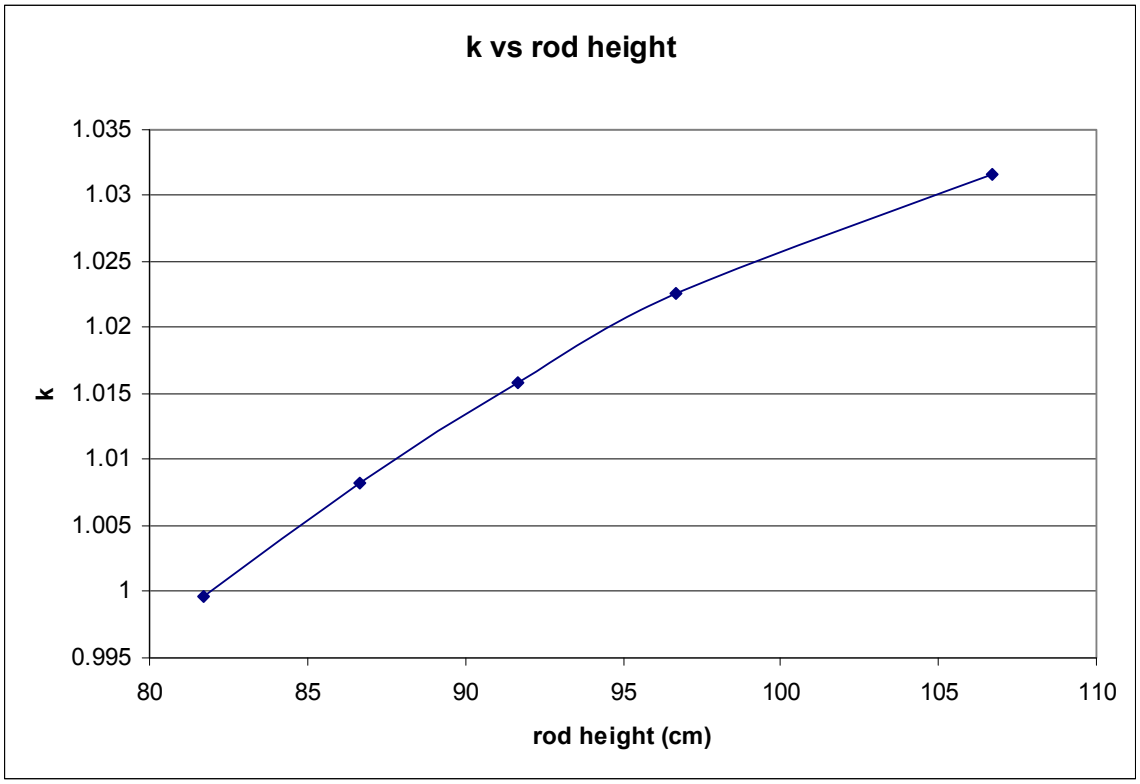

Figure 2.25 - BOC eigenvalue at various rod heights

The first reactivity feedback coefficient compared is the sodium void worth of the core. In order to calculate this value, the density of the sodium coolant was perturbed in the MCNP model. The density was reduced, or voided, 10%, 20%, 30%, 50%, 75%, and 100% and an eigenvalue calculation was run for each case. The eigenvalue for each case was then plotted against its respective void. This procedure was followed for both BOC and EOC and the plots can be seen in Figure 2.26 and Figure 2.27 respectively. When a linear curve is fit to this data, we find nearly all of the values lie within a single standard deviation of the line with R^2 values of 0.9991 and 0.9988 respectively, a very strong relationship. From this linear curve fit we obtain the reactivity feedback per sodium percent void of 0.0001. This value is relatively small, only about 4 cents per percent void, which is considered controllable in all but the most severe accidents.

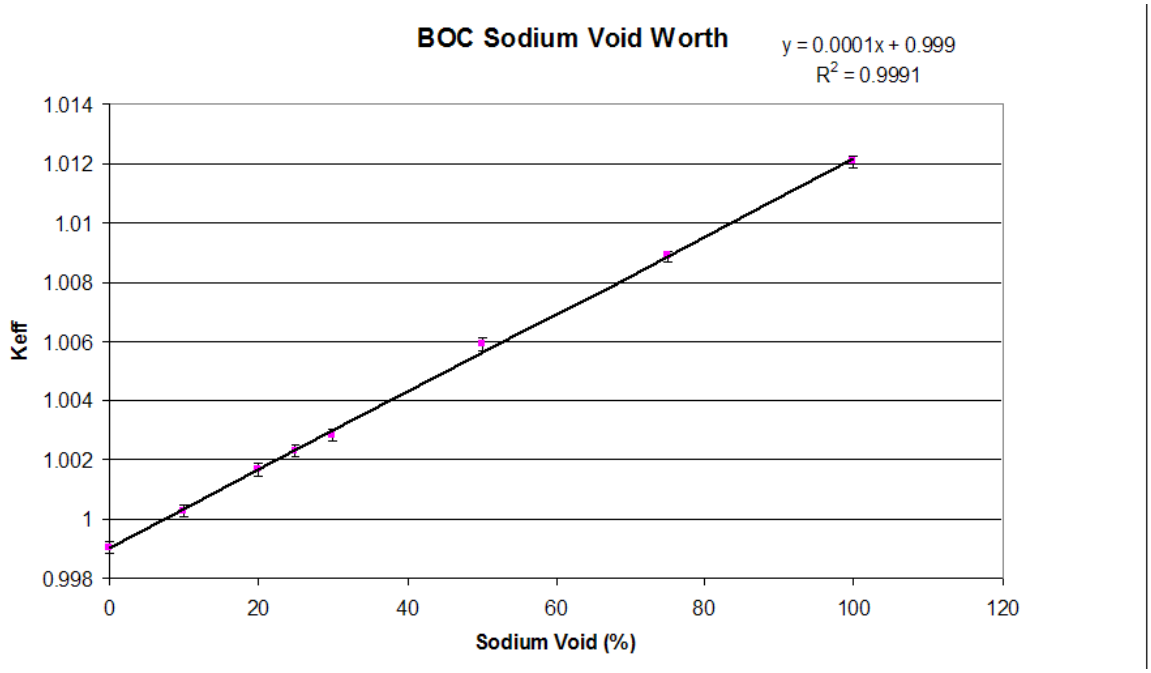

Figure 2.26 - BOC Sodium Void Worth

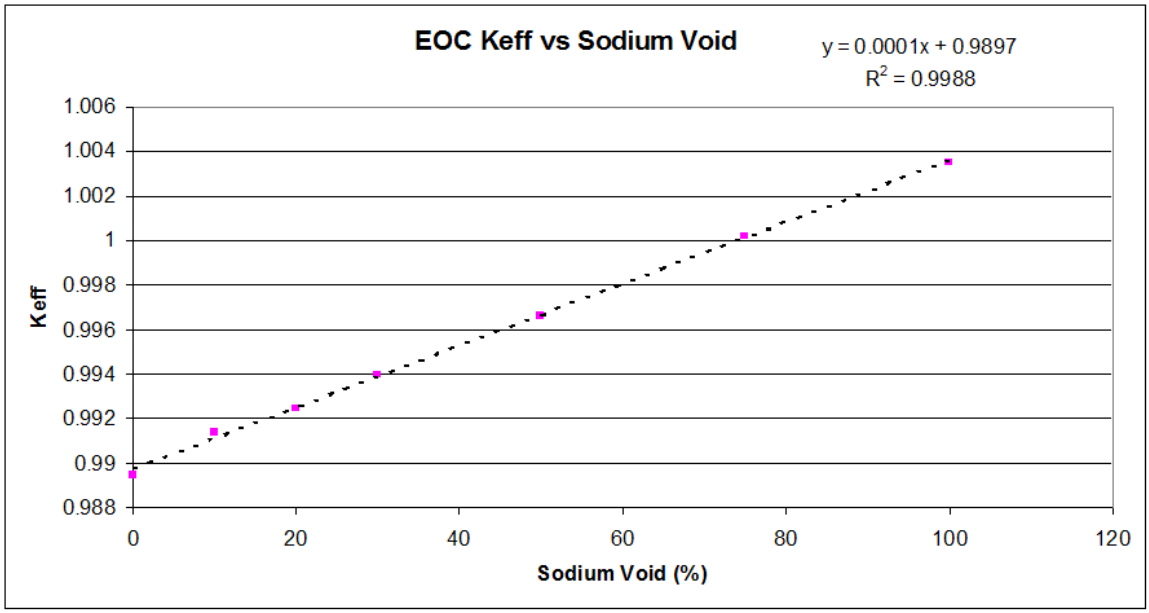

Figure 2.27 - EOC Sodium Void Worth

The next reactivity feedback coefficient considered is the axial expansion coefficient. It is important to note that this value was calculated assuming expansion only in the axial direction. This assumes axial expansion is independent of radial expansion which is accurate if the fuel is assumed to uniformly expand. To calculate the axial expansion coefficient, the active fuel height was uniformly increased by 1% and the density adjusted to conserve total fuel mass in the core. The change in eigenvalue between the base case and this perturbed case is calculated and then converted to a reactivity per degree K by multiplying by the linear expansion rate of the U-TRU metal fuel for the core height: this value is -0.35 c/K This differs from the quoted reference value of -0.34 c/K by 2.9%. These values are very close adding further confidence in the methods used in the depletion of the core and the method of calculating this reactivity feedback.

The parametric used in the verification of Monteburns depletion for a sodium cooled fast reactor is the doppler coefficient. This calculation presented a challenge due to the very small perturbation caused in eigenvalue. The small perturbation increases the statistical uncertainty in the calculation making it very hard to get an accurate prediction of the doppler. To address this large statistical uncertainty two methods were followed. One, the number of neutron histories was increased to reduce the statistical uncertain of each eigenvalue calculation. And two, a very large increase in fuel temperature, 500 K, was used. These two methods together predict a doppler of -0.067 c/K with an uncertainty of 0.008 c/K. The standard deviation in doppler is still greater than 10%, the current typical industry target standard for doppler uncertainty. When comparing against the reference doppler feedback coefficient of -0.047 we see a difference that could range from 25% to 80%. Further reduction of the statistical uncertainty in doppler could be accomplished by further increasing the number of neutron histories used in the MCNP calculations or using a larger increase in fuel temperature, but is left as future work.

Overall the comparison between the Monte Carlo model and the reference core are good. Axial and radial expansion and sodium void coefficients, as well as TRU and heavy metal consumption are all within 5%. The doppler coefficient and core mass values do not match up as well, but relatively large statistical uncertainties in these values could be partially to blame for the differences. Further quantification and reduction of error in these values are left as future work. Using the methods which have developed up until this point, a new fuel type core will be designed and analyzed.

2.7. Cermet Fuel Design

The final set of objectives of this thesis is the design of a TRU-cermet fueled SFR and comparison to the reference metal fueled reactor. The fuel will be a transuranic-oxide fuel contained in a Zirconium cermet matrix. First, the design limitations of the new fuel design will be discussed and used as the basis for the new fuel design. Next, the approach used to determine the final fuel loading and pin radius will be discussed and an equilibrium core composition obtained. Finally, a set of parametrics will be performed on the final equilibrium TRU-cermet fuel design will be performed and compared to the reference metal fueled core.

2.7.1. Design Considerations

A number of design limitations had to be imposed upon the new fuel design. These limitations were primarily for material and thermal-hydraulic concerns. The primary concern in the fuel design is related to the TRU loading. TRU loadings of greater than 50% begin to negatively affect the thermal conductivity of the fuel. This increases the characteristic time of transient accidents which can cause melting of the core without coolant interaction. In order to be as conservative as possible, a TRU loading as low as possible is preferred. The

second design consideration is the pin radius. The same total core mass can be maintained by a lower TRU loading if the pin radius can be increased. There is however a trade-off in thermal-hydraulic properties of the core. To avoid having to perform thermal-hydraulic calculations on the new TRU-cermet fueled core, a pin radius similar to those already analyzed in the references was considered. In Reference 3, pin radiuses between 0.295 cm and 0.34 cm were considered. For the TRU-cermet fuel, these same pin radiuses were considered.

2.7.2. Approach

Numerous calculations were performed with different combinations of TRU loadings and pin radii. The goal of these initial calculations is to obtain the same rodded eigenvalue as the fresh metal fueled core. The idea is this will maintain roughly the same shutdown margin as the metal fueled core. Figure 2.28 and Figure 2.29 show the results for various pin radii and TRU loadings. It is worth noting that Zr porosity has little effect on core eigenvalue. The final design chosen calls for a 10% Zr porosity to minimize the effect radiation damage has on the fuel while maintaining manufacturability. From Figure 2.28 we see that the 0.32 cm case has an eigenvalue that most closely matches that of the target metal fueled core. When the TRU loading for this case is slightly adjusted as seen in Figure 2.29 we arrive at our initial estimate for the final core design of 41.5% TRU.

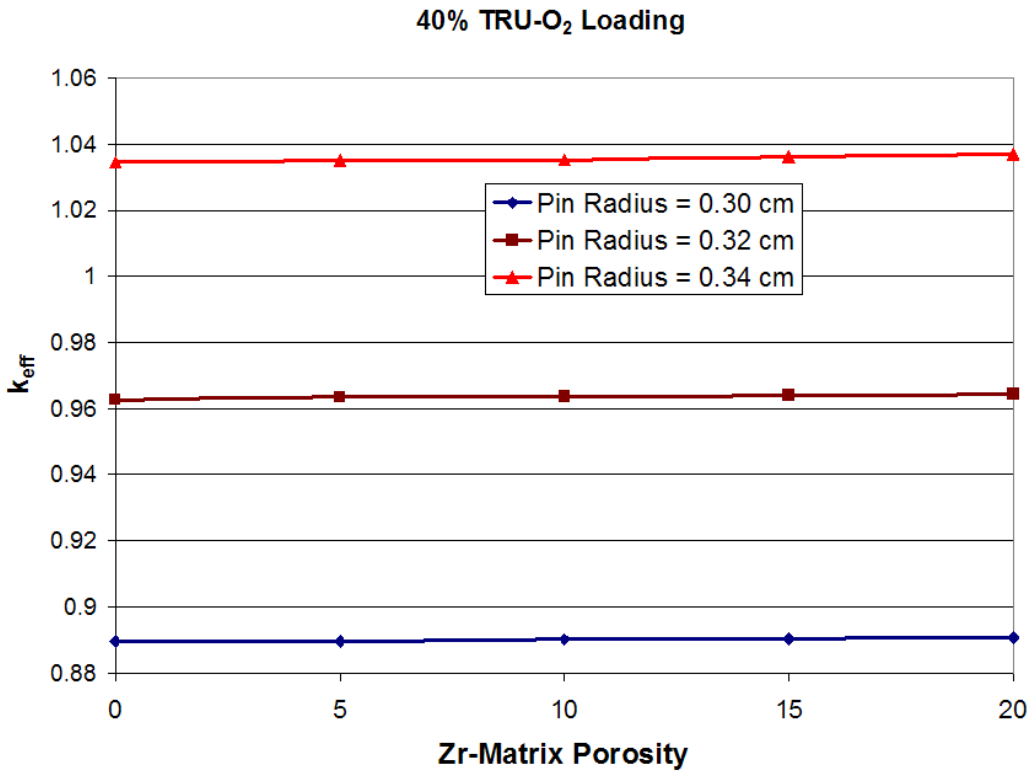

Figure 2.28 - ARI eigenvalue for 40% TRU loading

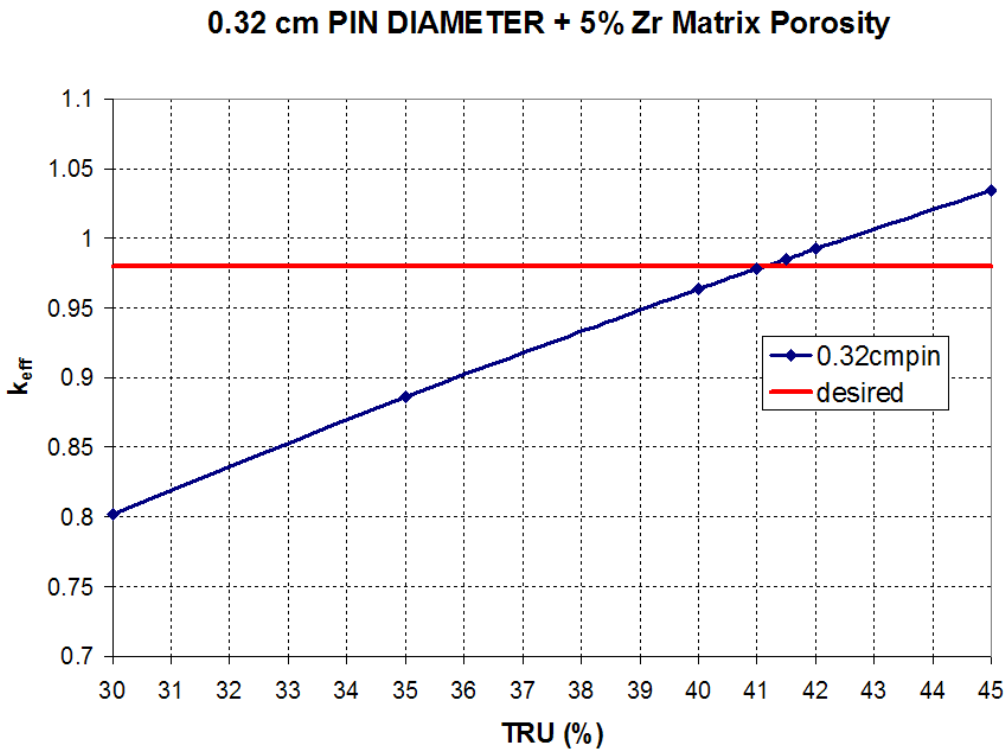

Figure 2.29 - ARI core eigenvalue for various TRU loadings

This initial core design is now depleted like the metal fueled core. A seven batch reloading scheme was used, removing 1/7th of the burned fuel and adding 1/7th fresh fuel for a total of 45 cycles to ensure convergence. What is found is that when the core is depleted to equilibrium, the final BOC and EOC eigenvalues are much higher than their metal fueled counterparts. This is primarily due to higher control rod worth, which in turn means the core initially has much more excess reactivity. The higher control rod worth is caused by the cermet fueled core having a softer spectrum due to the presence of the oxygen in the TRU-oxide fuel. Reloading a core while it is still capable of maintaining criticality is wasteful of fuel. As such, the TRU-oxide fueled core should be designed such that the EOC eigenvalue matches that of the metal fueled core, very nearly 1. The same pin radius is maintained and the TRU loading reduced. Equilibrium depletion calculations are first performed on two cases, 35% and 39% TRU. When neither

of these values produce the desired results, a third case, 38% TRU is tried. This case, 38% TRU finally produces the desired equilibrium EOC eigenvalue. These calculations can be seen in Figure 2.30.

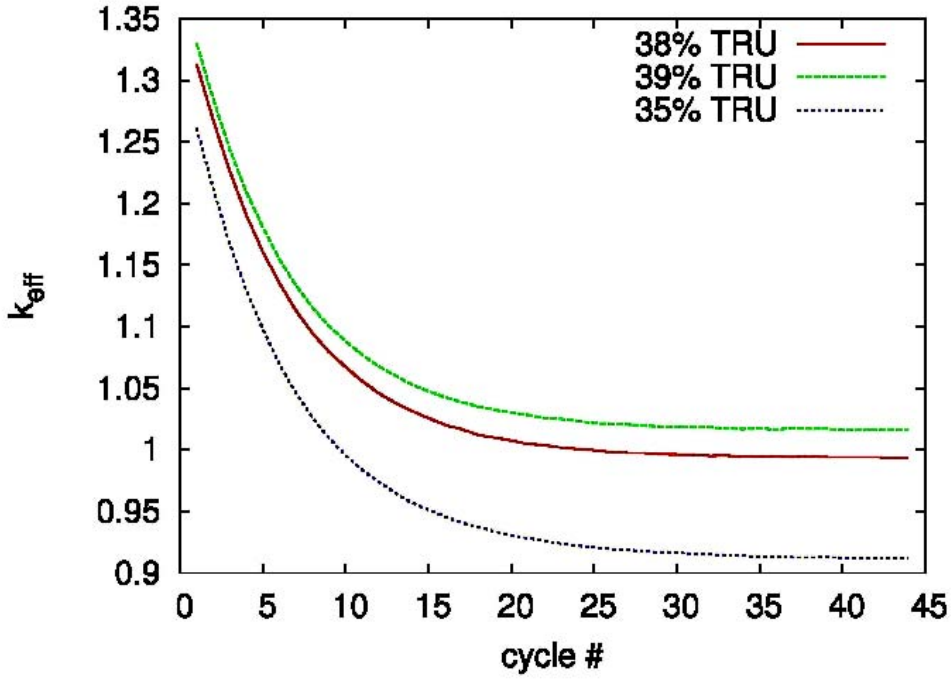

Figure 2.30 - EOC eigenvalue for three TRU loading configurations

The 38% w/o TRU, 0.32 cm radius pin fuel design now meets the initial design goal laid out. Now various parameters and reactivity coefficients will be computed to compare the performance of the reactor to that of its U-TRU metal counterpart.

2.7.3. Metal vs. Cermet Fuel Comparison

Many parameters are calculated following the same procedure as for the U-TRU metal fueled core. Parameters of specific interest are the TRU consumption rate, and reactivity feedback coefficients which affect the operability of the core.

The first two parameters considered are the full core fuel mass and TRU consumption rate. As can be seen in Table 2.6, there is a slightly lower TRU loading in the cermet fueled core. In addition to this, the heavy metal loading of the cermet core, which Is the same as the TRU loading, is significantly lower due to the absence of Uranium. The cermet core can maintain criticality with the lower heavy metal loading due to much better fuel utilization, again caused by the absence of the parasitic absorption in U-238. A secondary side effect of the absence of U-238 is a higher net TRU consumption rate. U-238 primarily acts as a neutron absorber which forms new TRU, reducing the overall consumption rate. This is also the reason the burnup reactivity loss is higher for the TRU core, 6.6% vs. 4.3% for the metal fueled core. The higher TRU consumption rate could be a good or a bad thing depending upon what goals GNEP decides upon. If the goal is to quickly and efficiently burn TRU, the cermet fueled core performs better by burning more TRU. If the goal is long term sustainability of the fuel cycle, the metal fueled core performs better by breeding some new TRU to offset some of what is lost.

Table 2.6 - Comparison of Cermet and Metal TRU Masses

	Cermet	Metal
BOC TRU Loading (kg)	2219	2250
Net TRU Consumption (kg/yr)	269	189.3

The next parameters of interest in comparison between the two cores are the reactivity feedback coefficients. Again, the same coefficients that were considered for the metal core are calculated. These values include delayed neutron fraction, sodium void worth, and axial and radial expansion coefficients. A table summarizing the comparison of these values can be found in Table 2.7.

Table 2.7 - Reactivity feedback comparison of metal and cermet fueled cores

	Cermet	Zr Metal
BOC Beta (pcm)	234.7	263.3
BOC Sodium Worth	$3.37	$4.91
EOC Beta (pcm)	236.6	256.7
EOC Sodium Worth	$4.20	$5.54
Axial Expansion (c/K)	-0.18	-0.35

Three significant differences in reactivity coefficients are worth noting. One, The effective delayed neutron fraction for the metal fueled core is consistently higher than that of the cermet core. This is due to the presence of U-238 in the metal fuel which has a much higher delayed neutron fraction when it undergoes fission than TRU. The next apparent difference between the reactivity feedback coefficients of the two cores is the lower sodium void worth of the TRU cermet core. There is a 31% decrease in the BOC sodium void worth and a 24% decrease in the EOC sodium void worth in terms of dollars. The smaller delayed neutron fraction of the cermet fueled core somewhat skews the data, meaning the difference in the feedback in terms of change in eigenvalue is even larger. The differences when only delta k is considered are 38% and 30% for BOC and EOC respectively. Plots used to compute the sodium void worth and to confirm the hypothesis of a linear relationship between reactivity feedback and sodium void are seen in Figure 2.31 and Figure 2.32.

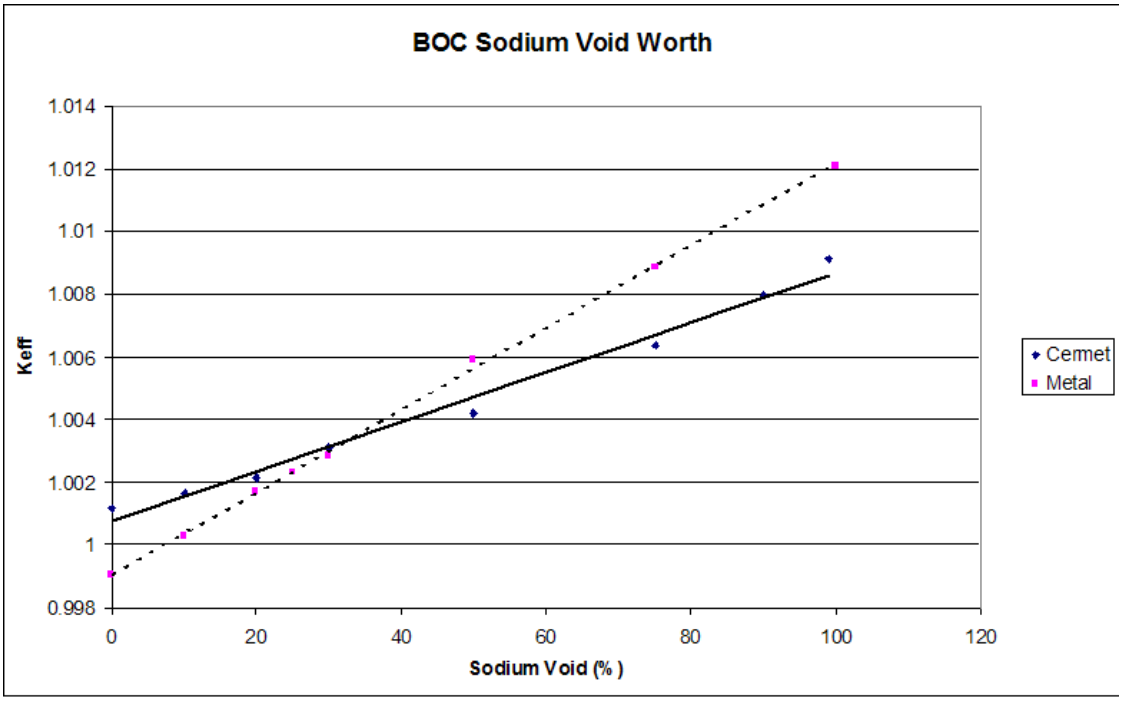

Figure 2.31 - BOC sodium void comparison of cermet and metal fueled cores

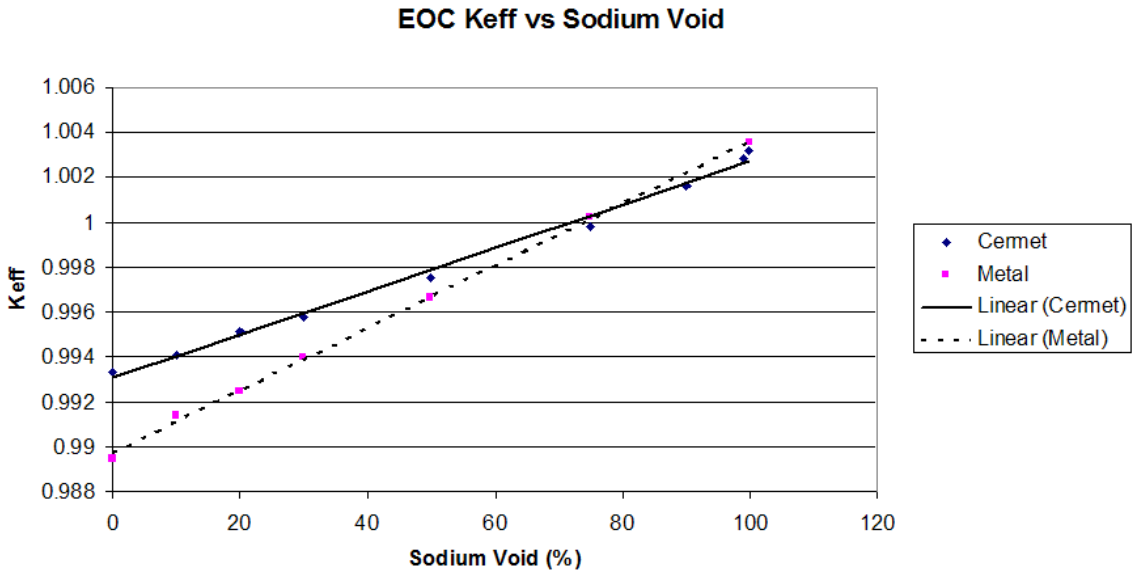

Figure 2.32 - EOC sodium void comparison of cermet and metal fueled cores

The final difference between the two cores is the smaller axial feedback coefficient. The immediate cause of this difference is not at first apparent. On possibility for the difference is the smaller fuel fraction in the Cermet fuel, 38% w/o TRU in the cermet fuel vs. 75% w/o U-TRU in the metal fueled core. An expansion of the core in the axial direction would thus affect the number densities of fissile isotopes much less in the cermet fuel which could cause the reactivity feedback to be smaller.

2.8. Summary, Conclusions, and Future Work

Monte Carlo based transport coupled with depletion, via *Monteburns*, is a powerful and accurate way to perform three-dimensional core depletion. As part of the model development, a number of parameters defining the model were investigated. While it is possible to make the MCNP model arbitrarily complex with an outer burn time step so small as to require hundreds, if not thousands, of cpu hours per simulation, this would be extremely inefficient and impractical. Since we are interested in understanding the burnup cycle of the reactor core and calculating the important safety parameters, it is important to strike a balance between the detail and accuracy provided in the solution and the computational efficiency. Those modeling parameters which significantly impact the final solution accuracy were considered in the equilibrium depletion of the core, whereas those factors which had a negligible effect on the final solution accuracy were neglected.

The first model parameter investigated was the control rod insertion depth which impacts the material burnup in the core since the control rods serve to reduce the neutron flux in the fuel by acting as neutron absorbers. This effect is most noticeable when the control rod is inserted at depths of greater than half the height of the core. Further calculations have shown that the amount of control rod insertion needed to suppress the excess reactivity of the equilibrium cores studied

here was significantly less than half the height of the core and thus could be neglected when performing equilibrium core calculations. The size of the outer burn step used in *Monteburns* does not affect the simulation result more than 80 pcm per cycle. Uncertainties in k_{eff} appear to be the primary reason and are within the statistical accuracy of an individual MCNP calculation. This effect is thus neglected in equilibrium core calculations.

The analysis here indicate the axial and radial mesh size significantly impacts the eigenvalue of the core in equilibrium depletion calculations. The results in the radial direction could justify the use of only two radial zones for material burnup (low enriched and highly enriched zones). However, axial flux variations are large enough to cause different material burnup rates at different axial locations in the fuel pins. This will result in different burnup reactivity swings and material compositions, depending on the mesh refinement. When equilibrium calculations are performed on a core with 2 depletion regions and on a core with 25 depletion regions a difference in final eigenvalue is found to be 700-800 pcm or approximately $3 for this core which is a very significant difference.

The equilibrium core condition for the ANL's compact core design was achieved by depleting the core for 45 cycles with a cycle length of 155.1 days. A homogenous reload scheme was used where $1/7^{th}$ of the burned fuel mass is removed at the end of each cycle and replaced $1/7^{th}$ fresh fuel. The burnup reactivity loss in term of Δk is 4267 pcm, which is in good agreement with the ANL calculations.

A number of parametrics were then performed to evaluate the accuracy of the models and methods. It was found that a number of parameters used in the comparison (i.e. sodium void worth, axial and radial expansion, delayed neutron fraction, TRU consumption, and burnup reactivity loss) were within 5% of the reference values which is sufficiently accurate for purposes here. A few other parameters do not compare as well, such as the Doppler coefficient and the discharge mass of certain isotopes. The discrepancy for these parameters was

greater than 10% compared to the reference values. The errors in these values are primarily attributable to statistical uncertainty. However, for the purpose of this study, the accuracy of the results is considered to be sufficient. Further quantification and reduction of these errors is left as future work.

Using the methods developed and validated for Monte Carlo analysis of a SFR, a new cermet fuel type was designed and compared to the reference metal core. Staying within the design considerations, a final design consisting of 38% w/o TRU with a pin radius of 0.32 cm was found to have similar operating characteristics when compared to the reference metal fueled core. The TRU consumption rate of the cermet core was found to be significantly higher than the metal fueled core. The sodium void worth was found to be less positive and the axial feedback coefficient was found to be less negative. The final design was found to have overall safety characteristics similar to the metal fueled core.

Overall, the models and methods developed here have accomplished the five objectives of this thesis. A $1/6^{th}$ model of a SFR was successfully modeled in MCNP. Methods were developed to accurately and efficiently deplete this model. A number of key parameters were calculated after depleting the model. These key parameters were then successfully benchmarked against current methods used in sodium fast reactor analysis. Based upon the calculation methods developed, a new TRU-cermet fuel type was designed to display similar operating characteristics for this reactor. Finally, the new TRU-cermet fueled reactor was compared to its metal fueled counterpart. It has been shown that Monte Carlo depletion is an accurate method of calculating critical core parameters for depletion and safety analysis. Statistical uncertainty in some parameters remains an issue. These uncertainties could be reduced by increasing the number of histories and should be considered in future work.

BIBLIOGRAPHY

1. Committee, U.S.D.o.E.R.A., *A Technology Roadmap for Generation IV Nuclear Energy Systems*. 2002.
2. Lineberry, M.J. and T.R. Allen, *The Sodium-Cooled Fast Reactor (SFR)*, Argonne National Laboratory.
3. Smith, M.A. and R.N. Hill, *Development and Analysis of a Compact Low-Conversion Ratio Fast Burner Reactor*. 6/30/2003, Argonne National Laboratory.
4. Seker, V., C. Glass, and T.J. Downar, *Monte Carlo Depletion Analysis of a TRU Burning Sodium Fast Reactor*. November 2007, Purdue University.
5. Group, X.-M.C., *MCNP - A General Monte Carlo N-Particle Transport Code, Version 5*, X-5, Editor. 2003, Los Alamos National Laboratory.
6. Croff, A.G., *A User's Manual for the ORIGEN2 Computer Code.* ORNL/TM-7175, 1980.
7. Poston, D.I. and H.R. Trellue, *User's Manual, Version 2.0 for Monteburns, Version 1.0*. 1999, Los Alamos National Laboratory: Los Alamos, NM.
8. Farlane, R.E.M., *RSICC Peripheral Shielding Routine Collection: NJOY99.0, Code System for Producing Pointwise and Multigroup Neutron and Photon Cross Sections from ENDF/B Data.* PSR-480 NJOY99.0, 1999.
9. Cetnar, J., W. Gudowski, and J. Wallenius, *User Manual for Monte-Carlo Continuous Energy Burnup (MCB) Code - Version 1C.* NEA-1643 MCB1C, 2002.
10. Hermann, O.W. and R.M. Westfall, *ORIGEN-S --SCALE System Module to Calculate Fuel Depletion, Actinide Transmutation, Fission Product Buildup and Decay, and Associated Radiation Source Terms", in SCALE: A Modular Code system for Performing Standardized Computer Analyses for Licensing Evaluations.* NUREG/CR-2000, 1993. **II**(I).
11. Smith, M.A., W.S. Yang, and R.N. Hill, *Preliminary Studies of a Nitride-Fueled Fast Burner Reactor.* ANL-AFCI-167, 2006.
12. *Provided by Kevin Kramer via Private Correspondence*. 2007.
13. Provided by Aaron Totemeier via Private Correspondence, 2007.

Appendix A. Monteburns Input Deck

AFCI single assembly 271 pins high enrichment .25 conversion 840MWt reactor
UNSU ! Type of Operating System
2 ! Number of MCNP materials
4 ! MCNP Material number
5 ! MCNP Material number
58605 ! Pin Volume (cc)
83722 ! Pin Volume (cc)
140 ! Power in MWt for system modeled
-200 ! Recov. energy/fission (MeV)
155.1 ! Total Number of days burned
6 ! Number of outer burn steps
40 ! Number of internal burn steps (multiple of 10)
1 ! Number of predictor steps
0 ! Step number to restart after
Fftfc ! Number of origen2 library -next line is origen2 lib. location
/g/g22/kramer12/work/mercury/depletion_work/ORIGEN22/origen22/libs
.005 ! fractional importance
1 ! Intermediate keff calc. 0)No 1)Yes
18 ! Number of isotopes to burn
92234.60c
92235.60c
92236.60c
92238.60c
93237.60c
94238.60c
94239.60c
94240.60c
94241.60c
94242.60c
95241.60c
95242.42c
95243.60c
96242.60c

96243.60c
96244.60c
96245.60c
96246.60c
18
92234.60c
92235.60c
92236.60c
92238.60c
93237.60c
94238.60c
94239.60c
94240.60c
94241.60c
94242.60c
95241.60c
95242.42c
95243.60c
96242.60c
96243.60c
96244.60c
96245.60c
96246.60

Appendix B. MCNP Input Deck

```
Title Card
c Moveable control rod Card
 120  0  -115 116 -117 118 -119 120 -903 910 fill=200 u=22
          trcl (0 0 120) imp:n=1
c  Low Enrichment
 1  4  -7.64316     -1     u=11 imp:n=1
 2  2  8.16103E-02  -2 1   u=11 imp:n=1
 3  3  2.22724E-02   2     u=11 imp:n=1
c
c  Universe fill
 4   3  2.22724E-02  -3 4 -5 6 -7 8 lat=2 imp:n=1
                     u=10 fill=-10:10 -10:10 0:0
       10 20R
       10  9R 11  9R  10
       10  8R 11 10R  10
       10  7R 11 11R  10
       10  6R 11 12R  10
       10  5R 11 13R  10
       10  4R 11 14R  10
       10  3R 11 15R  10
       10  2R 11 16R  10
       10  1R 11 17R  10
       10     11 18R  10
       10     11 17R  10  1R
       10     11 16R  10  2R
       10     11 15R  10  3R
       10     11 14R  10  4R
       10     11 13R  10  5R
       10     11 12R  10  6R
       10     11 11R  10  7R
       10     11 10R  10  8R
       10     11  9R  10  9R
       10 20R
 7  0 -9 10 -11 12 -13 14 -903 904 fill=10 u=12 imp:n=1
```

```
 8  2  8.16103E-02  -15 16 -17 18 -19 20 (9:-10:11:-12:13:-14)
         -903 904 u=12 imp:n=1
 9  3  2.22724E-02  (15:-16:17:-18:19:-20) -903 904 u=12 imp:n=1
c Lower Reflector
 10  12  6.25734E-02 -904 905 u=12 imp:n=1
c Lower Structure
 11   1  3.89085E-02 -905     u=12 imp:n=1
c Displaced Bond
 12  17  3.59964E-02 903 -907 u=12 imp:n=1
c Upper Plenum
 13  18  2.60327E-02 907 -908 u=12 imp:n=1
c Upper Structure
 14  19  6.24772E-02 908      u=12 imp:n=1
c
 31  5  -7.64316      -1     u=61 imp:n=1
 32  2  8.16103E-02  -2 1   u=61 imp:n=1
 33  3  2.22724E-02   2     u=61 imp:n=1
c
c  Universe fill
 34   3  2.22724E-02  -3 4 -5 6 -7 8 lat=2 imp:n=1
                    u=60 fill=-10:10 -10:10 0:0
       60 20R
       60  9R 61  9R  60
       60  8R 61 10R  60
       60  7R 61 11R  60
       60  6R 61 12R  60
       60  5R 61 13R  60
       60  4R 61 14R  60
       60  3R 61 15R  60
       60  2R 61 16R  60
       60  1R 61 17R  60
       60     61 18R  60
       60     61 17R  60  1R
       60     61 16R  60  2R
       60     61 15R  60  3R
       60     61 14R  60  4R
```

```
      60     61 13R  60  5R
      60     61 12R  60  6R
      60     61 11R  60  7R
      60     61 10R  60  8R
      60     61  9R  60  9R
      60 20R
 37  0 -9 10 -11 12 -13 14 -903 904 fill=60 u=62 imp:n=1
 38  2  8.16103E-02  -15 16 -17 18 -19 20 (9:-10:11:-12:13:-14)
        -903 904 u=62 imp:n=1
 39  3  2.22724E-02  (15:-16:17:-18:19:-20) -903 904 u=62 imp:n=1
c Lower Reflector
 40  12  6.25734E-02 -904 905 u=62 imp:n=1
c Lower Structure
 41   1  3.89085E-02 -905     u=62 imp:n=1
c Displaced Bond
 42  17  3.59964E-02 903 -907 u=62 imp:n=1
c Upper Plenum
 43  18  2.60327E-02 907 -908 u=62 imp:n=1
c Upper Structure
 44  19  6.24772E-02 908      u=62 imp:n=1
c ------------------------------------------------------------------------
c    Change TRCL (0 0 z) for cells 105 106 and 110 to move CR
c               Control Assembly
c
c ------------------------------------------------------------------------
 101   9  8.65633E-02  -101     u=21 imp:n=1
 102   2  8.16103E-02  -102 101   u=21 imp:n=1
 103   3  2.22724E-02   102     u=21 imp:n=1
 104   3  2.22724E-02  -103 104 -105 106 -107 108 lat=2 imp:n=1
                    u=20 fill=-6:6 -6:6 0:0
      20 20 20 20 20 20 20 20 20 20 20 20 20
      20 20 20 20 20 20 21 21 21 21 21 21          20
      20 20 20 20 20   21 21 21 21 21 21 21        20
      20 20 20 20     21 21 21 21 21 21 21 21      20
      20 20 20       21 21 21 21 21 21 21 21 21    20
      20 20         21 21 21 21 21 21 21 21 21 21  20
```

```
      20          21 21 21 21 21 21 21 21 21 21 20
      20            21 21 21 21 21 21 21 21 21   20 1R
      20              21 21 21 21 21 21 21 21 21     20 2R
      20                21 21 21 21 21 21 21 21       20 3R
      20                  21 21 21 21 21 21 21         20 4R
      20                    21 21 21 21 21 21           20 5R
      20 20 20 20 20 20 20 20 20 20 20 20 20
c  Moveable control rod cards
 105  0  -109 110 -111 112 -113 114  904 fill=20
              u=200 imp:n=1
 106  2  8.16103E-02  -115 116 -117 118 -119 120 -903 904
             (109:-110:111:-112:113:-114) u=200 imp:n=1
 107  3  2.22724E-02  -9 10 -11 12 -13 14 -903 904 #120 u=22 imp:n=1
 108  2  8.16103E-02  -15 16 -17 18 -19 20 (9:-10:11:-12:13:-14)
       -903 904 u=22 imp:n=1
 109  3  2.22724E-02  (15:-16:17:-18:19:-20) -903 904 u=22 imp:n=1
c Follower
 110  20 4.34150E-02  -904  u=200 imp:n=1
c Lower Reflector
 111  12  6.25734E-02 -904 905 #120 u=22 imp:n=1
c Lower Structure
 112   1  3.89085E-02 -905 #120 u=22 imp:n=1
c Upper Plenum
 113  18  2.60327E-02 903 -908 #120 u=22 imp:n=1
c Upper Structure
 114  19  6.24772E-02 908 #120 u=22 imp:n=1
c ------------------------------------------------------------------------
c
c               Reflector Assembly
c
c ------------------------------------------------------------------------
 201  11  7.247268E-02  -202     u=31 imp:n=1
c 202   2  8.16103E-02  -202 201   u=31 imp:n=1  $No cladding on reflector
 203   3  2.22724E-02   202     u=31 imp:n=1
 204   3  2.22724E-02  -203 204 -205 206 -207 208 lat=2 imp:n=1
                    u=30 fill=-6:6 -6:6 0:0
```

```
      30 30 30 30 30 30 30 30 30 30 30 30
      30 30 30 30 30 30 31 31 31 31 31 31          30
      30 30 30 30 30   31 31 31 31 31 31 31        30
      30 30 30 30     31 31 31 31 31 31 31 31      30
      30 30 30       31 31 31 31 31 31 31 31 31    30
      30 30         31 31 31 31 31 31 31 31 31 31  30
      30           31 31 31 31 31 31 31 31 31 31 31 30
      30            31 31 31 31 31 31 31 31 31 31  30 1R
      30              31 31 31 31 31 31 31 31 31   30 2R
      30               31 31 31 31 31 31 31 31     30 3R
      30                 31 31 31 31 31 31 31      30 4R
      30                   31 31 31 31 31 31       30 5R
      30 30 30 30 30 30 30 30 30 30 30 30 30
 205  0  -9 10 -11 12 -13 14 fill=30 u=32 imp:n=1
 208  2  8.16103E-02  -15 16 -17 18 -19 20 (9:-10:11:-12:13:-14) u=32 imp:n=1
 209  3  2.22724E-02  (15:-16:17:-18:19:-20) u=32 imp:n=1
c 210  0  -21 22 -23 24 -25 26  fill=32 imp:n=0
c ---------------------------------------------------------------------------
c
c               Shield Assembly
c
c ---------------------------------------------------------------------------
 301  11  8.24897E-02  -301     u=41 imp:n=1
 302   2  8.16103E-02  -302 301   u=41 imp:n=1  $No cladding on reflector
 303   3  2.22724E-02   302     u=41 imp:n=1
 304   3  2.22724E-02  -303 304 -305 306 -307 308 lat=2 imp:n=1
                    u=40 fill=-3:3 -3:3 0:0
            40  40  40  40  40  40  40
              40  40  40  41  41  41  40
                40  40  41  41  41  41  40
                  40  41  41  41  41  41  40
                    40  41  41  41  41  40  40
                      40  41  41  41  40  40  40
                        40  40  40  40  40  40  40
 305  0  -9 10 -11 12 -13 14 fill=40 u=42 imp:n=1
 308  2  8.16103E-02  -15 16 -17 18 -19 20 (9:-10:11:-12:13:-14) u=42 imp:n=1
```

```
 309  3  2.22724E-02  (15:-16:17:-18:19:-20) u=42 imp:n=1
c 310  0  -21 22 -23 24 -25 26  fill=42 imp:n=0
c ---------------------------------------------------
c
c             Reactor Fill
c
c ---------------------------------------------------
 500   0  -21 22 -23 24 -25 26 lat=2 imp:n=1
                    u=50 fill=0:10 0:10 0:0
      22  12  22  12  22  62  32  32  42     50  1R
        12  12  12  12  62  62  32  32  42   50  1R
          22  12  22  62  62  32  32  42     50  2R
            12  12  62  62  32  32  42       50  3R
              22  62  62  32  32  42         50  4R
                62  62  32  32  42           50  5R
                  32  32  32  42             50  6R
                    32  32  42               50  7R
                      42  42                 50  8R
                        50                   10R
                                           50 10R
c  fill
 700  0  900 901 -902 906 -909 fill=50  imp:n=1
c Void
 999  0  (-900:-901:902:909:-906)  imp:n=0

c  pin surfaces
1 cz 0.295
2 cz 0.345
c  window surfaces
3   px  0.448                    $ right side plane
4   px -0.448                    $ left  side plane
5   p   0.5774 1 0  0.5173         $ north-east side plane
6   p   0.5774 1 0 -0.5173         $ south-west side plane
7   p  -0.5774 1 0  0.5173         $ north-west side plane
8   p  -0.5774 1 0 -0.5173         $ south-east side plane
c
```

```
c  Big
c  window surfaces    (Assembly wall inside)
9   py  7.57                    $ top
10  py -7.57                    $ bottom
11   p   1.732050808  1 0  15.14      $ north-east side plane
12   p   1.732050808  1 0 -15.14      $ south-west side plane
13   p   1.732050808 -1 0  15.14      $ north-west side plane
14   p   1.732050808 -1 0 -15.14      $ south-east side plane
c  Assembly Wall outside
15   py  7.87                    $ top
16   py -7.87                    $ bottom
17   p   1.732050808  1 0  15.74      $ north-east side plane
18   p   1.732050808  1 0 -15.74      $ south-west side plane
19   p   1.732050808 -1 0  15.74      $ north-west side plane
20   p   1.732050808 -1 0 -15.74      $ south-east side plane
c  node boundary
21   py  8.07                    $ top
22   py -8.07                    $ bottom
23   p   1.732050808  1 0  16.14      $ north-east side plane
24   p   1.732050808  1 0 -16.14      $ south-west side plane
25   p   1.732050808 -1 0  16.14      $ north-west side plane
26   p   1.732050808 -1 0 -16.14      $ south-east side plane
c ---------------------------------------------------
c  Control Rod
c ---------------------------------------------------
c
101  cz 0.63
102  cz 0.70
c  window surfaces
103   px  0.71116                  $ right side plane
104   px -0.71116                  $ left  side plane
105   p   0.5774 1 0  0.821179          $ north-east side plane
106   p   0.5774 1 0 -0.821179          $ south-west side plane
107   p  -0.5774 1 0  0.821179          $ north-west side plane
108   p  -0.5774 1 0 -0.821179          $ south-east side plane
c
```

```
c  Big
c  window surfaces    (Inner Duct inside)
109   py  6.87                  $ top
110   py -6.87                  $ bottom
111   p   1.732050808  1 0  13.74      $ north-east side plane
112   p   1.732050808  1 0 -13.74      $ south-west side plane
113   p   1.732050808 -1 0  13.74      $ north-west side plane
114   p   1.732050808 -1 0 -13.74      $ south-east side plane
c  Inner Duct outside
115   py  7.17                  $ top
116   py -7.17                  $ bottom
117   p   1.732050808  1 0  14.34      $ north-east side plane
118   p   1.732050808  1 0 -14.34      $ south-west side plane
119   p   1.732050808 -1 0  14.34      $ north-west side plane
120   p   1.732050808 -1 0 -14.34      $ south-east side plane
c
c  Reflector specific surfaces
c
c
c 201  cz 0.549526
202  cz 0.782166
c  window surfaces
203   px  0.78362                $ right side plane
204   px -0.78362                $ left  side plane
205   p   0.5774 1 0  0.90485          $ north-east side plane
206   p   0.5774 1 0 -0.90485          $ south-west side plane
207   p  -0.5774 1 0  0.90485          $ north-west side plane
208   p  -0.5774 1 0 -0.90485          $ south-east side plane
c
c  Shield specific surfaces
c
c
301  cz 1.44408
302  cz 1.69408
c  window surfaces
303   px  1.69575                $ right side plane
```

```
304   px -1.69575                    $ left  side plane
305   p   0.5774 1 0  1.95808         $ north-east side plane
306   p   0.5774 1 0 -1.95808         $ south-west side plane
307   p  -0.5774 1 0  1.95808         $ north-west side plane
308   p  -0.5774 1 0 -1.95808         $ south-east side plane
c
c  Core Boundaries
c
899  cz 200
*900 px 0
*901 p  -0.5774 1 0 0          $ north-east side plane
902 cz  145.83
903 pz   90
904 pz  -23
905 pz  -83.3
906 pz  -133.54
907 pz   112.57
908 pz   210.59
909 pz   240.73
910 pz  -39.88

c
c    Materials : all materials are adjusted for thermal expansion
c
c    material 1 : lower structure - 3.89085E-02
c
m1     11023.60c   1.55907E-02
       26054.60c   9.28087E-04
       26056.60c   1.45690E-02
       26057.60c   3.36461E-04
       26058.60c   4.47768E-05
       28058.60c   2.21956E-03
       28060.60c   8.54967E-04
       28061.60c   3.71682E-05
       28062.60c   1.18482E-04
       28064.60c   3.01910E-05
```

```
      24050.60c   1.40584E-04
      24052.60c   2.71102E-03
      24053.60c   3.07408E-04
      24054.60c   7.65203E-05
      25055.60c   5.08461E-04
      42000.60c   4.35240E-04
c
c    material 2 : HT9 - 8.16103E-02
c
m2     26054.60c   4.08237E-03
      26056.60c   6.40845E-02
      26057.60c   1.47999E-03
      26058.60c   1.96960E-04
      28058.60c   2.93161E-04
      28060.60c   1.12925E-04
      28061.60c   4.90920E-06
      28062.60c   1.56492E-05
      28064.60c   3.98765E-06
      24050.60c   4.51224E-04
      24052.60c   8.70140E-03
      24053.60c   9.86669E-04
      24054.60c   2.45603E-04
      25055.60c   4.60068E-04
      42000.60c   4.90972E-04
c
c    material 3 : Sodium - 2.22724E-02
c
m3    11023.60c    2.22724E-02
c
c    material 4 : Inner core fuel - 3.24321E-02
c
m4     40000.60c  -2.33188E-01
      92234.60c  -4.89362E-11
      92235.60c  -8.29197E-04
      92236.60c  -9.78725E-06
      92238.60c  -4.13239E-01
```

```
      93237.60c  -2.32923E-02
      94238.60c  -9.70514E-03
      94239.60c  -1.71781E-01
      94240.60c  -8.15232E-02
      94241.60c  -2.42629E-02
      94242.60c  -1.84398E-02
      95241.60c  -1.64987E-02
      95242      -6.79360E-05
      95243.60c  -5.24078E-03
      96242.60c  -3.59090E-11
      96243.60c  -1.74693E-05
      96244.60c  -1.74693E-03
      96245.60c  -1.35872E-04
      96246.60c  -2.13513E-05
c  High Enrichment Zone
m5    40000.60c  -2.33188E-01
      92234.60c  -3.80615E-11
      92235.60c  -6.44931E-04
      92236.60c  -7.61230E-06
      92238.60c  -3.21408E-01
      93237.60c  -2.93686E-02
      94238.60c  -1.22369E-02
      94239.60c  -2.16593E-01
      94240.60c  -1.02790E-01
      94241.60c  -3.05923E-02
      94242.60c  -2.32501E-02
      95241.60c  -2.08028E-02
      95242      -8.56584E-05
      95243.60c  -6.60793E-03
      96242.60c  -4.52766E-11
      96243.60c  -2.20264E-05
      96244.60c  -2.20264E-03
      96245.60c  -1.71317E-04
      96246.60c  -2.69212E-05
c
c    material 7 : mixture of lower reflelctor - 6.25734E-02
```

```
c
m7    11023.60c   7.14545E-03
      26054.60c   2.77266E-03
      26056.60c   4.35248E-02
      26057.60c   1.00518E-03
      26058.60c   1.33771E-04
      28058.60c   1.99109E-04
      28060.60c   7.66960E-05
      28061.60c   3.33423E-06
      28062.60c   1.06286E-05
      28064.60c   2.70833E-06
      24050.60c   3.06460E-04
      24052.60c   5.90978E-03
      24053.60c   6.70122E-04
      24054.60c   1.66807E-04
      25055.60c   3.12468E-04
      42000.60c   3.33457E-04
c
c    material 8 : SS-316 - 7.64342E-02
c
m8    26054.60c   3.04219E-03
      26056.60c   4.77559E-02
      26057.60c   1.10289E-03
      26058.60c   1.46775E-04
      28058.60c   7.27553E-03
      28060.60c   2.80250E-03
      28061.60c   1.21834E-04
      28062.60c   3.88373E-04
      28064.60c   9.89635E-05
      24050.60c   4.60822E-04
      24052.60c   8.88649E-03
      24053.60c   1.00766E-03
      24054.60c   2.50827E-04
      25055.60c   1.66670E-03
      42000.60c   1.42668E-03
c
```

```
c    material 9 : CR absorber - 8.65633E-02
c
m9     6000.60c 3.9009E-03
       5010.60c 1.6450E-02
       5011.60c 6.6213E-02
c
c    material 10 : Shield absorber - 8.24897E-02
c
m10    6000.60c 3.7173E-03
       5010.60c 1.5676E-02
       5011.60c 6.3097E-02
c
c   material 11 : Reflector - 7.247268E-02
c
m11        11023.60c  3.4976E-3
          26000.50c  5.8380E-2
          28000.50c  3.4248E-4
          24000.50c  9.3228E-3
          25055.60c  3.9090E-4
          42000.60c  2.3890E-4
c
c    material 24 : mixture of lower reflelctor - 6.25734E-02
c
m12    11023.60c   7.14545E-03
      26054.60c   2.77266E-03
      26056.60c   4.35248E-02
      26057.60c   1.00518E-03
      26058.60c   1.33771E-04
      28058.60c   1.99109E-04
      28060.60c   7.66960E-05
      28061.60c   3.33423E-06
      28062.60c   1.06286E-05
      28064.60c   2.70833E-06
      24050.60c   3.06460E-04
      24052.60c   5.90978E-03
      24053.60c   6.70122E-04
```

```
     24054.60c   1.66807E-04
     25055.60c   3.12468E-04
     42000.60c   3.33457E-04
c
c    material 25 : SS-316 - 7.64342E-02
c
m13    26054.60c   3.04219E-03
     26056.60c   4.77559E-02
     26057.60c   1.10289E-03
     26058.60c   1.46775E-04
     28058.60c   7.27553E-03
     28060.60c   2.80250E-03
     28061.60c   1.21834E-04
     28062.60c   3.88373E-04
     28064.60c   9.89635E-05
     24050.60c   4.60822E-04
     24052.60c   8.88649E-03
     24053.60c   1.00766E-03
     24054.60c   2.50827E-04
     25055.60c   1.66670E-03
     42000.60c   1.42668E-03
c
c    material 26 : CR absorber - 8.65633E-02
c
m14    6000.60c 3.9009E-03
      5010.60c 1.6450E-02
      5011.60c 6.6213E-02
c
c    material 27 : Shield absorber - 8.24897E-02
c
m15    6000.60c 3.7173E-03
      5010.60c 1.5676E-02
      5011.60c 6.3097E-02
c
c    material 28 : Reflector 7.247268E-02
c
```

```
m16      11023.60c  3.4976E-3
         26000.50c  5.8380E-2
         28000.50c  3.4248E-4
         24000.50c  9.3228E-3
         25055.60c  3.9090E-4
         42000.60c  2.3890E-4
m17      11023.60c  1.7109E-2  $displaced bond(I)  .035996403
         26000.50c  1.6056E-2
         28000.50c  9.4190E-5
         24000.50c  2.5640E-3
         25055.60c  1.0751E-4
         42000.60c  6.5703E-5
m18      11023.60c  7.1453E-3  $Gas plenum(J)  .026032703
         26000.50c  1.6056E-2
         28000.50c  9.4190E-5
         24000.50c  2.5640E-3
         25055.60c  1.0751E-4
         42000.60c  6.5703E-5
m19      11023.60c  7.1453E-3  $upper structure(K)  .06247717
         26000.50c  4.7037E-2
         28000.50c  2.7594E-4
         24000.50c  7.5115E-3
         25055.60c  3.1495E-4
         42000.60c  1.9248E-4
m20      11023.60c  1.4317E-2  $follower(G)  .04341506
         26000.50c  2.4736E-2
         28000.50c  1.4511E-4
         24000.50c  3.9501E-3
         25055.60c  1.6563E-4
         42000.60c  1.0122E-4
kcode   20000 1.0 50 200
ksrc 13.25 23.5 0
```